


**Università degli Studi di Bari Aldo Moro**

DIPARTIMENTO DI FISICA "MICHELANGELO MERLIN"

Ph.D. degree in Physics (cycle XXXVIII)

Ph.D. thesis in Experimental Physics
Scientific Disciplinary Sector: FIS/01

# Design of a Ring Imaging Cherenkov detector for the next-generation heavy-ion experiment at the LHC

## Supervisors:

Prof. Domenico Di Bari

Prof. Giacomo Volpe

## Coordinator:

Prof. Vincenzo Spagnolo

## Presented by:

Nicola Nicassio

**FINAL EXAM 2026**

# Abstract

The ALICE Collaboration has proposed a new experiment, ALICE 3, to investigate the properties of the Quark-Gluon Plasma (QGP) beyond current limits in LHC Run 5. A key subsystem for charged-particle identification (PID) is a proximity-focusing Ring Imaging Cherenkov detector, composed of a central barrel (bRICH) and forward endcaps (fRICH). With its target PID performance, this detector will enable unique contributions to dielectron physics, to the heavy-flavour sector, and to precision studies of event-by-event fluctuations of conserved charges. The main goal of my PhD research was to design the bRICH system through dedicated feasibility and optimization studies, proposing an efficient and cost-effective solution, and demonstrating, via simulations and measurements, that it meets the ALICE 3 physics requirements in the most challenging environment of central (0-5%) Pb–Pb collisions. I proposed a modular, projective bRICH concept based on aerogel as Cherenkov radiator and SiPMs as photon sensors pointing to the interaction point to enhance the PID performance while minimising the total active area and costs. I further explored the use of an eco-friendly gas mixture in the bRICH proximity gap to enhance the electron identification capabilities. I also demonstrated the feasibility of Cherenkov-based charged-particle timing with the same SiPM modules, achieving time resolutions down to tens of picoseconds. The simulation activity included the development of fast machine-learning algorithms based on Boosted Decision Trees to learn Cherenkov ring topologies and to improve PID in the high-multiplicity Pb–Pb environment under realistic dark count rate (DCR) conditions. I complemented these studies by characterizing irradiated SiPMs and developing a realistic operation and ageing model that combines cooling below -40°C with annealing cycles above 70°C. To further mitigate the DCR, I investigated the use of smaller SiPMs with respect to the baseline $2 \times 2$ mm$^2$ size coupled to light concentrators. Characterization measurements of aerogel tiles revealed a refractive index gradient along their thickness, producing a natural focusing effect that improves the angular resolution in the proposed geometry. The detector concept was validated with multiple prototype beam tests at the CERN-PS T10 facility between 2022 and 2025, validating the detector parameters and confirming the expected angular resolution, photon yield, separation power, and the stability of the reconstruction at the DCR levels foreseen in ALICE 3. My work demonstrated the feasibility of the proposed projective proximity-focusing bRICH design and delivered a validated and cost-effective solution that, according to simulations and beam-test measurements, met the target ALICE 3 PID goals with unique contributions, in particular to dielectron physics. Thanks to the studies presented in this thesis, the proposed projective bRICH concept was adopted as the baseline layout in the ALICE 3 Scoping Document.

# Table of Contents

**Introduction** **1**

**1 The ALICE 3 experiment** **4**

1.1 An introduction to QGP . . . . . 5

1.1.1 Ultra-relativistic heavy-ion collisions . . . . . 6

1.1.2 Experimental signatures of QGP . . . . . 7

1.2 The Large Hadron Collider . . . . . 8

1.3 ALICE (Run 1 and 2) . . . . . 10

1.4 ALICE timeline . . . . . 11

1.5 Ion collisions at the LHC beyond Run 4 . . . . . 13

1.6 ALICE 3 physics motivations . . . . . 14

1.6.1 Understanding heavy-quark thermalisation in the QGP . . . . . 15

1.6.2 Accessing the QGP evolution with thermal radiation . . . . . 16

1.6.3 Characterising the cross-over to the QGP phase . . . . . 17

1.6.4 A new laboratory for hadronic and fundamental physics . . . . . 18

1.7 ALICE 3 detector requirements . . . . . 20

1.8 ALICE 3 detector concept . . . . . 22

1.8.1 Superconducting magnet . . . . . 24

1.8.2 Tracking detectors . . . . . 24

1.8.3 Time-of-Flight detector . . . . . 27
1.8.4 Ring Imaging Cherenkov detector . . . . . 27
1.8.5 Other subsystems . . . . . 29
1.8.6 ALICE 3 scoping options . . . . . 30
1.9 Expected ALICE 3 physics performance . . . . . 31
1.9.1 Dielectrons . . . . . 31
1.9.2 Multi-charm baryons . . . . . 33
1.9.3 Heavy-flavour correlations . . . . . 34

**2 ALICE 3 RICH technology options 36**

2.1 Charged particle identification . . . . . 36
2.2 Cherenkov radiation . . . . . 38
2.3 The RICH technique . . . . . 39
2.3.1 Separation power . . . . . 40
2.3.2 Single photon angular resolution . . . . . 40
2.3.3 Number of detected photons . . . . . 41
2.4 Aerogel radiators . . . . . 42
2.4.1 Aerogel refractive index . . . . . 43
2.4.2 Aerogel transparency . . . . . 43
2.5 Silicon Photomultipliers . . . . . 45
2.5.1 Photon detection efficiency . . . . . 47
2.5.2 Dark count rate and correlated background . . . . . 48
2.5.3 Single-photon time resolution (SPTR) . . . . . 49
2.5.4 Radiation damage in SiPMs . . . . . 50

**3 Design of the ALICE 3 bRICH 52**

3.1 ALICE 3 bRICH target PID coverage . . . . . 53

3.1.1 The choice of aerogel as Cherenkov radiator . . . . . 54
3.1.2 The choice of SiPMs as photon sensors . . . . . 55
3.1.3 Optimization of the aerogel thickness . . . . . 56
3.2 Evolution of the bRICH layout . . . . . 59
3.3 The original cylindrical bRICH layout . . . . . 59
3.3.1 Problems of the cylindrical geometry . . . . . 60
3.4 The projective proximity-focusing bRICH layout . . . . . 63
3.4.1 Projective bRICH geometry . . . . . 63
3.4.2 Radiator and photodetector . . . . . 65
3.4.3 The trapezoidal module concept . . . . . 66
3.4.4 The rectangular 17×18 $cm^2$ photodetector module . . . . . 67
3.4.5 Absorbing vs transparent walls between sectors . . . . . 69
3.4.6 Projective bRICH vs problems of the cylindrical layout . . . . . 70
3.5 Option: Gas-based $e^{\pm}$ ID enhancement . . . . . 72
3.5.1 Principle of operation . . . . . 73
3.5.2 Choice of the gas refractive index . . . . . 74
3.5.3 Eco-friendly gas mixtures . . . . . 75
3.5.4 Interfacing the gaseous radiator with aerogel . . . . . 76
3.5.5 Features of gas clusters in the bRICH geometry . . . . . 76
3.6 Option: charged-particle timing with bRICH . . . . . 80
3.6.1 Principle of operation . . . . . 80
3.6.2 Candidate window materials . . . . . 81
3.6.3 Pros and cons of combining oTOF and bRICH . . . . . 83
3.7 Option: 1×1 $mm^2$ SiPMs + light concentrators . . . . . 85
3.7.1 Light concentrators: Principle of operation . . . . . 86
3.7.2 Photon incidence angles on SiPMs in central Pb-Pb . . . . . 88

3.7.3 Optimization of concentrator size . . . . . 90
3.7.4 Impact on the bRICH aerogel and gas photon yield . . . . . 92
3.7.5 Concentrators vs charged-particle timing . . . . . 94
3.7.6 Implications on the module concept . . . . . 95
3.7.7 Feasibility and challenges . . . . . 96

**4 bRICH performance simulation 97**

4.1 Full simulation framework . . . . . 98
4.1.1 Detector geometry . . . . . 99
4.1.2 Event generation . . . . . 101
4.1.3 Custom digitizer . . . . . 102
4.2 Energy spectrum of detected photons . . . . . 105
4.3 Cherenkov angle reconstruction chain . . . . . 106
4.3.1 Single hit Cherenkov angle . . . . . 107
4.3.2 Angle selection: Cherenkov angle physical limit . . . . . 109
4.3.3 Timing selection: hit-track time matching . . . . . 109
4.3.4 Ring Cherenkov angle: the Hough transform . . . . . 110
4.4 Performance in single particle events . . . . . 111
4.4.1 Tested bRICH configurations . . . . . 111
4.4.2 Cherenkov angle analysis: resolution and yield . . . . . 113
4.4.3 Trapezoidal modules: performance with $2 \times 2$ mm$^2$ SiPMs . . . 117
4.4.4 Trapezoidal modules: performance vs SiPM size . . . . . 119
4.4.5 Trapezoidal modules: absorbing vs transparent walls . . . . . 120
4.4.6 Trapezoidal modules vs rectangular $17 \times 18$ cm$^2$ modules . . . . 122
4.4.7 Performance vs azimuthal angle . . . . . 122
4.4.8 Performance vs particle velocity . . . . . 124

4.5 Features of simulated Pb-Pb events . . . 127
4.5.1 Charged-track multiplicity and kinematics at the bRICH . . . 127
4.5.2 Projective bRICH acceptance for charged tracks . . . 129
4.5.3 Time profile of Pb-Pb events . . . 134
4.5.4 Photodetector occupancy in central Pb-Pb events . . . 136
4.5.5 Hit-track time matching vs SPTR and DCR . . . 137
4.5.6 Hit-track distance vs SPTR and DCR . . . 139
4.6 Particle identification: a Bayesian approach . . . 141
4.6.1 PID efficiency and purity . . . 142
4.6.2 Performance in pp collisions . . . 143
4.6.3 Pattern recognition in central Pb-Pb . . . 145
4.6.4 PID performance in central Pb-Pb . . . 148
4.7 Machine learning techniques for bRICH PID . . . 162
4.7.1 Boosted Decision Tree . . . 162
4.7.2 Results in pp collisions . . . 166
4.7.3 Results in Pb-Pb collisions . . . 169
4.8 Gas-based e-ID option in central Pb-Pb . . . 182
4.8.1 Background to gas clusters . . . 182
4.8.2 Pre-filtering of aerogel background photons . . . 182
4.8.3 Machine learning based e-ID with gas . . . 183
4.8.4 Results in pp collisions . . . 185
4.8.5 Results in Pb-Pb collisions . . . 187
4.9 Dielectron efficiency vs $m_{\mathrm{ee}}$ and $p_{\mathrm{T,ee}}$ . . . 192
4.9.1 Simulation strategy . . . 193
4.9.2 Results . . . 194
4.10 $\mathrm{D}^0 \to \mathrm{K}^-\pi^+$ efficiency vs $p_{\mathrm{T}}$ and $\eta$ . . . 200

**5 SiPM ageing in ALICE 3** **202**

5.1 SiPM DCR measurements . . . . . 202

5.1.1 Tested SiPM arrays . . . . . 203

5.1.2 History of irradiated arrays . . . . . 203

5.1.3 Measurement method . . . . . 204

5.1.4 Results . . . . . 204

5.1.5 DCR scaling model with fluence . . . . . 213

5.2 bRICH SiPM ageing model in ALICE 3 . . . . . 213

**6 Performance validation in beam tests** **218**

6.1 CERN-PS T10 beam line . . . . . 219

6.2 The ALICE 3 RICH prototypes . . . . . 220

6.2.1 Tested aerogel tiles . . . . . 221

6.2.2 Transparency characterization measurements . . . . . 221

6.2.3 Refractive index characterization measurements . . . . . 222

6.2.4 Aerogel ring SiPM arrays . . . . . 224

6.2.5 Charged-particle timing SiPM arrays . . . . . 225

6.2.6 SiPM cooling . . . . . 226

6.2.7 Gas flushing and humidity control . . . . . 226

6.2.8 Tracking system . . . . . 227

6.2.9 Cabling of the SiPMs to the front-end . . . . . 227

6.2.10 SiPM readout electronics . . . . . 228

6.2.11 The Petiroc board . . . . . 228

6.2.12 The RadioPico board . . . . . 229

6.3 Cherenkov angle reconstruction strategy . . . . . 231

6.4 Beam test of the 2022-2023 prototype . . . . . 231

6.4.1 Trigger and DAQ system . . . 233
6.4.2 Collected data . . . 233
6.4.3 Event selection . . . 234
6.4.4 Hit-track time matching and background sources . . . 235
6.4.5 Background modelling . . . 238
6.4.6 Single-hit Cherenkov angle and radius . . . 238
6.4.7 Uncorrelated background suppression using timing . . . 239
6.4.8 Ring angular resolution studies . . . 240
6.4.9 Charged-particle timing: efficiency and time resolution . . . 241
6.5 Beam test of the 2024-2025 prototype . . . 243
6.5.1 Trigger and DAQ system . . . 244
6.5.2 Collected data . . . 246
6.5.3 Event selection . . . 247
6.5.4 Hit-track time matching . . . 247
6.5.5 Single photon angular resolution at saturation . . . 249
6.5.6 Efficiency and S/B ratio vs time matching window . . . 250
6.5.7 Signal and background yield vs time matching window . . . 251
6.5.8 Extrapolation to the full ring acceptance . . . 252
6.5.9 Pattern recognition performance . . . 254
6.5.10 Performance stability with increasing background . . . 257
6.5.11 Extrapolation to the bRICH DCR levels . . . 258
6.5.12 Performance validation with simulations . . . 261
6.5.13 Charged-particle timing with picoTDC . . . 262
6.5.14 Validation of e-ID option using high-$n$ gas . . . 263

**Conclusions** **266**

**A Contributions to the single photon angular resolution 268**

A.1 Cherenkov angle reconstruction . . . . . 268

A.2 Localization and track incidence uncertainties . . . . . 270

A.3 Geometric uncertainty . . . . . 271

A.4 Chromatic uncertainty . . . . . 271

A.5 Evaluation of the rms uncertainties . . . . . 271

A.6 Magnetic field and multiple scattering errors . . . . . 272

**B Generation of the projective geometry 273**

B.1 Input parameters . . . . . 274

B.2 Output geometry specifications . . . . . 275

B.3 Intermediate variables . . . . . 277

B.4 Fundamental equations . . . . . 278

B.5 Algorithm implementation . . . . . 282

B.6 The baseline bRICH geometry . . . . . 283

**C Alignment, tracking and angle reconstruction in beam tests 284**

C.1 Track clusters in central and tracker arrays . . . . . 284

C.2 Alignment of arrays and tracker modules . . . . . 285

C.3 Candidate Cherenkov photon hits . . . . . 286

C.4 Most probable emission depth in the aerogel tile . . . . . 286

C.5 Emission point and the track direction . . . . . 287

C.6 Cherenkov angle extrapolation . . . . . 289

**References 290**

**Acknowledgements 303**

# Introduction

The ALICE Collaboration has proposed a completely new apparatus, ALICE 3, for the LHC Run 5 and beyond. The experiment will be completely realized using cutting-edge silicon technologies to study heavy-ion collisions collecting significantly higher luminosities than the current detector, providing a much larger acceptance, and providing unprecedented pointing resolution, by placing the vertex detector on a retractable structure inside the beam pipe. ALICE 3 will, on the one hand, enable novel studies of the Quark Gluon Plasma (QGP) and, on the other hand, open up important physics opportunities in other areas of QCD and beyond. The main new studies in the QGP sector focus on low-$p_{\mathrm{T}}$ heavy-flavour production, as well as on precise multi-differential measurements of dielectron emission to probe the mechanism of chiral-symmetry restoration and the time-evolution of the QGP phase. Besides QGP studies, ALICE 3 can uniquely contribute to hadronic physics, with femtoscopic studies of the interaction potentials between charm mesons and searches for nuclei with charm.

In this context, a key subsystem for high–energy charged–particle identification (PID) will be a proximity–focusing Ring Imaging Cherenkov, covering eight units of pseudo-rapidity ($|\eta| < 4$) and segmented in a central (bRICH, $|\eta| < 2$) and forward endcaps (fRICH, $2 < |\eta| < 4$). The design target is a better than $3\sigma$ e/$\pi$, $\pi$/K and K/p separation up to 2, 10 and 16 GeV/$c$, respectively. With this target PID performance, such a detector will enable unique contributions to dielectron physics, to the heavy-flavour sector, and to precision studies of event-by-event fluctuations of conserved charges.

The goal of my PhD research was to design the bRICH system through dedicated feasibility and optimization studies, proposing an efficient and cost-effective solution and demonstrating, via simulations and measurements, that it meets the ALICE 3 physics requirements in the most challenging environment of central Pb-Pb collisions.

I proposed and investigated a modular projective proximity-focusing geometry with modules equipped with aerogel tiles as Cherenkov radiator and SiPM-based photodetector modules oriented toward the nominal collision vertex to enhance the PID performance while minimising the total active area and costs. I also investigated the

option of flushing the bRICH expansion gap with an eco-friendly heavy-gas mixture to enhance the separation of electrons from pions up to about 4 GeV/$c$ momentum, as required for systematic multi-differential dielectron studies planned for ALICE 3.

I also explored the implementation of high-efficiency Cherenkov–based time measurements for charged particles, achieving resolutions of a few tens of picoseconds, by using the bRICH SiPMs coupled to a thin transparent window. This solution would open the possibility of combining the ALICE 3 outer TOF layer and the bRICH into a single detector using the same sensor layer, with substantial technical and cost advantages.

The simulation activity included the development of efficient and fast machine learning algorithms based on the Boosted Decision Tree concept, trained to learn the topology of aerogel Cherenkov rings and the electron clusters for the heavy gas option in the proposed geometry. These algorithms were specifically designed to push PID performance in the high multiplicity environment of central (0-5%) Pb–Pb collisions under extreme dark count rate (DCR) conditions beyond the limits of classical algorithms.

A major challenge for the feasibility of the project is indeed the increasing DCR of the SiPMs during operation due to their poor radiation tolerance under the high radiation load expected in the ALICE 3 environment. Ensuring DCR levels smaller than 4 MHz per channel is crucial for the long-term operation of the detector. In this context, I complemented the simulation studies, aimed at quantifying the impact of high DCR on the performance, with characterization measurements of irradiated SiPMs from Hamamatsu. These measurements were used to define an operating strategy and an ageing model based on cooling to temperatures below -40°C, with annealing cycles above 70°C. I also investigated the possibility of using smaller SiPMs with light concentrators to reduce the DCR keeping the same effective area and number of channels.

From the characterization measurements of the optical properties of hydrophobic aerogel tiles from Aerogel Factory Co., Ltd., I observed a systematic, unforeseen spatial gradient of the refractive index along the tile thickness. This produces a natural focusing effect that improves the angular resolution in the proposed bRICH geometry. This result may have an impact on future RICH detectors adopting a similar layout.

The simulation studies and characterization measurements were complemented and supported by beam tests of small-scale prototypes at the CERN-PS T10 facility between 2022 and 2025. I actively contributed to the planning of all runs, the design and characterization of the prototypes, the data taking, and I performed the full data analysis and simulation. The analysis validated the bRICH geometry and the expected performance in terms of angular resolution, photon yield, and separation power. It also demonstrated the stability of the ring reconstruction performance with the DCR levels expected during the ALICE 3 operation.

In this thesis I present my contributions largely following the chronological development of the project, from design and performance validation studies to the subsequent radiator and photodetector characterization and the prototyping for beam tests. In particular, this thesis is organized as follows.

An outline of the ALICE 3 experiment, focusing on the physics goals, the detector requirements, the state-of-the-art detector concept, and projections on the expected physics performance is presented in Chapter 1.

The principle of operation of the RICH technique and the main properties of the building blocks of the bRICH, aerogel and SiPMs, are summarized in Chapter 2.

The evolution of the bRICH design, from the original cylindrical layout in the ALICE 3 Letter of Intent to my final proposal for the current baseline modular projective layout, is discussed in Chapter 3. I also discuss the options for gas–based electron–identification, Cherenkov–based charged–particle timing, and the use of smaller SiPMs with light concentrators, and their simulation–based proofs of concept.

The simulation of detector performance, from the figures of merit in single–particle events to the efficiency and purity for e, $\mu$, $\pi$, K, and p in the most challenging central 0–5% Pb–Pb environment, also accounting for the SiPM DCR, the impact of the single photon time resolution (SPTR) on background suppression, and the photodetector module layout, is presented in Chapter 4. This chapter also introduces the machine–learning algorithms I developed for both aerogel and gas signals, highlighting the improvements over a classical Hough–transform plus Bayesian PID approach.

The characterization of SiPM arrays irradiated with neutrons at JSI in Ljubljana, together with the proposal for a SiPM operating strategy and ageing models I developed to describe the DCR evolution over the ALICE 3 lifetime, is presented in Chapter 5.

The main results from characterization measurements of the optical properties of various aerogel tiles and from beam tests of the various prototypes at CERN-PS T10 facility, focusing on the validation of the performance in terms of angular resolution, background suppression with timing, photon yield, pattern recognition, separation power, and reconstruction stability under high DCR, are finally reported in Chapter 6.

# Chapter 1

# The ALICE 3 experiment

The main experimental goal of the ALICE Collaboration is to study the microscopic dynamics of strongly interacting matter at extreme energy densities created in ultra-relativistic heavy-ion collisions, where the Quark–Gluon Plasma (QGP), a state of matter in which quarks and gluons are no longer confined within hadrons, is formed.

Despite the remarkable progress achieved with the ALICE experiment during LHC Runs 1 and 2, and the substantial improvements of the upgraded ALICE 2 detector for Run 3, as well as the further developments expected from the ALICE 2.1 upgrade planned for Run 4, several fundamental questions will remain open at the end of Run 4. These include our understanding of the properties of QGP that drive its constituents toward equilibrium, the temperature dependence of the partonic equation of state, the underlying dynamics of chiral-symmetry restoration, and the hadronization mechanisms of the QGP. Addressing these open questions requires a significant improvement in detector performance in terms of vertexing, tracking, and particle identification, calling for the development of a next-generation heavy-ion experiment.

In this context, the ALICE Collaboration is proposing a new detector, ALICE 3, designed to replace the current ALICE apparatus for the heavy-ion program planned for LHC Run 5, starting in 2036. The ALICE 3 proposal was first outlined in the Letter of Intent (LoI) published in 2022 [1], and further refined in the Scoping Document (SD) released in 2025 [2]. ALICE 3 is conceived to provide unprecedented capabilities in tracking, vertexing, particle identification, and data-rate handling, enabling a substantial reduction of both instrumental and physics backgrounds. The detector is optimized to perform efficiently from the low-multiplicity environment of pp collisions to the extreme high-multiplicity environment of the most central Pb–Pb events.

In this chapter I provide an overview of the ALICE 3 experiment. Section 1.1 provides a brief introduction to the QGP, its formation in ultra-relativistic heavy-ion collisions, and the key experimental signatures used to study it. Section 1.2 briefly summarizes the main features of the Large Hadron Collider, followed by a description of the current ALICE apparatus in Section 1.3 and the upgrade timeline toward ALICE 3 in Section 1.4. The LHC heavy-ion programme beyond Run 4 is summarized in Section 1.5. The physics motivations for the new detector are presented in Section 1.6, while the implications for the detector requirements and the detector concept are discussed in Sections 1.7 and 1.8. Projections of the target detector performance on the expected physics performance are finally presented in Section 1.9.

## 1.1 An introduction to QGP

The strong interaction between quarks and gluons, the fundamental building blocks of hadronic matter, is described by Quantum Chromodynamics (QCD). Under extreme conditions of temperature and energy density, QCD predicts a phase transition from the confined hadronic phase to a color-deconfined state of quarks and gluons [3], the Quark-Gluon Plasma (QGP), exhibiting the properties of a perfect fluid [4].

This QCD phase transition can be studied in the laboratory via ultra-relativistic heavy-ion collisions, which recreate the temperature, pressure, and energy density conditions necessary for QGP formation. The product of these collisions is a fireball in local thermal equilibrium that rapidly expands and cools down. The space-time evolution of this fireball is believed to reproduce the early stages of the Universe, when the partonic deconfined matter turned into confined hadrons a few µs after the Big Bang.

The first heavy-ion experiments date back to the 1980s at the Alternating Gradient Synchrotron (AGS) at Brookhaven National Laboratory (BNL) [5] and at the Super Proton Synchrotron (SPS) [6] at CERN, where fixed target experiments studied collisions at a centre-of-mass energy per nucleon pair $\sqrt{s_{\mathrm{NN}}}$ in the region $5 - 20$ GeV. High-energy heavy-ion collisions were then studied in collider experiments at the Relativistic Heavy-Ion collider (RHIC) [7] since 2000, reaching $\sqrt{s_{\mathrm{NN}}}$ values of 200 GeV for Au-Au collisions, and more recently also at the Large Hadron Collider (LHC) [8] since 2009, reaching $\sqrt{s_{\mathrm{NN}}}$ values of 5.36 TeV for Pb-Pb collisions.

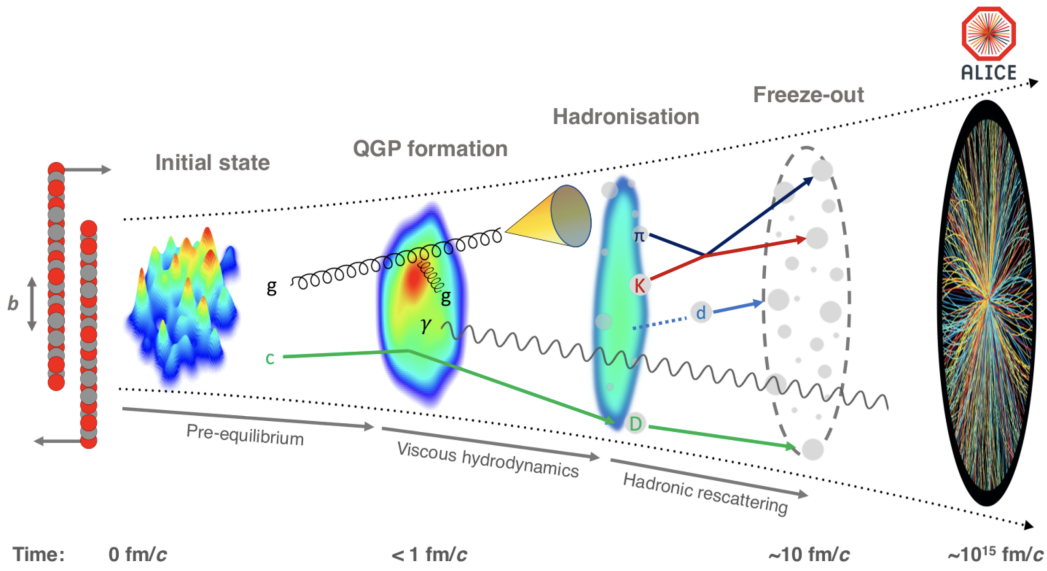


**Figure 1.1:** The evolution of a heavy-ion collision at LHC energies. Figure from [8].

### 1.1.1 Ultra-relativistic heavy-ion collisions

The evolution of an ultra-relativistic heavy-ion collision is usually described in terms of a series of stages, as schematically illustrated in Fig. 1.1.

- **Initial state.** Right before the collision, at $t < 0\,\mathrm{fm}/c$, two Lorentz-contracted nuclei with transverse diameter $2R$ and longitudinal thickness $2R/\gamma$ approach each other, where $\gamma$ is the Lorentz factor in the centre-of-mass reference frame. A large parton density is expected inside the nuclei. In this regime, the behaviour of nuclear matter is consistent with a state of Color Glass Condensate [9].

- **Pre-equilibrium.** The nuclei come close, initiating the interactions between their constituent partons. This stage is largely dominated by low-momenta gluons and evolves towards softer quarks and anti-quarks dynamically created through gluon fusion [10]. The system is highly anisotropic, and its shape resembles the overlap region between the two nuclei. Processes involving low momentum transfer determine the overall energy density and entropy deposition in the initial state [11]. Processes involving large momentum transfer ($Q^2 \gg 1$ GeV$^2$) allow for the creation of high-momenta gluons or heavy quarks, charm and beauty, interacting with the other constituents of the environment.

- **Thermalisation.** The partons produced in the primary interactions rescatter each other giving rise to a region of high energy density at thermal equilibrium leading to the formation of a strongly coupled QGP phase in $\approx 1$ fm/$c$.

- **Expansion.** Due to the internal pressure, the thermalised system undergoes a collective expansion and cools down as the energy density decreases. In this phase, the relative abundances of both gluons and up, down and strange quarks change due to multiple interactions as their mean free path is smaller than the size of the medium. During the expansion, the system behaves as a perfect liquid and can be described in the context of relativistic hydrodynamics [4].

- **Hadronisation.** When the critical energy density $\varepsilon_c \approx 1$ GeV/fm$^3$ is reached, the hadronisation process begins and the system evolves into an interacting hadron resonance gas. In this phase, the expansion and cooling of the system continue, as well as inelastic and elastic interactions among the hadrons within the system.

- **Decoupling.** The relative abundances of the different hadron species continue to change as long as the hadron gas undergoes inelastic interactions. Once the energy of these interactions becomes too low inelastic interactions cease and the so-called chemical freeze-out is reached. At this stage the abundances are fixed while elastic interactions are still present and keep modifying the kinetic properties of the hadrons. When the distances between hadrons exceed the range of the interaction, elastic collisions also cease and the so-called kinetic freeze-out is reached. At this stage the kinematical distributions of the hadrons are also fixed. Stable particles free-stream to the detectors, where they can be detected.

### 1.1.2 Experimental signatures of QGP

Due to the short lifetime of the QGP phase ($\approx$ 10 fm/$c$ $\approx 10^{-23}$ s), it cannot be studied directly and we can only access the final state of the collision, with final particles typically measured approximately $10^{15}$ fm/$c$ after the collision. However, theoretical models suggest certain observables as signatures of QGP production. These signatures, categorized based on their properties and the collision phase in which they are generated, are commonly classified as electromagnetic, hard, and soft probes.

- **Electromagnetic probes.** Real and virtual photons are produced in all the stages of a heavy-ion collision. They can be identified by measuring final state photons and lepton pairs. Since they are not interacting via the strong force, they leave the collision unscattered, making them ideal messengers to study the whole evolution of the collision [12]. They serve as a powerful probe for exploring the QGP temperature evolution and chiral-symmetry restoration mechanisms.

- **Hard probes.** Interactions with high-momentum transfer at the early stages of the collision result in the production of jets and particles containing heavy-

flavour quarks (c, b) in open charm/beauty and quarkonia. The study of such observables provides direct insight into QGP effects on the propagation of the parent quarks and gluons through the medium.

- **Soft probes.** Interactions with high-momentum transfer in the last stages of the fireball evolution dominate particle production processes and provide access to the phase transition and the medium bulk properties. These observables are mainly measured from low-momentum hadrons with light quarks (u, d, s).

A comprehensive overview of corresponding up-to-date results can be found in [8].

## 1.2 The Large Hadron Collider

The Large Hadron Collider (LHC) [13] operating at the European Organization for Nuclear Research (CERN) is the largest and most powerful hadron collider in the world. The LHC is a two-ring superconducting circular collider having a circumference of 26.7 km and is located underground at a depth between 50 m and 175 m. Inside the rings, two beams of protons or heavy ions circulate in opposite directions. The accelerator is designed to accelerate and collide protons with maximum achievable centre-of-mass energy $\sqrt{s} = 14$ TeV and Pb nuclei at $\sqrt{s_{\mathrm{NN}}} = 5.52$ TeV. The acceleration is caused by 16 superconducting radio-frequency (RF) cavities, 8 per ring. To avoid colliding with gas molecules inside the accelerator, the beams of particles travel in an ultra-high vacuum, at a pressure as low as $10^{-11}$ mbar. The system includes 1232 main dipole magnets operated at 1.9 K providing a magnetic field of about 8.3 T for bending the beam particles inside the rings, and 392 main quadrupole magnets for beam focusing. The LHC is the last step of the CERN accelerator complex, shown in Fig. 1.2, a series of machines which accelerate particles to increasingly high energies before injecting them into the next accelerator of the sequence.

To create a proton beam, a hydrogen bottle is used as primary source. Negative hydrogen ions ($H^-$) are obtained from hydrogen gas by applying an electric field. These ions are injected into a linear accelerator (LINAC 4) [15], where they are accelerated up to 160 MeV. The hydrogen ions are then stripped of their two electrons, leaving only protons, during injection from LINAC 4 into the Proton Synchrotron Booster (PSB) [16], where the proton energy is increased up to 2 GeV. Afterwards, the protons pass to the Proton Synchrotron (PS) [17] for further acceleration up to 26 GeV. They are then injected into the Super Proton Synchrotron (SPS) [18], which accelerates the particles in the beam up to 450 GeV, before the final injection into the LHC.

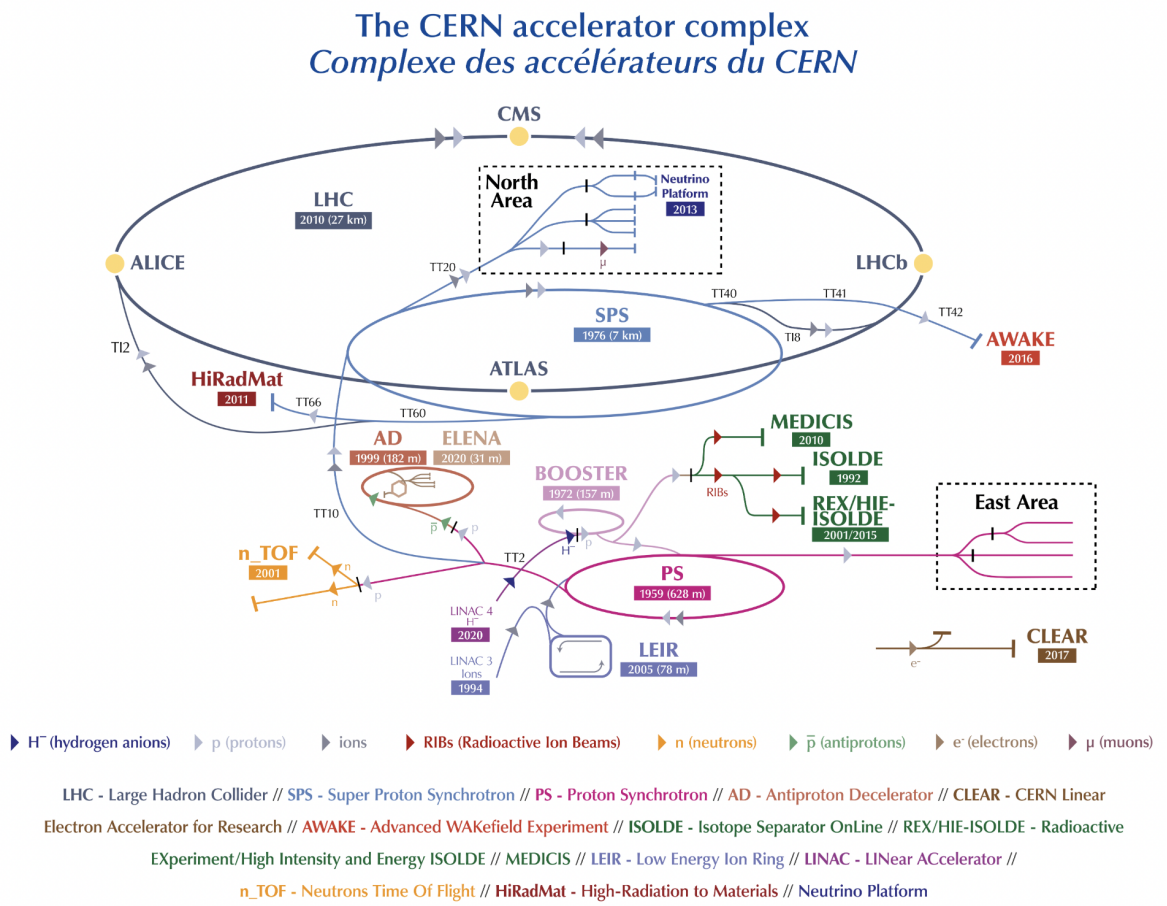


**Figure 1.2:** The CERN accelerator complex. Figure from [14].

Creating a heavy-ion beam involves a more complex process due to the heavier mass and multiple charges of the ions. To initiate a Pb-ion beam, vaporised lead is used as the primary source. An Electron Cyclotron Resonance (ECR) [19] source is required for the production of ions in highly charged states. The positive ions are then injected into a different linear accelerator (LINAC 3) [20], where they gain an energy boost up to 4.2 MeV per nucleon, and subsequently injected into the Low-Energy Ion Ring (LEIR) [21], where the ions are accelerated up to 72 MeV per nucleon, before being transferred to the PS. These ions pass through stripping foils to remove electrons.

Each interaction point along the LHC ring is covered by a large detector system. CMS (Compact Muon Solenoid) [22] and ATLAS (A Toroidal LHC ApparatuS) [23] were designed to study the properties of the Higgs boson and to explore BSM physics. The main purpose of the LHCb (Large Hadron Collider beauty) [24] experiment is to study the CP violation in the heavy-quark sector. Finally, ALICE (A Large Ion Collider Experiment) was built to study the QGP properties in heavy-ion collisions.

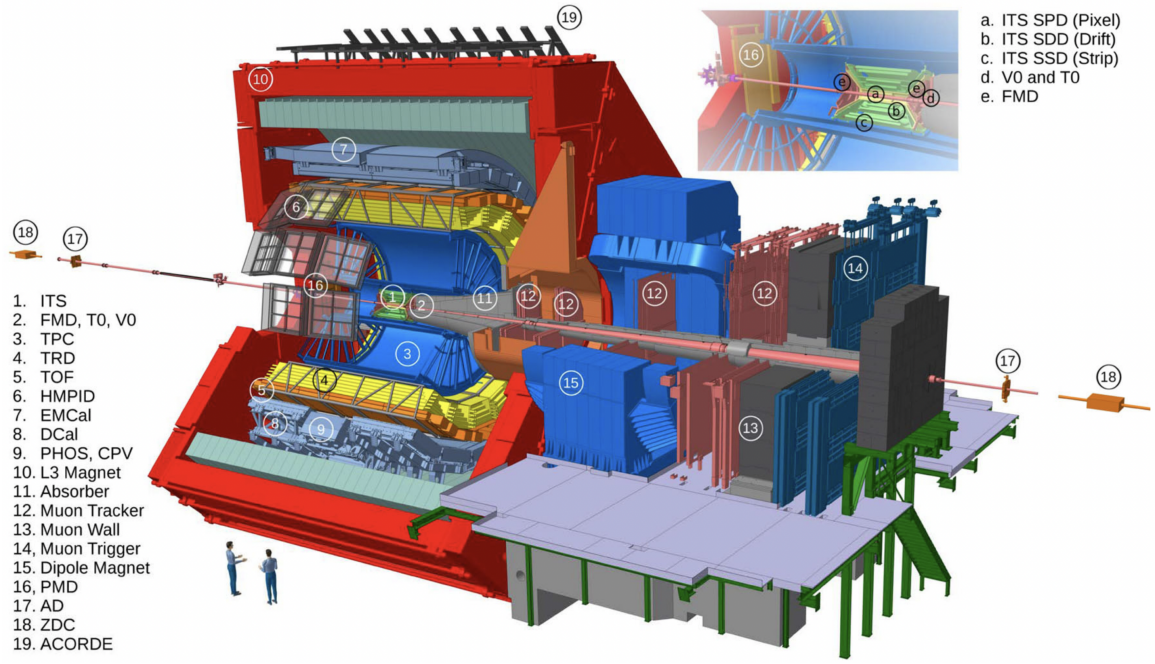


**Figure 1.3:** Schematic view of the ALICE detector.

## 1.3 ALICE (Run 1 and 2)

The ALICE detector is located at the interaction point IP2 of the LHC. The apparatus that was in operation in the LHC Runs 1 and 2, referred to as ALICE 1, is described in detail in Ref. [25]. Its performance is discussed in detail in Ref. [26]. The detector was designed to cope with the high particle multiplicity expected in the most central heavy-ion collisions and to provide robust PID down to $p_{\mathrm{T}} \sim 0.15$ GeV/$c$.

The ALICE detector is shown in Fig. 1.3. Its sub-detectors can be classified into three main groups: the central barrel detectors, covering central pseudorapidities, the forward detectors, placed at forward rapidity and the muon arm for muon identification.

The central barrel detectors are enclosed in the L3 solenoid magnet, which delivers a 0.5 T nominal magnetic field, and are mostly dedicated to vertex reconstruction, tracking and PID. Moving from the interaction point outward, they include:

- Inner Tracking System (ITS)
- Time Projection Chamber (TPC)
- Transition Radiation Detector (TRD)
- Time Of Flight (TOF)

These subsystems provide full azimuthal coverage ($0 \leq \phi \leq 2\pi$) with pseudorapidity acceptance $|\eta| < 0.9$. In the mid-rapidity region, there are additional detectors with limited acceptance:

- High-Momentum Particle IDentification (HMPID)
- PHOton Spectrometer (PHOS)
- ElectroMagnetic CALorimeter (EMCAL)
- Di-jet Calorimeter (DCal)

The forward detectors are placed in the high pseudorapidity region and are specialised systems for event triggering and measuring global event features. They include:

- Forward Multiplicity Detector (FMD) ($-3.4 < \eta < 5.1$)
- Photon Multiplicity Detector (PMD) ($-2.3 < \eta < 3.7$)
- Zero Degree Calorimeters (ZDC) ($|\eta| > 8.8$ for ZN, $6.6 < |\eta| < 7.4$ for ZP, $4.8 < |\eta| < 5.7$ for ZEM)
- V0 Detectors ($2.8 < \eta < 5.1$ for V0A and $-3.7 < \eta < -1.7$ for V0C)
- T0 Detectors ($4.6 < \eta < 4.9$ for T0A and $-3.3 < \eta < -2.9$ for T0C)

The muon spectrometer covers the forward pseudorapidity region $-4.0 \leq \eta \leq -2.5$. It consists of a dipole magnet, tracking and trigger chambers and is optimised to reconstruct heavy flavoured hadrons through their decays to $\mu^+\mu^-$ and single muons.

## 1.4 ALICE timeline

During LHC Run 1 (2009–2013) and Run 2 (2015–2018), ALICE conducted a comprehensive QCD programme, delivering key measurements that significantly advanced the characterization of QGP properties, as detailed in [8].

To fully exploit the LHC potential, ALICE underwent major detector upgrades during Long Shutdown 2 (2019–2021), including a new Inner Tracking System (ITS2), a substantial upgrade of the TPC and forward trigger detectors, and readout-electronics upgrades for the TRD, TOF, PHOS, and Muon Spectrometer. The upgraded system

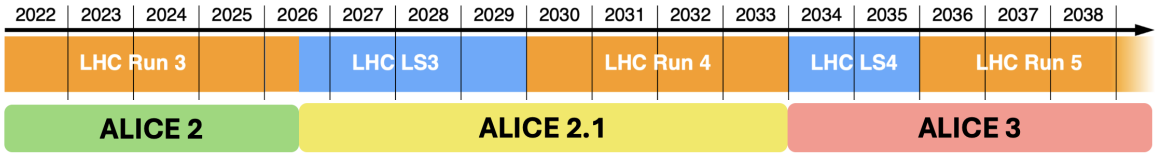


**Figure 1.4:** LHC schedule toward the ALICE 3 installation during LS4 and operation from Run 5.

is referred to as ALICE 2. Together with a new continuous-readout scheme, these improvements enable operation at the current interaction rates of Runs 3 [27].

Preparations are underway for a further upgrade, ALICE 2.1, during Long Shutdown 3 (2026–2029). Research and development for future subsystems has been substantially completed, and construction has begun on two new detectors: ITS3 [28], a bent, wafer-scale monolithic pixel system designed to replace the three innermost ITS2 layers, and FoCal [29], a forward electromagnetic and hadronic calorimeter. These upgrades will enable key heavy-ion measurements, including multi-charmed baryon production, the elliptic flow of dielectrons, and low-$p_{\mathrm{T}}$ photon production.

However, despite the wide-ranging capabilities of the upgraded apparatus, several open physics questions will remain to be addressed at the end of LHC Run 4.

Promising opportunities to extend the heavy-ion programme include the substantial increase in nucleon–nucleon luminosity at the LHC in Run 5 after LS4 and the use of intermediate-mass nuclei, such as Ar–Ar, Kr–Kr or Xe-Xe, which would provide novel QGP probes and enable a new era of precision measurements for rare observables in the Pb–Pb system. However, since the current ALICE tracking relies on the large TPC, such luminosities would saturate the maximum interaction rate the current experiment can sustain. A faster tracking technology is therefore required to replace the TPC.

To handle the increased interaction rates, a next-generation heavy-ion experiment, ALICE 3 [1, 2], has been proposed for installation at the LHC Interaction Point 2 during Long Shutdown 4 (2033-2034). ALICE 3 will be an all-silicon detector, exploiting technological advances in novel silicon technologies with unprecedented low mass. This design will allow exploration of an ultra-soft region of phase space, enabling the measurement of very low-$p_{\mathrm{T}}$ lepton pairs, photons, and hadrons at the LHC.

Fig. 1.4 shows the LHC schedule toward the ALICE 3 installation and operation. The start of data-taking with ALICE 3 is planned for LHC Run 5, currently scheduled to begin in 2036. Detector construction and pre-commissioning are planned for 2028–2031, allowing one year of contingency before the installation. The dismantling of the current ALICE detector, followed by the installation of ALICE 3, is expected to require a shutdown of two years, consistent with the current LHC schedule.

In the following sections of this chapter, the physics motivations of the ALICE 3 experiment will be outlined, followed by an overview of the system apparatus, and parametric projections on the expected physics performance.

## 1.5 Ion collisions at the LHC beyond Run 4

To address fundamental open questions in heavy-ion physics, it is crucial to fully exploit the LHC potential as a heavy-ion collider. While Pb ions provide the largest collision system and the strongest QGP effects, the luminosity is limited. Nevertheless, based on current projections, Run 5 will enable studies with more than five times the nucleon-nucleon luminosity achieved with Pb–Pb collisions in Runs 3 and 4. Several measurements will benefit from or only become possible with this increase in luminosity combined with vastly improved detector capabilities. Lighter ions, such as Ar, Kr and Xe, are also planned to be used in LHC Run 5. Due to their lower charge, they can be injected into the LHC with higher bunch intensities, resulting in higher nucleon-nucleon luminosity, thus enhancing the rate of hard processes. Table 1.1 shows the expected integrated luminosity and interaction rates for various collision systems under consideration. ALICE 3 is specifically optimised to fully exploit these luminosities.

| **Quantity** | **pp** | **O–O** | **Ar–Ar** | **Kr–Kr** | **Xe–Xe** | **Pb–Pb** |
|---|---|---|---|---|---|---|
| $\sqrt{s_{\mathrm{NN}}}$ (TeV) | 14.00 | 7.00 | 6.30 | 6.46 | 5.86 | 5.52 |
| $\langle L_{\mathrm{AA}} \rangle$ ($\mathrm{cm}^{-2}\mathrm{s}^{-1}$) | $3.0 \times 10^{32}$ | $9.5 \times 10^{29}$ | $2.0 \times 10^{29}$ | $5.0 \times 10^{28}$ | $1.6 \times 10^{28}$ | $3.3 \times 10^{27}$ |
| $\mathcal{L}_{\mathrm{AA}}^{\mathrm{month}}$ ($\mathrm{nb}^{-1}$) | $5.1 \times 10^{5}$ | $1.6 \times 10^{3}$ | $3.4 \times 10^{2}$ | $8.4 \times 10^{1}$ | $2.6 \times 10^{1}$ | 5.6 |
| $R_{\mathrm{max}}$ (kHz) | 24000 | 2169 | 821 | 344 | 187 | 93 |
| $\mathrm{d}N_{\mathrm{ch}}/\mathrm{d}\eta$ (MB) | 7 | 70 | 151 | 275 | 434 | 682 |

**Table 1.1:** Projected LHC performance for LHC Run 5. For various collision systems, the average luminosity $\langle L_{\mathrm{AA}} \rangle$, the luminosity integrated per month of operation $\mathcal{L}_{\mathrm{AA}}^{\mathrm{month}}$, the maximum interaction rate $R_{\mathrm{max}}$, the minimum-bias (MB) charged-particle pseudorapidity density $\mathrm{d}N_{\mathrm{ch}}/\mathrm{d}\eta$ are reported.

## 1.6 ALICE 3 physics motivations

The ALICE 3 detector concept is unique at the LHC in terms of pointing resolution of a few microns down to low transverse momentum over a large acceptance of eight pseudorapidity units, low material budget in the first tracking layers, and the identification of hadrons, electrons, and muons over a large transverse momentum range.

The ALICE 3 detector is designed to enable a broad physics program and provides unique opportunities to address open questions in the following areas of QCD.

- **Understanding the thermalisation of heavy quarks in the QGP**. Measurements of D–$\overline{\text{D}}$ azimuthal correlations and high-precision measurements of azimuthal asymmetries of beauty hadrons provide a direct measure of the degree of kinetic thermalisation and of the associated diffusion coefficients, to test first-principle calculations of quark diffusion in lattice QCD. The equilibration of charm quarks in the deconfined plasma produced in heavy-ion collisions can be studied with high sensitivity using the ratio of multi-charm to single-charm baryon yields, which is predicted to be hundred-times larger than in pp collisions.

- **Accessing the QGP evolution with thermal radiation**. High-precision measurements of dielectron (virtual photon) invariant-mass spectra, their transverse momentum dependence, and azimuthal anisotropy, provide a unique measure of the temperature of the QGP and its time evolution in the early stages of the collision, which is fundamental to the characterisation of the plasma.

- **Characterising the cross-over to the QGP phase**. Net-baryon (baryon minus antibaryon) and net-charm (charm minus anticharm) fluctuations measured over a large rapidity range characterise the critical behaviour near the cross-over transition between hadronic matter and the QGP, and are directly related to quantities calculable in lattice QCD. The dielectron spectral function in the $\rho^0$-meson mass region is directly sensitive to the manifestation of chiral symmetry restoration via mixing of vector and axial vector mesons.

- **Exploiting a new laboratory for hadronic physics**. Measurements of momentum correlations of charm hadrons provide unique experimental access to the hadron–hadron interaction potentials for heavy-flavour hadrons, to test lattice QCD calculations and to provide new insights in the nature of exotic hadrons (tetraquarks) with double-charm content. Searches for charm-nuclei such as the c-deuteron may lead to first observations of these novel states.

### 1.6.1 Understanding heavy-quark thermalisation in the QGP

#### High-precision beauty measurements

In order to establish a rigorous connection between parton transport, collective flow and hadronisation of the QGP, the study of parton energy loss needs to be extended down to the momenta typical of diffusion phenomena. To this end, measurements of the spectra and flow coefficients of beauty hadrons down to $\sim$1 GeV/$c$ are required. These measurements must include beauty hadrons ranging from the most abundant $\mathrm{B}^0$ or $\mathrm{B}^{\pm}$ mesons to $\mathrm{B}_s$ mesons and $\Lambda_b$ baryons, which are crucial to understand and constrain hadronisation models of b quarks in the presence of high-density QCD matter. The relaxation time of beauty quarks is expected to be about three times larger than for charm quarks (due to the ratio of masses). This aspect will provide unprecedented insight into the temperature dependence of heavy-quark diffusion in the QGP. This goal calls for a secondary vertexing performance far exceeding that of the present inner tracker of ALICE. In this context, ALICE 3 targets low-$p_{\mathrm{T}}$ beauty-hadron elliptic flow measurements in nucleus–nucleus collisions with $\approx 0.01$ precision.

#### D-$\overline{\mathrm{D}}$ azimuthal correlations

In order to discriminate between the different regimes of energy loss in the QGP and reveal the possible charm isotropisation by diffusion, novel and differential measurements, such as that of azimuthal angular correlations between fully-reconstructed charm hadron pairs over a wide rapidity range, are needed. The largest sensitivity to the energy loss mechanisms is expected for D mesons with transverse momenta below a few GeV/$c$, where radiative energy loss processes (gluon emission) lead to small angular deflections, while collisional processes (scattering on medium constituents) lead to large angular deflections and, potentially, to full isotropisation if the number of scatterings (i.e. coupling with the medium) is sufficiently large (diffusion regime). A first measurement of low-$p_{\mathrm{T}}$ angular D–$\overline{\mathrm{D}}$ correlations calls for high selection efficiency down to low transverse momentum of about 1 GeV/$c$, which requires an impact parameter resolution that exceeds the present technological limit, and for the ability to operate at rates that significantly exceed the capabilities of the present ALICE detector. In this context, the goal of ALICE 3 is to provide first measurements of the angular decorrelation of low-$p_{\mathrm{T}}$ charm mesons in nucleus-nucleus collisions.

#### Multi-charm baryons, p-wave quarkonia and exotic hadrons

A key goal of the next-generation high-energy heavy-ion programme is establishing the connection between the thermalisation of the QGP, including the initially-out-of-equilibrium charm quarks, and the formation of hadrons from deconfined quarks. Measuring, for the first time, the production of multi-heavy-flavour hadrons (like $\Xi_{cc}$, $\Omega_{cc}$, and ideally $\Omega_{ccc}$) and p-wave quarkonia ($\chi_{c1,2}$) will offer unprecedented sensitivity towards this goal. To achieve sufficient statistical significance for multi-heavy-flavour particles, a novel experimental approach, strangeness tracking [1], is needed to track all their decay products, such as $\Xi^{\pm}$ and $\Omega^{\pm}$ hyperons, before they decay further. This calls for tracking layers at distances as close as possible to the interaction point, hadron identification capabilities over a wide transverse momentum range from a few hundred MeV/$c$ to a few GeV/$c$, and high readout rates. Moreover, large pseudorapidity acceptance is required, not only to maximise the reconstructed signal yield, but also in order to investigate the dependence of the production of multi-heavy-flavour hadrons on the heavy-quark density that varies with rapidity. Access to p-wave quarkonia and exotic states requires quarkonium reconstruction capabilities down to zero $p_{\mathrm{T}}$, combined with high data-acquisition rates, and excellent soft–photon reconstruction capabilities for electromagnetic decays. These objects are still out of reach in nucleus–nucleus collisions with the present technology. The goal of ALICE 3 is to provide first measurements of multicharm baryons and p-wave charmonia in nucleus–nucleus collisions.

### 1.6.2 Accessing the QGP evolution with thermal radiation

#### Azimuthal asymmetry of electromagnetic radiation

Measurements of the non-uniform azimuthal angle distribution of particle production are a powerful tool to study fundamental properties of the QGP, such as its shear and bulk viscosities. Measurements planned for LHC Runs 3 and 4 will strongly constrain the initial conditions and geometry of the collision. This will allow us, for instance, to ascertain whether all hadron species truly emerge from a single, common flow field and to make precision measurements of the QGP viscosities. However, these insights will be limited to properties averaged over the system evolution. In order to gain access to the full time dependence of fundamental transport parameters (and hence to their temperature dependence), electromagnetic probes are required. This calls for a comprehensive study of the azimuthal asymmetry of the production of dileptons as a function of their transverse momentum and mass, which is directly connected to the emission time. Such a fully-differential measurement of the dilepton azimuthal asymmetries requires large data samples, excellent electron identification, and low

background, calling for a tracker with extremely low material budget to minimise photon conversions, and with high pointing resolution for the separation of electrons from the decays of heavy-flavour hadrons. These requirements make ALICE 3 design unique for thermal dilepton measurements differential in transverse momentum (time dependence of system temperature) and azimuthal angle relative to the reaction plane.

### 1.6.3 Characterising the cross-over to the QGP phase

#### Chiral symmetry restoration

The cross-over from confined to deconfined phase is accompanied by the restoration of chiral symmetry, leading to a modification of the dilepton spectrum in the light vector meson mass range, particularly in the region around the mass of the $a_1$ meson ($J^P = 1^+$), the chiral partner of the $\rho^0$ meson ($J^P = 1^+$). Since the $a_1$ is an axial vector meson, it does not couple to the dilepton channel in vacuum, but, as chiral symmetry is restored in the medium, it is expected to mix with the $\rho^0$, leading to a signature modification of the mass spectrum that would provide a first direct signal at the LHC conditions (baryochemical potential close to zero) of the admixture of the axial state, the so-called $\rho$-$a_1$ mixing [30]. The detection of this signal would elucidate the mechanisms of the chiral symmetry restoration in the QGP. The expected magnitude of this effect, a change of the dilepton yield of about 15% in the mass range close to the $\rho$ peak, is out of reach of the ALICE capabilities in Runs 3 and 4. The improvements offered by the ALICE 3 design, in particular the excellent electron identification, the small material budget and the high resolution vertexing capabilities down to low $p_{\mathrm{T}}$, will provide the precision required to observe the predicted effect at $3\sigma$ level [1]. Therefore, ALICE 3 will provide unique contributions to our understanding of chiral symmetry restoration mechanisms at vanishing baryochemical potential.

#### Fluctuations of conserved charges

Phase transitions in strongly-interacting matter can be addressed by investigating the response of the system to external perturbations via measurements of fluctuations of conserved charges. Such measurements provide information on critical behaviour near the phase boundary between QGP and hadronic matter. The fluctuations can be directly related to susceptibilities of conserved charges that can be computed in lattice QCD [31, 32]. The large coverage in pseudorapidity targeted by ALICE 3 ($|\eta| < 4$) is crucial to limit the fluctuations due to acceptance and to gain access to the intrinsic fluctuations and their $\Delta\eta$ dependence. Critical fluctuations in the vicinity of the cross-

over line to a second order phase transition are expected to strongly modify the sixth and higher-order cumulants of the net-baryon distribution. Therefore, extending the measurement for the first time to cumulants of order six and higher is one of the primary goals in ALICE 3. In addition, in ALICE 3, these studies can be extended to the strangeness and charm sector. Measurements of net-charm fluctuations require high reconstruction efficiency and high purity for open charm hadron reconstruction. Such studies are out of reach for the current generation of detectors.

### 1.6.4 A new laboratory for hadronic and fundamental physics

#### Nuclear bound states and hadronic interactions

The design of the ALICE 3 apparatus is ideal to address key topics at the interface of QGP, hadronic, and nuclear physics. High interaction-rate capabilities will grant for the first time access to rare phenomena, such as the production of nuclei, hypernuclei with mass number $A \geq 5$ and, combined with excellent heavy-flavour identification capabilities, possibly the as-yet undiscovered supernuclei (nuclei in which a proton is replaced by a charmed baryon $\Lambda_c$). Wide acceptance, again combined with outstanding heavy-flavour performance at low transverse momenta, will make it possible to extend for the first time the studies of hadron–hadron potentials via two-particle correlations to the charm–charm sector (for instance, using D$-$D and D$-$D$^*$ correlations), providing a new powerful tool to investigate the structure of the recently-discovered charmed exotic states, such as the $T_{cc}^+$ [33]. In ultra-peripheral collisions, the combination of wide acceptance and strong particle identification capabilities will also open up the possibility to explore more complex decays of photoproduced vector mesons than previously possible. In this context, ALICE 3 is designed to provide unique contributions to charm–charm hadronic interactions, the search for charmed nuclei, and the first measurement of (hyper)nuclei with $A = 5$ and $A = 6$ in hadronic collisions.

#### Ultra-soft photons and tests of quantum field theories

In high-energy hadronic collisions, bremsstrahlung photons are emitted in the production of prompt charged hadrons that are stable against strong decays. According to Low's theorem [34], for photon transverse momentum $k_T$ relative to the radiating hadron approaching zero (ultrasoft limit), the bremsstrahlung spectrum can be computed in a model- and process-independent way. This gives rise to the characteristic $1/k_T$ dependence of the photon spectrum and is a direct consequence of the conservation of electric charge. Low's theorem can be used to quantitatively test the infrared

limits of quantum field theories such as QED, QCD and quantum gravity. Low's theorem has not yet been conclusively verified in experiments, although its violation would constitute a crisis in theory. The large majority of tests of Low's theorem resulted in the observation of significant excesses of soft photons over what was predicted, typically by factors between four and eight. In ALICE 3, a dedicated forward tracker to reconstruct photon conversions at ultra-low transverse momenta of a few MeV/$c$ is planned to enable a new state-of-the-art measurement to test Low's theorem and thus the infrared limit of QED as a gauge theory.

### Collectivity in small systems

The discovery of collective effects in small collision systems [35, 36] has been one of the most remarkable LHC results so far. The investigation of the origin of these effects is one of the major goals of the Runs 3 and 4 campaign, with a dedicated high-multiplicity pp programme in ALICE, as well as runs with p–Pb and O–O collisions. However, high-multiplicity pp studies in Runs 3 and 4 will still be affected by the biases introduced by the limited pseudorapidity or low-momentum acceptance of the present LHC detectors, and any future measurement campaigns with lighter ions that may be warranted by the results of Runs 3 and 4 will require the capability of operating at data acquisition rates much larger than those of the current apparatus. Therefore, with its target rate capabilities, acceptance of eight pseudorapidity units and efficient reconstruction capabilities for $p_{\mathrm{T}}$ down to $\sim$50 MeV/$c$, ALICE 3 can provide unique contributions to our understanding of collective effects in small systems.

### Searches beyond the Standard Model

The search for physics beyond the Standard Model (BSM) is one of the main goals of the LHC. Heavy-ion collisions provide complementary and, at times, superior means as compared to pp collisions for searches of new phenomena not captured by the Standard Model. In particular, ultra-peripheral collisions (UPCs) of heavy ions offer the ideal conditions for the studies of photon-mediated processes, such as light-by-light scattering $\gamma\gamma \to \gamma\gamma$, axion-like particle searches and $\tau$ lepton anomalous magnetic moment measurements. ALICE 3 provides an opportunity to extend these studies to low-$p_{\mathrm{T}}$ photons for axion-like particle searches in $\gamma\gamma \to \gamma\gamma$, using photons reconstructed in an electromagnetic calorimeter and with conversions, and to low-$p_{\mathrm{T}}$ electrons or muons from $\tau$ decay. This will give access to kinematic regions that are inaccessible to other LHC experiments. The wide pseudorapidity coverage of the ALICE 3 detector provides an additional advantage for the selection of exclusive final states in

UPCs, making it suitable for the most sensitive axion-like particle search in the mass region down to 0.1 GeV/$c^2$.

## 1.7 ALICE 3 detector requirements

The measurements planned to address the physics goals outlined in the previous section rely on a series of observables defining the ALICE 3 subsystems and their design requirements in terms of vertexing, tracking, PID and rate capabilities. The target kinematic ranges for the ALICE 3 key physics objects are summarised in Table 1.2. The corresponding requirements for the ALICE 3 subsystems are reported in Table 1.3.

| **Observables** | **Kinematic Range** |
|---|---|
| Heavy-flavour hadrons | $p_{\mathrm{T}} \to 0$, $\lvert\eta\rvert < 4$ |
| Dielectrons | $p_{\mathrm{T,ee}} \approx 0.05$ to 3 GeV/$c$, $m_{\mathrm{ee}} \approx 0.05$ to 4 GeV/$c^2$ |
| Photons | $p_{\mathrm{T}} \approx 0.1$ to 50 GeV/$c$, $-2 < \eta < 4$ |
| Quarkonia and exotica | $p_{\mathrm{T}} \to 0$, $\lvert\eta\rvert < 2$ |
| Ultrasoft photons | $p_{\mathrm{T}} \approx 1$ to 50 MeV/$c$, $4 < \eta < 5$ |
| Nuclei | $p_{\mathrm{T}} \to 0$, $\lvert\eta\rvert < 4$ |

**Table 1.2:** Overview of the ALICE 3 key observables and the respective kinematic ranges of interest.

The key requirements are a retractable vertex detector featuring an unprecedented pointing resolution, a compact and light all-silicon tracker embedded in a superconducting solenoidal magnet, efficient identification of photons electrons, muons, pions, kaons and protons over a wide momentum range based on various subsystems, acceptance over eight units of pseudorapidity ($|\eta| < 4$) and forward subsystems for event characterisation, as well as continuous read-out combined with online data processing.

In particular, excellent pointing resolution, down to 10 µm, is required for tracks down to $p_{\mathrm{T}}$ of about 200 MeV/$c$. This is fundamental for the reconstruction of secondary vertices and decay chains, e.g. of heavy-flavoured hadrons. It is also a key ingredient for the rejection of heavy-flavour background for the dielectron measurements.

In addition, most of the observables of interest rely on charged-particle tracking. The detector is required to provide a relative $p_{\mathrm{T}}$ resolution $\Delta p_{\mathrm{T}}/p_{\mathrm{T}}$ down to 1-2% with excellent efficiency over the full target pseudorapidity range $\Delta\eta = 8$. The precision of the $p_{\mathrm{T}}$ measurement enters in the mass resolution, which is particularly important

| Physics goals | | Subsystems and specifications | | | | | | | |
|---|---|---|---|---|---|---|---|---|---|
| **Observable** | ***Uniqueness*** | **Magnet** | **IT** | **OT** | **TOF** | **RICH** | **ECAL** | **MID** | **FCT** |
| **Multi-charm baryons** | Observation of multi-charm baryons in AA collisions | **B = 1-2 T** | **$\sigma$ ~2.5 µm $R_{in}$= 5 mm $x/X_0$~0.1% $\lvert\eta\rvert$<4** | **$\sigma$ ~10 µm $R_{out}$> 65 cm $x/X_0$~1% $\lvert\eta\rvert$<4** | **Outer/Forward $\sigma$ ~ 20 ps** | Barrel **Forward** | | | |
| **D-Dbar correlations** | Angular de-correlation of soft charm | **B = 1-2 T** | " | " | **Outer/Forward $\sigma$ ~ 20 ps** | Barrel **Forward** | | | |
| **Beauty mesons and baryons** | Precision of 0.01 on elliptic flow | **B = 1-2 T** | " | " | **Outer $\sigma$ ~ 20 ps** | Barrel **Forward** | | $\lvert\eta\rvert$<1.3 | |
| **Quarkonia, $\chi_{c1}$(3872)** | Measurement at low $p_T$ and central rap. | **B = 1-2 T** | **$\lvert\eta\rvert$<1.3** | **$\lvert\eta\rvert$<1.3** | | | Pb/Scintillator | **$\lvert\eta\rvert$<1.3** | |
| **$\chi_{c1,2}$** | P-wave charmonia in AA collisions | **B = 1-2 T** | **$\lvert\eta\rvert$<1.3** | **$\lvert\eta\rvert$<1.3** | Outer $\sigma$ ~ 20 ps | Barrel | Crystals segment | **$\lvert\eta\rvert$<1.3** | |
| **Di-leptons (T, flow, $\chi$-symm)** | Time-evolution of thermal radiation; chiral symm. at $\mu_B$=0 | **B = 0.5-1 T** | **$\sigma$ ~2.5 µm $R_{in}$= 5 mm $x/X_0$~0.1% $\lvert\eta\rvert$<2** | **$\lvert\eta\rvert$<2** | **Inner/Outer $\sigma$ ~ 20 ps** | **Barrel** | | $\lvert\eta\rvert$<1.3 | |
| **Net-baryon fluctuations** | 6th order net-proton cumulants | **B = 1-2 T** | **$\lvert\eta\rvert$<4** | **$\lvert\eta\rvert$ < 4** | **Outer/Forward $\sigma$ ~ 20 ps** | **Forward** | | | |
| **Photon-jet, full jets** | High-precision low-$p_T$, large-R jet modification | | | | | | **Pb/Scintillator barrel/endcap** | | |
| **Hadronic physics (femtoscopy, nuclei)** | Charm-charm hadronic inter.; observation of charm-nuclei; (hyper)nuclei with A = 5 and 6 | **B = 1-2 T** | **$\sigma$ ~2.5 µm $R_{in}$= 5 mm $x/X_0$~0.1% $\lvert\eta\rvert$<4** | **$\sigma$ ~10 µm $R_{out}$> 65 cm $x/X_0$~1% $\lvert\eta\rvert$<4** | **Outer/Forward $\sigma$ ~ 20 ps** | Barrel **Forward** | | | |
| **Searches in $\gamma\gamma$ in UPCs** | ALPs m>0.1GeV and low coupling | **B = 1-2 T** | $\lvert\eta\rvert$<4 | $\lvert\eta\rvert$<4 | Inner/Outer/ Forward $\sigma$ ~ 20 ps | Barrel/Forward | **Pb/Scintillator barrel/endcap** | | |
| **Ultrasoft photons** | Validity and limits of Low theorem | **Small dipole B ~ 0.25 T** | | | | | | | **$4 < \eta < 5$ $x/X_0$~1%** |

**Table 1.3:** Subsystems and requirements to address the ALICE 3 physics programme [2].

for the extraction of signals for decays with a large background. Besides the gain in statistics, the large $\eta$ coverage is also crucial for the low $p_{\mathrm{T}}$ reach as well as studies of long-range correlations and for studies of the rapidity dependence of the yields.

The requirements for particle identification are also crucial in the ALICE 3 physics programme. Electrons must be identified in the $p_{\mathrm{T}}$ range from 50 MeV/$c$ up to about 2 GeV/$c$ and beyond. For muons, the challenge is to achieve an efficient identification from 1.5 GeV/$c$ upwards so that the combination of electrons and muons at low and high transverse momentum, respectively, ensures access to leptonic channels over a wide $p_{\mathrm{T}}$ range. In addition, the identification of light hadrons (pions, kaons and protons) must span the range from tens of MeV/$c$ up to a few tens GeV/$c$, in order to identify the products of heavy-flavour decays, while retaining high efficiency. For the detection of photons, the requirements are different for different measurements. While the measurement of photon-jet correlations calls for a large acceptance, the reconstruction of states such as the $\chi_c$ relies in addition on the measurement of photons at low energies. Finally, the detection of very low-$p_{\mathrm{T}}$ ($\geq$ 1 MeV/$c$) photons calls for a dedicated detector in the forward direction to exploit the longitudinal boost.

In addition, the apparatus must be optimized to fully exploit the expected integrated luminosities discussed in Section 1.5, ensuring stable operation at maximum interaction rates up to 24 MHz in pp collisions and 93 kHz in Pb–Pb collisions.

## 1.8 ALICE 3 detector concept

The combination of the above requirements led to the state-of-the-art reference detector concept sketched in Fig. 1.5 as outlined in the ALICE 3 Scoping Document [2].

The schematic longitudinal cross section of the reference detector is shown in Fig. 1.6. A silicon tracker (Inner Tracker and Outer Tracker) serves for vertexing and track reconstruction in the magnetic field provided by a superconducting magnet system. The three inner layers of the Inner Tracker are installed in secondary vacuum within the beam pipe. A compact layout covering eight units of pseudorapidity over the full azimuth is achieved by using a superconducting solenoid magnet with a 2 T field. For particle identification, Time-Of-Flight (TOF) layers, a Ring Imaging Cherenkov (RICH) detector system and an Electromagnetic Calorimeter (ECal), all housed in the superconducting magnet system, are employed. They are complemented, outside of the superconducting magnet, by a Muon Identifier (MID), including a hadron absorber and muon chambers, and a Forward Conversion tracker (FCT). The FCT is housed in a small dipole magnet. Forward Detectors (FD) are foreseen at either side of the

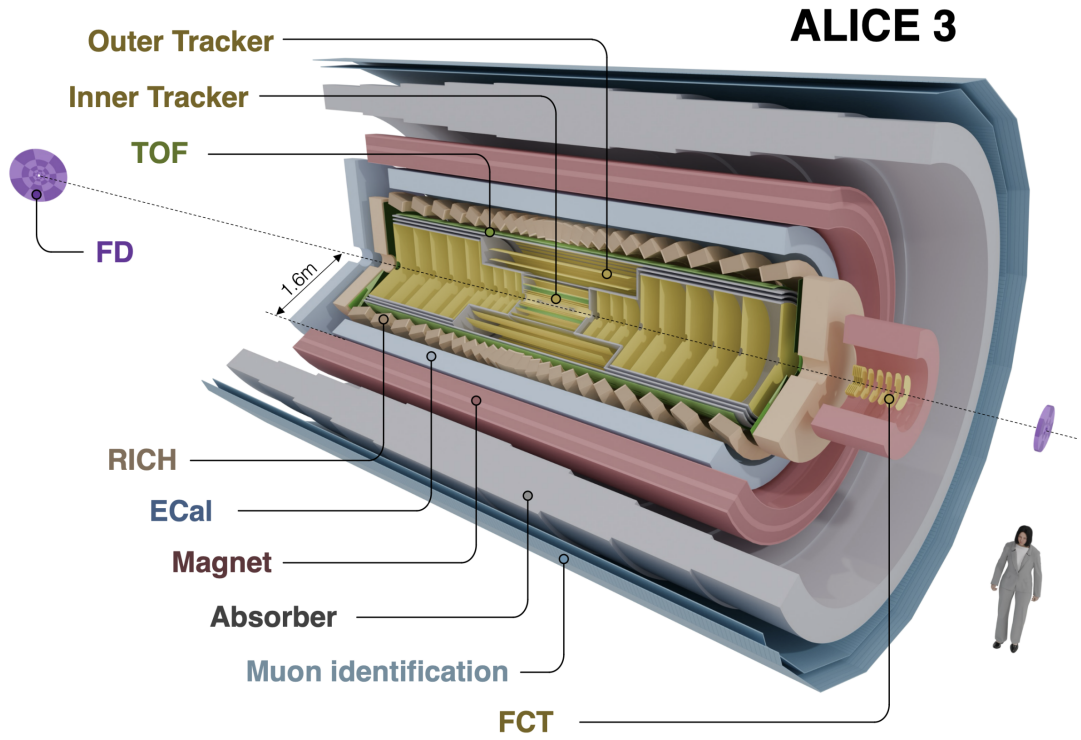


**Figure 1.5:** ALICE 3 state-of-the-art reference detector concept. A silicon tracker (Inner Tracker and Outer Tracker) serves for vertexing and track reconstruction in the magnetic field provided by a superconducting magnet. For PID a Time-Of-Flight detector (TOF), a Ring Imaging Cherenkov detector (RICH), an Electromagnetic Calorimeter (ECal), a Muon Identifier made of a hadron absorber followed by muon chambers (MID), and a Forward Conversion Tracker housed in a dipole magnet (FCT) are employed. Forward Detectors (FD) are installed at either side of the interaction point.

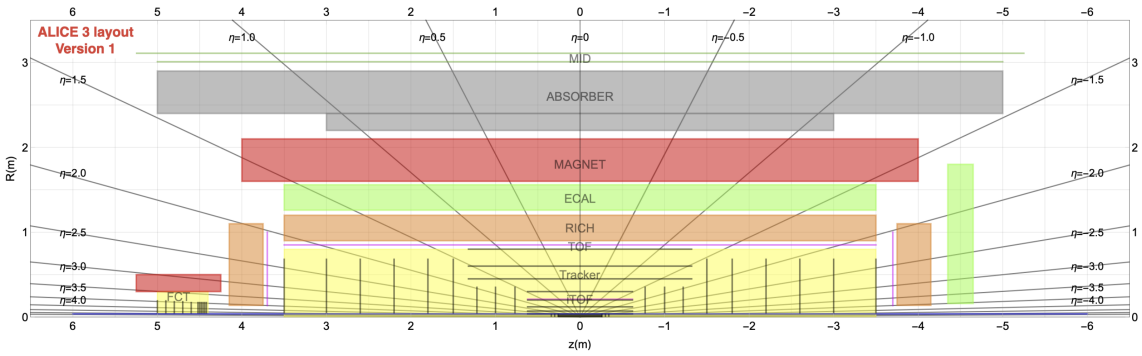


**Figure 1.6:** Longitudinal cross section of the ALICE 3 state-of-the-art reference detector shown in Fig. 1.5. The Inner and Outer Tracker, the TOF, the RICH, the superconducting magnet, the ECal, the hadron absorber, the MID and the FCT are shown. The FD layers at $|z| \geq 17$ m are not shown.

interaction point. The system is segmented into cylindrical layers in the barrel region, for $|\eta| < 2$, and disks for larger $|\eta|$. The result is a compact detector featuring a lightweight tracker capable of tracking over a wide momentum range with excellent pointing resolution, transverse momentum resolution, particle identification and high-rate capabilities based on the state-of-the-art technologies and innovative approaches.

In the following, I present the state-of-the-art ALICE 3 subsystems, with emphasis on the ones that impact the RICH performance, which is the subject of this thesis.

### 1.8.1 Superconducting magnet

The ALICE 3 superconducting magnet consists of a solenoid coil with a length of 7.5 m, a radius of 1.6 m and offering a field strength of 2 T. Alternative layouts with a radius of 1.25 m in a configuration without the ECal and a smaller magnetic field strength, down to 0.5 T, are also under study as scoping options, as discussed in Section 1.8.6. Various technology options are under study for the superconducting cable, with the baseline being Nb-Ti/Cu superconductor with aluminium cladding as stabilizer.

### 1.8.2 Tracking detectors

The ALICE 3 core detector component is a large silicon tracker arranged in 11 barrel layers and 12 forward disks on either side of the interaction point covering the range $|\eta| < 4$. These layers are equipped with Monolithic Active Pixel Sensors (MAPS) [37] and are grouped into the Inner Tracker and the Outer Tracker, as detailed below.

#### Inner Tracker

The ALICE 3 Inner Tracker (IT) consists of seven barrel layers and six disks on either side of the interaction point. It is divided into a Vertex Detector (VD) and Middle Layers (ML). The VD and ML barrel sections extend 50 cm and 124 cm along Z, respectively, and are complemented by disks with outer radii of 2.5 cm (VD) and 35 cm (ML). The specifications of the layers of VD and ML in terms of position, material budget and spatial resolution are given in Table 1.4.

The VD consists of the three innermost barrel layers and disks on either side of the interaction point. The goal is to ensure a pointing resolution better than 30 µm for $p_{\mathrm{T}}$ larger than 100 MeV. To achieve this resolution, the VD is designed as a retractable system based on curved wafer-scaled ultra-thin silicon MAPS installed in secondary

| Layer | Material thickness ($\%X_0$) | Intrinsic resolution (µm) | Barrel layers Length $\Delta z$ (cm) | Barrel layers Radius ($r$) (cm) | Forward disks Position ($\|z\|$) (cm) | Forward disks $R_{\text{in}}$ (cm) | Forward disks $R_{\text{out}}$ (cm) |
|---|---|---|---|---|---|---|---|
| 0 | 0.1 | 2.5 | 50 | 0.50 | 26 | 0.50 | 2.5 |
| 1 | 0.1 | 2.5 | 50 | 1.20 | 30 | 0.50 | 2.5 |
| 2 | 0.1 | 2.5 | 50 | 2.50 | 34 | 0.50 | 2.5 |
| 3 | 1 | 10 | 124 | 3.75 | 77 | 5 | 35 |
| 4 | 1 | 10 | 124 | 7 | 100 | 5 | 35 |
| 5 | 1 | 10 | 124 | 12 | 122 | 5 | 35 |
| 6 | 1 | 10 | 124 | 20 | | | |

**Table 1.4:** Specifications of the IT. VD: layers 0 to 2, ML: barrel layers 3 to 6, disks 3 to 5.

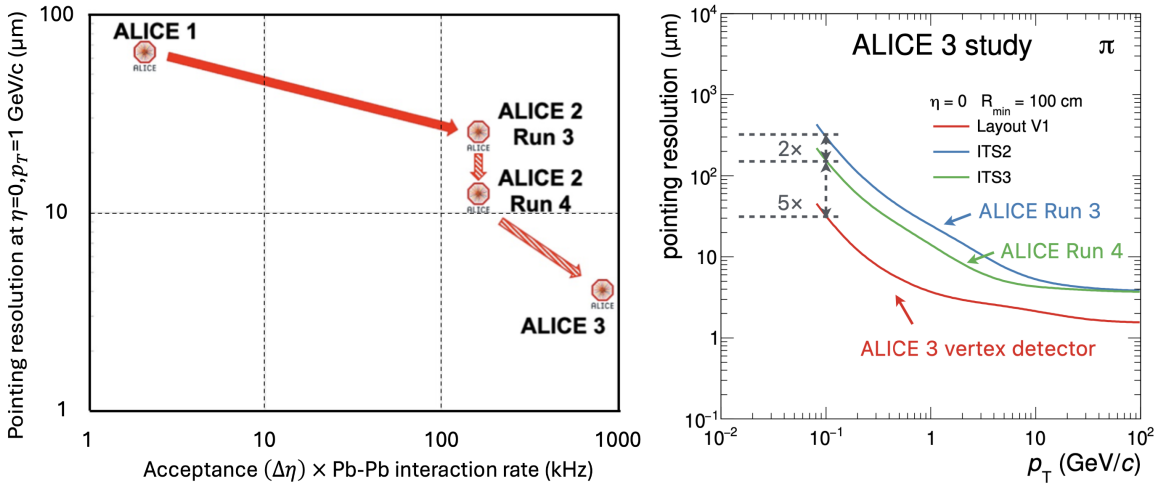


**Figure 1.7:** Left: Improvement of pointing resolution at $p_{\text{T}} = 1$ GeV/$c$ and $\eta = 0$ and effective Pb-Pb statistics from ALICE 1 to ALICE 3. Right: Expected pointing resolution for $\pi$ versus $p_{\text{T}}$.

vacuum inside the beampipe with the inner layer placed at 5 mm distance from the beam line after beam stabilisation. The resulting uniqueness of ALICE 3, combining pointing resolution and effective Pb–Pb statistics, is illustrated in Fig. 1.7. The VD geometry meets the resolution target and yields orders-of-magnitude improvements from ITS (Runs 1–2), ITS 2 (Run 3) and ITS 3 (Run 4) to the VD planned for Run 5.

The ML are located outside the beam pipe with primary vacuum and contribute to charged-particle tracking together with the Outer Tracker Layers. The target material thicknesses are 0.1% of a radiation length per layer for the VD and 1% for the ML.

| Layer | Det. | Material thickness ($\%X_0$) | Intrinsic resolution (μm) | Barrel layers | | Forward disks | |
|---|---|---|---|---|---|---|---|
| | | | | Full length ($\Delta z$) (cm) | Radius ($r$) (cm) | Position ($\|z\|$) (cm) | $R_{in}$–$R_{out}$ (cm) |
| 6 | IT/OT | 1 | 10 | 1×124 | 20 | 150 | 5–68 |
| 7 | OT | 1 | 10 | 1×129 | 30 | 180 | 5–68 |
| 8 | OT | 1 | 10 | 2×129 | 45 | 220 | 5–68 |
| 9 | OT | 1 | 10 | 2×129 | 60 | 260 | 5–68 |
| 10 | OT | 1 | 10 | 2×129 | 80 | 300 | 5–68 |
| 11 | OT | 1 | 10 | | | 350 | 5–68 |

**Table 1.5:** Specifications of the OT: barrel layers 7 to 10, disks 6 to 11.

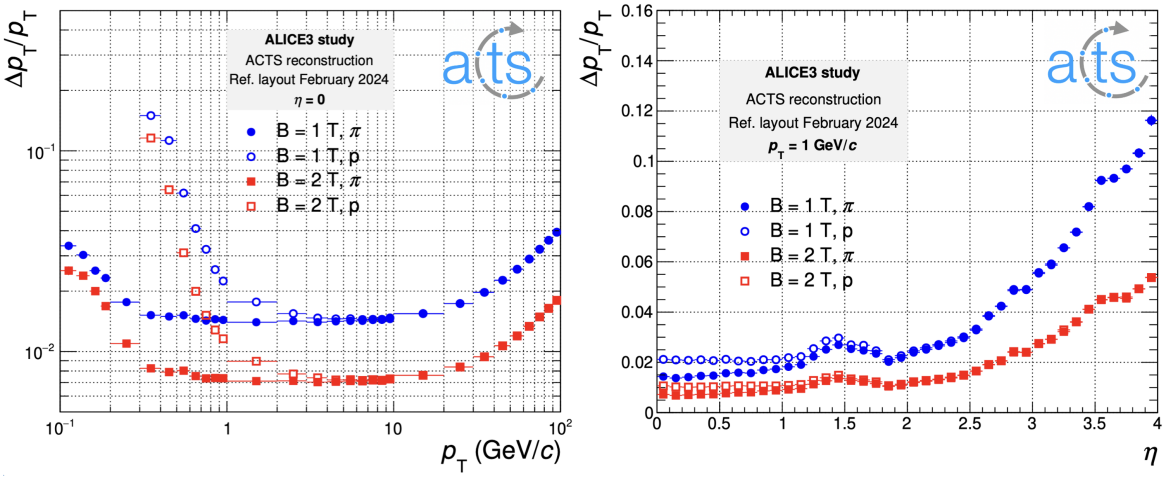


**Figure 1.8:** Expected relative $p_T$ resolution for $\pi$ and p as a function of both $p_T$ (left) and $\eta$ (right) assuming a magnetic field strength of $B = 1$ T and $B = 2$ T obtained with ACTS-based tracking [38].

### Outer Tracker

The Outer Tracker (OT) is located beyond the middle layers and disks of the IT. It consists of four barrel layers and six forward disks on either side of the interaction point, starting from a radius of 30 cm (barrel) and a longitudinal position of 150 cm (disks), with an overall longitudinal extent of 7 m and a radius of 80 cm for the outermost OT layer. The specifications of the OT layers in terms of position, material budget and spatial resolution are given in Table 1.5. The target material thickness is 1% of a radiation length per layer. The OT specifications are driven by the requirement of a relative $p_T$ resolution $\Delta p_T/p_T < 1\%$ over the widest possible $\eta$ interval.

Fig. 1.8 shows the resulting relative $p_T$ resolution for $\pi$ and p as a function of $p_T$ at $\eta = 0$ and as a function of $\eta$ at $p_T = 1$ GeV/$c$. The curves obtained assuming the baseline $B = 2$ T magnetic field are compared with the case of $B = 1$ T, highlighting

| | Inner TOF | Outer TOF | Forward TOF |
|---|---|---|---|
| Radius (m) | 0.19 | 0.85 | 0.15 to 1.0 |
| $z$ range (m) | -0.62 to 0.62 | -3.50 to 3.50 | $\pm$3.70 |
| Acceptance | $\|\eta\| < 2$ | $\|\eta\| < 2$ | $2 < \|\eta\| < 4$ |
| Granularity (mm$^2$) | 1×1 | 5×5 | 1×1 to 5×5 |
| Material thickness (%$X_0$) | 1 to 3 | 1 to 3 | 1 to 3 |
| Time resolution (ps) | 20 | 20 | 20 |

**Table 1.6:** Geometry and key specifications of the TOF layers.

the crucial role of the magnetic field in ensuring the target resolution. Although the target resolution is ensured up to $|\eta| \approx 2$, it worsens up to 5.5% for $|\eta| \to 4$.

### 1.8.3 Time-of-Flight detector

The Time-of-Flight system includes a cylindrical Inner TOF layer (iTOF) at a radius of 19 cm, a cylindrical Outer TOF barrel layer (oTOF) at a radius of 85 cm, and a forward disk (fTOF) at a longitudinal position of 370 cm on either side of the interaction point. The iTOF and the oTOF cover the region $|\eta| < 2$, while the fTOF covers the region $2 < |\eta| < 4$. The key specifications of the TOF layers are summarised in Table 1.6. The target material thickness is between 1% and 3% of a radiation length per layer.

The main requirement is a time resolution of 20 ps (rms) at full system level to ensure a better than 3$\sigma$ e/$\pi$, $\pi$/K and K/p separation up to 0.7, 2 and 4 GeV/$c$ momentum, respectively, as shown in Fig. 1.9, illustrating the PID reach in the $\eta$-$p_{\mathrm{T}}$ plane.

Low Gain Avalanche Diodes (LGADs), both hybrid [39, 40] and monolithic in CMOS technology [41], and Silicon Photomultipliers (SiPMs) [42] are under study as viable technology options for the TOF sensors, with CMOS LGADs being the baseline. Assuming SiPMs are validated for the oTOF, an appealing R&D option I investigated in this work is to integrate an SiPM-based oTOF with the SiPM photosensitive surface of the barrel RICH detector, yielding significant cost benefits, as discussed in Section 3.6.

### 1.8.4 Ring Imaging Cherenkov detector

The Ring Imaging Cherenkov system comprises two subsystems, one situated in the barrel (bRICH) in the radial region between 90 cm and 120 cm, covering the pseudo-rapidity region $|\eta| < 2$ , and the other positioned at forward and backward rapidities (fRICH) at 3.75 m longitudinal position, covering the region $2 < |\eta| < 4$.

| | **Barrel RICH** | **Forward RICH** |
|---|---|---|
| Radius (m) | 0.9 to 1.2 | 0.15 to 1.15 |
| $z$ range (m) | -3.60 to 3.60 | $3.75 < \|z\| < 4.15$ |
| Acceptance | $\|\eta\| < 2$ | $2 < \|\eta\| < 4$ |
| Radiator refractive index | 1.03 | 1.01 to 1.03 |
| Radiator material | Aerogel | Aerogel |
| Target ring angular resolution | 1.5 mrad | 1.5 mrad |
| Geometry | Projective | Disk |
| Max photodetector area ($m^2$) | 30.7 | 8.6 |
| Sensor technology | SiPMs | HRPPDs |
| Granularity ($mm^2$) | 2×2 | 1×1 to 2×2 |
| Single photon time resolution (ps) | 50 to 100 | 50 to 100 |

**Table 1.7:** Geometry and key specifications of the RICH subsystems.

The design target of the RICH systems is to extend the ALICE 3 particle identification capabilities beyond the TOF upper limits by ensuring a better than 3σ e/π, π/K and K/p separation for momenta up to at least 2, 10 and 16 GeV/$c$, respectively.

The key specifications, partly coming from the studies in this thesis, are reported in Table 1.7 and detailed below, highlighting my personal contributions to their definition.

### The bRICH detector

The required performance in the bRICH is achieved using a radiator with a refractive index of 1.03 and requiring an overall ring angular resolution better than 1.5 mrad at Cherenkov angle saturation. The target refractive index is obtained using aerogel as Cherenkov radiator. The baseline photodetector technology for the bRICH is represented by SiPMs with an area of $2 \times 2$ mm$^2$, a peak photon detection efficiency (PDE) of 40% at 450 nm and a single photon time resolution (SPTR) better than 100 ps.

To enhance the PID performance while minimising the total active area, I proposed a modular projective proximity-focusing bRICH geometry with 24 sectors segmented in 36 modules, each oriented toward the nominal ALICE 3 interaction point, as shown in Fig. 1.5. The resulting maximal bRICH photodetector area is about 30.7 m$^2$, assuming full coverage with SiPMs, while the total aerogel area is about 22 m$^2$. The resulting PID reach is shown in Fig. 1.9, highlighting the complementarity with the TOF.

Several R&D options are under investigation, including the use of a gaseous radiator in the bRICH expansion gap to extend electron identification in central Pb-Pb collisions up to 4 GeV/$c$, the integration of charged-particle timing using the bRICH SiPMs,

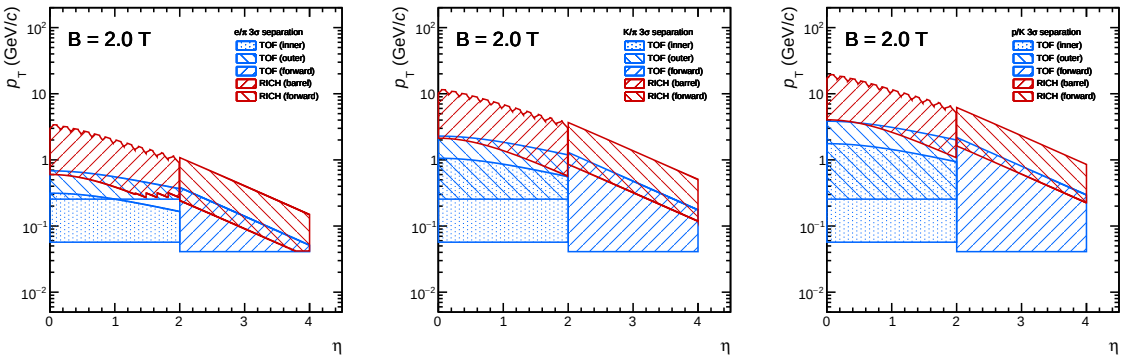


**Figure 1.9:** Expected $\eta$-$p_{\mathrm{T}}$ regions with larger than $3\sigma$ separation using ALICE 3 TOF and RICH systems for $B = 2$ T. The e/$\pi$, $\pi$/K and K/p separation plots are shown from left to right.

and the use of smaller SiPMs coupled with light concentrators to mitigate the SiPM DCR increase due to radiation damage. The study of these options was a central part of my research activity and will be discussed in the following chapters.

#### The fRICH detector

For the fRICH, a radiator with a lower refractive index, from 1.03 down to 1.01, is considered to account for both the larger upper momentum reach of the TOF and the Lorentz boost of the incoming particles. In this context, I performed dedicated optimization studies, resulting in an optimal index of 1.015. A granularity of $2{\times}2$ mm$^2$ is also targeted for the active area of the fRICH sensors.

A SPTR better than 100 ps is also required to ensure excellent background suppression for the pattern recognition of Cherenkov rings. Due to the significantly higher expected radiation dose compared to the bRICH, the fRICH photodetector surface is foreseen to be based on High-Resolution Picosecond Photodetectors (HRPPDs)[43]. The resulting photodetector area is approximately 4.3 m$^2$ per fRICH disk. The resulting PID reach is shown in Fig. 1.9, highlighting the complementarity with the fTOF up to $|\eta| = 4$.

### 1.8.5 Other subsystems

The ECAL, MID and the FCT are designed to provide identification of high-energy photons and electrons up to hundreds of GeV for $-4 < \eta < 1.5$, muons down to $p_{\mathrm{T}} \approx 1.5$ GeV/$c$ for $|\eta| < 1.3$ and soft photons with $p_{\mathrm{T}}$ down to 1 MeV/c for $4 < \eta < 5$, respectively. The ECAL is based on Pb-scintillator sampling technology and includes a high-energy resolution segment based on $PbWO_4$ crystals at $\eta = 0$ with

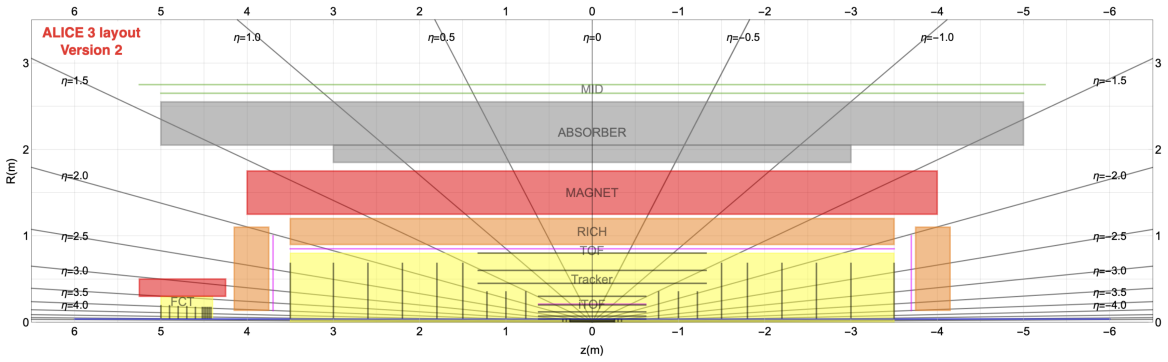


**Figure 1.10:** Longitudinal cross section of ALICE 3 layout in the scoping option without ECal.

SiPM readout. The MID consists of a steel hadron absorber followed by dedicated muon chambers made of scintillator bars read out using SiPMs. The FCT consists of forward disks equipped with MAPS using the same technology as the ML and the OT. Finally, the Forward Detectors (FD) provide event characterization and contribute to several key functions, including luminosity measurement and interaction triggering, LHC background monitoring, determination of the collision time and vertex position, and forward multiplicity and centrality estimation. They consist of two segmented disks placed at forward and backward rapidities ($4 < |\eta| < 7$), with the sensitive elements made of fast plastic scintillators.

### 1.8.6 ALICE 3 scoping options

Several detector scoping options for ALICE 3 are currently under investigation [2], including configurations with a reduced magnetic field strength, down to 1 T, which impacts the momentum-reconstruction performance, as illustrated in Fig. 1.8, or the removal of one or more subsystems.

The most relevant option for the studies presented in this thesis foresees the removal of the electromagnetic calorimeter (ECal). The longitudinal cross section of the corresponding detector layout is shown in Fig. 1.10. The main differences with respect to the reference layout, shown in Fig. 1.6, are the absence of the ECal barrel and endcap, and a reduction of the magnet and the MID radii by 35 cm.

The presence or absence of the calorimeter has a major influence on the radiation load of the surrounding detectors, in particular the SiPMs of the bRICH. This effect is mainly due to the backsplash of secondary particles originating from the showers developing inside the ECal. These secondaries significantly increase the radiation level in nearby regions, resulting in roughly an order of magnitude higher radiation load when the ECal is present relative to the case where it is not included.

At the time of writing this thesis, the configuration without the ECal is considered the most realistic option for the final ALICE 3 layout. Therefore, all radiation-load studies and projections for the bRICH presented in this work are based on this configuration.

## 1.9 Expected ALICE 3 physics performance

In this section, I report a selection of simulations of the expected ALICE 3 physics performance from the ALICE 3 Letter of Intent [1], highlighting the impact of each subsystem specifications on the physics programme, and in particular the RICH.

Here I focus on dielectrons, multi-charm baryon reconstruction, and heavy-quark correlation measurements. The studies reported here are obtained with a parametric simulation of both TOF and RICH PID considering the Letter of Intent version of those subsystems, originally accounting for a cylindrical bRICH geometry, assuming the target design specifications in terms of time resolution and angular resolution.

The projections take into account that, throughout LHC Run 5, ALICE 3 will collect integrated luminosities of 18 $\text{fb}^{-1}$ and 35 $\text{nb}^{-1}$ for pp and Pb-Pb collisions, respectively.

### 1.9.1 Dielectrons

Dileptons are produced in all the different stages of a heavy-ion collision. Since they are not interacting via the strong force, they leave the collision unscattered after production, making them ideal messengers to study the whole evolution of the collision as discussed in Section 1.6. Fig. 1.11 shows the ALICE 3 projection for the expected background-subtracted thermal dielectron invariant mass ($m_{\text{ee}}$) spectrum for central Pb-Pb collisions at centre-of-mass energy per nucleon pair $\sqrt{s_{\text{NN}}} = 5.02$ TeV.

Although first $T$ measurements are expected with ALICE 2 and 2.1 (LHC Runs 3 and 4), with the very large expected statistics, ALICE 3 will open the unique possibility to probe the time dependence of $T$ by extracting it as a function of mass or pair transverse momentum $p_{\text{T,ee}}$, as shown in the left panel of Fig. 1.12.

Similarly, the measurement of the thermal dielectron elliptic flow would, for the first time, be statistically achievable as a function of $m_{\text{ee}}$ and $p_{\text{T,ee}}$, as shown in the right panel of Fig. 1.12 labelled as "excess" dielectron $v_2$. The elliptic flow in different $m_{\text{ee}}$ and $p_{\text{T,ee}}$ regions provides key information to disentangle emission at early times of the collision from that produced later, after the medium has begun to cool.

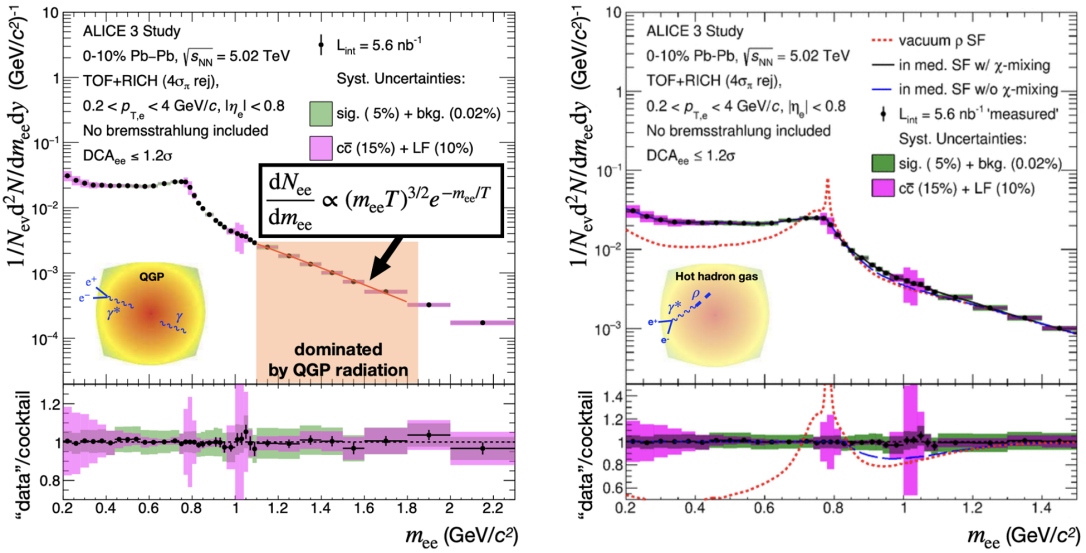


**Figure 1.11:** Simulated background-subtracted dielectron invariant mass spectrum in central (0-10%) Pb-Pb collisions at $\sqrt{s_{\rm NN}}$ = 5.02 TeV. Left: Fit of the spectrum in the $m_{\rm ee}$ range 1.1-1.8 GeV/$c^2$ to extract the early-stage QGP temperature. Right: Comparison of the spectrum obtained using the $\rho$ spectral function in medium under the hypothesis of $\rho$-$a_1$ mixing with expectations for the $\rho$ spectral function in vacuum and in medium without chiral mixing. Adapted from [1].

Such measurements probe the time evolution of the flow field and provide decisive inputs to the so-called photon puzzle, i.e. the simultaneous understanding of the yield and $v_2$ of direct real photons, which is also part of the ALICE 3 programme.

For $m_{\rm ee} < 1.2$ GeV/$c^2$, the shape of the thermal dielectron spectrum is dominated by thermal production of $\rho$ mesons. Their spectral function (SF) is modified in the hot medium where chiral symmetry restoration is predicted. The expected high-precision measurement of the $m_{\rm ee}$ spectrum in central Pb–Pb collision with ALICE 3 would enable the study of chiral symmetry restoration mechanisms like $\rho$-$a_1$ mixing [30], as shown in the right panel of Fig. 1.11.

The key ALICE 3 ingredients to achieve the required statistical and systematic precision are the excellent $e^{\pm}$ identification down to low $p_{\rm T}$ achieved with the combination of TOF and RICH, the small detector material budget to reduce the combinatorial background from $\gamma$ conversion or $\pi^0$ Dalitz decays and the excellent pointing resolution to efficiently suppress the dominant background from heavy-flavour hadron decays. In particular, the contribution of the RICH electron identification is crucial to cover the $m_{\rm ee}$ and $p_{\rm T,ee}$ regions above 1 GeV/$c^2$ and 1 GeV/$c$, respectively.

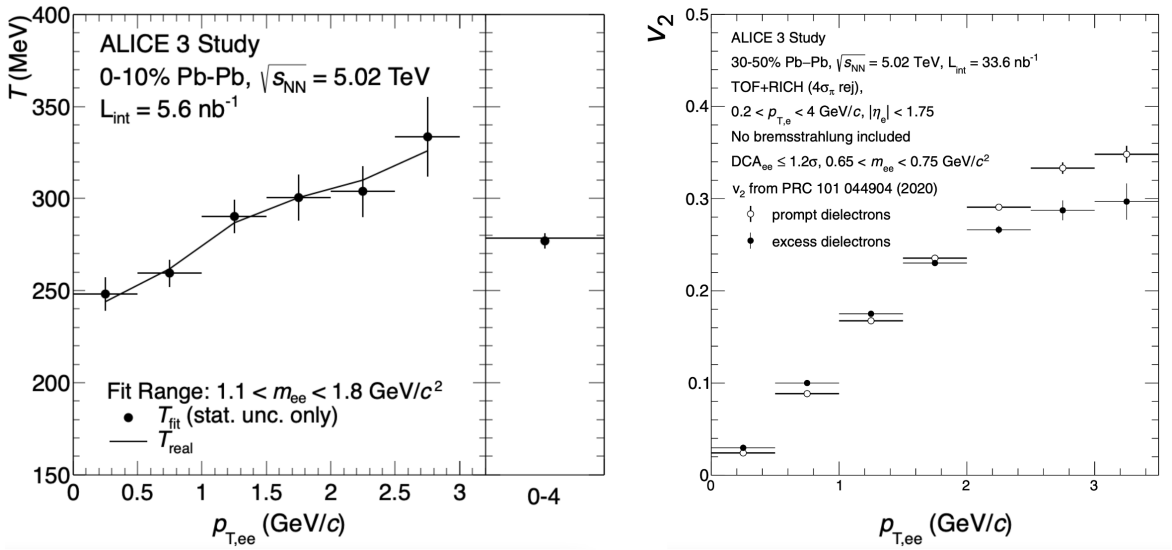


**Figure 1.12:** Left: Extracted temperature $T_{\mathrm{fit}}$ from the simulated $m_{\mathrm{ee}}$ dielectron spectrum for various $p_{\mathrm{T,ee}}$ intervals in central (0-10%) Pb–Pb collisions after one month of data taking with ALICE 3. Right: Projections for prompt and thermal dielectron $v_2$ measurements in $0.65 \leq m_{\mathrm{ee}} \leq 0.75$ GeV/$c^2$ with ALICE 3 in semi-central Pb–Pb collisions after six months of data taking. Adapted from [1].

### 1.9.2 Multi-charm baryons

Multi-charm baryon yields are powerful probes of the hadron formation mechanisms since they are expected to be produced through combination of uncorrelated charm produced in heavy-ion collisions [44]. The yields of multi-charm baryons relative to the number of produced charm quarks are predicted to be significantly enhanced in heavy-ion relative to pp collisions, as predicted by statistical hadronisation models [45].

ALICE 3 will enable systematic measurements of multi-charm states currently inaccessible, such as $\Xi_{cc}^{++}$ through decay to $\Xi_c^+\pi^+$ with the subsequent decay $\Xi_c^+ \rightarrow \Xi^- \pi^+ \pi^+$.

With the first tracking layer at 5 mm from the beam axis, strange baryons like $\Xi^-$ can be directly tracked before they decay, as shown in the left panel of Fig. 1.13. This increases significantly the pointing resolution of the reconstructed strange baryon trajectory to the primary vertex, improving the ability to distinguish weak decays from primary or secondary sources, which are characteristic of multi-charm baryons.

The resulting significance in central Pb-Pb at $\sqrt{s_{\mathrm{NN}}} = 5.52$ TeV as a function of $p_{\mathrm{T}}$ using standard selections and machine learning is shown in the right panel of Fig. 1.13.

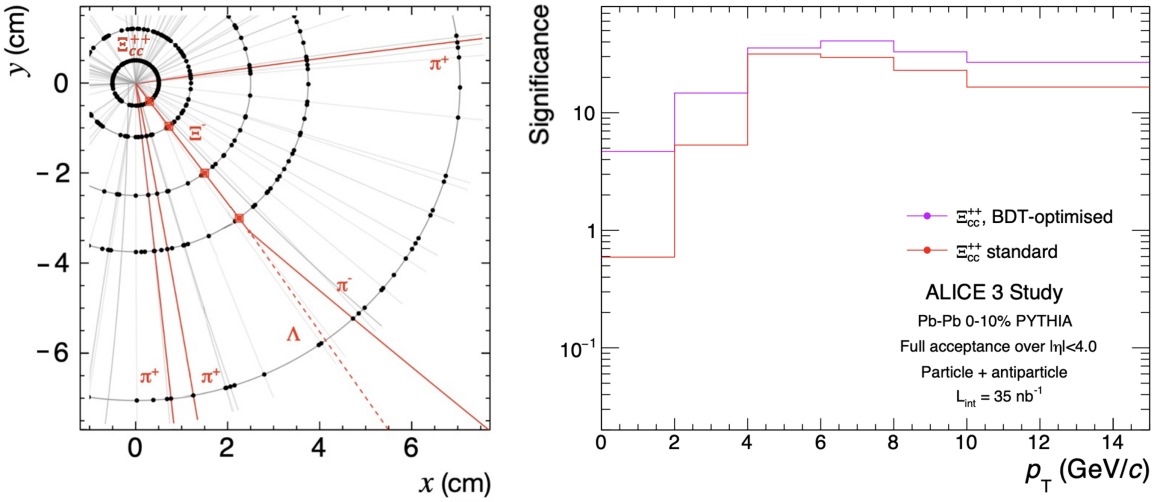


**Figure 1.13:** Left: ALICE 3 strangeness tracking in $\Xi_{cc}^{++} \to \Xi_c^+ + \pi^+$ with $\Xi_c^+ \to \Xi^- + 2\pi^+$. Right: Simulated $\Xi_{cc}^{++}$ significance in central (0-10%) Pb-Pb collisions at $\sqrt{s_{\rm NN}} = 5.52$ TeV as a function of $p_{\rm T}$ using standard selections and machine-learning–based selections. Adapted from [1].

### 1.9.3 Heavy-flavour correlations

The angular correlation of heavy-flavour hadrons pairs is a powerful probe of QGP scattering, since it is sensitive to the energy loss mechanisms and the degree of thermalization of heavy-quarks in the QGP, especially at low $p_{\rm T}$. The left panel of Fig. 1.14 shows the ALICE 3 projection for $\rm D^0\bar{D}^0$ correlation for minimum-bias Pb-Pb collisions at $\sqrt{s_{\rm NN}} = 5.52$ TeV. Such measurements are out of reach in Runs 3 and 4, since they require high $\rm D^0$ purity and reconstruction efficiency, as well as a large rapidity coverage, and will only be possible with ALICE 3.

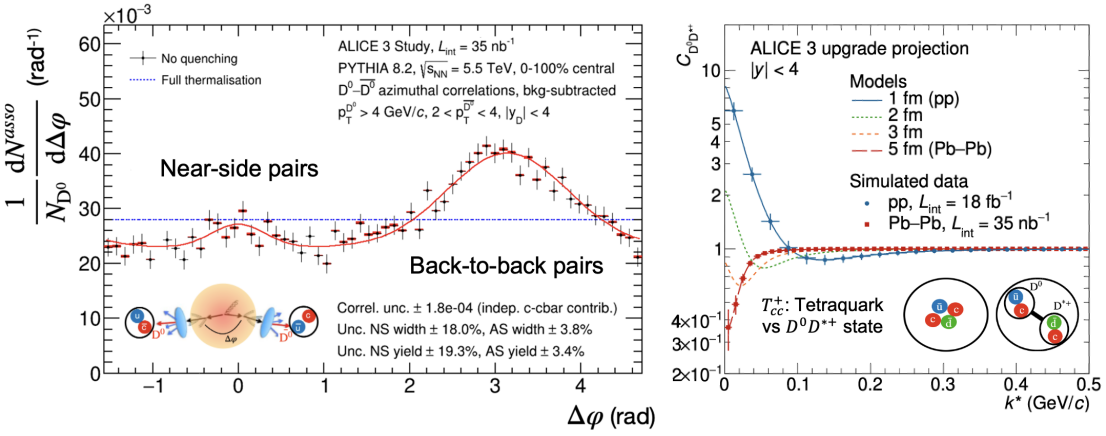


**Figure 1.14:** Left: Simulated $\rm D^0\bar{D}^0$ azimuthal correlation distribution in minimum-bias Pb-Pb collisions with ALICE 3 at $\sqrt{s_{\rm NN}} = 5.52$ TeV. Right: Simulated (dots) and predicted (lines) $\rm D^0D^{*+}$ correlation $C_{\rm D^0D^{*+}}$ as a function of the invariant relative momentum $k^*$ evaluated for different source sizes from pp to Pb-Pb collisions in the hypothesis of the presence of a bound state. Adapted from [1]

The momentum correlation of heavy-flavour hadron pairs is a powerful probe of the nature of exotic bound states. The nature of recently discovered exotic bound states, like $T_{cc}^{+}$ [33], is still unclear. The hypotheses of compact objects like tetraquarks or molecular $c\bar{c}$ states like $D^0D^{*+}$ for $T_{cc}^{+}$ are both not excluded. Measurements of the source size dependence of the two-particle momentum correlation function in different colliding systems, from pp to Pb-Pb, provide direct insight into the properties of the DD interaction potential [46]. The projections for the $D^0D^{*+}$ correlation function $C_{D^0D^{*+}}$ as a function of the invariant relative momentum $k^*$ in the hypothesis of the presence of a bound state are shown in the right panel of Fig. 1.14. These measurements will be out of reach in LHC Runs 3 and 4, since they require excellent pointing resolution, very high $D^0$ purity and reconstruction efficiency, as well as large $\eta$ acceptance, and they will only be possible with the performance targeted by ALICE 3.

# Chapter 2

# ALICE 3 RICH technology options

Ring Imaging Cherenkov (RICH) detectors are widely used in high energy physics to identify electrons and hadrons from a few to tens of GeV/$c$. The design starts from the choice of radiator and photodetector, which sets the PID performance over the momentum range of interest. The optical properties of the radiator determine both the momentum reach and the requirements on the photodetector through the transmittance of Cherenkov photons. With the target PID requirements of the ALICE 3 bRICH, these considerations lead to the choice of aerogel as Cherenkov radiator, with a refractive index of 1.03, and Silicon Photomultipliers (SiPMs) as photon sensors.

This chapter summarizes the RICH technique and the aerogel and SiPM properties relevant to this thesis. In particular, an overview of charged-particle identification, Cherenkov radiation, and the RICH technique is given in Sections 2.1, 2.2, and 2.3. A summary of aerogel features and optical properties is then provided in Section 2.4. Finally, a review of SiPMs and radiation-damage effects is presented in Section 2.5.

## 2.1 Charged particle identification

In order to identify a charged particle, it is necessary to determine its charge $Ze$ and its mass $m$. Although the mass cannot be measured directly, it can be deduced from the momentum $p$ and the velocity $\beta = v/c$ by exploiting the relation

$$p = \gamma m v \quad \Rightarrow \quad m = \frac{p}{c\beta\gamma}\,, \tag{2.1}$$

where $\gamma = (1-\beta^2)^{-1/2}$ is the relativistic Lorentz factor. Both the charge sign and the momentum are obtained by measuring the curvature of the track in a magnetic field.

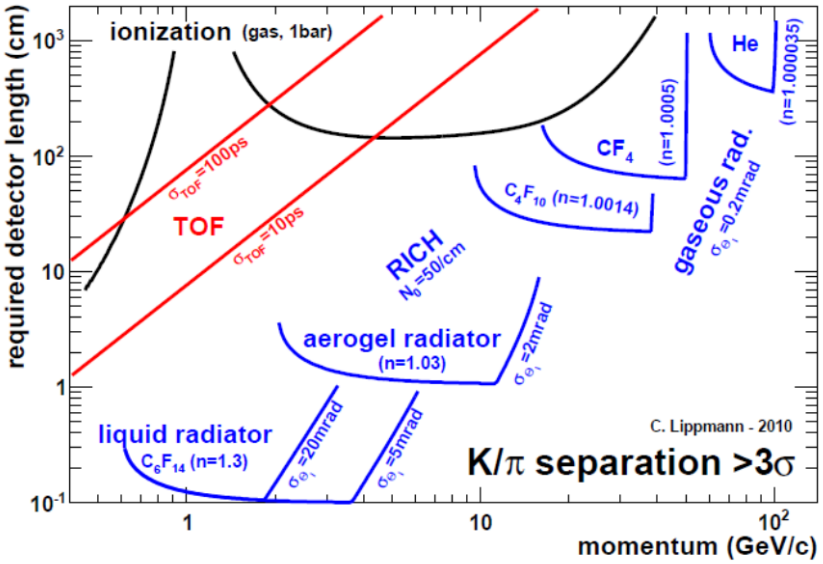


**Figure 2.1:** Minimum detector length required to achieve a K/$\pi$separation of $N_\sigma \geq 3\sigma$ with three different PID techniques [47]. For the energy loss technique, a gaseous detector is assumed. For the TOF technique, the detector length represents the particle flight path over which the time-of-flight is measured. For the RICH technique only the radiator thickness is reported and the thicknesses of an expansion gap and of the readout systems have to be added.

The particle velocity can be measured with various methods, such as the measurement of the energy deposit by ionization, time-of-flight measurements, the detection of Cherenkov radiation and the detection of transition radiation. The use of each of these method is restricted to specific momentum intervals and particle species.

The separation power $N_\sigma$ can be used to quantify the effectiveness of a technique. It defines the significance of the detector response $R$. If $R_\mathrm{A}$ and $R_\mathrm{B}$ are the mean values for particles of type A and B, respectively, and $\langle\sigma_\mathrm{A,B}\rangle$ is the average of the standard deviations of the measured distributions, the separation power $N_\sigma$ is defined as [47]:

$$N_\sigma = \frac{|R_\mathrm{A} - R_\mathrm{B}|}{\langle\sigma_\mathrm{A,B}\rangle}. \tag{2.2}$$

A summary of the allowed momentum coverage and the required detector lengths to achieve a separation power $N_\sigma \geq 3$ for K/$\pi$ separation with ionization, TOF and RICH systems under various assumptions on the TOF resolution, RICH angular resolution and considered radiator refractive index is shown in Fig. 2.1. In a general-purpose experiment like ALICE 3, the momentum reach of each of these PID techniques is ultimately limited by the constraints on each subsystem size, geometrical coverage, cost, and compatibility with other subsystems, making the combination of TOF layers with RICH systems the only viable option to fully cover the target momentum ranges.

## 2.2 Cherenkov radiation

Cherenkov radiation is electromagnetic radiation emitted when a charged particle passes through an optical medium of refractive index $n$ at a speed $v = \beta c$ greater than the phase velocity of light $c/n$ in that medium. Photons are emitted on the surface of a cone and have inherent polarization perpendicular to the cone surface [48]. The Cherenkov emission angle $\theta_c$ relative to the particle direction is given by the fundamental relation:

$$\cos\theta_c = \frac{1}{n\beta} , \tag{2.3}$$

while the emission angle $\phi_c$ in the plane normal to the particle direction has a flat distribution between 0 and $2\pi$. Recalling that the momentum $p$ of a particle with mass $m$, velocity $\beta$, and Lorentz factor $\gamma$ is given by $p = m\beta\gamma$, the momentum dependence of the Cherenkov angle is expressed by the relation:

$$\theta_c = \arccos\left(\frac{\sqrt{p^2+m^2}}{np}\right) . \tag{2.4}$$

For a given refractive index, the threshold velocity $\beta_{th} = 1/n$ corresponds to the mass-dependent momentum threshold:

$$p_{th} = \frac{m}{\sqrt{n^2-1}} . \tag{2.5}$$

In addition, independently of the mass of the particle, the Cherenkov angle reaches a maximum, or saturation value, $\theta_{c,max}$, in the limit $\beta \to 1$, given by:

$$\theta_{c,max} = \arccos(1/n) . \tag{2.6}$$

For a given momentum $p$, the emission angle $\theta_c$ depends on the frequency (i.e. wavelength) of the Cherenkov radiation, since $n$ is wavelength-dependent.

The number $N_{ph}$ of Cherenkov photons emitted per unit energy $\mathrm{d}E$ and length $\mathrm{d}x$ travelled by the charged particle in the medium is given by Frank-Tamm equation [48]:

$$\frac{d^2N_{ph}}{dE\,dx} = \left(\frac{\alpha}{\hbar c}\right) Z^2 \sin^2\theta_c(E) = \left(\frac{\alpha}{\hbar c}\right) Z^2 \left[1 - \left(\frac{1}{\beta n(E)}\right)^2\right] , \tag{2.7}$$

where $\alpha$ is the electromagnetic fine structure constant, $Z$ is the charge of the particle in units of electron charge and, because of the chromatic dispersion of the optical medium, $n$ is a function of the photon energy $E$. The corresponding wavelength spectrum is naturally obtained as $(d^2N_{ph}/d\lambda dx) = (d^2N_{ph}/dEdx)(dE/d\lambda)$ where $\lambda = hc/E$. The

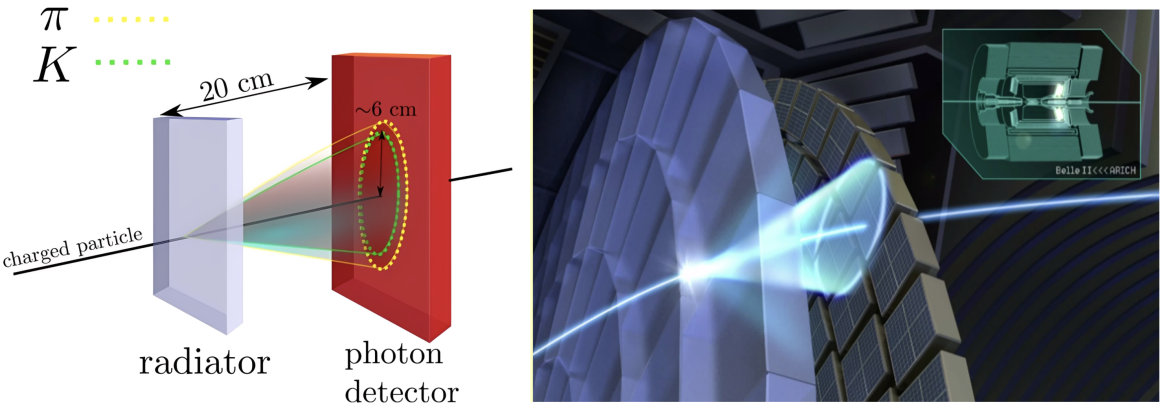


**Figure 2.2:** Schematic illustrations of a proximity-focusing RICH detector, showing the emission of Cherenkov photons in the radiator, their propagation through the expansion gap, and their detection on the photon sensor plane where the Cherenkov ring is formed.

mean number of produced photons is then obtained by integration of Eq. 2.7:

$$N_{\mathrm{ph}} = \left(\frac{\alpha}{\hbar c}\right) Z^2 \iint \left[1 - \left(\frac{1}{\beta n(E)}\right)^2\right] \mathrm{d}E \, \mathrm{d}x \,, \tag{2.8}$$

where the integral over $x$ extends from 0 to the total path length $L$ of the charged particle in the radiator and the integral over E extends over all possible photon energies.

## 2.3 The RICH technique

The main application of Cherenkov radiation in High Energy Physics is the identification of charged particles with known momentum. Particle identification is based on the dependence of the Cherenkov angle $\theta_{\mathrm{c}}$ on the particle mass $m$ at given momentum $p$. Inverting Eq. 2.4 for the particle mass:

$$m = \frac{p}{c}\sqrt{n^2 \cos^2(\theta_{\mathrm{c}}) - 1} \,. \tag{2.9}$$

Although Cherenkov detectors employing different identification techniques, such as Threshold Cherenkov Counters, have been developed in the last decades, the best performances are obtained through the RICH technique. In a RICH detector, the Cherenkov radiation emitted in a radiator is transmitted through an expansion gap either with a focusing optical system or without optics in a proximity-focusing configuration, onto a photodetector surface, where the detected photons form characteristic ring patterns, as shown in Fig. 2.2. The expansion gap is flushed with dry gas to keep

it clean, stabilize the refractive index, and control humidity and heat load.

Particle identification is achieved by measuring the Cherenkov emission angle $\theta_c$ of the photons associated to a given charged particle with known momentum $p$. Pattern recognition techniques are essential for associating the photon hits with the charged particle and rejecting background hits. Each detected photon provides a measurement with an uncertainty $\sigma_c^\gamma$ corresponding to the single photon angular resolution. For $N_{\rm det}$ detected photons, the ring Cherenkov angle resolution $\sigma_c^r$ can be expressed as:

$$\sigma_c^r = \frac{\langle \sigma_c^\gamma \rangle}{\sqrt{N_{\rm det}}} \oplus C \ , \tag{2.10}$$

where $\langle \sigma_c^\gamma \rangle$ is the average single photon angular resolution and $C$ accounts for tracking, alignment, multiple scattering, background hits. The main goal in the design of a RICH detector is to optimize $\sigma_c^r$ by minimizing $\langle \sigma_c^\gamma \rangle$ and maximizing $N_{\rm det}$.

### 2.3.1 Separation power

The capability of a RICH detector to resolve particles of different species is quantified by the separation power $N_\sigma$ defined by Eq. 2.2. Given two species of particles with same momentum $p$ and different mass $m_A$ and $m_B$ crossing a radiator with refractive index $n$, the corresponding mean Cherenkov angles $\theta_A$ and $\theta_B$ are measured with standard deviations $\sigma_A^{\rm ring}$ and $\sigma_B^{\rm ring}$. The separation power $N_\sigma$ is then given by:

$$N_\sigma = \frac{\mid \theta_A - \theta_B \mid}{\langle \sigma_{A,B}^{\rm ring} \rangle} \, . \tag{2.11}$$

### 2.3.2 Single photon angular resolution

Quantifying the contributions to the single-photon angular resolution $\sigma_c^\gamma$ is a key step in optimizing the detector geometry. Analytical expressions for the impact of individual detector parameters on $\sigma_c^\gamma$ for both proximity-focusing and mirror-focusing layouts are provided in [49, 50]. In both cases, Cherenkov photons emitted in the radiator form a set of nested light cones, which intersect the photodetector plane as finite-width shapes with elliptic- or hyperbolic-like profiles. The measurements necessary to define the Cherenkov angle $\theta_c$ are the photon detection point ($x$, $y$, $z$), the particle direction ($\theta_p$, $\phi_p$), the depth of the photon emission point in the radiator $z_e$ and the photon energy $E$. The assumption is made that these variables are uncorrelated. From the resulting functional dependence $\theta_c = \theta_c(E, z_e, x, y, z, \theta_p, \phi_p)$, the uncertainty on the

reconstructed Cherenkov angle at the single hit level can then be calculated as:

$$\sigma_c^{\gamma} = \sqrt{\sum_{\mathrm{i}} \left( \frac{\partial \theta_{\mathrm{c}}}{\partial v_{\mathrm{i}}} \sigma_{v_{\mathrm{i}}} \right)^2}, \tag{2.12}$$

where the variables $v_{\mathrm{i}}$ are $E$, $z_{\mathrm{e}}$, $x$, $y$, $z$, $\theta_{\mathrm{p}}$, $\phi_{\mathrm{p}}$ and the variables $\sigma_{v_{\mathrm{i}}}$ are their respective root-mean-square (rms) uncertainties. While the uncertainties on the photon energy $E$ (chromatic uncertainty) and the photon emission depth $z_{\mathrm{e}}$ (geometric uncertainty) are intrinsic to the radiator properties and they cannot be directly accessed, the uncertainties on the photon impact coordinates $x$, $y$, $z$ (localization uncertainty) and the charged-particle incidence angles $\theta_{\mathrm{p}}$, $\phi_{\mathrm{p}}$ (track incidence angle uncertainty) are determined by experimental conditions, like the photodetector specifications and the tracking quality. Since $E$ and $z_{\mathrm{e}}$ are not directly measured, the angle reconstruction is achieved by fixing them at the most probable values determined, respectively, by the convolution of the energy spectrum of the photons reaching the photodetector with the photodetector response curve, and the distribution of the emission point for photons not undergoing scattering or absorption in the radiator. Additional (=a) momentum-dependent contributions to $\sigma_c^{\gamma}$ come from multiple scattering and magnetic deflection in the radiator medium. They result in an uncertainty $\sigma_{\mathrm{a}} = p_{\mathrm{a}}/p$ to be added in quadrature to the other contributions in the $\sigma_c^{\gamma}$ definition. The analytical treatment of the derivatives and the rms uncertainties in Eq. 2.12, as well as the contributions due to multiple scattering and magnetic field deflection in the radiator, for the proximity-focusing RICH layout is presented in Appendix A.

### 2.3.3 Number of detected photons

The number of detected photons $N_{\mathrm{det}}$ is a crucial parameter to quantify the performance of a RICH detector. A large number of detected photons leads not only to improvements in the efficiency of pattern recognition of Cherenkov rings, but also to a significant improvement in the achievable ring angular resolution, according to Eq. 2.10. The mean number of detected photons is the result of the convolution of the statistics of emitted photons in the radiator, given by Eq. 2.8, the transmittance of materials characterizing the RICH components, the reflectance in case of a focusing optics, and the photodetector response. In particular, the expected mean number of detected photons $N_{\mathrm{det}}$ is limited by the photodetector photon detection efficiency PDE, the fraction of photodetector active area $F$, the transmittances $T_{\mathrm{i}}$ of the tra-

versed media and the reflectance of mirrors $R_{\mathrm{j}}$ according to the relation [49]:

$$N_{\mathrm{det}} = \left(\frac{\alpha}{\hbar c}\right) Z^2 F \iint \left[1 - \left(\frac{1}{n(E)\beta}\right)^2\right] \mathrm{PDE}(E) \prod_{\mathrm{i}} T_{\mathrm{i}}(E) \prod_{\mathrm{j}} R_{\mathrm{j}}(E) \mathrm{d}E \mathrm{d}x \ , \quad (2.13)$$

where PDE, $T_{\mathrm{i}}$ and $R_{\mathrm{j}}$ are averaged over the angular distribution of the corresponding incident photons. If Cherenkov photons are detected over an energy range in which the refractive index $n$ is approximately constant, Eq. 2.13 reduces to:

$$N_{\mathrm{det}} = N_0 Z^2 L \sin^2 \theta_{\mathrm{c}} \, , \quad (2.14)$$

where $N_0$, referred to as figure of merit, is defined as:

$$N_0 = \left(\frac{\alpha}{\hbar c}\right) F \int PDE(E) \prod_{\mathrm{i}} T_{\mathrm{i}}(E) \prod_{\mathrm{j}} R_{\mathrm{j}}(E) \mathrm{d}E \, . \quad (2.15)$$

The actual number of detected photons in a given event fluctuates around this mean according to Poisson statistics. The value of $N_{\mathrm{det}}$ plays a crucial role in the choice of the detector layout and the corresponding components.

## 2.4 Aerogel radiators

Silica aerogel is a highly porous material composed of a three-dimensional network of silica clusters, $(SiO_2)_n$ with sizes ranging from a few nm to tens of nm interconnected to form a rigid lattice with trapped air filling more than 90% of the total volume.

The combination of high optical transparency and a refractive index tunable during production in the range 1.003–1.26, intermediate between gases and liquids or solids, makes aerogels ideal Cherenkov radiators [48, 52]. Aerogel radiators have been successfully employed in past experiments such as HERMES [53], remain key components of current RICH systems in LHCb [54], AMS [55], BELLE II [56], and CLAS12 [57], and are also envisaged in future detectors, for example in ePIC at the EIC [58, 59].

In the following, unless otherwise specified, hydrophobic aerogel tiles from Aerogel Factory Co., Ltd. (Chiba, Japan) are considered. Detailed descriptions of the fabrication procedure for the production of hydrophobic silica aerogel tiles can be found in [60, 61, 62, 63]. Fig. 2.3 shows a photograph of an aerogel tile produced by Aerogel Factory Co., Ltd., together with a schematic representation of its internal nanostructure. The key details on the aerogel refractive index and transparency are given below.

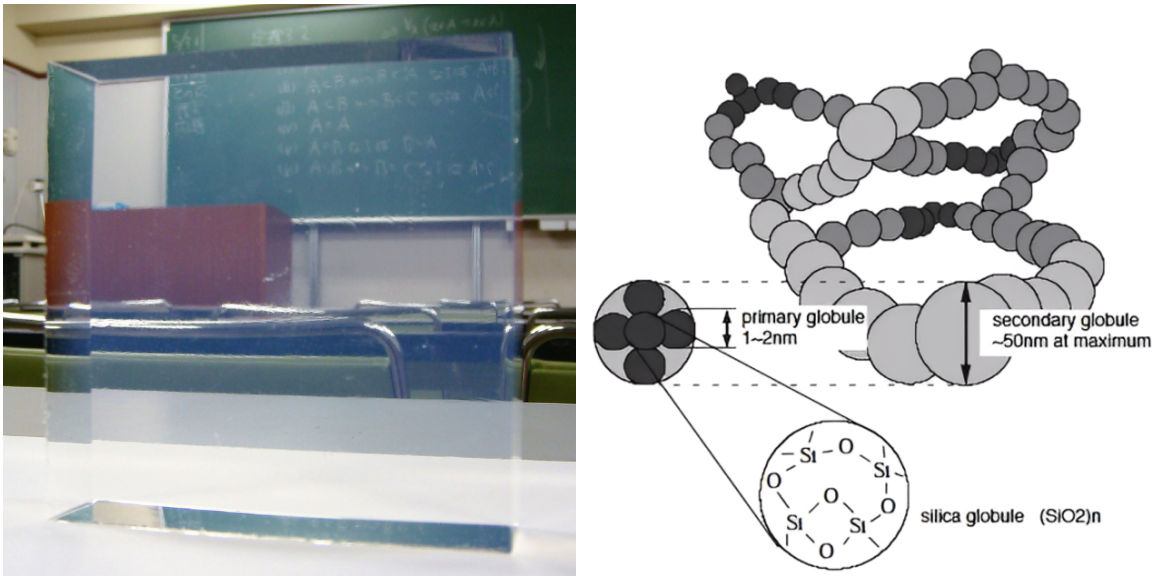


**Figure 2.3:** Left: Photograph of a hydrophobic silica aerogel tile produced by Aerogel Factory Co., Ltd. [51]. Right: Schematic representation of the internal nanostructure of silica aerogel.

### 2.4.1 Aerogel refractive index

The refractive index of an aerogel tile is related to its bulk density $\rho$, and is determined by the quantity of $SiO_2$ clusters in the volume of the tile by the approximate relation:

$$n(\lambda) = 1 + k(\lambda)\rho\,, \tag{2.16}$$

where $k$ depends on the wavelength $\lambda$ and the fabrication process [51, 61, 64]. A commonly used parametrization for the wavelength dependence of $n$ from the near-ultraviolet (NUV) to the near-infrared (NIR) range is a single-pole Sellmeier function:

$$n^2(\lambda) - 1 = \frac{a_0\lambda^2}{\lambda^2 - \lambda_0^2}\,. \tag{2.17}$$

Examples of the $n$ dependence on $\rho$ and data points of $n$ as a function of $\lambda$ for a 2 cm-thick tile from Aerogel Factory Co., Ltd. fitted with Eq. 2.17 are shown in Fig. 2.4.

### 2.4.2 Aerogel transparency

The aerogel transparency to impinging photons or Cherenkov photons emitted in a tile is limited by Rayleigh scattering and absorption, resulting in dispersion or loss.

Due to its granular structure, made of $SiO_2$ grains and pores with a typical length scale

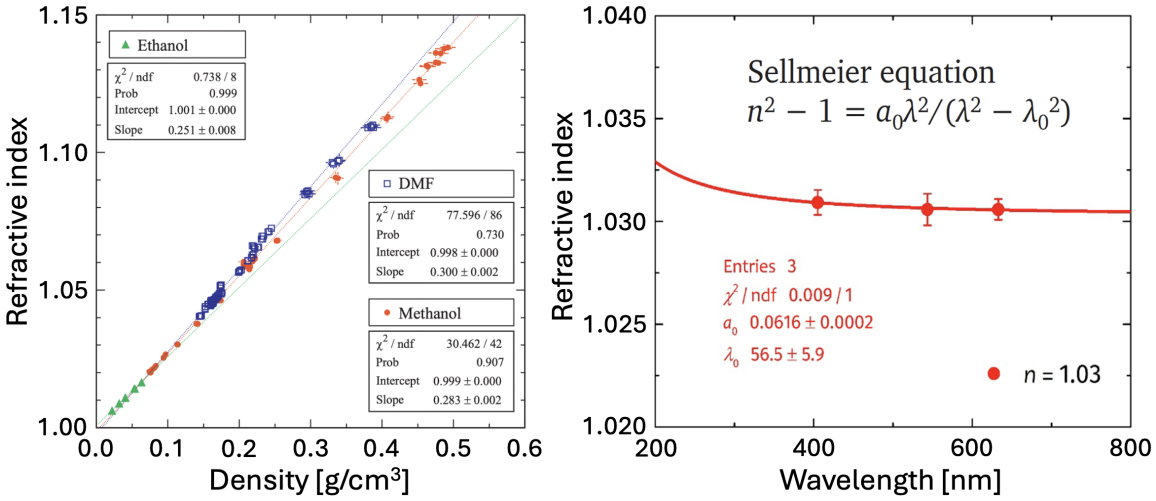


**Figure 2.4:** Left: Measured refractive index at $\lambda$ =405 nm as a function of density for aerogel tiles synthesized using various solvents. Taken from [61]. Right: Measured refractive index as a function of wavelength for an aerogel tile with a nominal refractive index of $n = 1.03$. Data points, provided by Aerogel Factory Co., Ltd., are fitted with a single-pole Sellmeier function.

of a few nm, the transport of near-ultraviolet (NUV) and visible photons in aerogel is affected by Rayleigh scattering, consisting in the elastic scattering of photons by atoms or molecules much smaller than the wavelength of the incident light [65, 66, 67]. The scattering intensity scales inversely with the fourth power of the wavelength, $\lambda^{-4}$. The probability density function $f(\cos\theta_s)$ for the scattering angle $\theta_s$ relative to the initial photon direction scales as $1 + \cos^2\theta_s$. When Rayleigh scattering occurs, Cherenkov photons lose their directionality and, if detected, contribute only as background.

Photons propagating through silica aerogel tiles can undergo absorption. Measurement results show that $\Lambda_A$ exhibits a pronounced $\lambda^8$-dependence around 250 nm, while it remains nearly constant throughout most of the visible region. At around 400 nm the typical absorption length $\Lambda_A$ is of the order of tens of cm, while the Rayleigh scattering length $\Lambda_S$ is only a few cm [68]. Within the wavelength range relevant for the studies presented in this work, internal absorption plays only a secondary role, while Rayleigh scattering remains the dominant limitation to photon transmission.

Absorption and scattering affect the transmittance $T$, defined as the fraction of incident light that remains in the forward direction after traversing the medium. It can be expressed in terms of the scattering length $\Lambda_S$ and the absorption length $\Lambda_A$ as [69]:

$$T = \exp\left(-\frac{t}{\Lambda_T(\lambda)}\right) \qquad \text{with} \qquad \Lambda_T(\lambda) \equiv \left(\frac{1}{\Lambda_S(\lambda)} + \frac{1}{\Lambda_A(\lambda)}\right)^{-1}, \tag{2.18}$$

where $t$ is the optical path length and $\Lambda_T$ is the transmission length of the sample.

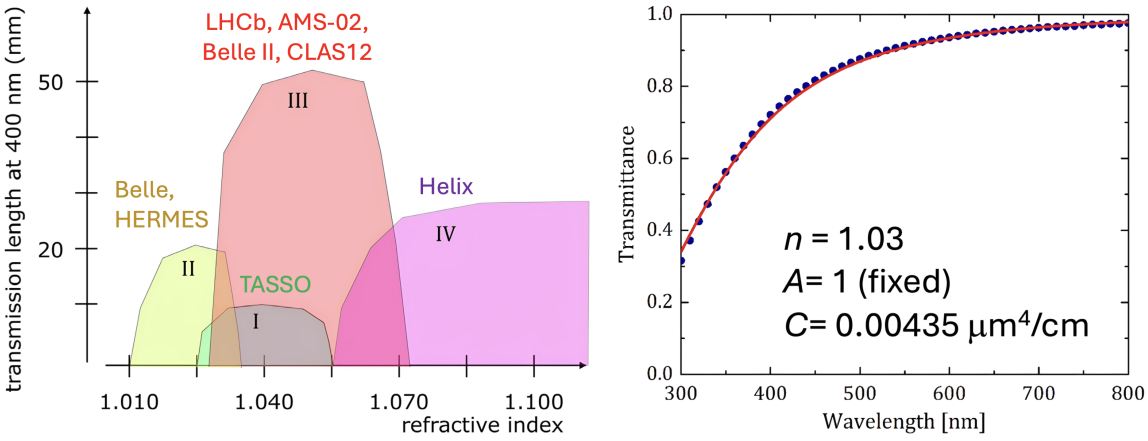


**Figure 2.5:** Left: Aerogel production history shown in the transmission length and refractive index plane [71]. Right: Transmittance as a function of wavelength for an aerogel tile with refractive index $n = 1.03$. Data points, provided by Aerogel Factory Co., Ltd., are fitted with Hunt's formula.

A common parametrization of the measured transmittance of an aerogel sample, valid for photons with wavelengths spanning from the near-ultraviolet (NUV) to the near-infrared (NIR) region over an effective path length $t$, is given by Hunt's formula [70]:

$$T = A \exp\left(-\frac{Ct}{\lambda^4}\right), \tag{2.19}$$

where $C$ is related to Rayleigh scattering, while $A$ accounts for absorption losses.

The left panel of Fig. 2.5 illustrates the history of the development of aerogel radiators for various experiments, highlighting the improvements in transmission length for various refractive indices at $\lambda =$ 400 nm [71]. In current production, tiles with $n \approx 1.03$ exhibit $\Lambda$ larger than 50 mm. The right panel of Fig. 2.5 shows the transmittance as a function of $\lambda$ for a tile from Aerogel Factory Co., Ltd. fitted with Eq. 2.19.

## 2.5 Silicon Photomultipliers

A Silicon Photomultiplier (SiPM) is a photon detector consisting of an array of passively quenched Single-Photon Avalanche Diodes (SPADs) connected in parallel to a common anode and cathode [42], as illustrated in the left panel of Fig. 2.6.

Each SPAD, hereafter referred to as microcell, is a digital (yes/no) photodiode with a typical pitch of 10 µm to 100 µm designed to operate in Geiger mode when reverse-biased above the breakdown voltage $V_{\mathrm{bd}}$, defined as the minimum bias required to initiate a self-sustaining avalanche. Typical $V_{\mathrm{bd}}$ values are between 20 V and 80 V at

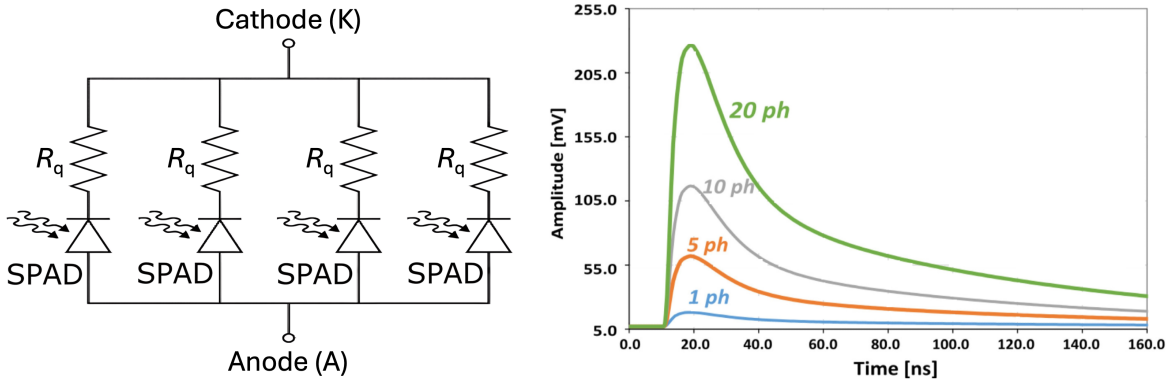


**Figure 2.6:** Left: Schematic representation of the structure of a SiPM. Right: Output signals from a SiPM with different number of triggered microcells. Reproduced from [72].

room temperature and decrease of up to 60 mV/°C with the decreasing temperature.

When a photon is absorbed in the depletion region of a SPAD, a primary electron-hole pair is produced. Under the action of the electric field, the charge carriers created in the depletion zone drift towards the amplification zone, where avalanche multiplication occurs, with a gain $G$, defined as the average number of carriers generated during an avalanche, typically in the range $10^5$–$10^9$ [73, 74]. After avalanche amplification, the charge carriers induce a detectable signal at the readout electrode. The discharge is quenched by the quenching resistor $R_q$, having typical values from 100 kΩ to 1 MΩ. The signal rise time is set by the rapid avalanche development, giving a pulse with a peaking time of a few hundred ps. Microcells have a typical capacitance $C_{pix} \approx 100$ fF. The large $R_q$ controls the decay time, typically 10 to 100 ns. The total collected charge is given by $Q_{pix} = C_{pix} V_{ov}$, where $V_{ov} = V_{bias} - V_{bd}$ is the overvoltage, typically a few volts. The gain is given by $G = Q_{pix}/e$, where $e$ is the elementary charge.

Each microcell in the SiPM operates independently with respect to the others. When a photon is absorbed, the resulting avalanche is confined to the microcell in which it was initiated, while all other microcells remain fully charged and ready to detect photons. The output signal of the SiPM is the sum of the signals from all firing microcells. An example of an output waveform is shown in the right panel of Fig. 2.6. If the number of incident photons is much smaller than the number of available microcells, as in the case of the single photon signals for a RICH detector, the SiPM response is linear, with the output current proportional to the number of absorbed photons.

For the applications in the ALICE 3 bRICH, the most relevant characteristics are the photon detection efficiency, the single-photon time resolution, the dark count rate, correlated noise, and radiation damage effects. The details are summarized below.

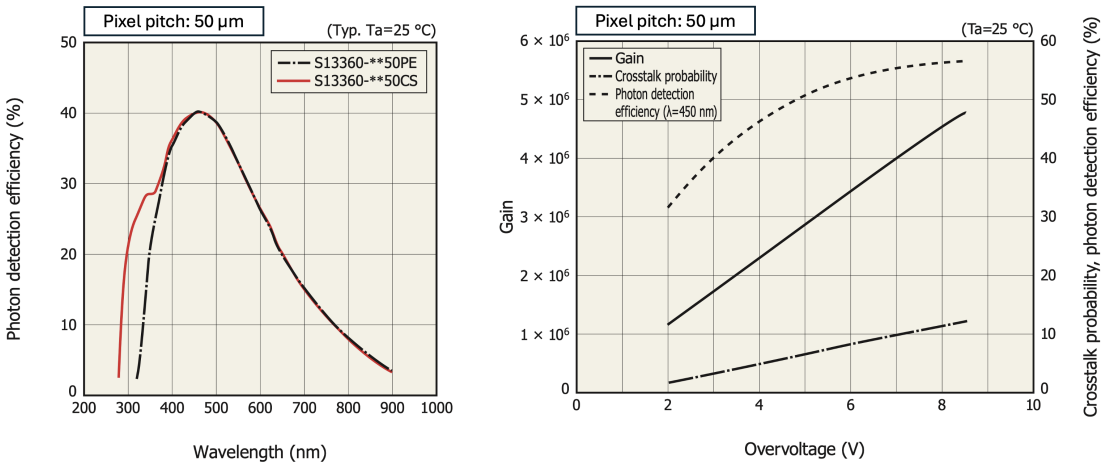


**Figure 2.7:** PDE as a function of photon wavelength (left) and overvoltage (right) at $T = 25°C$ with unpolarised normal incident light for Hamamatsu S13360 SiPMs. Reproduced from [75].

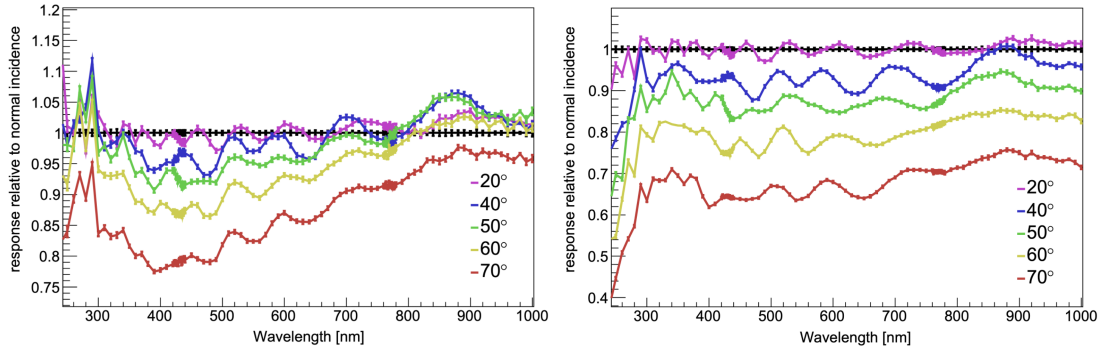


**Figure 2.8:** PDE as a function of photon wavelength for P polarisation (left) and S polarisation (right) at various photon incidence angles for Hamamatsu S13360 SiPMs. Reproduced from [76]

### 2.5.1 Photon detection efficiency

The photon detection efficiency (PDE) of a SiPM is the probability that an incident photon is absorbed and generates a self-sustaining avalanche in a microcell. It can be expressed as the product of three main contributions [42]:

$$\mathrm{PDE}(V_{\mathrm{ov}}, \lambda) = QE(\lambda) \cdot T_{\mathrm{p}}(V_{\mathrm{ov}}, \lambda) \cdot FF, \tag{2.20}$$

where $QE(\lambda)$ is the quantum efficiency for an electron-ion pair creation, $T_{\mathrm{p}}(V_{\mathrm{ov}}, \lambda)$ the avalanche triggering probability, and $FF$ the fill factor, defined as the fraction of active area. The PDE depends on the photon wavelength, the overvoltage, and the photon incidence angle and polarization, which is particularly relevant for the detection of Cherenkov photons. Figs. 2.7 and 2.8 show examples of the typical dependence of the PDE on these quantities for Hamamatsu S13360 SiPMs a microcell pitch of 50 µm.

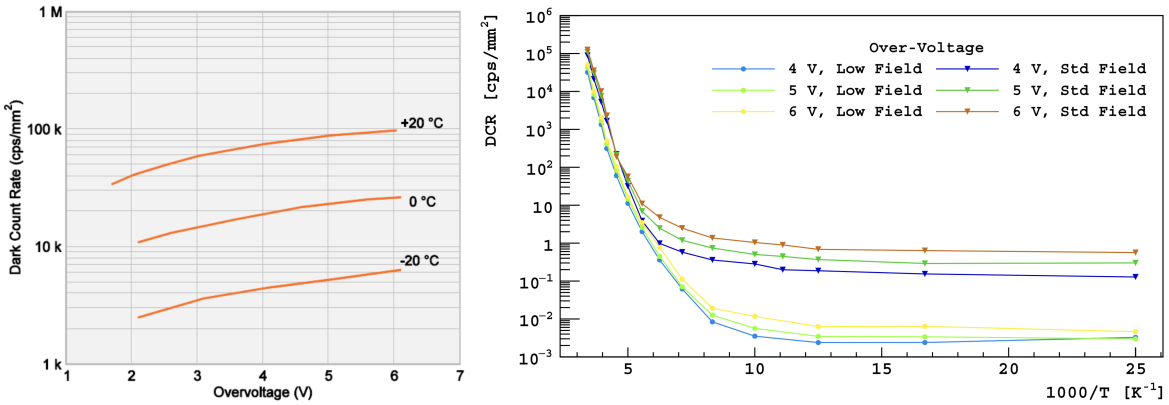


**Figure 2.9:** Examples of the measured DCR as a function of overvoltage and temperature for various FBK NUV-HD SiPMs. Reproduced from [77].

### 2.5.2 Dark count rate and correlated background

Even in the absence of incident photons, SiPMs produce output signals arising from both primary and correlated noise, including afterpulsing and optical cross-talk.

Primary noise, referred to as dark-count rate (DCR), consists of avalanches initiated by thermally generated carriers and is indistinguishable from avalanches triggered by real photons. In the temperature region of interest for this thesis, thermally generated events follow the Shockley–Read–Hall (SRH) generation–recombination mechanism, in which carriers are trapped in energy states located between the valence and conduction bands and can be released through thermal excitation mediated by phonons. Typical DCR values of SiPMs are about 50 kHz/mm$^2$ at room temperature. The DCR increases with increasing overvoltage and decreases with decreasing temperature. In particular, the DCR doubles (or halves) for every increase (or decrease) of about 10°C, making active cooling an effective means of DCR suppression. Fig. 2.9 shows examples of the typical dependence of the DCR on these quantities for FBK NUV-HD devices.

In SiPMs there are two main sources of correlated noise, originating from primary genuine photon events or DCR events, known as afterpulsing and optical cross-talk.

Afterpulses are delayed pulses created by charge carriers trapped during the avalanche amplification and released after a characteristic trapping time, typically 10-100 ns, thereby initiating new avalanches in the same microcell as the primary event. If the release occurs when the microcell is fully recharged, the afterpulse is indistinguishable from a primary dark-count event, while a release during the recharge phase produces a signal of reduced amplitude. An example is shown in the left panel of Fig. 2.10.

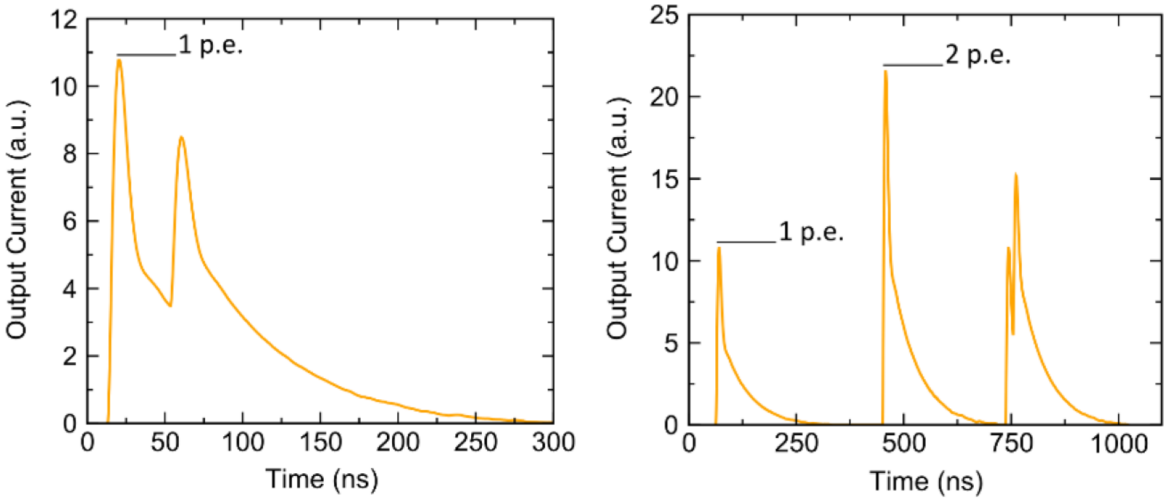


**Figure 2.10:** Left: Example of an afterpulse following a primary signal in a SiPM. Right: Examples of SiPM OC. From left to right it is possible to see a single-cell signal, a direct-OC signal (two cells fired at about the same time), and a delayed-OC (a second cell fired few ns after the first one).

Optical cross-talk (OC) signals result from photons created during the amplification process in a microcell [78, 79] reaching a neighbouring microcell, where they initiate another avalanche which can be prompt or delayed relative to the primary event. Prompt-OC occurs when an emitted photon reaches the active region of another microcell triggering an additional avalanche almost at the same time of the original avalanche. Delayed-OC involves photons that are absorbed in the undepleted region of the microcell. In this case the generated electron or hole can reach the multiplication region of the microcell by diffusion and trigger an avalanche with delays of several ns [72]. The right panel of Fig. 2.10 shows examples of direct and delayed OC.

The DCR and the contribution of correlated noise (CN) are related to the measured current $I_{\text{dark}}$ in dark conditions through the gain $G$ and the elementary charge $e$ as:

$$\text{DCR}\,(1+\text{CN}) = \frac{I_{\text{dark}}}{e\,G}\,. \tag{2.21}$$

### 2.5.3 Single-photon time resolution (SPTR)

The single-photon time resolution (SPTR) is a key performance parameter for applications involving Cherenkov photon detection. The fast rise time of SiPM signals allows the arrival time of detected photons to be determined with a precision of a few tens of picoseconds. In particular, modern SiPMs can achieve an intrinsic SPTR below 70 ps FWHM. However, the effective SPTR is limited by the performance of the front-end readout, in particular the available bandwidth and the contribution of electronic noise.

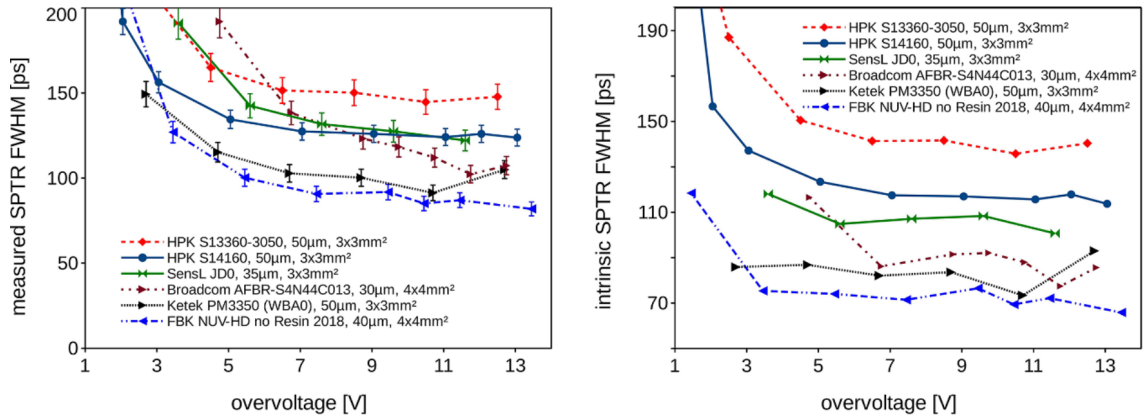


**Figure 2.11:** Measured SPTR (left) and the corresponding extrapolated intrinsic SPTR (right) for SiPMs from different manufacturers. The measurements were performed using a laser with a pulse width of 42 ps FWHM. The intrinsic SPTR was obtained by quadratically subtracting the estimated electronic noise contribution and the laser pulse width. Reproduced from [42].

Fig. 2.11 shows the measured SPTR for SiPMs from different manufacturers [42], highlighting that SPTR values better than 70 ps can be achieved with commercial SiPMs. The dominant limitation to the intrinsic SPTR arises from the terminal capacitance that the SiPM presents to the front-end electronics, which originates from the parasitic capacitances of all the microcells in the array and increases with the SiPM size [80].

### 2.5.4 Radiation damage in SiPMs

One of the main challenges in using SiPMs in high energy physics experiments is their high sensitivity to radiation damage. Comprehensive reviews on the theory of radiation damage in silicon sensors can be found in [81, 82]. Radiation damage in silicon sensors has two main effects: surface damage, caused by ionising events creating traps and fixed charges at the interface between the SiPM silicon and oxide [83], and bulk damage, due to the displacement of silicon atoms from the lattice in non-ionising events. These are typically quantified in terms of Total Ionising Dose (TID), expressed in rad or Gy, and Non Ionising Energy Loss (NIEL), expressed in 1 MeV $n_{eq}/cm^2$ [84]. The dominant observable consequence is an increase in current both below breakdown, referred to as the leakage current $I_{leak}$ and due to surface damage, and above breakdown, referred to as the dark current $I_{dark}$ and corresponding to an increased DCR due to bulk damage.

Fig. 2.12 shows the current–voltage characteristics at 20°C of an NUV HD cryo FBK SiPM irradiated with protons, thus experiencing both surface and bulk damage. The dark current $I_{dark}$, and therefore the DCR, increases linearly with fluence.

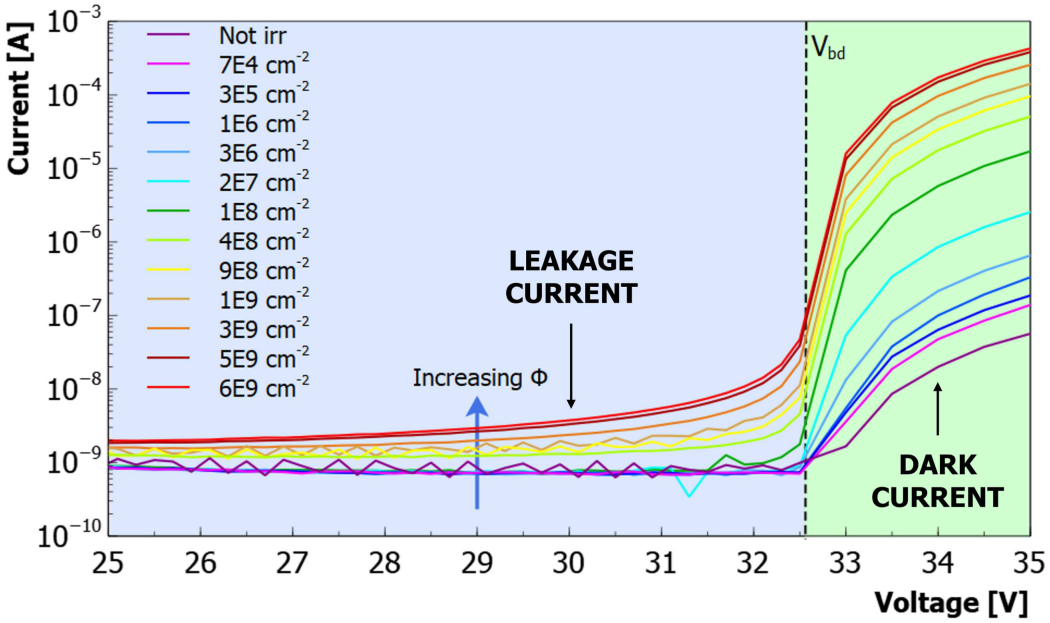


**Figure 2.12:** Reverse current–voltage characteristics at 20°C of a NUV-HD-cryo FBK SiPM irradiated with protons at different fluences. The current increase below (blue) and above (green) breakdown reflects the effects of surface and bulk damage, respectively. Reproduced from [85].

An increase of the DCR by about a factor $10^3$ is typically observed for commercially available SiPMs when irradiated to fluence levels of $10^{10}$ 1 MeV $n_{eq}/cm^2$ with respect to the pre-irradiation condition. An important consequence of the DCR increase is the loss of the single photon resolution. When cooled, the DCR is reduced and, below suitable temperatures, SiPMs can still resolve single photons even after severe irradiation. Radiation induced defects can be partially annealed at elevated temperatures [84]. The combined use of cooling and annealing cycles at high temperature is therefore crucial for defining a reliable operating strategy in any high-radiation environment.

# Chapter 3

# Design of the ALICE 3 bRICH

My research activity focused on the design and optimisation of the ALICE 3 barrel RICH (bRICH) detector. I conducted conceptual and feasibility studies on the detector layout and the photodetector module concept aimed at optimising the overall reconstruction performance and, consequently, the PID reach. All the conclusions reported in this chapter were obtained through and supervised with comprehensive performance simulation studies, with the ultimate benchmark being the detector response from pp to central Pb–Pb collisions, as discussed in detail in Chapter 4.

The ultimate concept for the bRICH proved to be a projective, proximity-focusing geometry segmented into 24 longitudinal sectors, each further divided into 36 modules combining an aerogel tile with a dedicated photodetector unit equipped with SiPMs.

Beyond the definition of the baseline configuration, I also carried out dedicated R&D studies on three possible upgrade options that preserve the main layout specifications while offering significant gains in the overall PID performance, physics reach and costs.

- The use of a proper gaseous radiator in the bRICH expansion gap to enhance the electron identification via threshold-based discrimination of heavier particles.
- The integration of Cherenkov-based charged-particle timing using the bRICH SiPMs in view of combining the bRICH and the oTOF in a single detector.
- The use of SiPMs with an active area of $1\times1$ mm$^2$ coupled with passive light concentrators in place of the baseline $2\times2$ mm$^2$ to reduce the SiPM DCR and cost by a factor of four while keeping the same number of channels and acceptance.

This chapter is structured as follows. In Section 3.1 I present the bRICH target PID coverage requirements that motivate the choice of aerogel as Cherenkov radiator and SiPMs as photon sensors. In Section 3.2 I summarize the evolution of the bRICH design from the original cylindrical layout, discussed in detail in Section 3.3, to my projective proximity-focusing layout, discussed in detail in Section 3.4. The possibility of enhancing the electron identification capabilities with respect to the aerogel reach by using a proper eco–friendly heavy-gas mixture is then detailed in Section 3.5. The possibility of integrating Cherenkov-based charged-particle timing measurements using the bRICH SiPMs is addressed in Section 3.6. Finally, the option of using smaller SiPMs coupled with light concentrators to reduce the SIPM DCR and cost, as well as preliminary performance studies, is discussed in Section 3.7.

## 3.1 ALICE 3 bRICH target PID coverage

Assuming the baseline specifications of the ALICE 3 iTOF and oTOF layers, with a target time resolution of 20 ps, a separation power greater than $3\sigma$ for e/$\pi$, $\pi$/K and K/p is expected from a few tens of MeV/$c$ (lower limit set by the curvature of charged tracks in the magnetic field) up to approximately 0.7, 2.3, and 3.8 GeV/$c$, respectively, at $\eta = 0$, where the path length travelled by the particles is minimal. At larger $|\eta|$, the momentum reach increases since particles travel longer distances before reaching the TOF layers. Fig. 1.9 shows the expected $\eta$–$p_{\mathrm{T}}$ regions covered by the TOF layers.

The goal of the ALICE 3 bRICH is to extend e/$\pi$, $\pi$/K and K/p discrimination enabling full PID coverage from the TOF upper limits up to at least 2, 10 and 16 GeV/$c$, respectively. A safety margin, with overlap between the expected TOF and RICH momentum coverage, must be foreseen to ensure robust PID performance under realistic operating conditions. This overlap mitigates, for instance, the impact of a TOF resolution potentially worse than the nominal 20 ps target. This imposes stringent requirements on the bRICH design in terms of radiator material, photodetector technology, and detector geometry. These considerations lead to the choice of aerogel with refractive index 1.03 as the Cherenkov radiator and Silicon Photomultipliers (SiPMs) as photon sensors, in a layout designed to achieve an overall ring angular resolution better than 1.5 mrad in the Cherenkov-angle saturation regime. Considerations on the available space and the positioning of aerogel tiles and SiPM modules lead to the choice of a proximity-focusing geometry to achieve the target ring angular resolution.

| Material | $n$ (400 nm) | $p_{\text{th}}$ [GeV/$c$] | | | |
|---|---|---|---|---|---|
| | | e | $\pi$ | K | p |
| Ar | 1.000287 | 0.021 | 5.84 | 20.66 | 39.11 |
| $CO_2$ | 1.000459 | 0.017 | 4.62 | 16.34 | 30.92 |
| $C_4F_{10}$ | 1.0014 | 0.010 | 2.64 | 9.35 | 17.70 |
| Aerogel | 1.02 | 0.003 | 0.70 | 2.46 | 4.66 |
| | 1.03 | 0.002 | 0.57 | 2.01 | 3.80 |
| | 1.04 | 0.002 | 0.49 | 1.73 | 3.28 |
| NaF | 1.33 | 0.0006 | 0.160 | 0.565 | 1.069 |
| $SiO_2$ | 1.47 | 0.0005 | 0.130 | 0.459 | 0.870 |

**Table 3.1:** Cherenkov momentum thresholds of common radiators for e, $\pi$, K, and p.

### 3.1.1 The choice of aerogel as Cherenkov radiator

The first design consideration is the choice of the radiator refractive index $n$, which defines the momentum range over which the detector can provide effective separation. The choice is primarily driven by the threshold for Cherenkov emission and the target upper momentum reach to ensure continuity with the ALICE 3 TOF PID capabilities.

Table 3.1 shows the Cherenkov momentum thresholds for e, $\pi$, K and p for materials in a wide $n$ range. Fig. 3.1 shows my analytical calculations for the Cherenkov angle, the mean number of detected photons and the expected ring angular resolution as a function of momentum for e, $\pi$, K and p with $n = 1.02, 1.03$, and 1.04, and the resulting e/$\pi$, $\pi$/K and K/p separation power. I assumed $N_0L = 400$ for the calculation of the number of detected photons with Eq. 2.14 and the target 1.5 mrad resolution at saturation. These calculations show that the optimal value of $n$ which allows the desired coverage for the ALICE 3 bRICH is approximately 1.03. Lower values of $n$ raise the threshold beyond the TOF upper limits, while higher values of $n$, despite the larger photon yield, reach saturation faster, limiting the upper momentum reach.

The requirement on the refractive index dictates the choice of aerogel as the radiator, since it is the only known solid material providing such a low refractive index, as discussed in Section 2.4. Possible alternatives, such as high-pressure gases or cryogenic liquids (e.g. helium with $n = 1.031$), are significantly more challenging to implement, leaving aerogel as the only practical solution.

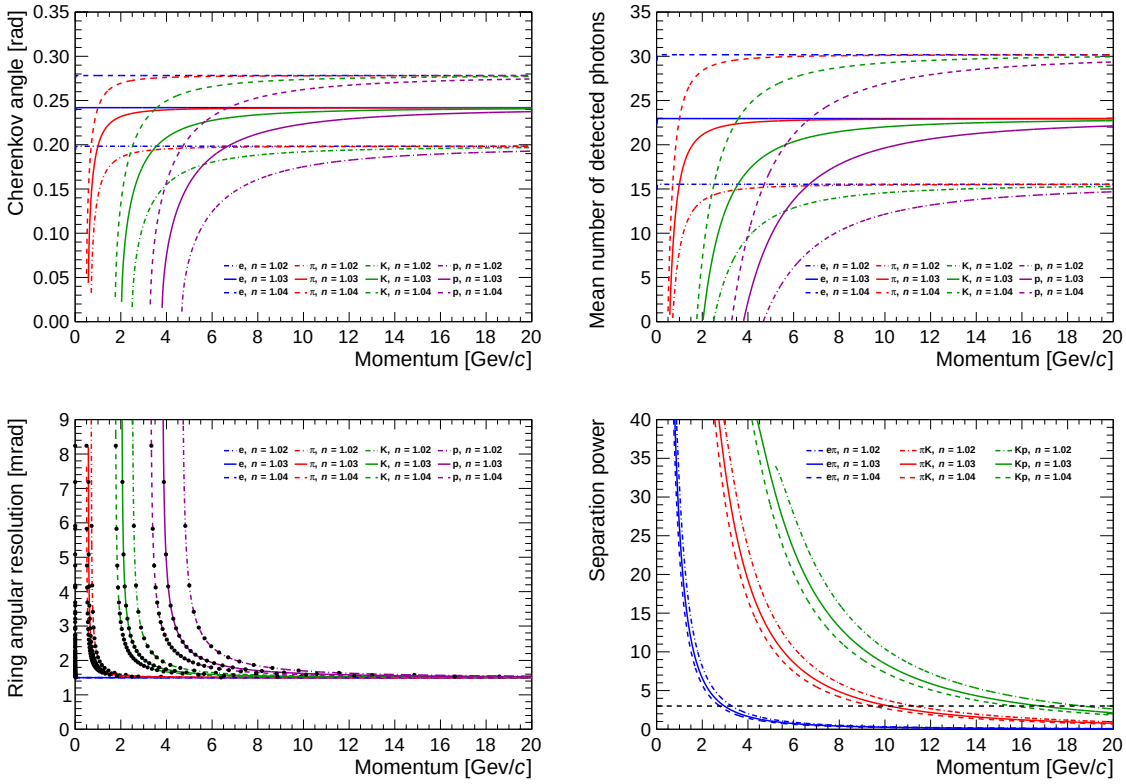


**Figure 3.1:** Cherenkov angle (top left), mean number of detected photons (top right) and the expected ring angular resolution (bottom left) as a function of momentum for e (blue), π(red), K (green) and p (magenta) with $n = 1.02$ (dash-dotted line), $n = 1.03$ (solid line) and $n = 1.04$ (dashed line). The bottom-right plot shows the separation power for π/e (blue), K/π (cyan) and p/K (red). The curves are obtained by setting $N_0 L$ at 400 and the saturation ring resolution at 1.5 mrad.

### 3.1.2 The choice of SiPMs as photon sensors

The choice of the photon sensors for the ALICE 3 bRICH is primarily driven by the radiator optical properties. As shown in Section 2.4, while transparent in the visible range, aerogel becomes opaque in the UV range, where most of the incident light is diffused by Rayleigh scattering. Therefore, the photon sensors must be sensitive to visible light, which rules out gaseous photon detectors. The following requirements are then defined to ensure efficient operation throughout the ALICE 3 lifetime.

- **Spectral sensitivity.** Sensors must be efficient for $\lambda > 300\,\text{nm}$. A photon-detection efficiency $> 30\%$ at $\lambda \approx 400$ nm is required for the target photon yield.
- **Granularity.** A pixel size of $1 \times 1$ mm$^2$ to $3 \times 3$ mm$^2$ is required to limit photon localization uncertainty in the Cherenkov angle while keeping the number of channels and the dark count per channel manageable.

- **Single-photon timing.** A time resolution better than 100 ps (rms) at the single-photon level is required. Fast timing is crucial for suppressing uncorrelated dark counts improving ring reconstruction and background rejection.
- **Insensitivity to magnetic field.** The photon sensors must operate stably in the 2 T solenoidal field, with field lines nearly parallel to the sensor planes.
- **Radiation tolerance.** Photon sensors must operate stably under the expected total ionising dose (TID) of units of $10^4$ rad and non-ionizing energy loss (NIEL) of units of $10^{11}$ 1-MeV $n_{eq}/cm^2$ over Run 5. The design goal is a dark count rate (DCR) lower than 1 MHz/mm$^2$ at the operating conditions.

The requirements on spectral sensitivity, granularity, and timing in the bRICH region can, in principle, be fulfilled by different technologies such as Silicon Photomultipliers (SiPMs) or vacuum-based devices, including Microchannel-Plate Photomultipliers (MCP-PMTs [86]), Large-Area Picosecond PhotoDetectors (LAPPDs) [87], and High-Resolution Picosecond PhotoDetectors (HRPPDs) [43].

However, vacuum-based detectors are highly sensitive to magnetic fields, making their application unfeasible for the bRICH. By contrast, SiPMs are almost unaffected by magnetic fields, making them the most suitable choice for this application [88]. A further advantage of using SiPMs is that they operate at relatively low bias voltages, typically a few tens of volts, in contrast to the high-voltage operation required by vacuum-based technologies. In addition, SiPMs offer clear advantages in terms of compactness and lower cost compared to these bulkier and more expensive alternatives.

The main limitations of SiPMs are the high DCR and the poor radiation tolerance. Increased DCR is expected due to the integrated TID and NIEL during operation. To ensure stable operation throughout the ALICE 3 lifetime, cooling to temperatures of -40°C or below is required, together with a strategy to mitigate the DCR during operation while preserving the target single-photon sensitivity. In this context, I developed a data-driven operation strategy and ageing models, as discussed in Chapter 5.

### 3.1.3 Optimization of the aerogel thickness

The optimal thickness of the aerogel tiles for the considered proximity-focusing layout is determined by both the aerogel transparency, mainly limited by the Rayleigh scattering of NUV photons, the impact on the single photon angular resolution through the geometric uncertainty on the photon emission depth, as discussed in Section 2.3.2, and the mean number of detected ring photons accounting for the SiPM PDE.

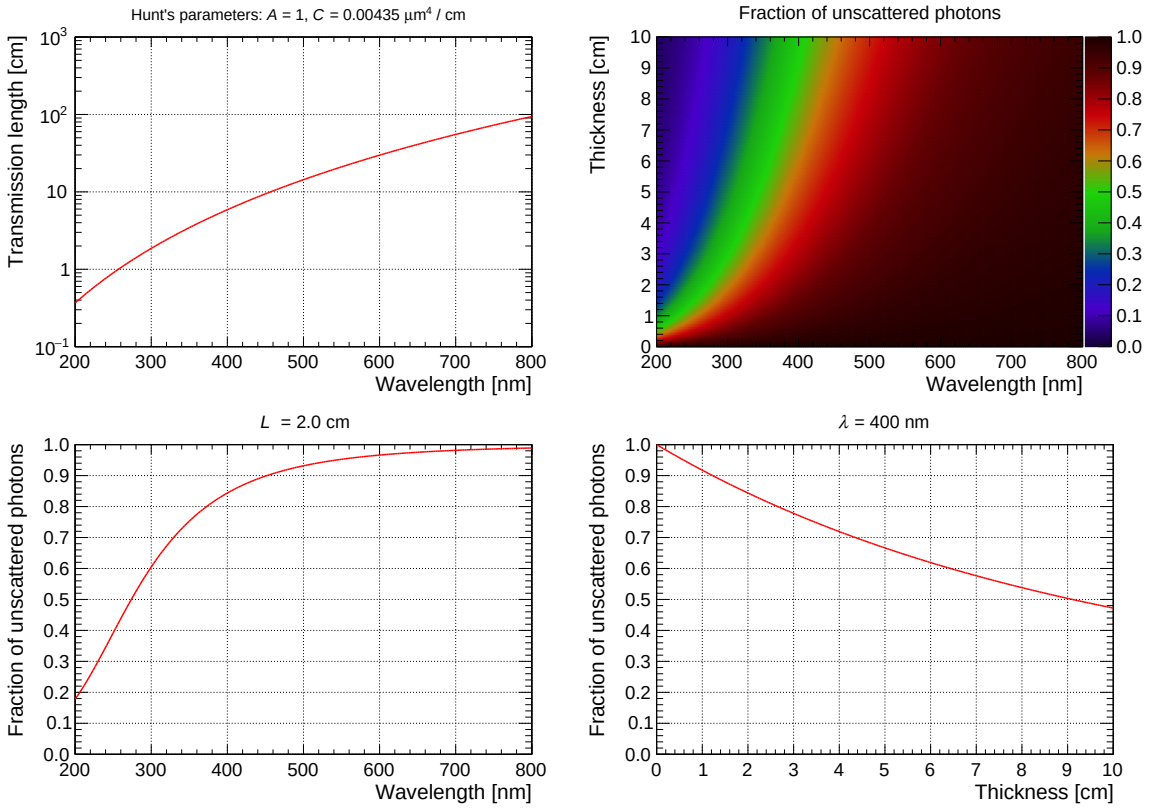


**Figure 3.2:** Aerogel transmission length as a function of wavelength used for calculations (top left) and expected fraction of unscattered photons as a function of wavelength $\lambda$ and radiator thickness $L$ (top right). The corresponding projections for $L = 2$ cm (bottom left) and for normally incident particles at saturation $\lambda = 400$ nm (bottom right) are also shown.

Fig. 3.2 shows the results of my calculations for the expected fraction of signal photons of wavelength $\lambda$ produced along the tile depth for normally incident tracks at saturation that traverse an aerogel sample of thickness $L$ without undergoing Rayleigh scattering as a function of both $\lambda$ and $L$ assuming the transmission length $\Lambda_{\mathrm{T}}(\lambda)$ calculated using the Hunt's parameters reported in the right panel of Fig. 2.5. The projections for $L = 2$ cm as a function $\lambda$ and for $\lambda = 400$ nm as a function of $L$ are also shown. The value of $F_{\mathrm{T}}$ increases with $\lambda$ and decreases with $L$. For example, $F_{\mathrm{T}} = 84\%$ at $\lambda = 400$ nm for $L = 2$ cm. This rises to nearly 93% for photons $\lambda = 500$ nm, while it decreases to about 78% if $L$ is increased to 3 cm. The useful production of Cherenkov light is effectively restricted to the visible range. In addition, although the number of photons increases linearly with the radiator thickness $L$, the number of useful photons for PID applications saturates due to scattering losses in the aerogel tile.

Fig. 3.3 shows my calculation results for the achievable single photon and ring angle resolutions at saturation as functions of the SiPM pixel size and the expansion gap thickness, assuming aerogel tiles with refractive index $n = 1.03$ and thickness 1.5, 2.0,

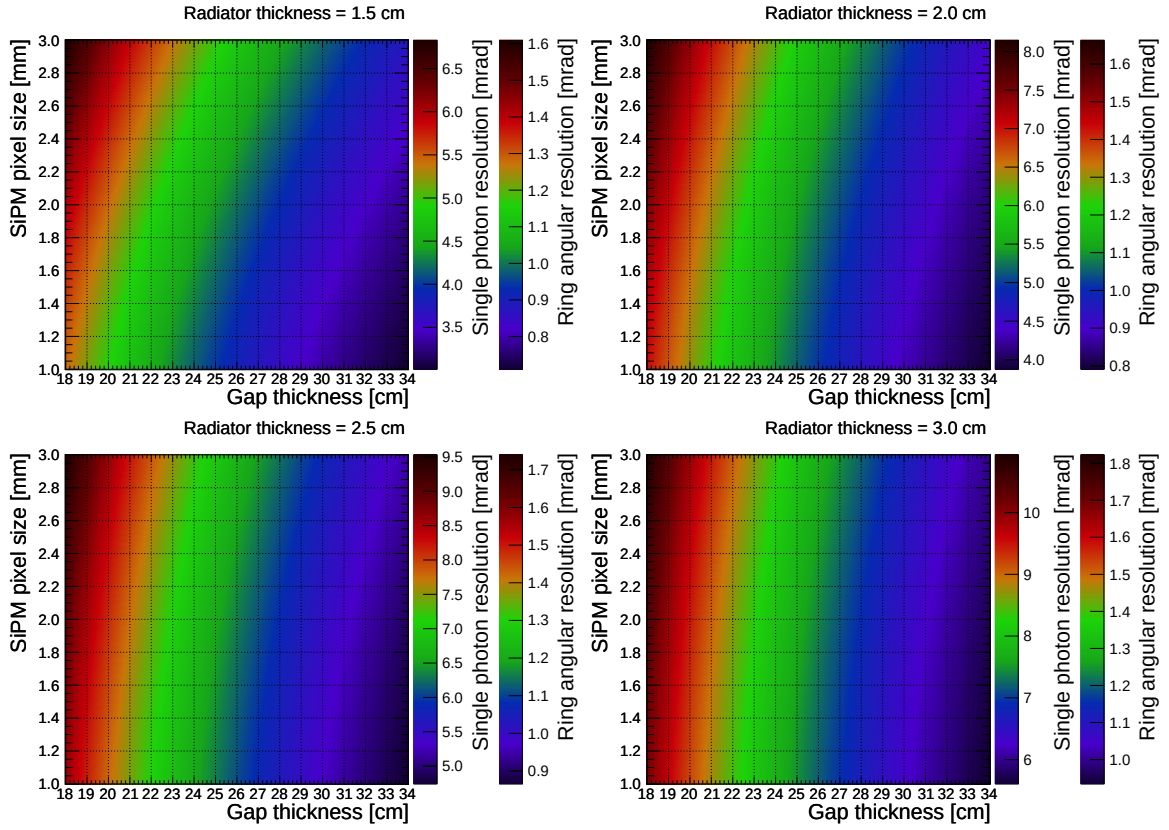


**Figure 3.3:** Single photon and ring angle resolutions at Cherenkov angle saturation in a proximity focusing geometry, as functions of the SiPM pixel size and the expansion gap thickness. Curves are shown for radiator thicknesses of 1.5 (top left), 2.0 (top right), 2.5 (bottom left), and 3.0 (bottom right) cm. The calculation assumes a uniform refractive index $n = 1.03$ and uses the detected photon yield derived from the reference PDE of Hamamatsu S13360-**50 SiPMs.

2.5, and 3.0 cm. For the ring resolution calculation, I used the detected photon yield corresponding to the PDE of Hamamatsu S13360-**50 SiPMs shown in Fig. 2.7. The explored SiPM pixel size and gap thickness ranges coincide with the full parameter space investigated in the bRICH optimization. Aerogel tiles thinner than 1.5 cm were discarded because the resulting photon yield was too small for stable pattern recognition. Conversely, for tiles thicker than 2.0 cm, despite the larger number of produced photons, the ring angle resolution is worse than in the 2.0 cm case due to the significant worsening of the geometric contribution to the single photon resolution and the enhanced photon scattering in the tile.

Therefore, the combination of these results on the fraction of unscattered photons, the expected yield at Cherenkov angle saturation for the reference SiPMs, and the thickness dependence of the single photon resolution indicates that the best compromise for the bRICH is obtained for a radiator thickness of 2.0 cm.

## 3.2 Evolution of the bRICH layout

The design of the bRICH evolved considerably over the course of my studies, beginning with the simple cylindrical proximity-focusing geometry originally proposed in the ALICE 3 Letter of Intent [1] and culminating in my proposal for the state-of-the-art projective proximity-focusing layout. Thanks to the studies discussed in this work, this solution was declared the baseline option in the ALICE 3 Scoping Document [2].

My design-development studies toward the final bRICH layout also passed through various intermediate configurations, including hybrid cylindrical–projective schemes and mirror-focusing designs employing spherical or parabolic mirrors.

The refinement of the design was driven, among other factors, by limitations in reconstruction performance in high-multiplicity Pb-Pb events, by the extension of the barrel acceptance from $|\eta| < 1.64$ to $|\eta| < 2.0$, by the challenges of data-load management under high DCR conditions, and by considerations on the overall cost.

In the following, after an overview of the original Letter of Intent cylindrical bRICH layout, highlighting its limitations, I focus on the latest projective bRICH geometry.

## 3.3 The original cylindrical bRICH layout

In the Letter of Intent configuration, the bRICH was initially conceived as a simple proximity-focusing cylindrical detector, chosen as the most straightforward solution in terms of mechanics, integration, and modularity.

A total longitudinal length of 5.6 m was adopted for both the aerogel radiator layer and the photodetector layer. The aerogel tiles were located at a radius of 90 cm, while the SiPM modules were located at 112 cm with respect to the beam axis, resulting in a pseudorapidity coverage up to $|\eta| = 1.64$ at the photodetector level.

An expansion gap of 20 cm was foreseen, flushed with argon gas ($n = 1.000287$ at 400 nm and 1 bar). Hydrophobic aerogel tiles with $n = 1.03$ and a thickness of 2 cm by Aerogel Factory Co., Ltd. [89] were taken as a reference for the radiator. Hamamatsu S13360-3050CS SiPMs [75] with an active area of $3 \times 3$ mm$^2$ and a microcell pitch of 50 µm were assumed were considered as a reference for the photon sensors, featuring a peak PDE of 40% at $\lambda = 450$ nm, as shown in Fig. 2.7, and an intrinsic SPTR of about 75 ps, as shown in Fig. 2.11, for operation at the recommended overvoltage $V_{\mathrm{ov}} = 3$ V.

Fig. 3.4 shows a schematic view of the cylindrical bRICH geometry, also accounting for a segmentation I defined for my preliminary studies. In particular, the system

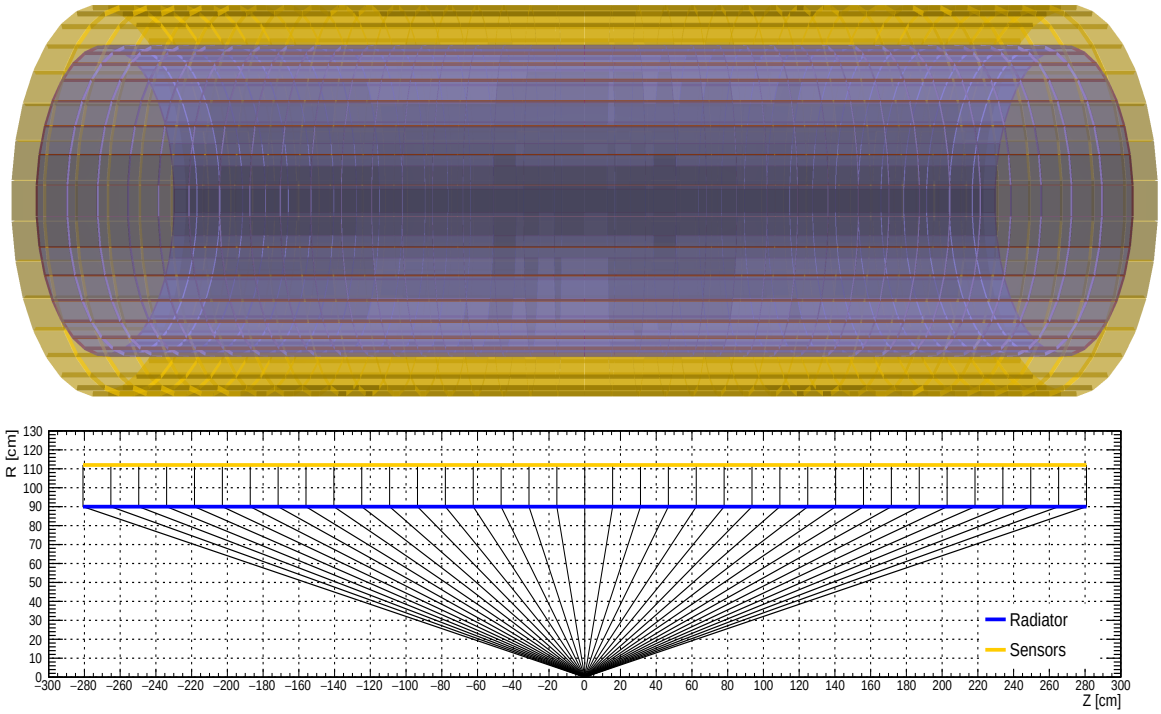


**Figure 3.4:** Schematic and longitudinal views of the original cylindrical bRICH geometry.

was segmented into 36 azimuthal sectors, each spanning an interval of 10° in the transverse plane and equipped with frames for the aerogel tiles and SiPM modules whose azimuthal length corresponds to the side of a regular polygon with 36 sides circumscribed around circumferences of 90 cm and 112 cm radius, respectively. Each sector was segmented into 36 longitudinal modules. This resulted in a maximal aerogel tile size of about $15.6 \times 15.7$ cm$^2$, corresponding to a total aerogel area of $\sim 31.7$ m$^2$. The corresponding SiPM modules reached a maximal size of about $15.1 \times 19.6$ cm$^2$, for a total SiPM area of $\sim 38.4$ m$^2$. An integration factor of 91% was originally assumed, resulting in about 3.75 million SiPM channels.

### 3.3.1 Problems of the cylindrical geometry

The combination of the design specifications in this cylindrical geometry ensures a ring angular resolution better than 1.5 mrad for charged tracks at Cherenkov angle saturation under ideal reconstruction conditions and at the single-track level. Nevertheless, several intrinsic limitations emerged from my simulation studies, as detailed below.

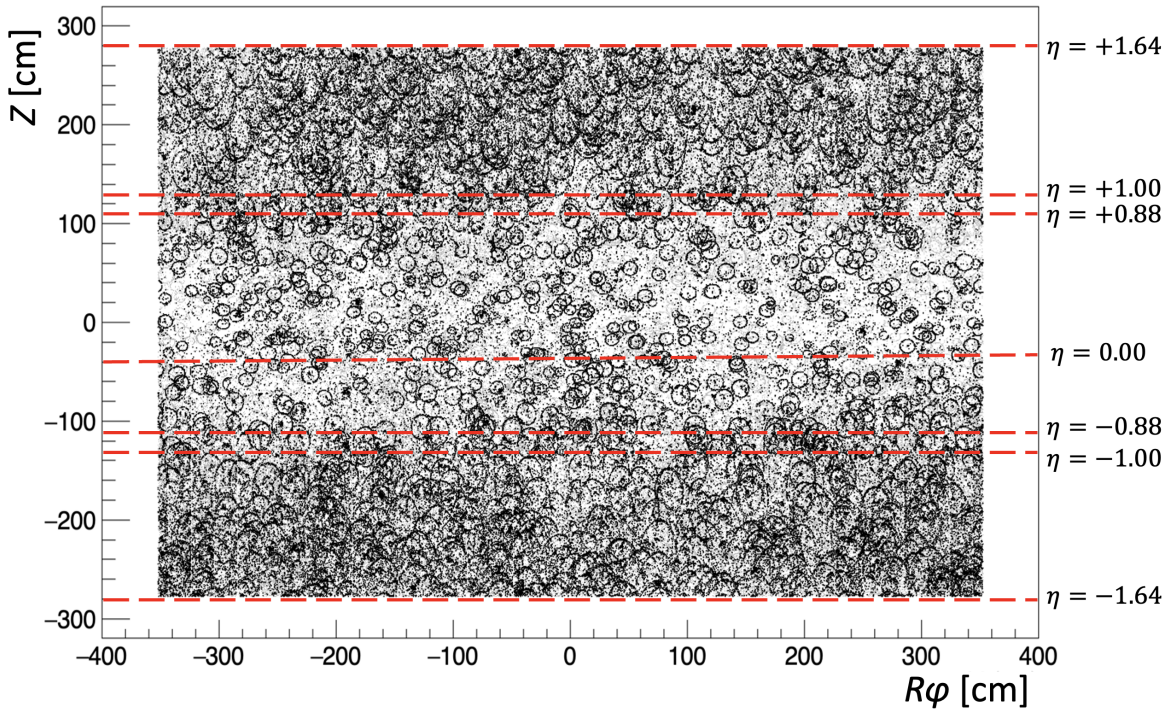


**Figure 3.5:** Photodetector hit-map in the $R\phi - Z$ plane of a single central Pb-Pb collision at $\sqrt{s_{\mathrm{NN}}} = 5.52$ TeV for the original cylindrical bRICH geometry. The SiPM PDE is not applied only for visualization purposes. The photodetector $Z$ values corresponding to various $\eta$ limits are indicated.

### Topology of Cherenkov rings at large $|\eta|$

Although the target PID performance is actually achieved at central pseudorapidities, up to $|\eta| < 1$, even in high-multiplicity Pb-Pb events, the reconstruction degrades rapidly for $|\eta| > 1$. This is clearly visible in Fig. 3.5, showing the photodetector hit-map in the $R\phi - Z$ plane of a single central Pb-Pb collision at $\sqrt{s_{\mathrm{NN}}} = 5.52$ TeV generated using my full simulation framework discussed in Section 4.1. As track inclination increases, the photons in the Cherenkov cone from the aerogel associated to a given charged track intersect the SiPM modules as an increasingly elongated ellipse, with longitudinal extensions exceeding 50 cm.

### Refraction at the aerogel–gas interface

This effect is further amplified by refraction at the aerogel–gas interface, where photons are refracted away from the normal to the aerogel tiles when entering the argon gas in the expansion gap. Because of the small refractive-index difference between aerogel and argon (1.03 for aerogel compared with 1.000287 for Ar at 400 nm), refraction remains negligible for photon incidence angles up to several tens of degrees. At larger

track inclinations, however, the associated photon angles increase and the refraction effect becomes progressively more pronounced. Beyond the critical angle, $\theta_{\mathrm{L}} \approx 76°$, photons undergo total internal reflection and fail to reach the sensor. As a result, the Cherenkov rings become increasingly larger, distorted, and eventually open.

#### Reconstruction in high-multiplicity events

In the high track-density environment of central Pb-Pb collisions, these enlarged and dispersed photon patterns overlap extensively, making Cherenkov-angle reconstruction extremely difficult due to the mutual background of photons from different tracks. This mutual background could even correlate tracks that are far apart in space, further complicating the pattern recognition and angle reconstruction, as shown in Fig. 3.5.

The reconstruction is further compromised for inclined tracks by the enhanced Rayleigh-scattering background that arises from the longer photon paths in the aerogel, with scattered photons propagating even to far-away sectors. This leads to photon patterns that extend across multiple sectors and overlap with those of unrelated tracks, ultimately compromising Cherenkov-angle reconstruction in high-multiplicity events.

For inclined tracks, the PDE of SiPMs is also degraded, as discussed in Section 2.5.1, reducing the number of detected ring photons and further complicating reconstruction.

#### Extension of bRICH acceptance to $|\eta| = 2$

In addition, with the redefinition of the ALICE 3 barrel acceptance from the original $|\eta| = 1.64$ to the baseline $|\eta| = 2$, this geometry would not only have required an extension of the total detector's longitudinal length up to 8.2 m for the radiator and 8.1 m for the photodetector, with a maximal radiator area of $\sim 46.4$ m$^2$ and a maximal photodetector area of $\sim 56.2$ m$^2$. ,but would in any case have remained suboptimal because of the refraction and total internal reflection effects discussed above.

#### Data load in high-DCR conditions

Another important limitation for this cylindrical layout emerged from the data load, driven in particular by the large SiPM DCR expected under ALICE 3 radiation conditions up to the MHz/mm$^2$ scale. This directly translates into stringent bandwidth demands on the front-end and readout electronics. An appealing mitigation strategy would be to apply a time gate, restricting the acquisition window down to 1 ns with sector-dependent timing. In this case, the number of recorded uncorrelated DCR hits

could be reduced by a factor of 25 compared to the full 25 ns bunch spacing. However, a problem arises again for $|\eta| > 1$, where highly inclined tracks cause photons from particles far apart in space to arrive at the same module with spreads of several ns. In these conditions, implementing such narrow gates is unfeasible, thus weakening the suppression of DCR hits and keeping the bandwidth requirements very challenging.

## 3.4 The projective proximity-focusing bRICH layout

The limitations above motivated the development of an alternative solution. In this context, I proposed a projective proximity-focusing layout, in which both the aerogel tiles and the SiPM modules are oriented toward the nominal collision vertex. In the following, I discuss the proposed layout in terms of geometry and module concept, and how it addresses the problems of the original cylindrical geometry.

### 3.4.1 Projective bRICH geometry

The proposed geometry is segmented into longitudinal sectors, each composed of a set of azimuthal modules. The sectors are housed in two different symmetric cylindrical vessels, leaving a gap at Z = 0 for services. Each module in a given sector includes an aerogel tile and the corresponding photodetector module, aligned parallel to one another within frames shaped as isosceles trapezoidal prisms whose upstream faces subtend the same solid angle, which varies with the sector, at the nominal interaction point. Modules are positioned such that the line connecting the intersection points of the diagonals of the upstream face of the photodetector and aerogel frames passes through the nominal interaction point and is normal to both frames.

I explored several segmentation schemes in order to cover the region $|\eta| < 2$ consistently with the space assigned to the bRICH in the ALICE 3 apparatus, corresponding to the radial region between 90 and 120 cm. I converged on a configuration with 24 sectors, each subdivided into 36 modules. The aerogel tiles and the SiPMs are arranged in the radial region between 90 cm and 117 cm, with the remaining space accounting for the target 2 cm thickness of the photodetector modules. The system spans a total longitudinal length of about 7.2 m, i.e., up to $|Z| \approx 3.6$ m on either side of the interaction point. I assumed a 1 cm gap at $R = 117$ cm and $Z = 0$ between the vessels housing the modules of the two 12-sector halves.

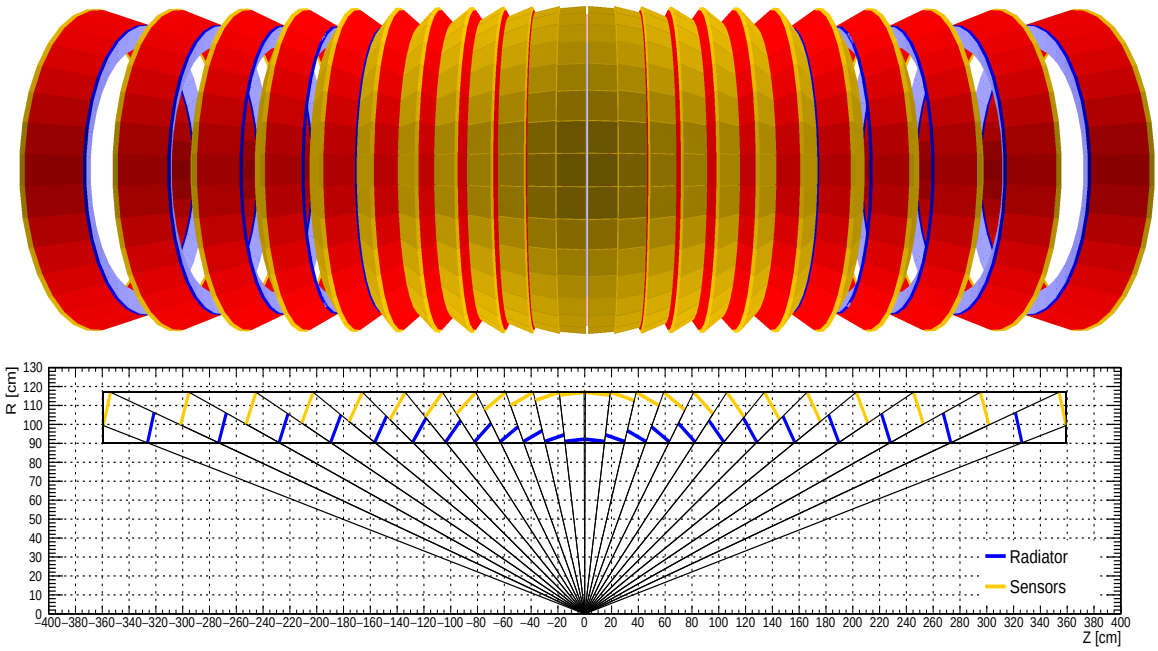


**Figure 3.6:** Schematic and longitudinal views of the proposed projective bRICH geometry.

A schematic view of the proposed projective bRICH geometry is shown in Fig. 3.6. The corresponding longitudinal view of the module positioning is also shown. The frames for the aerogel tiles and for the SiPM modules have trapezoidal profiles, tailored sector by sector. By construction, the expansion-gap width varies with the sector. I determined the optimal expansion-gap width and frame dimensions in each sector according to the following criteria.

- The expansion-gap thickness in each sector is maximized, within the radial space available to the bRICH, to optimize the single-photon angular resolution.
- The geometries of the frames for the aerogel tiles and the photodetector modules are chosen to ensure maximum acceptance for impinging charged particles originating from the nominal interaction point.

The values of the upper base, lower base and height of the trapezoidal frames for the aerogel tiles and the sensor modules for the sectors in the projective bRICH layout, as well as the corresponding thickness of the expansion gap, are shown in Fig. 3.7. A schematic view of the stacking of the frames for the sensor modules in each sector is also shown for visualization purposes. A systematic formulation of the algorithm I developed for the generation of this projective geometry is presented in Appendix B.

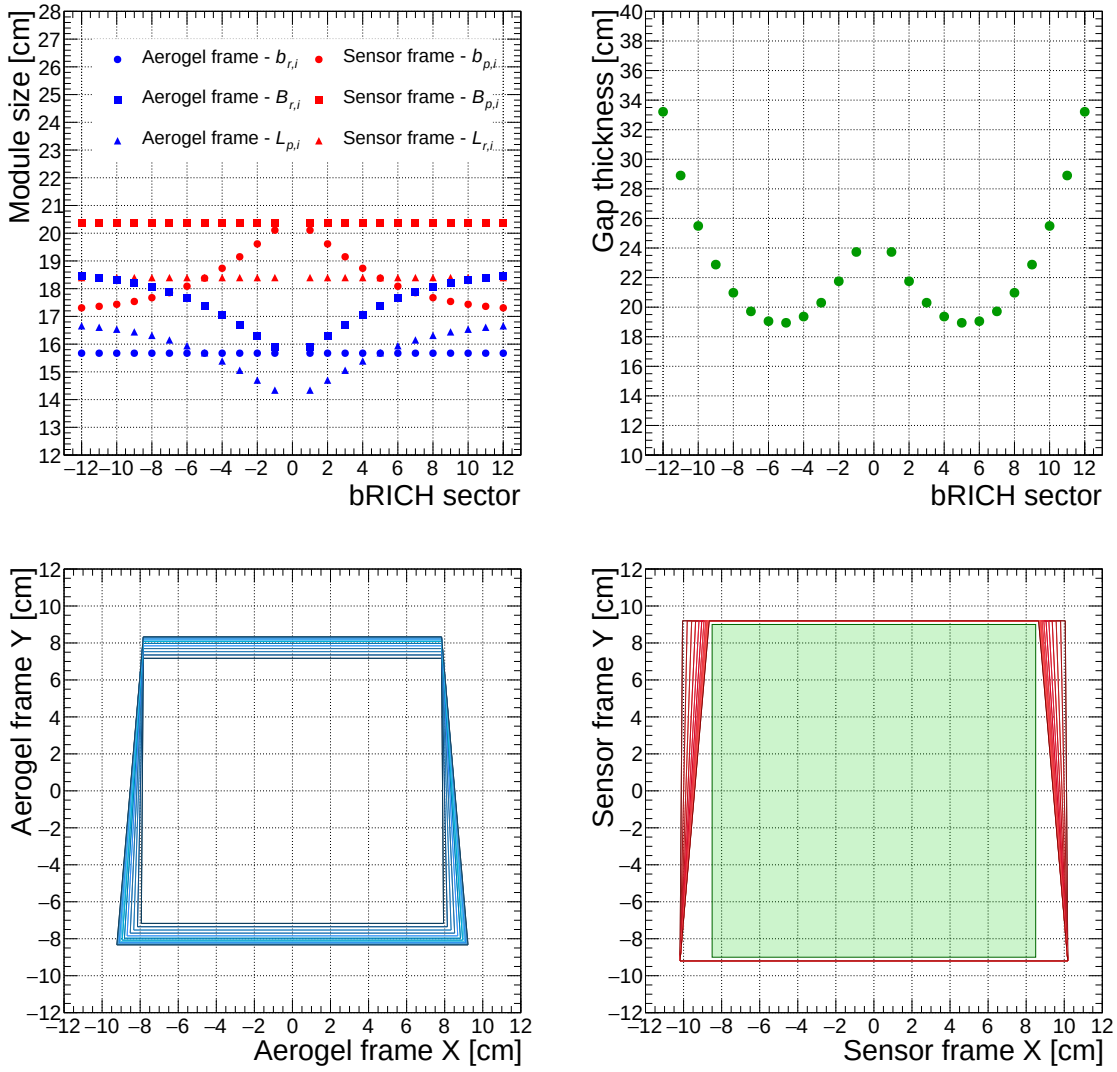


**Figure 3.7:** Top left: Upper base (squares), lower base (circles) and height (triangles) of the trapezoidal frames for the aerogel tiles (blue) and the sensor modules (red) for the sectors in the projective bRICH layout. Top right: Thickness of the expansion gap for the modules in each sector. Bottom left: Schematic view of the stacking of the frames for the aerogel tiles in each sector. Bottom right: Schematic view of the stacking of the frames for the sensor modules in each sector. The green rectangle marks the nominal 17×18 cm$^2$ module footprint considered in the modular option.

### 3.4.2 Radiator and photodetector

Hydrophobic aerogel tiles with n = 1.03 at 400 nm and a thickness of 2 cm produced by Aerogel Factory Co., Ltd. are still taken as the reference radiator option.

The same Hamamatsu S13360 SiPM technology as in the original cylindrical layout is also retained. However, the SiPM size is reduced from $3 \times 3$ mm$^2$ to $2 \times 2$ mm$^2$, to

gain angular resolution, reduce the per-channel DCR by more than a factor of two, lower the terminal capacitance, and improve timing when coupled to the electronics.

Due to the smaller SiPM size, a reference packaging factor of about 83% is assumed, compared to the 91% reference of the cylindrical geometry. This assumption is based on the commercial Hamamatsu S13361-2050AE-08 series arrays [90], featuring SiPMs with the target $2 \times 2$ mm$^2$ active area with a pitch of $2.2 \times 2.2$ mm$^2$.

Owing to the large SiPM DCR increase expected at NIEL levels of order $10^{11}$ (1-MeV $n_{eq}/cm^2$), cooling to -40°C or below is mandatory, together with an annealing scheme that heats the SiPMs to 70°C or above, as discussed in Chapter 5.

The front-end and readout electronics are still under active discussion. At the time of writing this thesis, the baseline front end is the DENEB ASIC, a 1024-channel, high-rate device under development at INFN Torino for the GRAIN detector at DUNE, building on the current ALCOR ASIC [91]. The 1024 channels are arranged in 32 columns, with one LVDS transceiver per column operating at 320 Mb/s in single data rate (SDR). This yields a total output bandwidth of $32 \times 320$ Mb/s, corresponding on average to about 10 Mb/s per channel. Each channel integrates four TDCs based on analog interpolation, with a target time-of-arrival resolution of 100 ps. The chip supports a leading-edge mode, in which all TDCs operate in parallel, as well as Time-over-Threshold (ToT) and Slew-Rate modes with the SiPMs coupled in pairs (2-by-2).

The baseline readout architecture foresees the use of Low Power GigaBit Transceivers (lpGBT) [92], developed at CERN, coupled to VTRx+ optical transceivers [93]. Data serialized by the lpGBT are transmitted via the VTRx+ optical links to the back-end readout system, where event building and data processing are performed. The lpGBT accepts up to 28 input data lines (e-links) in Forward Error Correction 5 (FEC5) mode (e-link clock of 320 MHz, corresponding to 320 Mb/s per e-link). When coupling the DENEB chip to the lpGBT with one e-link per column, only 28 of the 32 DENEB columns can be connected to a given lpGBT, allowing the readout of up to $28 \times 32 = 896$ channels per lpGBT (aggregate input $28 \times 320$ Mb/s $= 8.96$ Gb/s).

### 3.4.3 The trapezoidal module concept

The ideal bRICH coverage is achieved in the case of ideal packing, assuming the SiPMs and the aerogel tiles fit perfectly into the trapezoidal frames and neglecting inter-module gaps. Under these assumptions, this layout yields maximal aerogel and SiPM areas of about 22.7 m$^2$ and 30.7 m$^2$, respectively. The effective SiPM area, accounting for the 83% packaging factor, is about 25.4 m$^2$. These values are significantly reduced compared to those of the cylindrical geometry quantified in Section 3.3, providing a direct benefit in terms of cost while providing, at the same time, a larger $\eta$ acceptance.

This trapezoidal layout, implemented for the 12 pairs of symmetric sectors in the projective geometry of Fig. 3.6, implies the development of 12 distinct aerogel tiles and photodetector modules, as shown in Fig. 3.7.

For the aerogel, the required trapezoids have a variable height in the range ≈14.5–16.5 cm, a variable long base in the range ≈16.0–18.5 cm, and a fixed short base of ≈15.7 cm. The ≈ notation reflects mechanical details still under definition, which slightly reduce the effective tile size. These trapezoidal layouts are not an issue, as the hydrophobic aerogel tiles can be shaped to the required geometry (e.g., by water-jet cutting) as done, for example, for Belle II ARICH [56].

The photodetector module poses the main challenge. The trapezoids would have a variable short base in the range ≈17.3–20.4 cm, a fixed long base of 20.4 cm, and a height of 18.4 cm. Designing a fully trapezoidal module is non-trivial. Moreover, even if one were to adopt the maximal inscribed rectangle in each sector, one would still end up with 12 different footprints to develop, making this option impractical.

Nevertheless, I considered the trapezoidal module solution for the photodetector as the reference layout for all simulation studies presented in the following, providing a benchmark of the detector's limiting performance and a baseline for assessing the performance of more realistic, modular configurations.

### 3.4.4 The rectangular 17 × 18 cm$^2$ photodetector module

A realistic solution I found to ensure modularity, using the same module concept for all the bRICH modules, is to adopt a single rectangular module equal to the largest rectangle inscribed in the trapezoidal profile across the 12 frames. This yields a 17.3 × 18.4 cm$^2$ footprint. Including $\mathcal{O}$(mm) safety margins to accommodate mechanical tolerances, I set the current baseline module size to 17 × 18 cm$^2$.

Through dedicated optimization studies, I optimized the geometry of the SiPM packaging and positioning consistently with the specifications of the DENEB ASIC and the coupling with the lpGBT and VTRx+, which allows reading a maximum of 896 channels per DENEB chip. The optimization criterion was to achieve the best possible single-photon angular resolution while maintaining maximal module acceptance for incident charged tracks.

In the final layout, shown in Fig. 3.8, each rectangular 17 × 18 cm$^2$ module is equipped with 2 × 2 mm$^2$ SiPMs arranged into 360 dies of 11.0 × 6.6 mm$^2$, each die mounting 5 × 3 SiPMs with a pitch of 2.2 × 2.2 mm$^2$. These are grouped into 6 blocks (tiles) of 60 dies having size 8.5 × 6 cm$^2$, each tile read out by one DENEB ASIC. For each

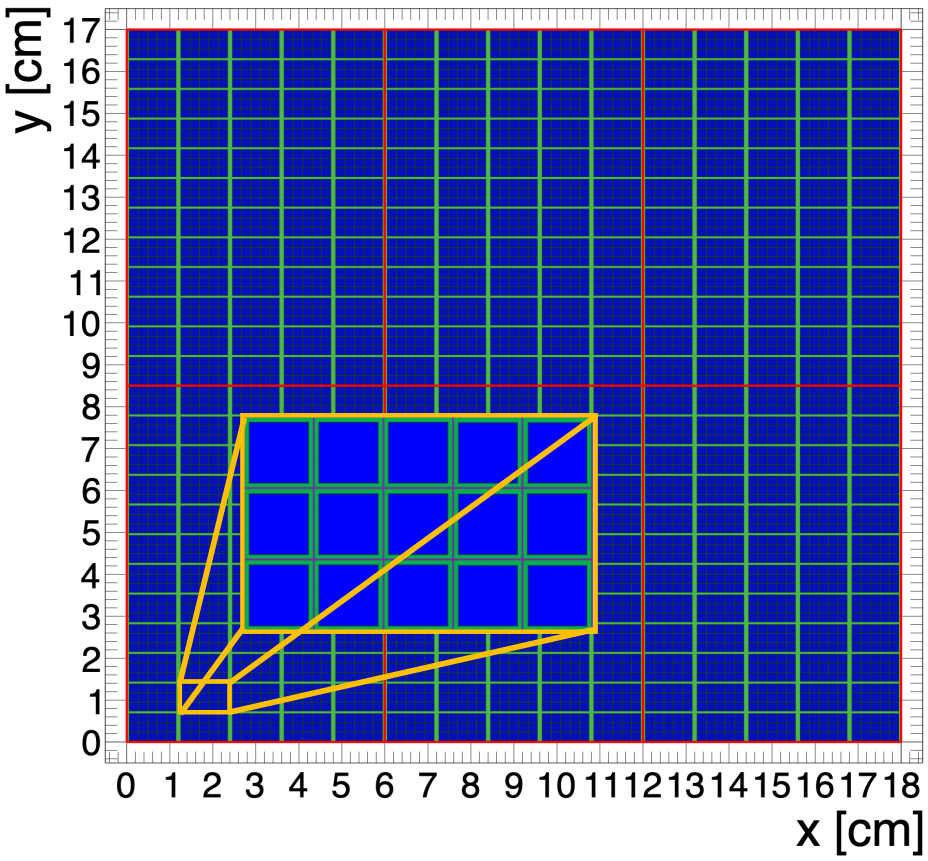


**Figure 3.8:** Geometry of the rectangular $17 \times 18$ cm$^2$ bRICH photodetector module layout. The blue squares correspond to the $2 \times 2$ mm$^2$ SiPMs. A zoom on a single $5 \times 3$ SiPM die is shown.

tile, there are 12 rows, each with five dies, resulting in 36 SiPMs per column along the 8.5 cm side and 25 SiPMs per row along the 6 cm side. The die-to-die gap is 0.48 mm along the 8.5 cm side and 1 mm along the 6 cm side, amounting to 900 SiPMs Neglecting the four corner sensors in each tile, this yields the design value of 896 SiPMs per tile and $6 \times 896 = 5376$ SiPMs per module.

The proposed rectangular $17 \times 18$ cm$^2$ geometry was assumed as a reference for preliminary studies on the integration of the electronics in the module. Fig. 3.9 shows a schematic view of the state-of-the-art module concept. The SiPM layer is connected to the front-end electronics (FEE) layer via a ceramic interposer that integrates two-phase $CO_2$ microchannel cooling [94] and enables annealing by forward-biasing the SiPMs [95]. Two additional PCBs are stacked to interface the FEE with the readout electronics, and the readout electronics to the external back-end readout system. The overall target module thickness, excluding cabling, is about 2 cm. Fig. 3.10 shows a schematic view of the bRICH layout accounting for this module implementation.

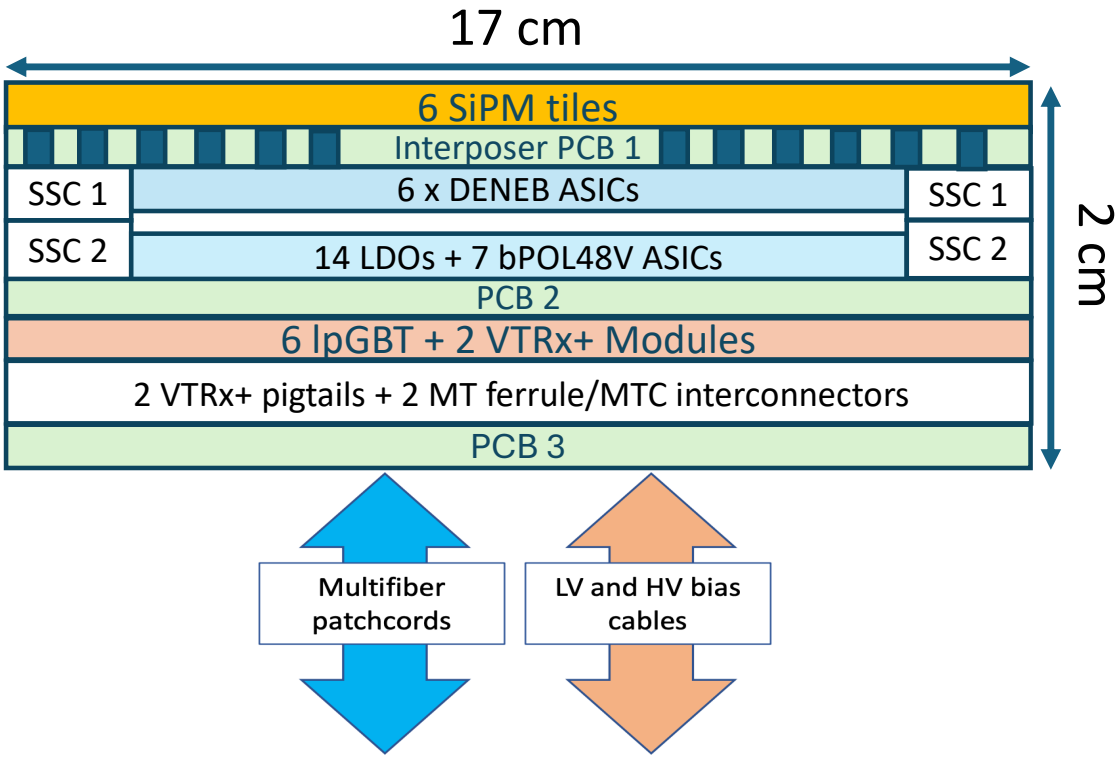


**Figure 3.9:** State-of-the-art module concept for the rectangular $17 \times 18$ cm$^2$ module geometry.

### 3.4.5 Absorbing vs transparent walls between sectors

For the nature of the walls separating adjacent sectors, corresponding to the red regions in Figs. 3.6 and 3.10, I investigated the following two design options.

- Photon absorbing walls, which prevent photons produced in one sector from reaching the photodetector modules of neighbouring sectors.
- Transparent walls, which allow photons emitted in one module within a sector to propagate and be detected in modules of the adjacent sectors.

They are schematically illustrated in Fig. 3.11. Although, in principle, transparent walls (or no walls) could increase the photon yield for tracks entering the aerogel tile in a module close to sector boundary, where a fraction of photons naturally escapes the module, the advantage is limited to low-multiplicity events. In high-multiplicity conditions, photons from different tracks reaching different sectors could significantly increase the mutual background and degrade the reconstruction performance.

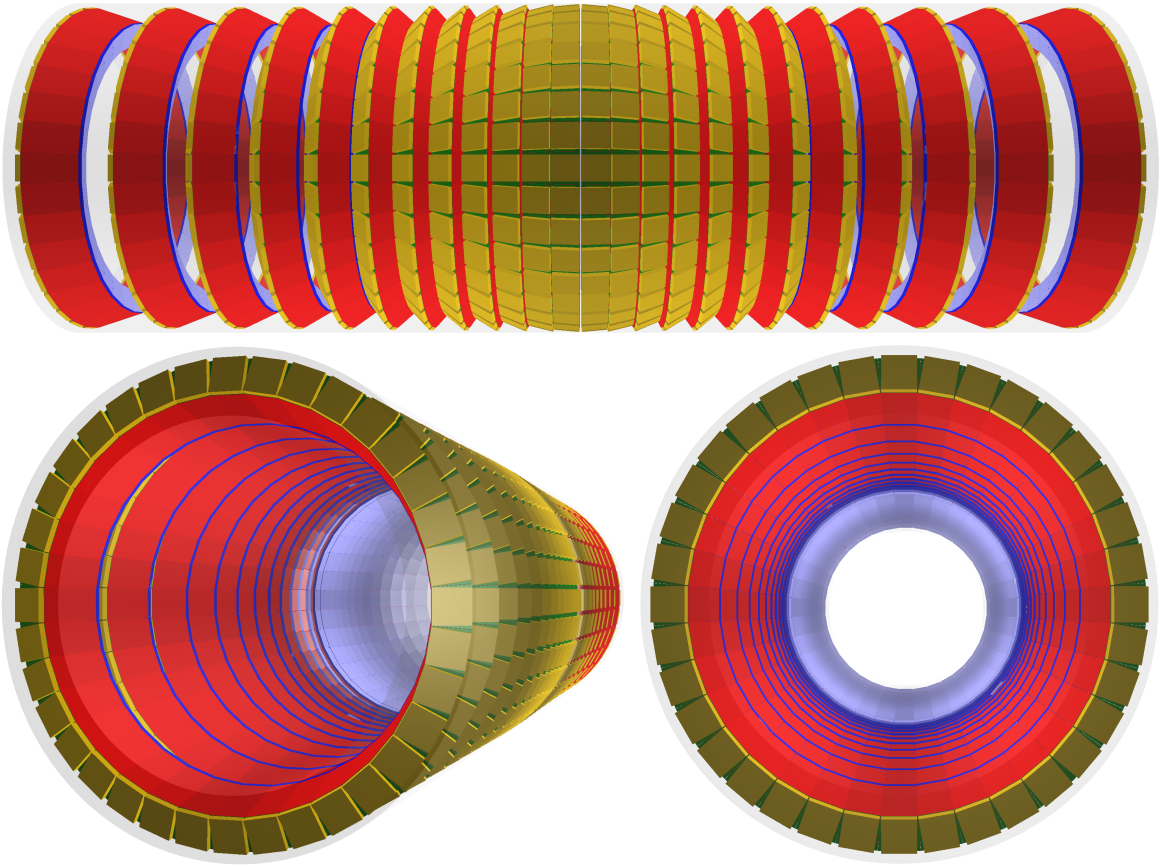

**Figure 3.10:** Schematic views of the bRICH layout with $17 \times 18$ cm$^2$ photodetector modules.

Conversely, photon-absorbing walls, which currently represent the baseline design, prevent photons leaving a sector from being detected elsewhere. In this configuration, all ring photons are confined within the incidence sector of the track, allowing each sector to operate independently and improving the separation of the rings from different tracks. Simulation studies comparing these configurations are presented in Section 4.4.5.

In both configurations, transparent walls (or no walls) are always assumed between adjacent modules within the same sector. Photons emitted in a given module can therefore be detected by the SiPMs of neighbouring modules within the same sector.

### 3.4.6 Projective bRICH vs problems of the cylindrical layout

Despite the added complications in terms of mechanics, integration, and modularity, the issues observed in the cylindrical layout are naturally solved in the projective one.

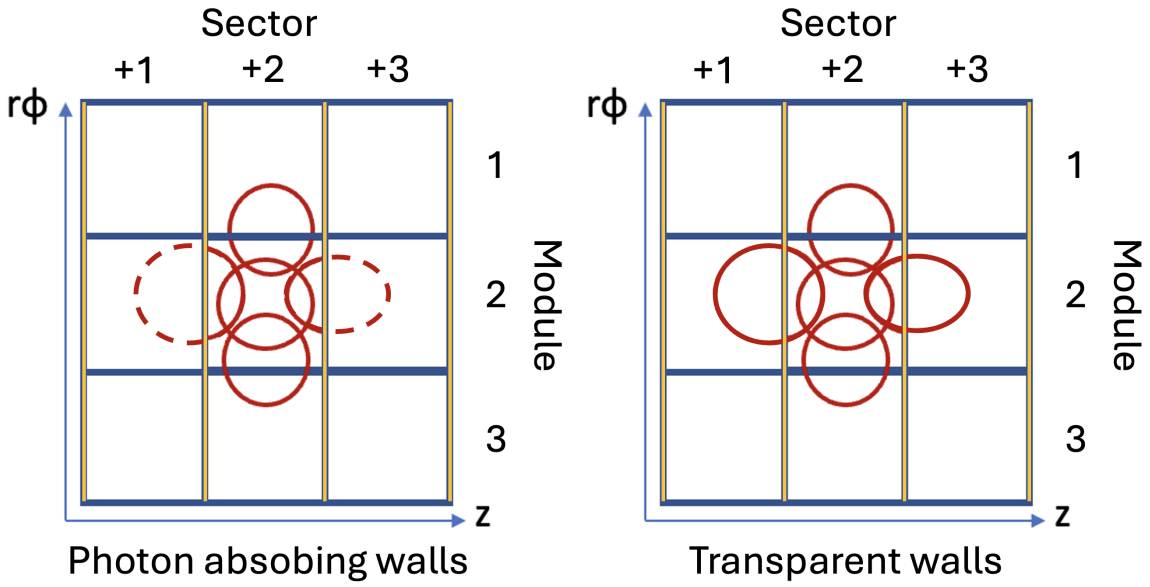


**Figure 3.11:** Schematic of the inter-sector photon-absorbing walls and transparent walls concept.

The reconstruction problems associated with inclined tracks disappear, since in each sector, also accounting for the track curvature in the magnetic field and the spread of the collision vertex, particles and their Cherenkov photons impinge on the sensors under conditions very close to normal incidence. As a result, the reconstructed rings remain compact, with a linear size not exceeding about 15 cm. This can be observed in Fig. 3.12, showing the photodetector hit-map of a single central Pb-Pb collision at $\sqrt{s_{\mathrm{NN}}} = 5.52$ TeV over the full bRICH acceptance. Despite the high-track multiplicity, the rings associated to the different charged tracks are clearly visible over the full detector acceptance.

Under the assumption of photon absorbing walls between adjacent sectors, all ring photons are confined within the track incidence sector, which allows the sectors to operate independently and ensures that rings from different tracks remain well separated, further stabilising pattern recognition.

Moreover, not only does the projective geometry mitigate Rayleigh scattering by limiting photon path lengths in the aerogel, but the addition of absorbing walls also prevents scattered photons from propagating into far-away sectors, as occurred in the cylindrical case, thus further reducing the background at the reconstruction level.

Finally, this confinement not only mitigates occupancy, but also minimises the spread in photon arrival times at the module level. It therefore becomes possible to apply an acquisition time gate of the order of ns, with sector-dependent offsets, efficiently suppressing the DCR background without sacrificing signal, as discussed in Section 4.5.3.

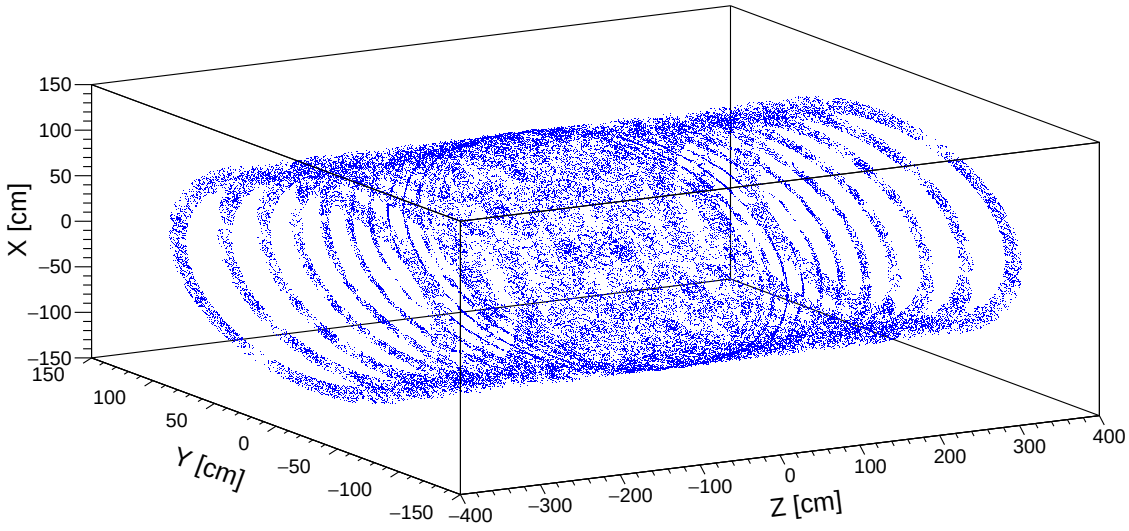


**Figure 3.12:** Photodetector hit-map of a single central Pb-Pb collision at $\sqrt{s_{\mathrm{NN}}} = 5.52$ TeV generated using my full simulation chain for my projective proximity-focusing bRICH geometry.

This substantially relaxes the requirements on bandwidth. The projective layout thus emerges as a robust solution for efficient PID in central Pb–Pb collisions.

The only downside of this layout is the loss of Cherenkov photons produced in the aerogel close to the sector boundaries. This results in a smaller number of detected photons per ring and a degradation of the ring angular resolution in those boundary regions. Nevertheless, owing to the excellent single-photon angular resolution achieved across all sectors, the overall ring resolution remains consistent with or even better than the leading bRICH requirement, as discussed in detail in Section 4.4.3.

## 3.5 Option: Gas-based $e^{\pm}$ ID enhancement

The baseline bRICH layout is designed to ensure better than $3\sigma$ e/$\pi$ separation up to approximately 2 GeV/$c$, using Cherenkov-ring information from photons emitted in the aerogel radiator in central (0-5%) Pb–Pb collisions, as discussed in Section 4.7.3.

However, ALICE physics groups focusing on channels including thermal dielectrons and quarkonia (such as $J/\psi \rightarrow \mathrm{e}^{+}\mathrm{e}^{-}$) have expressed interest in extending the e/$\pi$ separation capability up to 4 GeV/$c$ over the full bRICH acceptance.

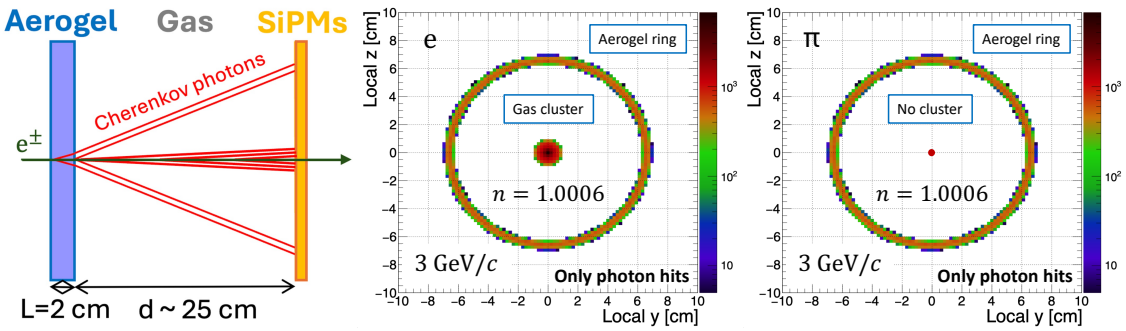


**Figure 3.13:** Principle of operation of the proposed threshold-based electron identification using clusters of fired SiPMs due to photons emitted in the gas filling the bRICH expansion gap assuming a refractive index of $n_g = 1.0006$ (left). For electrons at 3 GeV/$c$ both aerogel photons and gas clusters can be seen (middle), while for pions at the same momentum the gas cluster is missing (right).

The major challenge is pion contamination due to the much larger pion yield relative to electrons in the final state, requiring a $\pi$ rejection factor larger than $10^3$ in a momentum region where pions cannot be discriminated using only the aerogel signal.

To achieve this goal, I investigated the possibility of flushing the bRICH expansion gap with a proper gas mixture acting as an additional Cherenkov radiator for efficient threshold-based discrimination up to the target 4 GeV/$c$ momentum limit.

### 3.5.1 Principle of operation

The principle of operation of the proposed identification strategy is shown in Fig. 3.13. With a suitable choice of the gas refractive index, electrons are above the Cherenkov threshold in the target momentum range, while muons, pions, kaons, and protons are not. In this configuration, reconstructing clusters of SiPMs fired by aerogel photons, with a sufficiently large photon yield, can be used to unambiguously tag electrons.

This approach not only enables the extension of electron identification capabilities up to the target momenta, but also naturally provides a signature for electron identification at lower momenta (below 2 GeV/$c$), offering additional validation of electron tagging using the aerogel signals and potentially improving the overall electron identification performance in that region.

Potential backgrounds can still arise from non-electron tracks, including direct charged-particle interactions with the SiPMs and Cherenkov light produced in the SiPM protective layer or in a thin entrance window, with the timing option discussed in Section 3.6. Since the protective layer is about 100 µm thick and the timing windows under consid-

eration are about 1 mm, these signals are confined to a small area around the projected impact point, typically no larger than the nearest-neighbour SiPMs. Gas clustering is therefore preserved provided that hits within this critical region are excluded from the gas-cluster reconstruction.

### 3.5.2 Choice of the gas refractive index

The choice of the gas refractive index $n_g$ is crucial. Table 3.2 reports the Cherenkov momentum thresholds for electrons, muons, pions, kaons, and protons for various selected values of $n_g$, together with the expected mean number of detected photons per gas centimetre travelled by electrons, $N_{ph}$/cm, calculated assuming the baseline bRICH SiPM specifications and the same optical properties for all the values of $n_g$.

| Refractive index | $p_{th}$ [GeV/$c$] | | | | | $N_{ph}$/cm (e) |
|---|---|---|---|---|---|---|
| | e | μ | π | K | p | |
| 1.00030 | 0.02 | 4.31 | 5.69 | 20.15 | 38.30 | 0.13 |
| 1.00045 | 0.01 | 3.52 | 4.65 | 16.45 | 31.27 | 0.19 |
| 1.00060 | 0.01 | 3.04 | 4.02 | 14.24 | 27.08 | 0.26 |
| 1.00075 | 0.01 | 2.72 | 3.60 | 12.74 | 24.22 | 0.32 |

**Table 3.2:** Cherenkov momentum thresholds for e, $\mu$, $\pi$, K, and p at representative gas refractive indices, and the corresponding mean detected photon yield per gas cm travelled by electrons calculated assuming the baseline bRICH SiPM specifications and the same optical properties for all gases.

Although light gases, such as the Ar or the $N_2$ considered in the baseline bRICH layout, have a refractive index below about 1.0003 that satisfies the threshold requirement, the Cherenkov yield is too small for efficient electron identification. Since the yield scales with $\sin^2\theta_c$ according to Eq. 2.13, the mean number of detected photons is about 3 for a 25 cm path in gas, which leads to sizeable contamination from pions and other charged species through clustering of uncorrelated DCR hits. At the same time, gases with larger $n_g$ such as $CO_2$ ($n_g \approx 1.00046$ at 400 nm) or heavier mixtures provide a higher yield at the price of lower thresholds for μ, π and heavier particles. An optimal compromise is $n_g \approx 1.0006$, adopted as a reference for simulation studies discussed below. This choice introduces a slight μ contamination for momenta between 3 and 4 GeV/$c$, which is acceptable given the small muon fraction relative to electrons.

### 3.5.3 Eco-friendly gas mixtures

The target refractive index, $n_g = 1.0006$ at 400 nm, could be achieved under standard temperature and pressure conditions (0°C and 1 atm) by blending saturated fluorocarbons ($C_nF_{2n+2}$), such as $C_2F_6$ ($n \simeq 1.00082$) or $C_4F_{10}$ ($n \simeq 1.0014$), with light gases such as $N_2$ ($n \simeq 1.00030$) or $CO_2$ ($n \simeq 1.00046$). However, the high global-warming potentials (≈5,000–13,000 $CO_2$–equivalent) of fluorocarbons and the fact that their production is being progressively discontinued render them unsuitable for ALICE 3. Therefore, these gases are not a primary option for the bRICH.

I instead focused on gas mixtures using very small molar fractions of heavy fluoroketones ($C_nF_{2n}O$) diluted in $CO_2$ or $N_2$. For these studies, I considered $C_5F_{10}O$, which has $n \simeq 1.00175$ at 400 nm and offers the required optical properties, with an expected $CO_2$-equivalent GWP comparable to that of $CO_2$, enabling mixtures with orders-of-magnitude lower impact than saturated fluorocarbons [96].

The refractive index $n_g$ of a binary mixture can be expressed as:

$$n_g - 1 \;=\; w_1\,(n_1 - 1) \;+\; w_2\,(n_2 - 1), \qquad w_2 = 1 - w_1, \tag{3.1}$$

where $w_1$ is the molar fraction of the heavy component ($C_5F_{10}O$) with refractive index $n_1$, and $n_2$ is the refractive index of the diluent gas. Solving for $w_1$ at a target $n_g$ gives:

$$w_1 \;=\; \frac{n_g - n_2}{n_1 - n_2}. \tag{3.2}$$

- Inserting $n_g = 1.0006$ and $n_1 = 1.00175$ and using $CO_2$ as diluent ($n_2 = 1.00046$):

$$w_{C_5F_{10}O} \;=\; \frac{1.0006 - 1.00046}{1.00175 - 1.00046} \;\approx\; 10.85\%, \qquad w_{CO_2} \approx 89.15\%.$$

- Inserting $n_g = 1.0006$ and $n_1 = 1.00175$ and using $N_2$ as diluent ($n_2 = 1.00030$):

$$w_{C_5F_{10}O} \;=\; \frac{1.0006 - 1.00030}{1.00175 - 1.00030} \;\approx\; 20.69\%, \qquad w_{N_2} \approx 79.31\%.$$

Although pure $C_5F_{10}O$ has a normal boiling point of about 26.9°C, the reduced partial pressure associated with the considered mixture compositions lowers the effective condensation temperature, enabling safe operation at temperatures well below 0°C [97]. Such mixtures must be actively controlled during operation, since the relative molar fractions determine the stability of $n_g$. Monitoring solutions such as ultrasonic refractometry for real-time blending, first demonstrated in the 1990s for $C_5F_{12}/N_2$ in the SLD CRID at SLAC [98, 99], should then also be integrated into the detector design.

### 3.5.4 Interfacing the gaseous radiator with aerogel

For the integration of threshold-based electron identification in the bRICH, I investigated two options for the interfacing of the gaseous radiator with the aerogel tiles.
In the first option, I considered the coating of the upstream face of the aerogel tiles with an absorbing material, so that only gas photons emitted downstream of each tile reach the SiPM plane. This yields clusters that are uniform across each sector, with a size determined solely by the thickness of the expansion gap in the considered sector.
In the second option, I considered the upstream face uncoated, allowing photons produced in the vessel upstream of the aerogel, from $R = 90$ cm, to reach the SiPMs. Given the inclination of the photodetector modules shown in the longitudinal view in Fig. 3.6, clusters become larger at smaller $|\eta|$ than at larger $|\eta|$, resulting in an increase of the overall mean cluster size. However, a drawback of the second option is that upstream photons must traverse the full aerogel tile, where Rayleigh scattering can lead to losses or introduce additional background that must be accounted for.

### 3.5.5 Features of gas clusters in the bRICH geometry

In this section I report my simulation results for the features of gas clusters for the two options above in terms of topology in the ALICE 3 baseline 2 T solenoidal magnetic field, number of fired SiPMs, total number of photoelectrons and their distributions within the SiPMs. All the results presented in this section are obtained assuming a mixture of 10.85% $CO_2$ + 89.15% $C_5F_{10}O$, with a refractive index of 1.0006 at 400 nm.

The left panel of Fig. 3.14 illustrates the curvature of electrons with various $p_T$ in the ALICE 3 baseline 2 T solenoidal magnetic field. For each track, the path of a photon emitted at the entrance of the aerogel vessel ($R = 90$ cm) in the direction of maximal separation at the photodetector radius ($R = 117$ cm) is also displayed. The right panel presents the cumulative hit map of gas photon hits from electrons with $p = 3$ GeV/$c$ and $\eta = 0.1$ in the bRICH obtained with my full simulation chain.

The curvature in the magnetic field, together with the uniform emission of Cherenkov photons along the electron path in the gas, produces asymmetric clusters. For $p_T < 1$ GeV/$c$ the maximum distance of photon hits from the track impact point exceeds 2 cm. Since these outliers are few, to avoid clustering hits far from the track that are likely due to other tracks or SiPM DCR, in the following I adopted a fiducial clustering region. I defined it sector-by sector and as a circle of radius depending on $p_T$, the path length of the charged track in gas, and the curvature in the magnetic field.

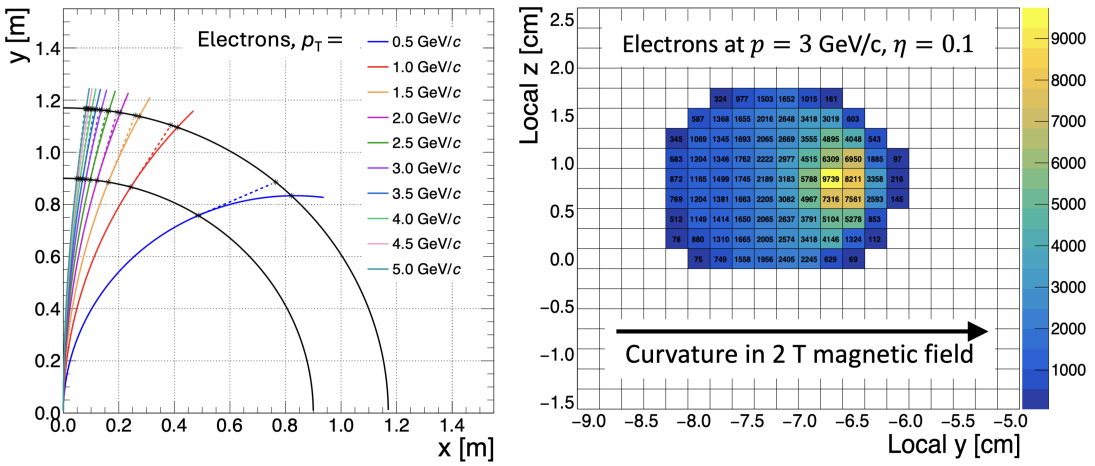


**Figure 3.14:** Left: Illustration of the curvature of electrons with various $p_T$ in the ALICE 3 baseline 2 T solenoidal magnetic field. For each track, the trajectory of a photon emitted at the entrance of the aerogel vessel ($R = 90$ cm) in the direction where it is expected to be detected farthest from the track impact point at the reference photodetector radius ($R = 117$ cm) is shown. Right: cumulative hit-map of gas photons from electrons with $p = 3$ GeV/$c$ and $\eta = 0.1$ in the bRICH.

Fig. 3.15 shows my simulation results for the features of gas and pion clusters under the hypothesis that the upstream face of the aerogel tiles is coated with an absorbing material, over the full bRICH acceptance, for tracks with $p = 3$ GeV/$c$. The figure reports the distributions of the number of fired SiPMs, the distance between photon hits and the most probable track impact point on the SiPM module, the total number of photoelectrons (p.e.), and the number of p.e. per SiPM for the considered mixture.

The mean number of fired SiPMs as a function of the pseudorapidity $\eta$, highlighting the sector dependence, is also shown, together with the fraction of electron events passing simultaneous requirements on the minimum number of fired SiPMs and on the minimum number of p.e. With the baseline SiPM size, pitch, and PDE, the number of fired SiPMs for electron events ranges from 7 to 13, reflecting the thickness of the expansion gap in each sector, as shown in Fig. 3.7. The reduction at sector boundaries corresponds to truncated clusters. The electron signature is a cluster dominated by single-p.e. hits, with an increased number of p.e. in the cells closest to the track impact point. The hit–track distance distribution supports a fiducial clustering radius up to 2 cm, depending on the sector, for electrons at 3 GeV/$c$. I repeated the analysis by scanning $p$ and $\eta$ to define the corresponding fiducial radius in each sector.

For pions, hits are still recorded due either to direct interactions or to Cherenkov photons emitted in the considered 100 µm silicone resin layer ($n = 1.41$ at 400 nm) on top of the SiPMs. From the hit–track distance distribution it can be observed that these signals lie very close to the track impact point, typically within the nearest cells, and can be easily discarded without significantly affecting gas clustering.

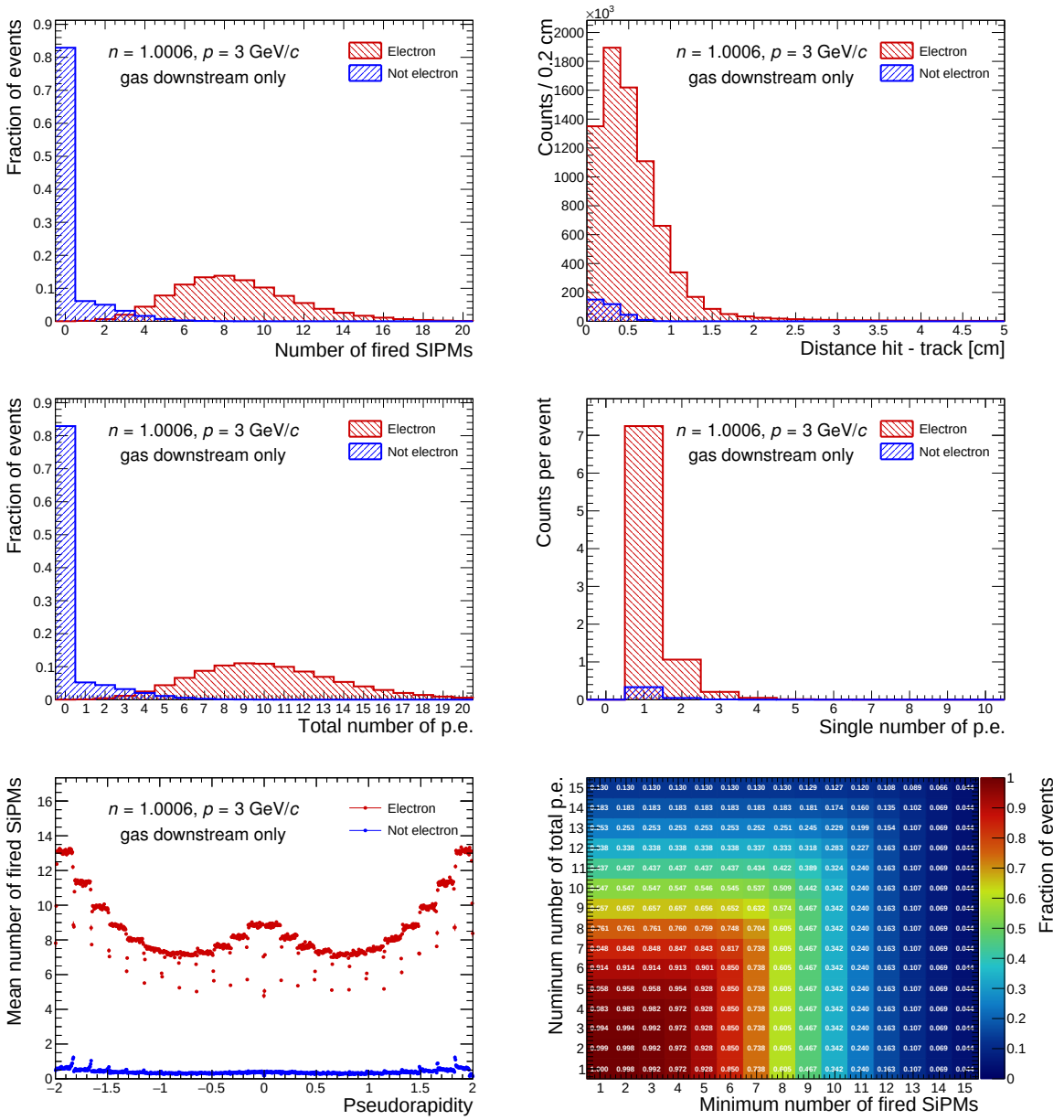


**Figure 3.15:** Simulation results for gas-cluster features for electrons (red) and pions (blue) at 3 GeV/$c$ over the full bRICH acceptance, in the hypothesis of an absorbing coating on the upstream face of the aerogel tiles, for the mixture 10.85% $C_5F_{10}O$ + 89.15% $CO_2$ ($n$ = 1.0006). Top left: Distribution of the number of fired SiPMs. Top right: Distribution of the distance between gas-photon hits and the most probable track impact point on the SiPM module. Middle left: Distribution of the total number of p.e. Middle right: Distribution of the number of p.e. per SiPM. Bottom left: Mean number of fired SiPMs as a function of $\eta$. Bottom right: Fraction of electron events featuring a minimum number of fired SiPMs and on the minimum number of total p.e.

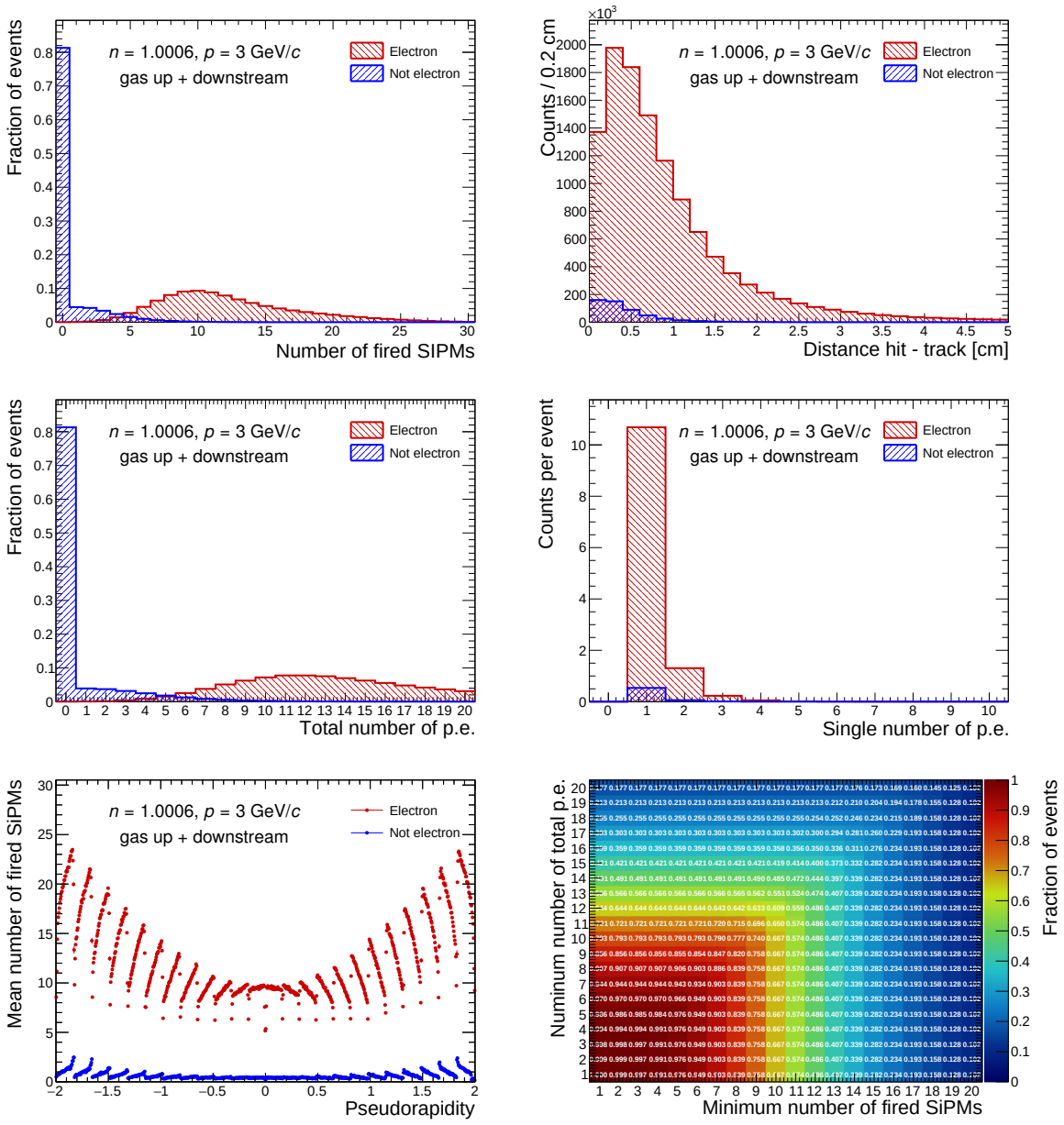


**Figure 3.16:** Simulation results for gas-cluster features for electrons (red) and pions (blue) at 3 GeV/$c$ over the full bRICH acceptance, assuming no absorbing coating on the upstream face of the aerogel tiles, for the mixture 10.85% $C_5F_{10}O$ + 89.15% $CO_2$ ($n = 1.0006$). Top left: Distribution of the number of fired SiPMs. Top right: Distribution of the distance between gas-photon hits and the most probable track impact point on the SiPM module. Middle left: Distribution of the total number of p.e. Middle right: Distribution of the number of p.e. per SiPM. Bottom left: Mean number of fired SiPMs as a function of $\eta$. Bottom right: Fraction of electron events featuring a minimum number of fired SiPMs and on the minimum number of total p.e.

Fig. 3.16 shows the analogous figures of merit for electrons and pions at 3 GeV/$c$ when the upstream face of the aerogel tiles is left uncoated. As expected, clusters become larger at smaller $|\eta|$ than at larger $|\eta|$, with more SiPMs firing due to single photons in regions farther from the track impact point. This yields a broader distribution of hit–track distances on the SiPM module, without any change in the p.e. per cell in the cluster core, which is driven by photons emitted close to the track impact point.

The analysis of these features is important not only to define proper clustering criteria aimed at minimizing the clustering of background hits, but also to identify the relevant inputs for machine-learning–based e-ID algorithms, as discussed in Section 4.8.3.

## 3.6 Option: charged-particle timing with bRICH

An appealing R&D option I investigated for the bRICH concerns the possibility of implementing high-efficiency Cherenkov-based charged-particle timing measurements, with a resolution down to tens of ps, directly using the bRICH SiPMs coupled with a thin window of transparent material. This solution would open the possibility of combining the oTOF and the bRICH into a single detector using the same sensor layer, with substantial technical and cost advantages.

### 3.6.1 Principle of operation

Previous studies have already investigated the use of SiPMs for the direct detection and timing of incident charged particles [100, 101]. In such cases, the signals mainly originate from Cherenkov photons emitted in the SiPM protective layer, typically a few hundred µm of epoxy or silicone resin. However, these signals are typically confined to the single SiPM where the interaction occurs. This confinement, combined with the limited packaging factor of SiPMs in arrays, significantly reduces their overall efficiency for the direct detection of the impinging charged particles.

To overcome this limitation, I explored the approach of directly coupling to a SiPM array a thin transparent slab, with a thickness of a few mm, as illustrated in Fig. 3.17. With a suitably chosen refractive index, this slab acts as an additional Cherenkov radiator for the incident charged particles. The promptly emitted Cherenkov photons ($\approx$ ps) then generate clusters of contiguous fired SiPMs on the photosensitive surface.

The topology of these clusters in terms of radius, average number of fired SiPMs, and distribution of photoelectrons is determined by the slab refractive index, transmittance and thickness, as well as and SiPM granularity, and PDE.

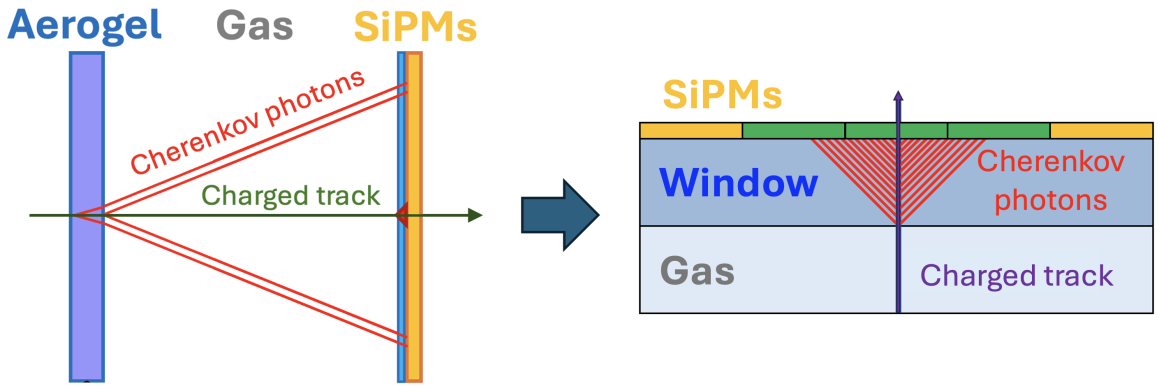


**Figure 3.17:** Cherenkov-based charged-particle timing using the bRICH SiPMs

The track timing is then obtained by combining the timing information from SiPMs in the cluster. The precision of each individual measurement is determined by the intrinsic resolution of the SiPMs and the contributions of the electronics, primarily the time jitter and the TDC resolution. This method offers two complementary advantages.

- In the cluster core, where signals correspond to multiple photoelectrons, yielding the best intrinsic time resolution and the lowest time jitter, scaling with the number of photoelectrons $N_{pe}$ as $1/\sqrt{N_{pe}}$, and $1/N_{pe}$, respectively [102].
- At the cluster periphery, where single-photoelectron statistics dominates, additional timing measurements are still available, enhancing the overall precision.

As a result, even with SiPMs combined with their associated electronics chain, yielding a SPTR of about 100 ps, track time resolutions at the level of a few tens of ps can be achieved. In addition, this approach mitigates the limitation imposed by the SiPM packaging factor, enabling charged-particle detection efficiencies approaching 100%.

In the following sections, I present a detailed discussion of the choice of window material, as well as the benefits and challenges of merging oTOF and bRICH.

### 3.6.2 Candidate window materials

The choice of the window material for the proposed Cherenkov-based charged-particle timing strategy is driven by strict PID requirements. With the bRICH SiPMs placed at a radius $R$ larger than 100 cm from the beam axis, only charged particles with transverse momentum $p_T$ above approximately $0.3 \cdot B \cdot R/2 = 0.3$ GeV/$c$ reach the sensors, accounting for the curvature in the baseline 2 T solenoidal magnetic field. In addition, the ALICE 3 iTOF is designed to achieve better than $3\sigma$ separation

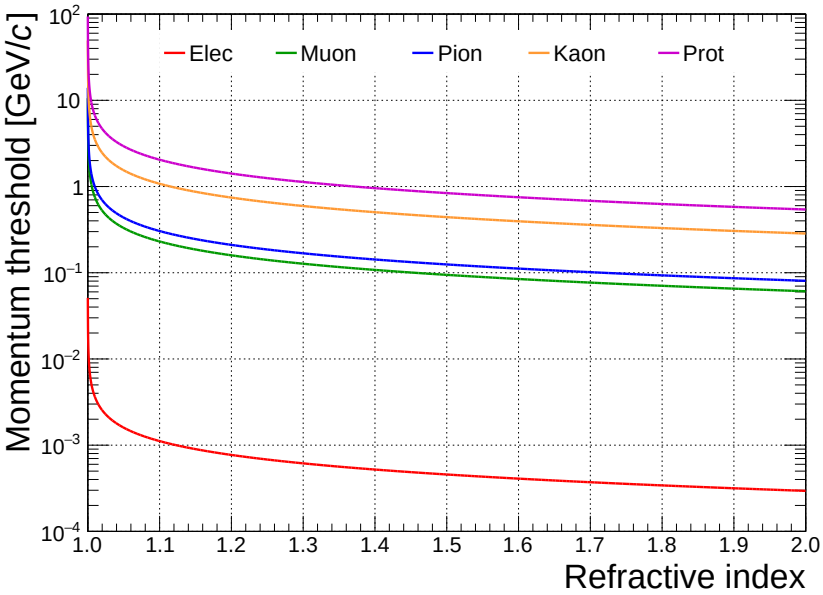


**Figure 3.18:** Cherenkov momentum thresholds for e, μ, π, K and p as a function of refractive index.

for e/π, π/K, and K/p up to momenta of about 0.3, 1, and 2 GeV/$c$, respectively. These momentum values, together with a safety margin of overlap with the iTOF coverage, define the lower identification limits that must be guaranteed in the scenario of integrating the oTOF layer with the bRICH SiPMs. The PID upper limits, on the other hand, are required to remain consistent with those of the baseline oTOF design.

In the proposed charged-particle timing strategy, these requirements are primarily addressed by minimizing the Cherenkov emission threshold for the different particle species, ensuring that particles reach Cherenkov angle saturation at the lowest possible momenta, while maximizing the emission angle. Fig. 3.18 shows the momentum threshold $p_{\mathrm{th}}$ for e, μ, π, K and p as a function of the refractive index. From the plot it can be deduced that a transparent material with a refractive index greater than 1.3 is required. Candidate materials for the sensor window include NaF ($n \approx 1.33$), $MgF_2$ ($n \approx 1.38$) and fused silica ($n \approx 1.47$), which also offer excellent transparency and optical coupling to typical SiPM protective layers.

Materials with higher refractive indices are characterized by lower momentum thresholds $p_{\mathrm{th}}$, larger Cherenkov emission angles $\theta_{\mathrm{c}}$, and higher photon yields $N_{\mathrm{ph}}$, which scale as $N_{\mathrm{ph}} \propto \sin^2\theta_{\mathrm{c}}$ according to Eq. 2.8, thus leading to larger clusters. However, the optical coupling to the SiPMs becomes more challenging, and photons experience increased time delays and spatial displacements, together with stronger reflection effects that can either reduce acceptance for external photons (e.g., from the bRICH aerogel) or introduce background via multiple total-internal reflections. As a result, using materials with $n >$ 1.5-1.6 is non convenient for this application.

### 3.6.3 Pros and cons of combining oTOF and bRICH

The combination of the ALICE 3 oTOF and bRICH detectors into a single system based on the same SiPM layer offers several advantages, together with some limitations. The main pros and cons I identified are detailed in the following.

#### Pros

A major benefit is the significant cost reduction. According to the oTOF cost reported ALICE 3 Scoping Document [2], savings of more than 15 MCHF can be achieved. In the proposed approach, the only additional cost with respect to the bRICH baseline arises from the sensor window material and its optical coupling to the SiPM layer.

The proposed timing strategy ensures a charged-particle detection efficiency close to 100% in the regions covered by the bRICH modules, with the window cluster topology, with the emitted Cherenkov photons hitting multiple contiguous SiPMs, overcoming the limitations imposed by the finite SiPM packaging factor ($< 90\%$).

An intrinsic advantage of the presence of this window is that the centroid of the corresponding clusters delivers a tracking point at a larger radius with a spatial resolution of a few hundred microns ($\sigma_x \approx 2/\sqrt{12}$ mm for the baseline 2×2 mm$^2$ SiPMs). This improves track propagation to the aerogel radiator and thus enhances the reconstruction of the Cherenkov angle in the bRICH. This feature alone could justify the inclusion of the window, regardless of whether oTOF and bRICH are integrated or not. In addition, a better track matching with the tracker layers is expected when using $2 \times 2$ mm$^2$ SiPMs compared to the larger $5 \times 5$ mm$^2$ granularity of the stand-alone oTOF baseline.

Window photon signals are also easily distinguished from those produced in the upstream aerogel radiator. Clusters from the window or resin typically contain many photoelectrons distributed across a few adjacent SiPMs, while aerogel photons appear as isolated single-photoelectron signals, albeit with correlated SiPM background. This separation allows more robust signal identification. In addition, for physics analyses focused exclusively on TOF measurements, the possibility exists to further reduce background due to both aerogel photons and DCR signals by raising thresholds to a few photoelectrons at the cost of sacrificing the bRICH signals.

An additional advantage is the possibility of exploiting the radial space originally allocated to the stand-alone oTOF in the ALICE 3 apparatus to enlarge the expansion gap of the bRICH sectors, thereby improving the angular resolution in the reconstruction of photons from the upstream aerogel radiator, or to more easily accommodate thermal shielding, front-end electronics, and other services.

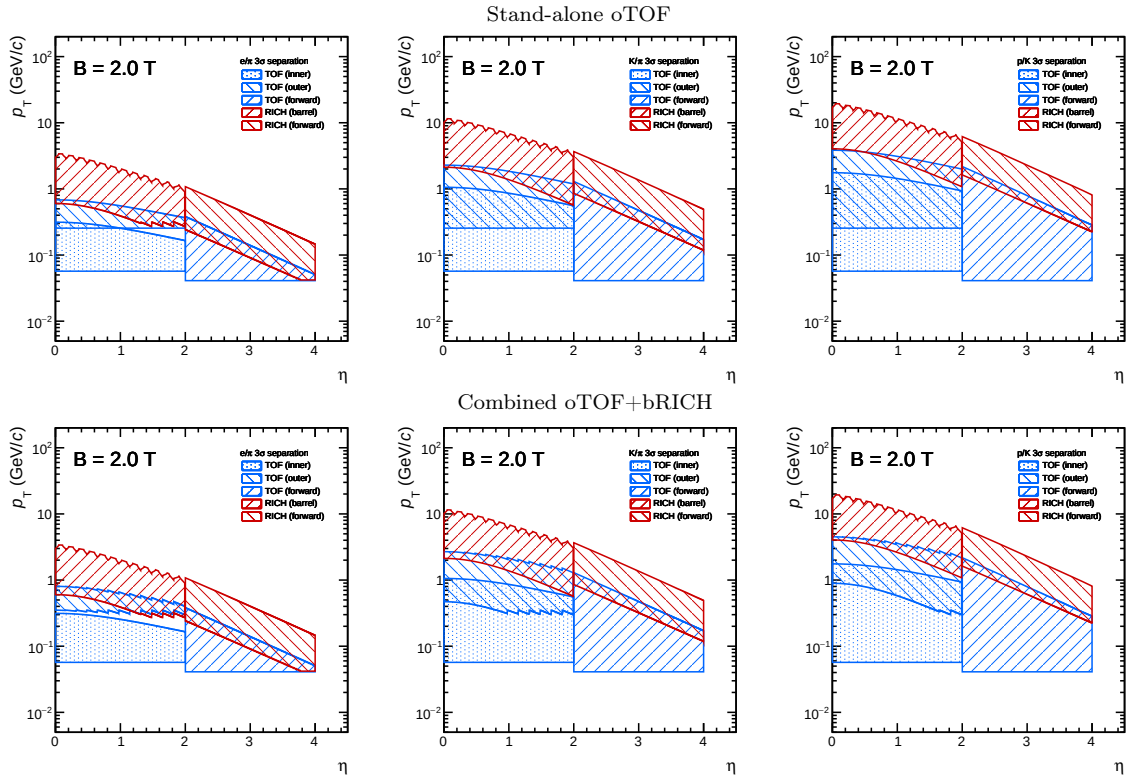


**Figure 3.19:** Expected $\eta$-$p_{\mathrm{T}}$ regions where a larger than 3σ e/π (left), π/K (middle) and K/p (right) separation is achieved assuming a magnetic field strength $B = 2$ T using the ALICE 3 TOF and RICH systems in the hypothesis of stand-alone oTOF (top) and of oTOF combined with bRICH (bottom).

Finally, the longer lever arm $L_{\mathrm{trk}}$ associated with the bRICH sensors at a mean radius $\langle R_{\mathrm{bRICH}} \rangle \approx 110$ cm, compared to the baseline oTOF radius $R_{\mathrm{oTOF}} = 85$ cm, can either provide the same PID performance while relaxing the 20 ps resolution requirement of the baseline design, or deliver improved PID at the same target time resolution, since the separation power scales proportionally to $L_{\mathrm{trk}}/\sigma_t$, as shown in Fig. 2.1. Fig. 3.19, shows my calculation results for a comparison of the expected $\eta$-$p_{\mathrm{T}}$ regions where a larger than 3σeπ, π/K and K/p separation is achieved for $B = 2$ T using the baseline ALICE 3 TOF and RICH systems in the hypothesis of stand-alone oTOF and of oTOF combined with bRICH. In the latter case, I considered a 1 mm thick fused silica window coupled to 2×2 mm$^2$ Hamamatsu S13360 series SiPMs with a microcell pitch of 50 µm and intrinsic SPTR in Fig. 2.11 for the calculations. A larger overall PID separation power is potentially achieved compared to the baseline oTOF layout, at the cost of slightly sacrificing coverage at low-$p_{\mathrm{T}}$ due to both the larger radius and the window thresholds for Cherenkov emission. However, these losses mostly occur in regions already almost fully covered by the iTOF, so the practical cost is primarily a reduction of the oTOF–iTOF overlap region, as detailed below.

### Cons

The combined approach also presents some challenges. In the 2 T solenoidal field, the curvature of charged-particle tracks requires a minimum transverse momentum above about 300 MeV/$c$ for particles to reach the bRICH sensors compared to the lower limit of the baseline oTOF. This results in a gap of about 150 MeV in transverse momentum between the iTOF and oTOF+bRICH for $3\sigma$ $e/\pi$ separation at $|\eta| \to 2$. For comparison, the baseline oTOF layout already exhibits a 100 MeV gap in the same kinematic region, as shown in the top-left panel of Fig. 3.19. This gap is recovered when operating in configurations with a reduced magnetic field.

In addition, the window introduces Cherenkov emission thresholds that constrain the low momentum reach for PID. For K and p, the corresponding momentum thresholds lie above the magnetic field limit, as shown in Fig. 3.18. Nevertheless, this does not represent a significant drawback, since the low-$p_{\mathrm{T}}$ region is already well covered by the iTOF, as illustrated in the bottom–middle and bottom–right panels of Fig. 3.19.

Another limitation arises from the requirement to operate at the single-photoelectron level when combining aerogel ring measurements with timing measurements. This makes charged-particle timing sensitive to inefficiencies caused by radiation damage to the SiPMs, primarily through dead-time effects in high DCR conditions.

Acceptance limitations also arise from the specifications of the module concept. In the case of the projective bRICH geometry with rectangular $17 \times 18$ cm$^2$ modules discussed in Section 3.4.4, acceptance losses are expected in the regions between contiguous modules in the same sectors and in the regions between adjacent sectors.

In summary, the combination of all these advantages and limitations must be carefully considered toward a final design choice. Nevertheless, the crucial aspect remains the validation of the achievable performance in terms of charged-track detection efficiency and time resolution. In this context, I tested various SiPM types coupled with different sensor window materials in beam conditions. Preliminary results, discussed in Chapter 6, confirm the feasibility of approaching the required efficiency and resolution.

## 3.7 Option: $1 \times 1$ mm$^2$ SiPMs + light concentrators

One of the main challenges for the feasibility of the bRICH system is to keep the SiPM DCR per channel within the 1 MHz/mm$^2$ safety limit throughout the ALICE 3 operation. This corresponds to 4 MHz for the baseline $2 \times 2$ mm$^2$ SiPM. Due to the poor radiation tolerance of the SiPMs, keeping the DCR below this limit is not trivial

| Module layout | Total area ($m^2$) | Active area ($m^2$) | N channels |
|---|---|---|---|
| Trapezoidal (83% integration factor) | 30.72 | 25.50 (baseline 2x2$mm^2$) 6.35 (light conc.+1x1 $mm^2$) | ≈ 6.99 M |
| Rectangular 17x18 $cm^2$ (896 x 6 channels / module) | 26.44 | 18.58 (baseline 2x2$mm^2$) 4.64 (light conc.+1x1 $mm^2$) | ≈ 4.64 M |

**Table 3.3:** Photodetector active area and number of channels for the proposed projective bRICH geometry with the trapezoidal module layout and the rectangular $17 \times 18$ $cm^2$ module layout considering both the $2 \times 2$ $mm^2$ pixel size and the $1 \times 1$ $mm^2$ option with light concentrators.

even accounting for cooling and annealing, as discussed in detail in Chapter 5, where I developed a data-driven ageing model based on my measurements on the current reference SiPM technology.

A significant reduction of the DCR could in principle be achieved using smaller SiPMs, e.g. with size $1 \times 1$ $mm^2$, resulting in a DCR reduction by a factor of four. However, using smaller SiPMs keeping the same acceptance would require an increase by a factor of four in the number of SiPMs, DENEB chips, lpGBTs and VTRx+ ASICs, as well as the other module components, making the simple smaller SiPM option unfeasible.

An appealing option I investigated involves coupling $1 \times 1$ $mm^2$ SiPMs with light concentrators with a collection area of $2.2 \times 2.2$ $mm^2$, consistent with the baseline pixel pitch, to concentrate the impinging photons onto the smaller target SiPM active area. The concentrator option would enable the possibility of covering the same effective area as the baseline option keeping the same number of SiPMs and the corresponding positioning on the photodetector module with a four times smaller active area.

This would not only result in a reduction of the DCR by a factor of four, but also in the overall bRICH photodetector active area and SiPM cost by about the same amount, as shown in Table 3.3. The overall active area would decrease from about 25.50 $m^2$ to about 6.34 $m^2$ for the trapezoidal module layout and from about 18.58 $m^2$ to about 4.64 $m^2$ for the rectangular $17 \times 18$ $cm^2$ module layout.

In addition, with sufficient manufacturing tolerances, adjacent concentrators can be packed without gaps, recovering photons that in the baseline $2 \times 2$ $mm^2$ option with $2.2 \times 2.2$ $mm^2$ pitch would fall into dead regions between adjacent SiPMs.

### 3.7.1 Light concentrators: Principle of operation

The use of light concentrators to reduce the active area of photon sensors has been deeply investigated in applications ranging from high-energy physics [103] to photo-

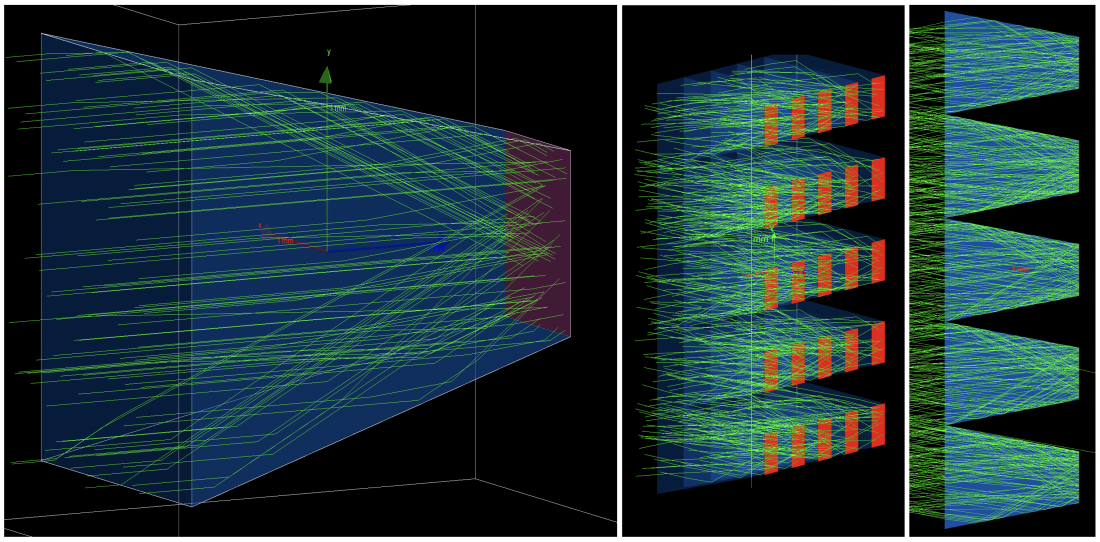

**Figure 3.20:** Ray tracing simulation in the Geant4 framework showing the principle of operation of a light concentrator made of a solid truncated pyramid made of fused silica and an array of concentrators coupled with SiPMs. The red squares correspond to the active area of the SiPMs.

voltaic [104]. Various implementations have been studied, including solid pyramids, Winston cones, compound parabolic concentrators and immersion graded index optics. For the studies presented in this work, I focused on the solid concentrator option, considering truncated pyramids made of fused silica coupled with SiPMs. The principle operation is illustrated in Fig. 3.20. Photons reaching the gas–fused silica interface refract into the concentrators. With an optimised pyramid height, they undergo multiple total reflections (for incidence angles above the limit angle) and Fresnel reflections (for incidence angles below the limit angle) along the concentrator walls and are focused onto the SiPM active area. In this way, photons from a large area with a narrow field of view are concentrated into a smaller area.

These concentrators are an example of non-imaging optic, since the information about the incidence angle is lost by the exit aperture. This is not a problem for my application, where I am assuming that each SiPM has its own concentrator, provided the Cherenkov-angle reconstruction for an expansion gap of thickness $T_g$, defined relative to the SiPM active area, is performed using an effective gap $T_g - l_c$, where $l_c$ is the height of the concentrator, instead of the baseline $T_g$.

The main limitation concerns the photon collection efficiency, which significantly decreases for incidence angles above the total reflection regime. Fixing the upper and lower base of the pyramids, the angular region where photons are efficiently collected depends on the pyramid height. The angular region to be covered by the concentrators for the bRICH application is determined by the angular distribution of the impinging Cherenkov photons emitted by the considered charged-particle species of interest.

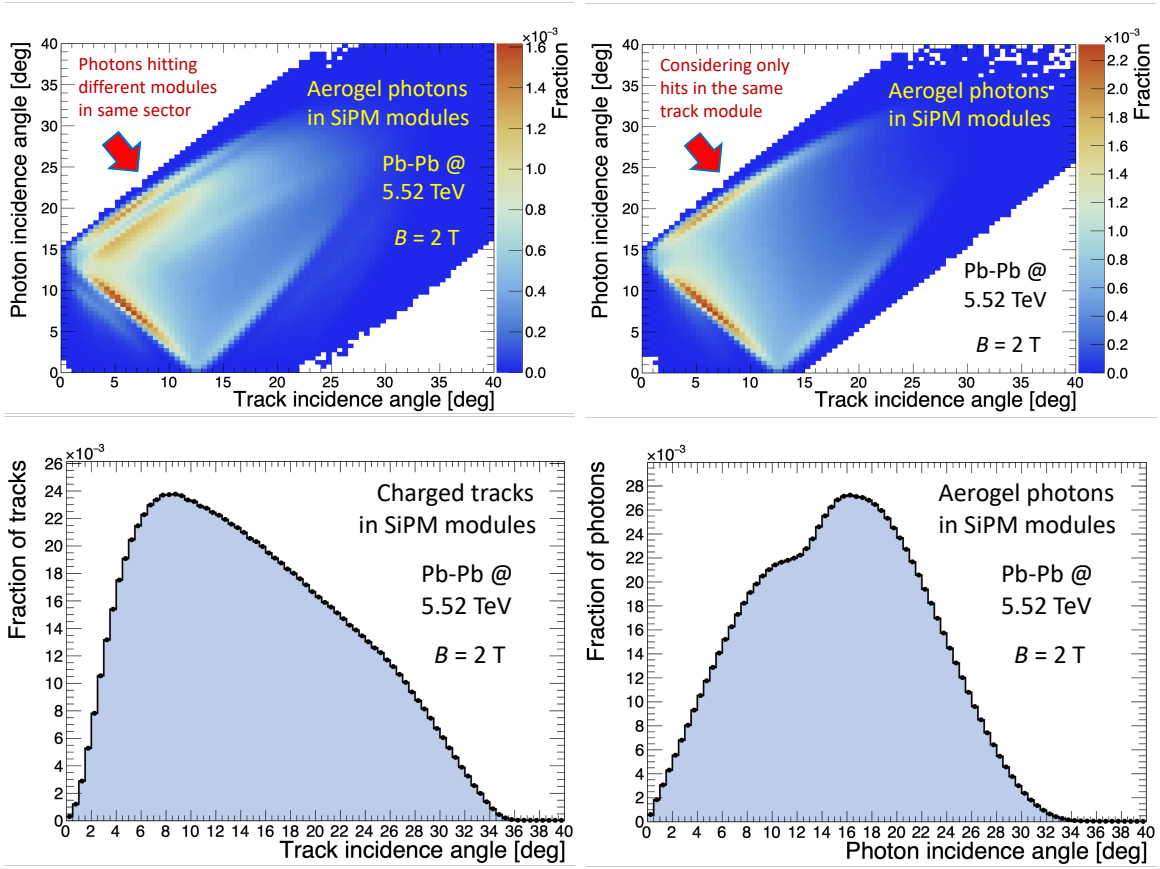


**Figure 3.21:** 2D angular distributions of the charged-track incidence angles and the aerogel photon incidence angle for all particle species, considering both all detected photons (top left) and only photons detected by the SiPMs in the same module in which they are emitted (top right) over the full bRICH acceptance for central Pb-Pb collision at $\sqrt{s_{\mathrm{NN}}} = 5.52$ TeV. The corresponding 1D track incidence angle and photon incidence angle distributions considering all detected photons are shown in the bottom-left and the bottom-right panel, respectively.

### 3.7.2 Photon incidence angles on SiPMs in central Pb-Pb

The 2D angular distributions of the charged-track incidence angles and the aerogel photon incidence angle for all particle species, considering both all detected photons and only photons detected by the SiPMs in the same module in which they are emitted, for central Pb-Pb collision at $\sqrt{s_{\mathrm{NN}}} = 5.52$ TeV generated using my full simulation chain, discussed in Section 4.1, are shown in Fig. 3.21. The corresponding 1D distributions considering all detected photons are also shown. The end-point of the distributions is at about 34-35°. In the case of photons from gas, in the gas-based $e^{\pm}$ ID enhancement option outlined in Section 3.5, due to the small emission angle ($< 2°$), the corresponding angular distribution almost mirrors the track incidence angle one.

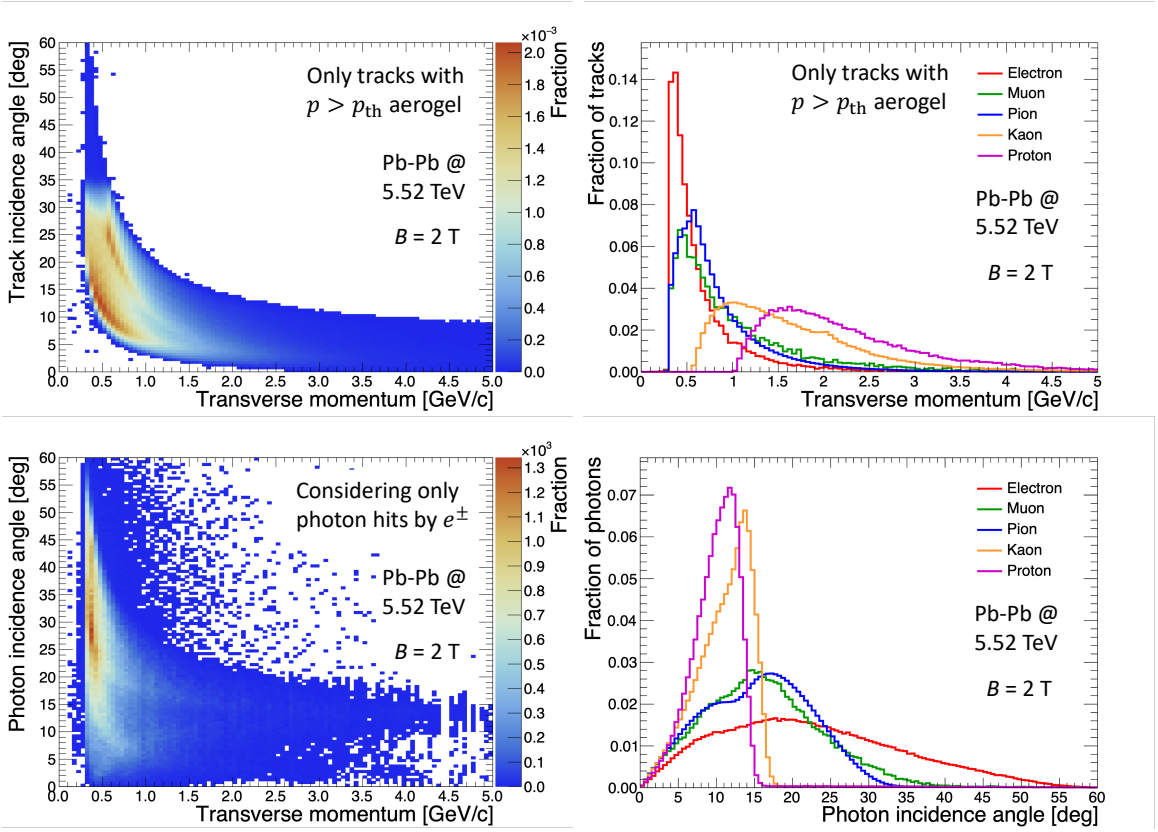


**Figure 3.22:** Top left: 2D distribution of the track incidence angle and transverse momentum at the bRICH SiPMs for tracks with momentum larger than the threshold for Cherenkov emission in the aerogel over the full bRICH acceptance for central Pb-Pb collision at $\sqrt{s_{\mathrm{NN}}}$ = 5.52 TeV. Top right: Transverse momentum distributions for e, μ, π, K and p. Bottom left: 2D distribution of the photon incidence angle and transverse momentum for electrons. Bottom right: Photon incidence angle distributions for e, μ, π, K and p.

Fig. 3.22 shows the 2D distribution of the track incidence angle and transverse momentum at the bRICH SiPMs for tracks with a momentum beyond the threshold for Cherenkov emission in the aerogel over the full bRICH acceptance in the generated Pb-Pb events. The 1D transverse momentum distributions for e, μ, π, K and p are also shown. These distributions highlight that the largest track incidence angles are due to the curvature of low-$p_{\mathrm{T}}$ tracks in the 2 T magnetic field.

The largest per-species contribution to the $p_{\mathrm{T}}$ comes from electrons and positrons due to their lower threshold for Cherenkov emission. The resulting 2D distribution of the photon incidence angle and the transverse momentum for electrons and the $p_{\mathrm{T}}$-integrated photon incidence angle distributions for e, μ, π, K and p are shown in the bottom panels of Fig. 3.22. These plots highlight the presence of a non negligible electron component for photon incidence angles above the 35° maximum angle reference value I considered for my optimization studies.

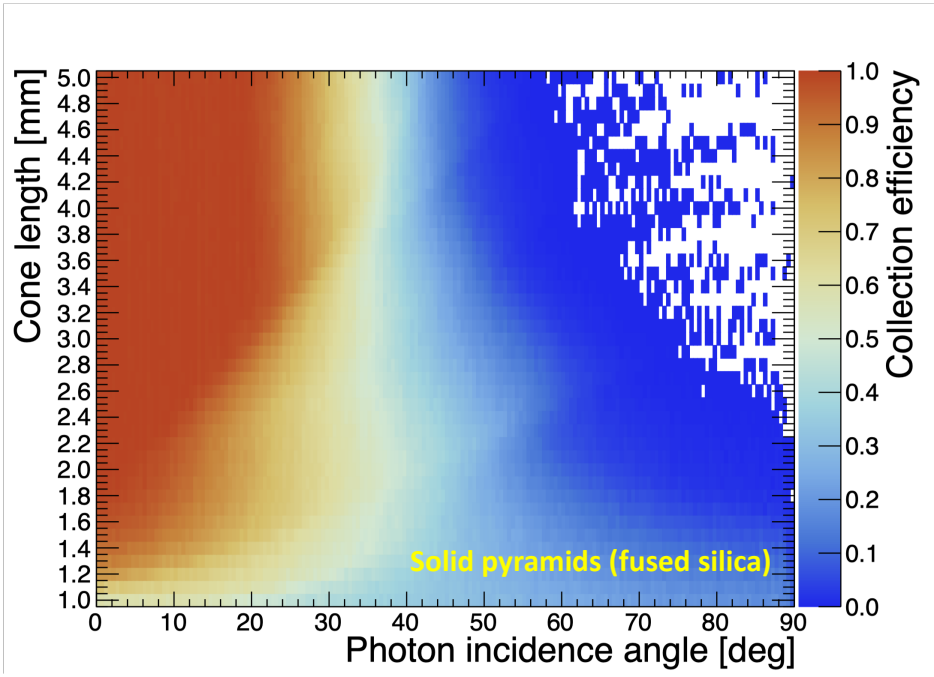


**Figure 3.23:** Scan over the pyramid height of the photon collection efficiency as a function of the photon incidence angle on a light concentrator consisting of a truncated pyramid made of fused silica with a larger base of $2.2 \times 2.2$ mm$^2$.

In particular, extending the high-efficiency collection region beyond this limit is not compatible with the considered implementation of concentrators as solid truncated pyramids with $2.2 \times 2.2$ mm$^2$ input area and $1 \times 1$ mm$^2$ output area. Therefore, this concentrator option comes at the cost of sacrificing the bRICH identification of electrons and positions in the $p_{\mathrm{T}}$ region between the 2 T magnetic field limit, about 0.3 GeV/$c$, and 0.5 GeV/$c$. Nevertheless, this region is already covered by the ALICE 3 oTOF system. Therefore the use of concentrators would just result in a reduction of the overlap between the oTOF and the bRICH identification region.

### 3.7.3 Optimization of concentrator size

I performed dedicated ray tracing simulations in the Geant4 [105] framework to investigate and optimize the size of the considered solid truncated pyramids. For all these studies, I assumed an input area of $2.2 \times 2.2$ mm$^2$, assuming no gap between contiguous pyramids, and an output area of $1 \times 1$ mm$^2$, matching the corresponding SiPM active area. The parameter to be optimized is the pyramid height.

Fig. 3.23 shows a scan over the pyramid height of the photon collection efficiency as a function of the photon incidence angle on a light concentrators. For this simulation

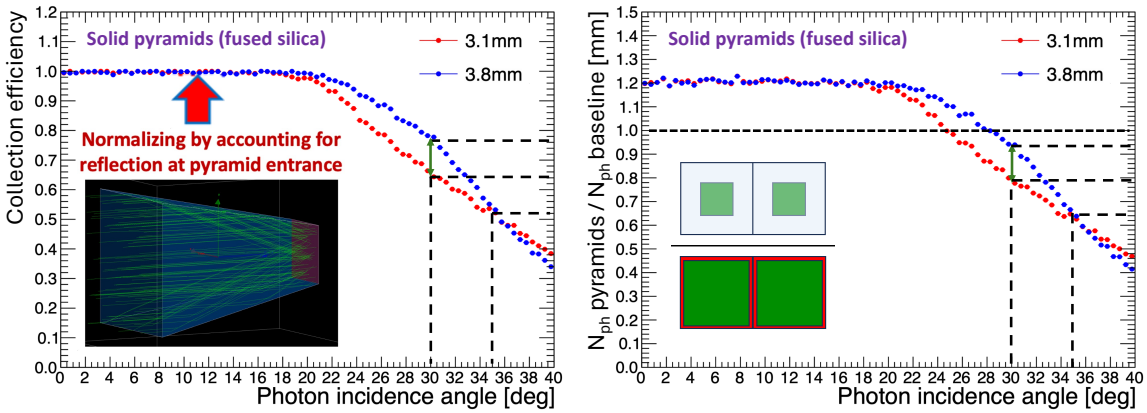


**Figure 3.24:** Left: Simulated photon detection efficiency as a function of the photon incidence angle using truncated pyramids made of fused silica with a larger base of $2.2 \times 2.2$ mm$^2$, a smaller base of $1 \times 1$ mm$^2$ and heights of 3.1 mm (red) and 3.8 mm (blue). Right: Ratio of the number of detected photons considering an array of $1 \times 1$ mm$^2$ SiPMs coupled with contiguous light concentrators to the number of detected photons with the baseline $2 \times 2$ mm$^2$ SiPMs with $2.2 \times 2.2$ mm$^2$ pitch.

I provided the refractive index and chromatic dispersion of fused silica [106] and the photon wavelength spectrum resulting from the convolution of the Cherenkov emission spectrum, given by Eq. 2.7, the measured transmittance of aerogel tiles from Aerogel Factory Co., Ltd. shown in Fig. 2.5 and the PDE of Hamamatsu S13360-**50CS SiPMs shown in Fig. 2.7. The plot shows that the optimal height required to maximize the photon collection efficiency for incidence angles as close as possible to the 35° reference end-point with considered input and output bases is about 3.8 mm. Higher values of this height result in a negligible improvement of the efficiency at the cost of a larger material budget in front of the SiPMs.

Fig. 3.24 shows the resulting photon detection efficiency using truncated pyramids with heights of 3.1 mm and 3.8 mm. The two curves intersect at 35°, where they show a collection efficiency of about 52%. The 3.8 mm case offers larger collection efficiency for smaller angles, increasing to 77% at 30° incidence angle, at the cost of a sharper end-point with respect to smaller values of the height. The reported efficiencies are normalized by accounting for Fresnel reflection at the pyramid entrance face. Due to the similarities in the refractive index of fused silica with the typical protection layers of SiPMs ($n \approx 1.5$), the amount of photons that would be lost due to this reflection is approximately the same that would be lost for photons directly traversing the protection layer of SiPMs in the baseline option.

The right panel of Fig. 3.24 shows the ratio of the number of photons considering an array of $1 \times 1$ mm$^2$ SiPMs coupled with contiguous light concentrators with heights of 3.8 mm and 3.1 mm to the number of detected photons with the baseline $2 \times 2$ mm$^2$

SiPMs with $2.2 \times 2.2$ mm$^2$ pitch. As anticipated in Section 3.7, the use of light concentrators would enable the possibility of recovering photons in the dead regions between contiguous SiPMs. With respect to the baseline SiPM array specifications, the use of light concentrators would ideally result in an increase by up to 21% for photon incidence angles in the total reflection regime. In addition, for larger angles, in the Fresnel reflection regime, this also mitigates the loss of collection efficiency. In particular, for the optimal 3.8 mm case, this ratio is larger than 1 up to about 28°, and it decreased to 94% and 64% at 30° and 35°, respectively.

These results show that the considered simple geometry provides almost full coverage of the photon incidence angle region of interest for the bRICH physics. Even better coverage could be achieved with more complex geometries, such as compound parabolic concentrators [103], or materials, such as immersion graded index optics [104].

### 3.7.4 Impact on the bRICH aerogel and gas photon yield

For a charged track reaching the photodetector at a given incidence angle, the Cherenkov photons emitted in the aerogel radiator or in the gas filling the expansion gap reach the SiPM area at various incidence angles.

Moreover, the considered truncated pyramids made of fused silica ($n \approx 1.47$) behave as additional Cherenkov radiators for the impinging charged particles. The photons produced inside the concentrators are emitted with a Cherenkov angle of about 45° and are not expected to be efficiently trapped in the same concentrator hit by the impinging charged track. These photons may in principle fire multiple SiPMs near the pyramid where they are emitted, thus representing a source of background, especially in the case of the high-n gas-based $e^{\pm}$ ID enhancement option. In particular, due to the low threshold for Cherenkov emission, photons emitted inside the concentrators may result in the formation of mini-clusters around the track impact point for all particle species with momentum above this threshold. This could potentially harm the purity of the electron signal based on the analysis of gas clusters.

The top-left panel of Fig. 3.25 shows the event display of the simulation of an electron at 3 GeV/$c$ momentum and the resulting photons emitted in the aerogel tile, in gas and in the light concentrators assuming truncated pyramids made of fused silica with a height of 3.8 mm, a larger base of 2.2 mm$^2$ and coupled with $1 \times 1$ mm$^2$ SiPMs on the smaller base in the Geant4 framework.

The top-right panel of the same figure shows the mean number of fired SiPMs due to photons emitted within the concentrators as a function of the track incidence angle resulting from the simulation. This value increases from 2 to 3 for track incidence

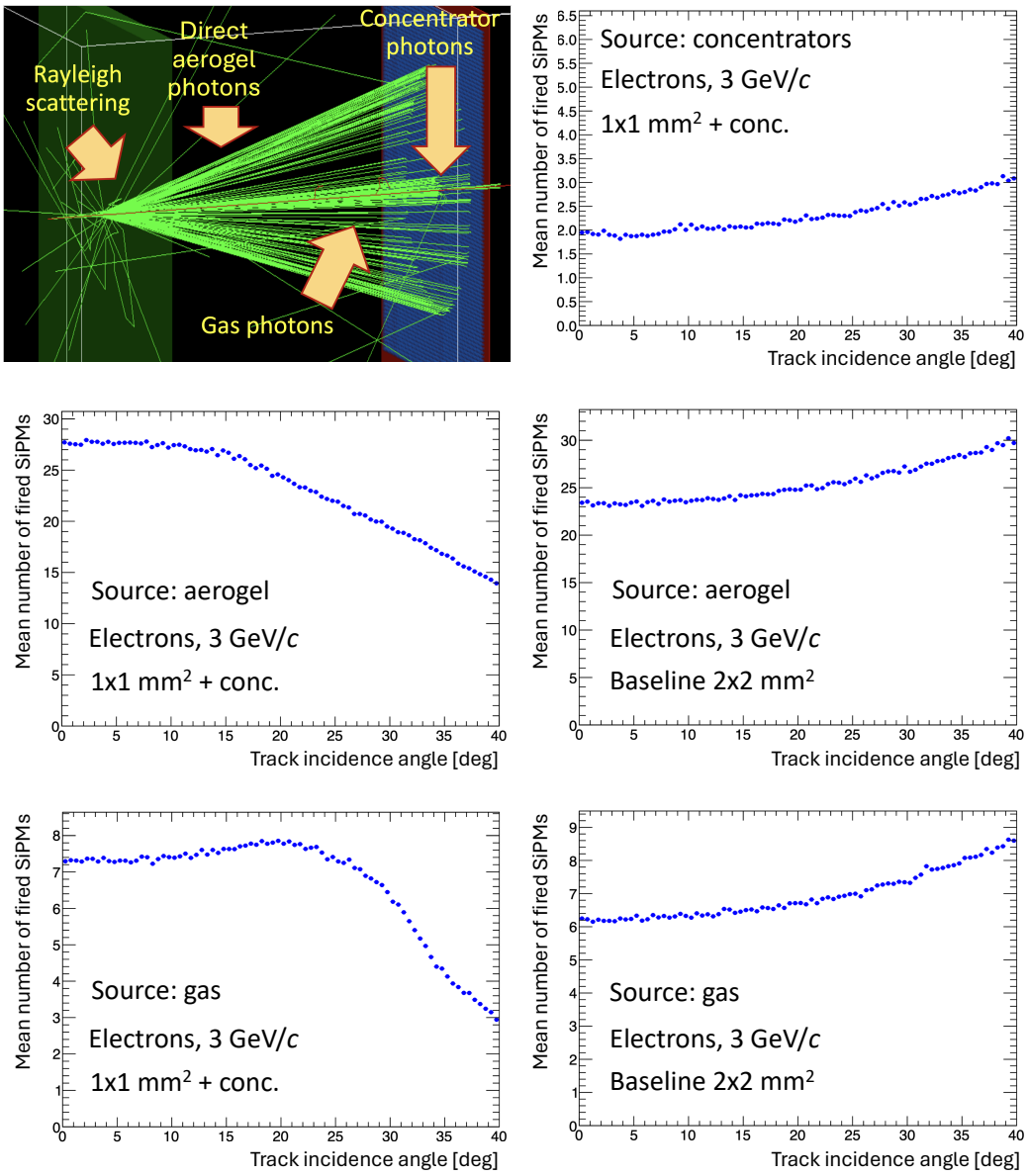


**Figure 3.25:** Top left: Simulation of an electron at 3 GeV/$c$ momentum emitting photons in aerogel, gas and light concentrators assuming truncated pyramids made of fused silica with a height of 3.8 mm, a larger base of 2.2 mm$^2$ and coupled with $1 \times 1$ mm$^2$ SiPMs on the smaller base. Top right: Mean number of fired SiPMs due to photons emitted within the concentrators as a function of the track incidence angle. Middle: Mean number of fired SiPMs due to photons emitted in the aerogel tile as a function of the track incidence angle with both the concentrator option (left) and the baseline SiPM size (right). Bottom: Mean number of fired SiPMs due to photons emitted in the gas filling the expansion gap as a function of the track incidence angle with both the concentrator option (left) and the baseline SiPM size (right) assuming the mixture 10.85% $C_5F_{10}O$ + 89.15% $CO_2$ ($n = 1.0006$).

angles up to 40°. I found equivalent results for pions, kaons and protons at the same momentum. I verified that these photons are always first nearest neighbours to the pyramid hit by the track, making them easy to discard by excluding hits in the corresponding fiducial region when searching for $e^{\pm}$ gas clusters.

The middle and bottom panels of Fig. 3.25 show the mean number of fired SiPMs due to photons emitted in the aerogel tile and in the gas by electrons at 3 GeV/$c$ momentum as a function of the track polar angle with both the concentrator option and the baseline SiPM size. In the case of aerogel photons, the number of fired SiPMs with smaller SiPMs coupled with light concentrators is higher than with the baseline SiPM size up to about 24° track incidence angle, then it becomes smaller. The increase observed in the baseline case at larger angles is due to the larger path length of charged particles in the aerogel tile with the increasing incidence angle, scaling with $1/\cos(\theta_{\text{trk}})$, where $\theta_{\text{trk}}$ is the track incidence angle. The same considerations also apply to gas photons. Owing to their small relative angle to the track ($< 2°$), concentrators yield a larger number of fired SiPMs for track-incidence angles up to about 26°.

These results show that light concentrators coupled with smaller SiPMs are not only a powerful tool for mitigating the SiPM DCR, but they also integrate well with the photon-detection requirements of the ALICE 3 bRICH, achieving performance that may potentially exceed the baseline option within specific angular regions.

### 3.7.5 Concentrators vs charged-particle timing

The formation of mini-clusters due to photons emitted within the concentrators may at first sound similar to the SiPM-based charged-particle timing as discussed in Section 3.6, where fused silica is also one of the most promising materials. However, the considered geometry does not allow efficient collection of photons emitted directly inside the concentrators due to the large photon-emission angles. Most of these photons are expected to leave the concentrator and, due to the smaller considered SiPM area of $1 \times 1$ mm$^2$ compared with the baseline $2 \times 2$ mm$^2$ with the same $2.2 \times 2.2$ mm$^2$ pitch, they are just lost. In addition, despite the reference 3.8 mm height, particles traversing the regions close to the boundary between adjacent concentrators only travel a short path length in the concentrator material, resulting in a limited Cherenkov emission yield. As a result, a significant fraction of the impinging particles result in small mini-clusters of fired SiPMs with a very limited number of photoelectrons per SiPM. Therefore, the concentrator option is not compatible with the efficient SiPM-based charged-particle timing approach discussed in Section 3.6.

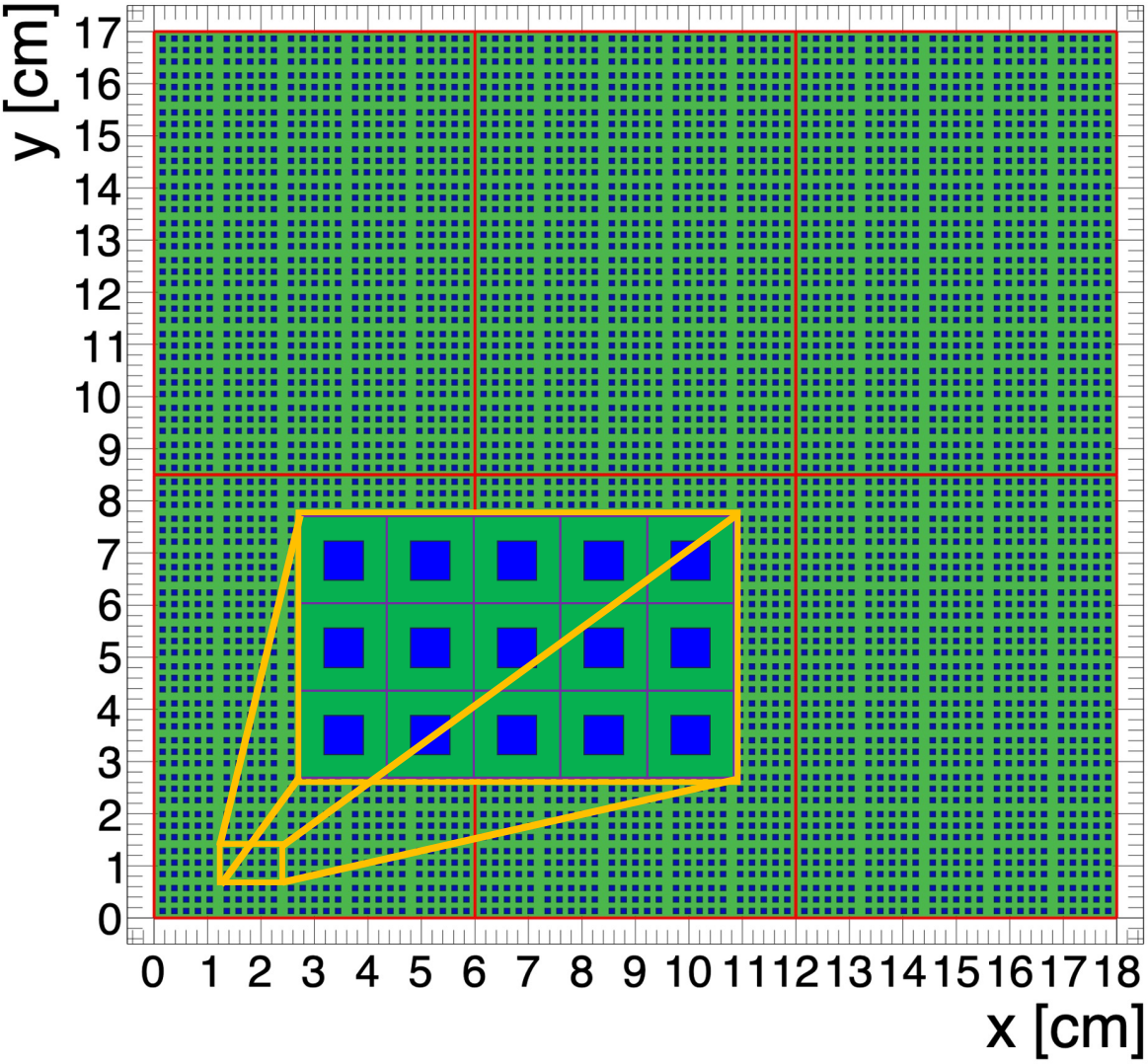


**Figure 3.26:** Geometry of the rectangular $17 \times 18$ cm$^2$ bRICH photodetector module layout using $1 \times 1$ mm$^2$ SiPMs coupled with light concentrators. The blue squares correspond to the SiPMs.

### 3.7.6 Implications on the module concept

Using $1 \times 1$ mm$^2$ SiPMs coupled with light concentrators in place of the baseline $2 \times 2$ mm$^2$ devices, and keeping the same number of channels and the reference $2.2 \times 2.2$ mm$^2$ SiPM pitch per die, impacts the module layout. In particular, the smaller SiPM footprint yields extra free space on the module PCB of about 160 cm$^2$ per module, as shown in Fig. 3.26 compared with the baseline module layout shown in Fig. 3.8. This extra free space is beneficial for integrating passive components, as well as for SiPM routing, cabling, and bi-phase $CO_2$ microchannel cooling.

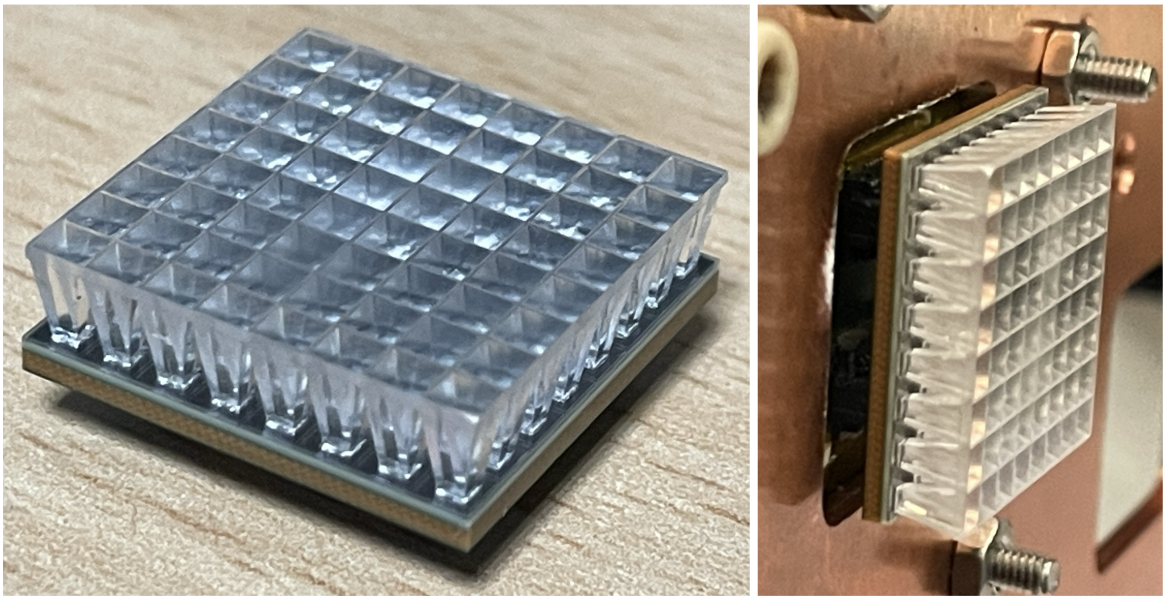

**Figure 3.27:** First prototypes of $8 \times 8$ SiPM arrays mounting the reference truncated pyramids with an upper base of $2.2 \times 2.2$ mm$^2$, a smaller base of $1 \times 1$ mm$^2$ and a height of 3.8 mm.

### 3.7.7 Feasibility and challenges

My optimization studies presented in the previous section led to the production of the first prototypes of $8 \times 8$ SiPM arrays mounting the reference truncated pyramids with an upper base of $2.2 \times 2.2$ mm$^2$, a smaller base of $1 \times 1$ mm$^2$ and a height of 3.8 mm, as shown in Fig. 3.27. First results on optical characterization and beam test measurements of these arrays will be available shortly after the end of this thesis work.

A stringent requirement for application in the bRICH is adherence to tight manufacturing tolerances over a total effective area of approximately 25.50 m$^2$ for the trapezoidal module layout or 18.58 m$^2$ for the rectangular layout. The main challenge concerns the stability of the concentrator arrays at the expected Total Ionizing Dose (TID), as well as the glue used to couple them to the SiPMs, across the required temperature range, from operation at -40°C or below to annealing at 70°C or higher.

# Chapter 4

# bRICH performance simulation

To study the PID performance of the proposed bRICH layout, I developed a dedicated custom full simulation framework enabling the generation and analysis of events from single particles to pp and Pb–Pb collisions. Within this framework, I implemented dedicated Cherenkov-angle reconstruction and particle identification algorithms to carry out a comprehensive performance assessment. The simulation also accounts for the other ALICE 3 subsystems contributing to the overall bRICH performance.

I first focused on the evaluation of the single-photon angular resolution, the mean number of detected photons, and the ring angular resolution over the full bRICH acceptance to quantify the limiting bRICH performance. The studies cover both the trapezoidal and the rectangular $17 \times 18$ cm$^2$ photodetector module layouts. I also quantified the impact of transparent and absorbing walls between contiguous sectors.

The core of my work targets the most challenging environment of central (0–5%) Pb–Pb collisions in extreme DCR conditions. After a detailed analysis of track acceptance and the space–time topology of Pb–Pb events, aimed at defining robust selection criteria for background suppression, I studied pattern recognition and PID performance in terms of efficiency and purity for e, $\mu$, $\pi$, K, and p. The Pb–Pb results were compared to the ones in pp collisions, serving as a benchmark under near-ideal conditions.

For the performance assessment, I first adopted a classical approach based on the Hough transform method for pattern recognition combined with a Bayesian approach for PID. Due to the performance limitations observed in high-multiplicity events, I then developed a machine-learning algorithm based on XGBoost, trained to learn Cherenkov-ring topologies in the projective geometry. This approach outperforms the classical method and provides a state-of-the-art reference for bRICH performance.

I also implemented an XGBoost-based algorithm to study the performance of the gas-based electron identification option in pp and Pb-Pb events. Finally, I evaluated the bRICH contribution to ALICE 3 dielectron physics by studying the PID efficiency versus $m_{\mathrm{ee}}$ and $p_{\mathrm{T,ee}}$, showing that the bRICH is essential to fully explore this channel.

This chapter is structured as follows. In Section 4.1 I present the simulation framework. In Section 4.2 I study the energy spectrum of detected signal-photon hits to characterize Rayleigh-scattering background and the expected spectral response. In Section 4.3 I describe the Cherenkov-angle reconstruction algorithm. In Section 4.4 I report the performance in single-particle events for the tested configurations, establishing the limiting reference performance. In Section 4.5 I discuss the features of the generated Pb–Pb events. The corresponding PID efficiency and purity obtained with a classical Bayesian PID approach are discussed in Section 4.6. In Sections 4.7 and 4.8 I present my XGBoost-based PID algorithms and their performance in pp and central (0–5%) Pb–Pb events using the aerogel signal and the gas clusters. In Section 4.9 I discuss the bRICH contribution to ALICE 3 dielectron physics. Finally, in Section 4.10 I discuss the bRICH contribution to the $\mathrm{D}^0 \to \mathrm{K}^-\pi^+$ identification.

## 4.1 Full simulation framework

The full simulation framework I developed for this study is based on the integration of Pythia 8.304 [107] for event generation and Geant4 11.0.3 [105] transport tools These tools enable a detailed modelling of particle propagation in matter, including decays and interactions, such as the emission, propagation, and detection of Cherenkov photons from the RICH radiator, as well as the interactions of charged and neutral particles across the traversed detector layers. In addition, they also takes care of the magnetic field. The particles then leave hits in the defined sensitive volumes containing information on the particle type, momentum, nominal position and deposited energy. I then developed a custom digitizer to simulate the actual detector response, accounting for features including the pixelization, dead areas, the time resolution, the detection efficiency, the dark counts and the dead time of the sensors. The output of the digitizer is then used for the analysis. A diagram of the simulation steps is shown in Fig. 4.1. For the generation of Pb-Pb Pythia 8 includes a machinery based on the Angantyr model [108], in which simulation of heavy-ion collisions are implemented combining multiple nucleon–nucleon collisions. For all the simulation studies presented in this work, I used the Geant4 FTFP_BERT and the G4OpticalPhysics physics lists.

In the following sections, I describe the implementation of the detector geometry, the event generation, my custom digitizer, and the set of observables stored for the analysis.

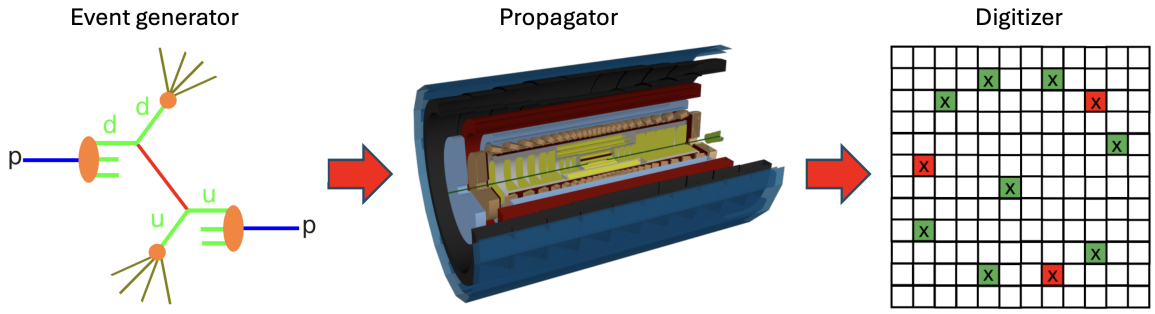


**Figure 4.1:** Diagram of the simulation workflow: event generation, transport, and digitization.

### 4.1.1 Detector geometry

The simulation includes the bRICH layout of interest, along with all other upstream ALICE 3 subsystems potentially affecting tracking and the background due to interactions with the materials, including the beam pipe, the barrel tracker layers, the outer tracker disks and the iTOF and oTOF layers. I implemented the bRICH geometry according to the various configurations under study presented in Chapter 3, while all the other subsystems were implemented according to their state-of-the-art specifications [2] and were kept fixed throughout this work. Fig. 4.2 shows the simulated geometry for the proposed projective proximity-focusing bRICH layout. The two vessels and walls at sector boundaries are not shown for visualization purpose.

In particular, for the bRICH geometry, I considered both the options with the trapezoidal photodetector module concept and the rectangular $17 \times 18$ cm$^2$ module concept. For the refractive index and transmission length for the 2 cm thick aerogel tiles and the PDE of the SiPMs I assumed the typical curves of hydrophobic aerogel tiles from Aerogel Factory Co., Ltd., and Hamamatsu S13360-**50 SiPMs, reported in Fig. 4.3.

For the additional detector subsystems, I considered silicon cylinders and disks, with geometric specifications and material budgets as listed in Tables 1.4, 1.5, and 1.6, for the inner tracker, outer tracker, and TOF layers, respectively, surrounded by air. For the beam pipe, I considered a beryllium cylinder of radius 3.0 cm and thickness 0.8 mm, corresponding to about 0.23% of a radiation length $X_0$.

All studies reported in this chapter used a uniform 2 T field along the beam direction, as an approximation of the field provided by the ALICE 3 superconducting magnet.

I considered the standard ALICE coordinate system, where the origin (0, 0, 0) corresponds to the nominal interaction point of the beams, and the Z-axis is aligned with the nominal beam axis. The X-axis points horizontally outward from the beam line, and the Y-axis points vertically upward, forming a right-handed coordinate system.

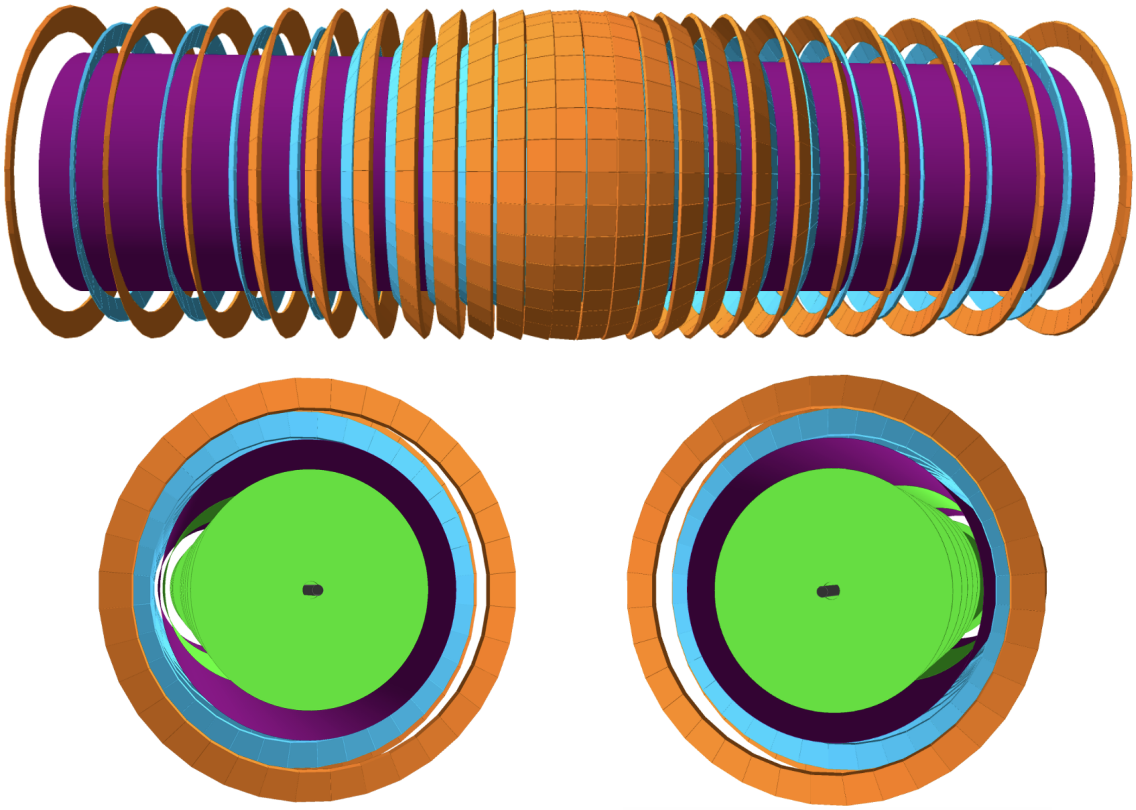

**Figure 4.2:** Full simulated geometry for the projective bRICH layout, including the beam pipe (gray), the barrel and disk tracker layers (green) and the iTOF and oTOF layers (purple)

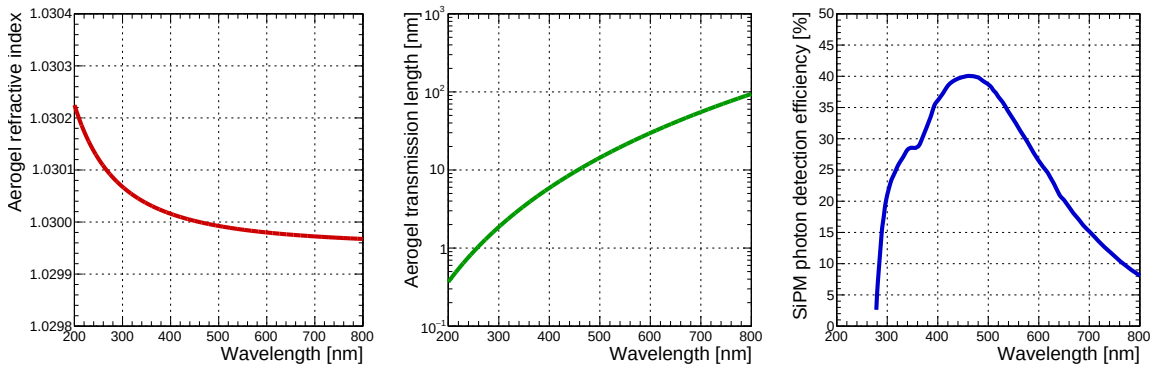


**Figure 4.3:** Reference aerogel refractive index (left), aerogel transmission length (middle) and SiPM PDE (right) as a function of the photon wavelength used for the simulation.

| **Pythia settings** | **pp** | **Pb-Pb** |
|---|---|---|
| Version | 8.304 | 8.304 |
| Tune | Monash 2013 | Monash 2013 |
| Beams:idA | 2212 | 1000822080 |
| Beams:idB | 2212 | 1000822080 |
| Beams:eCM | 14000 #GeV | 5520 #GeV |
| ParticleDecays:limitTau0 | on | on |
| ParticleDecays:tau0Max | 10 #mm/$c$ | 10 #mm/$c$ |
| HardQCD:hardccbar | on | // |
| HardQCD:hardccbar | on | // |
| HeavyIon:SigFitNGen | // | 0 |
| HeavyIon:SigFitDefPar | // | 14.82,1.82,0.25,0,0,0,0,0 |
| HeavyIon:bWidth | // | 20 #fm |

**Table 4.1:** Simulation settings used for event generation in pp and Pb-Pb collisions.

### 4.1.2 Event generation

For all the results presented in this chapter, I used the following categories of events.

- Single-particle events with a single e, μ, π, K or p.
- $c\bar{c}$ and $b\bar{b}$ biased pp collisions at centre-of-mass energy $\sqrt{s} = 14$ TeV.
- Central (0-5%) Pb-Pb collisions at centre-of-mass energy $\sqrt{s_{\mathrm{NN}}} = 5.52$ TeV.

I generated single-particle events using the Geant4 General Particle Source (GPS) [109], a generator allowing full control over the energy and angular distributions of the primary particles. I used these events to assess the limiting detector performance.

I then considered pp and Pb–Pb collisions, generated using Pythia 8.304, to test the stability of the detector performance in the effective occupancy conditions planned for the ALICE 3 detector and to quantify the PID performance of the considered RICH configurations. The settings used for the event generation in both collision systems are summarised in Table 4.1. Samples of central (0-5%) Pb-Pb events were generated using the Angantyr model [108] with HeavyIon:bWidth set to 20 fm [110] and considering the 5% events in the sample featuring the largest primary track multiplicity.

Fig. 4.4 shows the event display with 500 primary tracks from the nominal collision vertex, showing the propagation of both tracks and photons in the system. For visualization purposes, only photons passing the reference SiPM PDE check are shown.

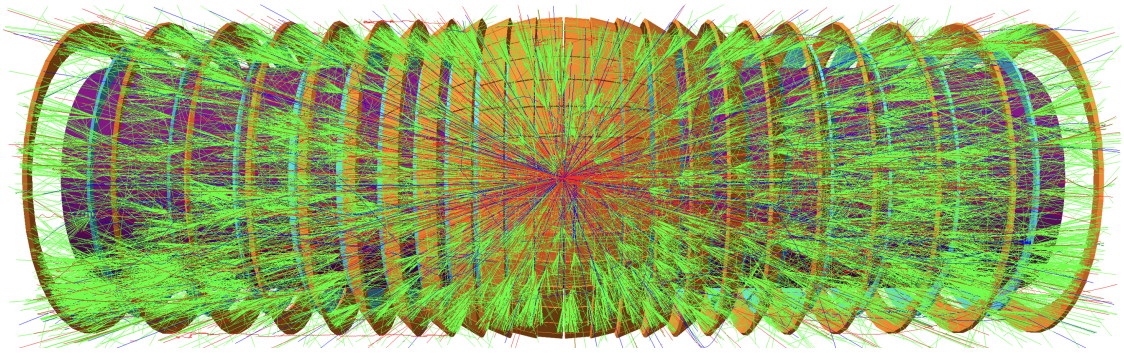

**Figure 4.4:** Event display of a Pb-Pb event with 500 primary charged tracks entering the bRICH showing the propagation of both charged tracks (blue and red) and photons (green) in the system. For visualization purposes, only photons passing the reference SiPM PDE check are shown.

#### Raw data

For each simulated event an output file is written storing the information required for later digitization. It includes all new primary particles and all secondary particles created by interactions with the detector materials and by decays. For each generated particle, my simulation code configures Geant4 to store the PDG code identifying the particle species, the process that produced it, the parent track labels, the space–time coordinates and four-momentum at the production point, and the same quantities at every hit in the tracker, TOF, and RICH sensitive volumes.

### 4.1.3 Custom digitizer

Starting from the hits recorded in the generic sensitive volumes, I implemented a custom digitizer that models the detector response of the subsystems used in this analysis, including pixelization, time resolution, detection efficiency, recovery time and dark counts. The most relevant details are summarised in the following.

#### Charged-particle detection and timing

For the tracker and TOF layers, I assumed a charged-particle detection efficiency of 100% in order to decouple the intrinsic RICH performance from that of the other subsystems. Consequently, all bRICH PID efficiency results presented in the following are normalized to the fraction of reconstructed good tracks for each particle species. For the charged-particle hit times provided by the TOF layers, I assumed the ALICE 3 TOF target resolution of $\sigma_{t,\mathrm{ch}} = 20$ ps. The measured hit times were obtained by smearing the nominal arrival times with a Gaussian fluctuation of width $\sigma_{t,\mathrm{ch}}$.

### Photodetector pixelization

For each available hit on the bRICH photodetector modules, I mapped its position relative to the SiPM layout and discarded all hits falling outside the active SiPM areas. For the rectangular $17 \times 18$ cm$^2$ module layout in Section 3.4.4, the discarded hits correspond to photons impinging within the 200 µm gaps between adjacent SiPMs on the same die or within the inactive regions separating neighbouring dies. For hits falling within the area of a given SiPM, I assigned the coordinates of the corresponding pixel centre $(x_{\mathrm{ph}}, y_{\mathrm{ph}}, z_{\mathrm{ph}})$. An example of this step for a single particle event with the rectangular $17 \times 18$ cm$^2$ module layout is shown in the left panel of Fig. 4.5.

### Photon detection efficiency

For the detection of photons with the bRICH SiPMs, I used the wavelength-dependent PDE curve shown in the right panel of Fig. 4.3. For each optical-photon hit, I generated a random number uniformly distributed between 0 and 1 and accepted the hit only if this number was smaller than the PDE value at the photon's wavelength.

### Single photon time resolution

For the optical photon hits on the RICH photodetector modules, one of the goals of this chapter is to highlight the impact of the overall single-photon time resolution (SPTR), including both the SiPM and electronics contributions. Accordingly, I considered several SPTR scenarios in the range 50–200 ps, and computed the measured hit times by adding a Gaussian fluctuation of width $\sigma_{t,\mathrm{ph}}$ to the nominal times.

### Simulation of SiPM dead time effects

A critical consideration at high DCR and for a given acquisition window $\Delta t$ is the SiPM recovery time. SiPMs can fire due to DCR, together with correlated cross-talk and afterpulsing, before the gate opens and may still be recovering when a true signal arrives, failing to register the threshold crossing. To account for this, I implemented a custom simulation, based on the method proposed in [111], to evaluate the probability that a SiPM is still recovering at the gate opening. The right panel of Fig. 4.5 shows this probability as a function of the DCR for $2 \times 2$ mm$^2$ SiPMs under various assumptions for the recovery time $\tau$ assuming the cross-talk and afterpulsing probabilities and characteristic times of commercial Hamamatsu SiPMs, showing how operation becomes

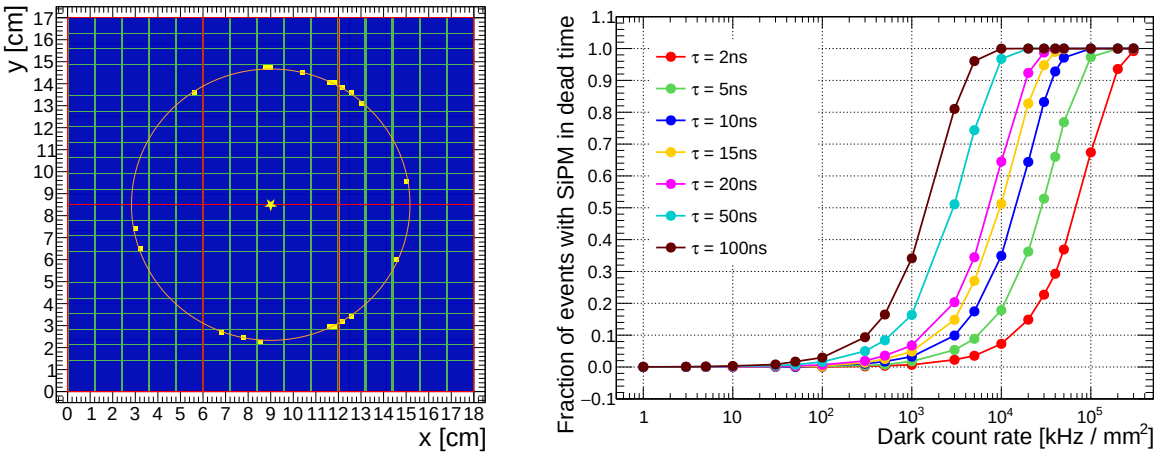


**Figure 4.5:** Left: Single-particle event with digitized hits on the $17 \times 18$ cm$^2$ rectangular module layout. Right: Simulated probability that a SiPM is still recovering at the acquisition time gate opening as a function of DCR under various assumptions for the recovery time $\tau$.

critical beyond the MHz/mm$^2$ level. In this chapter I assumed $\tau = 20$ ns and, event by event, disabled a random fraction of SiPMs with probability taken from Fig. 4.5.

### Simulation of SiPM DCR

For a reference DCR per unit area (e.g. 1 MHz/mm$^2$), a SiPM active area $A_{\mathrm{SiPM}}$ (4 mm$^2$ for the reference $2 \times 2$ mm$^2$ SiPMs), an acquisition time gate $\Delta t$, and a number of available (i.e. not disabled in the previous step) SiPMs $N_{\mathrm{av}}$ in the bRICH, I extracted the effective number of dark counts $N_{\mathrm{DCR}}$ from a Poisson distribution with mean:

$$\langle N_{\mathrm{DCR}} \rangle = \mathrm{DCR} \cdot A_{\mathrm{SiPM}} \cdot N_{\mathrm{av}} \cdot \Delta t. \tag{4.1}$$

For each generated count, I randomly selected one of the available SiPMs and assigned a hit time $t_{\mathrm{ph}}$ uniformly distributed in the $\Delta t$ window with a sector-dependent origin.

### Clustering of multiple hits in the same SiPM

From the steps described above, multiple counts, either signal hits passing the PDE check or background hits, can occur on the same SiPM in the same event. In such cases, I treated the SiPM as firing once, with the number of photoelectrons equal to the total number of counts and the detection time corresponding to the earliest hit.

**Digitizer output**

For each event, my digitizer records the relevant information on all the accepted charged tracks and the hits in the bRICH SiPM modules for the analysis. For each track, it stores the hit coordinates and time $(x_{\mathrm{TOF}}, y_{\mathrm{TOF}}, z_{\mathrm{TOF}}, t_{\mathrm{TOF}})$, as well as the momentum components $(p_{x,\mathrm{TOF}}, p_{y,\mathrm{TOF}}, p_{z,\mathrm{TOF}})$, at the oTOF layer, and the particle species ID. The space–time coordinates and four-momentum at the production point are also stored. For each hit in the bRICH SiPM modules, the digitizer stores the position and time $(x_{\mathrm{ph}}, y_{\mathrm{ph}}, z_{\mathrm{ph}}, t_{\mathrm{ph}})$, the number of photoelectrons, and the parent label. The coordinates and momenta are used for the reconstruction of the Cherenkov angle, while the species IDs and parent labels are employed to quantify the detector performance, efficiencies, and separation power among different particle species.

## 4.2 Energy spectrum of detected photons

I studied the wavelength spectrum of detected photons to quantify the impact of Rayleigh scattering and to determine the average radiator refractive index $\langle n_r \rangle$ to be used in the analysis. The detected $\lambda$ spectrum results from the convolution of the Cherenkov emission spectrum, the aerogel transmittance, and the PDE of the SiPMs.

For this study, I simulated single $\pi^-$ events with momentum $p = 10$ GeV/$c$, directed towards the centre of the aerogel tile of module 1 in the central sector (+1) assuming photon absorbing walls between contiguous sectors. Fig. 4.6 shows the resulting wavelength spectra of both direct unscattered and Rayleigh scattered Cherenkov photons reaching the photodetector active area (left) and those passing the reference PDE selection (right). Scattered photons not reaching the SiPMs are also shown.

Despite significant Rayleigh scattering at short wavelengths ($\lambda < 350$ nm), the projective geometry naturally rejects most scattered photons, with only about 9% detected per event. With the reference SiPM PDE in Fig. 4.3, the detection efficiency at short wavelengths is further suppressed, leading to fewer than one detected scattered photon per event on average, compared to approximately 24 expected unscattered photons at saturation. From a scan over the bRICH sectors, I found the mean number of detected scattered photons to be below 0.5–0.6 per event, depending on the sector gap. Under these conditions, the Rayleigh contribution is therefore almost negligible.

From the spectrum of detected unscattered photons, I extracted a mean detected wavelength of $\langle \lambda \rangle = 460$ nm, leading to the choice of the dispersion curve in Fig. 4.3, with the nominal $n = 1.03$ at 460 nm. I also extracted the standard deviation of the

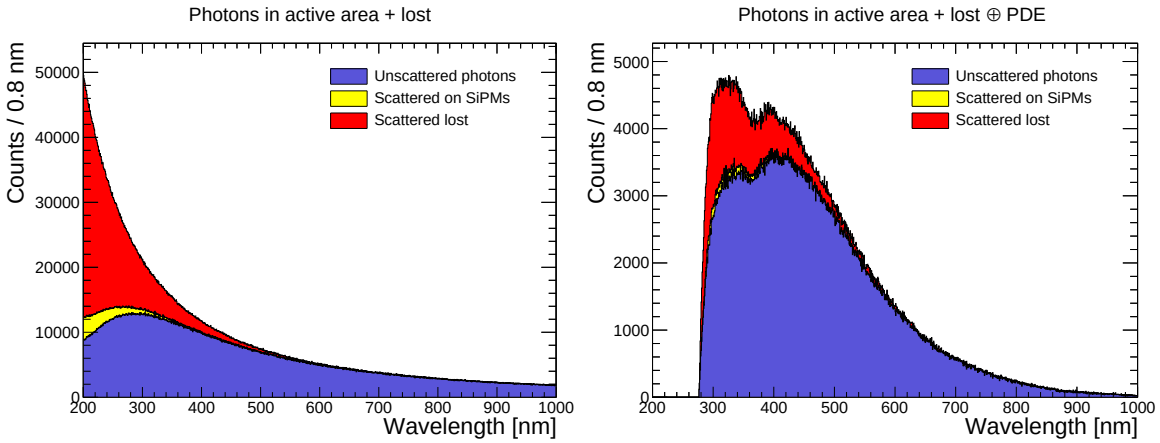


**Figure 4.6:** Spectrum of all Cherenkov photons (left) and of photons passing the SiPM PDE selection (right) for $\pi^-$ at $p = 10$ GeV/$c$. The blue and yellow areas correspond to unscattered and scattered photons reaching the SiPMs. The red area indicates scattered photons not reaching the SiPMs.

detected wavelength spectrum, $\sigma_\lambda = 125$ nm, which I used in the analytical calculation of the chromatic contribution to the angular resolution in Appendix A.

## 4.3 Cherenkov angle reconstruction chain

I implemented a C++ pattern recognition algorithm for reconstructing the charged-particle Cherenkov emission angle in aerogel using the hits produced in the bRICH.

For all available charged tracks, I required at least one hit in the oTOF layer for track selection. This condition rejects tracks that do not reach the RICH systems due to low $p_\mathrm{T}$ in the 2 T magnetic field or interactions with the traversed material. I further required the oTOF track extrapolation to reach a hypothetical cylindrical layer with radius 117 cm, to ensure acceptable conditions for reconstruction.

From the hit on the oTOF layer and the corresponding track momentum, I extrapolated the track to the most probable emission depth $T_\mathrm{em}$ of detected unscattered photons in the aerogel radiator, with space–time coordinates $(x_\mathrm{rad}, y_\mathrm{rad}, z_\mathrm{rad}, t_\mathrm{rad})$, while accounting for curvature in the 2 T magnetic field. I determined $T_\mathrm{em}$ with a dedicated simulation following the procedure discussed in Appendix C.4. For the reference aerogel sample I found $T_\mathrm{em}$ to lie 650 µm beyond the median plane of the tiles.

For each track, I evaluated the hypothetical Cherenkov emission angle associated to each measured hit, treated as a candidate photon emitted by the considered track at the most probable emission depth in the radiator, using the algorithm in Section 4.3.1.

I applied selections on the track–photon relative detection time and on the reconstructed single hit angle to suppress background hits due to photons produced by other charged particles and the SiPM DCR, as discussed in Sections 4.3.3 and 4.3.2.

Finally, I processed the surviving hits with a Hough-like pattern recognition method [112] to determine, for each track, the ring Cherenkov angle, as detailed in Section 4.3.4.

### 4.3.1 Single hit Cherenkov angle

Given a track and a hit on the photodetector, I performed a geometrical backtracking to reconstruct the angle under which a hypothetical photon causing the hit would be emitted if produced by the considered track [112]. The following assumptions are made.

- The origin of all candidates photons is assumed at the extrapolation point of the charged track to the most probable emission depth of detected unscattered photons in the aerogel radiator, 650 µm beyond the median plane of the tiles.
- All candidates are assumed to have the same wavelength $\langle\lambda\rangle$, corresponding to the mean wavelength of detected unscattered photons, evaluated in Section 4.2.

The following parameters are required to perform the angle extrapolation:

- $T_r, T_g$ = aerogel tile and gap thickness in the considered module,
- $T_{\rm em}$ = most probable emission depth in the aerogel tile,
- $\langle n_r\rangle$, $\langle n_g\rangle$ = aerogel and argon refractive indices at wavelength $\langle\lambda\rangle$.

The following variables are then required to perform the angle extrapolation:

- $\mathbf{r}_{rad} = (x_{rad},\, y_{rad},\, z_{rad})$ : track extrapolation to $T_{\rm em}$ in the aerogel tile,
- $\mathbf{r}_{ph} = (x_{ph}, y_{ph}, z_{ph})$ : hit coordinates on the photodetector,
- $\mathbf{p}_{rad} = (p_{x,\rm rad},\, p_{y,\rm rad},\, p_{z,rad})$ : track momentum extrapolation at $\mathbf{r}_{rad}$,
- $\mathbf{u}_{em}$ : vector normal to the aerogel tile in the considered module.

The angle reconstruction procedure consists of the following steps:

1. The variation of the photon coordinates $\delta\mathbf{r}$ from the most probable emission point $\mathbf{r}_{rad}$ to the detection point $\mathbf{r}_{ph}$ is evaluated as $\delta\mathbf{r} = \mathbf{r}_{ph} - \mathbf{r}_{rad}$

2. The apparent emission angle $\theta_{ap}$ between $\delta\mathbf{r}$ and the normal vector to the radiator tile in the considered radiator module $\mathbf{u}_{em}$ is calculated as:

$$\theta_{ap} = \arccos\left(\frac{\delta\mathbf{r}\cdot\mathbf{u}_{em}}{|\delta\mathbf{r}||\mathbf{u}_{em}|}\right) \tag{4.2}$$

3. The angle $\theta_{rad}$ between the candidate photon direction in the radiator and $\mathbf{u_{em}}$ is obtained from $\theta_{ap}$ by taking into account refraction at the interface between aerogel and gas using Snell's law with the relation:

$$\theta_{rad} = \arcsin\left(\frac{(T_r - T_{em}) + T_g}{(T_r - T_{em}) + T_g\langle n_r\rangle/\langle n_g\rangle}\ \sin\theta_{ap}\right) \tag{4.3}$$

4. The angle $\delta\theta = \theta_{ap} - \theta_{rad}$ is evaluated and a rotation $R_{\mathbf{u}}(\delta\theta)$ by an angle $\delta\theta$ is applied to $\delta\mathbf{r}$ around the axis passing through the point $\mathbf{r_{rad}}$ and perpendicular to both $\delta\mathbf{r}$ and $\mathbf{u}_{em}$ with positive direction given by the unit vector $\mathbf{u}$ defined as:

$$\mathbf{u} = \frac{\delta\mathbf{r}\times\mathbf{u}_{em}}{|\delta\mathbf{r}\times\mathbf{u}_{em}|} \tag{4.4}$$

   The vector resulting from the rotation $\delta\mathbf{r}'$ is then given by:

$$\delta\mathbf{r}' = R_{\mathbf{u}}(\delta\theta)\delta\mathbf{r} = \mathbf{u}(\mathbf{u}\cdot\delta\mathbf{r}) + \cos(\delta\theta)(\mathbf{u}\times\delta\mathbf{r})\times\mathbf{u} + \sin(\delta\theta)(\mathbf{u}\times\delta\mathbf{r}) \tag{4.5}$$

5. The most probable Cherenkov emission angle $\theta_c$ is finally obtained as the angle between $\delta\mathbf{r}'$ and the charged-particle direction $\mathbf{p}$ as:

$$\theta_c = \arccos\left(\frac{\delta\mathbf{r}'\cdot\mathbf{p}_{rad}}{|\delta\mathbf{r}'|\ |\mathbf{p}_{rad}|}\right) \tag{4.6}$$

This method is general and is valid for any track incidence on the modules of the considered bRICH implementations. The result is equivalent to one obtained through the treatment discussed in Appendix A with the change of variables:

$$(\mathbf{r}_{rad}, \mathbf{r}_{ph}, \mathbf{p}_{rad}) \longmapsto (z_e, x, y, z, \theta_p, \phi_p). \tag{4.7}$$

The corresponding uncertainty, $\sigma_c^\gamma$, representing the single photon angular resolution, can then be evaluated with the procedure discussed in Section 2.3.2.

### 4.3.2 Angle selection: Cherenkov angle physical limit

Considering all available hits as candidate Cherenkov photons for a given track, uncorrelated background hits can yield reconstructed angles above the physical Cherenkov maximum in aerogel. For the analysis I only keep hits within the physically allowed range. The theoretical limit $\theta_{c,\max}$ for $\langle n_r \rangle = 1.03$ is about $\theta_{c,\max} \approx 241.9$ mrad. Accounting for measurement effects, including tracking, the pixel size, the emission-depth uncertainty and chromatic dispersion, determining the single-photon resolution $\sigma_c^\gamma$, I only retain hits such that $\theta_c < \theta_{c,\max} + 3\,\sigma_c^\gamma$ , and treat larger angles as background.

### 4.3.3 Timing selection: hit-track time matching

With a single-photon time resolution (SPTR) better than 200 ps, a time cut on hit–track matching can be applied to substantially suppress contamination from the SiPM DCR and from photons emitted by other particles in the same event.

For each detected hit with detection time $t_{ph}$ at the position $\mathbf{r}_{ph}$ on a photodetector module, and the most probable emission point $\mathbf{r}_{rad}$ when regarded as candidate Cherenkov photon by a given track, I evaluated the time $t_D$ required to travel the total path length from $\mathbf{r}_{rad}$ to $\mathbf{r}_{ph}$. For the calculation I assumed straight line propagation in the aerogel tile and the gas filling the expansion gap, with refraction at their interface, and the corresponding group velocities derived from their dispersion curves at $\langle \lambda \rangle = 460$ nm. I then evaluated the most probable emission time as $t_{em} = t_{ph} - t_D$. Comparing to the extrapolated track arrival time $t_{rad}$ at $\mathbf{r}_{rad}$, we keep hits satisfying:

$$|\Delta T| \equiv |t_{em} - t_{rad}| < N\,\sigma_{\Delta T} \tag{4.8}$$

where $\sigma_{\Delta T}$ is the spread in the $\Delta T$ distribution of true Cherenkov photons associated to the considered tracks and $N$ can be tuned to optimize the selection.

For the analysis of pp and Pb-Pb events, I investigated the impact of the time-matching requirement for an overall SPTR ranging from the target 50 ps to 200 ps. For all these studies I assumed the baseline track-time resolution $\sigma_{t,\mathrm{ch}} = 20$ ps from the oTOF. As a first approximation, the expected spread of the $\Delta T$ distribution is then given by:

$$\sigma_{\Delta T}^{\mathrm{exp}} = \sqrt{\mathrm{SPTR}^2 + \sigma_{t,\mathrm{ch}}^2}\,, \tag{4.9}$$

which gives $\sigma_{\Delta T}^{\mathrm{exp}} \approx 54$ ps for SPTR = 50 ps and $\approx 201$ ps for SPTR = 200 ps. I found that the optimal compromise among the achievable efficiency, purity and signal to background ratio was achieved for $N \approx 2$, as detailed in Section 4.5.5.

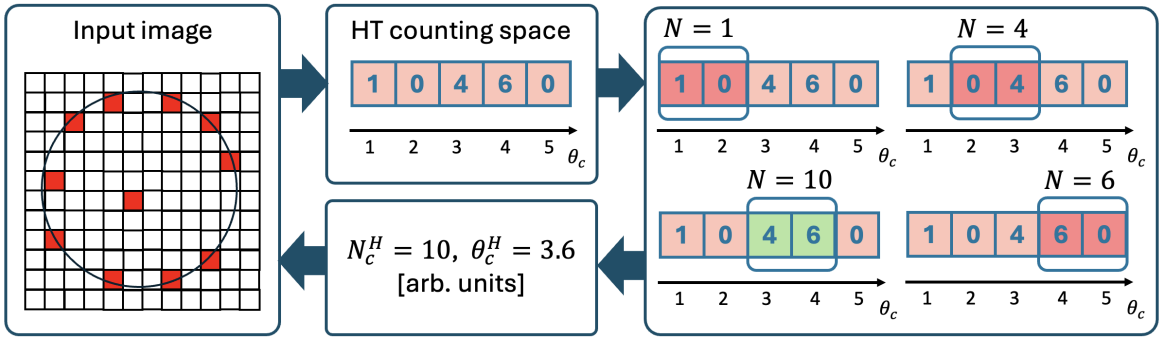


**Figure 4.7:** Illustrative example of the application of the Hough transform method for the reconstruction of the Cherenkov angle associated to a given charged track in a RICH detector.

### 4.3.4 Ring Cherenkov angle: the Hough transform

For the determination of the ring Cherenkov angle for a given track I used a modified Hough-transform method [113, 114], similar to that employed in the ALICE HMPID detector [112], to account for the uncertainty $\sigma_c^\gamma$ on the measured single hit angles $\theta_c$. The method is based on a sampling band approach to scan the $\theta_c$ angular spectrum of the candidate photon hits. The extraction of the angle consists of the following steps:

1. A sliding window having a width $b$ of units of $\sigma_c^\gamma$ is used to scan the angular range of interest $[\theta_{\min}, \theta_{\max}]$ in the $\theta_c$ measured spectrum with a step size $\Delta\theta_c$. At each step the number of hits found within the window is counted.

2. A search is made for the interval with the largest number of counted hits. The information on the number $N_c^H$ of photodetector hits falling in the selected sampling band and the corresponding angles $\theta_{c,i}$, with $i = 1, ..., N_c^H$ is recorded.

3. A threshold $N_{\min}^H$ is set on the number of recorded hits $N_c^H$ to avoid the clustering of background hits for charged tracks below or slightly above the threshold for Cherenkov emission. If $N_c^H < N_{\min}^H$, the considered track is discarded.

4. The mean Cherenkov angle $\theta_c^H$ associated with the track is finally calculated by averaging the measured angles of the hits falling in the selected window:

$$\theta_c^H = \frac{1}{N_c^H} \sum_{i=1}^{N_c^H} \theta_{c,i}. \tag{4.10}$$

An illustrative example of the application of the Hough transform for reconstruction of the Cherenkov angle associated to a charged track is shown in Fig. 4.7. The algorithm performance and computational load depend on the step size $\Delta\theta_c$, the considered range

$[\theta_{\min}, \theta_{\max}]$, the width of the sliding window $b$ and the threshold $N^H_{\min}$ on the number of counted hits $N^H_c$. The step size and the range determine the number of steps $N_{\text{steps}} = (\theta_{\max} - \theta_{\min})/\Delta\theta_c$, i.e. the number of iterations required to fill the counter.

I found that the optimal range for the bRICH aerogel tiles was between $\theta_{\min} = 30$ mrad and $\theta_{\max} = \arccos(1/\langle n_r \rangle) + 3\,\sigma^\gamma_c$, where $\sigma^\gamma_c$ is the single photon angular resolution at saturation in the considered sector and module. Hits with $\theta_c < 30$ mrad are discarded since they may be due to photons emitted in gas or in the SiPM protection layer, which may result in clusters of hits potentially harming the Hough counting. I also considered a step size $\Delta\theta_c = 1$ mrad. I found the optimal band width for reconstruction in high-multiplicity events and in high DCR conditions to be $b \approx 2 \times (2\sigma^\gamma_c)$.

The threshold $N^H_{\min}$ sets the effective lower-momentum PID limit and impacts efficiency and purity, as tracks with fewer than $N^H_{\min}$ detected photons are rejected. An appropriate choice of $N^H_{\min}$ suppresses tracks at or below the Cherenkov threshold, where Hough-selected hits are predominantly background. A typical working point is $N^H_{\min} = 3$ to ensure high-efficiency reconstruction. Higher values can increase PID purity at the cost of a reduced efficiency, as discussed in Sections 4.6.3 and 4.6.4.

.

## 4.4 Performance in single particle events

I evaluated the projective bRICH performance over the full acceptance in terms of the single photon angular resolution, the mean number of detected ring photons, and the resulting ring angular resolution from Hough transform reconstruction.

To quantify the intrinsic performance limits, I considered single particle events with e, μ, π, K and p. I primarily focused on the reconstruction at the Cherenkov angle saturation, which is the most critical region for PID since rings from different species have comparable radii and the best possible resolution is required. I also mapped the scaling with the particle velocity $\beta$ and momentum $p$ for e, μ, π, K and p.

I compared the effects on the performance of several design choices discussed in Chapter 3, including the photodetector module layout, the optical properties of the walls between contiguous sectors, the SiPM size, and the microcell pitch.

### 4.4.1 Tested bRICH configurations

The results reported here refer to the following configurations, summarised in Table 4.2.

| Module geometry | Inter sector walls | SiPM size ($mm^2$) | SiPM pitch ($mm^2$) | Microcell pitch ($\mu m^2$) | PDE at 450 nm (%) |
|---|---|---|---|---|---|
| Trapezoidal | absorbing | $1 \times 1$ | $1.1 \times 1.1$ | $50 \times 50$ | 40 |
| Trapezoidal | absorbing | $2 \times 2$ | $2.2 \times 2.2$ | $50 \times 50$ | 40 |
| Trapezoidal | absorbing | $3 \times 3$ | $3.3 \times 3.3$ | $50 \times 50$ | 40 |
| Trapezoidal | transparent | $1 \times 1$ | $1.1 \times 1.1$ | $50 \times 50$ | 40 |
| Trapezoidal | transparent | $2 \times 2$ | $2.2 \times 2.2$ | $50 \times 50$ | 40 |
| Trapezoidal | transparent | $3 \times 3$ | $3.3 \times 3.3$ | $50 \times 50$ | 40 |
| Rectangular $17 \times 18$ $cm^2$ | absorbing | $2 \times 2$ | $2.2 \times 2.2$ ($3 \times 5$ tile) | $50 \times 50$ | 40 |
| Rectangular $17 \times 18$ $cm^2$ | absorbing | $2 \times 2$ | $2.2 \times 2.2$ ($3 \times 5$ tile) | $75 \times 75$ | 50 |

**Table 4.2:** Photodetector configurations used for the bRICH performance studies.

- Trapezoidal SiPM modules with photon absorbing walls and transparent walls between adjacent sectors, equipped with $2 \times 2$ $mm^2$ SiPMs with $2.2 \times 2.2$ $mm^2$ pitch and $50 \times 50$ $\mu m^2$ microcell pitch. The reference PDE curve of S13360–**50CS in Fig. 4.3 is considered, corresponding to about 40% at 450 nm at recommended overvoltage. The options with smaller $1 \times 1$ $mm^2$ and larger $3 \times 3$ $mm^2$ SiPMs with pitches $1.1 \times 1.1$ and $3.3 \times 3.3$ $mm^2$, preserving the same 83% packaging factor as the $2 \times 2$ $mm^2$ case, have been studied for comparison.
- Rectangular $17 \times 18$ $cm^2$ SiPM modules with photon absorbing walls between adjacent sectors, equipped with $2 \times 2$ $mm^2$ SiPMs with $2.2 \times 2.2$ $mm^2$ in $3 \times 5$ tiles packaged as discussed in Section 3.4.4, with $2.2 \times 2.2$ $mm^2$ pitch within each $3 \times 5$ SiPM tile and $50 \times 50$ $\mu m^2$ microcell pitch. The PDE curve follows S13360–**50CS, corresponding to about 40% at 450 nm at recommended overvoltage. The option with $75 \times 75$ $\mu m^2$ microcell pitch, assuming the reference PDE curve of Hamamatsu S13360–**75CS SiPMs [75], corresponding to about 50% at 450 nm, has been studied for comparison.

### Simulation strategy

For the evaluation of the single photon angular resolution, the mean number of Hough-clustered ring photons, and the ring angular resolution in the tested configurations, I generated single-particle events over the full bRICH acceptance. I assumed a Gaussian spread of the production $Z$ around the nominal collision vertex, as expected for real pp and Pb-Pb events. Defining $\theta_{\rm rad}$ and $\phi_{\rm rad}$ as the polar and azimuthal angles the

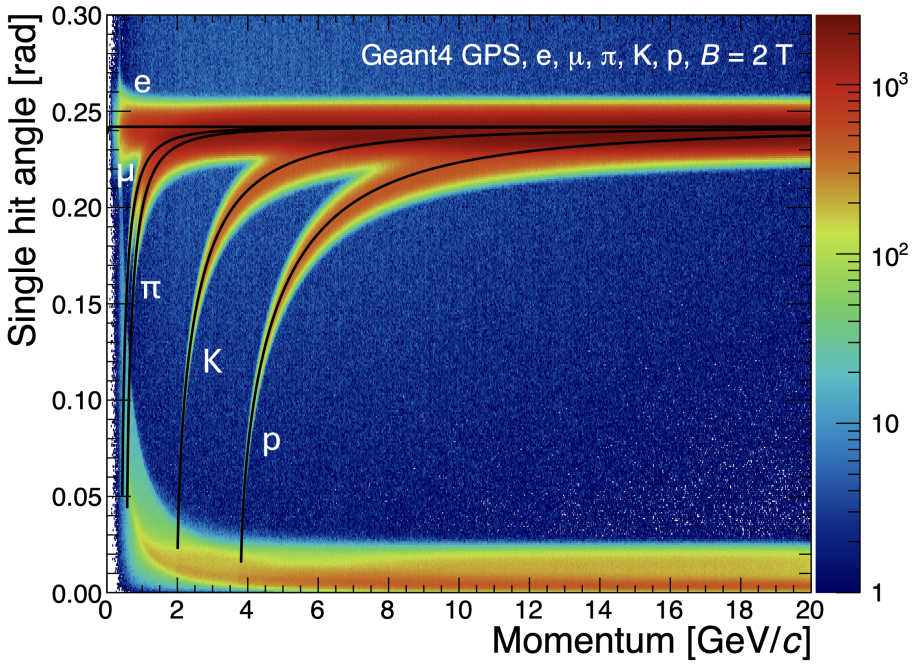


**Figure 4.8:** Distributions of the reconstructed single hit angle as a function of momentum for single particle events with e, μ, π, K and p over the full bRICH acceptance. The trapezoidal bRICH photodetector module layout with photon absorbing inter-sector walls is assumed.

most probable emission point in the radiator $\mathbf{r}_{rad}$, I mapped the performance versus $-\log\big(\tan(\theta_{\rm rad}/2)\big)$, hereafter the radiator (geometric) pseudorapidity $\eta_{\rm rad}$ (not coincident with the particle's physical $\eta$ due to the curvature in the magnetic field), together with $\phi_{\rm rad}$ and the velocity $\beta$. I extracted the single photon angular resolution $\sigma_{\rm c}^{\gamma}$ as the standard deviation of the single hit Cherenkov angle distribution around the signal region. This was preferred over a Gaussian fit given the expected non-Gaussian shape dominated by the almost uniform emission-depth uncertainty. Applying the Hough transform I obtained the number of clustered ring photons and the reconstructed Cherenkov angle. From the mean and standard deviation of these distributions, I extracted the mean number of detected photons and the ring angular resolution.

### 4.4.2 Cherenkov angle analysis: resolution and yield

Figs. 4.8 and 4.9 show examples of the distributions of the reconstructed Cherenkov angle at the single hit level and the resulting ring Cherenkov angle obtained with the Hough transform as a function of momentum for a sample of 5M e, μ, π, K and p, with 1M events per species and uniform momentum distribution up to 20 GeV/$c$ over the full bRICH acceptance. The plots refer to the reference trapezoidal bRICH photodetector module layout with photon absorbing inter-sector walls.

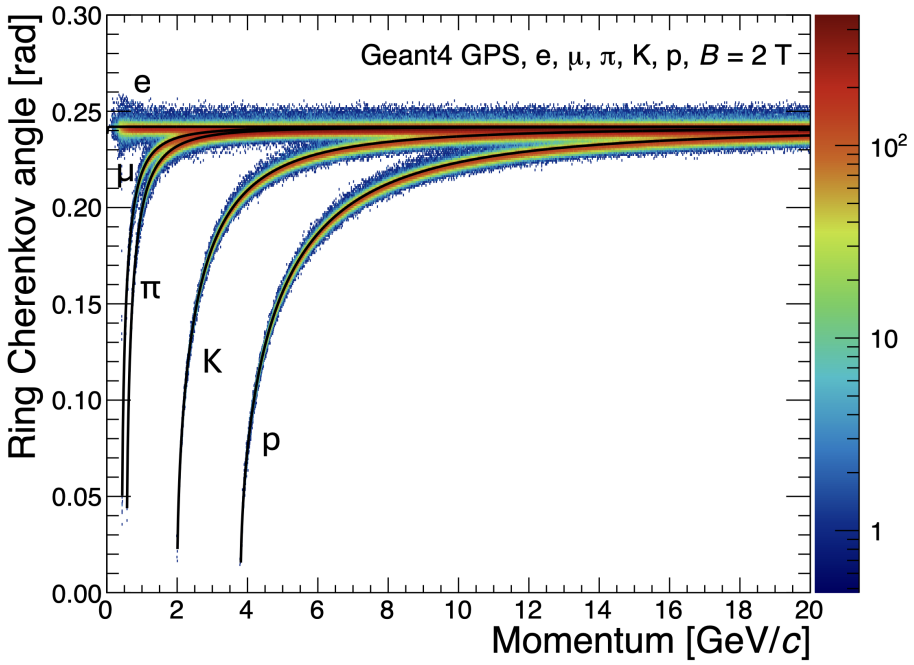


**Figure 4.9:** Distribution of the reconstructed ring Cherenkov angle using the Hough transform as a function of momentum for single particle events with e, μ, π, K and p over the full bRICH acceptance. The trapezoidal photodetector module layout with photon absorbing walls is assumed.

The bands corresponding to the different particle species are clearly distinguishable. The nearly uniform background visible in the single hit Cherenkov angle distribution arises mainly from photons undergoing Rayleigh scattering in the aerogel tiles and from secondaries produced by interactions with the materials. The horizontal band at small angles corresponds to Cherenkov photons emitted in the argon filling the expansion gap and in the considered 100 μm silicone resin layer on top of the SiPMs. With a mean number of correlated background hits below one per event in the region $\theta_c < 260$ mrad, the Hough transform successfully clusters the signal hits, yielding ring Cherenkov angles consistent with the expected values across the full momentum range.

The projections of these distributions for each species, momentum interval, and bRICH sector, allow the extraction of the angular resolutions. Fig. 4.11 illustrates the distributions of the reconstructed single-hit Cherenkov angle in three representative sectors for π at 10 GeV/$c$. The results correspond to sector +1, the central sector, sector +5, which hosts modules with the smallest expansion gap and therefore exhibits the poorest resolution, and sector +12, the outermost sector characterized by the largest expansion gap and consequently the best expected angular resolution.

The extracted sector-averaged single-photon Cherenkov angle resolutions $\sigma_c^\gamma$ are approximately 5.8 mrad, 7.1 mrad, and 4.2 mrad for the three sectors, respectively. The corresponding expectations derived from the combination of geometric, localiza-

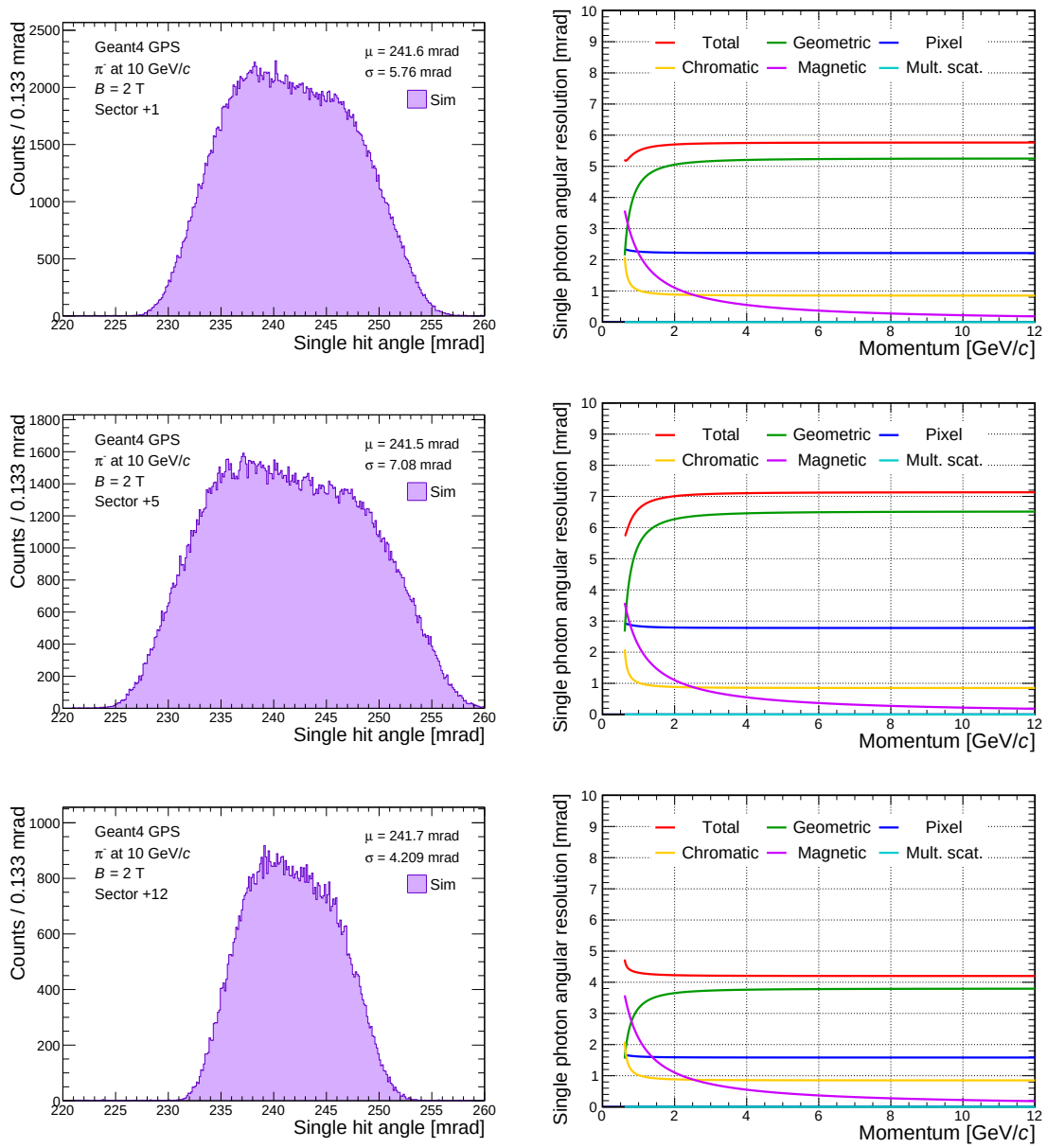


**Figure 4.10:** Left: Distributions of the single hit Cherenkov angle in sectors +1 (top), +5 (middle), +12 (bottom) for simulated single particle events with negative π at 10 GeV/$c$ momentum. Right: Expected single photon angular resolution and the corresponding geometric, localization, chromatic, magnetic field and aerogel multiple scattering contributions as a function of momentum. The trapezoidal photodetector module layout with photon absorbing inter-sector walls is assumed.

tion, chromatic, magnetic field, and multiple-scattering contributions are also shown in Fig. 4.10 demonstrating good agreement with the simulation results.

Fig. 4.11 shows the distributions of the number of Hough-selected hits and the reconstructed ring Cherenkov angle for the same sectors. The shape of the multiplicity

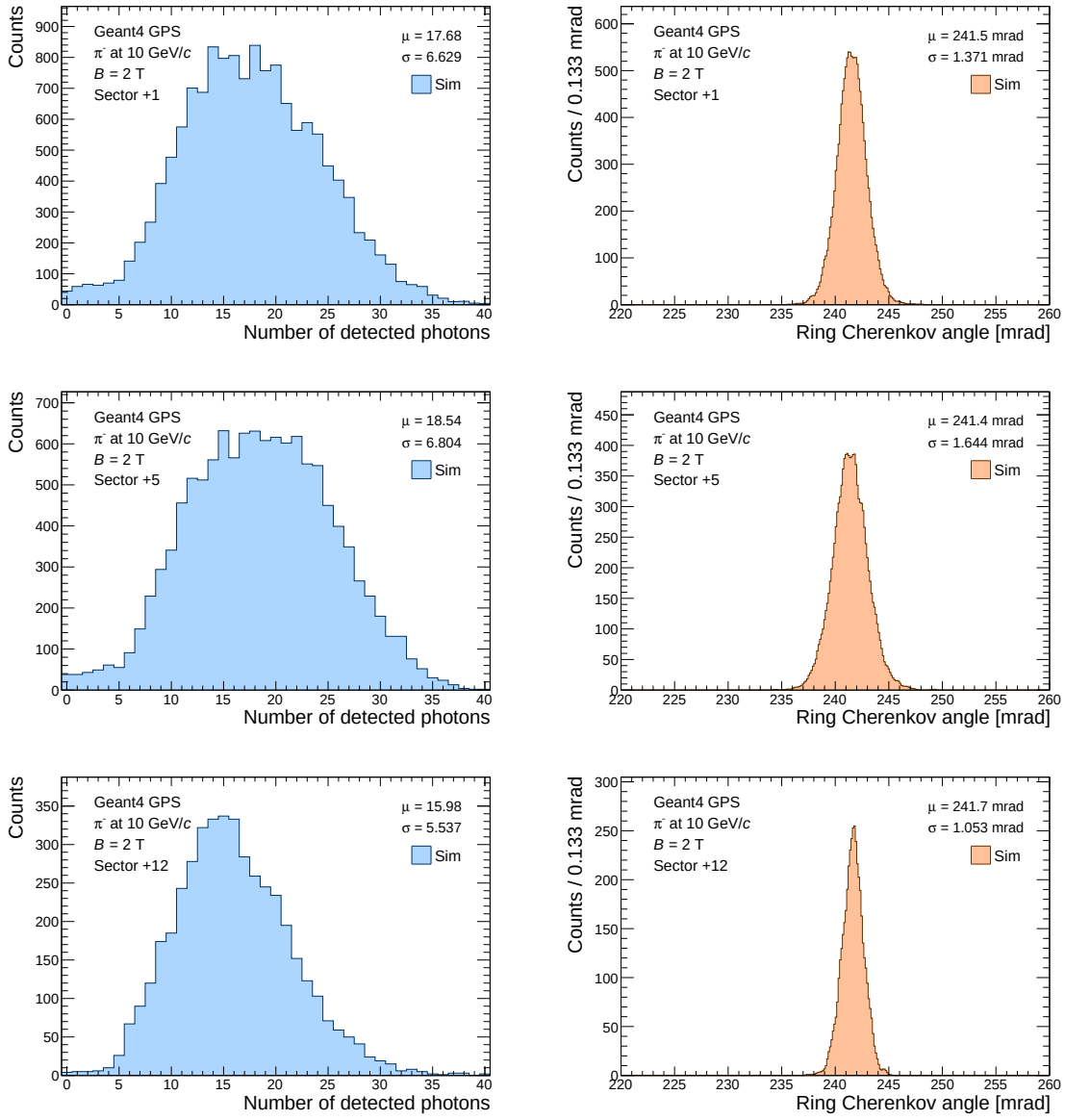


**Figure 4.11:** Distributions of the number of Hough selected hits (left) and the reconstructed ring Cherenkov angle using the Hough transform (right) in sectors +1 (top), +5 (middle), +12 (bottom) for simulated single particle events with $\pi$ at 10 GeV/$c$ impinging uniformly on the sector modules. The trapezoidal photodetector module layout with photon absorbing inter-sector walls is assumed.

distributions reflects the dependence of photon yield on the track impact position in the aerogel, since a fraction of the photons emitted near sector boundaries is lost. The mean number of detected photons, about 17.7, 18.5, and 16.0 in sectors +1, +5, and +12 respectively, indicates that smaller expansion gaps correspond to smaller ring radii and thus to larger regions of full photon acceptance. Overall, the reconstructed ring angular resolutions meet the ALICE 3 design target of approximately 1.5 mrad.

In the following sections, the same study is extended to the single-track level, both as a sector-averaged measurement and through a detailed scan across the module area, to map the local variations in angular resolution for the different tested configurations.

### 4.4.3 Trapezoidal modules: performance with 2×2 mm² SiPMs

Fig. 4.12 shows the sector average and the local fine sector scan of the single photon angular resolution, the mean number of detected ring photons, and the ring angular resolution from Hough transform reconstruction for simulated $\pi$ at 10 GeV/$c$ as a function of the radiator pseudorapidity $\eta_{\mathrm{rad}}$, for the trapezoidal bRICH photodetector module layout with the reference $2 \times 2$ mm$^2$ SiPMs with photon absorbing walls.

#### Single photon angular resolution

The single photon angular resolution $\sigma_{\mathrm{c}}^{\gamma}$ in Fig. 4.12 follows the trend of the expansion gap width $T_{\mathrm{g}}$ in the bRICH sectors, shown in Fig. 3.7. This is expected since the dominant contributions to the angular resolution, the uncertainties on the emission depth and the hit localization on the SiPMs, scale as $1/T_g$, as discussed in Appendix A. The resolution is 5.8 mrad at midrapidity, 7.1 mrad for $|\eta_{\mathrm{rad}}| \approx 0.8$, and 4.2 mrad for $|\eta_{\mathrm{rad}}| \to 2$. The largest $\sigma_{\mathrm{c}}^{\gamma}$ corresponds to the sectors with the smallest gap of 19 cm. The local fine scan in Fig. 4.12 shows that in the considered configuration with absorbing walls, so that all signal photons hit the same photodetector module, $\sigma_{\mathrm{c}}^{\gamma}$ is almost independent of the $\eta_{\mathrm{rad}}$ and it mostly depends on the geometry of the system.

#### Mean number of detected ring photons

The extrapolated number of detected ring photons $N_{\mathrm{det}}$ shown in Fig. 4.12 is the result of the convolution of the Cherenkov emission yield, which also depends on the considered aerogel thickness of 2 cm, with the photodetector module acceptance for the rings. The fine sector scan shows that the detected photon yield strongly depends on the position of the track impact point in terms of $\theta_{\mathrm{rad}}$, with a loss of a fraction of photons for particles entering the aerogel close to sector boundaries. In particular, about 23-24 photons are clustered for tracks at Cherenkov angle saturation that enter the central $\eta_{\mathrm{rad}}$ region of the modules in a given sector. This number is almost halved, down to about 12-13, at the extreme $\eta_{\mathrm{rad}}$, where roughly half of the ring photons fall outside the sector acceptance and are absorbed by the sector walls.

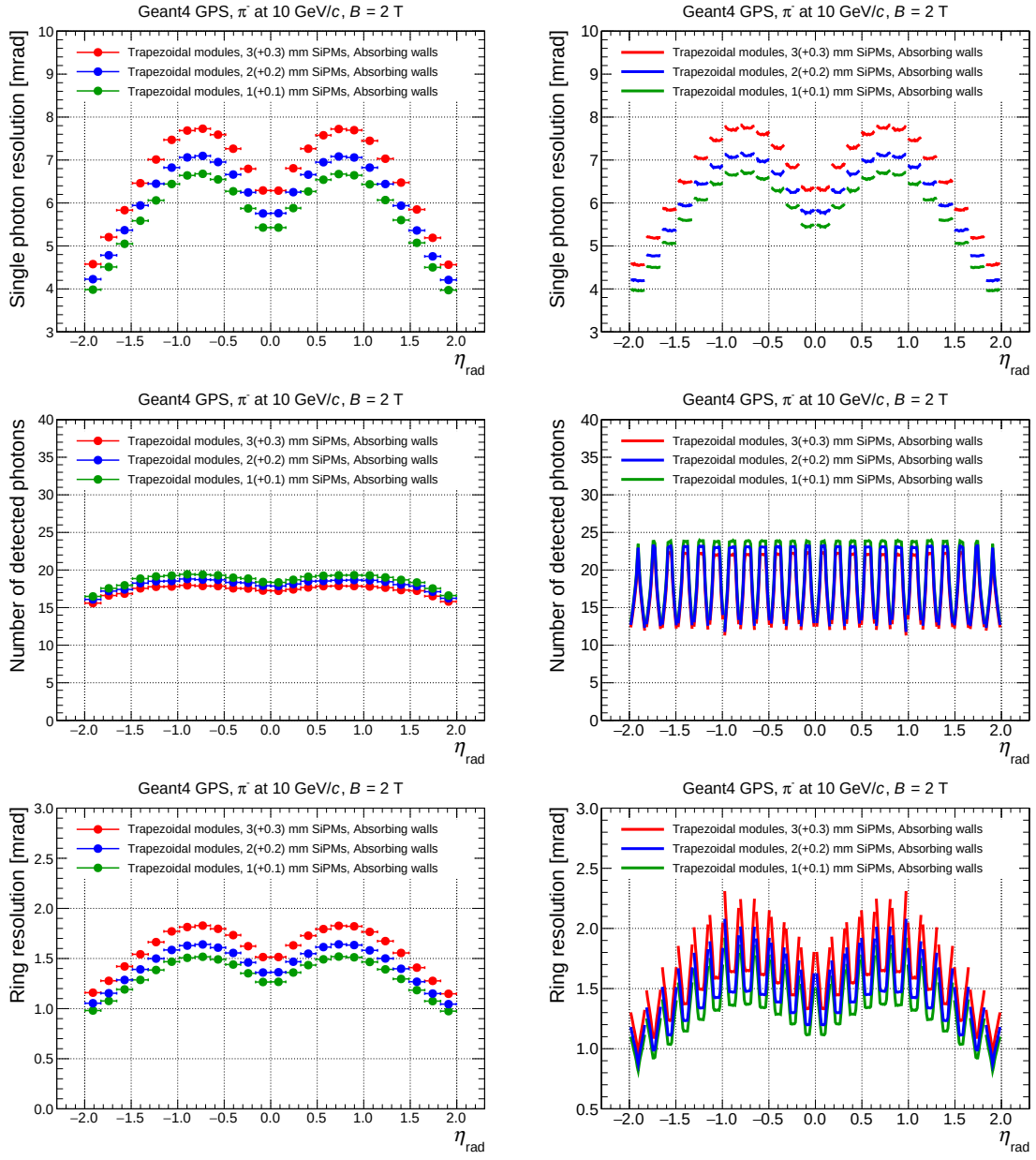


**Figure 4.12:** Sector average (left) and local fine sector scan (right) of single photon angular resolution (top), mean number of detected ring photons (middle), and resulting ring angular resolution (bottom) from Hough transform reconstruction for simulated $\pi$ at 10 GeV/$c$ as a function of the radiator pseudorapidity $\eta_{\mathrm{rad}}$. The panels refer to the trapezoidal bRICH photodetector module layout with photon absorbing walls between contiguous sectors. The results relative to the reference $2 \times 2$ mm$^2$ SiPMs with $2.2 \times 2.2$ mm$^2$ pitch and $50 \times 50$ µm$^2$ microcell pitch (green) are compared with the cases of $1 \times 1$ mm$^2$ SiPMs (red) and $3 \times 3$ mm$^2$ SiPMs (blue), using the same packaging factor of 83% to define the pitch, the same microcell pitch and PDE.

The $\theta_{\rm rad}$ region where full acceptance is ensured in each detector depends on the sector gap thickness $T_g$. A larger gap corresponds to a ring radius, $R_c \propto T_g$ and to a smaller full acceptance region. This balances the trend of $\sigma_{\rm c}^{\gamma}$, since regions with the worst $\sigma_{\rm c}^{\gamma}$ are more likely to have larger acceptance, thus improving the ring resolution.

#### Ring angular resolution

The resulting ring angular resolution at saturation shown in Fig. 4.12 follows the expected $\sigma_{\rm c}^{\gamma}/\sqrt{N_{\rm det}}$ scaling across the full $\eta_{\rm rad}$ range accounting for the combined behaviour of $\sigma_{\rm c}^{\gamma}$ and $N_{\rm det}$ discussed above. For the considered photodetector module layout geometry a ring angular resolution better than the 1.5 mrad bRICH target is achieved in the central region of almost all sectors, with a worsening up to 2 mrad limited to the regions corresponding to the sector boundaries, particularly for the sectors at $|\eta_{\rm rad}| \approx 0.8$, due to the combined effect of reduced ring acceptance and the larger single photon angular resolution $\sigma_{\rm c}^{\gamma}$ caused by the smaller expansion gap.

### 4.4.4 Trapezoidal modules: performance vs SiPM size

In Fig. 4.12, the angular resolution and the number of detected ring photons for the reference $2\times2$ mm$^2$ SiPMs are compared to those for $1\times1$ mm$^2$ and $3\times3$ mm$^2$ devices assuming the same 83% packaging factor, as indicated in Table 4.2.

The single photon angular resolution $\sigma_{\rm c}^{\gamma}$ worsens with increasing SiPM size as expected due to the larger uncertainty on the hit localization on the photodetector, scaling with the pixel size, as discussed in Appendix A. Despite the same packaging factor being assumed, the detected photon yield is slightly smaller for larger pixels, since multiple photons are more likely to enter the same pixel and be counted as a single hit. Nevertheless, the overall difference in resulting ring resolution $\sigma_{\rm c}^{\rm r}$ is not larger than 0.3 mrad when comparing the $1 \times 1$ mm$^2$ to the $3 \times 3$ mm$^2$ configuration.

These results highlight that the impact of pixel size on physics performance is marginal, and that the choice is mostly technical. Larger pixels minimize the number of channels, 4/9 relative to $2\times2$ mm$^2$ SiPMs, but suffer more from radiation damage, 9/4 relative to $2\times2$ mm$^2$ SiPMs. Smaller pixels are better in terms of per pixel DCR after irradiation, with an expected DCR about four times smaller than for $2\times2$ mm$^2$, but would require four times more channels, making the module integration unfeasible within the current spatial constraints. A possibility to use smaller SiPMs to cover the same effective area is using light concentrators, as discussed in Section 3.7. For the studies reported in the following, unless stated otherwise, the $2 \times 2$ mm$^2$ option is always assumed.

### 4.4.5 Trapezoidal modules: absorbing vs transparent walls

Fig. 4.13 shows the same results as Fig. 4.12 for the option with transparent inter-sector walls discussed in Section 3.4.5 to improve the yield for tracks at sector boundaries.

The wall properties have a significant impact on the single photon angular resolution $\sigma_c^\gamma$ and on the mean number of detected photons $N_{\rm det}$ in the region $|\eta_{\rm rad}| < 0.8$.

In this region, $N_{\rm det}$ at sector boundaries is always larger than in the absorbing wall case due to the extra collected photons. However, $\sigma_c^\gamma$ at boundaries for sectors in this region is not flat, unlike the photon absorbing wall case. In particular, as shown in the top-right panel of Fig. 4.13, $\sigma_c^\gamma$ in a given sector is better for the boundary at larger $|\eta_{\rm rad}|$, and worse for the boundary at smaller $|\eta_{\rm rad}|$.

This behaviour is expected, and can be interpreted from the longitudinal view of the projective bRICH geometry in Fig. 3.6. The extra photons detected in the modules of adjacent sectors are seen through an effective expansion gap that can be smaller or larger than the gap of the sector where they are produced. These extra photons enter the distribution used to extract $\sigma_c^\gamma$, increasing or reducing the corresponding standard deviation relative to the case where only photons produced in the same sector are considered. This results in spikes close to the sector boundaries, with the worst $\sigma_c^\gamma$ reaching 8.7 mrad at $|\eta_{\rm rad}| = 0.5$. Nevertheless, the extra collected photons lead to an overall better ring angular resolution $\sigma_r$ at sector boundaries relative to the case of absorbing walls throughout the region $|\eta_{\rm rad}| < 0.8$.

The impact of transparent walls becomes negligible or even negative for $|\eta_{\rm rad}| > 0.8$, where the projective geometry and segmentation prevents photons emitted in the module of a given sector from reaching modules in the adjacent sectors.

A drawback of transparent walls is the increase of the mutual ring background in high multiplicity events, especially close to midrapidity. In particular, photons emitted by different tracks in adjacent sectors can reach the module of a neighbour sector, causing potential ring overlaps and larger mutual background in angle reconstruction. Photon absorbing walls naturally avoid this problem, by fully disentangling the ring reconstructions for tracks traversing different sectors, and by suppressing mutual background, at the cost of reduced ring acceptance. Therefore, the absorbing wall option was preferred to the transparent one, and, unless stated otherwise, all studies presented in the following were performed under this assumption.

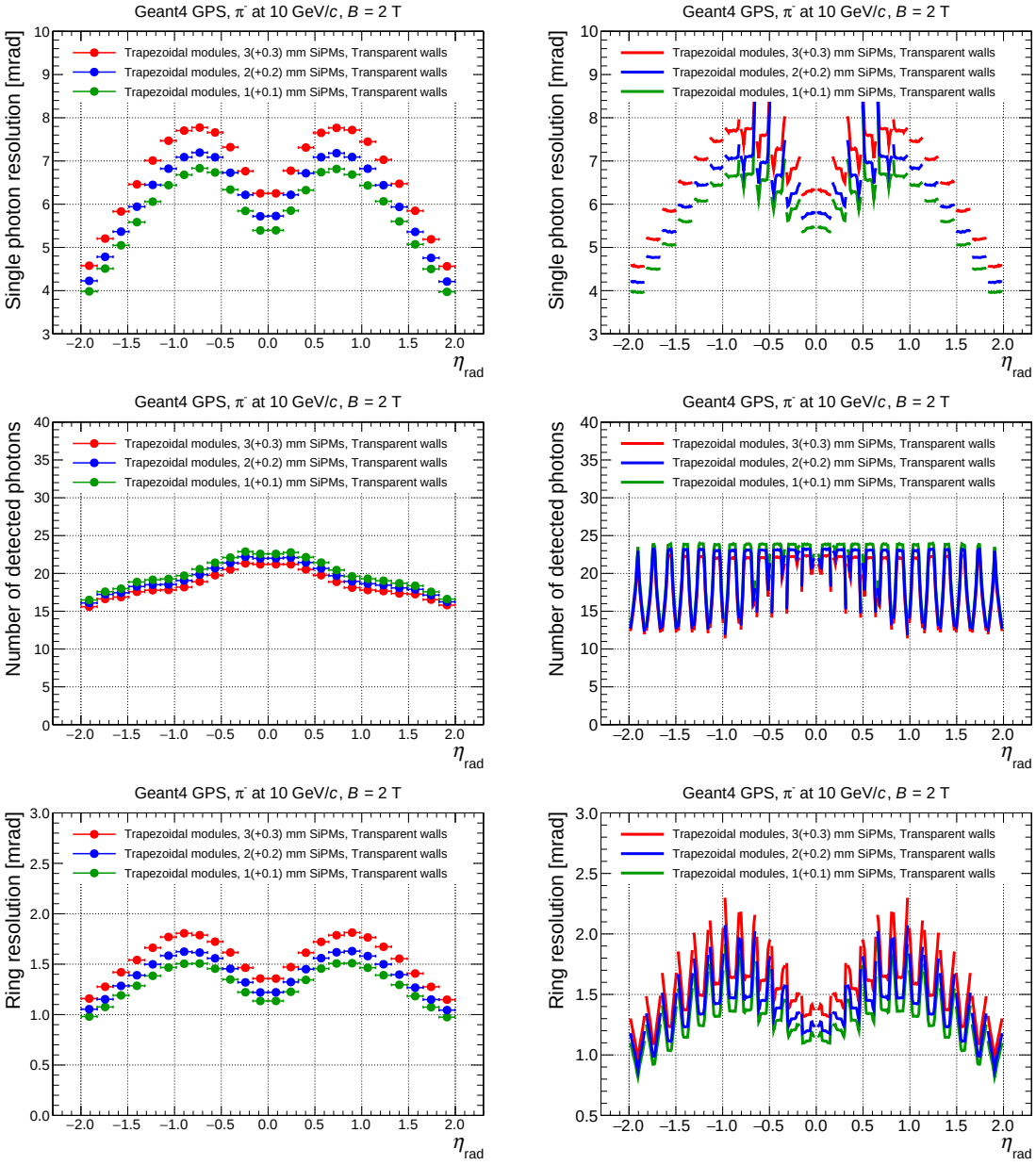


**Figure 4.13:** Sector average (left) and local fine sector scan (right) of single photon angular resolution (top), mean number of detected ring photons (middle), and resulting ring angular resolution (bottom) from Hough transform reconstruction for simulated $\pi$ at 10 GeV/$c$ as a function of the module pseudorapidity $\eta_{\mathrm{rad}}$. The panels refer to the trapezoidal bRICH photodetector module layout with transparent walls letting photons emitted in one sector reach an adjacent sector. The results relative to the reference $2 \times 2$ mm$^2$ SiPMs with $2.2 \times 2.2$ mm$^2$ pitch and $50 \times 50$ µm$^2$ microcell pitch (green) are compared with the cases of $1 \times 1$ mm$^2$ SiPMs (red) and $3 \times 3$ mm$^2$ SiPMs (blue), using the same packaging factor of 83% to define the pitch, the same microcell pitch and PDE.

### 4.4.6 Trapezoidal modules vs rectangular $17 \times 18$ cm$^2$ modules

In Fig. 4.14 the performance of the reference trapezoidal bRICH photodetector module layout with $2 \times 2$ mm$^2$ SiPMs, $2.2 \times 2.2$ mm$^2$ pitch, and $50 \times 50$ μm$^2$ microcell pitch is compared with the rectangular module layout of the same SiPM size and microcell pitch. Results for the rectangular layout with a larger microcell pitch, $75 \times 75$ μm$^2$, which provides a higher PDE, are also shown for comparison.

The single photon angular resolution $\sigma_c^\gamma$ is unaffected by the layout when the same SiPM size is considered. The main difference between the two layouts concerns the number of detected ring photons $N_{\rm det}$. Photons entering the regions of the trapezoidal frames not covered by the rectangular modules are systematically lost. These regions amount to a fractional loss of 14%, relative to the maximal coverage. Additional losses occur in the dead regions between different dies, as discussed in Section 3.4.4. Photons falling between SiPMs within the same die, with size $2 \times 2$ mm$^2$ and pitch $2.2 \times 2.2$ mm$^2$, are lost in both layouts. As a result, the effective active area, determined by the $6 \times 896 = 5376$ SiPMs per rectangular module, corresponds to about 73% of the active area in the trapezoidal layout, consistently with the values in Fig. 4.14.

A fraction of these photons can be recovered when using SiPMs with larger microcell pitch. Considering, for example, Hamamatsu S13360-$**$75CS SiPMs, with $75 \times 75$ μm$^2$ microcells and a PDE about 25% larger than the $50 \times 50$ μm$^2$ case (50% vs 40% at 450 nm), the effective loss relative to the trapezoidal geometry is reduced from about 27% to about 9%. These larger microcell SiPMs are therefore a viable backup option.

The profile of $N_{\rm det}$ affects the ring angular resolution $\sigma_c^{\rm r}$. With the rectangular module layout and the reference $50 \times 50$ μm$^2$ microcell pitch, $\sigma_c^{\rm r}$ worsens by less than 0.3 mrad relative to the trapezoidal layout. This is most critical in sectors with $|\eta_{\rm rad}| \approx 0.8$, where $\sigma_c^{\rm r}$ exceeds the 1.5 mrad design target. The $75 \times 75$ μm$^2$ option improves the resolution, recovering the target at least in the full ring acceptance regions.

In the following, all studies with both rectangular and trapezoidal modules are reported for the reference $50 \times 50$ μm$^2$ microcell pitch, in order to explore the worst case scenario.

### 4.4.7 Performance vs azimuthal angle

All results on the angular resolution and on the number of detected photons presented above were discussed as a function of $\eta_{\rm rad}$. Here, the dependence on $\phi_{\rm rad}$ is investigated. As specified in Section 3.4.5, while both absorbing and transparent inter-sector walls are studied, transparent walls are always assumed between the modules within a sector.

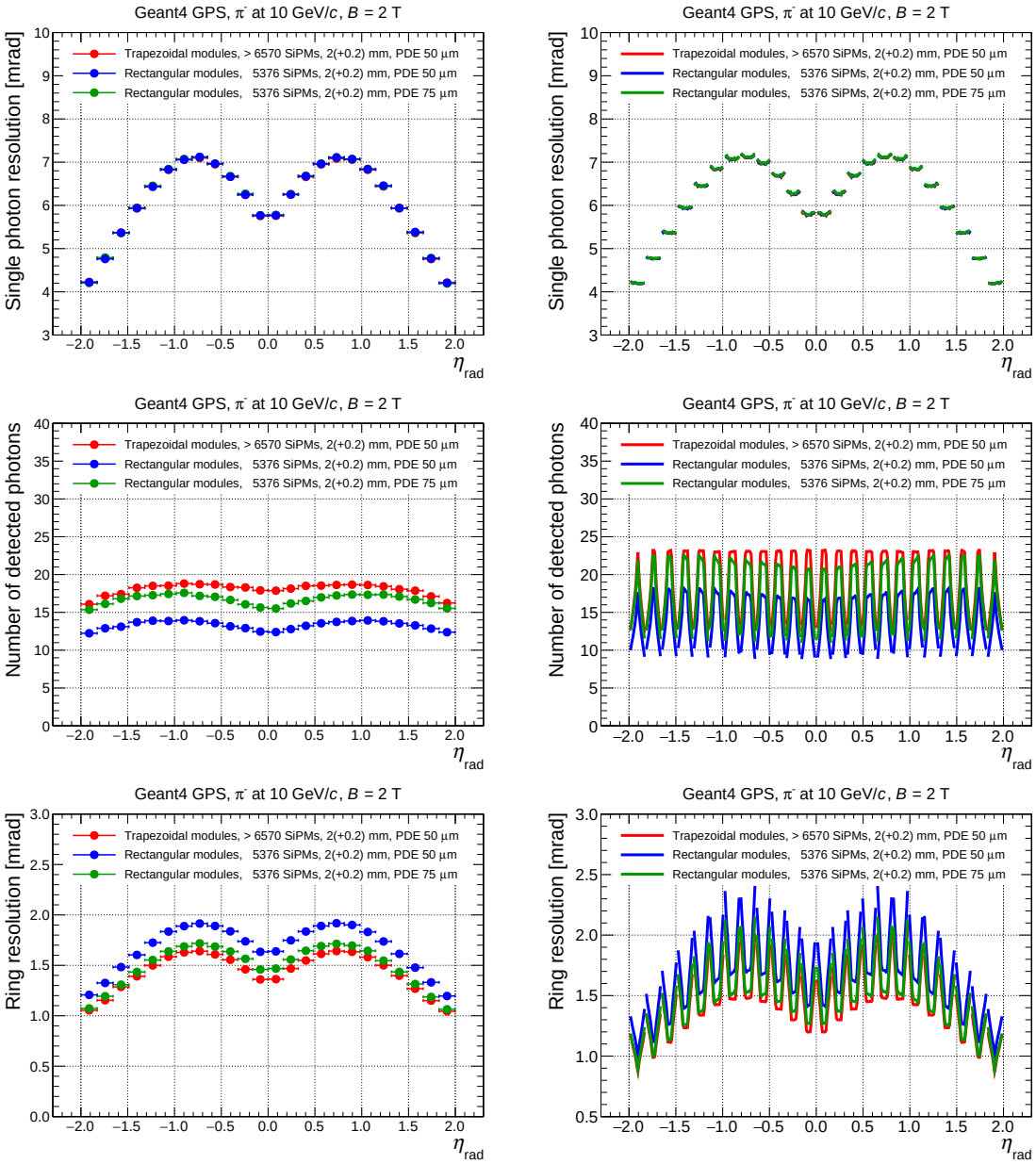


**Figure 4.14:** Sector average (left) and local fine sector scan (right) of single photon angular resolution (top), mean number of detected ring photons (middle), and ring angular resolution (bottom) from Hough transform reconstruction for simulated $\pi$ at 10 GeV/$c$ as a function of $\eta_{\mathrm{rad}}$. The results relative to the trapezoidal bRICH photodetector module layout with $2 \times 2$ mm$^2$ SiPMs, $2.2 \times 2.2$ mm$^2$ pitch, and $50 \times 50$ µm$^2$ microcell pitch (red curve) are compared with those for the rectangular $17 \times 18$ cm$^2$ module layout of the same SiPM size with microcell pitches of $50 \times 50$ µm$^2$ and $75 \times 75$ µm$^2$ shown in blue and green. Photon absorbing walls are assumed between contiguous sectors.

Fig. 4.15 shows the local fine scan of the single photon angular resolution, the mean number of detected ring photons, and the resulting ring angular resolution for simulated $\pi$ at 10 GeV/$c$ in module 1 of sector +1, as functions of $\theta_{\rm rad}$ and $\phi_{\rm rad}$, for both the trapezoidal bRICH module layout and the rectangular $17 \times 18$ cm$^2$ layout.

The single photon angular resolution, $\sigma_{\rm c}^{\gamma}$, is unaffected by the module layout, shows almost no dependence on $\phi_{\rm rad}$, and remains almost uniform in both $\theta_{\rm rad}$ and $\phi_{\rm rad}$. The largest impact of the module geometry is on the number of detected photons, $N_{\rm det}$.

For trapezoidal modules, which have no uncovered regions other than the 200 μm gap between adjacent SiPMs, the $N_{\rm det}$ values show the expected $\theta_{\rm rad}$ scaling as discussed in Section 4.4.3. At fixed $\theta_{\rm rad}$, it is almost uniform in $\phi_{\rm rad}$. A slight worsening is observed in the two extreme $\phi_{\rm rad}$ bins, where some tracks traverse the aerogel tile close to the edges and exit before the full depth, resulting in a lower photon yield. The same trend appears in the ring angular resolution, $\sigma_{\rm c}^{\rm r}$, following the expected $1/\sqrt{N_{\rm det}}$ behaviour.

For the rectangular $17 \times 18$ cm$^2$ layout, the behaviour is more complex. In addition to the reduction of $N_{\rm det}$ in $\theta_{\rm rad}$ regions close to sector boundaries, the $\phi_{\rm rad}$ profile, at fixed $\theta_{\rm rad}$ exhibits an absolute maximum near $\phi_{\rm rad} = 0°$ and local maxima around $\pm 3.5°$. This occurs since the rectangular modules leave uncovered areas at the boundaries of the trapezoidal frames. Depending on the track impact point in the radiator, a larger or smaller fraction of the ring, with radius $R_c \approx 6$ cm at Cherenkov saturation for the considered module, intercepts these uncovered regions, which locally reduces or enhances the mean $N_{\rm det}$. This structure is absent in the trapezoidal layout, where the full frame region is equipped with SiPMs, providing maximal acceptance for the rings.

### 4.4.8 Performance vs particle velocity

The results presented in the previous sections characterized the performance at the Cherenkov angle saturation. In this section, I report the results on the dependence on the particle velocity $\beta$. In particular, I explored the range from $\beta = 0.97$, corresponding to the Cherenkov velocity threshold in aerogel with refractive index $n = 1.03$, to $\beta \to 1$.

Fig. 4.16 shows the results for the single photon angular resolution, the mean number of detected ring photons, and the resulting ring angular resolution for simulated $\pi$, as functions of $\eta_{\rm rad}$ and $\beta$ for both the trapezoidal and the rectangular module layouts.

In each of the 24 bRICH sectors, for a fixed $\beta$, the single photon angular resolution, $\sigma_{\rm c}^{\gamma}$, is almost uniform versus $\eta_{\rm rad}$. The value in each sectorincreases with $\beta$, yielding the worst resolution at saturation for $\beta \to 1$, for the sectors in the region $|\eta_{\rm rad}| \approx 0.8$.

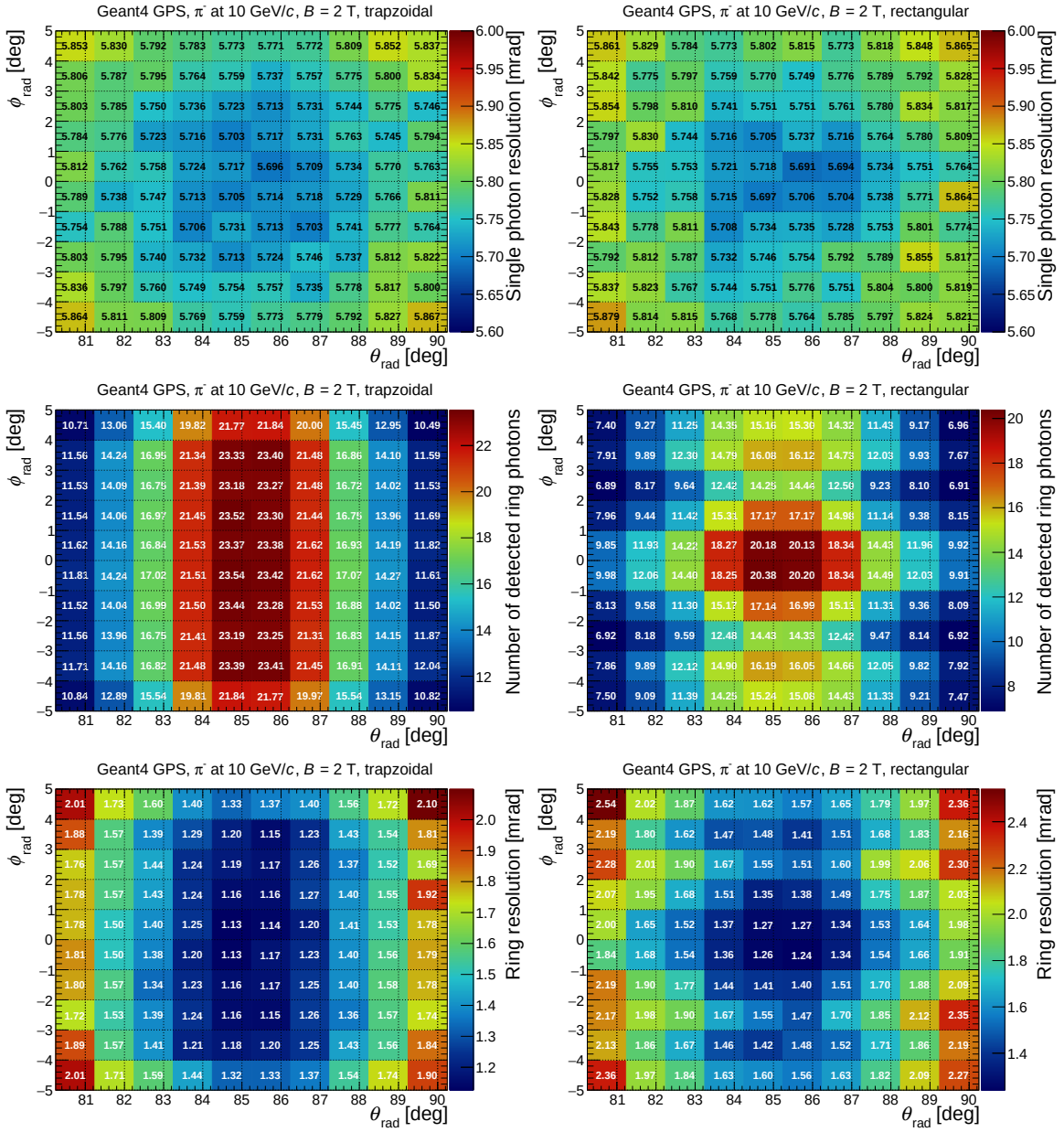


**Figure 4.15:** Local fine scan of single photon angular resolution (top), mean number of detected ring photons (middle), and ring angular resolution (bottom) from Hough transform reconstruction for simulated $\pi$ at 10 GeV/$c$, for module 1 of sector +1, shown as functions of $\theta_{\rm rad}$ and $\phi_{\rm rad}$. The left panels refer to the trapezoidal bRICH photodetector module layout and the right panels to the rectangular 17 × 18 cm$^2$ layout. All results are obtained with the reference 2 × 2 mm$^2$ SiPMs with 50 × 50 µm$^2$ microcell pitch. Photon absorbing walls are assumed between contiguous sectors.

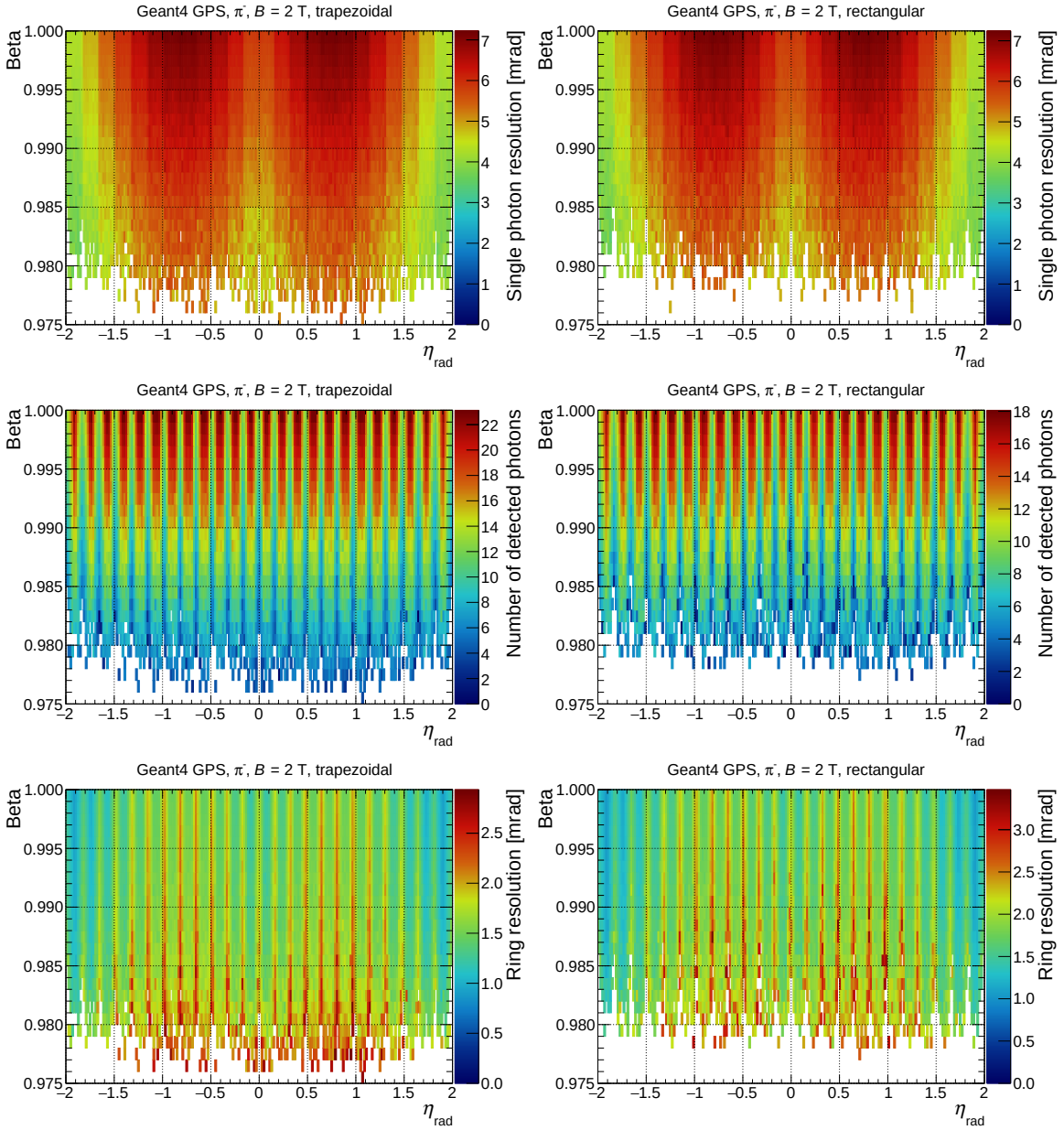


**Figure 4.16:** Local fine sector scan of single photon angular resolution (top), mean number of detected ring photons (middle), and resulting ring angular resolution (bottom) from Hough transform reconstruction for simulated $\pi$ shown as functions of $\eta_{\mathrm{rad}}$ and $\beta$. The left panels refer to the trapezoidal bRICH photodetector module layout and the right panels to the rectangular $17 \times 18$ cm$^2$ layout. All results are obtained with the reference $2 \times 2$ mm$^2$ SiPMs with $50 \times 50$ µm$^2$ microcell pitch. Photon absorbing walls are assumed between contiguous sectors.

The mean number of detected photons, $N_{\rm det}$, shows the expected acceptance-driven variation at sector boundaries convolved with the reduction with decreasing $\beta$ from the Cherenkov emission spectrum, given by the Frank–Tamm relation in Eq. 2.7. Comparing the rectangular and trapezoidal layouts, the $N_{\rm det}$ ratio (rectangular over trapezoidal) is consistent with the relative fraction of active area over the full $\beta$ range. The resulting ring angular resolution, $\sigma_{\rm c}^{\rm r}$, is almost uniform in the central $\theta_{\rm rad}$ regions of each sector and, for all $\beta$, follows the expected $\sigma_{\rm c}^{\gamma}/\sqrt{N_{\rm det}}$ scaling.

A slight worsening of $\sigma_{\rm c}^{\rm r}$ is observed at sector boundaries with decreasing $\beta$. As expected, the effect is more evident for the rectangular photodetector layout. This resolution degradation at small $\beta$, unlike the saturation region $\beta \to 1$, is not harmful for particle identification performance, because it occurs where the Cherenkov angles for the considered particle species are well separated from those of other species. However, an excessively low $N_{\rm det}$ near sector boundaries may affect the feasibility itself of the angle reconstruction, thus reducing the angle reconstruction efficiency.

## 4.5 Features of simulated Pb-Pb events

In the following I discuss the simulation results of the bRICH performance obtained for central (0-5%) Pb–Pb collisions at $\sqrt{s_{\rm NN}} = 5.52$ TeV, representing the most challenging environment with a charged-particle multiplicity $\mathrm{d}N_{\rm ch}/\mathrm{d}\eta$ at the collision vertex of about 2000 at midrapidity. For all these studies I generated the Pb–Pb datasets as described in Section 4.1.2, using minimum bias collisions and selecting the 5% of events in the sample with the largest charged-track multiplicity at the collision vertex.

This section covers the properties of the simulated events in terms of charged-track multiplicity and kinematics at the bRICH, the geometric acceptance of the aerogel tiles and of the photodetector modules to those tracks, the time profile of the photodetector hits, the photodetector occupancy in central Pb–Pb events, and the aerogel tile acceptance together with the resulting photodetector acceptance. Except for the lower occupancy, all the considerations presented for Pb-Pb are also valid for pp events.

### 4.5.1 Charged-track multiplicity and kinematics at the bRICH

Fig. 4.17 shows the features of simulated Pb–Pb collisions at $\sqrt{s_{\rm NN}} = 5.52$ TeV in terms of tracks entering the bRICH. The top–left panel shows the distribution of the charged–track multiplicity of accepted tracks with centrality classes indicated to illustrate the selection strategy. The top–right panel reports the mean number of

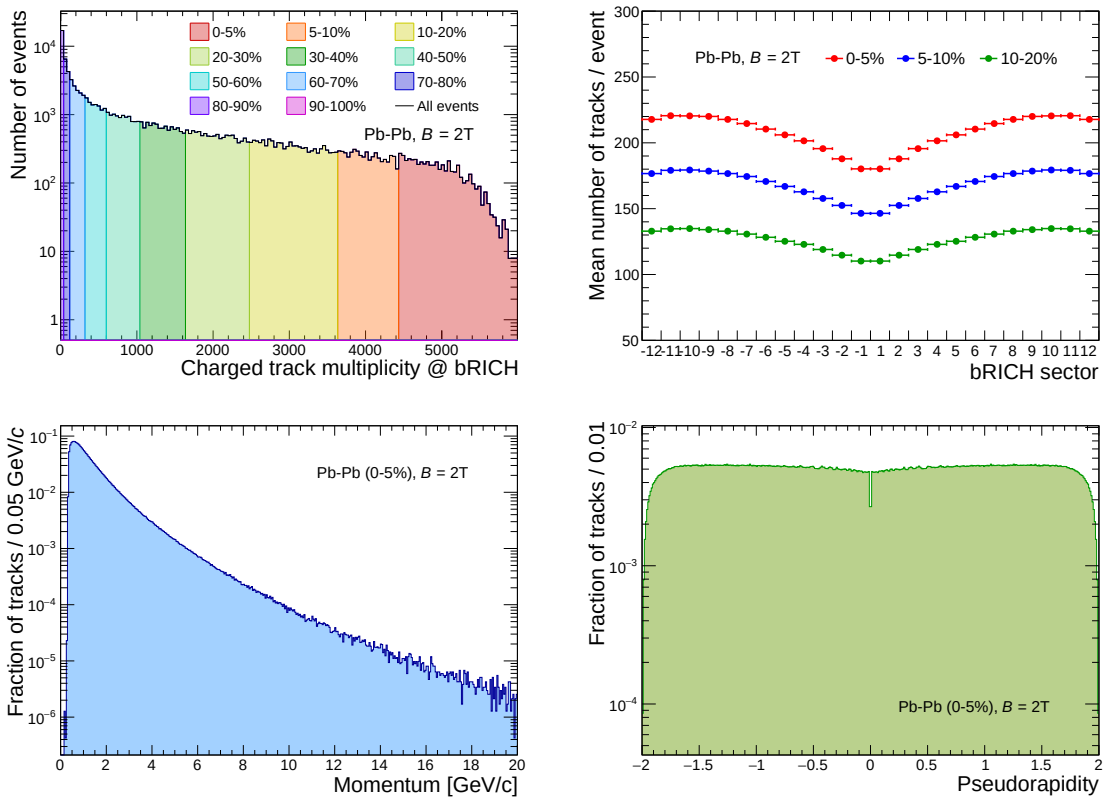


**Figure 4.17:** Features of simulated 0-5% Pb–Pb collisions at $\sqrt{s_{\mathrm{NN}}} = 5.52$ TeV in terms for tracks reaching the bRICH. Top left: Charged–track multiplicity of accepted tracks for the bRICH analysis with centrality classes indicated to show the selection strategy. Top right: Mean number of tracks per bRICH sector for 0-5%, 5-10% and 10-20% Pb-Pb events. Bottom left: Momentum distribution of tracks at the bRICH. Bottom right: Pseudorapidity distribution of tracks at the bRICH.

tracks per bRICH sector for 0–5% events, compared to 5–10% and 10–20% selections. The bottom panels show the momentum and $\eta$ distributions of the accepted tracks.

The 0-5% events of interest correspond to more than 4.4k tracks entering the bRICH per event, corresponding to about 200 tracks per sector (following the expected $\mathrm{d}N_{\mathrm{ch}}/\mathrm{d}\eta$ across the different sectors) and 5-6 charged tracks per bRICH module.

The lower number relative to the about 8k on average at the collision vertex is expected due to both the curvature in the 2 T magnetic field, preventing particles with $p_{\mathrm{T}} \lesssim 0.3$ GeV/$c$ from reaching the RICH position, and the interactions with the traversed material budget, as shown in the corresponding momentum distribution.

### 4.5.2 Projective bRICH acceptance for charged tracks

A crucial aspect of the projective geometry to be investigated is the geometric acceptance for impinging charged particles in pp and Pb–Pb collisions. The geometry is optimized to collect straight tracks from the nominal collision point. The stability of the acceptance for low momentum tracks in the baseline 2 T solenoidal magnetic field and in the presence of the expected spread of the collision point is not trivial.

I studied the charged-track acceptance both at the radiator module level, which controls the production of Cherenkov photons in aerogel, and at the photodetector module level, which is relevant for charged-particle timing with SiPMs and for the gas-based e identification option. For the photodetector module I considered both the ideal trapezoidal module layout and the rectangular $17 \times 18$ cm$^2$ module layout.

#### Simulation strategy

In the full bRICH simulation I introduced two continuous normalization sensitive volumes. The first was positioned immediately downstream of the aerogel tiles. The second was positioned immediately downstream of the SiPM modules. Their segmentation followed the trapezoidal profiles of the frames for both the aerogel tiles and the photodetector modules, with all trapezoids interconnected so that every impinging charged track was registered with unit efficiency inside these normalization volumes.

I determined the geometric acceptance at the radiator level or at the photodetector level as the fraction of charged tracks that enter the corresponding normalization volume and also enter an aerogel tile or a photodetector module within the frame.

In the following I report the acceptance results for simulated central (0-5%) Pb–Pb collisions at $\sqrt{s_{\rm NN}} = 5.52$ TeV assuming a Gaussian spread of the primary vertex along the beam direction with the typical $\sigma_{\rm Z} = 10$ cm relative to the nominal collision vertex. I evaluated the acceptance as a function of the track momentum $p$, the pseudorapidity $\eta$, and the azimuthal angle $\phi$ of the charged track at the production point.

#### Acceptance at the radiator level

The left panels of Fig. 4.18 show the accepted fraction of tracks at the radiator as functions of $p_{\rm T}$, $\eta$, and $\phi$. The top-right and middle-right panel show the two dimensional acceptance maps in the planes ($p_{\rm T}$, $\eta$) and ($\eta$, $\phi$), highlighting the corresponding correlations. The bottom right panel shows the map of track impact points on the radiator tiles in terms of ($\eta_{\rm rad}$, $\phi_{\rm rad}$), where $\eta_{\rm rad}$ and $\phi_{\rm rad}$ are the geometrical pseudorapidity,

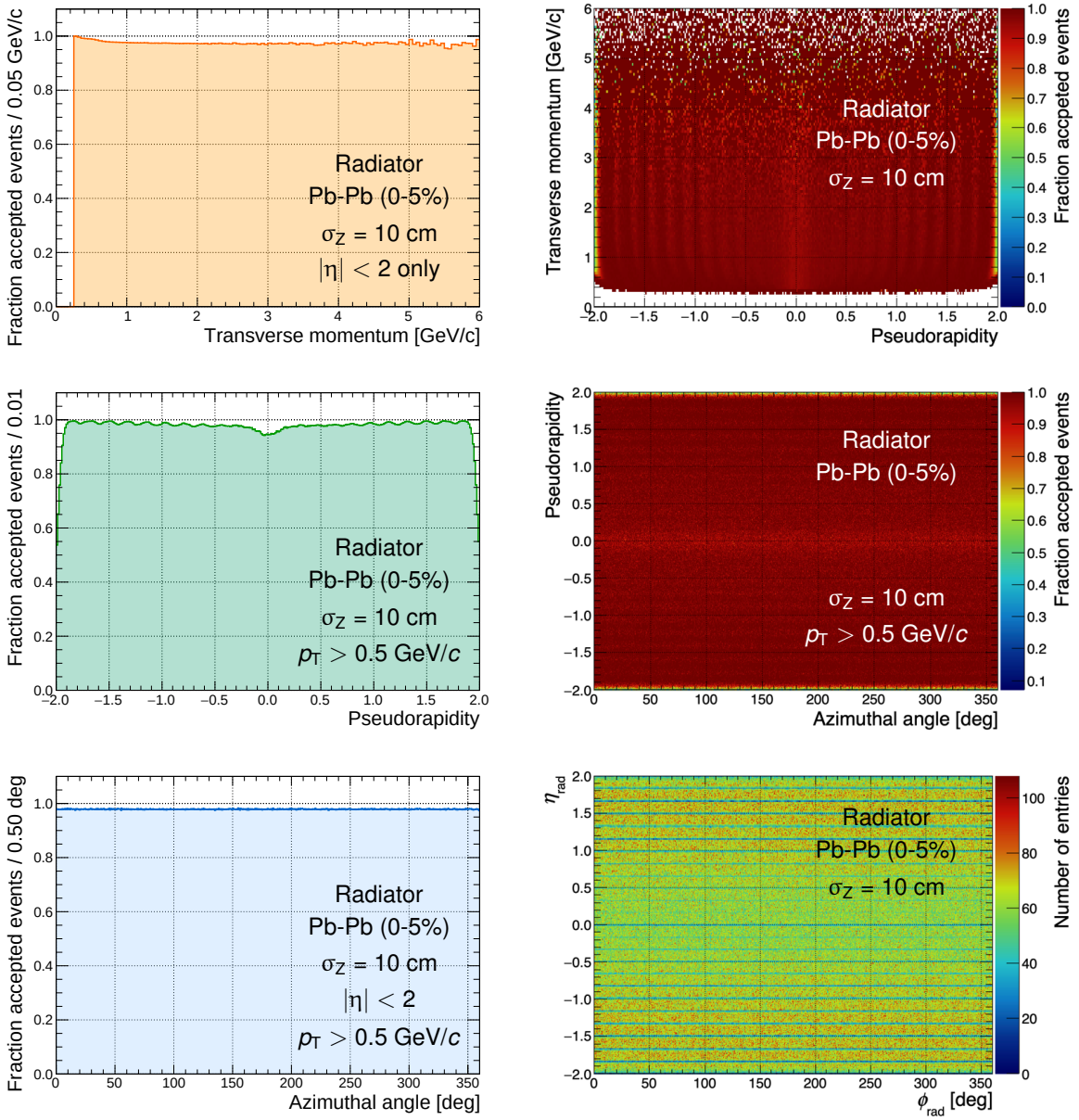


**Figure 4.18:** Fraction of accepted tracks at the radiator for simulated central (0–5%) Pb–Pb collisions at $\sqrt{s_{\mathrm{NN}}} = 5.52$ TeV. Left (top to bottom): acceptance versus the track $p_{\mathrm{T}}$, $\eta$, and $\phi$. Top-right and middle-right: two-dimensional acceptance maps in the $(p_{\mathrm{T}}, \eta)$ and $(\eta, \phi)$ planes, illustrating their correlations. Bottom-right: map of track impact points on the radiator in $(\eta_{\mathrm{rad}}, \phi_{\mathrm{rad}})$.

$-\log(\tan(\theta_{\mathrm{rad}})/2)$, and the azimuthal angle of the impact point on the radiator.

The lower limit near $p_{\mathrm{T}} \simeq 0.3$ GeV/$c$ in the one dimensional $p_{\mathrm{T}}$ plot and in the two dimensional $p_{\mathrm{T}}$ versus $\eta$ map arises from track curvature in the 2 T field, which prevents soft tracks from entering the bRICH and the normalization layers. The one dimensional distributions in $\eta$ and $\phi$ and the corresponding two dimensional map are thus shown only for $p_{\mathrm{T}} > 0.5$ GeV/$c$ in order to highlight purely geometric effects.

The trapezoidal aerogel tile profile provides an overall acceptance larger than 98% in polar and azimuthal coverage, also accounting for the spread of the Z coordinate of the collision vertex. A shallow minimum around 95% at $\eta = 0$ is visible and corresponds to the 1 cm gap between the two bRICH vessels introduced in Section 3.4.1.

The slight acceptance loss close to $|\eta| = 2$ is expected since the design bRICH boundary at $|\eta| = 2$ corresponds to the case of straight tracks from the nominal vertex. With a distributed vertex along Z, tracks with $\eta \to 2$ and $\eta \to -2$ produced at positive and negative Z, respectively, can be lost by the bRICH. Those tracks are not actually lost in the full ALICE 3 system, since they are still expected to enter the fRICH disks.

The impact point map of accepted tracks also shows only a minor loss at boundaries between contiguous modules and sectors, validating the effectiveness of the proposed trapezoidal radiator tile layout in terms of geometric track acceptance in Pb-Pb events.

#### Acceptance at the photodetector level

Figs. 4.19 and 4.20 show the same set of plots as Fig. 4.18 at the photodetector level for the trapezoidal and the rectangular $17 \times 18$ cm$^2$ layouts, respectively. The impact point maps are given in terms of ($\eta_{\mathrm{det}}$, $\phi_{\mathrm{det}}$), the geometrical pseudorapidity and the azimuthal angle of the impact point of accepted tracks on the photodetector modules.

For trapezoidal photodetector modules the behaviour closely follows that of the aerogel tiles, including the effect of the vertex spread. For rectangular modules a significant loss appears. Tracks that would cross regions of the trapezoidal frame outside the inscribed rectangular modules are lost as illustrated schematically in Fig. 3.7. These losses correspond to the white areas in the ($\eta_{\mathrm{det}}$, $\phi_{\mathrm{det}}$) map.

The largest loss occurs at midrapidity where the azimuthally integrated acceptance is about 78%. The loss is mitigated toward $|\eta| \to 2$ where the geometric efficiency exceeds 90%. The stronger loss at midrapidity follows from the ratio of active module area to frame area, which is smallest at midrapidity by construction. The loss is almost uniform as a function of $\phi$, with an $\eta$ integrated acceptance close to 87%.

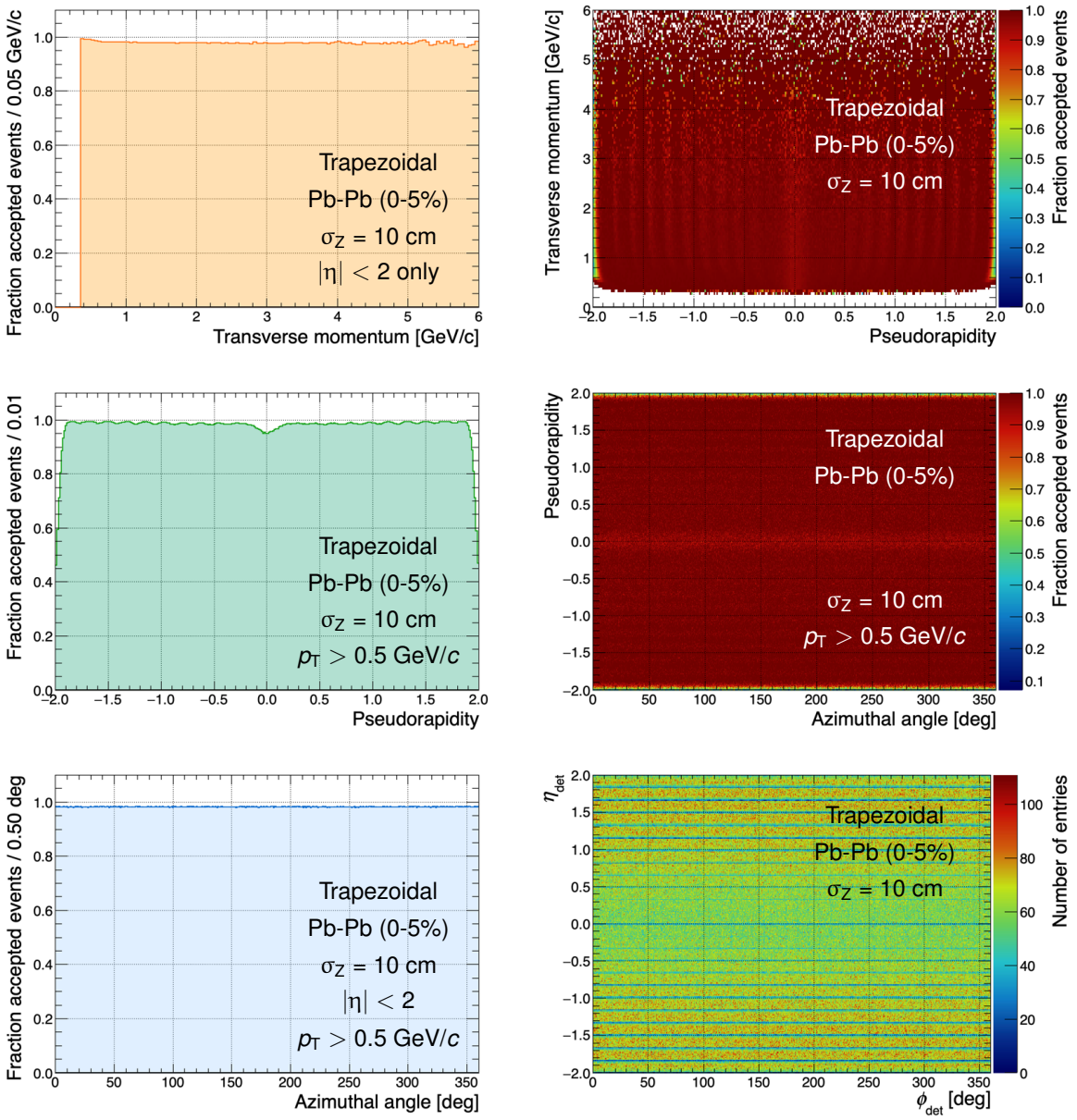


**Figure 4.19:** Fraction of accepted tracks at the photodetector for the trapezoidal module layout for simulated central (0–5%) Pb–Pb collisions at $\sqrt{s_{\mathrm{NN}}} = 5.52$ TeV. Left (top to bottom): acceptance versus the track $p_{\mathrm{T}}$, $\eta$, and $\phi$. Top-right and middle-right: two-dimensional acceptance maps in the $(p_{\mathrm{T}}, \eta)$ and $(\eta, \phi)$ planes, illustrating their correlations. Bottom-right: map of track impact points on the photodetector in $(\eta_{\mathrm{det}}, \phi_{\mathrm{det}})$.

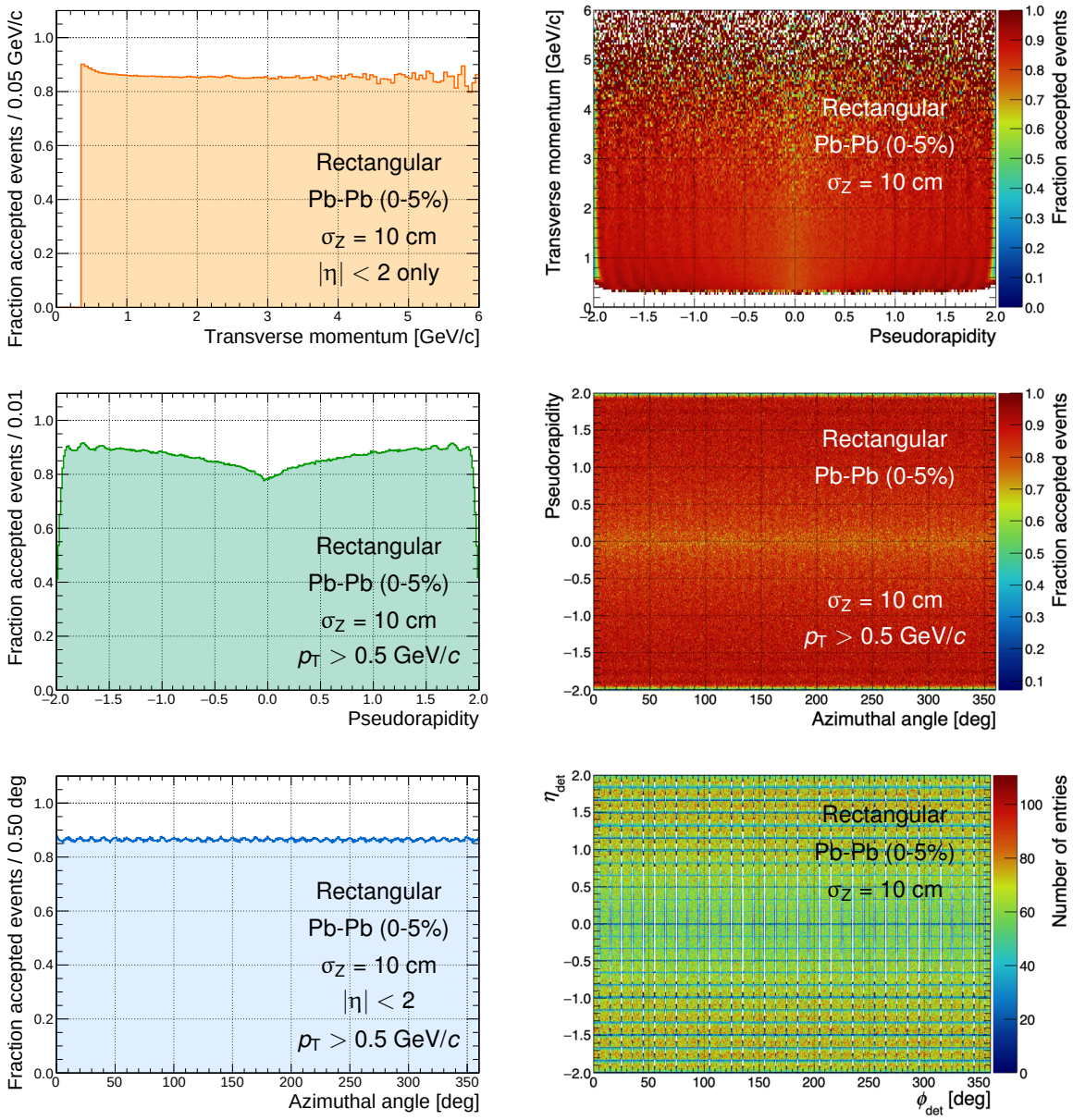


**Figure 4.20:** Fraction of accepted tracks at the photodetector for the rectangular $17 \times 18$ cm$^2$ module layout for simulated central (0–5%) Pb–Pb collisions at $\sqrt{s_{\mathrm{NN}}} = 5.52$ TeV. Left (top to bottom): acceptance versus the track $p_{\mathrm{T}}$, $\eta$, and $\phi$. Top-right and middle-right: two-dimensional acceptance maps in the $(p_{\mathrm{T}}, \eta)$ and $(\eta, \phi)$ planes, illustrating their correlations. Bottom-right: map of track impact points on the photodetector in $(\eta_{\mathrm{det}}, \phi_{\mathrm{det}})$.

It is important to note that acceptance losses at the photodetector plane are not critical for Cherenkov angle reconstruction as long as the track enters the radiator. Because of the finite ring size, a fraction of the photons remains detectable by the rectangular modules. The reduced acceptance nonetheless lowers the number of detected photons and degrades the achievable angular resolution, as discussed in Section 4.4.6.

However, the photodetector acceptance loss is critical for gas-based electron identification and charged-particle timing with SiPMs, where the signal photons are clustered within a region smaller than one centimetre around the predicted track impact point. For tracks falling outside the active module area, gas photons are lost, and for SiPM based timing there is no signal at all because the track does not traverse any SiPM region. This directly limits the timing performance and gas-based e tagging efficiency.

### 4.5.3 Time profile of Pb-Pb events

With SiPM DCR levels of order 1 MHz/mm$^2$, the overall data load expected when collecting all SiPM hits within a broad acquisition window become a serious concern. A central motivation for proposing the projective bRICH geometry is the expected time clustering of signal Cherenkov photons and charged–track hits into narrow time windows of the order of nanoseconds. Quantifying the intrinsic arrival–time structure of charged particles and photons at the bRICH SiPMs is therefore essential to define and validate the front–end electronics requirements.

Fig. 4.21 shows the intrinsic time profiles (i.e. without smearing from the time resolution) relative to the collision time for simulated central (0–5%) Pb–Pb events. The contributions from charged–track hits, aerogel photons, gas photons, and DCR are highlighted. Two DCR operating conditions are considered, 50 kHz/mm$^2$, corresponding to brand-new SiPMs operated at room temperature, and 1 MHz/mm$^2$, corresponding to the reference DCR safety limit. The left panels display the cumulative signal and DCR hits across all 24 bRICH sectors, while the right panels show the cumulative time profile for a single module including its own signal photons and DCR hits.

As expected, the projective geometry results in pronounced signal spikes in each sector superimposed on the uncorrelated DCR hits. Accounting for the time walk and the finite sensor time resolution, all signal hits within a sector cluster within time windows shorter than 2 ns. This enables an efficient reduction of the data volume by applying per–sector acquisition gates shorter than 2–3 ns with a different origin for each sector.

If the gate is opened at most once per bunch crossing, every 25 ns, the data load is reduced by about a factor 12.5 for a 2 ns window and about 8.3 for a 3 ns window, compared with continuous readout. This gating is foreseen directly at the front-end

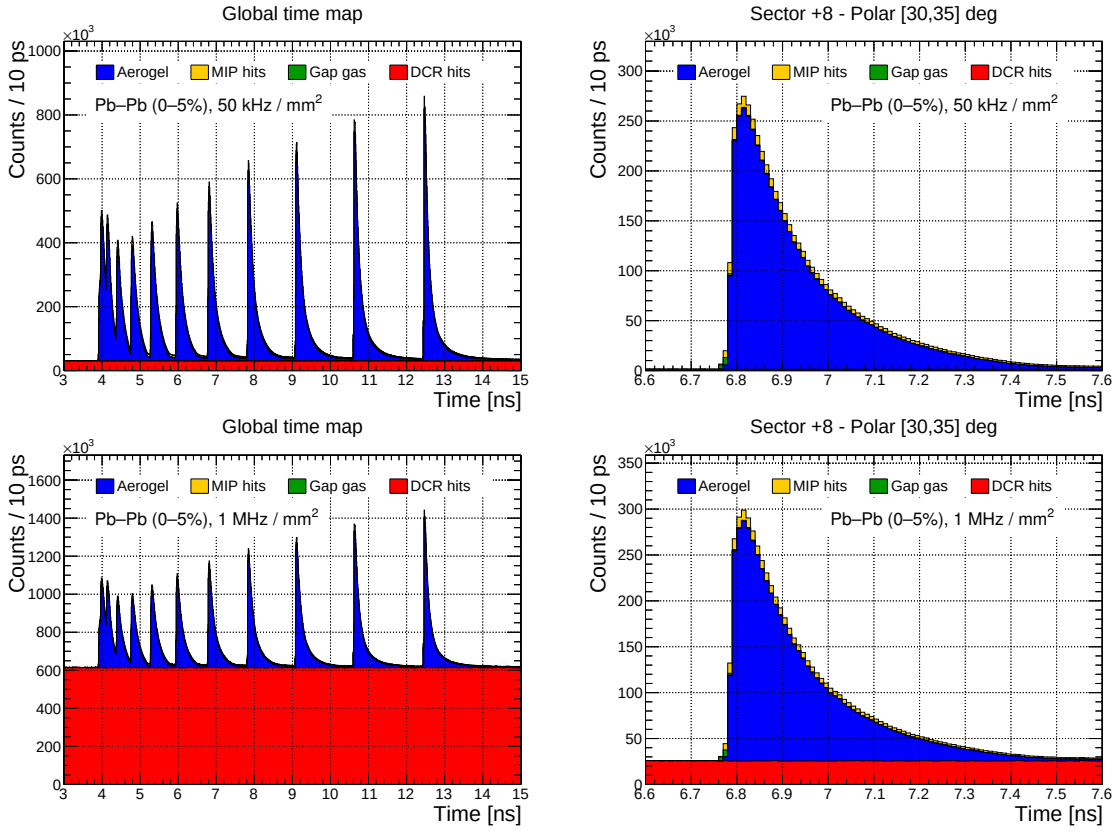


**Figure 4.21:** Intrinsic time profiles of charged-track hits and Cherenkov photons at the bRICH sensors for simulated central (0–5%) Pb–Pb events at $\sqrt{s_{\rm NN}} = 5.52$ TeV relative to the collision time assuming DCR = 50 kHz/mm$^2$ (top) and DCR = 1 MHz/mm$^2$ (bottom) and considering all the 24 bRICH sectors (left) and only sector +8 (right). The contributions from charged-track hits, aerogel photons, gas photons, and DCR are highlighted.

level by vetoing the DENEB ASIC discriminators outside the fiducial time window. This feature is already included in the ongoing DENEB design studies.

It is interesting to note that, in central (0-5%) Pb–Pb events, the track and photon multiplicity is so large that the number of detected signal hits within such a time gate exceeds the number of DCR hits. On the contrary, in low multiplicity events such as pp, the signal yield is so small that the time spikes are barely distinguishable from the DCR bands, which account for more than 99% of the recorded hits.

To report results in a worst-case scenario, all simulation studies presented in the following that include a time gate use a 4 ns window starting 1 ns before the nominal arrival time of the fastest tracks in each sector relative to the collision time.

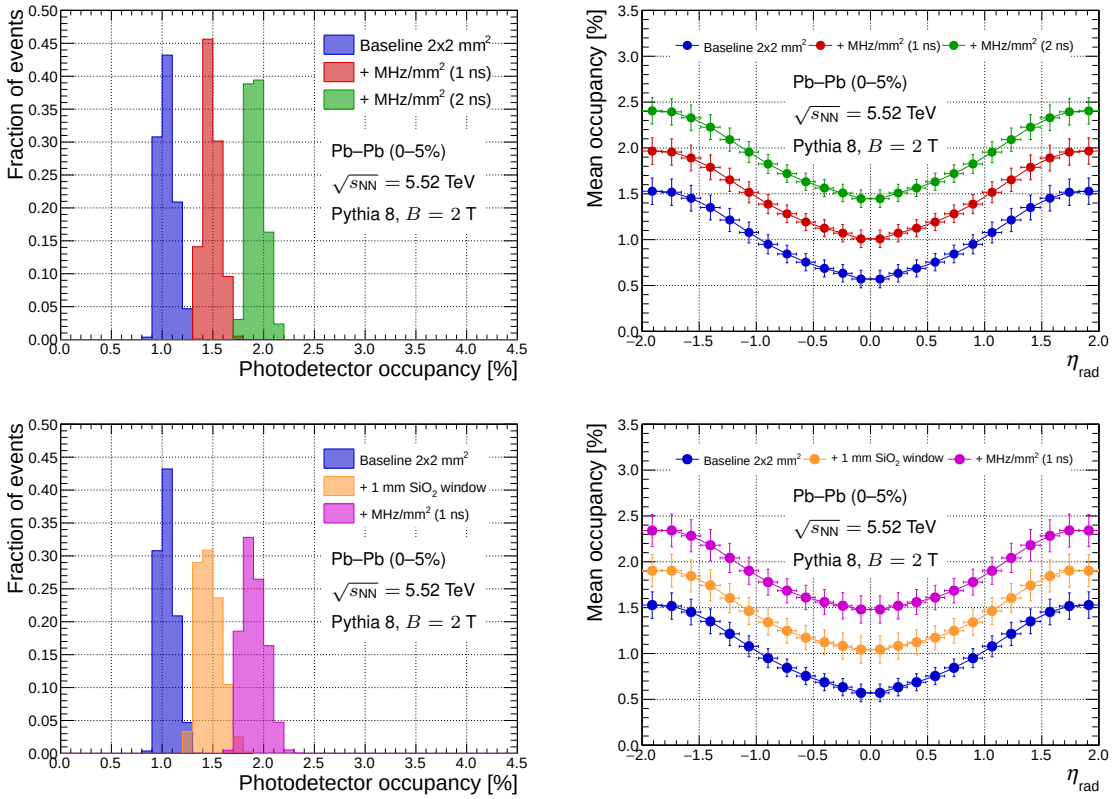


**Figure 4.22:** Overall (left) and per sector (right) photodetector occupancy in simulated central (0–5%) Pb-Pb collisions at $\sqrt{s_{\mathrm{NN}}} = 5.52$ TeV. The values obtained in the reference layout without DCR (blue), adding the hits from a DCR of 1 MHz/mm$^2$ sampled in a sector-specific acquisition time gate of 1 ns (red) and 2 ns (green) are shown. Also shown is the option with the modules coupled to a 1 mm thick $SiO_2$ window used to enhance charged-particle timing without DCR (orange) and with a DCR of 1 MHz/mm$^2$ sampled in a 1 ns gate (magenta).

### 4.5.4 Photodetector occupancy in central Pb-Pb events

Due to the large expected track and hit multiplicity in central Pb-Pb events as well as the large expected SiPM DCR relative to the considered acquisition time gate, I investigated the photodetector occupancy in those events, also accounting for the DCR and the photons from a hypothetical 1 mm $SiO_2$ window for timing.

Fig. 4.22 shows the photodetector occupancy in simulated central 0 to 5% Pb-Pb collisions at $\sqrt{s_{\mathrm{NN}}} = 5.52$ TeV, comparing the reference layout without DCR, the contribution of hits from a DCR of 1 MHz/mm$^2$ sampled in sector-specific acquisition gates of 1 ns and 2 ns, as well as the option with a 1 mm $SiO_2$ window directly coupled to the SiPM either without DCR or with hits from a DCR of 1 MHz/mm$^2$ sampled in a 1 ns gate. The occupancy is shown averaged over the full acceptance and per sector.

Most of the hits come from the Cherenkov photons produced in the aerogel tiles. They result in an average occupancy of 1%, ranging from 0.6% in the central sectors and increasing up to 1.6% at forward rapidities. A DCR of 1 MHz/mm$^2$ results in an increase of the occupancy of about 0.5% per 1 ns acquisition time gate. A further systematic increase of about 0.5% is observed in the case of the $SiO_2$. These results highlight that with a time gate of 1 to 2 ns, despite the large DCR, in central (0-5%) Pb-Pb events the largest contribution still comes from the products of the collision. In this case the main concern for the pattern recognition of Cherenkov rings comes from the mutual background of hits by different particles in the same events.

### 4.5.5 Hit-track time matching vs SPTR and DCR

A crucial design parameter for the bRICH is the overall single photon time resolution (SPTR) accounting for both SiPMs and front-end. In this section I investigate the impact of the SPTR on the time matching between charged tracks and the corresponding signal photon hits, also accounting for the background from the SiPM DCR.

Fig. 4.23 shows the distributions of the difference $\Delta T$ between the extrapolated emission time of candidate photon hits and the extrapolated charged-track arrival time at the most probable emission point in the radiator, calculated as discussed in Section 4.3.3, for central (0-5%) Pb-Pb collisions at $\sqrt{s_{\rm NN}} = 5.52$ TeV. Only hits with reconstructed single hit angle less than 260 mrad are considered. The results obtained with an assumed SPTR of 50 ps, 100 ps, and 200 ps under hypotheses of both no DCR, where only physical hits are detected, and a DCR of 1 MHz/mm$^2$ sampled in an acquisition time window of 4 ns, are compared.

In all cases, the observed distribution of true signal photon hits is a Gaussian with mean about 0 and a standard deviation dominated by the SPTR, with the extra contribution of the track time based on the oTOF time resolution of 20 ps being almost negligible.

From the plots, it can be observed that even with DCR levels of the order of MHz/mm$^2$, the hit multiplicity in central Pb-Pb events was still dominated by the correlated background from particles within the same event. The panels also show how effectively improving the SPTR separates signal and background hits.

From the scan of the Cherenkov angle reconstruction versus the time cut $\Delta T$, I found that the best compromise among efficiency, purity, and signal-to-background ratio for pattern recognition and PID was obtained by selecting only hits with $|\Delta T| < 2\,\mathrm{SPTR}$. In the following, I always adopted this assumption, unless stated otherwise.

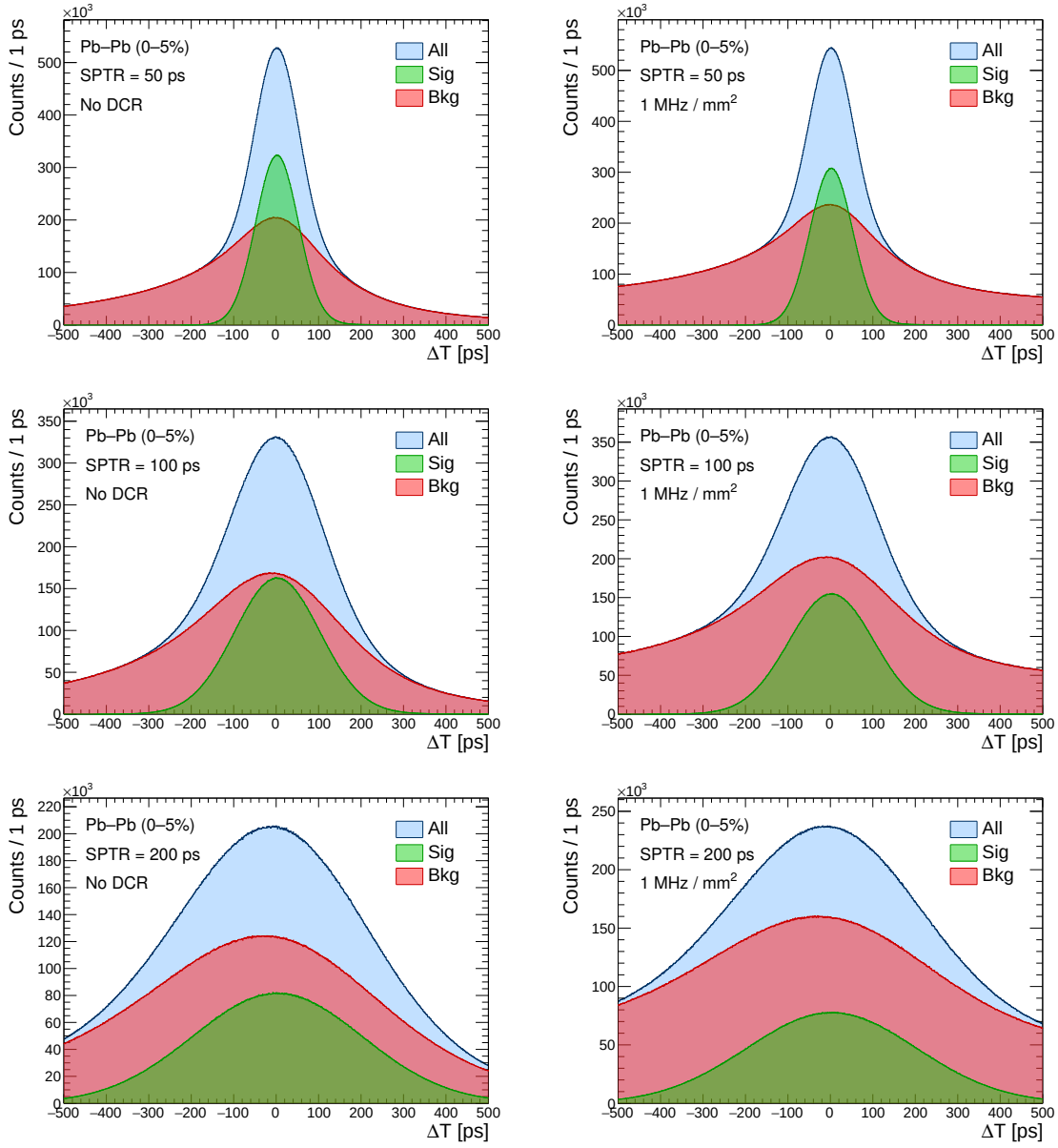


**Figure 4.23:** Distribution of the difference $\Delta T$ between the extrapolated emission time of candidate photon hits and the extrapolated charged-track arrival time at the most probable emission point in the radiator for central (0-5%) Pb-Pb collisions at $\sqrt{s_{\mathrm{NN}}} = 5.52$ TeV, considering only hits with single hit angle less than 260 mrad. The panels correspond to the assumption of a SPTR of 50 ps (top), 100 ps (middle), and 200 ps (bottom), shown for the case without DCR (left) and with a DCR of 1 MHz/mm$^2$ sampled in a 4 ns acquisition window per sector (right). The contribution of signal (green) and background (red) hits is highlighted.

### 4.5.6 Hit-track distance vs SPTR and DCR

To characterize the topology of the Cherenkov rings on the photosensitive surface, I investigated the spatial distribution of detected signal and background hits relative to the most probable charged-track impact point on the photodetector modules. I determined the track impact point extrapolating the track from the most probable photon emission point in aerogel to the photodetector modules, using the same procedure discussed in Section 4.3 for the extrapolation from the oTOF layer to the bRICH aerogel.

Fig. 4.24 shows the distribution of the distance between candidate photon-hit positions and the extrapolated track impact point on the photodetector modules for central (0–5%) Pb–Pb collisions at $\sqrt{s_{\mathrm{NN}}} = 5.52$ TeV. Only hits with reconstructed single hit angle less than 260 mrad, corresponding to the physical Cherenkov angle region, are considered. The left and right panels correspond to the cases without DCR and with a DCR of 1 MHz/mm$^2$ sampled in a 4 ns acquisition window per sector.

The results with SPTR = 50 ps and 100 ps, both with a $\pm 2\,$SPTR hit–track time-matching cut, are compared to the case where no time matching is applied, highlighting the significant background suppression. In particular, excellent suppression of the uncorrelated DCR hits is achieved with a SPTR of 200 ps or better. This also partially mitigates the correlated background due to hits from different tracks in the same event.

The peak below 2 mm corresponds to the pixel crossed by the track, where photons are produced in the considered 100 µm silicone resin layer in front of the SiPMs. Although they originate from the track of interest, they still represent background for the selection of signal photon hits used to reconstruct the Cherenkov angle in aerogel.

One of the main design features of the proposed projective bRICH geometry is that it maintains near-normal track incidence on the radiator even toward forward rapidities, yielding localized rings and limiting the photon spread. This is crucial to suppress mutual track background in such a high-multiplicity environment.

Signal hits are in fact confined within a maximum distance of 9 cm relative to the track. The multiple signal peaks in Fig. 4.24 mirror the width of the expansion gap across sectors, as the detected ring radius scales proportionally with the gap.

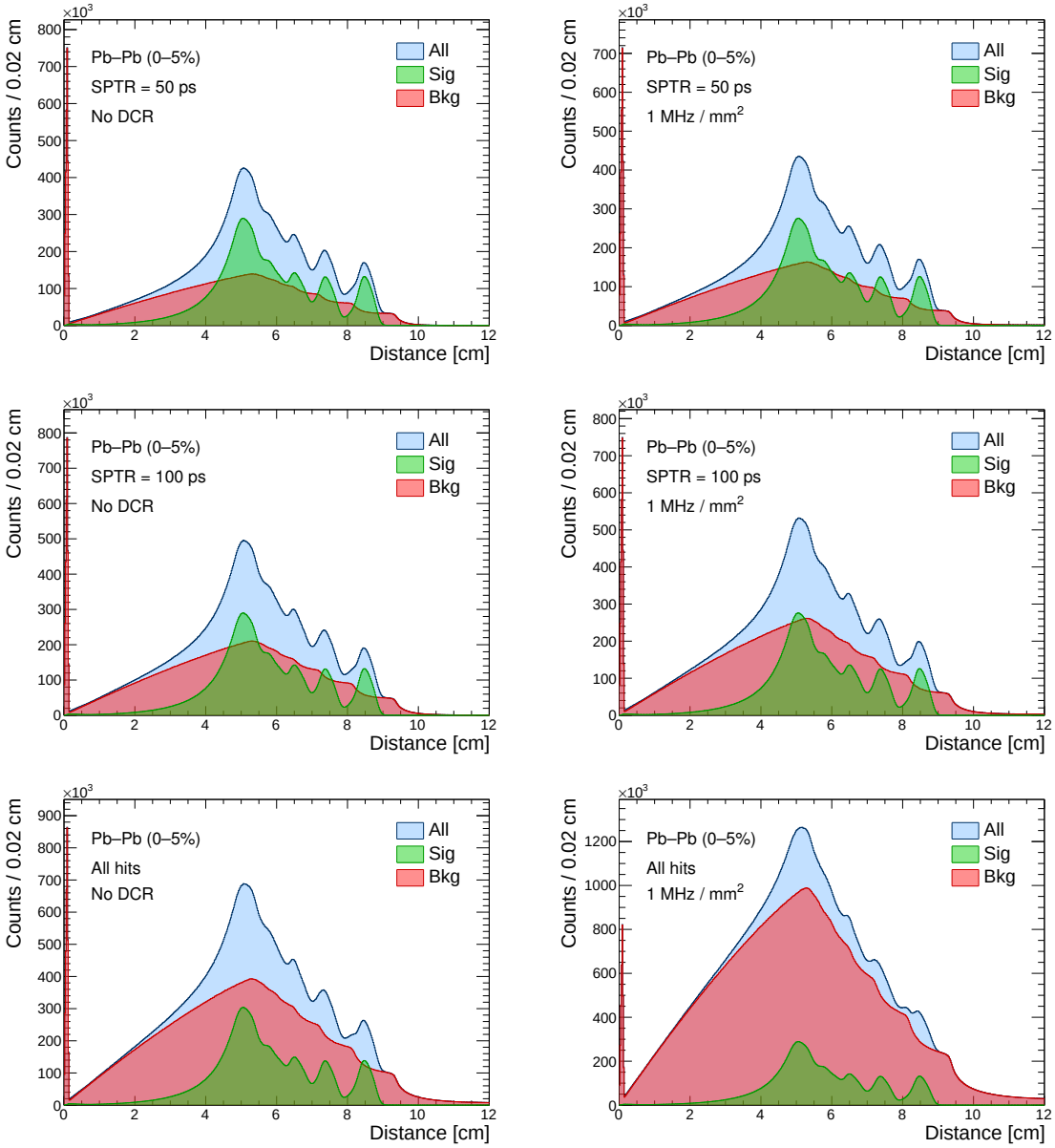


**Figure 4.24:** Distribution of the distance between candidate photon-hit positions and the extrapolated track impact point on the photodetector modules for central (0–5%) Pb–Pb collisions at $\sqrt{s_{\mathrm{NN}}} = 5.52$ TeV, considering only hits with single hit angle $< 260$ mrad. The panels correspond to the case without DCR (left) and with a DCR of 1 MHz/mm$^2$ sampled in a 4 ns acquisition window per sector (right). Rows correspond to the cases with SPTR = 50 ps (top) and 100 ps (middle), both with a $\pm 2\,$SPTR hit–track time-matching cut, and to all hits without timing selection (bottom). The contribution of signal (green) and background (red) hits is highlighted.

## 4.6 Particle identification: a Bayesian approach

In order to study the PID performance of the tested bRICH configurations in pp and Pb-Pb events, I implemented a dedicated algorithm based on a Bayesian approach [115]. The considered approach is based on computing, track by track, the probability $P(i|S)$ that the measured signal $S$ corresponds to a given particle species $i$, namely e, μ, π, K and p. The main ingredients of Bayesian PID are the following:

- the probability $A(S|i)$ to register the signal $S$ for each mass hypothesis $i$;
- the a priori relative abundances $C_i$ of each particle species $i$ in the sample.

I defined the probability for the mass hypothesis $i$ as:

$$P(i|S) = \frac{C_i \; A(S|i)}{\sum_j^{\text{all species}} C_j \; A(S|j)} \tag{4.11}$$

I assigned the final track identity according to the maximum $P(i/S)$ among all mass hypotheses. In this context, I studied the impact on PID efficiency and purity of setting a minimum requirement $P_{\text{max}}^{\text{min}}$ on this maximum, leaving tracks untagged when:

$$P_B \equiv \max_i P(i \mid S) < P_{\text{max}}^{\text{min}}. \tag{4.12}$$

Larger $P_{\text{max}}^{\text{min}}$ values increase PID purity at the cost of reduced efficiency, and vice versa. Tuning this threshold is therefore possible to optimize tagging in terms of efficiency and purity depending on the needs of any specific physics analysis.

### Measured signal

For the bRICH performance analyses with the Bayesian approach, I assumed the measured signal $S$ to be the reconstructed ring Cherenkov angle $\theta_{\text{rec}}$, evaluated with the Hough-transform estimator $\theta_c^H$, as discussed in Section 4.3.4.

The reconstructed angle $\theta_{\text{rec}}$ is accompanied by the information on the number of clustered hits $N_{\text{rec}}$. Since low $N_{\text{rec}}$ values are likely to correspond to the clustering of background hits, I investigated the impact the impact on PID efficiency and purity of imposing a minimum requirement $N_{\text{rec}}^{\text{min}}$ for $N_{\text{rec}}$, by leaving tracks untagged when:

$$N_{\text{rec}} < N_{\text{rec}}^{\text{min}}. \tag{4.13}$$

Larger $N_{\text{rec}}^{\text{min}}$ values increase PID purity at the cost of reduced efficiency, and vice versa.

### Detector response

For the calculation of the detector response $A(S|i)$, I assumed a Gaussian with mean equal to the expected Cherenkov angle $\theta^i_{\rm th}$, calculated using Eq. 2.4, and standard deviation given by mean ring angular resolution $\sigma_{{\rm r},\,i}$ from the simulation of the considered RICH configuration, evaluated at the track pseudorapidity $\eta$ and momentum $p$ for the tested mass hypothesis $i$:

$$A(S \mid i) = \frac{1}{\sigma_{{\rm r},i}\sqrt{2\pi}} \exp\left[-\frac{\left(\theta_{\rm rec} - \theta_{{\rm th},i}\right)^2}{2\,\sigma^2_{{\rm r},i}}\right] . \tag{4.14}$$

If the track momentum $p$ is below the aerogel Cherenkov threshold for mass hypothesis $i$, the response is set to zero, $A(S \mid i) = 0$, for that hypothesis. In order to limit the PID contamination due to the random clustering of background yields, yielding $\theta_{\rm rec}$ values totally unrelated with any of considered mass hypotheses, tracks with

$$|\theta_{\rm rec} - \theta_{{\rm th},i}| > 4\sigma_{{\rm r},i} \quad \text{for all mass hypotheses } i = {\rm e}, \mu, \pi, {\rm K}, {\rm p} \tag{4.15}$$

are discarded. This choice leads to an improvement of the PID purity at the cost of efficiency loss depending on the collision system, track multiplicity, and DCR level.

### Relative abundances

For the relative abundances $C_i$, I used the Monte Carlo fractions of e, μ, π, K, and p (particle + antiparticle) entering the bRICH modules in the considered pp and Pb-Pb collisions. The reference values employed in the analysis are reported in Table 4.3.

| $C$(e) | $C$(μ) | $C$(π) | $C$(K) | $C$(p) |
|---|---|---|---|---|
| 0.32% | 0.08% | 83.58% | 10.17% | 5.85% |

**Table 4.3:** Relative abundances of e, μ, π, K, and p entering the bRICH used for the analysis.

## 4.6.1 PID efficiency and purity

For each tested configuration, I evaluated the tagging performance for the considered collision systems in terms of $e$, μ, π, K, and p PID efficiency and purity, in intervals of momentum and pseudorapidity $(p, \eta)$. For a given interval, let $N_i^{\rm true}$ be the number of true particles of species $i$ entering the bRICH, $N_{i\to j}$ the number of those tagged as

species $j$, and $\sum_j N_{j\to i}$ the total number tagged as $i$, irrespective of their true species. Untagged tracks are included in $N_i^{\text{true}}$ but excluded from $\sum_j N_{j\to i}$.

The efficiency $\varepsilon_i$ and the purity $\mathcal{P}_i$ of the sample tagged as species $i$ are given by:

$$\varepsilon_i \;=\; \frac{N_{i\to i}}{N_i^{\text{true}}} \qquad \text{and} \qquad \mathcal{P}_i \;=\; \frac{N_{i\to i}}{\sum_j N_{j\to i}}\,. \tag{4.16}$$

The corresponding uncertainties on $\varepsilon_i$ and $\mathcal{P}_i$ are evaluated according to the relations:

$$\sigma_{\varepsilon_i} \;=\; \sqrt{\frac{\varepsilon_i(1-\varepsilon_i)}{N_i^{\text{true}}}} \qquad \text{and} \qquad \sigma_{\mathcal{P}_i} \;=\; \sqrt{\frac{\mathcal{P}_i(1-\mathcal{P}_i)}{\sum_j N_{j\to i}}}\,. \tag{4.17}$$

### 4.6.2 Performance in pp collisions

To benchmark the limiting bRICH performance, I report pattern-recognition and PID results in pp under the ideal reference conditions with SPTR = 50 ps and no DCR.

Fig. 4.25 shows the performance of the Hough-transform-based pattern recognition combined with Bayesian PID in 1.8M simulated $c\bar{c}$ biased pp collisions at $\sqrt{s} = 14$ TeV. Results are provided for both the trapezoidal photodetector module layout and the rectangular $17 \times 18$ cm$^2$ layout. Tracks are accepted only if the number of Hough-selected hits is $\geq 3$ and tagged when the maximum Bayesian probability exceeds 50%.

The reconstructed Cherenkov angles follow the expected momentum dependence for all particle species, with an almost negligible fraction of events with a fake reconstructed angle due to hits from the mutual track background and secondaries.

The corresponding efficiencies and purities indicate near-ideal PID performance between threshold and saturation in these low-multiplicity events. Electrons are separated from pions up to 2–2.5 GeV/$c$, kaons from pions up to 8–10 GeV/$c$, and protons from pions and kaons beyond 14 GeV/$c$. The analysis reported here is limited to 14 GeV/$c$ by sample statistics at higher momenta rather than intrinsic performance.

The main challenge for PID is keeping performance as close as possible to the limiting ones reported here in terms of efficiency and purity even in the high-multiplicity environment of the most central Pb–Pb collisions under extreme DCR conditions, a key objective of my research and the focus of the next sections.

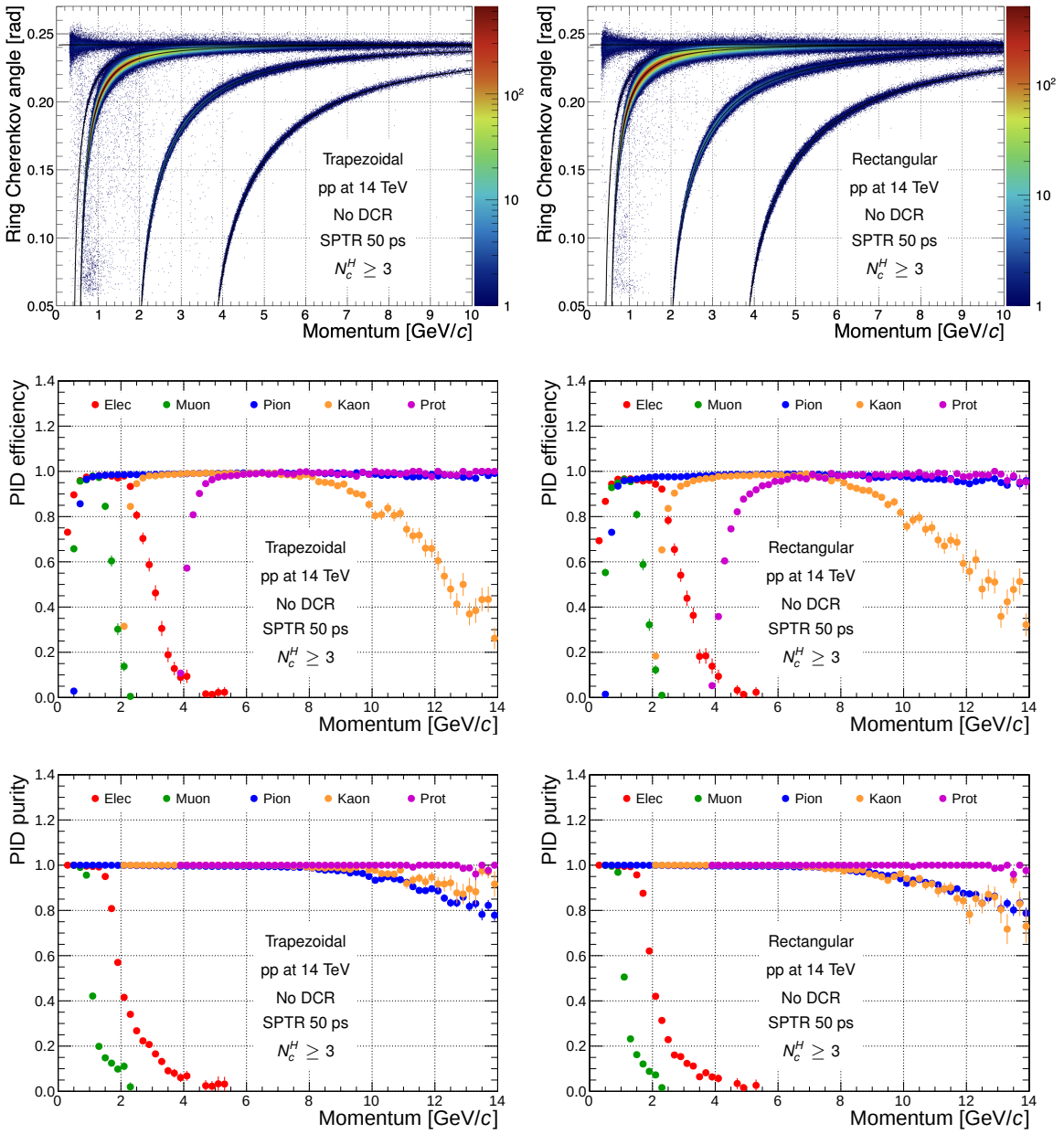


**Figure 4.25:** Distributions of the reconstructed ring Cherenkov angle (top), PID efficiency (middle) and purity (bottom) versus momentum for e, μ, π, K and p, obtained with the Hough transform and Bayesian PID for simulated pp collisions at $\sqrt{s} = 14$ TeV assuming SPTR = 50 ps, a $\pm 2\,\sigma$ SPTR hit-track matching cut, no DCR, an acquisition time gate of 4 ns per sector, and both the trapezoidal layout (left) and the rectangular $17 \times 18$ cm$^2$ layout (right). Tracks are accepted only if the number of Hough-selected hits is $\geq 3$ and tagged when the maximum Bayesian probability exceeds 50%.

### 4.6.3 Pattern recognition in central Pb-Pb

To visualize the complexity of pattern recognition in central Pb-Pb, Fig. 4.26 shows the distributions of the reconstructed ring Cherenkov angle versus momentum obtained with the Hough transform method for simulated central (0-5%) Pb-Pb collisions at $\sqrt{s_{\rm NN}} = 5.52$ TeV for the trapezoidal photodetector module layout. A DCR of 1 MHz/mm$^2$ sampled in an acquisition time gate of 4 ns is assumed, representing a worst case scenario. The results obtained with a $\pm 2$ SPTR cut on the hit-track time matching assuming the ideal target SPTR of 50 ps (on the left) and the worst case scenario of 200 ps (on the right) are compared. The three rows correspond to cuts on the minimum number of Hough-selected hits required to accept a track of 3, 7 and 11. The corresponding plots for rectangular $17 \times 18$ cm$^2$ modules are shown in Fig. 4.27.

The signal bands of e, $\mu$, $\pi$, K and p become wider relative to the pp case due to the clustering of both uncorrelated DCR hits and mutual track background hits, resulting in the worsening of the ring angular resolution.

The main problem arises for charged tracks below the threshold for Cherenkov emission, where there are not signal photon hits to cluster. In this case, only background hits are clustered together by the Hough transform. This results in the vertical bands in Figs. 4.26 and 4.27 where the momentum steps corresponding to $\pi$, K and p are clearly visible. In particular, below 0.6 GeV/$c$, corresponding to the $\pi$ threshold in aerogel, $\pi$, K and p all contribute to the vertical band. Between 0.6 GeV/$c$ and 2 GeV/$c$, corresponding to the K threshold, both K and p contribute to the band. Finally between 2 GeV/$c$ and 4 GeV/$c$ mostly protons contribute to the band.

Fake Cherenkov angles reconstructed in those region could invade the bands associated to the different particle species, significantly affecting the purity. Although this background can be suppressed by setting a threshold on the minimum number of Hough-selected hits, discarding those tracks and enhancing the purity, this comes at the cost of a reduced efficiency, as discussed in Section 4.6.4.

The effects of this background are particularly relevant for electrons, due to low relative abundance, about 0.3% of the tracks, compared to all the other species, while the best possible efficiency and purity are required for their identification.

Comparing results with a SPTR of 50 ps and 200 ps, the benefit of the best resolution on the background suppression is clear, favouring a SPTR better than 100 ps.

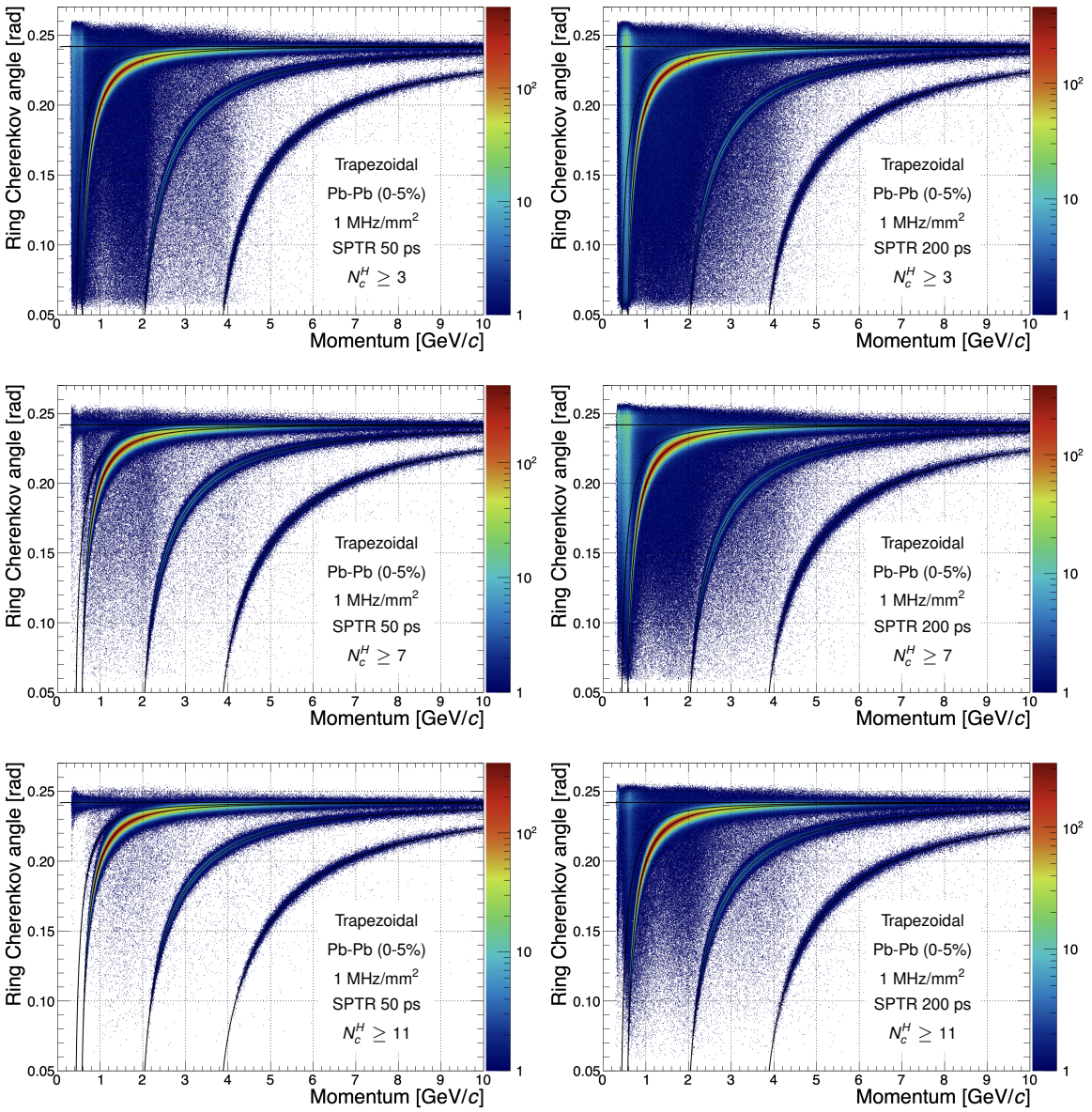


**Figure 4.26:** Distributions of the reconstructed ring Cherenkov angle versus momentum obtained with the Hough transform method for simulated central (0-5%) Pb-Pb collisions at $\sqrt{s_{\mathrm{NN}}} = 5.52$ TeV assuming a DCR of 1 MHz/mm$^2$, an acquisition time gate of 4 ns and trapezoidal photodetector modules. Columns correspond to a SPTR of 50 ps (left) and 200 ps (right). A $\pm 2\,\mathrm{SPTR}$ hit-track matching cut is assumed. Rows correspond to cuts on the minimum number of Hough-selected hits required to accept a track, namely 3 (top), 7 (middle), and 11 (bottom).

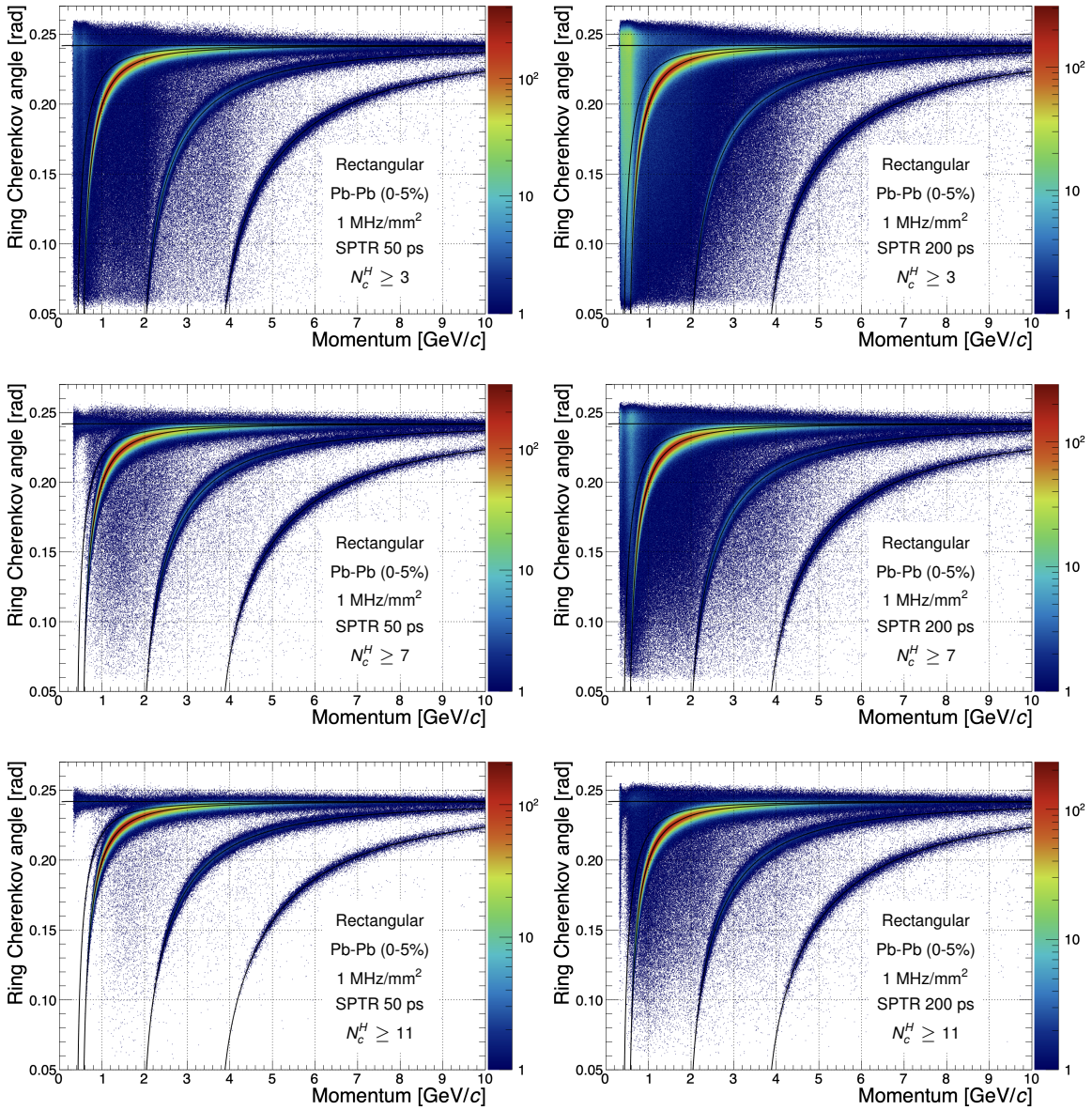


**Figure 4.27:** Distributions of the reconstructed ring Cherenkov angle versus momentum obtained with the Hough transform method for simulated central (0-5%) Pb-Pb collisions at $\sqrt{s_{\mathrm{NN}}} = 5.52$ TeV assuming a DCR of 1 MHz/mm$^2$, an acquisition time gate of 4 ns and rectangular $17 \times 18$ cm$^2$ photodetector modules. Columns correspond to a SPTR of 50 ps (left) and 200 ps (right). A $\pm 2\,$SPTR hit-track matching cut is assumed. Rows correspond to cuts on the minimum number of Hough-selected hits required to accept a track, namely 3 (top), 7 (middle), and 11 (bottom).

### 4.6.4 PID performance in central Pb-Pb

Figs. 4.28–4.33 show the PID efficiency and purity versus momentum for e, μ, π, K and p obtained with the Hough transform and Bayesian PID for 5k central (0-5%) Pb–Pb collisions at $\sqrt{s_{\rm NN}} = 5.52$ TeV for the trapezoidal photodetector module layout. To quantify the intrinsic limitations due to the high hit/track multiplicity of the events, the contribution of the DCR, the impact of the SPTR and the effect of the requirement of a minimum number of Hough-selected hits $N^H_{\rm min}$, the six figures refer to cases with SPTR = 50, 100, and 200 ps, both without DCR and with a DCR of 1 MHz/mm$^2$. In all cases, a 4 ns acquisition window per sector is used. For pattern recognition, a ±2 SPTR hit–track time matching requirement is applied. Tracks are tagged only if the maximum Bayesian probability exceeds 50%. The rows correspond to $N^H_{\rm min} = 3$, 7, 11. The same results for rectangular 17 × 18 cm$^2$ modules are shown in Figs. 4.34–4.39. The results in the case of no DCR show the intrinsic performance, limited only by correlated mutual track background due to the high-multiplicity of the collision, while those with a DCR of 1 MHz/mm$^2$ represent the worst-case operating scenario.

#### Hadron identification

Analysing the plots relative to the trapezoidal module layout, it can be observed that, for the considered selections, the purities of π, K and p are almost unaffected by $N^H_{\rm min}$, with purities larger than 95% for momenta between the Cherenkov threshold and the overlap regions, even with $N^H_{\rm min} = 3$ in the worst scenario of DCR and SPTR.

In the momentum regions where the bands associated to π, K and p begin to overlap, the purities start worsening. The major loss above 10 GeV/$c$ is observed for kaons. as expected also considering the relative fractions of K relative to pions.

In the momentum region where the species are intrinsically well separated, efficiencies larger than 95% are found for the trapezoidal module layout for $N^H_{\rm min} = 3$ even in the worst case scenario of DCR and SPTR. The efficiency could be further increased by softening the Bayes probability cut relative to the 50% considered for these plots at the cost of a reduction in the corresponding PID purity.

Increasing $N^H_{\rm min}$ leads to marginal improvements of the hadron purities at the cost of a significant reduction of the PID efficiency, dropping down to 90%. The π, K and p efficiency loss with increasing $N^H_{\rm min}$ is particularly evident at low momenta, close to the corresponding thresholds for Cherenkov emission. The efficiency loss is partly due to the loss of photons for tracks entering the bRICH aerogel tiles close to the sector boundaries, which are more easily discarded by higher $N^H_{\rm min}$ thresholds.

Comparing the results on hadron PID obtained for trapezoidal modules with the case of rectangular $17 \times 18$ cm$^2$ modules, comparable purities are achieved with an efficiency lower by about 2-3% for $N^H_{\rm min} = 3$. Raising $N^H_{\rm min}$ to 7 or 11 improves PID purity but degrades efficiency much more than the option of trapezoidal modules. In particular, for $N^H_{\rm min} = 11$ the maximum efficiency decreases from about 90–95% with trapezoidal modules to roughly 80% or less with rectangular modules. This behaviour is expected, since the rectangular layout provides only $\sim 73\%$ of the active area of the trapezoidal design, yielding fewer signal and background hits. Consequently, looser $N^H_{\rm min}$ requirements are needed for rectangular modules to mitigate efficiency losses.

Despite the worsening with respect to low-multiplicity pp collisions, these results show that, even in the high-multiplicity environment of Pb–Pb collisions, with a SPTR of 200 ps and a DCR of 1 MHz/mm$^2$, the proposed rectangular $17 \times 18$ cm$^2$ module layout enables the Hough-transform plus Bayesian-PID selections to be optimized to achieve excellent $\pi$/K separation up to 8–10 GeV/$c$ with both efficiency and purity above 80%, and excellent K/p separation beyond 14 GeV/$c$.

### Electron identification

The main limitation of the Hough-transform plus Bayesian PID approach in Pb–Pb, relative to the pp limiting performance discussed in Section 4.6.2, concerns the identification of electrons below 2 GeV/$c$. The dominant contamination arises from the clustering of background hits for tracks below the Cherenkov threshold.

For analyses focused on electron identification, this background can be substantially reduced by increasing $N^H_{\rm min}$. Since electrons entering the bRICH are always in the saturation regime, the associated efficiency loss is limited. Further improvements are obtainable by tuning the Bayesian probability threshold relative to the 50% used here, loosening it to raise efficiency or tightening it to raise purity.

With SPTR values of 50 ps or 100 ps, both efficiency and purity above 80% remain achievable up to 1.5–2 GeV/$c$ with suitable tuning. However, performance worsens markedly for poorer SPTR, rendering such projections unstable. This behaviour reflects intrinsic limits of Hough-based pattern recognition under the high multiplicity of central Pb–Pb events combined with large SiPM DCR, particularly at low momentum.

In the following, I show that custom machine-learning algorithms trained on aerogel-ring patterns in the proposed projective geometry result in better PID, improving the electron identification efficiency and purity, and thereby validating the expected bRICH performance across all the considered operating scenarios. This is particularly important for the rectangular module layout due to the reduced acceptance for photons.

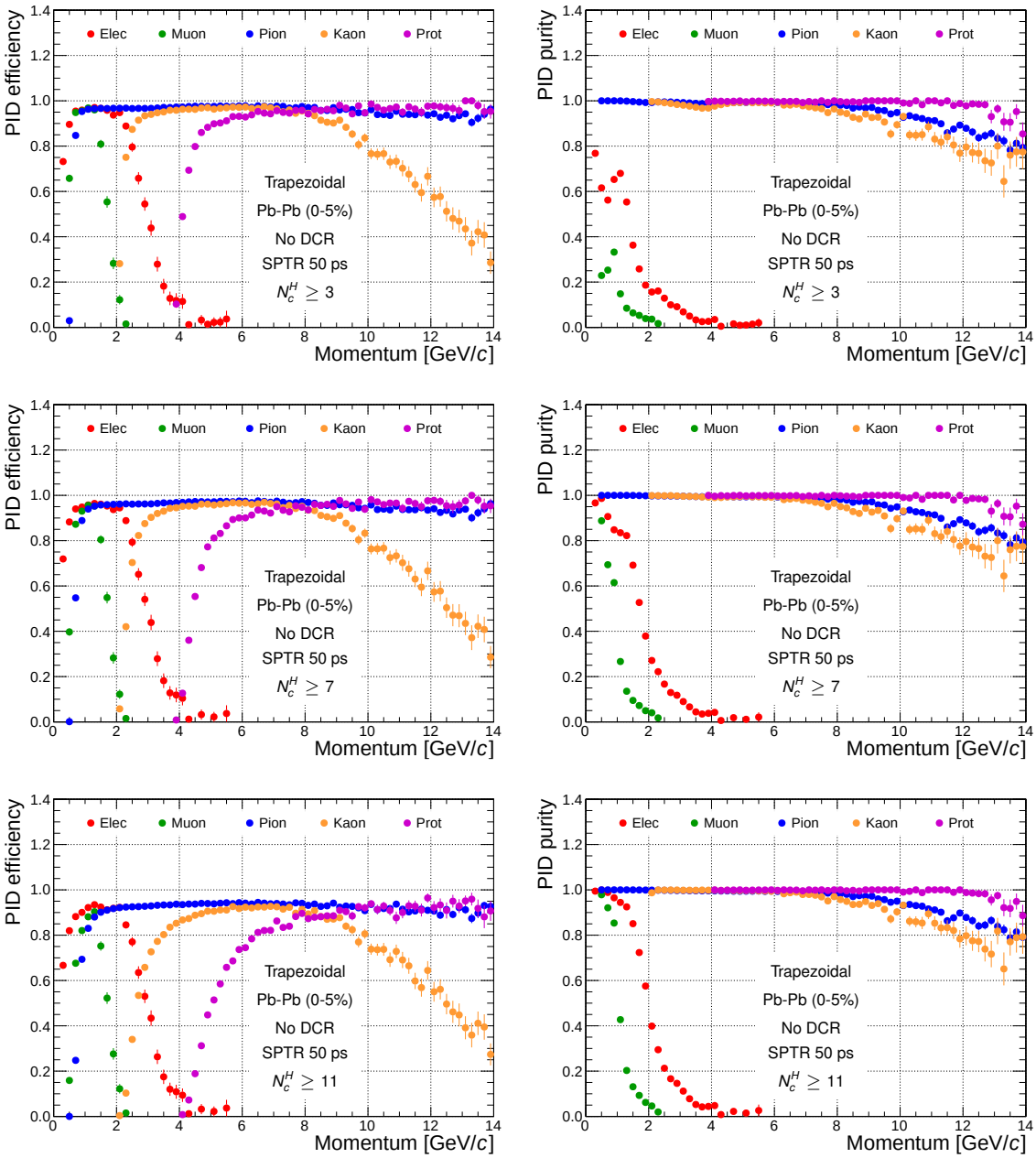


**Figure 4.28:** PID efficiency (left) and purity (right) versus momentum for e, μ, π, K, and p, obtained with the Hough transform and Bayesian PID for central (0–5%) Pb–Pb collisions at $\sqrt{s_{\mathrm{NN}}} = 5.52$ TeV, assuming SPTR = 50 ps, a $\pm 2\,\sigma$ SPTR hit-track matching cut, no DCR, an acquisition time gate of 4 ns per sector, and trapezoidal photodetector modules. Rows correspond to cuts on the minimum number of Hough-selected hits to accept a track, namely 3 (top), 7 (middle), and 11 (bottom), with the requirement that the maximum Bayesian probability is at least 50%.

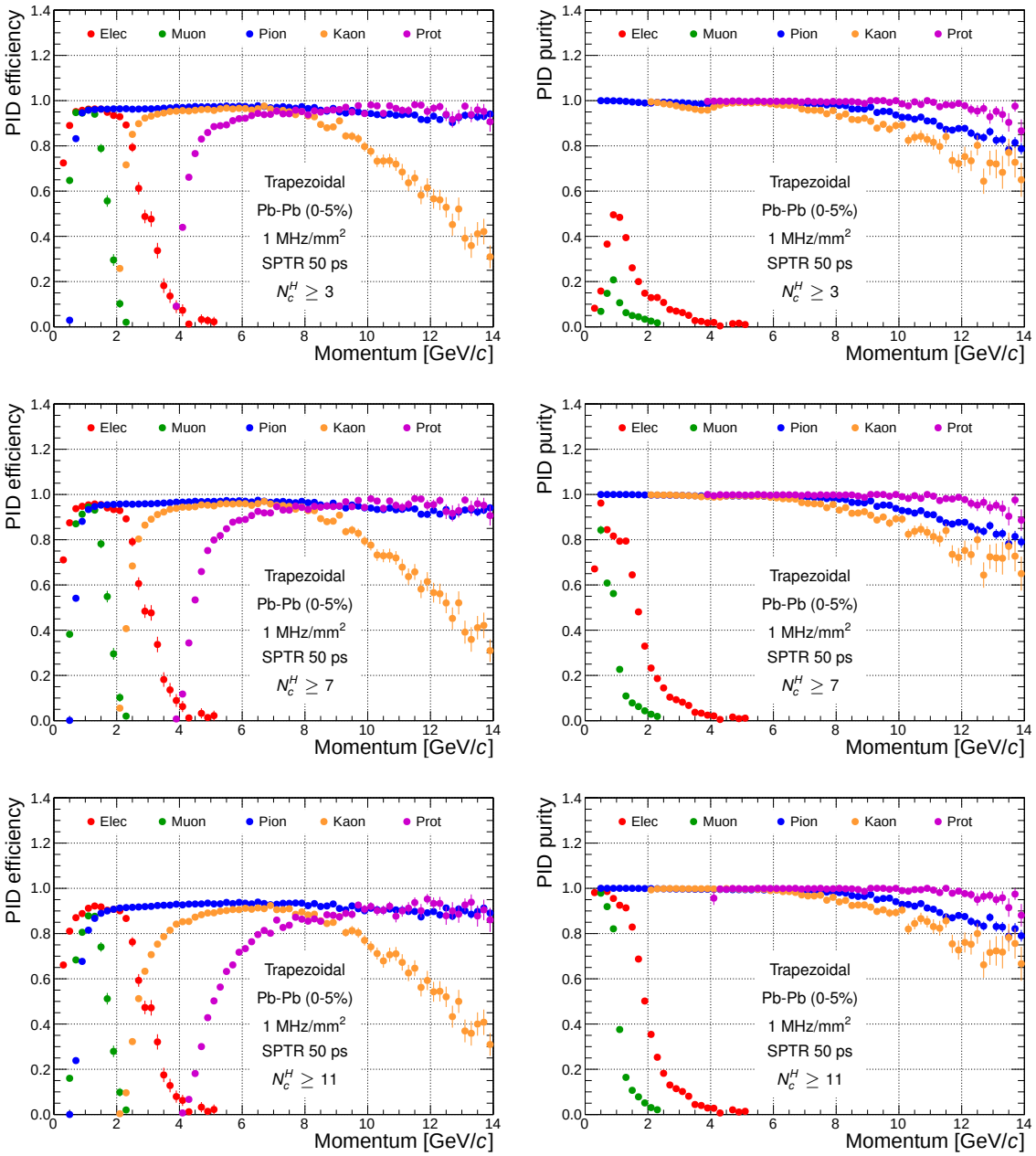


**Figure 4.29:** PID efficiency (left) and purity (right) versus momentum for e, μ, π, K, and p, obtained with the Hough transform and Bayesian PID for central (0–5%) Pb–Pb collisions at $\sqrt{s_{\mathrm{NN}}} = 5.52$ TeV, assuming SPTR = 50 ps, a $\pm 2\,\sigma$ SPTR hit-track matching cut, DCR= 1 MHz/mm$^2$, an acquisition time gate of 4 ns per sector, and trapezoidal photodetector modules. Rows correspond to cuts on the minimum number of Hough-selected hits to accept a track, namely 3 (top), 7 (middle), and 11 (bottom), with the requirement that the maximum Bayesian probability is at least 50%.

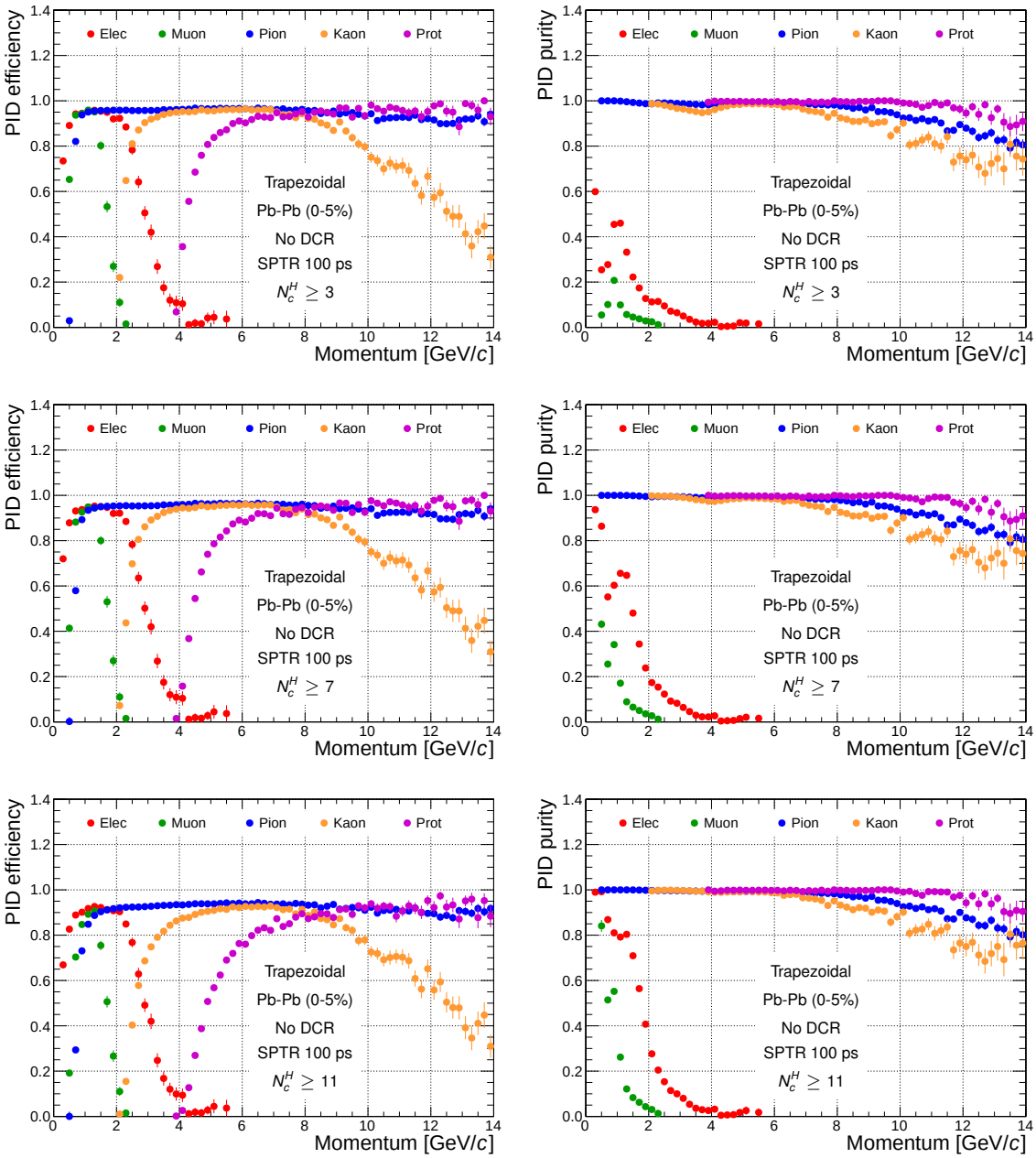


**Figure 4.30:** PID efficiency (left) and purity (right) versus momentum for e, μ, π, K, and p, obtained with the Hough transform and Bayesian PID for central (0–5%) Pb–Pb collisions at $\sqrt{s_{\mathrm{NN}}} = 5.52$ TeV, assuming SPTR = 100 ps, a $\pm 2\,\mathrm{SPTR}$ hit-track matching cut, no DCR, an acquisition time gate of 4 ns per sector, and trapezoidal photodetector modules. Rows correspond to cuts on the minimum number of Hough-selected hits to accept a track, namely 3 (top), 7 (middle), and 11 (bottom), with the requirement that the maximum Bayesian probability is at least 50%.

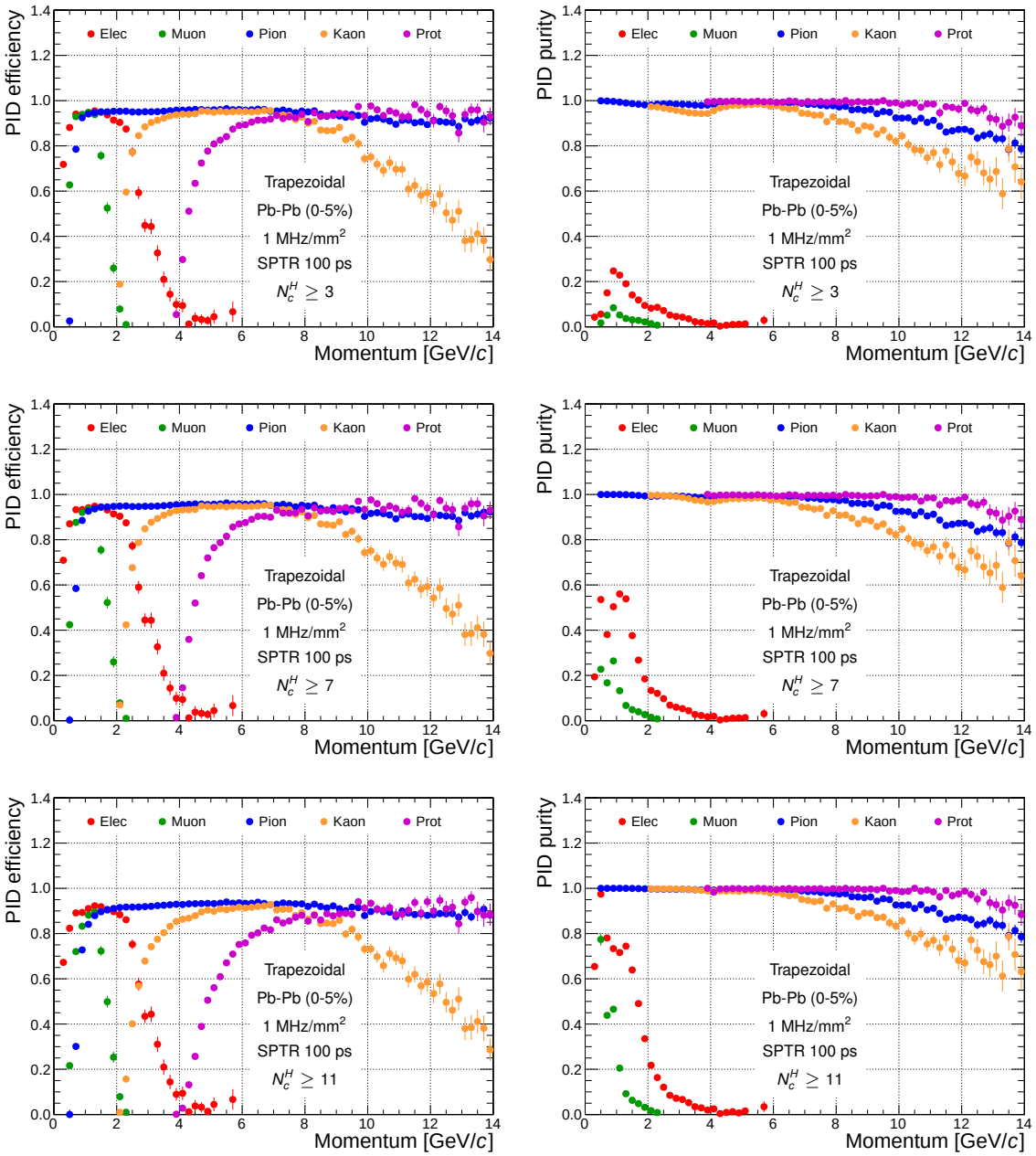


**Figure 4.31:** PID efficiency (left) and purity (right) versus momentum for e, μ, π, K, and p, obtained with the Hough transform and Bayesian PID for central (0–5%) Pb–Pb collisions at $\sqrt{s_{\mathrm{NN}}} = 5.52$ TeV, assuming SPTR = 100 ps, a $\pm 2\,\sigma$ SPTR hit-track matching cut, DCR= 1 MHz/mm$^2$, an acquisition time gate of 4 ns per sector, and trapezoidal photodetector modules. Rows correspond to cuts on the minimum number of Hough-selected hits to accept a track, namely 3 (top), 7 (middle), and 11 (bottom), with the requirement that the maximum Bayesian probability is at least 50%.

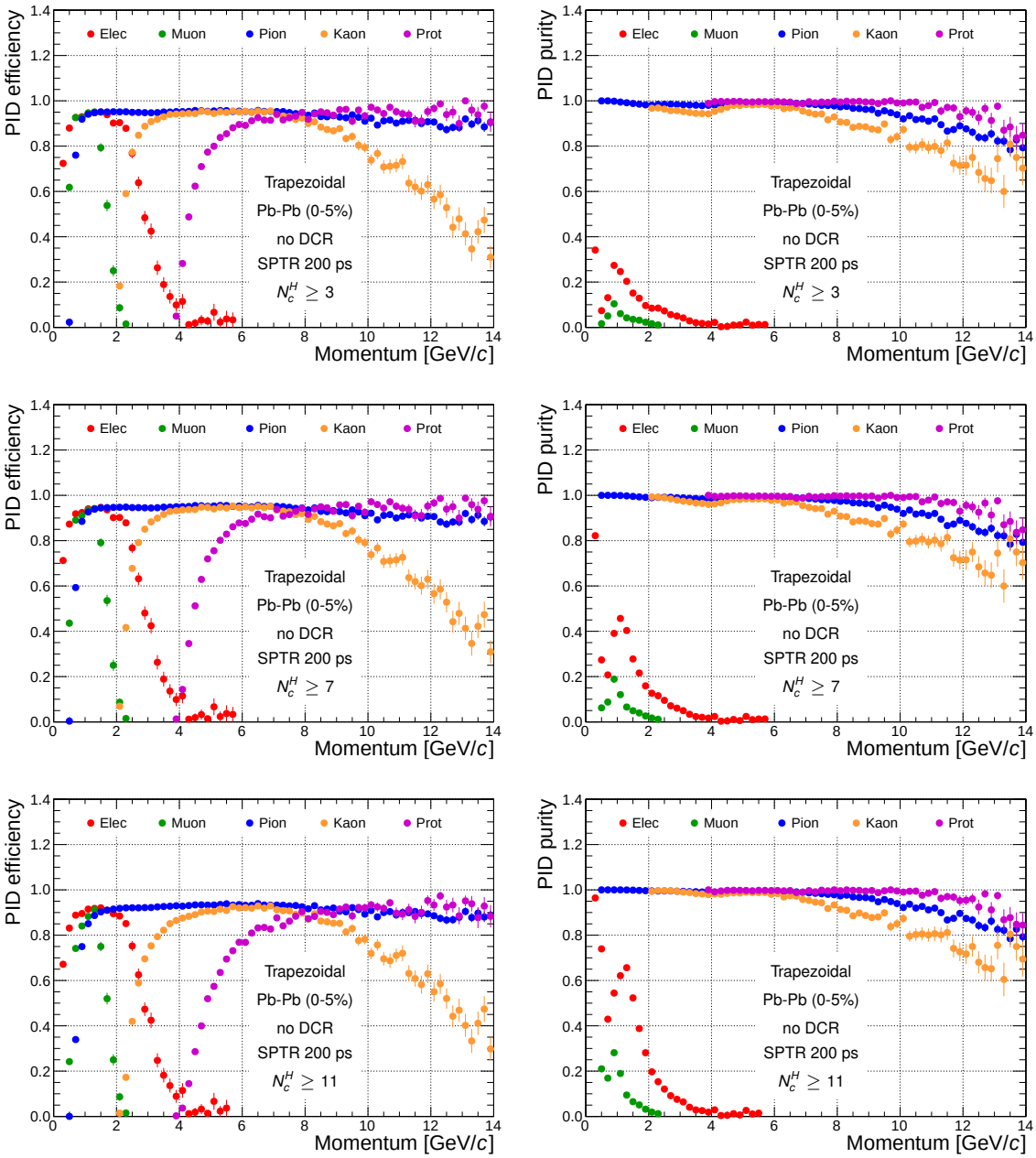


**Figure 4.32:** PID efficiency (left) and purity (right) versus momentum for e, μ, π, K, and p, obtained with the Hough transform and Bayesian PID for central (0–5%) Pb–Pb collisions at $\sqrt{s_{\mathrm{NN}}} = 5.52$ TeV, assuming SPTR = 200 ps, a $\pm 2\,\mathrm{SPTR}$ hit-track matching cut, no DCR, an acquisition time gate of 4 ns per sector, and trapezoidal photodetector modules. Rows correspond to cuts on the minimum number of Hough-selected hits to accept a track, namely 3 (top), 7 (middle), and 11 (bottom), with the requirement that the maximum Bayesian probability is at least 50%.

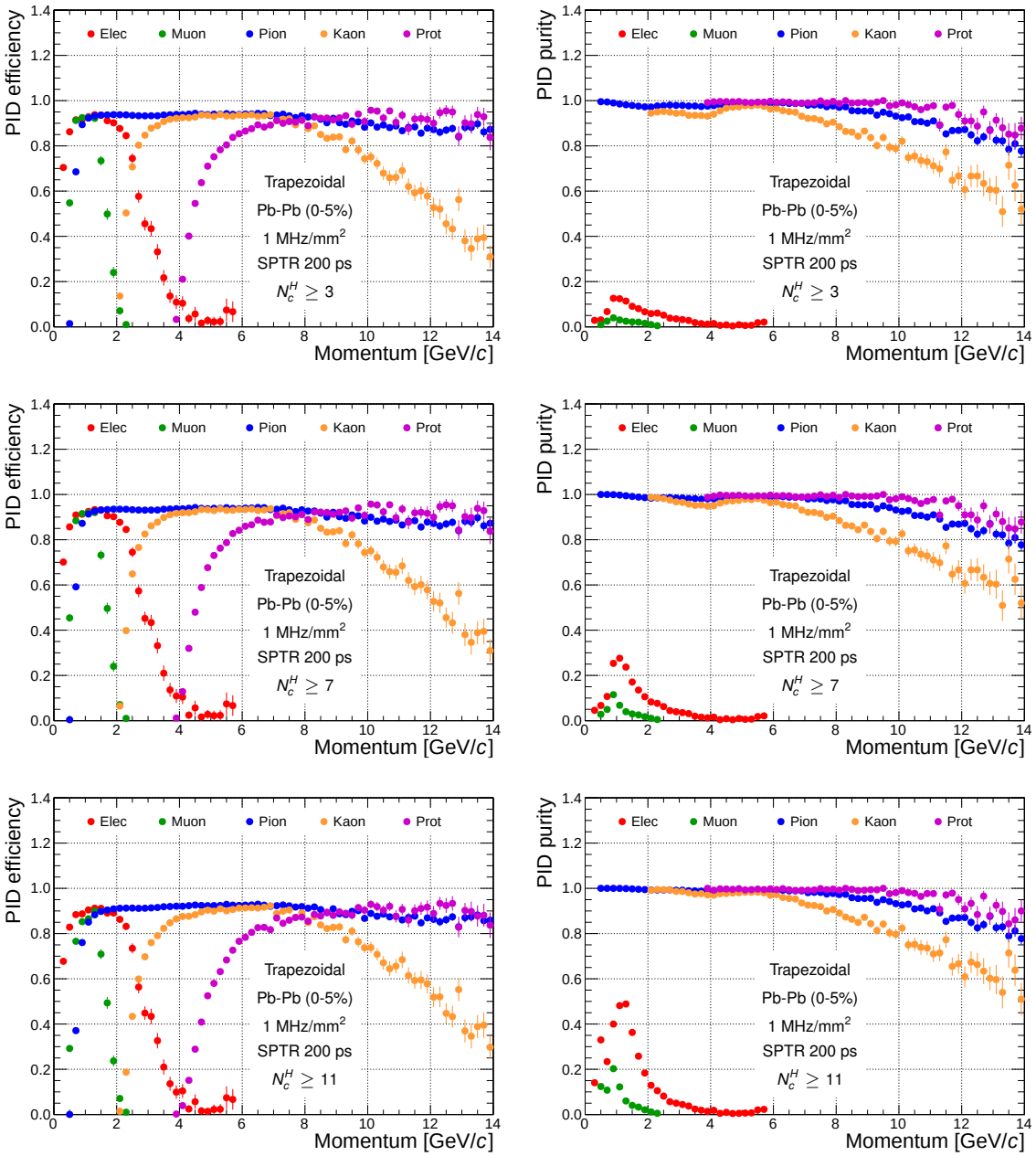


**Figure 4.33:** PID efficiency (left) and purity (right) versus momentum for e, μ, π, K, and p, obtained with the Hough transform and Bayesian PID for central (0–5%) Pb–Pb collisions at $\sqrt{s_{\rm NN}} = 5.52$ TeV, assuming SPTR = 200 ps, a $\pm 2\,\sigma$ SPTR hit-track matching cut, DCR= 1 MHz/mm$^2$, an acquisition time gate of 4 ns per sector, and trapezoidal photodetector modules. Rows correspond to cuts on the minimum number of Hough-selected hits to accept a track, namely 3 (top), 7 (middle), and 11 (bottom), with the requirement that the maximum Bayesian probability is at least 50%.

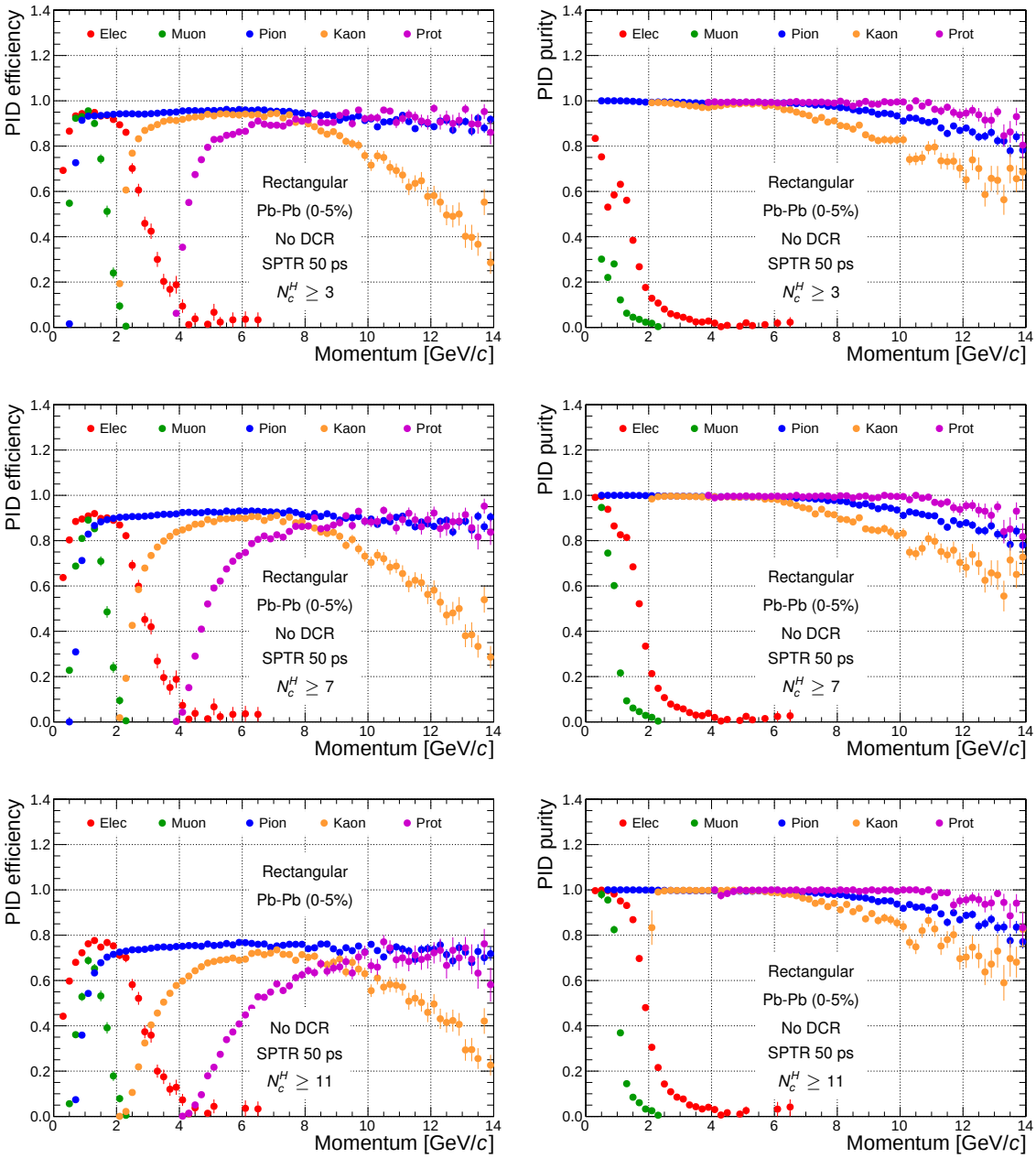


**Figure 4.34:** PID efficiency (left) and purity (right) versus momentum for e, μ, π, K, and p, obtained with the Hough transform and Bayesian PID for central (0–5%) Pb–Pb collisions at $\sqrt{s_{\mathrm{NN}}} = 5.52$ TeV, assuming SPTR = 50 ps, a $\pm 2\,\sigma$ SPTR hit-track matching cut, no DCR, an acquisition time gate of 4 ns per sector, and rectangular $17 \times 18$ cm$^2$ photodetector modules. Rows correspond to cuts on the minimum number of Hough-selected hits to accept a track, namely 3 (top), 7 (middle), and 11 (bottom), with the requirement that the maximum Bayesian probability is at least 50%.

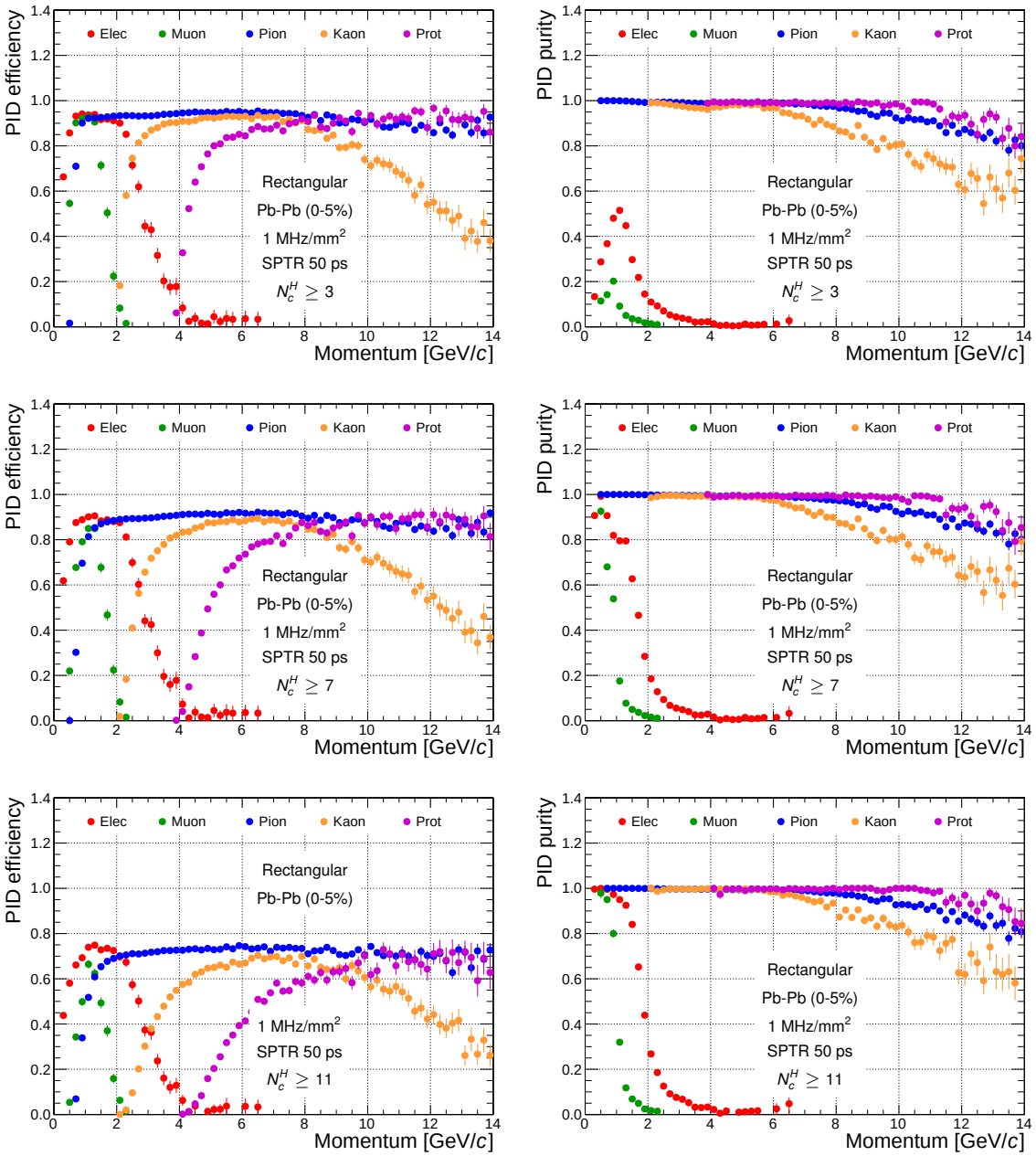


**Figure 4.35:** PID efficiency (left) and purity (right) versus momentum for e, μ, π, K, and p, obtained with the Hough transform and Bayesian PID for central (0–5%) Pb–Pb collisions at $\sqrt{s_{\rm NN}} = 5.52$ TeV, assuming SPTR = 50 ps, a $\pm 2\,\sigma$ SPTR hit-track matching cut, DCR= 1 MHz/mm$^2$, an acquisition time gate of 4 ns per sector, and rectangular $17 \times 18$ cm$^2$ photodetector modules. Rows correspond to cuts on the minimum number of Hough-selected hits to accept a track, namely 3 (top), 7 (middle), and 11 (bottom), with the requirement that the maximum Bayesian probability is at least 50%.

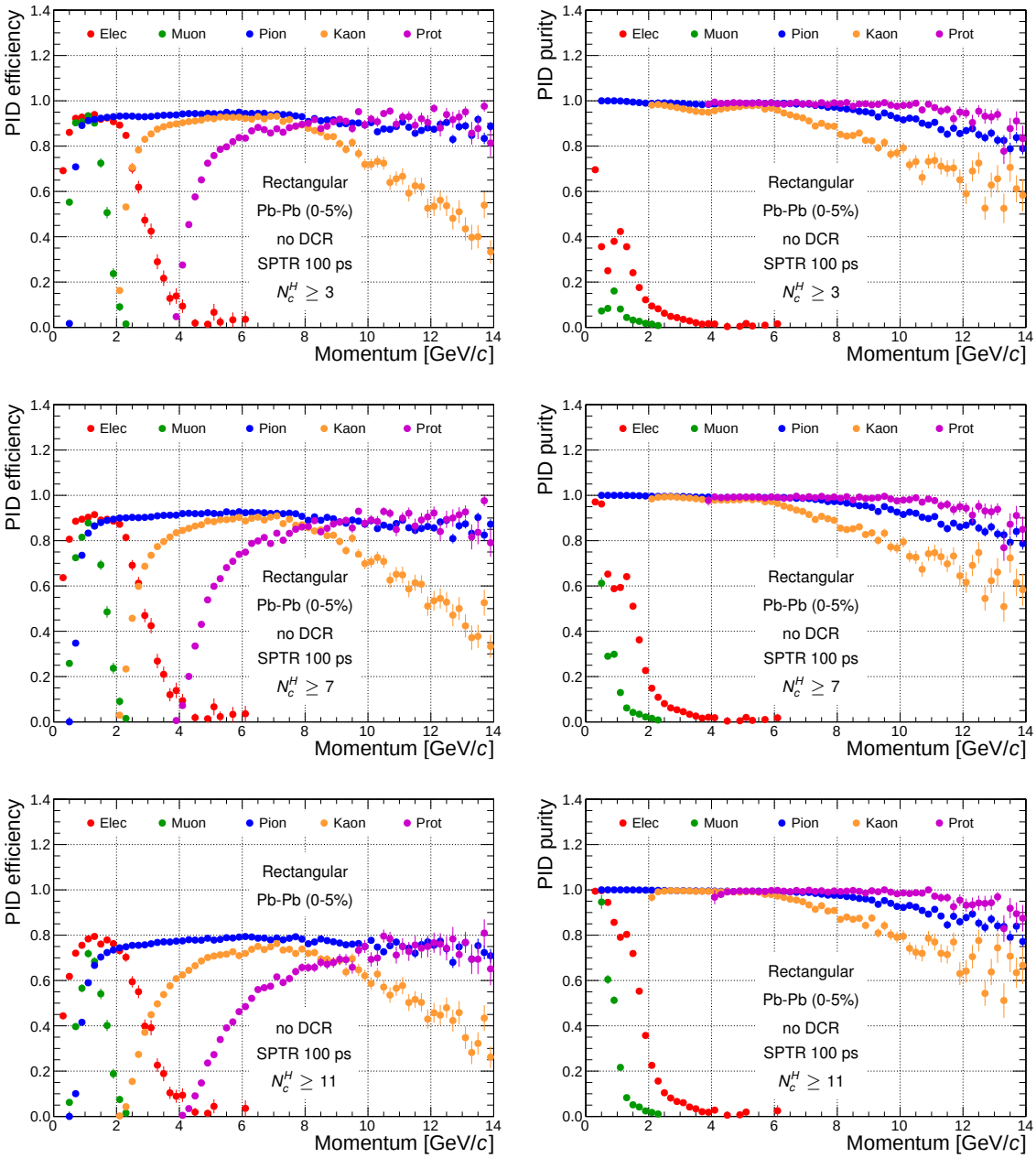


**Figure 4.36:** PID efficiency (left) and purity (right) versus momentum for e, μ, π, K, and p, obtained with the Hough transform and Bayesian PID for central (0–5%) Pb–Pb collisions at $\sqrt{s_{\mathrm{NN}}} = 5.52$ TeV, assuming SPTR = 100 ps, a $\pm 2\,\mathrm{SPTR}$ hit-track matching cut, no DCR, an acquisition time gate of 4 ns per sector, and rectangular $17 \times 18$ cm$^2$ photodetector modules. Rows correspond to cuts on the minimum number of Hough-selected hits to accept a track, namely 3 (top), 7 (middle), and 11 (bottom), with the requirement that the maximum Bayesian probability is at least 50%.

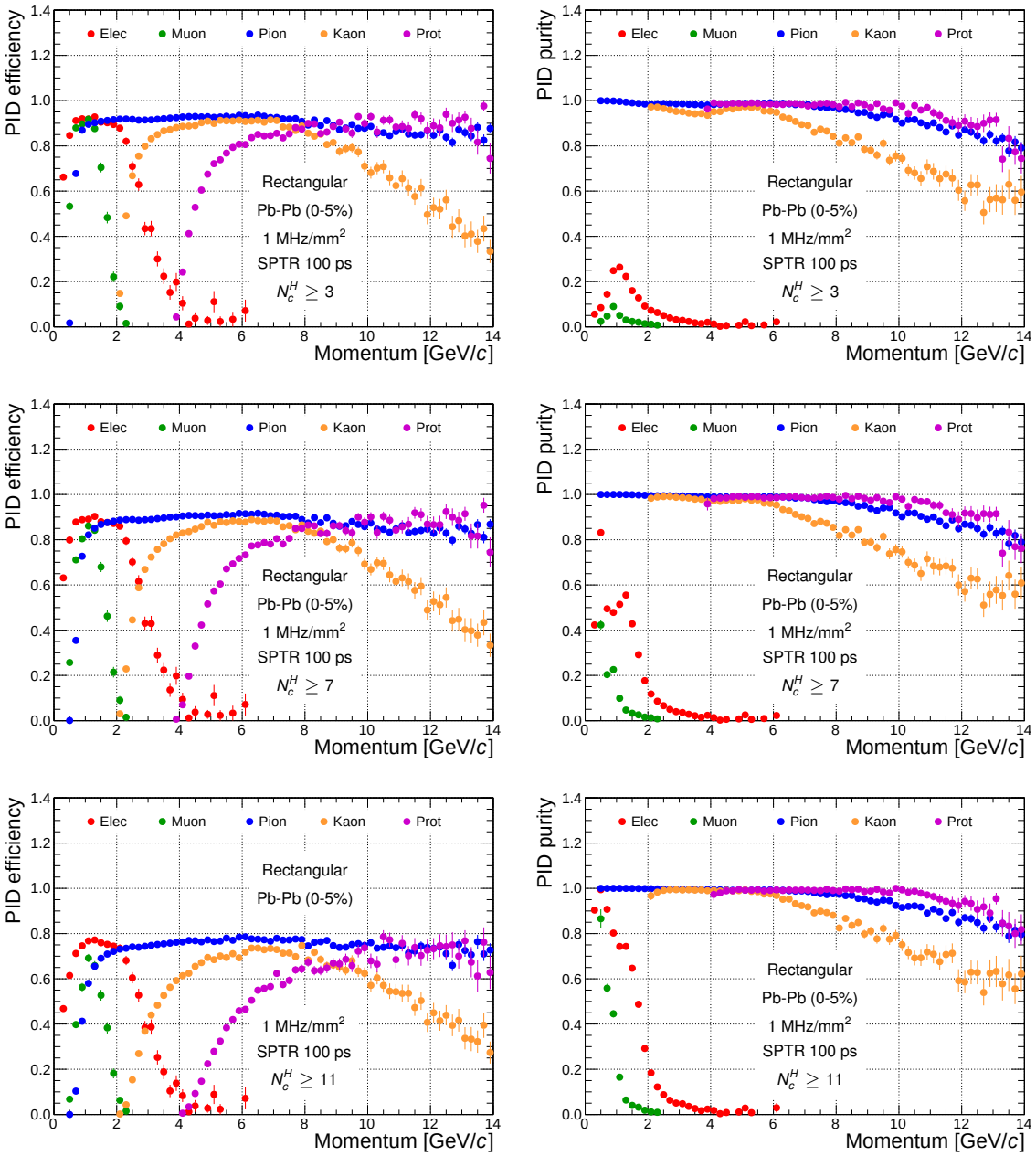


**Figure 4.37:** PID efficiency (left) and purity (right) versus momentum for e, μ, π, K, and p, obtained with the Hough transform and Bayesian PID for central (0–5%) Pb–Pb collisions at $\sqrt{s_{\mathrm{NN}}} = 5.52$ TeV, assuming SPTR = 100 ps, a $\pm 2\,\sigma$ SPTR hit-track matching cut, DCR= 1 MHz/mm$^2$, an acquisition time gate of 4 ns per sector, and rectangular $17 \times 18$ cm$^2$ photodetector modules. Rows correspond to cuts on the minimum number of Hough-selected hits to accept a track, namely 3 (top), 7 (middle), and 11 (bottom), with the requirement that the maximum Bayesian probability is at least 50%.

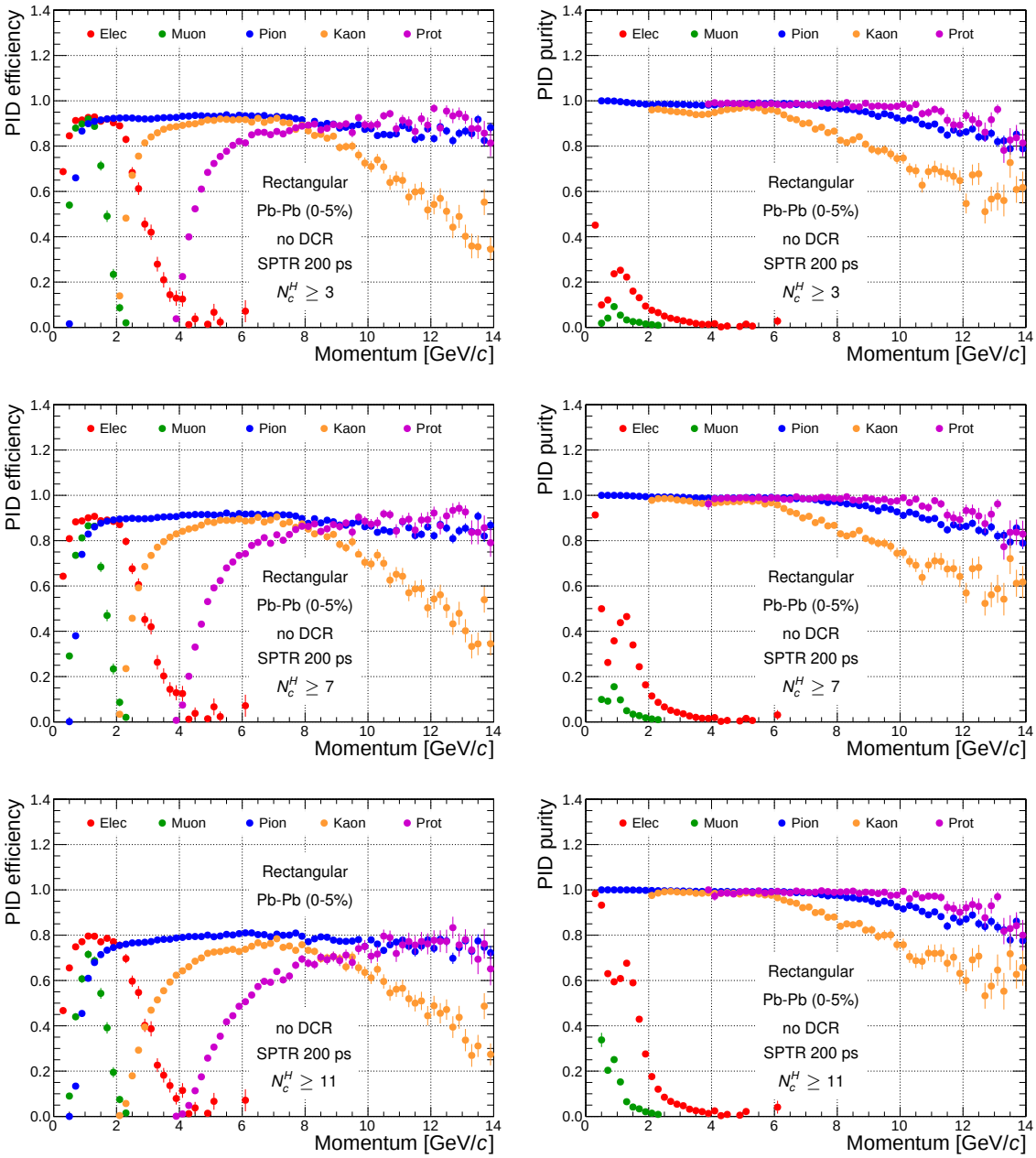


**Figure 4.38:** PID efficiency (left) and purity (right) versus momentum for e, μ, π, K, and p, obtained with the Hough transform and Bayesian PID for central (0–5%) Pb–Pb collisions at $\sqrt{s_{\mathrm{NN}}} = 5.52$ TeV, assuming SPTR = 200 ps, a $\pm 2\,\mathrm{SPTR}$ hit-track matching cut, no DCR, an acquisition time gate of 4 ns per sector, and rectangular $17 \times 18$ cm$^2$ photodetector modules. Rows correspond to cuts on the minimum number of Hough-selected hits to accept a track, namely 3 (top), 7 (middle), and 11 (bottom), with the requirement that the maximum Bayesian probability is at least 50%.

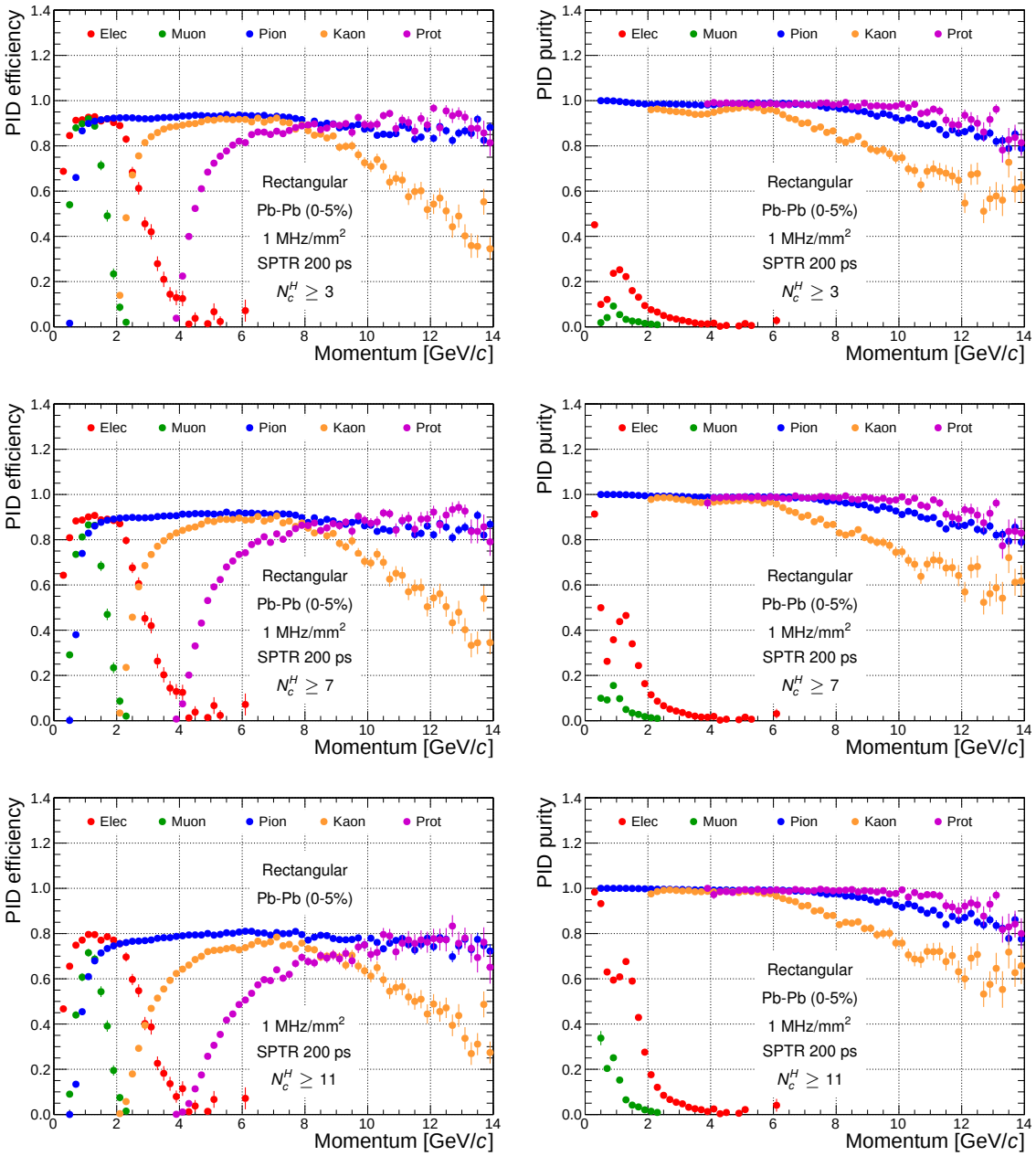


**Figure 4.39:** PID efficiency (left) and purity (right) versus momentum for e, μ, π, K, and p, obtained with the Hough transform and Bayesian PID for central (0–5%) Pb–Pb collisions at $\sqrt{s_{\mathrm{NN}}} = 5.52$ TeV, assuming SPTR = 200 ps, a $\pm 2\,\sigma$ SPTR hit-track matching cut, DCR= 1 MHz/mm$^2$, an acquisition time gate of 4 ns per sector, and rectangular $17 \times 18$ cm$^2$ photodetector modules. Rows correspond to cuts on the minimum number of Hough-selected hits to accept a track, namely 3 (top), 7 (middle), and 11 (bottom), with the requirement that the maximum Bayesian probability is at least 50%.

## 4.7 Machine learning techniques for bRICH PID

A part of my research project was focused on the development of fast and efficient machine-learning-based pattern recognition algorithms for PID in central Pb-Pb. Although the classical Hough-transform based pattern recognition algorithm and the Bayesian PID approach perform well in low-multiplicity environments, limitations arise in high-multiplicity events and in high DCR conditions. A key difficulty is taking into account the complex ring topology in the projective bRICH geometry, e.g. open rings for tracks entering aerogel near sector boundaries, when defining a cut on the minimum number of clustered hits optimal for all $\eta$, $p$ and mass hypotheses.

To address this, I explored various machine-learning classifiers trained to learn the space–time signature of aerogel rings, thereby potentially improving PID performance relative to classical analyses. In particular, I implemented and tested various algorithms based on Artificial Neural Networks [116], Random Forests [117], and Boosted Decision Trees [118] developed in Python using the `tensorflow`, `sklearn` and `xgboost` libraries, respectively. I found that a well-trained Boosted Decision Tree based on Extreme Gradient Boosting (XGBoost) demonstrated the highest performance. The details on the configuration, training and results are presented in the following.

### 4.7.1 Boosted Decision Tree

The Boosted Decision Tree (BDT) concept is based on the binary decision tree. A binary decision tree is a supervised machine-learning model that recursively partitions an input space with threshold splits on the input variables until a stopping condition is met (e.g., maximum depth). Each split defines a decision rule, and each leaf outputs a prediction, such as class scores or probabilities. As a supervised model, a decision tree is trained on labelled data by optimizing an appropriate loss function and tuning the split variables, thresholds, and number of partitions. In the training phase, the model "learns" how to classify events through the patterns shown in their input variables.

The performance of a single decision tree can be improved through ensemble boosting. A boosted decision tree builds an additive model of many shallow trees, each a weak learner, added in sequence so that each new tree reduces the residual errors of the current ensemble. The procedure optimizes a regularized loss with gradient-based updates, which reduces prediction error while controlling model complexity. The resulting ensemble acts as a strong learner that combines the predictive power of its constituents, thus outperforming any individual tree. For the studies reported in the following, I used Extreme Gradient Boosting (XGBoost [119]) as the boosting engine.

## Datasets

In order to directly compare the performance achieved with the classical approach based on the Hough transform and the Bayesian approach, I used the same full raw datasets employed for the classical analysis, 18M pp collisions at $\sqrt{s} = 14$ TeV and 5k central (0–5%) Pb-Pb collisions at $\sqrt{s_{\mathrm{NN}}} = 5.52$ TeV, corresponding to about $25 \times 10^6$ charged particles reaching the bRICH in the 2 T magnetic field, as the test datasets.

For the training and validation of the algorithms, I generated new raw datasets using the same procedure followed for the main pp and central Pb-Pb datasets, but with a different random seed. In the following, I report the results relative to SPTR values of 50 ps, 100 ps and 200 ps and limiting DCR values of 0 and 1 MHz/mm$^2$.

For all considered cases, in the training phase I used a stratified 5% of the events as a validation set to monitor the validation metric at each boosting step. Stratification is important for e and μ, due to the lower than 0.35% relative abundance in the sample.

## Features

The features I selected for both pattern recognition and tagging studies with the bRICH include both track parameters and high-level space–time clustering observables computed for each of the five considered mass hypotheses, namely e, μ, π, K and p.

- **Track parameters**:
  - $p$: Momentum at the most probable emission point in aerogel.
  - $\eta$: Pseudorapidity at the most probable photon emission point in aerogel.
  - $\theta_{\mathrm{rad}}$: Polar angle of the most probable emission point in aerogel.
  - $\phi_{\mathrm{rad}}$: Azimuthal angle of the most probable emission point in aerogel.
- **Per–hypothesis space–time clustering counts:**

  For each accepted charged track, with the corresponding set of candidate Cherenkov photon hits on the photodetector, the following observables are first computed:
  - The single–hit Cherenkov angle $\theta_{\mathrm{rec}}$, using the procedure in Section 4.3.1.
  - The single-hit Cherenkov azimuthal angle $\phi_{\mathrm{rec}}$, defined as the projection of the candidate photon direction in the plane perpendicular to the track and calculated with respect to the positive Z direction.
  - The relative hit–track time $\Delta T$ at the most probable emission point in the traversed aerogel tile, calculated as discussed in Section 4.3.3.

Then, for each mass hypothesis $i = \mathrm{e}, \mu, \pi, \mathrm{K}$ and p, given the expected angle $\theta_{\mathrm{th},i}$, the single photon angular resolution $\sigma_{\mathrm{c}}^{\gamma}(i)$, and the single photon time resolution SPTR, counts are formed in angular windows $n \in \{1,2,3\}$, time windows $m \in \{1,2\}$, and azimuthal intervals $k \in \{0,1,2,3\}$ with $\phi_{\mathrm{rec}} \in [\,k\pi/2, (k{+}1)\pi/2\,]$. The corresponding features are:

$$N_{\mathrm{hits}}(i;n,m,k) = N_{\mathrm{hits}} \left\{ \begin{array}{c} \left|\theta_{\mathrm{rec}} - \theta_{\mathrm{th},i}\right| < n\,\sigma_{\mathrm{c}}^{\gamma}(i) \\ |\Delta T| < m\,\mathrm{SPTR} \\ \phi_{\mathrm{rec}} \in \left[\,k\pi/2, (k{+}1)\pi/2\,\right] \end{array} \right\}.$$

The track parameters correspond to 4 features. The space–time counts correspond to $5 \times 3 \times 2 \times 4 = 120$ additional features. The total feature count is 124.

## Particle identification labels

For the classification task, the label associated to each track is the categorical mass hypothesis $i = \mathrm{e}, \mu, \pi, \mathrm{K}$ and p. For tracks with momentum below the aerogel threshold for Cherenkov emission, I introduced a sixth label to tag them as below threshold.

## Particle identification: One-vs-rest strategy

Tagging the five particle species in the considered dataset constitutes a multi-class classification problem. I addressed it with a one-vs-rest scheme, training five independent binary XGB classifiers (e vs. all, $\mu$ vs. all, $\pi$ vs. all, K vs. all, p vs. all). For each classifier, tracks of the target species with momentum above its aerogel Cherenkov threshold are assigned label 1 (positive class), while all other tracks, including those below threshold, are assigned label 0 (negative class).

Each of these models outputs a score interpreted as the probability $p\,(i \mid \boldsymbol{x})$ that the corresponding feature vector $\boldsymbol{x}$ results from a particle of species $i$. Finally, I assigned the final track identity according to the maximum score among all mass hypotheses.

As in the case of the Bayesian PID approach discussed in Section 4.6, a minimum-confidence threshold $P_{\mathrm{min}}^{\mathrm{max}}$ can be applied to leave low-confidence tracks untagged, thereby increasing PID purity at the cost of reduced efficiency. The selection and the impact of this threshold for PID in central (0-5%) Pb-Pb is discussed in Section 4.7.3.

## Classifier configuration

For each of the five XGB classifiers in the one-vs-rest scheme, I optimized the hyperparameters through a grid search. Table 4.4 reports the optimal configuration used for training and inference with `XGBClassifier` in the aerogel–based PID with the bRICH.

| Hyperparameter | Value |
|---|---|
| `objective` | `binary:logistic` |
| `reg_alpha` | 0.10 |
| `reg_lambda` | 0.03 |
| `n_estimators` | 250 |
| `learning_rate` | 0.10 |
| `max_depth` | 10 |
| `min_child_weight` | 3 |
| `subsample` | 0.30 |
| `colsample_bytree` | 0.90 |

**Table 4.4:** Configuration of `XGBClassifier` aerogel-based PID with the bRICH.

Let the training set be $\mathcal{D} = \{(\boldsymbol{x}_k, i_k)\}_{k=1}^{N}$ for $N$ events with features $\boldsymbol{x}_k$ and labels $i \in \{0, 1\}$. The ensemble outputs a class probability $p_k \equiv p(\, i_k{=}1 \mid \boldsymbol{x}_k)$. The training objective, or loss function, $\mathcal{L}$ minimized by the classifier during the training procedure consists of a data term $\mathcal{L}_{\text{data}}$ and a tree-level regularization term $\Omega$,

$$\mathcal{L} \;=\; \mathcal{L}_{\text{data}} \;+\; \Omega. \tag{4.18}$$

With `objective=binary:logistic`, the data term is set to the binary cross-entropy:

$$\mathcal{L}_{\text{data}} \;=\; \sum_{k=1}^{N} \Big[ -\, i_k \,\log p_k \;-\; (1 - i_k) \log(1 - p_k) \Big]. \tag{4.19}$$

The tree-level regularization term considered for this study is given by:

$$\Omega \;=\; \sum_{m=1}^{M} \left[ \alpha \sum_{j=1}^{T_m} |w_{mj}| \;+\; \frac{\lambda}{2} \sum_{j=1}^{T_m} w_{mj}^2 \right], \tag{4.20}$$

where $M$ is the number of trees, $T_m$ the number of leaves in tree $m$, and $w_{mj}$ the leaf weight. The coefficients $\alpha$ and $\lambda$ are controlled by `reg_alpha` and `reg_lambda` in Table 4.4. The $\alpha$ term ($L_1$ regularization) promotes sparsity in leaf weights, while the $\lambda$ term ($L_2$ regularization) shrinks large weights, improving generalization.

The other hyperparameters control model complexity, learning rate, and sampling.

- The parameter `n_estimators`=250 sets the number of boosting rounds.
- The parameter `learning_rate`=0.10 applies step-size shrinkage to the feature weights, so that after each boosting step, the new tree's feature weights are scaled by the learning rate, making updates more conservative to prevent overfitting.
- The parameter `max_depth`=10 limits the tree complexity by constraining the number of splits along any path of each tree.
- The parameter `min_child_weight`=3 enforces a minimum effective sample number of entries in every leaf, preventing overly fine splits.
- The parameter `subsample`=0.30 applies random row subsampling, drawing 30% of the training instances once per boosting iteration to reduce variance, improve generalization, and mitigate overfitting.
- The parameter `colsample_bytree`=0.90 defines the subset of features, which are randomly sampled, used for split finding when constructing each tree.

All remaining hyperparameters not reported in Table 4.4 and not explored in the grid search were kept at the corresponding `XGBClassifier` default values (version 1.7.5).

### 4.7.2 Results in pp collisions

As in the case of Bayesian PID, to benchmark the limiting PID performance achievable with my XGBoost-based PID algorithm, here I report the PID results in pp collisions under the ideal reference conditions of SPTR = 50 ps and no DCR.

Figs. 4.40 and 4.41 show PID efficiency and purity versus momentum for e, μ, π, K, and p, obtained with my XGBoost-based algorithm for the test dataset of simulated $c\bar{c}$-biased pp collisions at $\sqrt{s} = 14$ TeV. Fig. 4.40 refers to the trapezoidal module layout, while Fig. 4.41 refers to the rectangular $17 \times 18$ cm$^2$ layout. The rows correspond to minimum XGBoost score thresholds of 20%, 50%, and 80%.

As expected, for low-multiplicity events my XGBoost-based PID yields efficiencies and purities comparable to those obtained with the Bayesian approach, shown in Fig. 4.25, by properly matching the XGBoost score threshold and the maximum Bayesian probability threshold. A slight purity gain can actually be observed at fixed efficiency, especially for e and μ, for the XGBoost analysis, due to the better performance dealing with open rings close to the sector boundaries. Overall, electrons are separated from pions up to 2–2.5 GeV/$c$, kaons from pions up to 8–10 GeV/$c$, and protons from pions and kaons beyond 14 GeV/$c$. This validates the reliability of the algorithm.

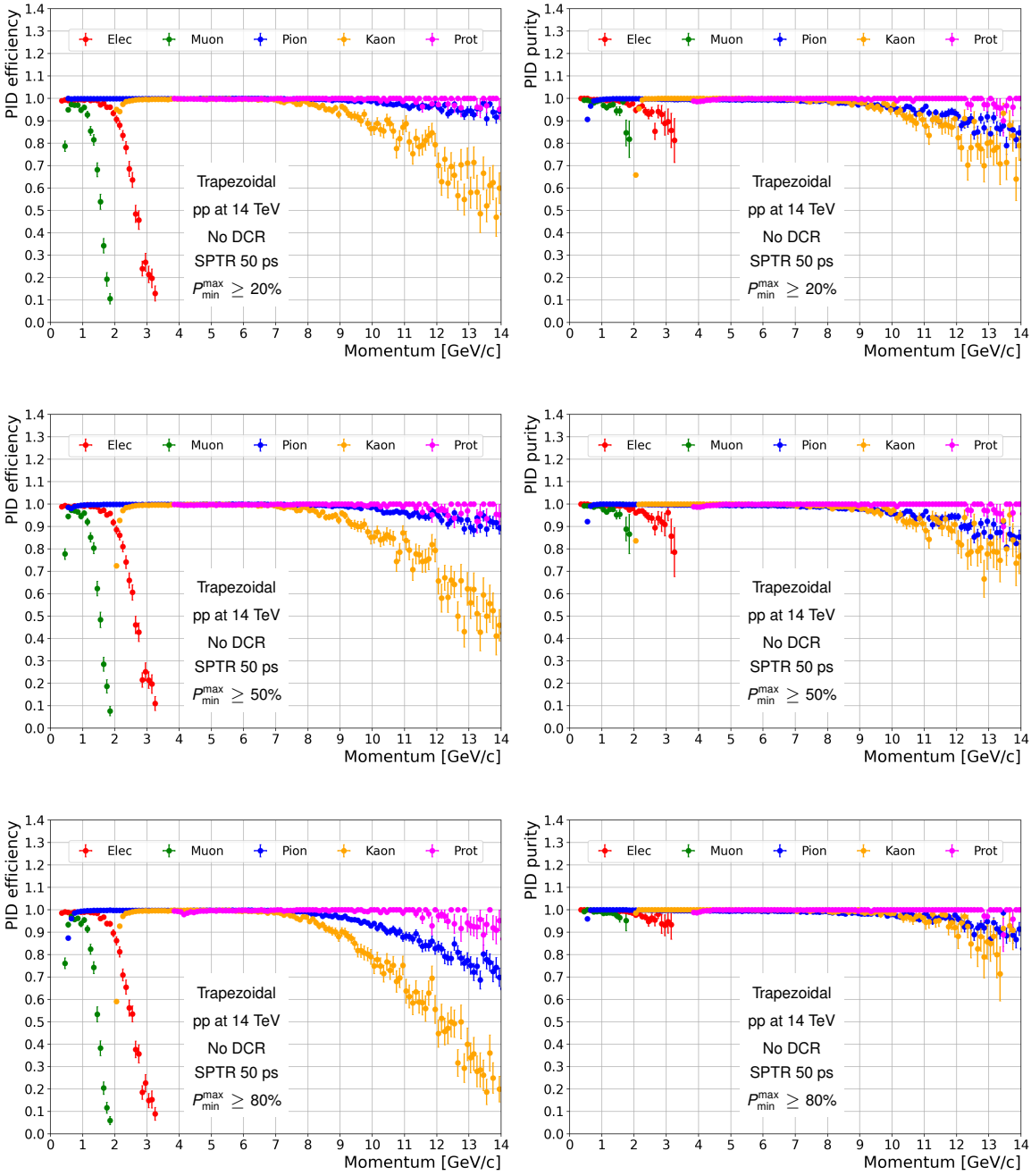


**Figure 4.40:** PID efficiency (left) and purity (right) versus momentum for e, μ, π, K, and p, obtained with my XGBoost-based PID algorithm for the test dataset of simulated pp collisions at $\sqrt{s} = 14$ TeV, assuming SPTR = 50 ps, no DCR, an acquisition time gate of 4 ns per sector, and trapezoidal photodetector modules. Rows correspond to minimum score thresholds of 20% (top), 50% (middle), and 80% (bottom) applied to the highest-scoring mass hypothesis.

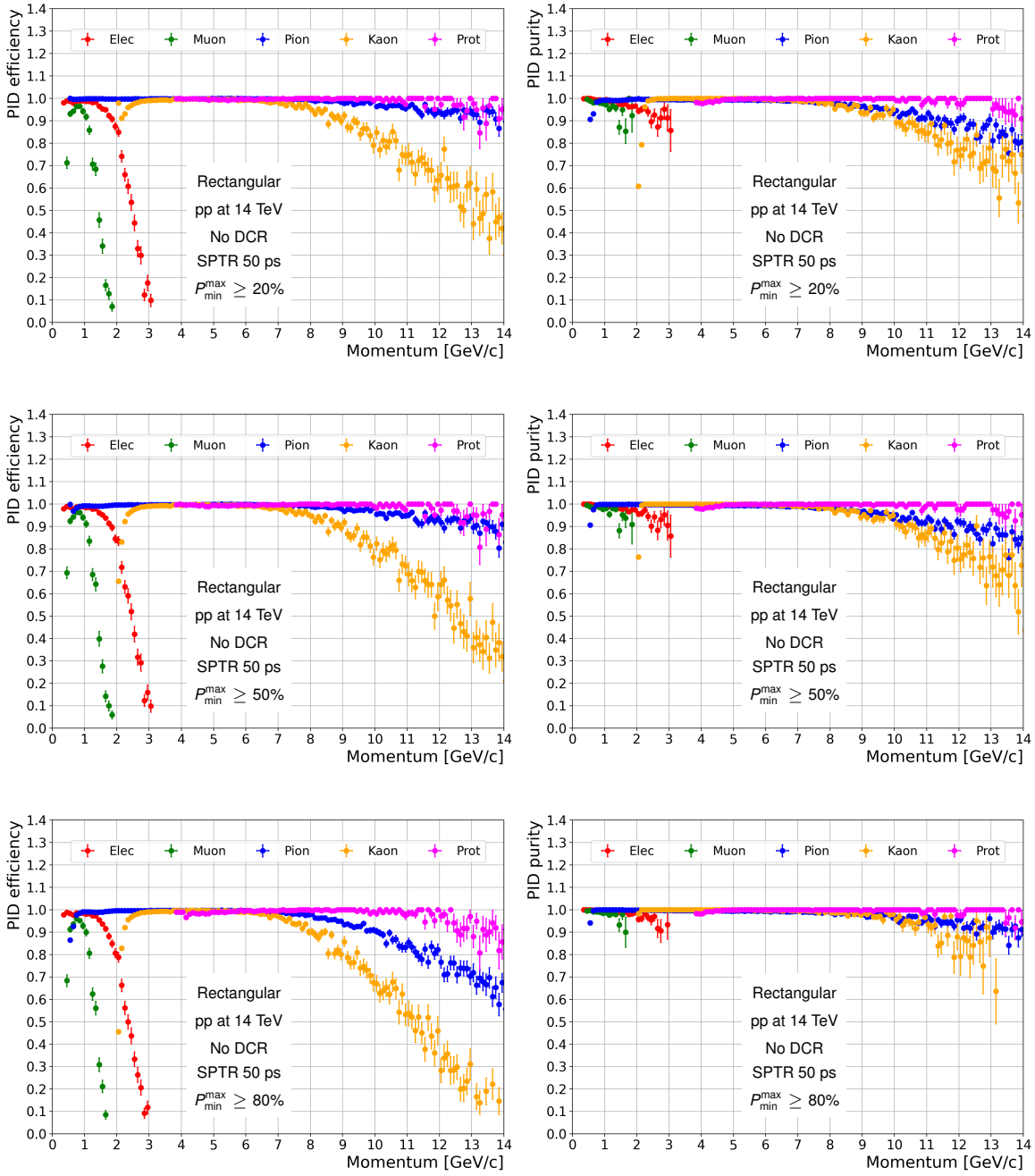


**Figure 4.41:** PID efficiency (left) and purity (right) versus momentum for e, μ, π, K, and p, obtained with my XGBoost-based PID algorithm for the test dataset of simulated pp collisions at $\sqrt{s} = 14$ TeV, assuming SPTR = 50 ps, no DCR, an acquisition time gate of 4 ns per sector, and rectangular $17 \times 18$ cm$^2$ photodetector modules. Rows correspond to minimum score thresholds of 20% (top), 50% (middle), and 80% (bottom) applied to the highest-scoring mass hypothesis.

### 4.7.3 Results in Pb-Pb collisions

Figs. 4.42–4.47 show the PID efficiency and purity versus momentum for e, μ, π, K and p obtained with my XGBoost-based PID algorithm for the full test dataset of central (0-5%) Pb–Pb collisions at $\sqrt{s_{\mathrm{NN}}} = 5.52$ TeV for the trapezoidal photodetector module layout. The figures refer to cases with SPTR = 50, 100, and 200 ps, both without DCR and with a DCR of 1 MHz/mm$^2$. In all cases, a 4 ns acquisition window per sector is used. The rows correspond to minimum XGBoost score thresholds of 20%, 50%, and 80%. The results for rectangular 17 × 18 cm$^2$ modules are shown in Figs. 4.48–4.53. The results in the case of no DCR show the intrinsic performance, limited only by correlated mutual track background due to the high-multiplicity of the collision, while those with a DCR of 1 MHz/mm$^2$ represent the worst-case operating scenario.

Similar considerations to those discussed in Section 4.6.4 still apply to these results. However, the efficiencies and purities are systematically higher than those obtained with the classical Hough-transform plus Bayesian PID analysis. In particular, comparable purities are achieved at significantly larger efficiencies, reaching values close to 100% in the momentum range between the Cherenkov threshold and saturation for hadrons with PID limits up to or beyond 10 GeV/$c$ depending on the particle species. The electron identification performance is notably improved across all tested configurations, with combined efficiency and purity exceeding 90–95% for SPTR = 50 and 100 ps, and remaining above 80–85% for 200 ps, up to 1.5–2 GeV/$c$, for both the trapezoidal and rectangular 17 × 18 cm$^2$ module layouts.

Comparing the panels for different score thresholds, one can observe that the efficiency–purity trade-off can be optimized by tuning the minimum XGBoost score threshold to the requirements of the specific physics analysis and particle species.

The only region where a slight degradation is observed corresponds to kaons above 8 GeV/$c$, where the kaon and pion mass hypotheses become compatible. This effect is mainly due to limited statistics in the training sample at high momentum, causing the algorithm to preferentially assign the pion hypothesis. Further improvement is therefore expected with larger training datasets. Nevertheless, these results highlight the capability of proposed algorithm trained on aerogel-ring patterns to effectively learn and exploit the ring topology in the considered projective bRICH geometry, clearly outperforming the classical Hough-transform plus Bayesian PID approach.

The main conclusion of this analysis is that, despite the reduced active area and photon acceptance of the rectangular 17 × 18 cm$^2$ module layout, acceptable performance is achieved even in the worst-case scenario of central (0–5%) Pb–Pb events with a DCR of 1 MHz/mm$^2$ and a SPTR of 200 ps, validating it as a viable bRICH design option.

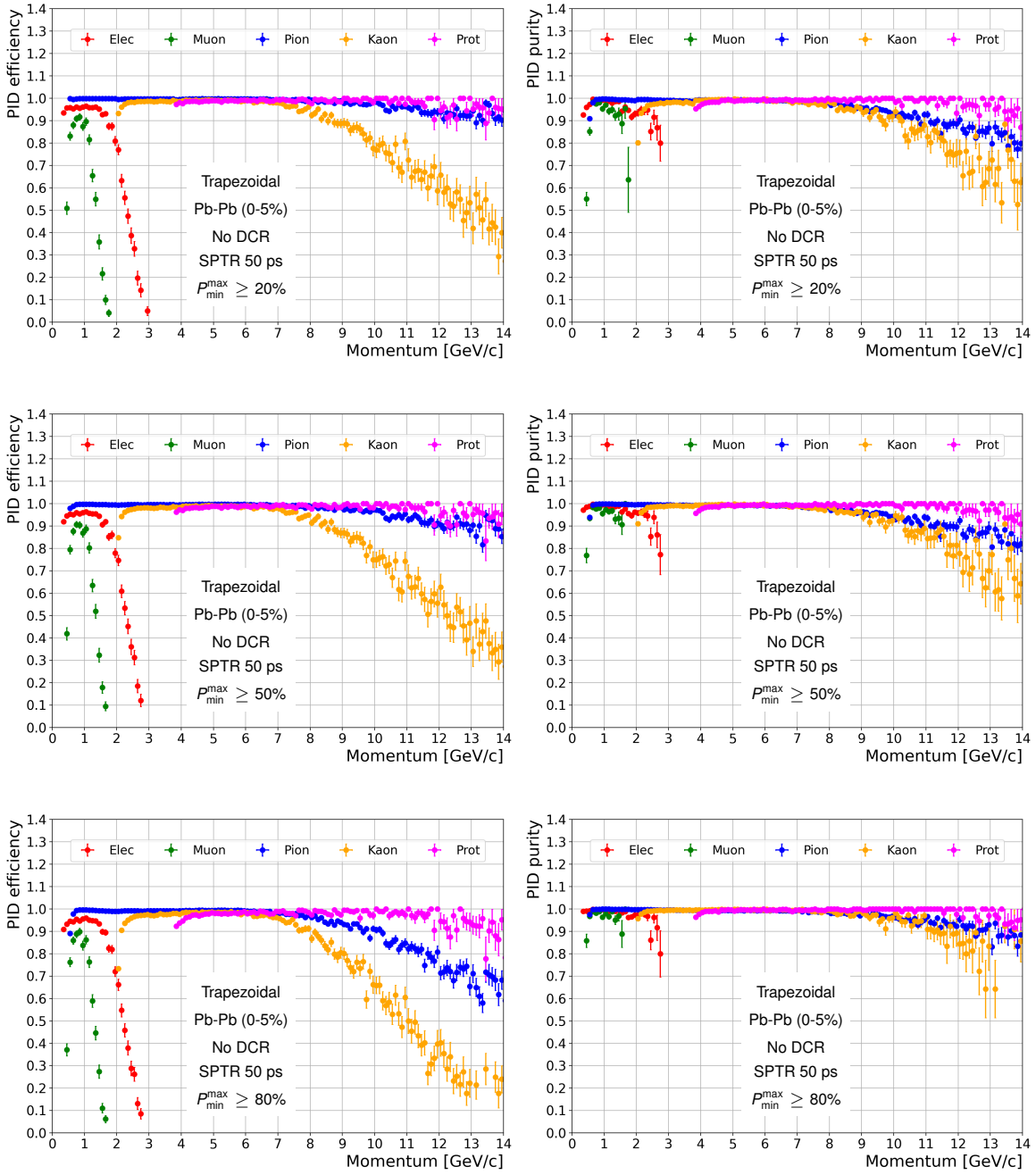


**Figure 4.42:** PID efficiency (left) and purity (right) versus momentum for e, μ, π, K, and p, obtained with my XGBoost-based PID algorithm for the test dataset of central (0–5%) Pb–Pb collisions at $\sqrt{s_{\mathrm{NN}}} = 5.52$ TeV, assuming SPTR = 50 ps, no DCR, an acquisition time gate of 4 ns per sector, and trapezoidal photodetector modules. Rows correspond to minimum score thresholds of 20% (top), 50% (middle), and 80% (bottom) applied to the highest-scoring mass hypothesis.

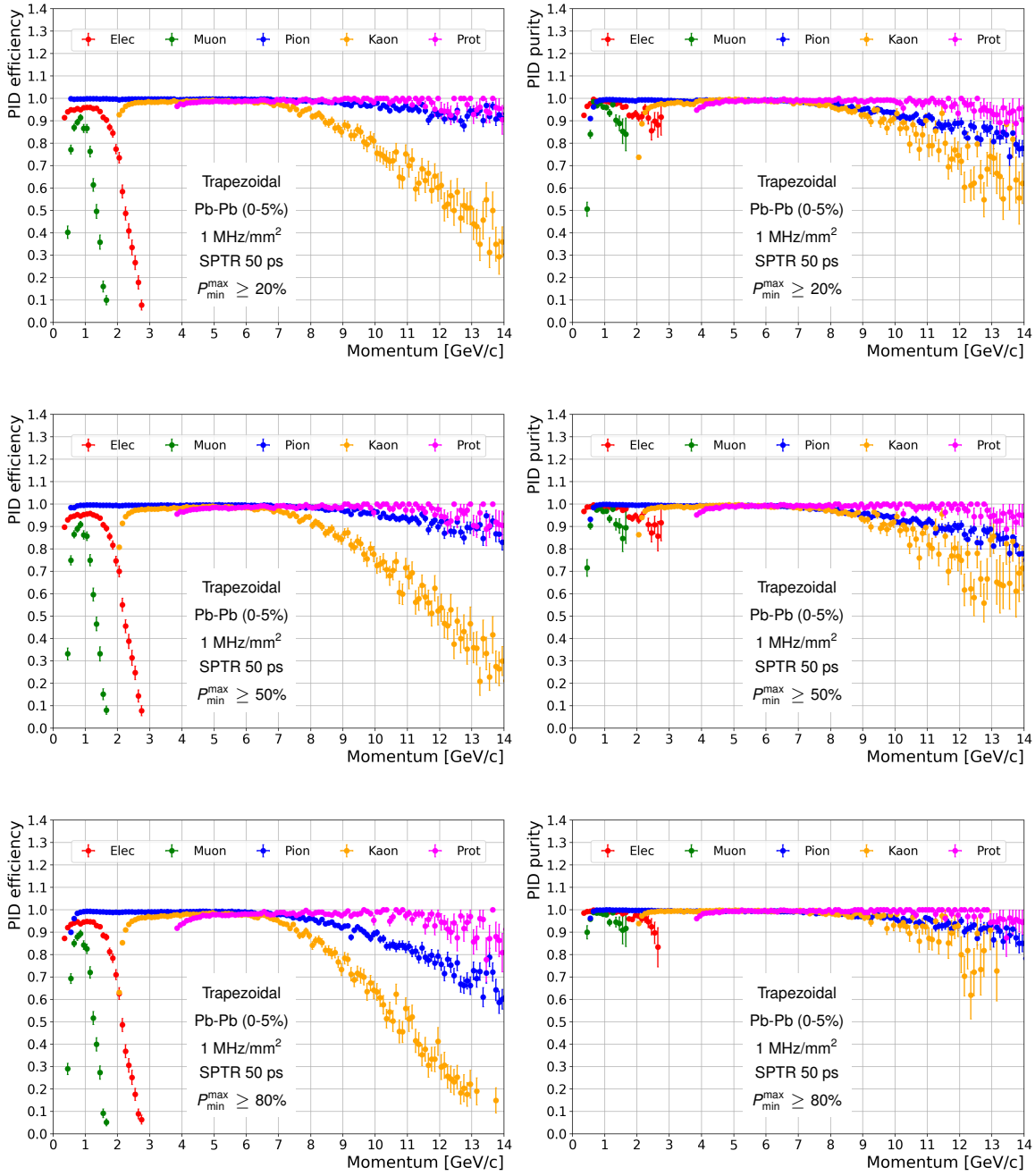


**Figure 4.43:** PID efficiency (left) and purity (right) versus momentum for e, μ, π, K, and p, obtained with my XGBoost-based PID algorithm for the test dataset of central (0–5%) Pb–Pb collisions at $\sqrt{s_{\mathrm{NN}}} = 5.52$ TeV, assuming SPTR = 50 ps, DCR= 1 MHz/mm$^2$, an acquisition time gate of 4 ns per sector, and trapezoidal photodetector modules. Rows correspond to minimum score thresholds of 20% (top), 50% (middle), and 80% (bottom) applied to the highest-scoring mass hypothesis.

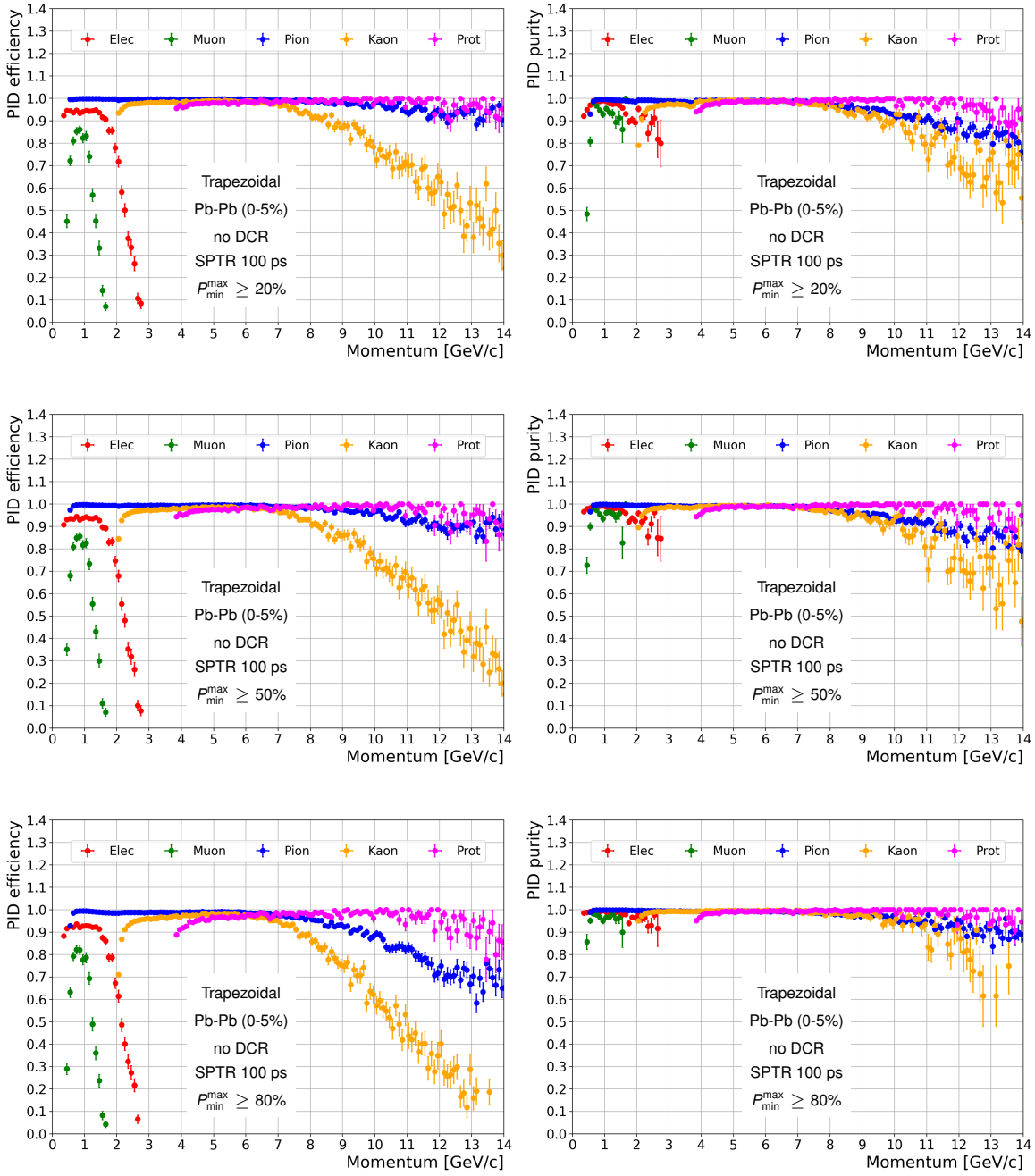


**Figure 4.44:** PID efficiency (left) and purity (right) versus momentum for e, μ, π, K, and p, obtained with my XGBoost-based PID algorithm for the test dataset of central (0–5%) Pb–Pb collisions at $\sqrt{s_{\mathrm{NN}}} = 5.52$ TeV, assuming SPTR = 100 ps, no DCR, an acquisition time gate of 4 ns per sector, and trapezoidal photodetector modules. Rows correspond to minimum score thresholds of 20% (top), 50% (middle), and 80% (bottom) applied to the highest-scoring mass hypothesis.

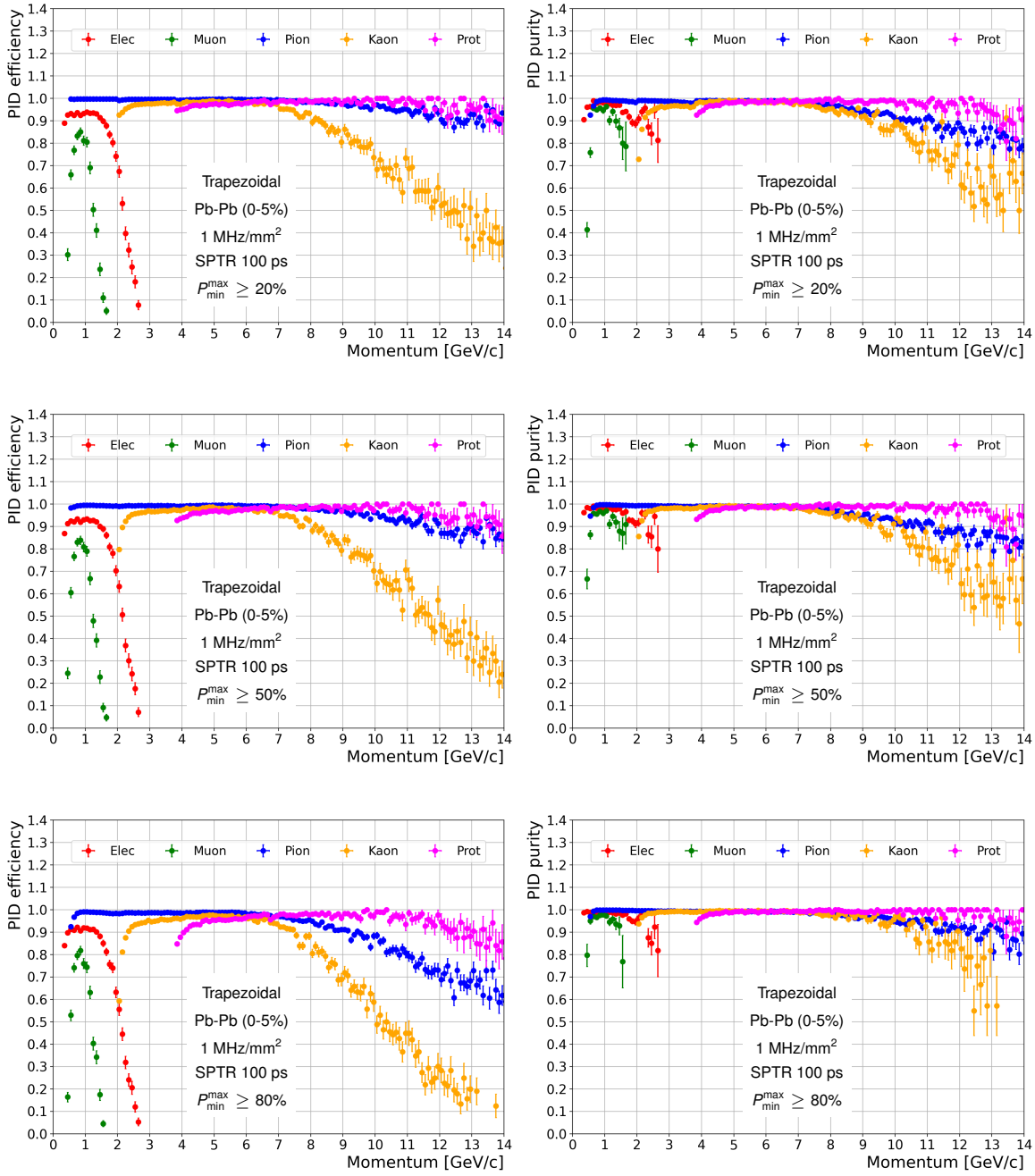


**Figure 4.45:** PID efficiency (left) and purity (right) versus momentum for e, μ, π, K, and p, obtained with my XGBoost-based PID algorithm for the test dataset of central (0–5%) Pb–Pb collisions at $\sqrt{s_{\text{NN}}} = 5.52$ TeV, assuming SPTR = 100 ps, DCR= 1 MHz/mm$^2$, an acquisition time gate of 4 ns per sector, and trapezoidal photodetector modules. Rows correspond to minimum score thresholds of 20% (top), 50% (middle), and 80% (bottom) applied to the highest-scoring mass hypothesis.

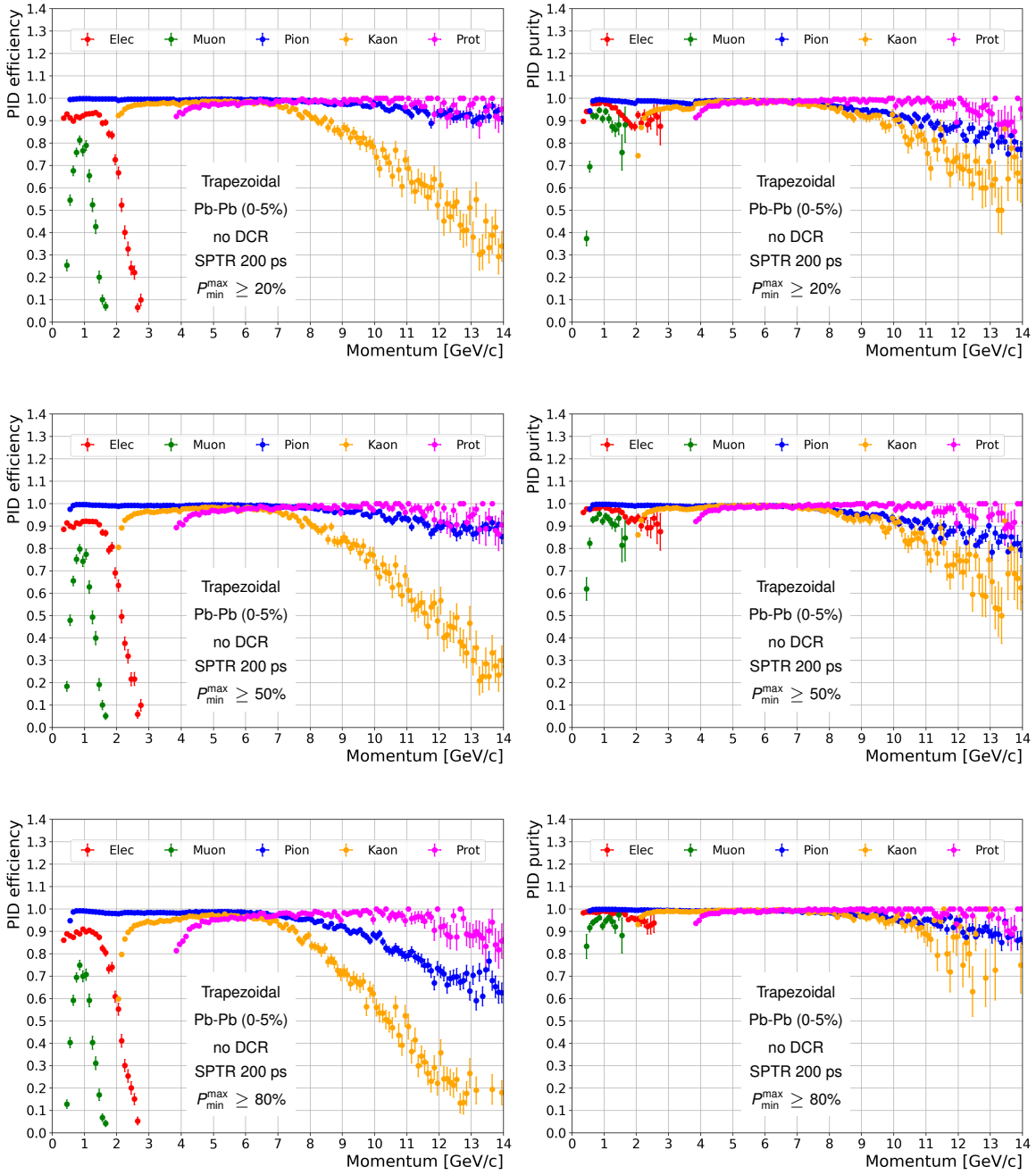


**Figure 4.46:** PID efficiency (left) and purity (right) versus momentum for e, μ, π, K, and p, obtained with my XGBoost-based PID algorithm for the test dataset of central (0–5%) Pb–Pb collisions at $\sqrt{s_{\mathrm{NN}}} = 5.52$ TeV, assuming SPTR = 200 ps, no DCR, an acquisition time gate of 4 ns per sector, and trapezoidal photodetector modules. Rows correspond to minimum score thresholds of 20% (top), 50% (middle), and 80% (bottom) applied to the highest-scoring mass hypothesis.

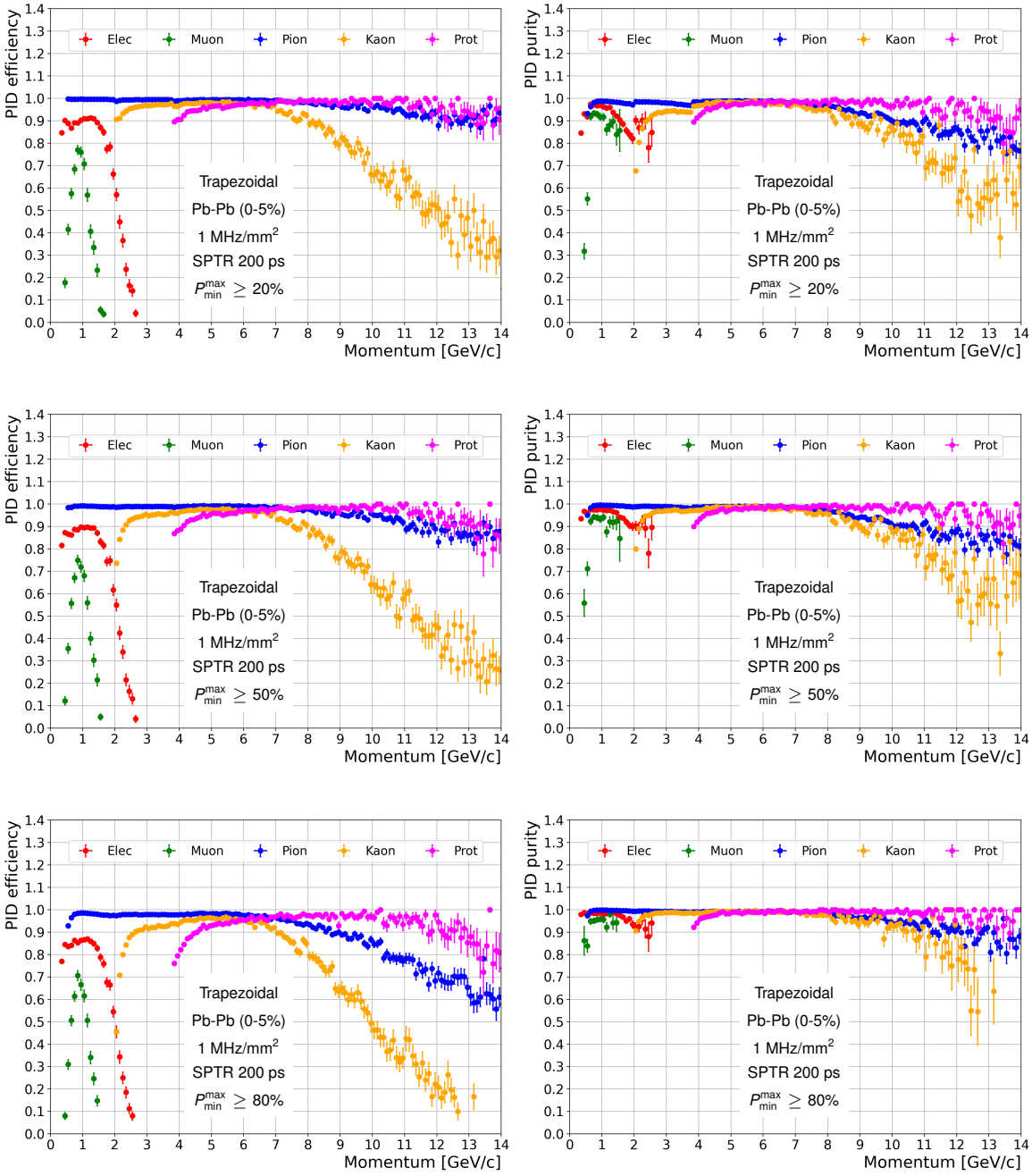


**Figure 4.47:** PID efficiency (left) and purity (right) versus momentum for e, μ, π, K, and p, obtained with my XGBoost-based PID algorithm for the test dataset of central (0–5%) Pb–Pb collisions at $\sqrt{s_{\text{NN}}} = 5.52$ TeV, assuming SPTR = 200 ps, DCR= 1 MHz/mm$^2$, an acquisition time gate of 4 ns per sector, and trapezoidal photodetector modules. Rows correspond to minimum score thresholds of 20% (top), 50% (middle), and 80% (bottom) applied to the highest-scoring mass hypothesis.

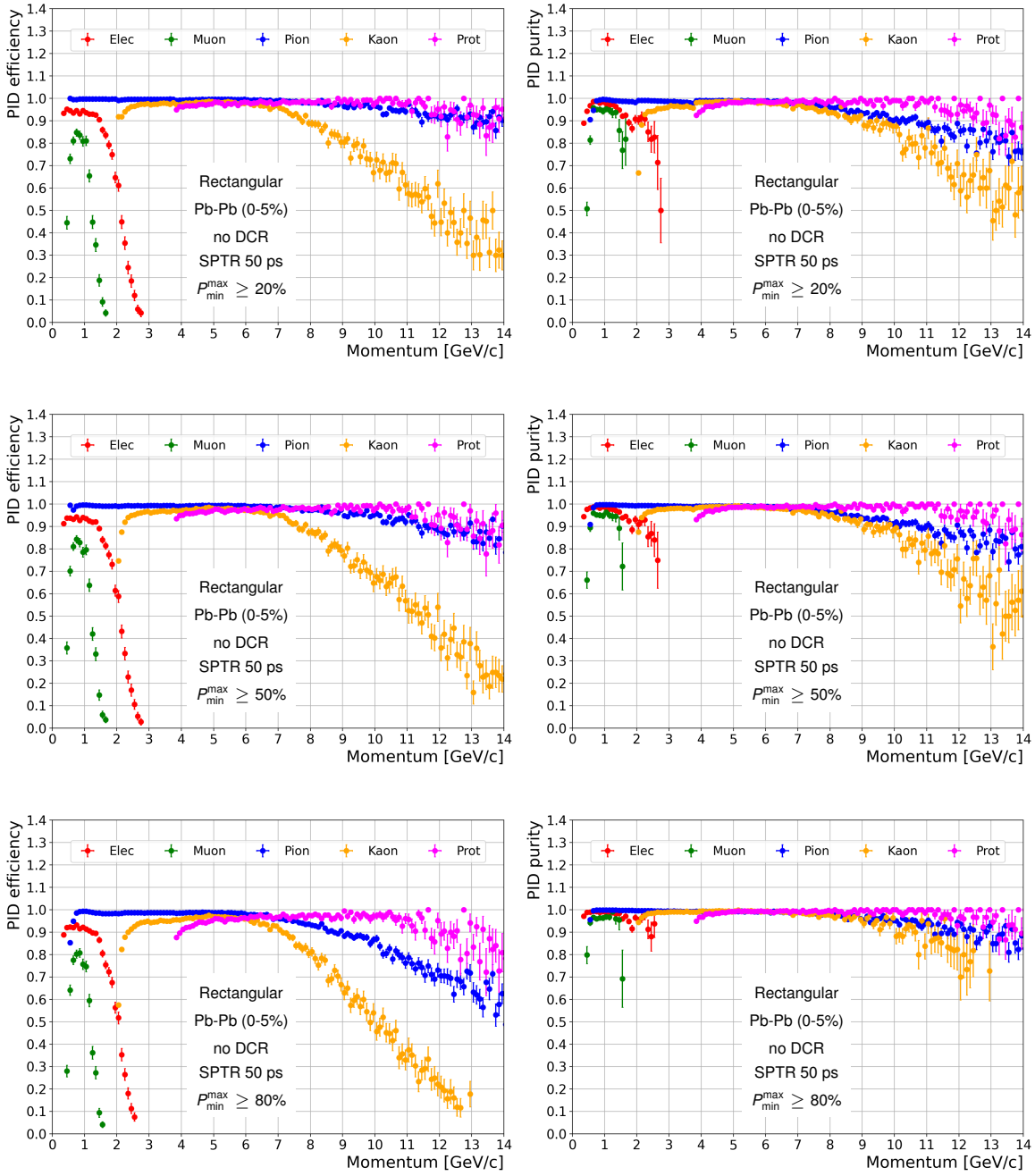


**Figure 4.48:** PID efficiency (left) and purity (right) versus momentum for e, μ, π, K, and p, obtained with my XGBoost-based PID algorithm for the test dataset of central (0–5%) Pb–Pb collisions at $\sqrt{s_{\mathrm{NN}}} = 5.52$ TeV, assuming SPTR = 50 ps, no DCR, an acquisition time gate of 4 ns per sector, and rectangular $17 \times 18$ cm$^2$ photodetector modules. Rows correspond to minimum score thresholds of 20% (top), 50% (middle), and 80% (bottom) applied to the highest-scoring mass hypothesis.

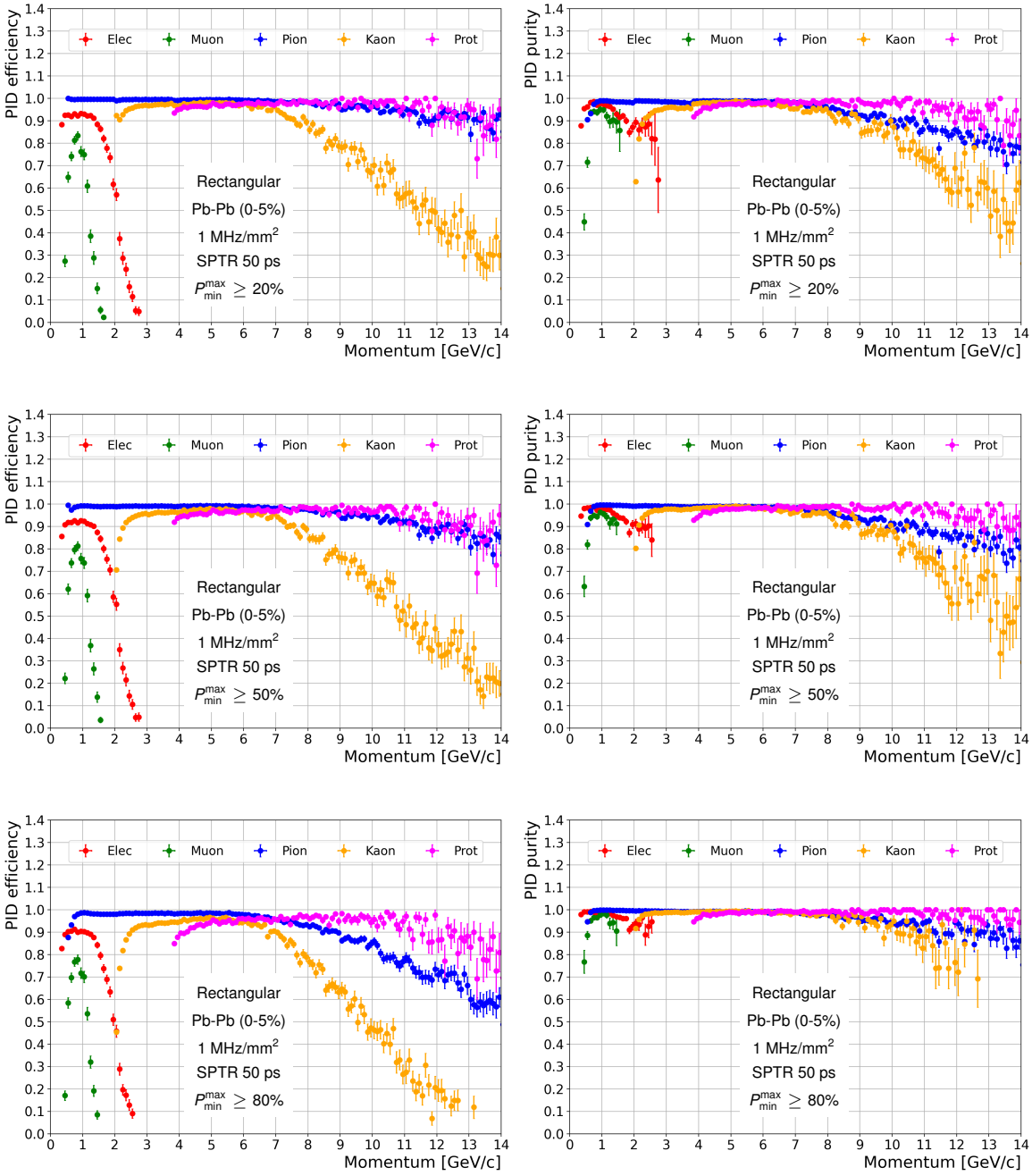


**Figure 4.49:** PID efficiency (left) and purity (right) versus momentum for e, μ, π, K, and p, obtained with my XGBoost-based PID algorithm for the test dataset of central (0–5%) Pb–Pb collisions at $\sqrt{s_{\text{NN}}} = 5.52$ TeV, assuming SPTR = 50 ps, DCR= 1 MHz/mm$^2$, an acquisition time gate of 4 ns per sector, and rectangular $17 \times 18$ cm$^2$ photodetector modules. Rows correspond to minimum score thresholds of 20% (top), 50% (middle), and 80% (bottom) to the highest-scoring mass hypothesis.

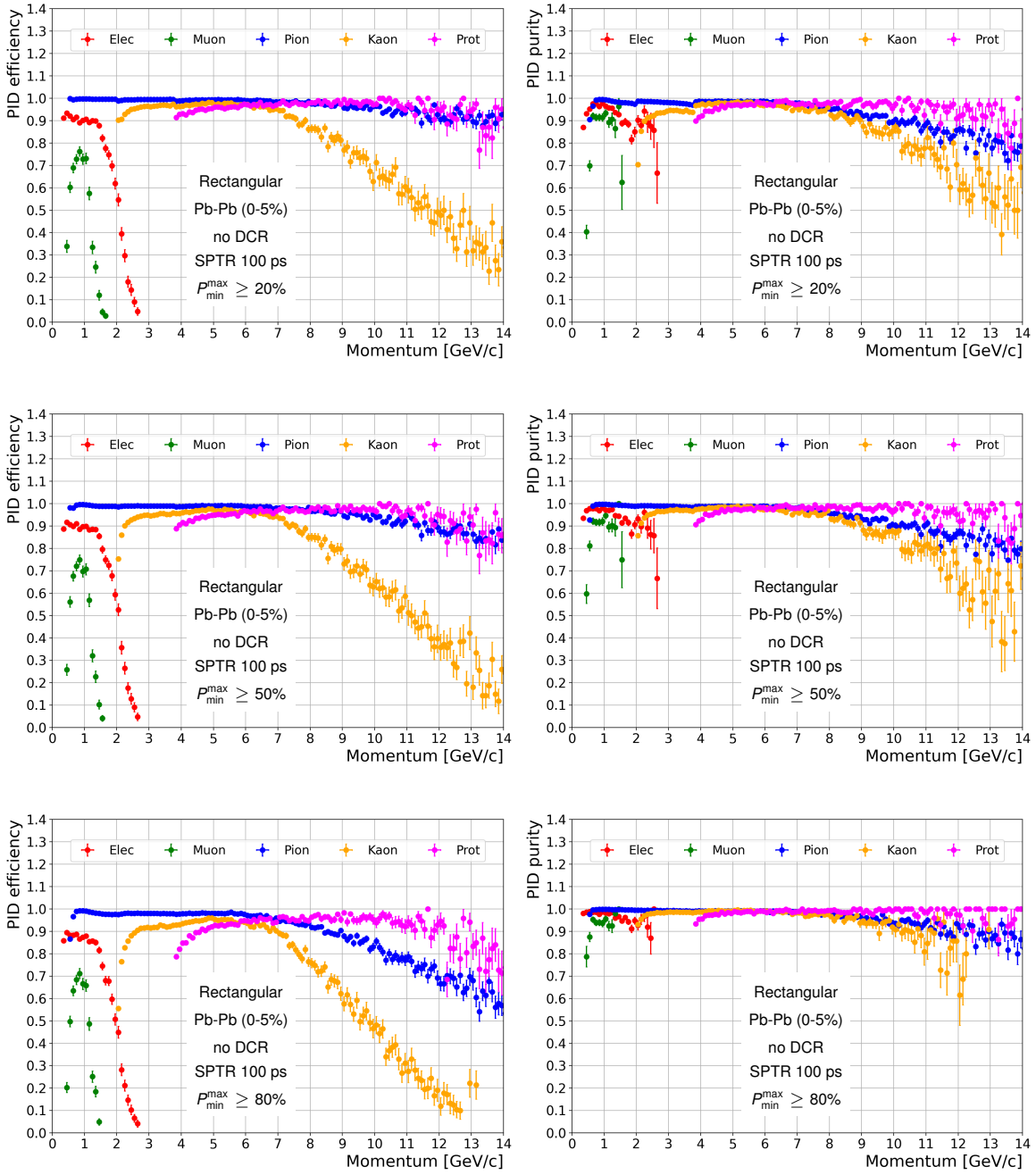


**Figure 4.50:** PID efficiency (left) and purity (right) versus momentum for e, μ, π, K, and p, obtained with my XGBoost-based PID algorithm for the test dataset of central (0–5%) Pb–Pb collisions at $\sqrt{s_{\mathrm{NN}}} = 5.52$ TeV, assuming SPTR = 100 ps, no DCR, an acquisition time gate of 4 ns per sector, and rectangular $17 \times 18$ cm$^2$ photodetector modules. Rows correspond to minimum score thresholds of 20% (top), 50% (middle), and 80% (bottom) applied to the highest-scoring mass hypothesis.

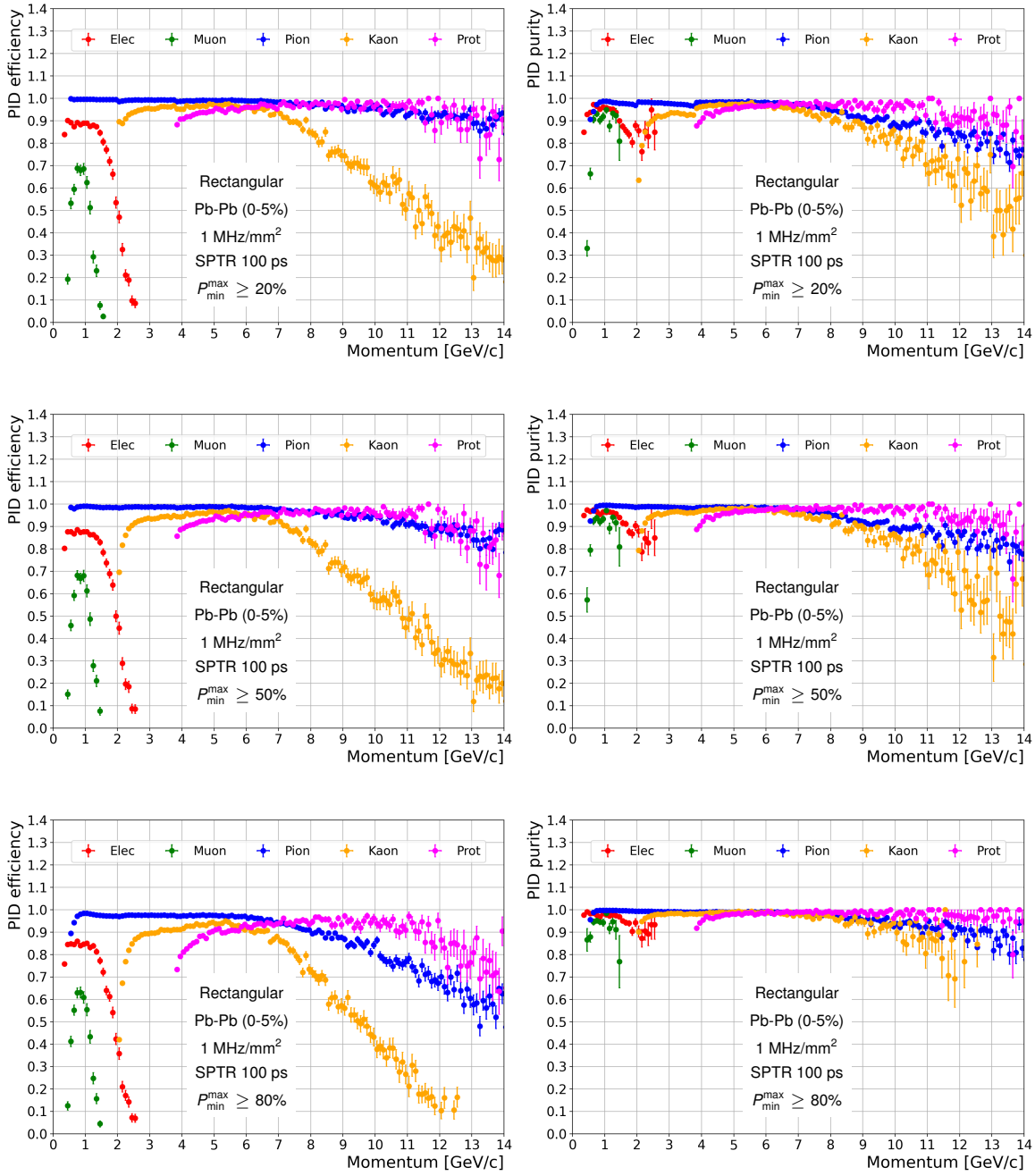


**Figure 4.51:** PID efficiency (left) and purity (right) versus momentum for e, μ, π, K, and p, obtained with my XGBoost-based PID algorithm for the test dataset of central (0–5%) Pb–Pb collisions at $\sqrt{s_{\text{NN}}} = 5.52$ TeV, assuming SPTR = 100 ps, DCR= 1 MHz/mm$^2$, an acquisition time gate of 4 ns per sector, and rectangular $17 \times 18$ cm$^2$ photodetector modules. Rows correspond to minimum score thresholds of 20% (top), 50% (middle), and 80% (bottom) to the highest-scoring mass hypothesis.

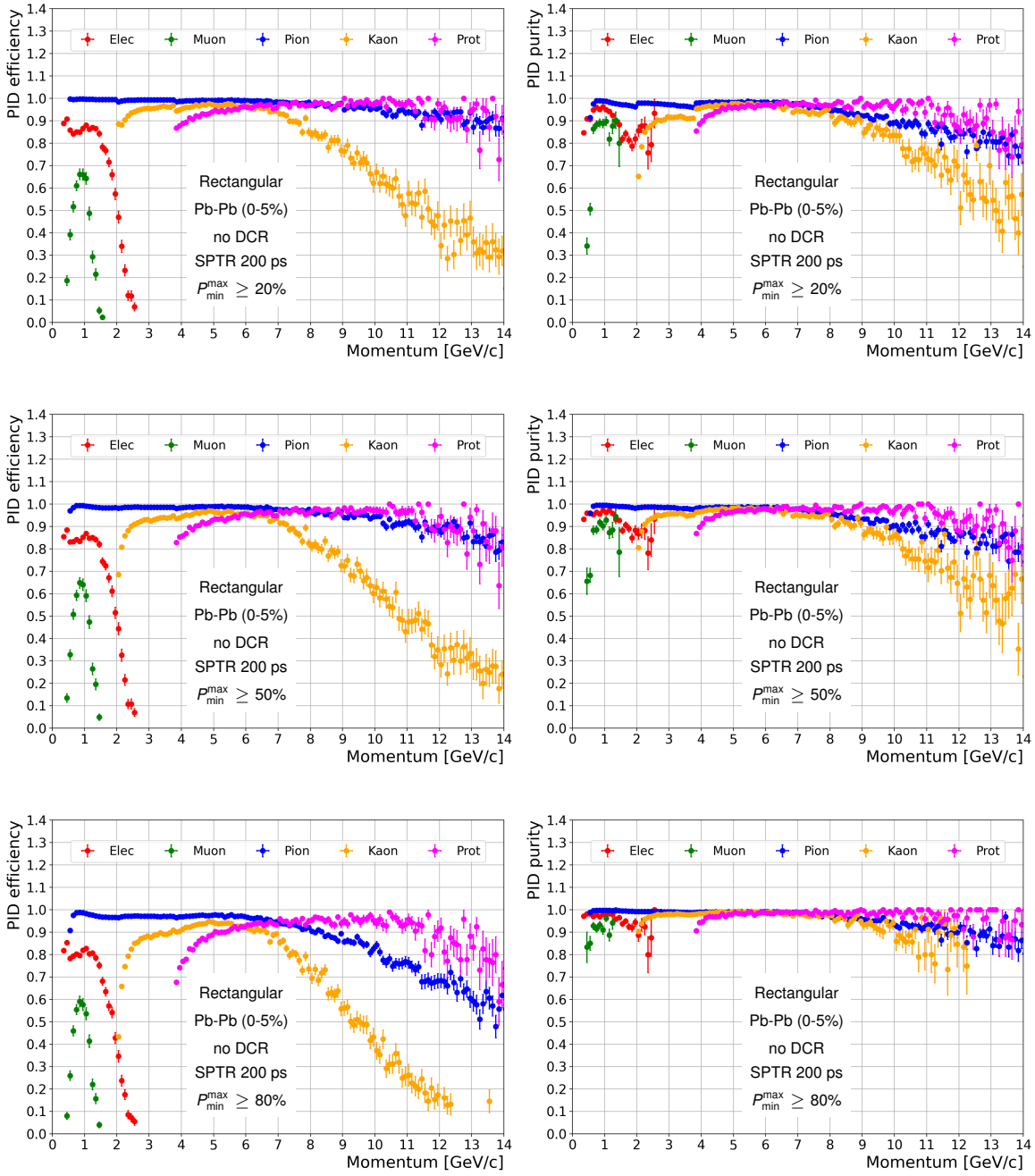


**Figure 4.52:** PID efficiency (left) and purity (right) versus momentum for e, μ, π, K, and p, obtained with my XGBoost-based PID algorithm for the test dataset of central (0–5%) Pb–Pb collisions at $\sqrt{s_{\mathrm{NN}}} = 5.52$ TeV, assuming SPTR = 200 ps, no DCR, an acquisition time gate of 4 ns per sector, and rectangular $17 \times 18$ cm$^2$ photodetector modules. Rows correspond to minimum score thresholds of 20% (top), 50% (middle), and 80% (bottom) applied to the highest-scoring mass hypothesis.

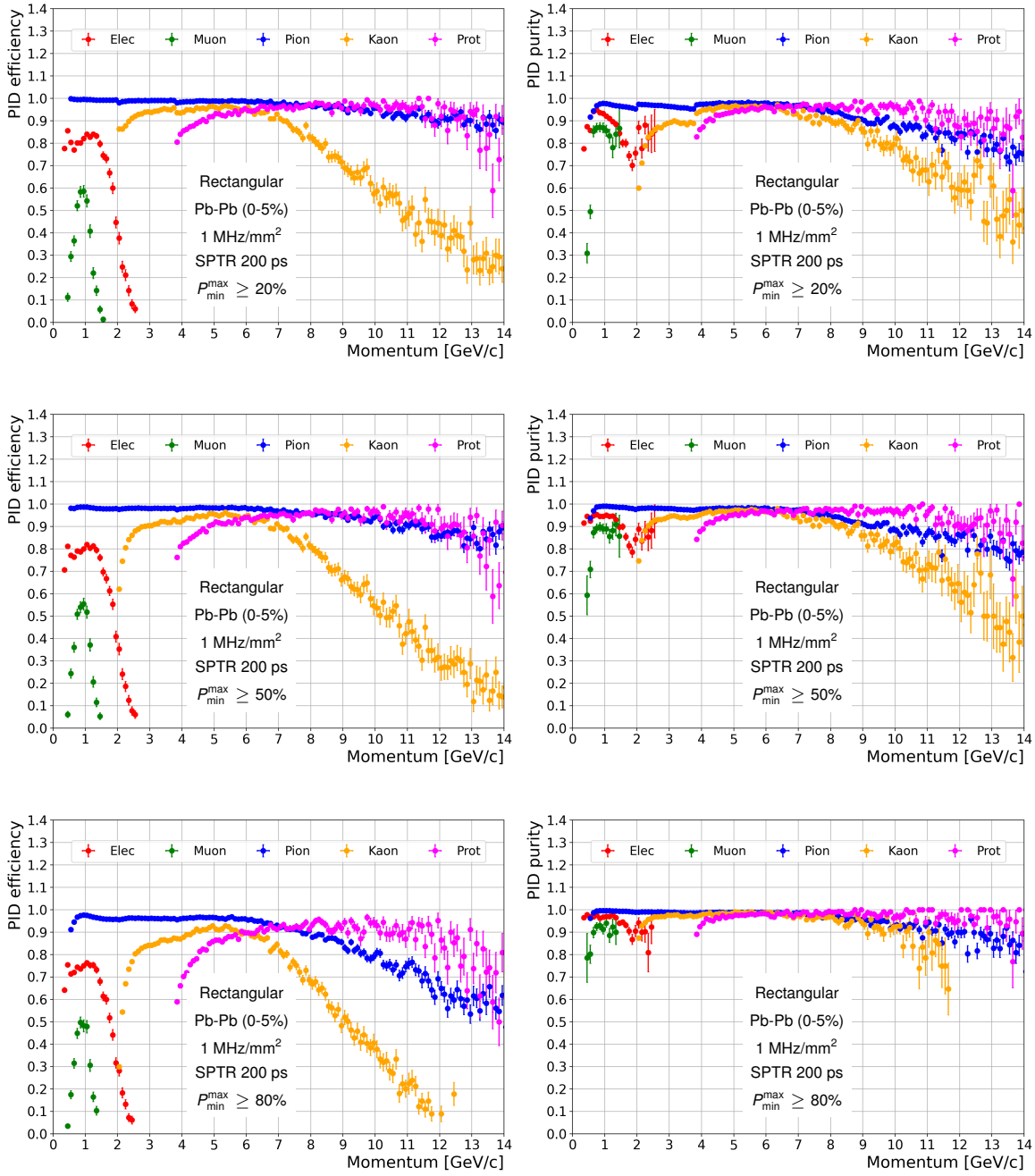


**Figure 4.53:** PID efficiency (left) and purity (right) versus momentum for e, μ, π, K, and p, obtained with my XGBoost-based PID algorithm for the test dataset of central (0–5%) Pb–Pb collisions at $\sqrt{s_{\mathrm{NN}}} = 5.52$ TeV, assuming SPTR = 200 ps, DCR= 1 MHz/mm$^2$, an acquisition time gate of 4 ns per sector, and rectangular $17 \times 18$ cm$^2$ photodetector modules. Rows correspond to minimum score thresholds of 20% (top), 50% (middle), and 80% (bottom) to the highest-scoring mass hypothesis.

## 4.8 Gas-based e-ID option in central Pb-Pb

The Cherenkov rings from the aerogel tiles enable efficient identification of electrons and positrons up to about 2 GeV/$c$ in central (0–5%) Pb–Pb events. The threshold gas–based e-ID option introduced in Section 3.5, using a green-gas mixture such as 10.85% $C_5F_{10}O$+ 89.15% $CO_2$ with refractive index $n = 1.0006$, provides an additional observable, the gas cluster, to tag electrons. This not only strengthens coverage below 2 GeV/$c$, but also enables the possibility to extend e-ID up to 4 GeV/$c$ and beyond.

To validate the effectiveness of this option under ALICE 3 operating conditions, I investigated the corresponding e-ID performance in central (0–5%) Pb–Pb events. Here I considered both the case in which all photons emitted in gas, both upstream and downstream of the traversed aerogel tiles, can reach the photodetector modules, and the case in which upstream-emitted photons are absorbed, so that only photons produced downstream can be detected. I evaluated the two limiting DCR scenarios of no DCR and 1 MHz/mm$^2$ considering an overall SPTR of 100 ps. For this study, I assumed trapezoidal photodetector modules. In the rectangular 17 × 18 cm$^2$ option, similar purities are expected but with lower efficiencies, due to the systematic loss of gas photons from tracks falling into inactive regions outside the module boundaries.

### 4.8.1 Background to gas clusters

The discrimination capabilities of the proposed gas-based e-ID option are affected by background hits, mainly from Cherenkov photons emitted in aerogel by the various charged tracks in the events, particularly relevant at high multiplicity, the SiPM DCR, and hits arising from secondaries. These hits can cluster near the most probable impact points of a track on the photodetector modules, creating fake clusters that mimic true electron clusters. Given the low e relative abundance, even small fractions of non-electron tracks misclassified as electrons significantly harm the achievable purity.

### 4.8.2 Pre-filtering of aerogel background photons

To mitigate the large correlated background from aerogel photons in each event, I first applied, track-by-track, the XGBoost-based aerogel PID classifier discussed in Section 4.7 for the considered DCR level and SPTR. I then used the predicted label $i$ to discard all hits in the event satisfying

$$\left|\theta_{\rm rec} - \theta_{{\rm th},i}\right| < 3\,\sigma_{\rm c}^{\gamma}(i)\,, \tag{4.21}$$

where $\theta_{\rm rec}$ is the single-hit candidate Cherenkov angle computed as in Section 4.3.1, $\theta_{{\rm th},i}$ is the theoretical Cherenkov angle for species $i$, and $\sigma_{\rm c}^{\gamma}(i)$ is the single-photon angular resolution for the considered particle species and sector.

With this simple pre-filtering, most of the unscattered Cherenkov photons from other tracks are therefore removed. However, photons that undergo Rayleigh scattering in the aerogel before leaving the tiles, and hits from secondaries produced in material interactions, cannot be rejected and constitute an irreducible background. The main drawback of this procedure is the possible removal of true electron gas-cluster photons when the cluster lies within the fiducial ring area of any other track to which the filter is applied, leading to an efficiency loss. However, this is crucial to ensure PID purities larger than 90% at the considered track multiplicities.

### 4.8.3 Machine learning based e-ID with gas

For this analysis, I developed a classification algorithm trained in a one-vs-rest scheme, using a binary XGB classifier to discriminate e from any other mass hypothesis.

#### Datasets

For the training, validation, and testing of the algorithm, I generated new datasets by replacing Ar in the vessel with a 10.85% $C_5F_{10}O$ + 89.15% $CO_2$ mixture, following the same procedure used for the main pp and central Pb–Pb datasets. The pp and Pb–Pb training and test datasets comprised 18M and 5k collisions, respectively. For all considered cases, in the training phase I used a stratified 5% of the events as a validation set to monitor the validation metric at each boosting step. Stratification is important for e and μ, due to the lower than 0.35% relative abundance in the sample.

#### Features

The features I used for electron tagging with gas are both track parameters and high-level observables describing the cluster topology, namely the number of fired SiPM channels and the number of detected photoelectrons within the cluster fiducial region.

- **Track parameters**:
  - $p$: Momentum at the most probable photon emission point in aerogel.
  - $\eta$: Pseudorapidity at the most probable photon emission point in aerogel.

– $\theta_{\mathrm{det}}$: Polar angle of the track impact point on the SiPM module.

– $\phi_{\mathrm{det}}$: Azimuthal angle of the track impact point on the SiPM module.

In particular, I considered the $p$ and $\eta$ extrapolated at the most probable emission point in aerogel also for the study with gas, to enable a direct comparison of purity and efficiency with the aerogel only option. The track impact point on the SiPM modules was obtained by extrapolating the track from the most probable photon emission point in aerogel to the photodetector modules, accounting for the 2 T magnetic field. Tracks not reaching any SiPM module were discarded.

- **Gas cluster topology**:

  For each accepted charged track, extrapolated to the position $\mathbf{r}_{\mathrm{trk}}^{\mathrm{det}}$ on the corresponding photodetector module, and for the pre-filtered set of candidate gas photons with hit positions $\mathbf{r}_{\mathrm{hit}}^{\mathrm{det}}$, I counted the number of hits $N_{\mathrm{hits}}$ and the number of photoelectrons $N_{\mathrm{pe}}$ in five cluster regions, defined by the radial limits

$$d_k \in \{\,0,\ 0.32\ \mathrm{cm},\ 0.70\ \mathrm{cm},\ 1.05\ \mathrm{cm},\ 1.40\ \mathrm{cm},\ 2.00\ \mathrm{cm}\,\}, \qquad k = 0, \ldots, 5,$$

  and indexed by $j = 0, \ldots, 4$ as the five annuli $[d_j,\, d_{j+1})$ around $\mathbf{r}_{\mathrm{trk}}^{\mathrm{det}}$, given by:

$$N_{\mathrm{hits}}(j) = N_{\mathrm{hits}}\big\{ d_j \le \big\|\mathbf{r}_{\mathrm{hit}}^{\mathrm{det}} - \mathbf{r}_{\mathrm{trk}}^{\mathrm{det}}\big\| < d_{j+1} \big\}\,,$$

$$N_{\mathrm{pe}}(j) = N_{\mathrm{pe}}\big\{ d_j \le \big\|\mathbf{r}_{\mathrm{hit}}^{\mathrm{det}} - \mathbf{r}_{\mathrm{trk}}^{\mathrm{det}}\big\| < d_{j+1} \big\}\,.$$

  In addition, within the same disk of radius $R_\star = 1.40$ cm centred at $\mathbf{r}_{\mathrm{trk}}^{\mathrm{det}}$, I counted the cumulative number of recorded hits, the corresponding number of photoelectrons and the number of SiPM hits with charge $Q$ exceeding four fixed thresholds $Q_{\mathrm{min}} \in \{2, 3, 4, 5\}$ in units of photoelectrons, yielding the six features:

$$N_{\mathrm{hits}}(R_\star) = N_{\mathrm{hits}}\big\{ \big\|\mathbf{r}_{\mathrm{hit}}^{\mathrm{det}} - \mathbf{r}_{\mathrm{trk}}^{\mathrm{det}}\big\| < R_\star \big\}\,,$$

$$N_{\mathrm{pe}}(R_\star) = N_{\mathrm{pe}}\big\{ \big\|\mathbf{r}_{\mathrm{hit}}^{\mathrm{det}} - \mathbf{r}_{\mathrm{trk}}^{\mathrm{det}}\big\| < R_\star \big\}\,,$$

$$N_{\mathrm{hits}}(R_\star,\, Q_{\mathrm{min}}) = N_{\mathrm{hits}}\Big\{ \big\|\mathbf{r}_{\mathrm{hit}}^{\mathrm{det}} - \mathbf{r}_{\mathrm{trk}}^{\mathrm{det}}\big\| < R_\star,\ Q \ge Q_{\mathrm{min}} \Big\}.$$

  Assuming a single photon time resolution SPTR, these hit-related features are computed only if relative hit–track time on the photodetector $\Delta T_{\mathrm{det}}$ satisfies:

$$\big|\Delta T_{\mathrm{det}}\big| < 2\,\mathrm{SPTR}\,. \tag{4.22}$$

The track parameters correspond to 4 features. The gas cluster topology features correspond to 5+5+6 = 16 additional features. The total feature count is 20.

### Labels

Electron/positron tracks are assigned label 1, while other tracks are assigned label 0.

### Classifier configuration

As in the case of Section 4.7.1, for the XGB classifier developed for gas studies, I optimized the hyperparameters through a grid search. Table 4.5 reports the optimal configuration used for training and inference with `XGBClassifier` in the gas–based e-ID bRICH option. The definition of the hyperparameters is provided in Section 4.7.1.

| Hyperparameter | Value |
|---|---|
| `objective` | `binary:logistic` |
| `reg_alpha` | 0.05 |
| `reg_lambda` | 0.05 |
| `n_estimators` | 250 |
| `learning_rate` | 0.10 |
| `max_depth` | 9 |
| `min_child_weight` | 3 |
| `subsample` | 0.30 |
| `colsample_bytree` | 1.00 |

**Table 4.5:** Configuration of `XGBClassifier` gas-based e-ID with the bRICH.

## 4.8.4 Results in pp collisions

To benchmark the limiting gas-based e-ID performance achievable with my XGBoost-based PID algorithm, here I report the results for pp collisions under the ideal reference conditions of SPTR = 100 ps, a $\pm 2\,\mathrm{SPTR}$ hit-track matching cut, and no DCR for the two tested configurations. In particular, Figs. 4.54 and 4.58 show the results for the test dataset of simulated $c\bar{c}$-biased pp collisions at $\sqrt{s} = 14$ TeV considering both the configuration in which gas photons emitted both upstream and downstream of the aerogel radiator tiles are detected, and the configuration where only gas photons emitted downstream of the aerogel tiles are considered. The panels show the score probability distributions for electrons versus all other species, the e-ID purity and efficiency, integrated over the full momentum spectrum, as a function of the threshold on the XGB score, and the efficiency and purity as a function of momentum setting a minimum score threshold of 50%.

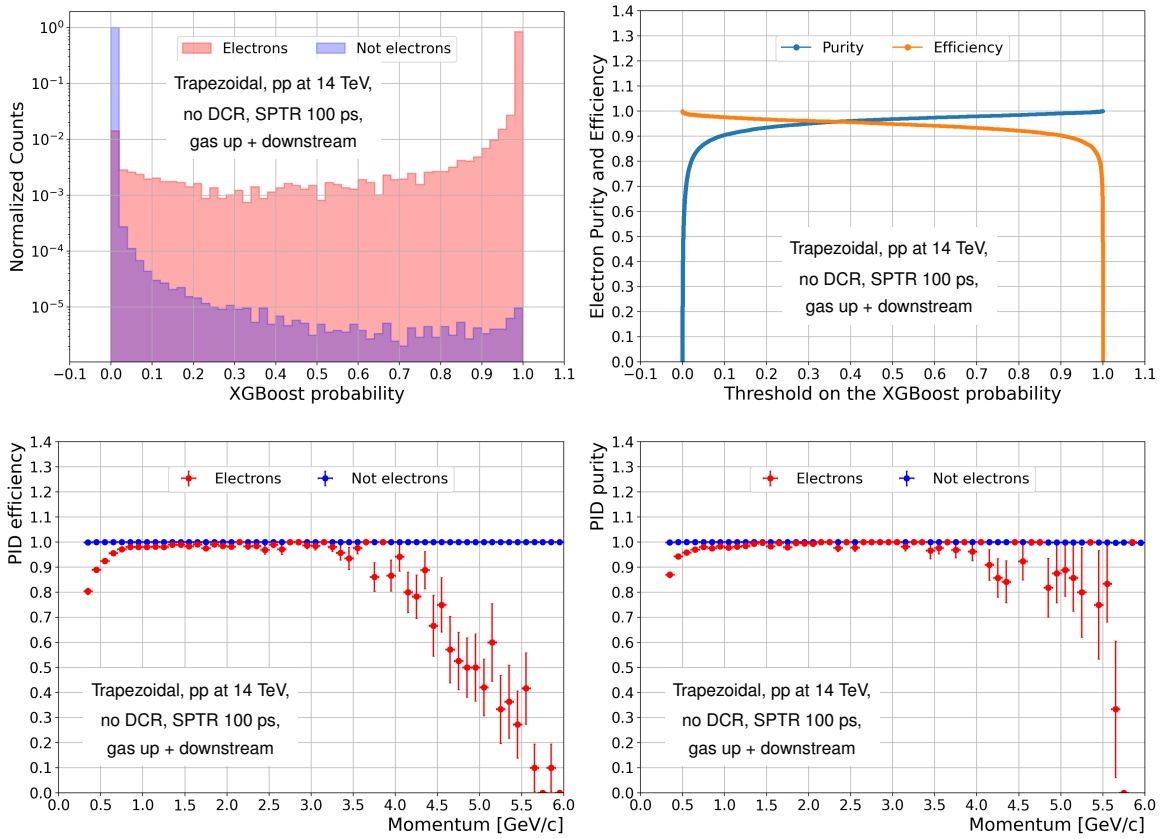


**Figure 4.54:** Performance of the gas-based e-ID option using my XGBoost-based algorithm for the test dataset of pp collisions at $\sqrt{s} = 14$ TeV assuming SPTR = 100 ps, a $\pm 2$ SPTR hit-track matching cut, no DCR, an acquisition time gate of 4 ns per sector, trapezoidal photodetector modules, the bRICH vessel filled with $C_5F_{10}O$+$CO_2$, and considering gas photons emitted both upstream and downstream of the aerogel tiles. Score probability distributions for electrons and all other species (top left), integrated electron-identification purity and efficiency as a function of the threshold on the XGB score (top right), and electron efficiency (bottom left) and purity (bottom right) as functions of momentum for a minimum score threshold of 50%.

The target e-ID coverage is achieved up to 4 GeV/$c$ and above, with purities and efficiencies close to unity. The observed efficiency and purity loss below 0.5 GeV/$c$ is mainly due to the curvature in the 2 T magnetic field, resulting in a too large separation between photons emitted upstream in the gas and the track impact point on the photodetector, and preventing those photon hits from being included in the clusters. In the momentum region where enough statistics is available for training, comparable results are achieved both in the case where only photons produced downstream of the aerogel tiles are detected and in the case in which upstream photons are also included. This is expected since the latter configuration provides a larger photon yield without introducing significant additional background in the low-multiplicity pp environment.

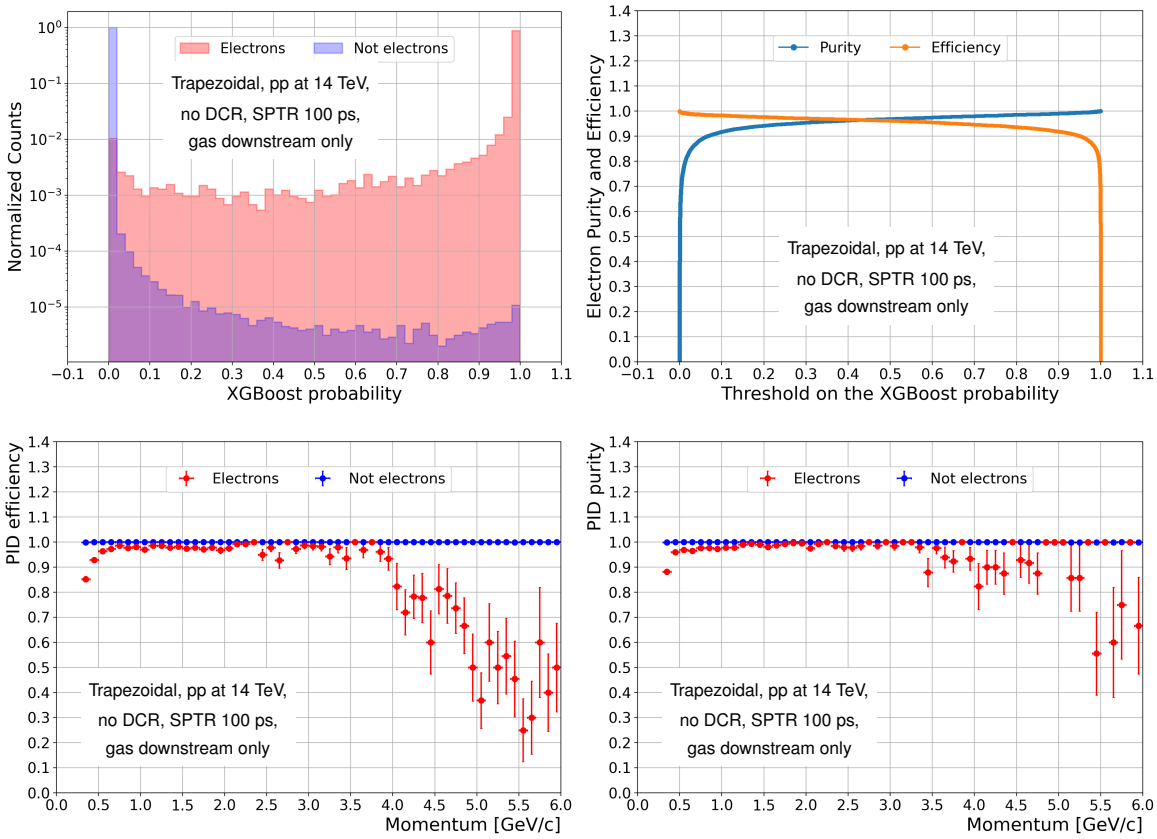


**Figure 4.55:** Performance of the gas-based e-ID option using my XGBoost-based algorithm for the test dataset of pp collisions at $\sqrt{s} = 14$ TeV assuming SPTR = 100 ps, no DCR, a $\pm 2$ SPTR hit-track matching cut, an acquisition time gate of 4 ns per sector, trapezoidal photodetector modules, the bRICH vessel filled with $C_5F_{10}O$+$CO_2$, and considering only gas photons emitted downstream of the aerogel tiles. Score probability distributions for electrons and all other species (top left), integrated electron-identification purity and efficiency as a function of the threshold on the XGB score (top right), and electron efficiency (bottom left) and purity (bottom right) as functions of momentum for a minimum score threshold of 50%.

As for the aerogel-based analysis, the real challenge arises in central Pb–Pb collisions, especially under high-DCR operation, as detailed in the following section.

### 4.8.5 Results in Pb-Pb collisions

In this section, I report the results for the gas-based e-ID performance achieved with my XGBoost-based algorithm for the test dataset of central (0–5%) Pb–Pb at $\sqrt{s_{\rm NN}} = 5.52$ TeV assuming an acquisition time gate of 4 ns per sector, a SPTR of 100 ps, a $\pm 2$ SPTR hit-track matching cut, and the limiting cases of no DCR, to study correlated background, and 1 MHz/mm$^2$ for the trapezoidal photodetector module layout.

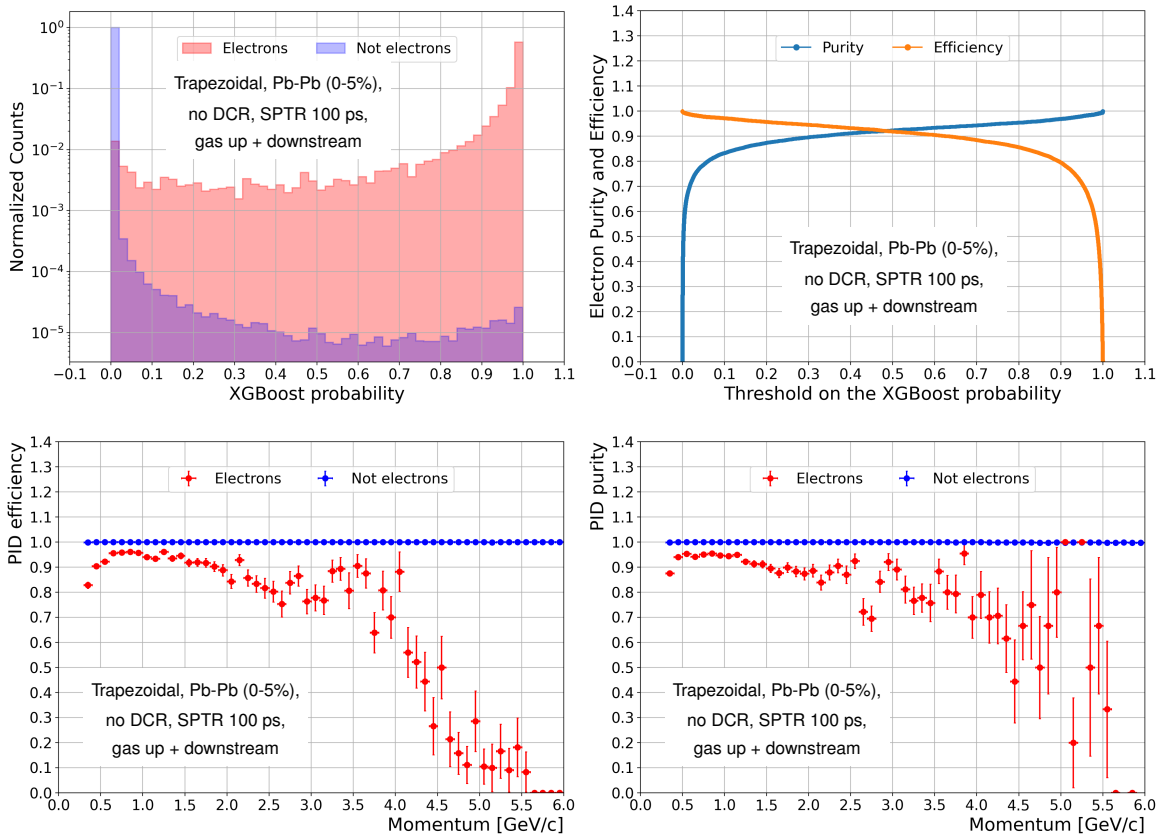


**Figure 4.56:** Performance of the gas-based e-ID option using my XGBoost-based algorithm for the test dataset of central (0–5%) Pb–Pb collisions at $\sqrt{s_{\mathrm{NN}}} = 5.52$ TeV assuming SPTR = 100 ps, a $\pm 2$ SPTR hit-track matching cut, no DCR, an acquisition time gate of 4 ns per sector, trapezoidal photodetector modules, the bRICH vessel filled with $C_5F_{10}O$+$CO_2$, and considering gas photons emitted both upstream and downstream of the aerogel tiles. Score probability distributions for electrons and all other species (top left), integrated electron-identification purity and efficiency as a function of the threshold on the XGB score (top right), and electron efficiency (bottom left) and purity (bottom right) as functions of momentum for a minimum score threshold of 50%.

Figs. 4.56 and 4.57 show the results for the configuration in which gas photons emitted both upstream and downstream of the aerogel radiator tiles are detected for the cases with no DCR and a DCR = 1 MHz/mm$^2$, respectively. The panel layout is identical to that of Figs. 4.54 and 4.55 relative to the pp case.

The corresponding results for the configuration in which only gas photons emitted downstream of the aerogel radiator tiles are detected are shown in Figs. 4.58 and 4.59.

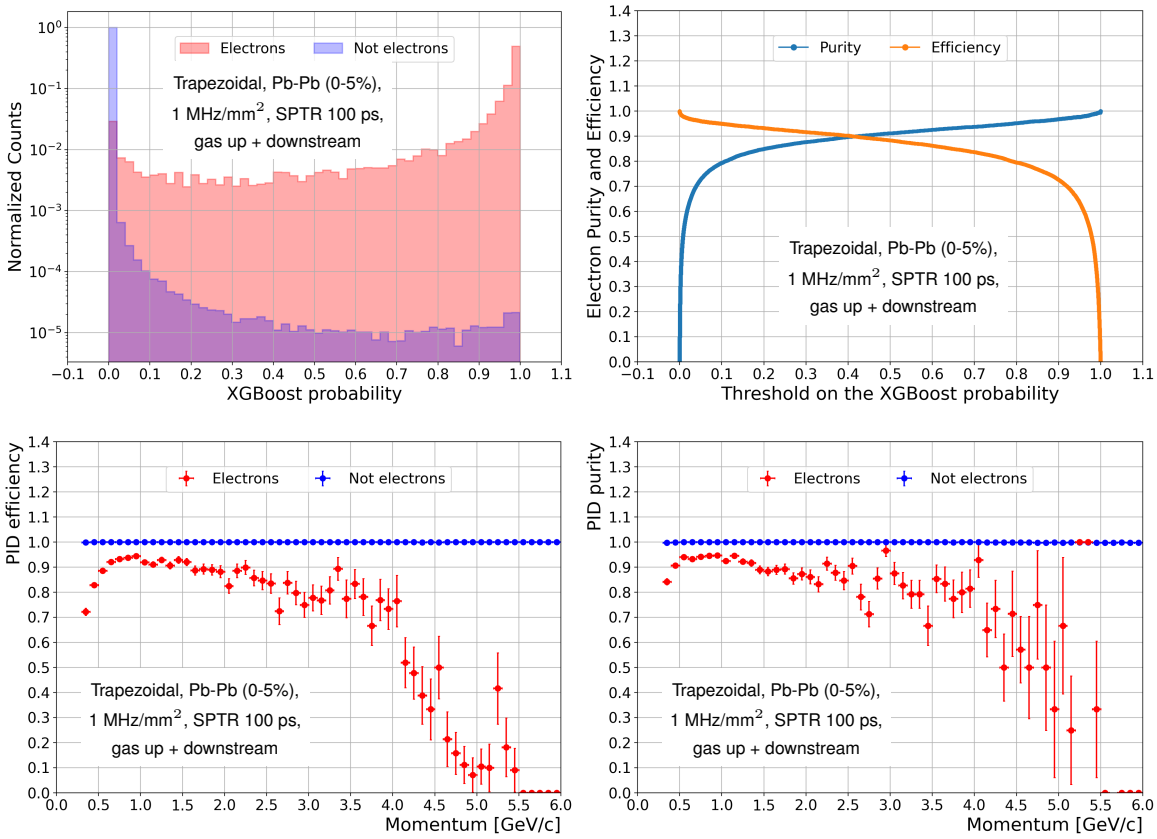


**Figure 4.57:** Performance of the gas-based e-ID option using my XGBoost-based algorithm for the test dataset of central (0–5%) Pb–Pb collisions at $\sqrt{s_{\mathrm{NN}}} = 5.52$ TeV assuming SPTR = 100 ps, a $\pm 2\,\mathrm{SPTR}$ hit-track matching cut, DCR = 1 MHz/mm$^2$, an acquisition time gate of 4 ns per sector, trapezoidal photodetector modules, the bRICH vessel filled with $C_5F_{10}O$+$CO_2$, and considering gas photons emitted both upstream and downstream of the aerogel tiles. Score probability distributions for electrons and all other species (top left), integrated electron-identification purity and efficiency as a function of the threshold on the XGB score (top right), and electron efficiency (bottom left) and purity (bottom right) as functions of momentum for a minimum score threshold of 50%.

### Performance without DCR

From the plots of efficiency and purity versus momentum, with DCR = 0 and a 50% score threshold, e-ID efficiencies and purities above 90% are achieved up to 2 GeV/$c$, and above 80% up to 4 GeV/$c$. The larger efficiencies observed below 1 GeV/$c$ arise from the effective suppression of correlated background using the ±2 SPTR hit–track time matching cut. In this momentum range, electrons have velocity $\beta \to 1$, while other species with smaller $\beta$ result in hit times that are naturally separated, which limits random clustering of background hits from different tracks and preserves purity.

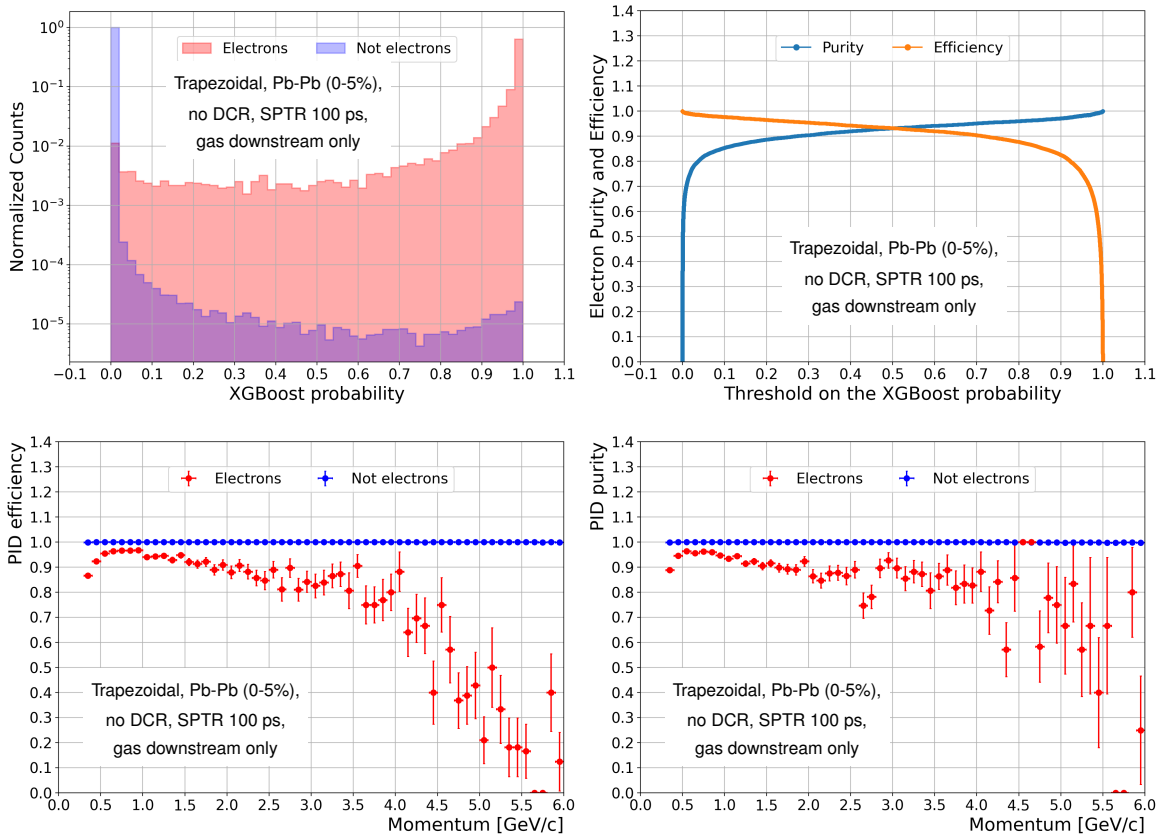


**Figure 4.58:** Performance of the gas-based e-ID option using my XGBoost-based algorithm for the test dataset of central (0–5%) Pb–Pb collisions at $\sqrt{s_{\mathrm{NN}}} = 5.52$ TeV assuming SPTR = 100 ps, a $\pm 2\,\mathrm{SPTR}$ hit-track matching cut, no DCR, an acquisition time gate of 4 ns per sector, trapezoidal photodetector modules, the bRICH vessel filled with $C_5F_{10}O$+$CO_2$, and considering only gas photons emitted downstream of the aerogel tiles. Score probability distributions for electrons and all other species (top left), integrated electron-identification purity and efficiency as a function of the threshold on the XGB score (top right), and electron efficiency (bottom left) and purity (bottom right) as functions of momentum for a minimum score threshold of 50%.

At higher momenta, $\beta \to 1$ also for other species, the nominal time differences shrink, and the timing cut becomes less effective at rejecting correlated background.

The probability distributions show the expected trade-off between efficiency and purity varying the score threshold. Increasing the threshold raises purity at the cost of efficiency, while decreasing the threshold raises efficiency at the cost of purity.

Above 4 GeV/$c$ the efficiency progressively decreases because $\mu$ and $\pi$ are above the Cherenkov threshold in gas and can produce clusters similar to those of e. Given the small e fraction compared with other species, the classifier tends to label some true e as $\pi$ in this regime, losing efficiency. The fluctuations observed at high momentum

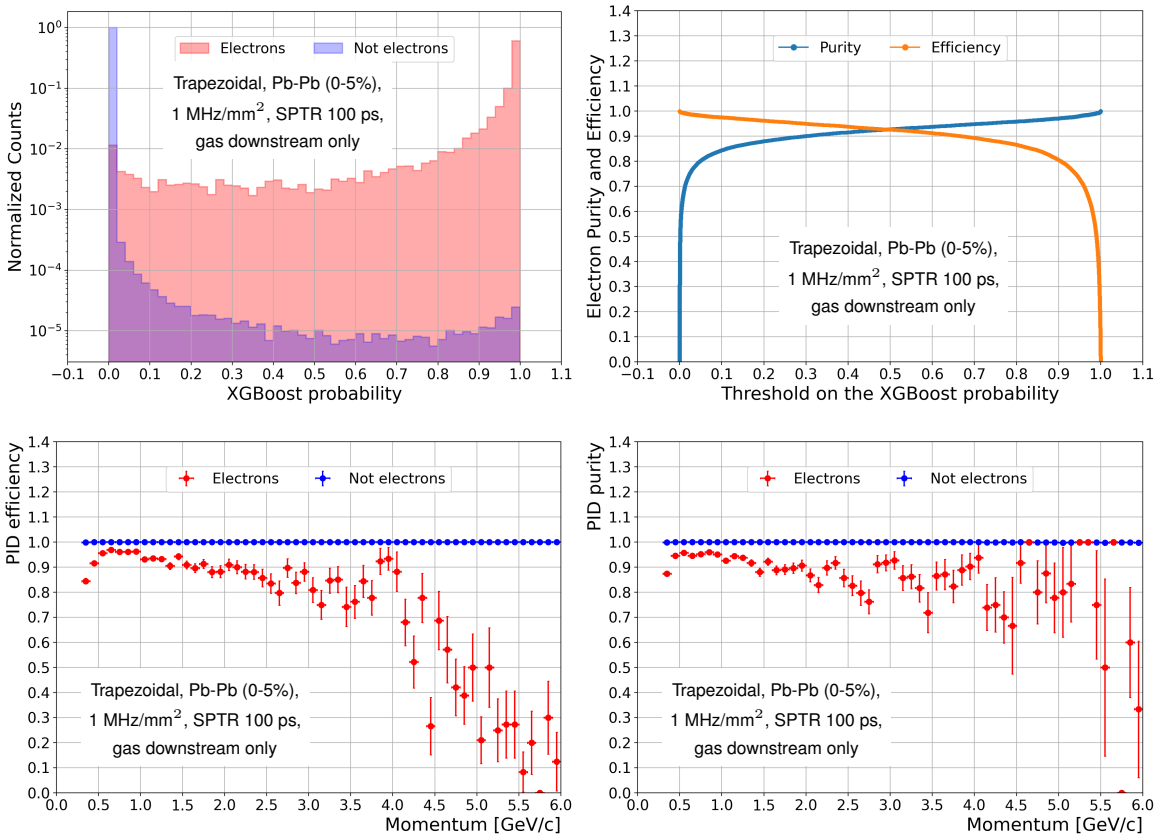


**Figure 4.59:** Performance of the gas-based e-ID option using my XGBoost-based algorithm for the test dataset of central (0–5%) Pb–Pb collisions at $\sqrt{s_{\mathrm{NN}}} = 5.52$ TeV assuming SPTR = 100 ps, a $\pm 2\,\mathrm{SPTR}$ hit-track matching cut, DCR = 1 MHz/mm$^2$, an acquisition time gate of 4 ns per sector, trapezoidal photodetector modules, the bRICH vessel filled with $C_5F_{10}O$+$CO_2$, and considering only gas photons emitted downstream of the aerogel tiles. Score probability distributions for electrons and all other species (top left), integrated electron-identification purity and efficiency as a function of the threshold on the XGB score (top right), and electron efficiency (bottom left) and purity (bottom right) as functions of momentum for a minimum score threshold of 50%.

are due to limited electron statistics in the 5k events used in this study.

Across the full momentum range, the efficiencies and purities for all species other than electrons are about unity. Tracks from these species are rarely tagged as electrons, which preserves high efficiency. Moreover, even if a fraction of electrons is classified as other species, their low abundance ($\sim 0.3\%$) makes the impact on purity negligible.

With DCR = 0, background arises from correlated hits due to primary tracks, including Cherenkov photons produced in aerogel, and from secondaries generated in material. The excellent efficiencies and purities indicate that the pre-filtering of aerogel photons effectively suppresses the background from unscattered aerogel signal photons.

#### Performance with DCR = 1 MHz/mm$^2$

When considering the worst case scenario with a DCR of 1 MHz/mm$^2$, both efficiency and purity are systematically reduced. Nevertheless, within the full bRICH acceptance, efficiencies and purities remain above 80% below 4 GeV/$c$, with a momentum integrated purity and efficiency of about 90%. The largest losses appear below 1 GeV/$c$. This is expected, since the uniformly distributed in space and time DCR affects all tracks within the ±2 SPTR hit–track time matching window. Maintaining a SPTR no worse than 100 ps is thus crucial to prevent random clustering of background hits and to ensure optimal e-ID with the expected multiplicity and DCR.

#### Impact of photons produced upstream of the aerogel tiles

Slightly worse performances are achieved in the configuration in which gas photons emitted both upstream and downstream are detected relative to the configuration in which only downstream photons are detected for the considered central Pb-Pb events.

This is partly due to training limitations, since the variable electron cluster size within the same sector depending on the track entrance region in the bRICH vessel requires much more statistics to fully learn the topology of the electron clusters relative to the case where only photons produced downstream of the aerogel tiles are detected.

In addition, although larger clusters can occur for certain track entrance regions enabling the collection of all gas photons, the absence of any focusing optics causes upstream emitted photons to strike SiPMs at larger distances from the track, extending the cluster with sparse hits over a wider fiducial area. Extra hits in the peripheral regions of the clusters result in patterns also found for non-electron tracks due to background hits from other tracks or the SiPM DCR, thus affecting efficiency and purity.

Because of additional Rayleigh scattering in aerogel for photons emitted upstream of the tile, which must traverse the full thickness of the tile, these extra photons in Pb-Pb events provide little net benefit for electron identification. Therefore, the results shown here indicate that operating with only photons emitted downstream of the aerogel tiles and absorbing upstream photons seems to be the optimal design choice.

## 4.9 Dielectron efficiency vs $m_{\mathrm{ee}}$ and $p_{\mathrm{T,ee}}$

One of the main physics contributions of the bRICH in ALICE 3 is the reconstruction of dielectrons originating from virtual photons emitted throughout all stages of Pb–Pb

collisions. These electromagnetic probes enable measurements of the time evolution of the QGP temperature and studies of chiral symmetry restoration in the $\rho$–$a_1$ sector. As discussed in Section 1.9.1, these analyses require efficient double-differential $e^+e^-$ measurements in ($m_{ee}$, $p_{T,ee}$) with robust particle identification for $m_{ee} < 4$ GeV/$c^2$ and $p_{T,ee} < 3$ GeV/$c$, while keeping contamination, dominated by pions, as low as possible. Using the ALICE 3 iTOF and oTOF alone provides limited reach, effectively constraining the sensitivity to $m_{ee} \lesssim 0.7$ GeV/$c^2$ and $p_{T,ee} \lesssim 0.7$ GeV/$c$ even with the ideal 20 ps time resolution. The identification capabilities provided by the bRICH with aerogel rings and gas clusters are thus mandatory to achieve the target coverage.

In this section I present results obtained with a dedicated fast-simulation tool I developed to map the dielectron selection efficiency, requiring both $e^+$ and $e^-$ to be identified, as a function of ($m_{ee}$, $p_{T,ee}$) using the efficiency curves relative to central (0-5%) Pb-Pb at $\sqrt{s_{NN}} = 5.52$ TeV obtained in the full simulation framework.

To ensure coverage of dielectron pairs with one hard and one very soft electron, or with both electrons soft, which may not enter the bRICH acceptance, the iTOF and oTOF remain essential. I therefore quantified the performance of each subsystem alone, requiring both $e^+$ and $e^-$ to be identified by that single subsystem, to highlight intrinsic limitations, and then evaluated the combined performance by accepting pairs when each track is identified by at least one among bRICH aerogel, bRICH gas, iTOF, or oTOF, thereby illustrating their complementarity.

### 4.9.1 Simulation strategy

The simulation workflow used in this dielectron study includes the following steps.

- I scanned the dielectron phase space in ($m_{ee}$, $p_{T,ee}$) by generating virtual photons with fixed ($m_{ee}$, $p_{T,ee}$) and rapidity $y_{ee}$ sampled uniformly in $[-2, 2]$, with corresponding pseudorapidity $\eta_{ee}$. They were then decayed to $e^+e^-$ with standard two body kinematics, providing the $p_T$ and $\eta$ of each daughter electron.
- I propagated each daughter through the detectors accounting for the ALICE 3 baseline 2 T solenoidal magnetic field and evaluated whether the track entered the acceptance of the PID subsystems, namely the iTOF, oTOF and bRICH. If a track entered a subsystem I applied particle identification for that subsystem.
- For iTOF and oTOF I assumed the ALICE 3 target time resolution $\sigma_{TOF} = 20$ ps. I classified a track as an electron only when its measured time-of-flight, including the Gaussian spread due to $\sigma_{TOF}$, was consistent with the e hypothesis within

$3\,\sigma_{\mathrm{TOF}}$ and differed from the $\pi$ hypothesis by more than $3\,\sigma_{\mathrm{TOF}}$, independently of event multiplicity. This ideal TOF performance was chosen to best highlight the bRICH contribution to this physics channel.

- For the bRICH, I used the full-simulation single-electron efficiency curves for central (0–5%) Pb–Pb collisions at $\sqrt{s_{\mathrm{NN}}} = 5.52$ TeV with DCR = 1 MHz/mm$^2$ and SPTR = 100 ps, considering both aerogel and the gas option, and employing my XGBoost-based PID algorithms for aerogel and gas signals. For each track I drew a uniform random number in $[0, 1]$ and tagged the track as an electron when the number was smaller than the efficiency value at the track $p_{\mathrm{T}}$ and $\eta$.
- I evaluated the counts of correctly tagged events both at the single subsystem level, by requiring both $\mathrm{e}^+$ and $\mathrm{e}^-$ to be identified by the same subsystem, and at the combined level, by accepting pairs when each track was identified by at least one among bRICH aerogel, bRICH gas, iTOF, or oTOF. Counts were normalized to the accepted events to get the final efficiencies in each ($m_{\mathrm{ee}}$, $p_{\mathrm{T,ee}}$) bin.

For the bRICH, I tested both the reference trapezoidal photodetector layout and the rectangular $17 \times 18$ cm$^2$ module layout, using the aerogel-ring and gas-cluster information. For both module layouts, I modelled the aerogel response with the efficiency curves specifically obtained for the considered configuration, while for gas signals I first required the track to fall within a photodetector module, leaving tracks hitting regions beyond the module boundaries untagged. For tracks satisfying this geometric requirement, I applied the same gas-efficiency curves as in the trapezoidal layout.

### 4.9.2 Results

In the following I present dielectron efficiency results across ($m_{\mathrm{ee}}, p_{\mathrm{T,ee}}$), including the iTOF and oTOF only, the standalone contribution of the bRICH with the information on aerogel rings and gas clusters, and their combination to reach the target coverage. For the bRICH I compare the performance obtained with the trapezoidal photodetector module layout with that of the rectangular $17 \times 18$ cm$^2$ module layout, focusing on the associated efficiency losses and their kinematic dependence.

#### Dielectron efficiency with iTOF and oTOF

Fig. 4.60 shows the simulated dielectron pair efficiency as functions of $m_{\mathrm{ee}}$ and $p_{\mathrm{T,ee}}$ using TOF PID. The top-left panel requires both $\mathrm{e}^+$ and $\mathrm{e}^-$ identified by the iTOF. The top-right panel requires both identified by the oTOF. The bottom-left panel accepts

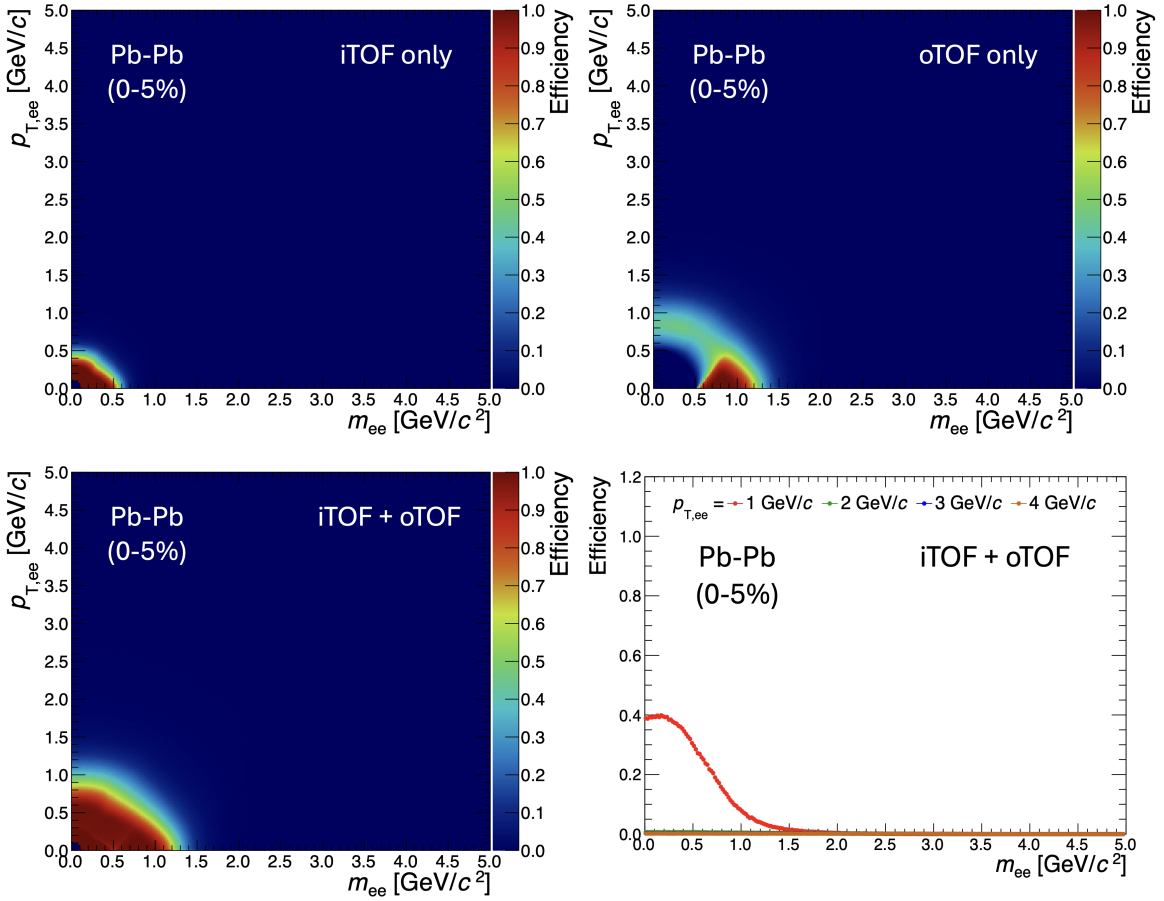


**Figure 4.60:** Simulated dielectron efficiency versus $m_{ee}$ and $p_{T,ee}$ for central (0–5%) Pb–Pb at $\sqrt{s_{NN}} = 5.52$ TeV. The top-left panel requires both $e^+$ and $e^-$ to be identified by the iTOF. The top-right panel requires both $e^+$ and $e^-$ to be identified by the oTOF. The bottom-left panel accepts pairs when each track is identified as an electron by either the iTOF or the oTOF. The bottom-right panel shows the corresponding projections for $p_{T,ee} = 1, 2, 3, 4$ GeV/$c$.

pairs when each track is identified as an electron by either the iTOF or the oTOF. The bottom-right panel reports the corresponding one dimensional efficiency curves for $p_{T,ee} = 1, 2, 3, 4$ GeV/$c$ for the OR selection. As expected, TOF systems alone provides useful coverage primarily in the region $m_{ee} \lesssim 0.7$ GeV/$c^2$ and $p_{T,ee} \lesssim 0.7$ GeV/$c$.

### Dielectron efficiency with bRICH aerogel rings and gas clusters

Figs. 4.61 and 4.62 show the contribution of the bRICH for the trapezoidal photodetector module layout and for the rectangular $17 \times 18$ cm$^2$ module layout, respectively. In each figure, the top-left panel requires both $e^+$ and $e^-$ identified by bRICH using aerogel only. The top-right panel requires both identified using gas clusters only. The middle-left panel accepts pairs when each track is identified by at least one among

bRICH aerogel, iTOF, or oTOF. The middle-right panel accepts pairs when each track is identified by at least one among bRICH aerogel, bRICH gas, iTOF, or oTOF. The bottom panels show the one dimensional efficiency for $p_{\mathrm{T,ee}} = 1, 2, 3$ and 4 GeV/$c$.

Considering aerogel only or gas only for the identification of both tracks, the bRICH extends the PID reach up to about 3 GeV/$c$ for $m_{\mathrm{ee}}$ and $p_{\mathrm{T,ee}}$ with aerogel and up to about 5 GeV/$c$ with gas. However, the region near $m_{\mathrm{ee}} \to 0$, especially at large $p_{\mathrm{T,ee}}$, remains poorly covered since the pairs in this region often include one hard and one soft electron, with the soft one failing to enter the bRICH acceptance. These soft electrons are efficiently recovered by iTOF and oTOF. Combining the iTOF, oTOF and bRICH thus ensures an almost symmetrical coverage in both $m_{\mathrm{ee}}$ and $p_{\mathrm{T,ee}}$.

Using both the aerogel ring and the gas cluster information is particularly effective below about 2 GeV/$c$ at the single electron level, where the two observables provide efficient and largely independent separation power. The 1D curves of the dielectron efficiency as a function of $m_{\mathrm{ee}}$ at fixed $p_{\mathrm{T,ee}}$ in Figs. 4.61 and 4.62 best highlight the strong impact of the gas information on the target $(m_{\mathrm{ee}}, p_{\mathrm{T,ee}})$ reach.

### Rectangular 17 × 18 cm² versus trapezoidal photodetector module layout

To quantify the performance loss with the rectangular module layout, Fig. 4.63 shows the ratios of the dielectron efficiencies obtained with the rectangular $17 \times 18$ cm$^2$ layout to those with the ideal trapezoidal layout, for the same set of selections described above.

From the ratio maps and curves, one observes a systematic efficiency reduction for both the aerogel and gas signals due to the extra dead regions within the trapezoidal frames housing each rectangular photodetector module relative to the ideal coverage of the trapezoidal module layout, as shown in Fig. 3.7. The nearly flat 2D ratio of about 74% in the gas only case is consistent, to first order, with the square of the rectangular photodetector module single track acceptance integrated over the full $\eta$ range covered by the bRICH, which is about 86%, since both $\mathrm{e}^+$ and $\mathrm{e}^-$ must be detected.

Nevertheless, combining iTOF, oTOF, bRICH aerogel, and bRICH gas information, an overall efficiency larger than 75% is observed in the full $(m_{\mathrm{ee}}, p_{\mathrm{T,ee}})$ range up to 5 GeV/$c^2$ and 4 GeV/$c$, respectively, for the rectangular $17 \times 18$ cm$^2$ module layout relative to the trapezoidal one. Both configurations provide the required PID capabilities for dielectron measurements. Since comparable purity is expected under the same operating conditions, and considering the advantages in the reduced overall SiPM area, modularity, and integration, these results indicate that the rectangular option is a robust and physically viable choice for dielectron studies despite its lower acceptance.

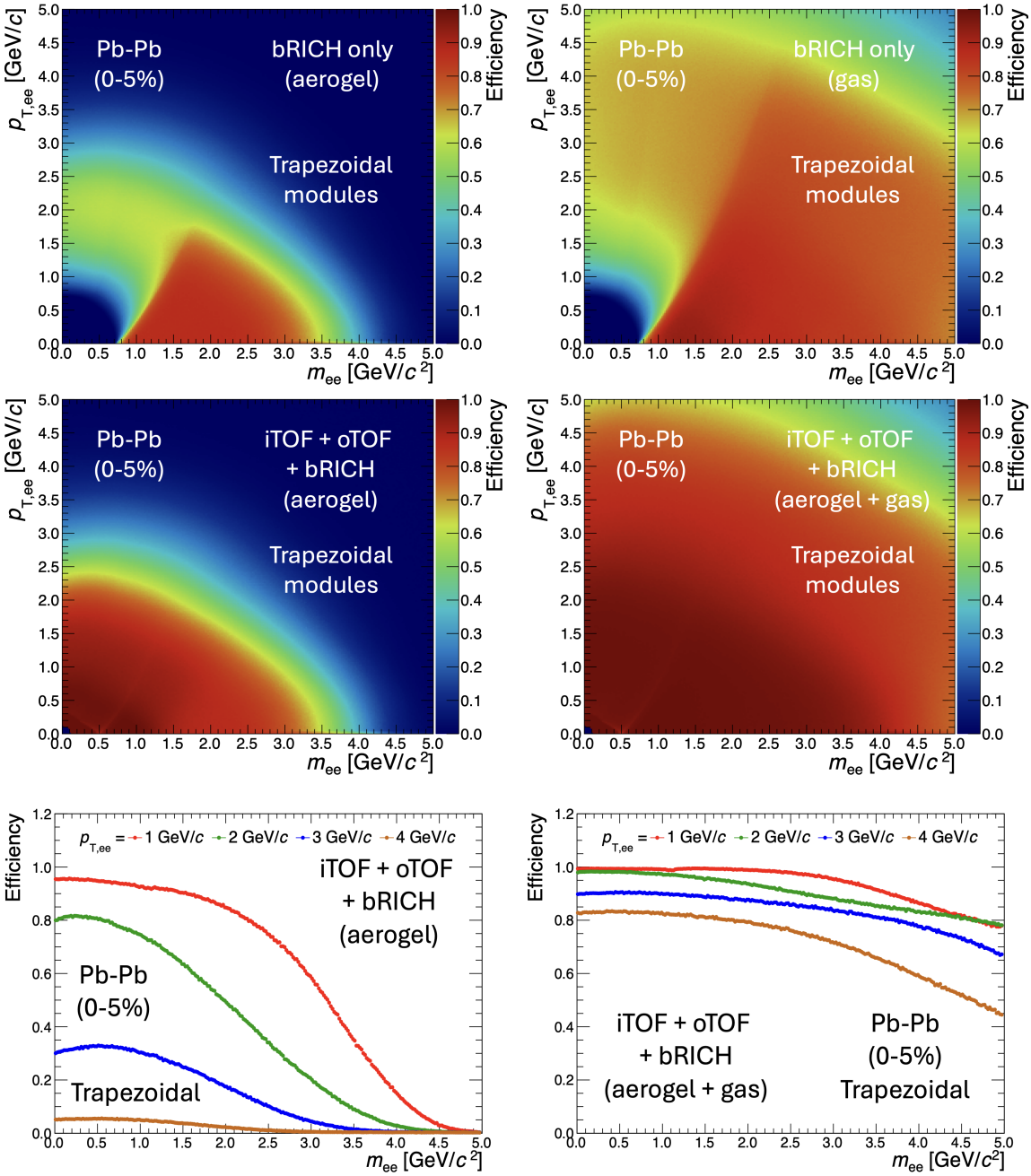


**Figure 4.61:** Simulated dielectron efficiency versus $m_{ee}$ and $p_{T,ee}$ for central (0–5%) Pb–Pb at $\sqrt{s_{NN}} = 5.52$ TeV assuming SPTR = 100 ps, DCR = 1 MHz/mm$^2$, trapezoidal photodetector modules and the bRICH vessel filled with $C_5F_{10}O$+$CO_2$. The top panels require both $e^+$ and $e^-$ identified by the bRICH using only the aerogel rings (left) and only gas clusters (right). The middle-left panel accepts pairs when each track is identified by at least one among bRICH aerogel, iTOF, or oTOF. The middle-right panel accepts pairs when each track is identified by at least one among bRICH aerogel, bRICH gas, iTOF, or oTOF. The bottom panels show the 1D projections for $p_{T,ee} = 1, 2, 3, 4$ GeV/$c$.

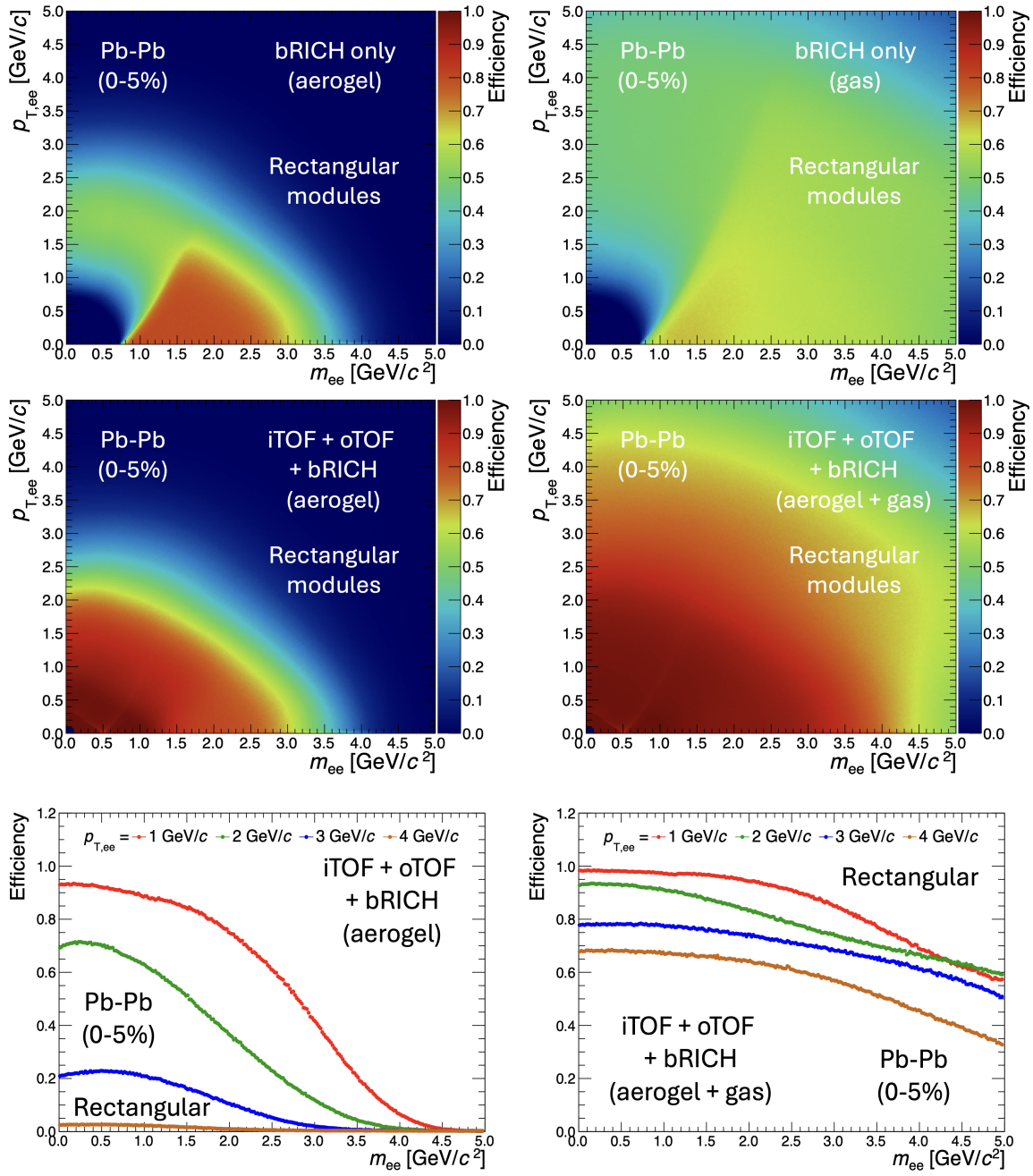


**Figure 4.62:** Simulated dielectron efficiency versus $m_{ee}$ and $p_{T,ee}$ for central (0–5%) Pb–Pb at $\sqrt{s_{NN}} = 5.52$ TeV assuming SPTR = 100 ps, DCR = 1 MHz/mm$^2$, trapezoidal $17 \times 18$ cm$^2$ modules and the bRICH vessel filled with $C_5F_{10}O$+$CO_2$. The top panels require both $e^+$ and $e^-$ identified by the bRICH using only the aerogel rings (left) and only gas clusters (right). The middle-left panel accepts pairs when each track is identified by at least one among bRICH aerogel, iTOF, or oTOF. The middle-right panel accepts pairs when each track is identified by at least one among bRICH aerogel, bRICH gas, iTOF, or oTOF. The bottom panels show the 1D projections for $p_{T,ee} = 1, 2, 3, 4$ GeV/$c$.

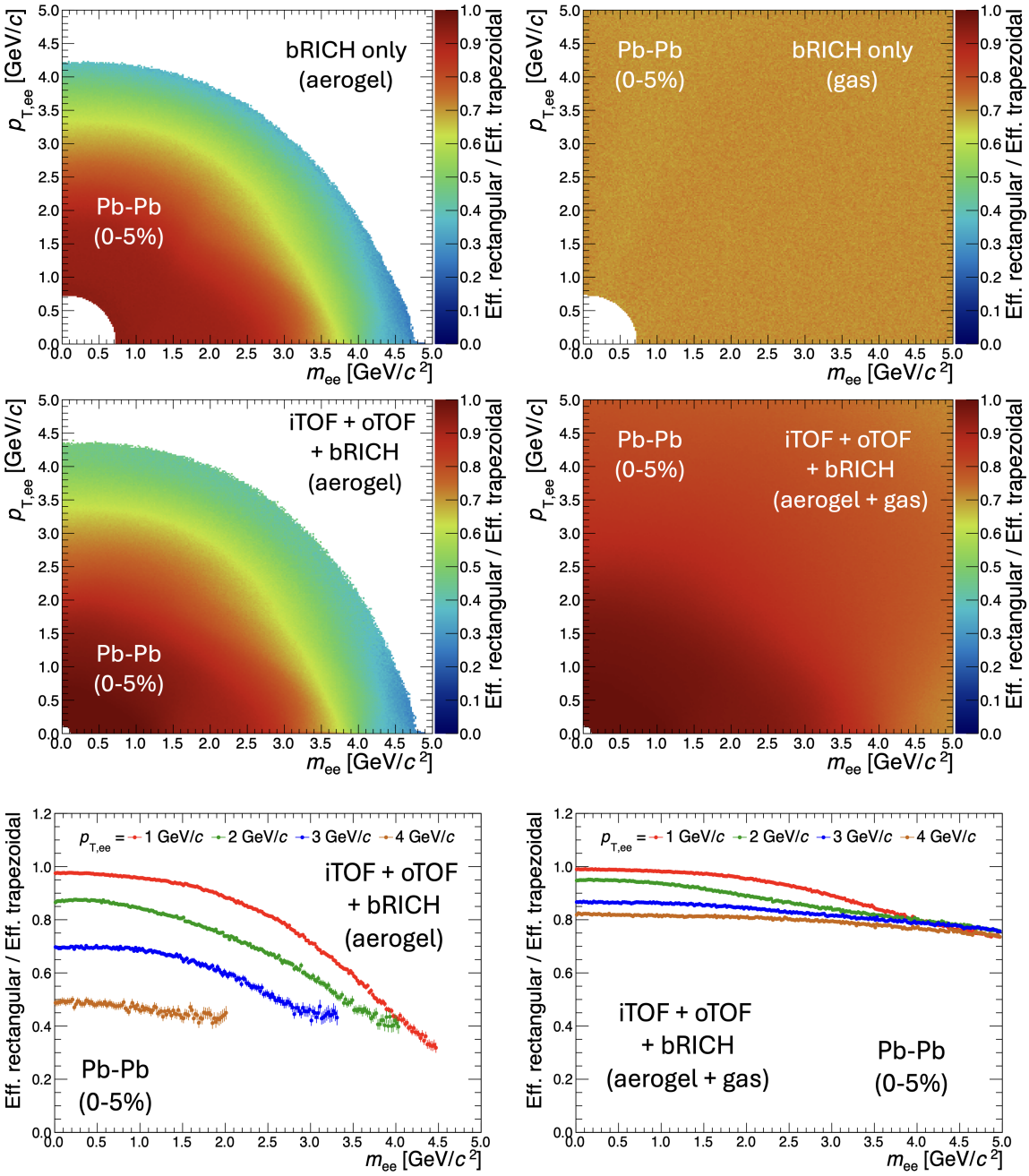


**Figure 4.63:** Ratios of the dielectron efficiency with the rectangular $17 \times 18$ cm$^2$ bRICH photodetector layout relative to that with the ideal trapezoidal layout, shown versus $m_{ee}$ and $p_{T,ee}$, for central (0–5%) Pb–Pb at $\sqrt{s_{NN}} = 5.52$ TeV assuming SPTR = 100 ps and DCR = 1 MHz/mm$^2$. The top-left panel requires both $e^+$ and $e^-$ identified by the bRICH using only the aerogel signal. The top-right panel requires both identified by the bRICH using gas clusters only. The middle-left panel accepts pairs when each track is identified by at least one among bRICH aerogel, iTOF, or oTOF. The middle-right panel accepts pairs when each track is identified by at least one among bRICH aerogel, bRICH gas, iTOF, or oTOF. The bottom panels show the 1D projections for $p_{T,ee} = 1, 2, 3, 4$ GeV/$c$.

## 4.10 $D^0 \to K^-\pi^+$ efficiency vs $p_T$ and $\eta$

A significant contribution of the bRICH to the ALICE 3 physics programme is the identification of decay products of high-$p_T$ hadrons, which is crucial, for instance, for measuring azimuthal correlations between heavy-flavour hadrons, such as $D^0\bar{D}^0$, as discussed in Section 1.9.3. These measurements require high $D^0$ purity up to and beyond $p_T = 4$ GeV/$c$, as indicated in the left panel of Fig. 1.14.

In this section I report a preliminary study of the $D^0$ efficiency in the decay channel $D^0 \to K^-\pi^+$ in pp collisions for the rectangular $17 \times 18$ cm$^2$ bRICH photodetector layout. The goal is to quantify the impact of the bRICH and its interplay with the iTOF and oTOF, which remain mandatory for kaon identification at momenta $p <$ 2 GeV/$c$, i.e. below the Cherenkov threshold in aerogel. For the results reported here, I performed particle identification using the bRICH probability cuts chosen to maximize the overall efficiency×purity for $\pi$/K separation.

To map the $D^0$ $(\eta, p_T)$ phase space, I generated $D^0$ events with the decay fixed to $K^-\pi^+$ and propagated the daughters through the ALICE 3 apparatus. I accepted events in which both $K^-$ and $\pi^+$ enter the bRICH, embedded the corresponding simulated hits with hits from a dataset of pp events to include the corresponding background, and then applied PID selections for the iTOF, oTOF, and bRICH systems.

For the TOF I assumed a target time resolution of $\sigma_{TOF} = 20$ ps and classified a track as $\pi$ or K when its measured time-of-flight was consistent with that hypothesis within $3\,\sigma_{TOF}$ and differed from the alternative hypothesis by more than $3\,\sigma_{TOF}$. For the bRICH I used my XGBoost-based PID algorithm trained on pp at $\sqrt{s} = 14$ TeV. I evaluated the $D^0$ efficiency as the fraction of parent $D^0$ for which both daughters were identified, either by the same subsystem or by at least one of them.

Fig. 4.64 shows the reconstructed Cherenkov-angle distributions for the daughter $K^-$ and $\pi^+$ as a function of momentum using the Hough transform, together with the parent $D^0$ identification efficiency as a function of $\eta$ and $p_T$ for the bRICH alone, iTOF+oTOF, and the combined iTOF+oTOF+bRICH configuration.

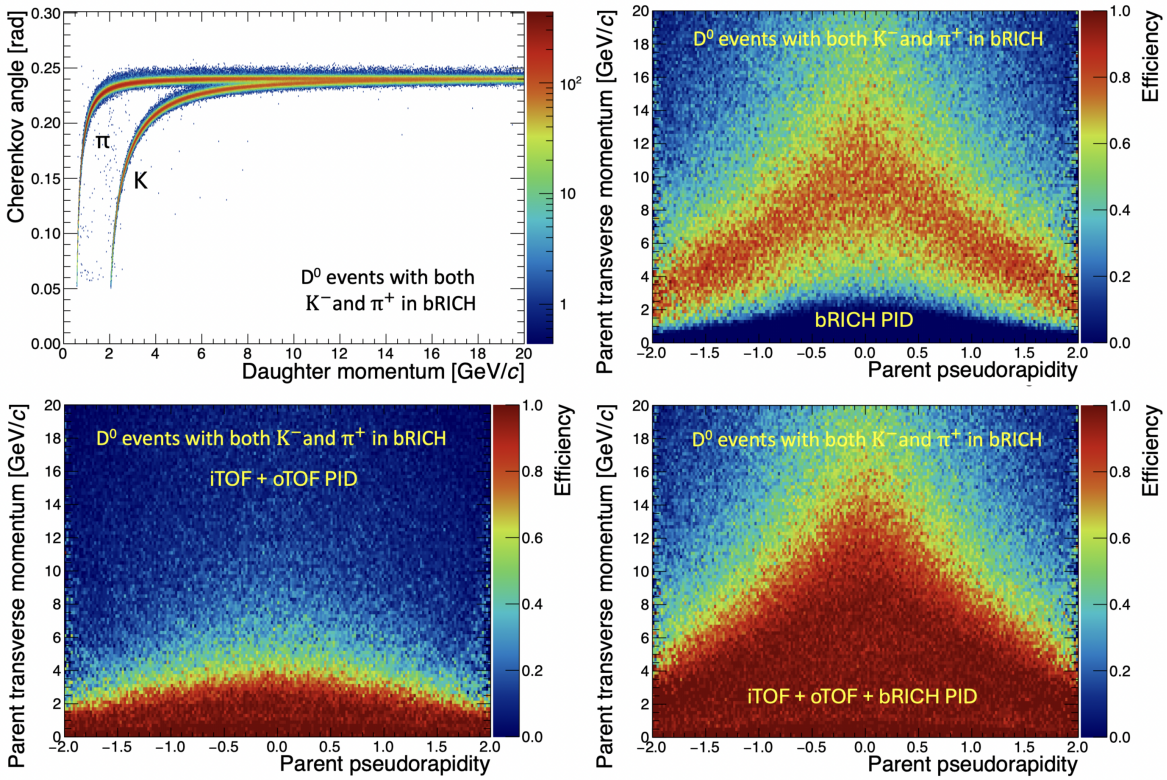


**Figure 4.64:** $D^0 \to K^-\pi^+$: reconstructed Cherenkov-angle distributions for the daughter tracks as a function of momentum using the Hough transform (top left), together with the resulting parent $D^0$ identification efficiency versus $\eta$ and $p_T$ for bRICH alone (top right), iTOF+oTOF (bottom left), and the combined iTOF+oTOF+bRICH configuration (bottom right).

As expected, the bRICH alone yields limited overall efficiency due to events where the daughter $K^-$ has momentum below the aerogel threshold, $p < 2$ GeV/$c$. The iTOF and oTOF identify these tracks efficiently, providing high overall $D^0$ efficiency up to $p_T \simeq 3.5$–4 GeV/$c$ at $\eta = 0$, with lower reach at larger $|\eta|$. Only the combination with the bRICH, which extends coverage to high-momentum pions and kaons, enables efficient $D^0$ identification up to about 14–15 GeV/$c$ at $\eta = 0$ and about 4 GeV/$c$ as $|\eta| \to 2$ with minimum contamination, as required for the correlation measurements.

Although a slight degradation is expected in the high-multiplicity environment of Pb–Pb collisions, these results highlight the strong contribution that the proposed bRICH can offer to the ALICE 3 physics programme.

# Chapter 5

# SiPM ageing in ALICE 3

Due to the limited radiation tolerance of the SiPMs, it is crucial to ensure their operation within a DCR safety limit of approximately 1 MHz/mm$^2$ at the expected fluences of units of $10^{11}$ MeV $n_{eq}$/cm$^2$ in the bRICH to guarantee stable and reliable detector performance throughout the ALICE 3 lifetime. This limit is derived from a combined analysis of the SiPM recovery characteristics and the operational constraints of the reference front-end, the DENEB ASIC. In particular, the conversion times of the TDCs, the available data bandwidth, and their impact on pattern recognition and particle identification performance have been considered. Operating within this DCR threshold is therefore essential to maintain the efficiency and accuracy of the detector, ultimately determining the achievable physics reach of the system.

In this context, I performed characterization measurements of Hamamatsu SiPM arrays irradiated up to fluences of $10^{12}$ MeV $n_{eq}$/cm$^2$ aimed at quantifying the scaling of DCR with fluence and its mitigation through cooling and annealing. Based on these results, I constructed a SiPM ageing model describing the progressive DCR increase with integrated luminosity and its mitigation under various operating conditions.

## 5.1 SiPM DCR measurements

In order to develop a realistic scaling model for the DCR as a function of fluence, and a bRICH SiPM ageing model for the reference devices used in my design study, accounting for both cooling and annealing, I performed dedicated characterization measurements. Specifically, I extrapolated the DCR of five $8 \times 8$ Hamamatsu S13361 series arrays made of $2 \times 2$ mm$^2$ SiPMs irradiated with neutrons at the TRIGA reactor at JSI in Ljubljana [120], up to fluences of $10^{12}$ MeV $n_{eq}$/cm$^2$. Measurements were per-

formed down to -60°, with annealing up to 70°C. The target operation and annealing temperatures were achieved using a Climats EXCAL 1423-HA climatic chamber [121]. The specifications of the tested SiPM arrays and their annealing history, the measurement procedures and DCR extrapolation, and the resulting DCR scaling and SiPM ageing models are detailed in the following.

### 5.1.1 Tested SiPM arrays

Five $8 \times 8$ Hamamatsu S13361-2050AE-08 arrays [90] made of $2 \times 2$ mm$^2$ SiPMs with a microcell pitch of 50 µm and mounting epoxy resin were tested. In the following, the arrays are identified by their serial numbers: S438, S439, S440, S441, and S442. Arrays S441 and S442 were not irradiated to serve as references, while arrays S439, S438, and S440 were irradiated to fluences of $10^{10}$, $10^{11}$, and $10^{12}$ MeV $n_{eq}/cm^2$, respectively.

### 5.1.2 History of irradiated arrays

Documenting the post-irradiation history of the arrays is essential to account for passive annealing and to quantify the impact of subsequent active annealing.

Arrays S439, S438, and S440 were irradiated to their target fluences at the TRIGA reactor at JSI in Ljubljana [120] in July 2024. One week later, the first set of measurements on all five arrays was performed at room temperature ($T = 25$°C). For the three irradiated samples, a ∼20% reduction in DCR relative to the immediately post-irradiation condition is already expected from the literature [122].

Between September and October 2024, arrays S439, S438 and S440 were kept at room temperature for about one month during additional characterization and beam tests, a period over which a 40–50% DCR decrease relative to the immediately post-irradiation state is expected. The arrays were then stored in a freezer at -20°C, where annealing is expected to be negligible, until February 2025, when I performed a second DCR measurement campaign, scanning the temperature range from 20°C down to -40°C using a Climats EXCAL 1423-HA climatic chamber [121].

Subsequently, S439, S438, and S440 were again kept at -20°C until May 2025, when I repeated the DCR measurements prior to active annealing at 70°C for a total of 611 h. DCR measurements were taken after 135 h and again at the end of the 611 h anneal, after which the arrays were returned to -20°C for storage. In this final campaign, temperatures were extended down to -60°C for S439 and to -40°C for S438 and S440.

### 5.1.3 Measurement method

The set-up for characterization measurements is shown in Fig. 5.1. The arrays were placed inside the climatic chamber mounted on dedicated PCBs providing access to the individual SiPMs with cables routed through a sealed feedthrough and connected to an iseg SHR Series High Precision HV Source Measuring Unit [123]. For each array and operation temperature, I measured the reverse current $I_{\mathrm{rev}}$ of each SiPM as a function of the reverse bias voltage $V_{\mathrm{bias}}$.

The measured current $I_{\mathrm{rev}}$ accounts for both the leakage current $I_{\mathrm{leak}}$ and the bulk current $I_{\mathrm{dark}}$ according to the relation:

$$I_{\mathrm{rev}} = I_{\mathrm{leak}} + I_{\mathrm{dark}} \tag{5.1}$$

For the determination of the breakdown voltage $V_{\mathrm{bd}}$ of each measured channel of the considered arrays at each temperature I used the method of the Inverse Logarithmic Derivative [124]. From the measured I–V curves, I estimated the leakage component $I_{\mathrm{leak}}$ by fitting the pre-breakdown region with a constant, and I obtained $I_{\mathrm{dark}}$ by subtraction relative to the measured $I_{\mathrm{rev}}$. I then computed the DCR at $V_{\mathrm{ov}}$ as:

$$\mathrm{DCR}\,(1 + \mathrm{CN}) = \frac{I_{\mathrm{dark}}}{q\,G}, \tag{5.2}$$

where $q$ is the elementary charge and $G$ is the gain at the operating overvoltage $V_{\mathrm{ov}}$. The factor $(1 + \mathrm{CN})$ accounts for correlated-noise contributions in addition to primary dark counts. For the measurements reported in the following, I did not disentangle $(1 + \mathrm{CN})$ from the DCR, and I report only their product $\mathrm{DCR}\,(1 + \mathrm{CN})$. For all my calculations, I used the nominal gain of the considered arrays at the operation overvoltage [90], and I assumed that the gain associated with each dark count is independent of fluence. This assumption proved to be reasonable for all tested arrays and operating temperatures, except for array S440 irradiated to $10^{12}$ MeV $\mathrm{n_{eq}/cm^2}$ operated at room temperature. In that case, the very high DCR causes pile-up of multiple dark count events occurring in the same microcell before it fully recharges, reducing the effective gain and consequently leading to an underestimation of the DCR.

### 5.1.4 Results

The main results on the scaling of DCR with fluence and its mitigation through cooling and annealing based on my measurements are detailed in the following subsections.

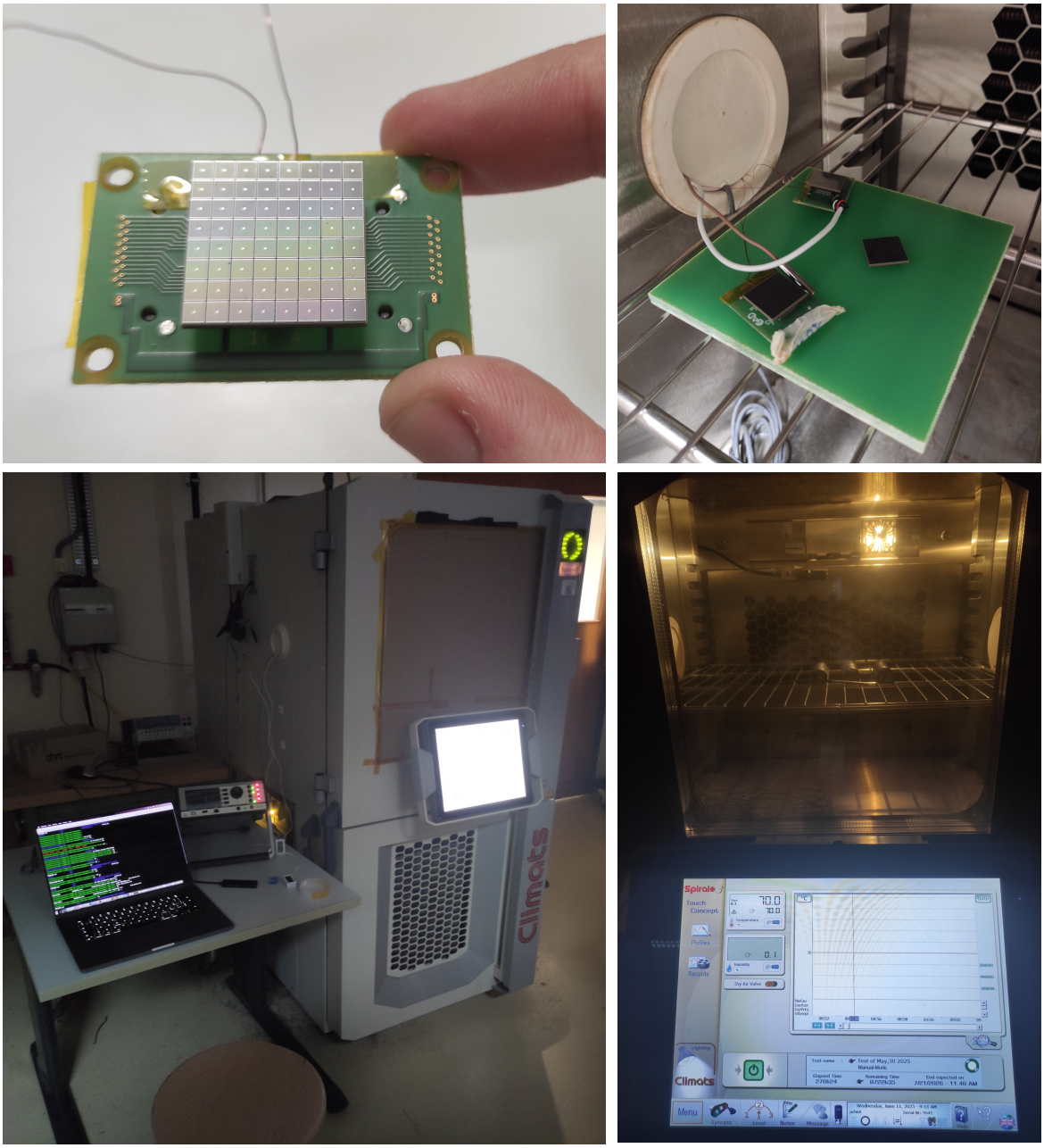


**Figure 5.1:** Setup for SiPM DCR studies with cooling and annealing. Top left: SiPM array mounted on a dedicated PCB providing access to individual channels. Top right: Arrays placed inside the climatic chamber, with SiPM signal and temperature-sensor routed outside the chamber through a sealed feedthrough. Bottom left: Full setup with climatic chamber and HV source-measure unit during data-taking. Bottom right: Annealing of the irradiated arrays at 70°C in the chamber.

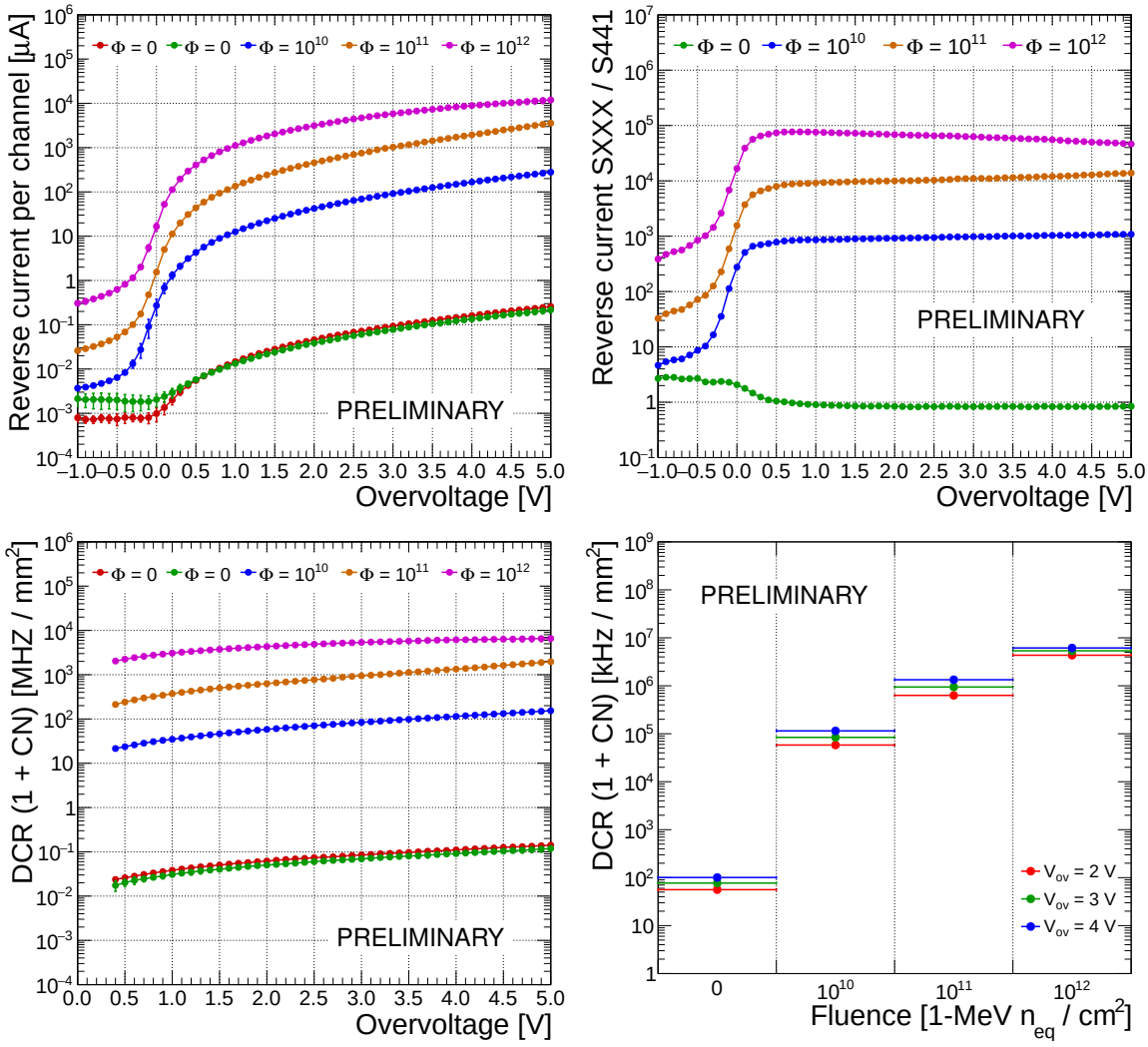


**Figure 5.2:** Mean reverse current per channel for the five tested arrays (top left), reverse current ratio of each array to the non-irradiated S441 (top right) and extrapolated DCR(1+CN) (bottom left) as a function of the overvoltage for data taken at room temperature one week after irradiating arrays S439, S438, and S440. The bottom-left plot shows a comparison of the extrapolated DCR(1 + CN) at the different fluences at overvoltages of 2 V, 3 V and 4 V.

### DCR scaling with fluence

Fig. 5.2 shows the mean reverse current per channel for the five tested arrays, the reverse current ratio of each array to the non-irradiated S441, and the extrapolated DCR(1 + CN) as a function of the $V_{ov}$ . The data were taken at room temperature in July 2024, one week after irradiating S439, S438, and S440. A comparison of the extrapolated DCR(1 + CN) at different fluences at $V_{ov}$ of 2, 3, and 4 V is also shown.

Relative to the non-irradiated reference, I observed increases in the mean reverse cur-

rent by a factor of $10^3$ for the sample irradiated to $10^{10}$ MeV $n_{eq}/cm^2$, by $10^4$ for $10^{11}$ MeV $n_{eq}/cm^2$, and by $5 \times 10^4$ for $10^{12}$ MeV $n_{eq}/cm^2$. As expected, the response is linear between $10^{10}$ and $10^{11}$, while at $10^{12}$ the increase is only a factor of five relative to $10^{11}$ instead of the expected ten. As discussed in Section 5.1.3, this deviation is likely due to pile-up of successive dark counts in the same microcell before full recharge, which lowers the effective gain. Consequently, the DCR obtained with the procedure in Section 5.1.3 is underestimated at $10^{12}$ for operation at 25°C.

The two non-irradiated samples, S441 and S442, feature the same bulk current $I_{dark}$, while a difference in the leakage current $I_{leak}$ by about a factor of two is observed. The resulting DCR(1+CN) is between 60 kHz/mm$^2$ and 120 kHz/mm$^2$ for operation at overvoltages between 2 V and 4 V.

The corresponding measured DCR(1+CN) values for the arrays irradiated at $10^{10}$ and $10^{11}$ MeV $n_{eq}/cm^2$ span the intervals 6–12 and 60–120 MHz/mm$^2$, respectively. These results show that SiPM operation at room temperature is not feasible in the ALICE 3 radiation environment. Cooling and annealing are therefore mandatory.

### DCR mitigation with cooling

Fig. 5.3 shows the mean reverse current per channel as a function of both the bias voltage and the overvoltage and the extrapolated DCR(1+CN) as a function of the overvoltage for the non-irradiated array S441 with measurements taken between -20°C and 20°C. The resulting DCR(1+CN) curves at overvoltages between 2 V and 4 V are also plotted as a function of temperature.

The corresponding plots for array S439, irradiated to $10^{10}$ MeV $n_{eq}/cm^2$, are shown in Fig. 5.4. The data were taken in May 2025 after room-temperature annealing and after 611 h at 70°C in the climatic chamber, with operation down to -60°C.

Independently of the fluence, a decrease in the breakdown voltage consistent with the nominal 0.054 mV/°C was observed. A significant reduction of the DCR, by up to two orders of magnitude, was observed approaching temperatures below -20°C. To quantify it, I fitted the DCR(1+CN) curves versus temperature with the function:

$$\mathrm{DCR}(1+\mathrm{CN}) = \alpha\, 2^{-(T-\beta)/T_{1/2}}\,, \tag{5.3}$$

where $\beta$ is fixed to the maximum operating temperature in the dataset and $\alpha$ is the corresponding DCR(1 + CN) at $T = \beta$, while $T_{1/2}$ denotes the temperature drop required to halve the DCR. I found $T_{1/2}$ values of about 8.8°C for the SiPMs of the two non-irradiated arrays and about 10.7°C for the arrays irradiated to $10^{10}$ MeV $n_{eq}/cm^2$

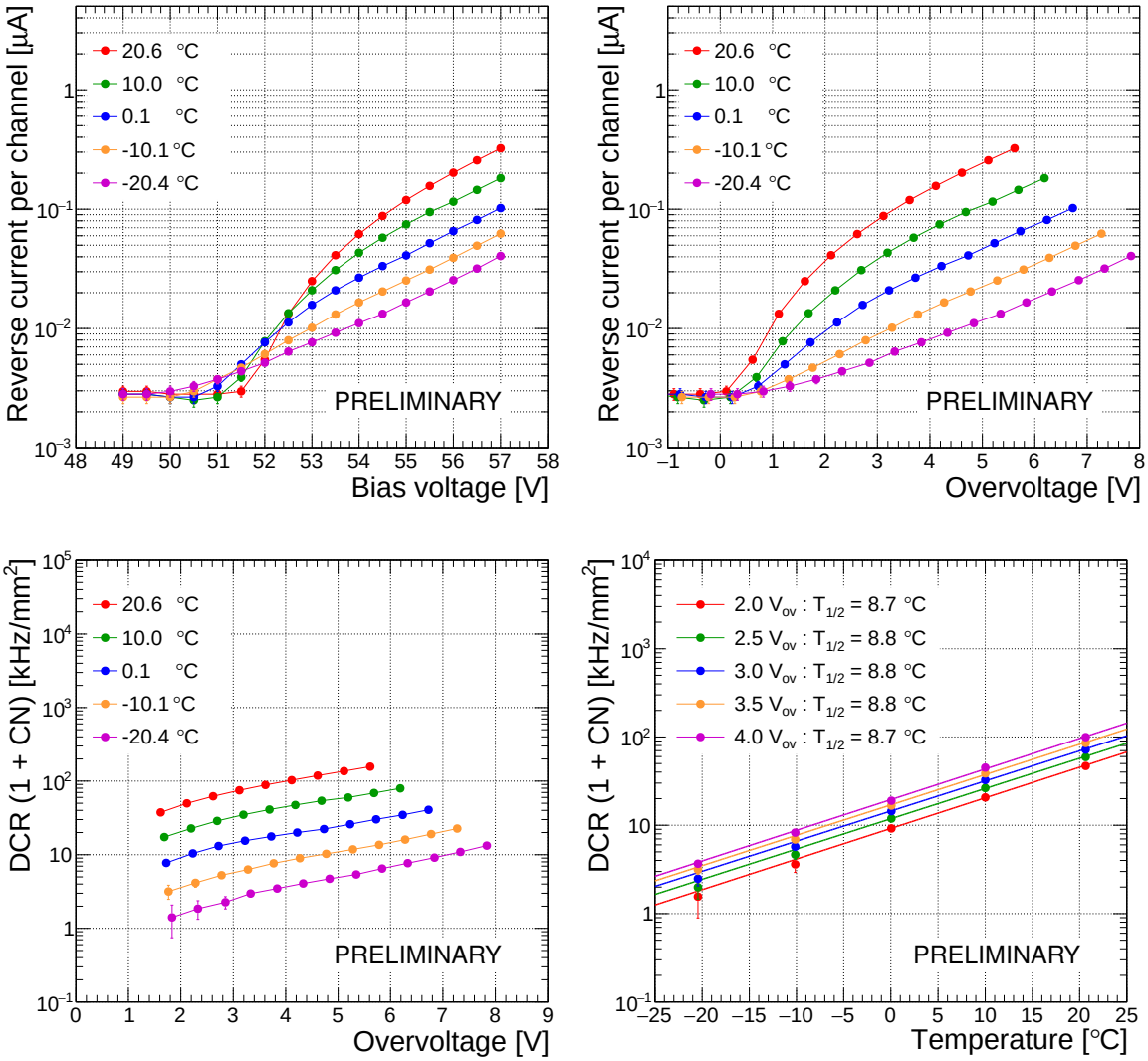


**Figure 5.3:** Mean reverse current per channel as a function of both the bias voltage (top left) and the overvoltage (top right) and extrapolated DCR(1+CN) as a function of the overvoltage (bottom left) for the non-irradiated array S441 between -20°C and 20°C. The bottom-right panel shows the resulting DCR(1+CN) curves at $V_{ov}$ between 2 and 4 V plotted versus temperature.

and $10^{11}$ MeV $n_{eq}/cm^2$. These values are almost independent on the considered operating overvoltage. The observed increase by about 2°C in $T_{1/2}$ for the irradiated arrays is consistent with the literature. These values indicate a reduction in DCR(1 + CN) by about a factor of 167 for the non-irradiated arrays and 65 for the irradiated arrays when operated at -40°C instead of 25°C. Further mitigation is achieved operating the SIPMs at even lower temperatures. For the irradiated arrays, operation at -60°C yields a reduction by about a factor of 234 relative to 25°C.

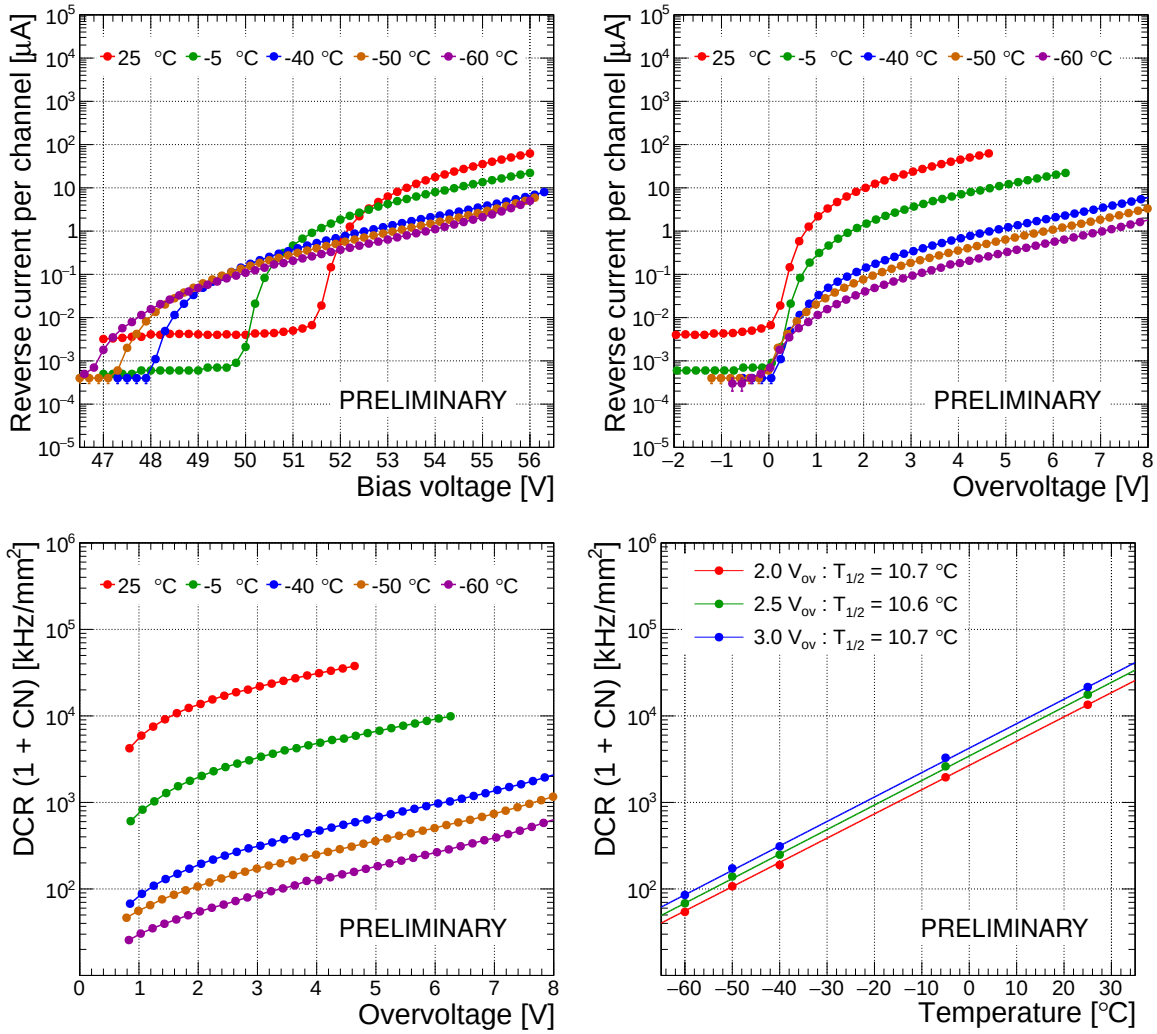


**Figure 5.4:** Mean reverse current per channel as a function of both the bias voltage (top left) and the overvoltage (top right) and extrapolated DCR(1+CN) as a function of the overvoltage (bottom left) for the array irradiated to $10^{10}$ MeV $n_{eq}/cm^2$ after room-temperature annealing and after 611 h at 70°C in the climatic chamber between -60°C and 25°C. The bottom-right panel shows the resulting DCR(1+CN) curves at $V_{ov}$ between 2 and 3 V plotted versus temperature.

### DCR mitigation with annealing

Fig. 5.5 shows a comparison of the extrapolated DCR(1 + CN) for the tested SiPM arrays at the different fluences at overvoltages of 2 V and 3 V for operation at 25°C and -40°C for data collected throughout the annealing history outlined in Section 5.1.2.

I measured DCR(1 + CN) down to 300 kHz/mm$^2$, 3 MHz/mm$^2$, and 30 MHz/mm$^2$ for arrays irradiated to $10^{10}$, $10^{11}$, and $10^{12}$ MeV $n_{eq}/cm^2$, respectively, when cooled to -40°C and operated at an overvoltage of 3 V. At an overvoltage of 2 V, the corre-

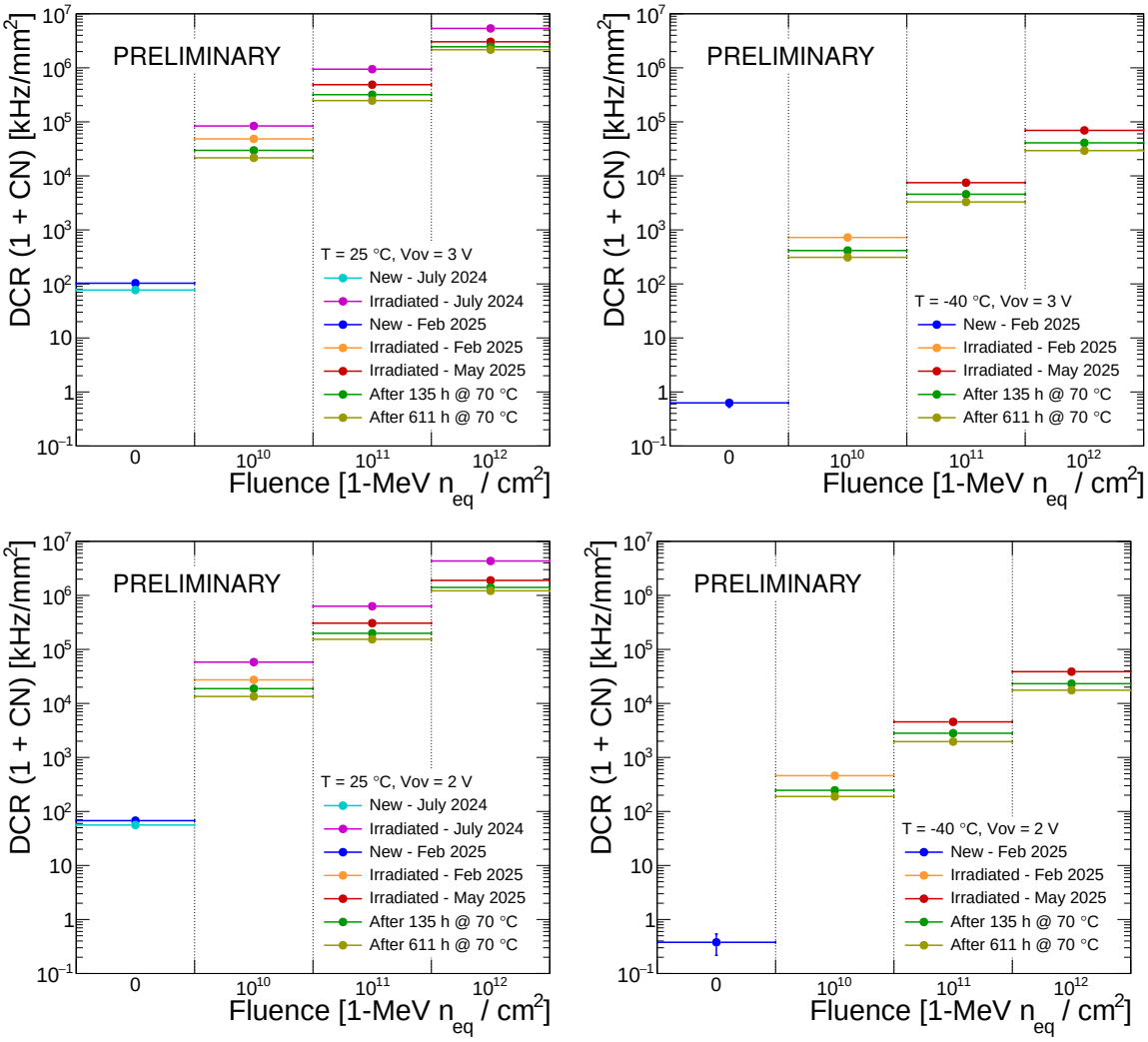


**Figure 5.5:** Comparison of the extrapolated DCR(1+CN) for the tested SiPM arrays at the different fluences at overvoltages of 2 V (bottom) and 3 V (top) for operation at 25°C (left) and -40°C (right) for data collected throughout the annealing history outlined in Section 5.1.2.

sponding values are approximately 200 kHz/mm$^2$, 2 MHz/mm$^2$, and 20 MHz/mm$^2$.

It is worth noting that the linear scaling of DCR(1 + CN) with fluence is recovered for the array irradiated to $10^{12}$ MeV $n_{eq}$/cm$^2$ at -40°C, in contrast to room temperature where the pile-up of dark counts in the same microcell reduces the effective gain.

Fig. 5.6 shows, for each fluence, the ratios of the extrapolated DCR(1 + CN) at successive annealing steps, normalized to the value measured one week after irradiation, with the SiPMs annealed at room temperature, and immediately before the 70°C annealing, evaluated at 25°C, -5°C, and -40°C for overvoltages of 2 V and 3 V.

I observed a reduction to about 60% of the value measured immediately before the

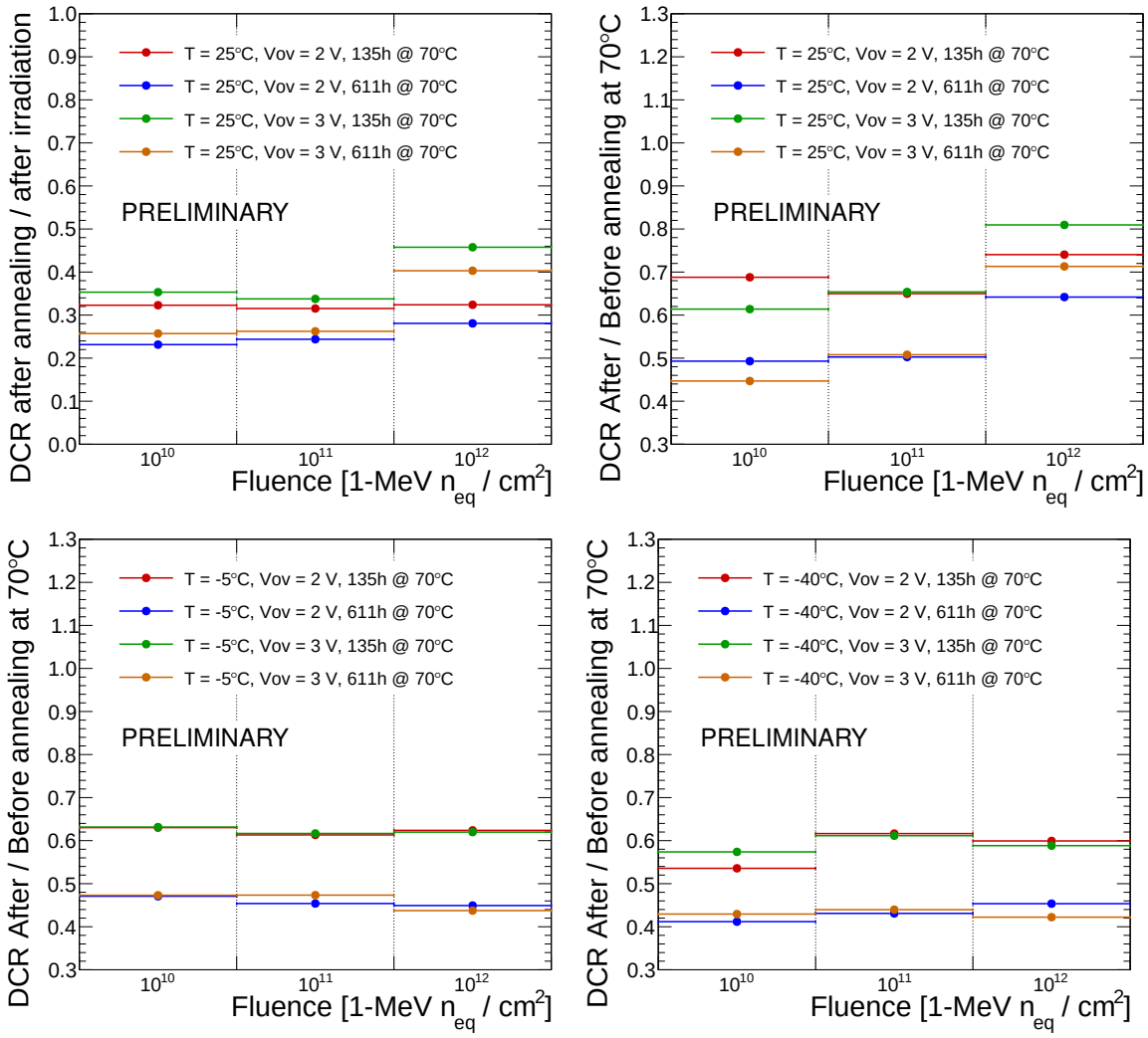


**Figure 5.6:** Ratios of the extrapolated DCR(1 + CN) for each tested fluence at successive annealing steps, normalized to the value measured one week after irradiation, with the SiPMs annealed at room temperature, evaluated at 25°C (top left), and immediately before the 70°C annealing, evaluated at 25°C (top right), -5°C (bottom left), and -40°C (bottom right) for overvoltages of 2 V and 3 V.

70°C anneal after 135 hours at 70°C, and to about 45% after 611 hours at 70°C, with no significant dependence on overvoltage, operating temperature, or fluence. The only exception is the array irradiated to $10^{12}$ MeV $n_{eq}/cm^2$ at 25°C, as discussed above.

The effectiveness of DCR mitigation decreases with the annealing time because annealable defects are removed. Spontaneous annealing at room temperature, with a small additional contribution from storage at -20°C, already reduced the DCR(1 + CN) to between 60% and 50% of the value measured one week after irradiation.

Finally, it must be observed that the values measured one week after irradiation are

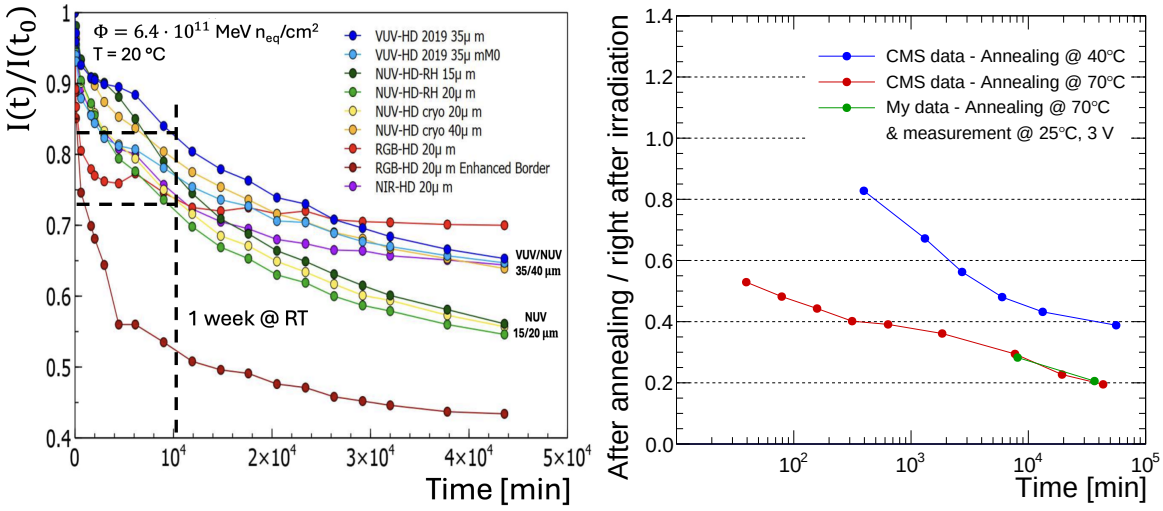


**Figure 5.7:** Left: Dark current decrease for several FBK SiPMs annealed at room temperature as a function of time, normalised to the value immediately after irradiation. Adapted from [122]. Right: Mean DCR(1 + CN) reduction extrapolated from my measurements during annealing at 70°C as a function of time, relative to the state immediately after irradiation, compared with results reported for Hamamatsu SiPMs based on the same technology [125].

underestimated relative to those immediately after irradiation, due to passive annealing. This effect is well documented in the literature [122] and is illustrated in the left panel of Fig. 5.7, where the dark current of several FBK SiPMs decreases to about 75% to 85% after one week at room temperature. Taking 80% as a reference, the DCR reduction I measured after annealing at 70°C, when referred to the state immediately after irradiation, is consistent with results reported in the literature for other Hamamatsu SiPMs based on the same technology, as shown in the right panel of Fig. 5.7. For this comparison, I assumed that the defects that annealed spontaneously during the extended room-temperature storage would have annealed in a much shorter time if the arrays had been placed at 70°C immediately after irradiation.

All these measurements show that DCR(1 + CN) decreases to about 30% of the value measured immediately after irradiation after 135 hours at 70°C (about 6 days), and to about 20% after 611 hours at 70°C (about 25 days).

From these data, a long-term DCR(1+CN) annealing limit around 10% can be foreseen. For my ALICE 3 bRICH studies, this is useful to develop ageing models that account for annealing during the months of LHC stops between data-taking periods.

### 5.1.5 DCR scaling model with fluence

On the basis of the measurement results discussed in the previous section, I developed a simple DCR scaling model with fluence, temperature and overvoltage. My baseline model is based on data collected at -40°C. The model allows the prediction of the SiPM DCR after collecting a fluence $\Delta\Phi$ for operation at temperature $T$ and overvoltage $V_{\mathrm{ov}}$ using the following equation:

$$\mathrm{DCR}\,(\Phi, T, V_{\mathrm{ov}}) = [\mathrm{DCR}\,(\Phi = 0, T = \text{-}40°\mathrm{C}, V_{\mathrm{ov}}) + \alpha_{\Phi}\ \Phi] \cdot\ 2^{-(T-40°\mathrm{C})/T_{1/2}} \tag{5.4}$$

where $\mathrm{DCR}\,(\Phi = 0, T = -40°\mathrm{C}, V_{\mathrm{ov}})$ is the measured DCR for the non-irradiated arrays operated at $-40°$C at the considered overvoltage $V_{\mathrm{ov}}$ and $T_{1/2} \approx 10.8°$C is the corresponding measured temperature drop required to halve the DCR for the arrays after irradiation. The coefficient $\alpha_{\Phi}$ was extracted as the slope of a linear fit of the measured DCR$(1 + \mathrm{CN})$ versus fluence at fixed $V_{\mathrm{ov}}$, after correcting the data for the expected reduction due to annealing prior to measurement. To avoid underestimating the actual DCR, I adopted a conservative approach and treated $(1 + \mathrm{CN})$ as fully contributing to the dark counts. I obtained $\alpha_{\Phi} \approx 110$ kHz/mm$^2$ per $10^9$ MeV $\mathrm{n_{eq}}$/cm$^2$ at $V_{\mathrm{ov}} = 3$ V and $\alpha_{\Phi} \approx 73$ kHz/mm$^2$ per $10^9$ MeV $\mathrm{n_{eq}}$/cm$^2$ at $V_{\mathrm{ov}} = 2$ V.

The DCR increase $\Delta$ DCR for an increase $\Delta\Phi$ in the fluence is then given by:

$$\Delta\ \mathrm{DCR}\,(\Phi, T, V_{\mathrm{ov}}) = \alpha_{\Phi}\ \Delta\Phi \cdot\ 2^{-(T-40°\mathrm{C})/T_{1/2}} \tag{5.5}$$

Fig. 5.8 shows my model predictions for the DCR as a function of fluence from $10^9$ to $10^{12}$ MeV $\mathrm{n_{eq}}$/cm$^2$ for operation at -40°C and -60°C at overvoltages of 2 V and 3 V. The figure also shows the extrapolated long-term annealing limits at 20°C and 70°C, assumed to reach 40% and 10% of the values measured immediately after irradiation.

## 5.2 bRICH SiPM ageing model in ALICE 3

From the DCR scaling model discussed above, I developed a SiPM ageing model to account for the progressive increase of the bRICH SiPM DCR during operation with the increasing integrated luminosity and its mitigation using annealing.

The ALICE 3 baseline monthly operation schedule for LHC Run 5 is shown in Fig. 5.9. It includes pp data taking lasting five to seven months per year. Each year a dedicated one-month heavy-ion period follows. Long technical stops are scheduled between the end of one year and the start of the next. Shorter technical stops of about one week each are expected within the data-taking period.

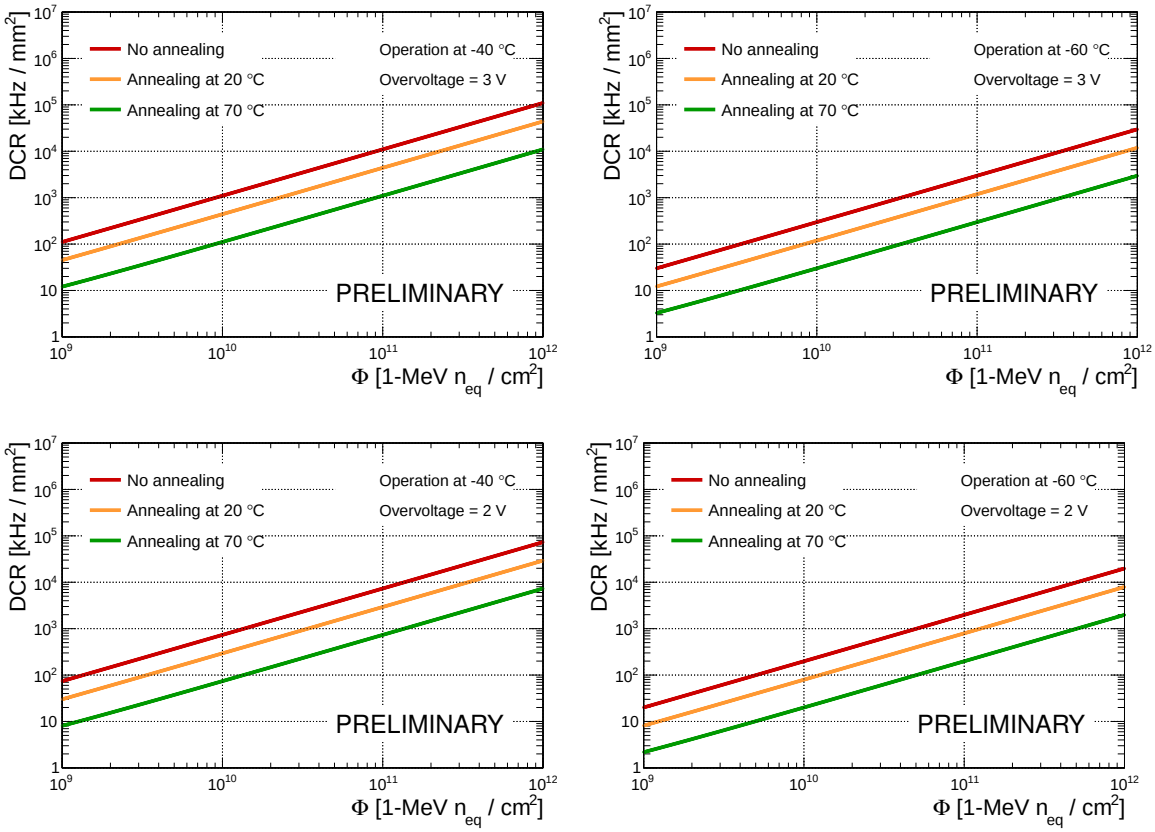


**Figure 5.8:** Model predictions for the DCR as a function of fluence from $10^9$ to $10^{12}$ MeV $n_{eq}/cm^2$ for SiPM operation at -40°C (left) and -60°C (right) at overvoltages of 3 V (top) and 2 V (bottom). The extrapolated long-term annealing limits at 20°C and 70°C are also shown.

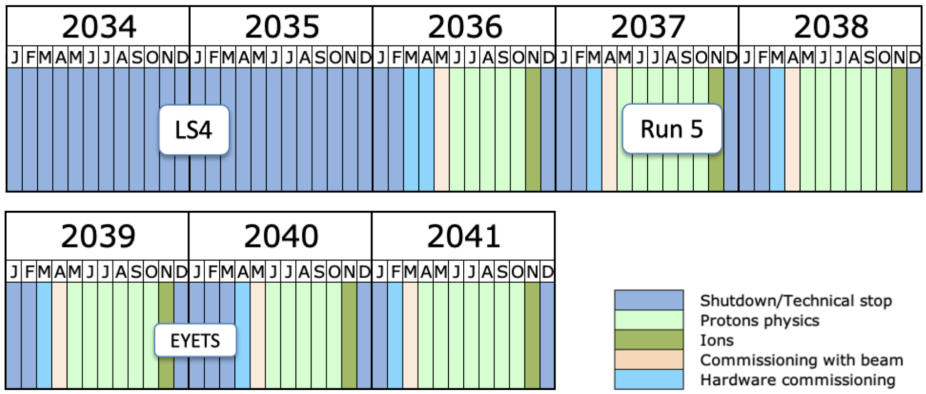


**Figure 5.9:** ALICE 3 baseline monthly operation schedule during LHC Run 5.

For my SiPM ageing studies, I considered the ALICE 3 layout without the ECal and with a reduced magnet radius, as discussed in Section 1.10. Table 5.1 summarizes the expected Total Ionizing Dose (TID) and the corresponding 1 MeV $n_{eq}/cm^2$ fluence

corresponding to expected Non-Ionizing Energy Loss (NIEL) at the target Run 5 luminosities and maximum interaction rate for pp and Pb-Pb collisions, based on simulations from the ALICE 3 radiation load group.

| System | $\mathcal{L}^{\text{month}}$ | $\mathcal{L}^{\text{Run5}}$ | Max interaction rate (MHz) | TID (rad) | NIEL (1 MeV $n_{eq}/cm^2$) |
|---|---|---|---|---|---|
| pp | 0.5 $fb^{-1}$ | 18 $fb^{-1}$ | 24 | $1.7\times10^4$ | $7.5\times10^{11}$ |
| Pb-Pb | 5.6 $nb^{-1}$ | 33.6 $nb^{-1}$ | 0.093 | $2.5\times10^2$ | $1.1\times10^{10}$ |

**Table 5.1:** Expected TID and NIEL at the target Run 5 luminosities and maximum interaction rate for pp and Pb-Pb collisions resulting from simulation studies by the ALICE 3 radiation load group.

My ageing model is based on the following assumptions:

- Fluence accumulates uniformly during pp and Pb–Pb data taking. The total fluence expected by the end of Run 5 is distributed across the corresponding data-taking months, and the DCR increase for each step is given by Eq. 5.5.
- During LHC shutdowns between consecutive years and during technical stops within data taking (three one-week stops), the bRICH SiPMs are annealed by forward biasing them through the electronics of the bRICH module.
- For annealing at 70°C, short anneals during technical stops mitigate about 70% of the incremental damage accumulated since the previous anneal, leaving a 30% residual DCR. Long-term anneals in the months corresponding to the LHC shutdowns mitigate about 90% of the incremental damage, leaving a 10% DCR residual relative to the state after the previous long-term anneal.

Fig. 5.10 shows the predictions for the integrated luminosity assuming a 24 MHz interaction rate during the whole pp period, the corresponding 1 MeV $n_{eq}/cm^2$ NIEL at the bRICH SiPMs, and the expected DCR for operation at -40°C with $V_{ov} = 3$ V and annealing at 70°C. For comparison, the expected DCR assuming operation only during the Pb-Pb period is also shown.

Both Table 5.1 and Fig. 5.10 show that most of the SiPM damage comes from pp data taking and that, without additional mitigation, the DCR would exceed the baseline 1 MHz/$mm^2$ bRICH safety level. The pp contribution is almost twenty times larger than that from Pb-Pb alone, where cooling and annealing would keep the DCR always below the baseline 1 MHz/$mm^2$ bRICH safety level.

Due to ALICE 3 commissioning, operating at a pp interaction rate that increases with time rather than fixed at the target 24 MHz is also being considered, with 1 MHz in

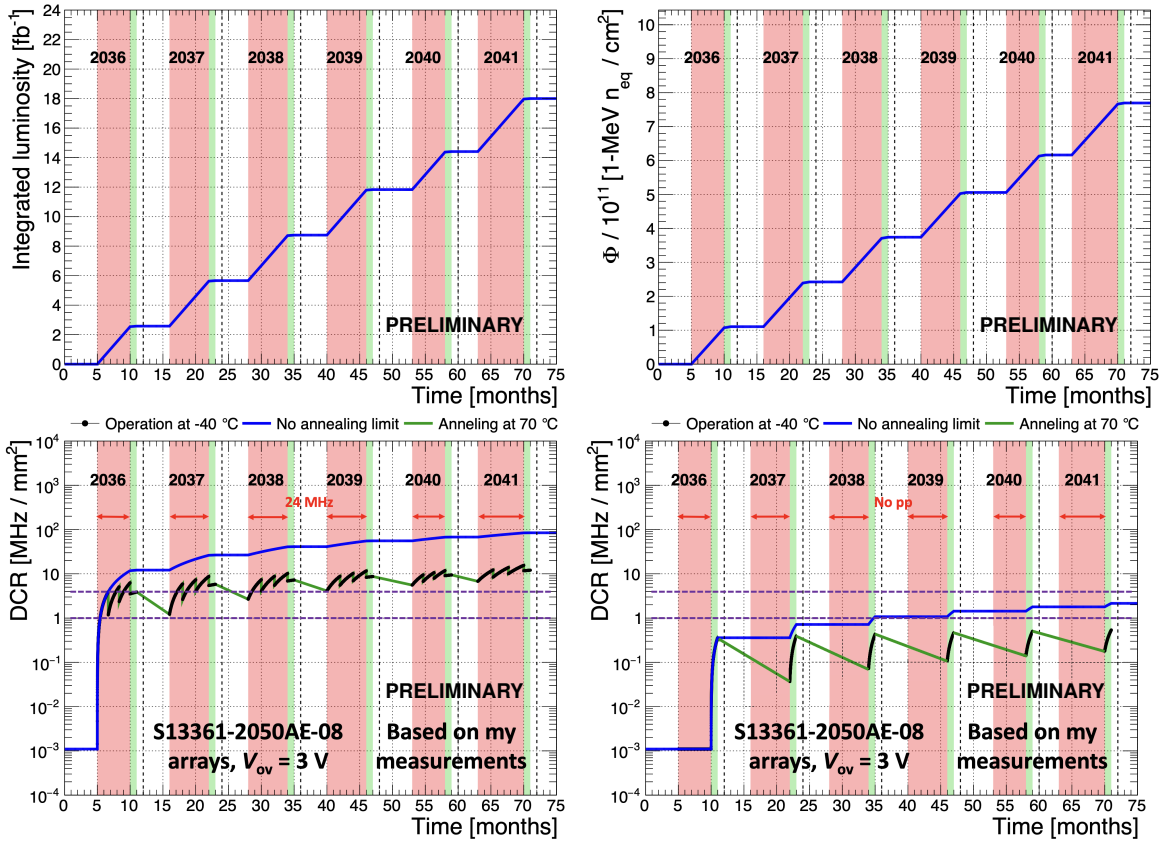


**Figure 5.10:** Predictions for the integrated luminosity assuming a 24 MHz interaction rate during the whole pp period (top left), the corresponding 1 MeV $n_{eq}/cm^2$ NIEL at the bRICH SiPMs (top right), and the expected DCR for operation at -40°C with $V_{ov} = 3$ V and annealing at 70°C (bottom left). The expected DCR for operation only during the Pb-Pb period is also shown (bottom right).

the first year, 6 MHz in the second, and 24 MHz in the remaining operational years. Fig. 5.11 shows my SiPM ageing projection for operation at -40°C with $V_{ov} = 2$ V and 3 V under this scenario. The plots show a significantly lower DCR in the first years, with values below the 1 MHz/mm$^2$ bRICH safety limit, ensuring safer operation during the corresponding Pb-Pb periods. Operating at $V_{ov} = 2$ V yields a DCR reduction of about 30% relative to the 3 V baseline at the cost of a reduced PDE.

A significant DCR reduction can be achieved by operating the SiPMs at a lower temperature relative to the baseline -40°C. The bottom panels of Fig. 5.11 also show my ageing projection for operation at -60°C with $V_{ov} = 3$ V and 2 V, and annealing at 70°C. Although this temperature is not compatible with the baseline microchannel bi-phase $CO_2$ cooling, requiring a different implementation of cooling, a DCR reduction by about a factor of 4 is expected relative to the baseline operation at -40°C.

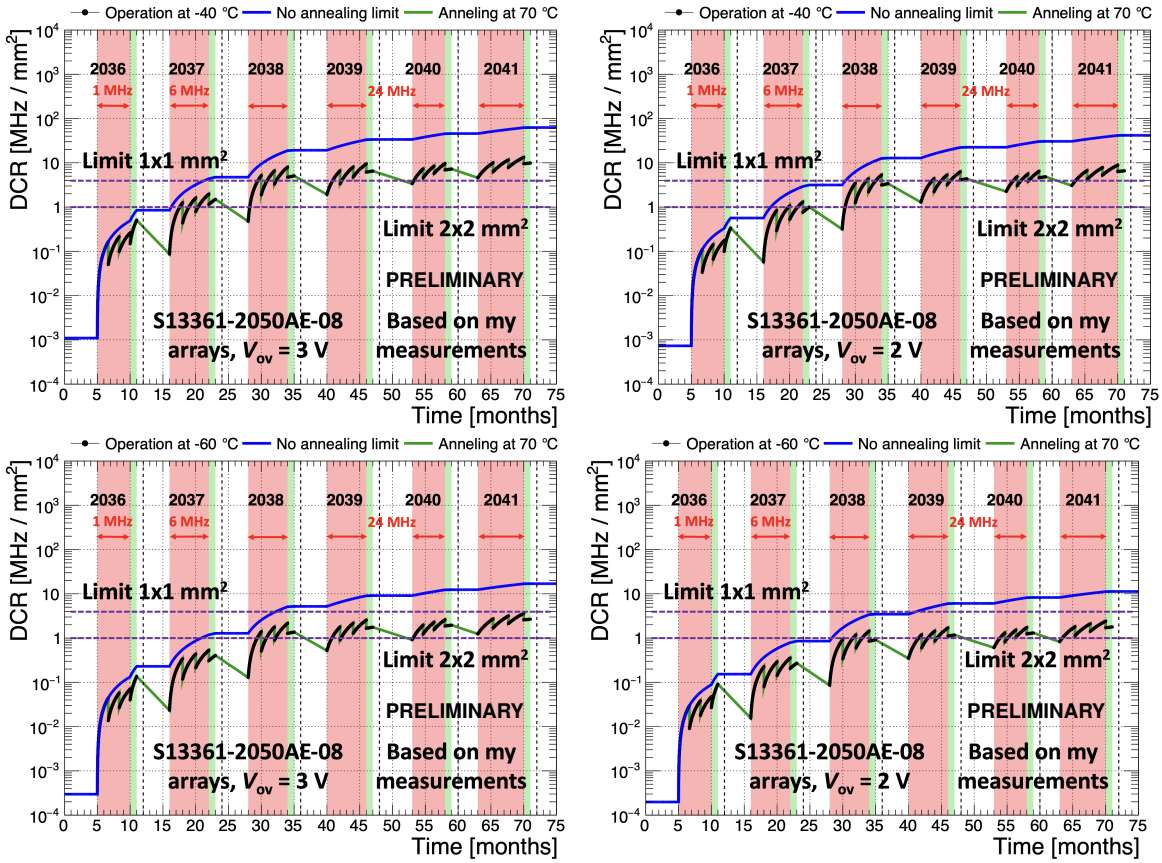


**Figure 5.11:** SiPM ageing projection for operation at -40°C (top) and -60°C (bottom) with $V_{ov}$ = 3 V (left) and 2 V (right), and annealing at 70°C assuming a pp interaction rate of 1 MHz in the first year, 6 MHz in the second, and 24 MHz in the remaining operational years.

A further and faster mitigation of radiation-damage effects could be achieved by annealing the SiPMs at temperatures higher than the reference 70°C by increasing the forward-bias voltage applied to the SiPMs. Annealing at temperatures up to 150°C, as considered in ongoing studies for the future ePIC dual RICH (dRICH) detector, can cure up to 97% of the radiation-damage effects [126]. However, despite the encouraging results in terms of DCR mitigation, the risks, including potential damage to the SiPM modules and documented alteration of the protective resin with a consequent reduction of the overall PDE, are not negligible and must be addressed properly.

Replacing the baseline $2 \times 2$ mm$^2$ SiPMs with $1 \times 1$ mm$^2$ SiPMs coupled to light concentrators, as discussed in Section 3.7, raises the reference limit from 1 MHz/mm$^2$ (i.e., 4 MHz per $2 \times 2$ mm$^2$ channel) to 4 MHz/mm$^2$, extending the bRICH lifetime by a further factor of four. Therefore, accounting also for operation at temperatures below the baseline -40°C and for annealing at temperatures above 70°C, the combination of these options provides additional margin to mitigate the expected DCR.

# Chapter 6

# Performance validation in beam tests

Various prototypes of the proposed bRICH configuration were successfully tested on beam at the CERN-PS T10 facility between 2022 and 2025. In this context, I actively contributed to the planning of all the beam tests, the design and the characterisation of the prototypes, the data-taking, and performed the full data analysis and simulation.

The results of these measurements validated the baseline design bRICH specifications in terms of expansion gap, aerogel thickness and pixel size, as well as the aerogel refractive index to achieve the target photon yield, angular resolution and separation power in the required momentum intervals. From characterization measurements of the tested aerogel tiles, I found an unexpected systematic gradient of the refractive index along the tile depth leading to a natural focusing effect improving the angular resolution. Then, I retrieved a single photon angular resolution of about 4.2 mrad at the Cherenkov angle saturation value of 241.5 mrad with 2 cm thick aerogel tiles featuring a refractive index of 1.03 and an expansion gap of about 23 cm with the baseline $2 \times 2$ mm$^2$ pixel size, yielding the target $3\sigma$ $\pi$/K separation at 10 GeV/$c$ momentum with as few as ten detected photons per ring. The measurements also demonstrated that excellent DCR background suppression is achieved using timing. All the prototypes included SiPM arrays mounted along the beamline coupled with various window materials, which allowed probing the possibility of achieving charged-track time resolutions better than 70 ps with a detection efficiency better than 99%. Measurements also validated the proposed gas-based option for e-ID up to 4 GeV/$c$.

This chapter is structured as follows. In Section 6.1 I summarize the features of the CERN-PS T10 beam line. In Section 6.2 I describe the different tested bRICH prototypes. In Section 6.3 I present the general Cherenkov angle reconstruction strategy used across all setups. Finally, the main results from the 2022-2023 and 2024–2025 campaigns are discussed in Sections 6.4 and 6.5, respectively.

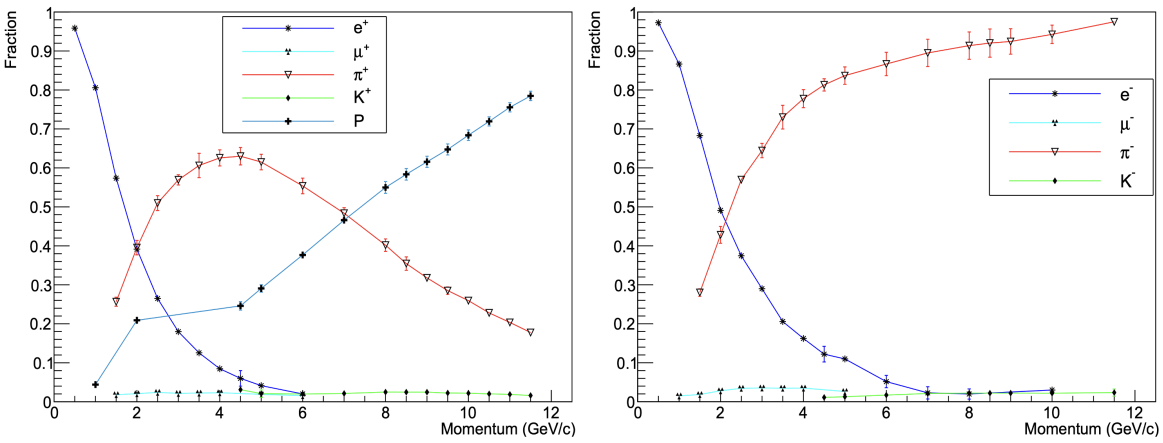


**Figure 6.1:** T10 beam composition at the end of the beam line for positive (left) and negative (right) particles over the momentum range from 0.5 GeV/$c$ to 11.5 GeV/$c$. Adapted from [129].

## 6.1 CERN-PS T10 beam line

The CERN-PS T10 beam line is a secondary beam line at the CERN East Area. It is driven by 24 GeV/$c$ protons slow-extracted from the Proton Synchrotron (PS) over a period of 0.4 s, with such cycles flexibly scheduled as needed within the overall PS supercycle. The beam impinges on a beryllium/tungsten target producing secondary particles [127]. The target consists of a 10 mm diameter and 200 mm length beryllium rod, housed in a hollow aluminium cylinder with an inner diameter of 11 mm and an outer diameter of 20 mm. It is capped on the upstream side with a 3 mm-thick aluminium cap and on the downstream side with a 3 mm-thick tungsten cap. The T10 line consists of a series of magnets transporting secondary charged particles produced at a vertical production angle of 35 mrad to the experimental zone [128]. Collimators along the beam line allow for flexible selection of the beam intensity and momentum spread around the central momentum defined by the magnet settings.

The reference beam composition at the end of the line for positive and negative particles in the full momentum range, from 0.5 GeV/$c$ to 11.5 GeV/$c$, is shown in Fig. 6.1 [129]. Contributions from minority particle species, such as antiprotons, are omitted. The positive beam is dominated by electrons at low momenta, by pions at intermediate momenta, and by protons at the higher momenta. The negative beam is dominated by electrons at low momenta and by pions at higher momenta.

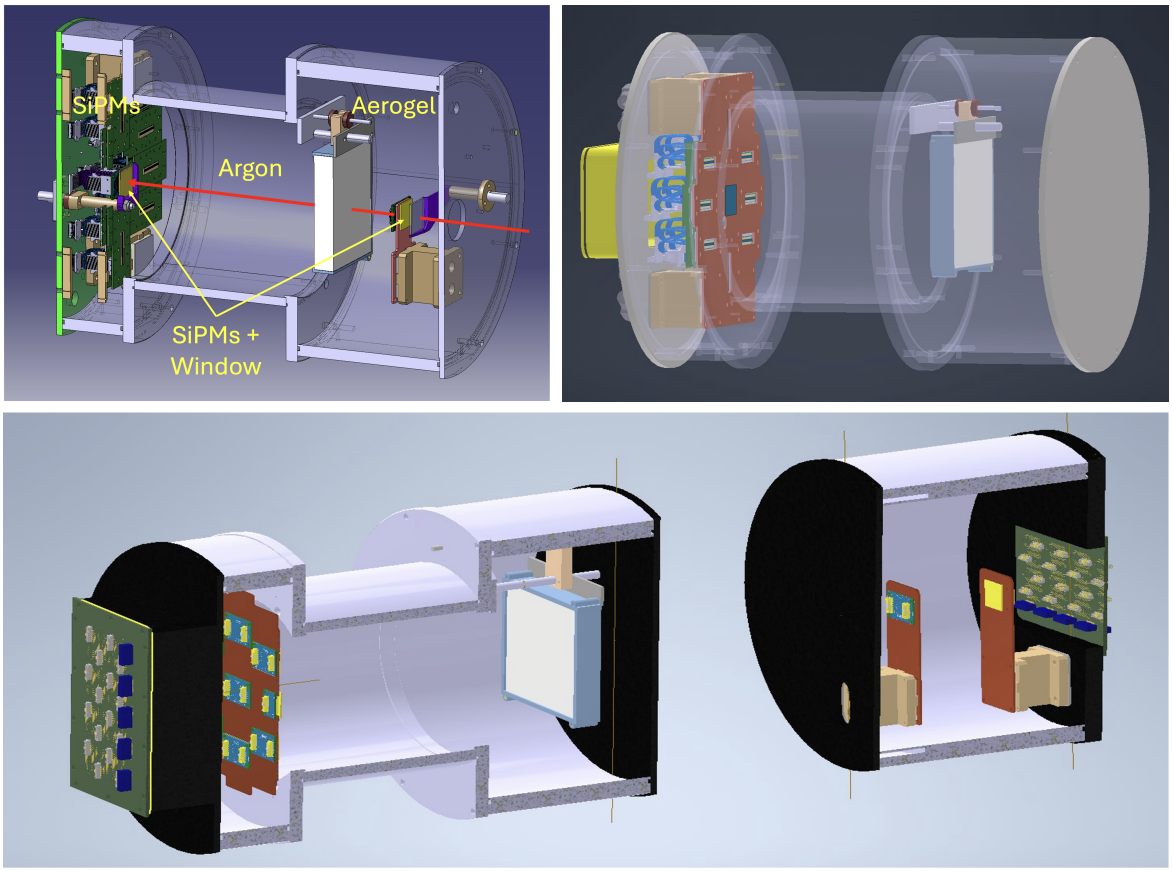


**Figure 6.2:** Schematic of the 2022-2023 prototype (top) and the 2024-2025 prototype (bottom).

## 6.2 The ALICE 3 RICH prototypes

Two prototypes of the proposed proximity-focusing bRICH configuration were successfully tested at the CERN-PS T10 beam line since 2022 [130, 131, 132, 133]. In the following they are referred to as the 2022-2023 prototype and the 2024-2025 prototype, respectively. The corresponding schematic diagrams are shown in Fig. 6.2. All tested prototypes were based on a cylindrical vessel housing hydrophobic aerogel tiles from Aerogel Factory Co, Ltd. separated by an expansion gap, with thickness varying from 23 to 24 cm in the different prototypes, flushed with a dry gas from a copper plate equipped with SiPM arrays from Hamamatsu mounted on custom printed circuit boards (PCBs). Additional arrays for charged-particle timing were installed along the beam line and mounted on dedicated copper plates with custom PCBs in the same vessel as the aerogel tile (2022-2023) or in an additional vessel placed upstream relative to the aerogel one (2024-2025). The SiPM arrays were cooled down to -5°C to reduce the DCR. The data were collected with a complete chain of front-end and readout electronics based on the Petiroc 2A ASIC [134] for the 2022-2023 prototype and the

Radioroc 2 ASIC [135] coupled with a picoTDC [136] for the 2024-2025 prototype. For charged-particle tracking, external tracker modules based on plastic scintillating fibers coupled with SiPM arrays with Petiroc 2A front-end were used. The details on the tested aerogel tiles and SiPM arrays, the cooling system, gas flushing, the tracking system and the front end and readout electronics are reported in the following.

### 6.2.1 Tested aerogel tiles

Various $11 \times 11\,\mathrm{cm}^2$ aerogel tiles were tested with different refractive indices and thicknesses. The main datasets were taken using tiles with $n = 1.03$ and $t = 2\,\mathrm{cm}$ (LEC4-1b, LEC4-2a, LEC6-1a, LEC6-2b). Additional runs included a 2 cm tile with $n = 1.04$ (LEC12-6), two 1 cm tiles with $n = 1.0299$ and 1.0320 (AG23V002 and AG23V004), and a monolithic dual-layer tile of 1 cm + 1 cm with $n = 1.0300$ and 1.0328 (A2407CE).

Prior to the beam tests, I characterised the optical properties of the tiles in terms of transmittance, transmission length, Rayleigh scattering length, absorption length, and the refractive index chromatic dispersion and homogeneity. These measurements were crucial for the interpretation and validation of beam test results with simulations.

### 6.2.2 Transparency characterization measurements

I measured the linear transmittance in the wavelength interval between 200 nm and 900 nm using an Agilent 900 External Diffuse Reflectance Accessory (DRA) [137] integrating sphere installed in an Agilent Cary 4000 UV-Vis spectrophotometer [138]. From the measured forward (or linear) transmittance I extracted the transmission length $\Lambda(\lambda)$ by inverting Eq. 2.18 using the thickness of each tile for the path length. I then performed an Extended Hunt fit [89, 139] to extract the corresponding Rayleigh scattering length $\Lambda_\mathrm{S}(\lambda)$ and absorption length $\Lambda_\mathrm{A}(\lambda)$, assuming the $\lambda$ dependence discussed in Section 2.4.2. Fig. 6.3 shows an example of the measured linear transmittance and the extrapolated transmission, scattering and absorption lengths as a function of $\lambda$ for tile LEC6-1a in a region directly hit by the beam, denoted as Point 3. The results for the linear transmittance, transmission length, scattering length, and absorption length in the same region as a function of $\lambda$ for all tested tiles are reported in Fig. 6.4. As expected, the dominant limitation to the transparency in the $\lambda$ region of interest, between about 300 and 700 nm, comes from Rayleigh scattering, with a measured scattering length at 400 nm between 5 and 6 cm for all tested tiles.

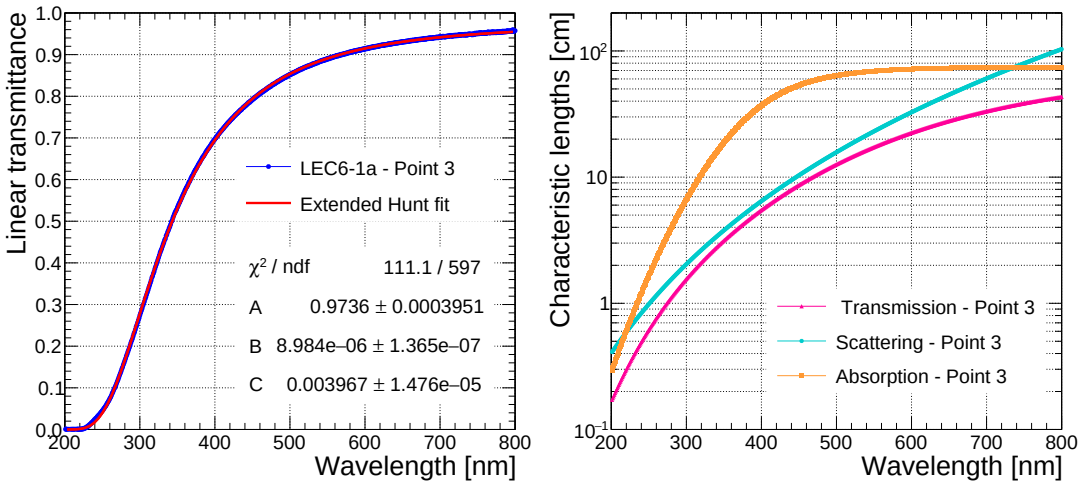


**Figure 6.3:** Measured linear transmittance and extended Hunt fit (left), and extrapolated transmission, scattering, and absorption lengths (right) as functions of $\lambda$ for tile LEC6-1a near the tile centre.

### 6.2.3 Refractive index characterization measurements

The refractive index of the tested tile was measured with the minimum deviation method [140, 141] using three Thorlabs laser modules at 405, 532, and 365 nm [142]. Measurements were taken at depths of 3, 10, and 17 mm from a reference face. Fig. 6.5 shows the setup and the mean refractive index obtained by averaging measurements at the four corners for tiles LEC6-1a and LEC6-2b at fixed depths relative to the reference face as a function of $\lambda$ and at fixed $\lambda$ as a function of depth.

The expected chromatic dispersion, with the refractive index decreasing with the increasing wavelength is observed. At a depth of 3 mm, both tiles show a decrease in $n$ from about 1.0305 at 405 nm to about 1.0295 at 635 nm. At 17 mm, $n$ decreases from about 1.0320 to about 1.0305 over the same wavelength range. To extrapolate a dispersion curve, useful for refined simulation inputs, I fitted the measurements at each depth with the single-pole Sellmeier function in Eq. 2.17.

The measurements reveal, for both tiles and at all tested wavelengths, a surprising systematic refractive index gradient across the depth with magnitude up to 0.0015. I attributed this effect to density inhomogeneities arising during the fabrication process. The observed gradient is nonlinear. At 3 mm the index is lower than at 10 mm by no more than 0.0005, whereas the change at 17 mm reaches values up to 0.0015. This result is surprising, since with the face featuring the lower index placed upstream with respect to the impinging charged particles, such a gradient is expected to produce a "self-focusing" effect reducing the geometric uncertainty in the Cherenkov angle reconstruction and improving the angular resolution compared with a uniform index.

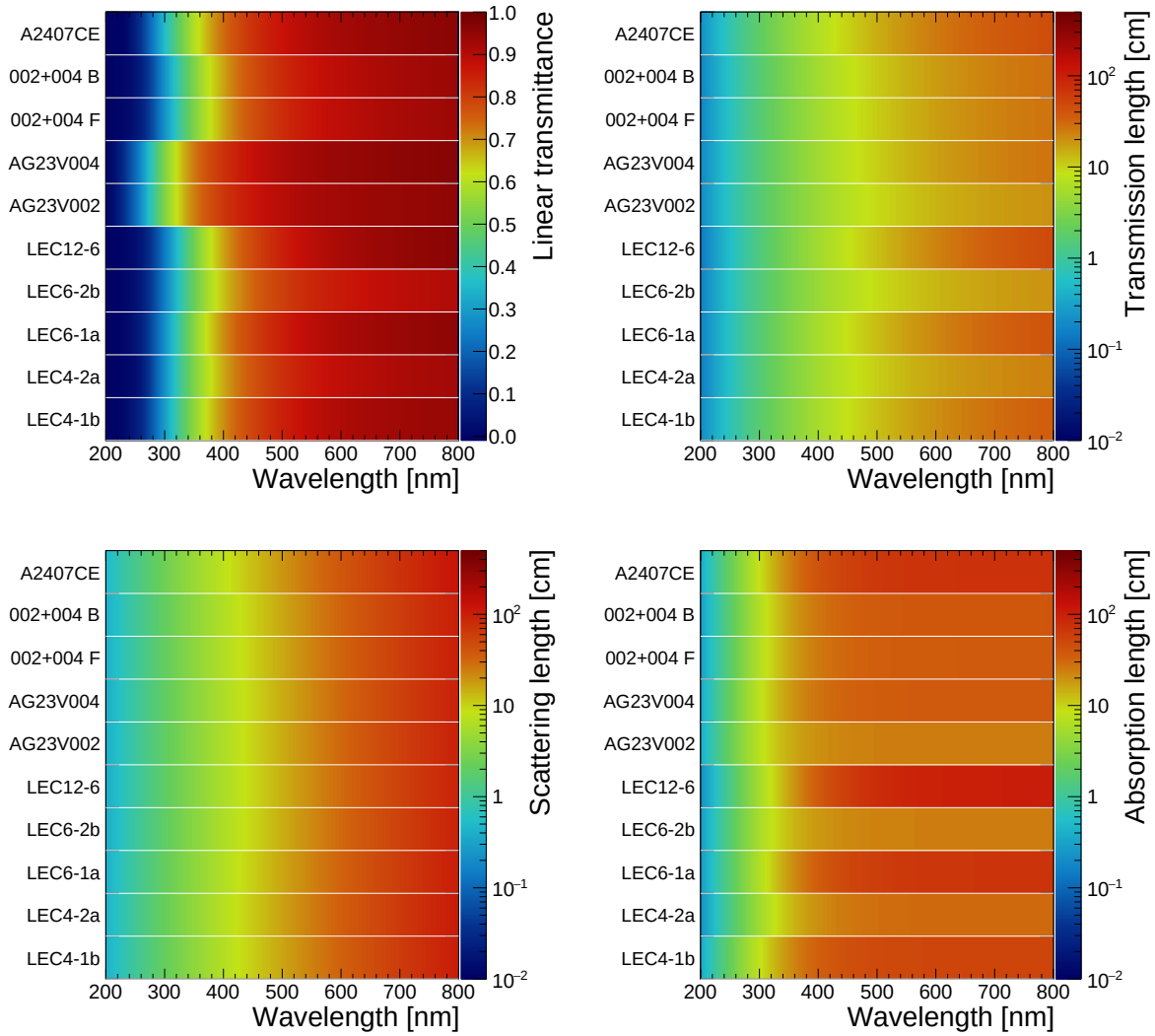


**Figure 6.4:** Transmittance (top left), and transmission (top right), scattering (bottom left) and absorption lengths (bottom right) of the tested aerogel samples as a function of $\lambda$ near the tile centre.

For most of the beam test measurements, the tiles were mounted in such a configuration, confirming the expected focusing effect. To derive refractive index gradient curves that could be used as simulation inputs to reproduce and validate the data, with measurements available at only three depths, I parametrized the index at each wavelength as a quadratic function of depth constrained to pass through the measured points. Although the present data indicate reproducibility across the measured tiles, measurements on additional samples are needed to confirm this conclusion.

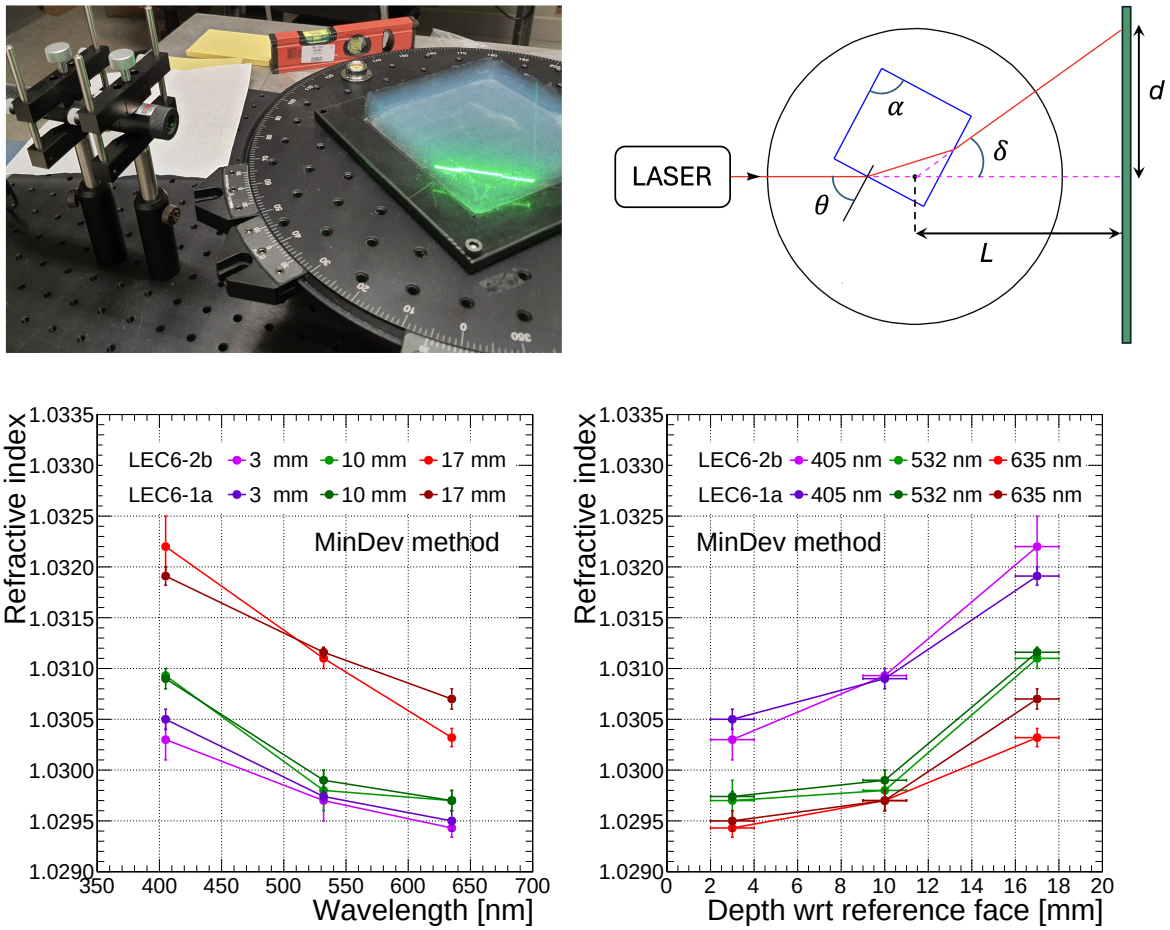


**Figure 6.5:** Top: Photograph (left) and schematic illustration (right) of the setup used for the measurement of aerogel refractive index with the minimum deviation method. Bottom: Mean measured refractive index of the aerogel tiles LEC6-1a and LEC6-2b at fixed depths relative to the reference face as a function of $\lambda$ (left) and at fixed $\lambda$ as a function of depth (right).

### 6.2.4 Aerogel ring SiPM arrays

For the detection of Cherenkov photons produced in the aerogel radiator, SiPM arrays from Hamamatsu were mounted on the main copper plate of the aerogel vessel.

In the 2022-2023 prototype, the aerogel photon detector consisted of eight Hamamatsu S13552 linear arrays [143] with 128 SiPMs, each $0.23 \times 1.625$ mm$^2$ in size packaged with a 0.25 mm linear pitch and a $57.5 \times 62.5$ µm$^2$ microcell pitch. The centres of each S13552 array were located at a radius of 6.5 cm with respect to the geometric centre of the system, as shown in Fig. 6.6. The 128 channels of each array were arranged into 32 groups, each consisting of four adjacent SiPMs (OR-4), through custom PCBs, resulting in an effective readout pitch of $1 \times 1.625$ mm$^2$. The eight arrays provided an acceptance of about 3% for the aerogel Cherenkov rings at saturation.

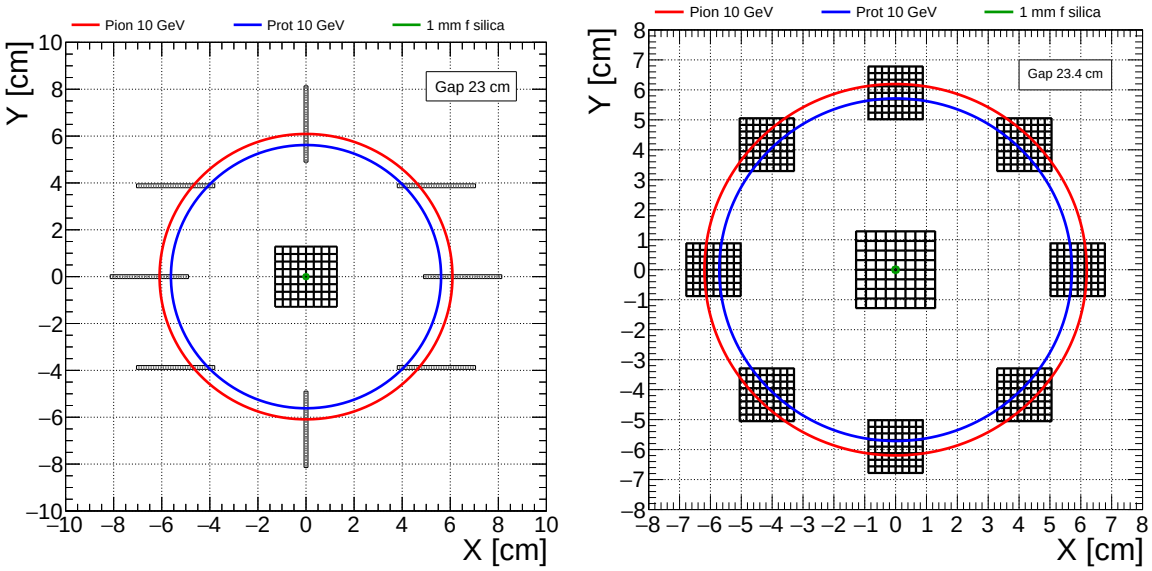


**Figure 6.6:** Schematic view of the aerogel ring and timing SiPM array positioning on the copper plate of the aerogel vessel in the 2022-2023 prototype (left) and in the 2024-2025 prototype (right).

In the 2024-2025 prototype the aerogel photon detector was upgraded by replacing the linear arrays with eight Hamamatsu S13361-2050AE-08 arrays [90] with $8 \times 8$ SiPMs, each $2 \times 2$ mm$^2$ in size packaged with a $2.2 \times 2.2$ mm$^2$ pitch and a 50 µm microcell pitch. From dedicated design studies, I found that the optimal placement of the arrays was with their centres at a radius of 5.9 cm from the geometric centre of the system, as shown in Fig. 6.6. The available front-end boards could read out at most five ring arrays, resulting in an acceptance for saturated aerogel Cherenkov rings of about 25%.

### 6.2.5 Charged-particle timing SiPM arrays

For charged-particle timing studies, additional SiPM arrays were installed along the beam line and mounted on dedicated copper plates. In 2022-2023 prototype they were located in the aerogel vessel. In the 2024-2025 prototype they were deployed in both the aerogel vessel and an additional upstream vessel. These arrays also provided additional tracking points, complementing the dedicated tracker modules.

The 2022-2023 prototype included two mounting slots for the central SiPM arrays. One slot was at the centre of the main copper plate of the aerogel vessel (M1) and another was on the side opposite the aerogel tile (M0), as shown in the right panel of Fig. 6.6. A Hamamatsu S13361-3075AE-08 array [75], mounting $8 \times 8$ SiPMs, each $3 \times 3$ mm$^2$ in size packaged with a $3.2 \times 3.2$ mm$^2$ pitch and a 75 µm microcell pitch, coupled to a 1 mm thick fused-silica window via a 100 µm silicone resin layer was kept in the M1

position. Three different arrays were tested in the M0 position. First, a Hamamatsu S13361-1350AE-08 array [75] with $8 \times 8$ SiPMs, each $1.3 \times 1.3$ mm$^2$ in size packaged with a $1.5 \times 1.5$ mm$^2$ pitch and a 50 µm microcell pitch, coupled to a 2 mm thick fused-silica window via a 100 µm epoxy resin layer. Second, a Hamamatsu S13361-3075AE-08 array coupled to a 1 mm thick $MgF_2$ window via a 100 µm silicone resin layer. Third, a Hamamatsu S13361-3075AE-08 array without an external window, relying only on the built-in 100 µm epoxy layer.

In the 2024-2025 prototype a S13361-3075AE-08 array coupled to a 1 mm thick fused-silica window via a 100 µm silicone resin layer was kept at the centre of the main copper plate of the aerogel vessel (N2) as in 2023. Two additional Hamamatsu S13361-2050AE-08 arrays coupled to a 1 mm thick fused-silica window via a 100 µm epoxy resin layer (N0 and N1) were mounted in another vessel placed upstream relative to the aerogel one, as shown in the bottom panel of Fig. 6.2. EJ-500 optical cement [144] was used to glue the windows to the SiPM arrays.

### 6.2.6 SiPM cooling

The SiPMs in the vessel were cooled to -5°C to reduce the DCR. Cooling was provided by Peltier cells coupled to a low-temperature water loop. The copper plates on which the SiPM arrays were assembled served as cold plates. On the side opposite the arrays, Peltier cells were installed in a sandwich configuration, with thermal paste between the SiPM cooling plate and a copper cooling block through which water at 5°C, supplied by a Huber Minichiller 600 [145], was circulated. The resulting cooling system enabled the possibility to keep the SiPM temperature below 0°C. On the main copper plate carrying the SiPM arrays aimed at detecting Cherenkov photons produced in the aerogel tiles, one Peltier module was mounted at each of the four corners. For each array installed along the beam line, a single Peltier module was mounted on its dedicated copper plate. Analog temperature sensors TT4-10KC3-T125-M5-500 [146] were assembled on the edges of the copper plates to monitor their temperature by using a Raspberry Pi 3 with ADS1115 16-bit ADCs [147].

### 6.2.7 Gas flushing and humidity control

The vessels of the tested prototypes were flushed with Ar to prevent condensation by keeping the relative humidity below 2.5%, corresponding to a dew point temperature inside the cylinder of approximately -25°C, significantly lower than the considered SiPM operation temperature. Humidity sensors SHT31-D [148] were used to monitor

both the room and the vessel humidity. For the last measurement campaign with the 2024-2025 prototype, mixtures of $CO_2$ and $C_4F_{10}$ were used, with a $C_4F_{10}$ molar fraction up to 32%, to study the threshold-based option for e-ID enhancement.

### 6.2.8 Tracking system

For charged-particle tracking, all tested prototypes employed X–Y tracking modules consisting of staggered arrays of round plastic scintillating fibers coupled to 128-channel Hamamatsu S13552-series SiPM arrays [143], originally developed by INFN Bari for space applications [149, 150]. Each module used fibers with diameters of 500 or 750 µm, with either single-ended or dual-ended readout in both the X and Y views. For the tests of the 2022–2023 prototype, two tracking modules were mounted, one upstream at 31 cm and one downstream at 94 cm from the median plane of the 2 cm thick aerogel tile. For the tests of the 2024-2025 prototype, the distances were changed, respectively, to 167 cm and 123 cm. The larger distance of the upstream tracking module from the aerogel relative to the 2022-2023 setups is due to the presence of the additional vessel with two SiPM arrays mounted along the beam line for charged-particle timing. The resulting contribution of the tracking uncertainty on the angular resolution was evaluated to be smaller than 1 mrad constraining the track direction with the two tracking modules and the SiPM arrays along the beam line.

### 6.2.9 Cabling of the SiPMs to the front-end

All SiPM arrays were bonded on one side of custom PCBs routing the channels to Samtec LSHM-120 multi-channel connectors [151] bonded on the opposite side of the PCBs. For the arrays reading the tracking modules, the Samtec LSHM-120 multi-channel connectors were connected directly to the Front-End Boards (FEBs) by means of high-speed 50 Ohm multi-channel Samtec HLCD-20 cables [152]. For the arrays mounted inside the vessels the Samtec LSHM-120 multi-channel connectors were first connected to a feed-through PCB connector using Samtec HLCD-20 cables, and then an additional cable was plugged for each array to route the analogue signals from the feed-through PCB connector to the FEBs placed outside. The SiPM bias voltages were provided through four of the HLCD channels by bias modules connected to the readout boards. The SiPM PCBs were equipped with 1-wire digital temperature sensors DS18B20 [153] routed by means of one HLCD channel.

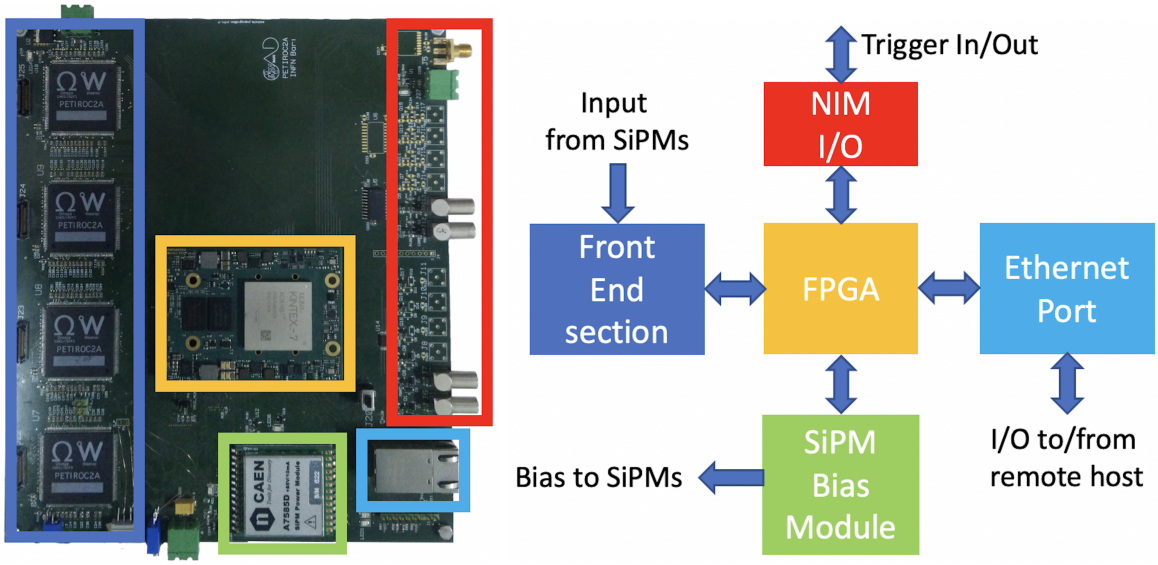


**Figure 6.7:** Picture (left) and block diagram (right) of the Petiroc board. Adapted from [154].

### 6.2.10 SiPM readout electronics

The data were collected with a complete chain of front-end and readout electronics based on the Petiroc 2A ASIC [134] for the 2022-2023 prototype and the Radioroc 2 ASIC [135] coupled with a picoTDC [136] for the 2024-2025 prototype. The details on the boards used for data acquisition are summarised in the following sections.

### 6.2.11 The Petiroc board

In the 2022-2023 prototype, the readout electronics for the SiPM arrays in the aerogel vessel and the tracker modules was based on custom front-end boards, hereafter referred to as Petiroc boards, developed by the Electronics Service of the INFN unit of Bari [149, 154]. A picture of the board and its block diagram are shown in Fig. 6.7.

The board is equipped with four Petiroc 2A ASICs developed by Omega-Weeroc [134]. The Petiroc 2A is a 32-channel front-end ASIC providing per-channel arrival time and charge readout. Each channel integrates a 10-bit analog-to-digital converter (ADC) for charge measurement and a 10-bit time-to-digital converter (TDC) with 40 ps LSB for timing. A nominal time jitter smaller than 150 ps FWHM is expected for larger than two PE-signals for operation at 0.5 PE threshold (ASIC only). Four LSHM-120 Samtec multi-channel connectors [152] are used to route 32 SiPM signals to each ASIC. Besides the front-end ASICs, the Petiroc board hosts a CAEN A7585D SiPM voltage supply module [155] to bias the SiPMs and a Kintex-7 FPGA mounted on a

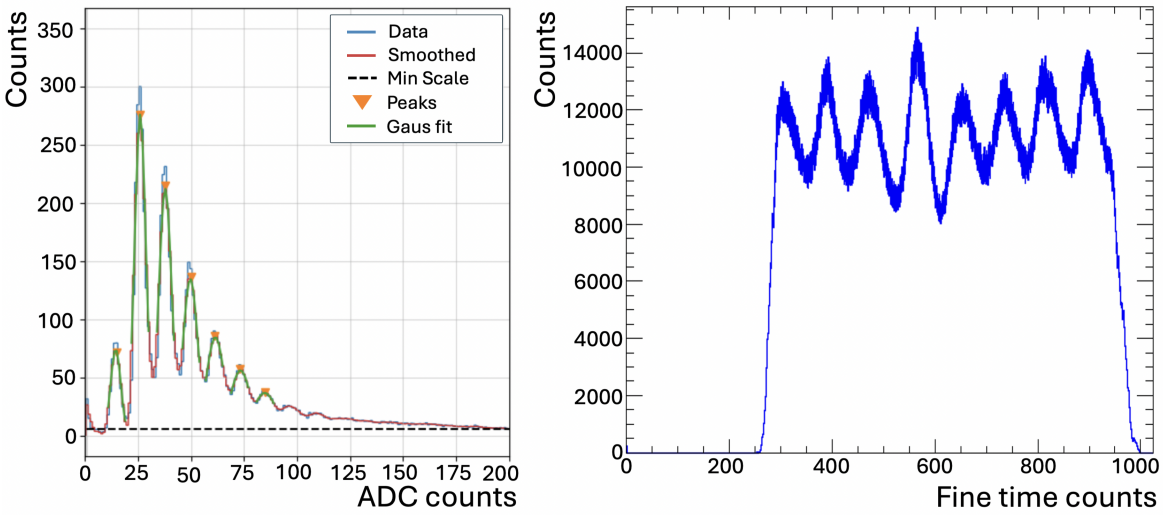


**Figure 6.8:** Example Petiroc 2A ADC counts (left) and fine time counts (right) distributions from a S13552 array under laser illumination, recorded with the Petiroc board in periodic-trigger mode.

Mercury+ KX2 module [156]. The board and DAQ infrastructure are based on the MOSAIC system [157]. The FPGA handles the ASICs and trigger configurations as well as the data acquisition. There are six NIM input and output lines for external trigger operation and synchronous multi-board operation. The FEB is connected to a host with TCP/IP network interface through an Ethernet port.

Fig. 6.8 shows representative distributions of ADC counts and fine time counts measured with a Hamamatsu S13552 SiPM array under laser illumination, acquired with the Petiroc 2A board in periodic trigger mode. These distributions are then used to perform charge calibration by identifying the peaks corresponding to photoelectron equivalent signals in the ADC spectrum, and time calibration by mapping the fine time counts into sub-bins within the 25 ns window associated with each coarse TDC count. More details about the calibration method are reported in [149, 150].

### 6.2.12 The RadioPico board

In the 2024-2025 prototype, the readout electronics for the SiPM arrays in the tracker modules was still based on the Petiroc boards, while for the arrays in the two vessels it was based on mezzanines developed by the Electronics Service of the INFN unit of Bari in collaboration with Weeroc, connected to MOSAIC readout boards [157], hereafter referred to as RadioPico boards. Fig. 6.9 shows a photograph of the RadioPico board and example input and output signals on the oscilloscope. The corresponding block diagram is equivalent to that of the Petiroc board in the right panel of Fig. 6.7. The

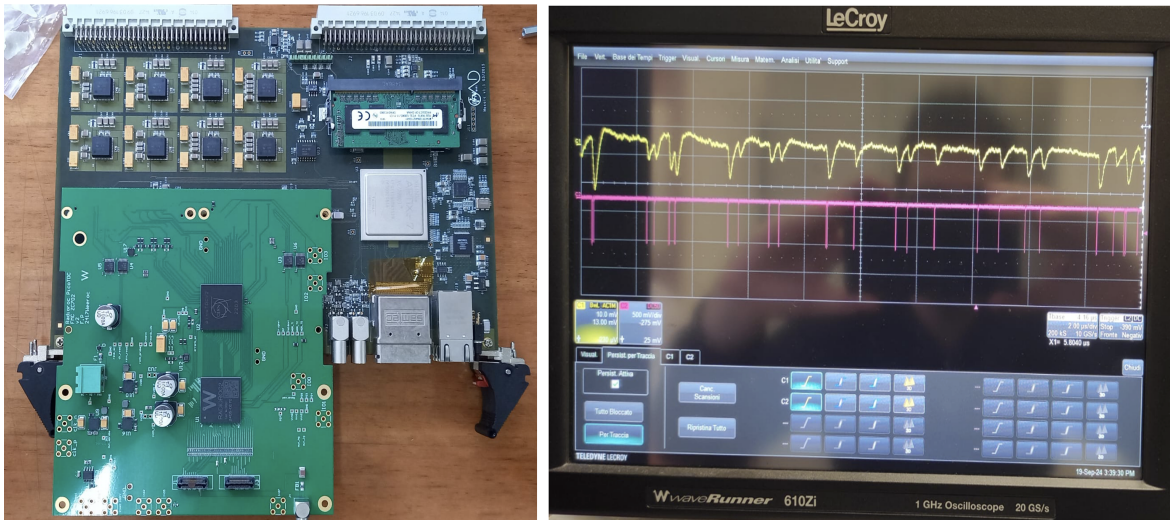


**Figure 6.9:** Left: Photograph of the RadioPico board. Right: Waveforms of analog input and Radioroc 2 discriminator output for a Hamamatsu S13361-3075AE-08 array operated in dark conditions.

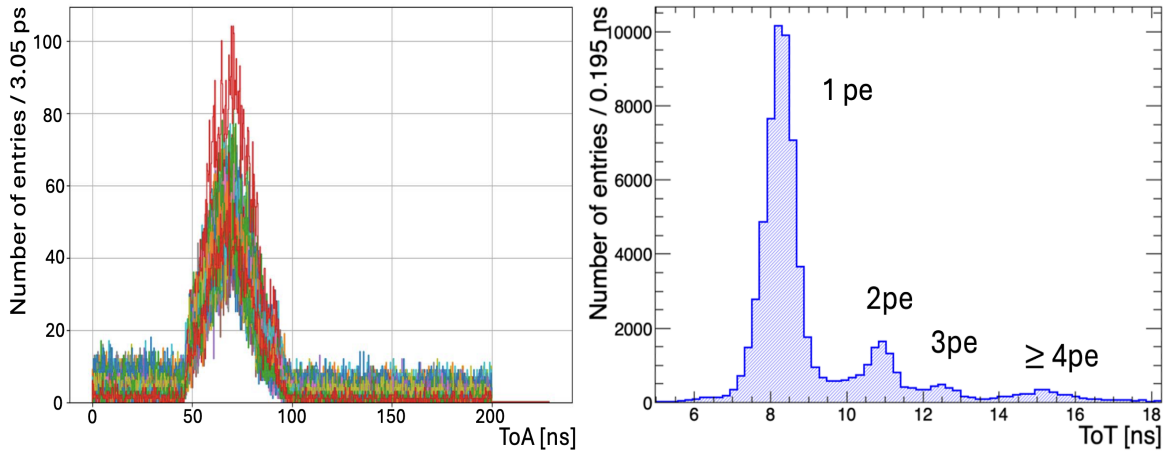


**Figure 6.10:** Example picoTDC ToA (left) and ToT (right) distributions from a S13361-3075AE-08 SiPM array under laser illumination, recorded with the RadioPico board in periodic-trigger mode.

board is equipped with one Radioroc 2 ASIC developed by Weeroc [135] coupled with one picoTDC ASIC developed by CERN [136]. The ASICs have 64 channels, allowing the readout of an $8 \times 8$ SiPM array with each board. Two LSHM-120 Samtec multi-channel connectors are used to route 32 SiPMs each to the Radioroc 2 ASIC. In the RadioPico board, the signals entering Radioroc 2 are fed to the time-preamplifier and discriminated by setting a threshold. The ASIC is configured to provide a differential output digital signal of each input channel, with an expected jitter as low as 35 ps FWHM on a single p.e. (ASIC only). This signal is fed as input to the picoTDC ASIC, working with a 40 MHz differential clock provided through dedicated SMA connectors, enabling a LSB as low as 3.05 ps. At each external trigger occurrence, a

match between the trigger, with a programmable latency, and a hit is detected within a programmable time window, where all digital signals, i.e. hits, registered by the picoTDC are acquired by the FEB-MOSAIC system. Besides the mezzanine with the front-end ASICs, the RadioPico board hosts a Xilinx Artix-7 FPGA handling the ASICs and trigger configurations as well as the data acquisition. There are NIM input lines for external trigger and spill signals, and an output line for a single-ended copy of the clock with LEMO connectors. The FEB is connected to a host with TCP/IP network interface through an Ethernet port. External bias to the SiPMs is provided by a CAEN A7585D module through an additional LEMO connector on the mezzanine.

For all characterization and beam test measurements discussed in this chapter, the picoTDC was configured to operate in time-over-threshold mode to measure time of arrival (ToA) with an LSB of 3.05 and 16-bit resolution, and time over threshold (ToT) with a LSB of 195.31 ps and 11-bit resolution. From the latter, it was possible to count the number of photoelectrons, as shown in Fig. 6.10 for SiPM characterization studies under laser illumination in periodic-trigger mode. The acquisition was performed by operating picoTDC in triggered mode and setting an acquisition time window of 200 ns.

Fig. 6.10 shows examples of the picoTDC ToA and ToT distributions measured with a Hamamatsu S13361–3075AE–08 SiPM array under laser illumination, acquired with the RadioPico board in periodic-trigger mode. The peaks in the ToT distribution associated with increasing number of photoelectrons are clearly resolved.

## 6.3 Cherenkov angle reconstruction strategy

For Cherenkov angle reconstruction with beam test measurements, I implemented a Cherenkov angle reconstruction algorithm based on the one used for the simulation studies discussed in Section 4.3.1. The reconstruction requires the photon hit point on the SiPM arrays, the most probable emission point in the aerogel tile and the track direction at that point. The details on the steps performed for the alignment, charged-particle tracking to the most probable emission point in the aerogel tile and the final single hit angle reconstruction are reported in Appendix C.

## 6.4 Beam test of the 2022-2023 prototype

The 2022-2023 prototype was tested on beam in a two-week period in October 2022 and in a two-week period between September and October 2023. The setup for the beam test of the 2022-2023 prototype is shown in Fig. 6.11. The positions of the

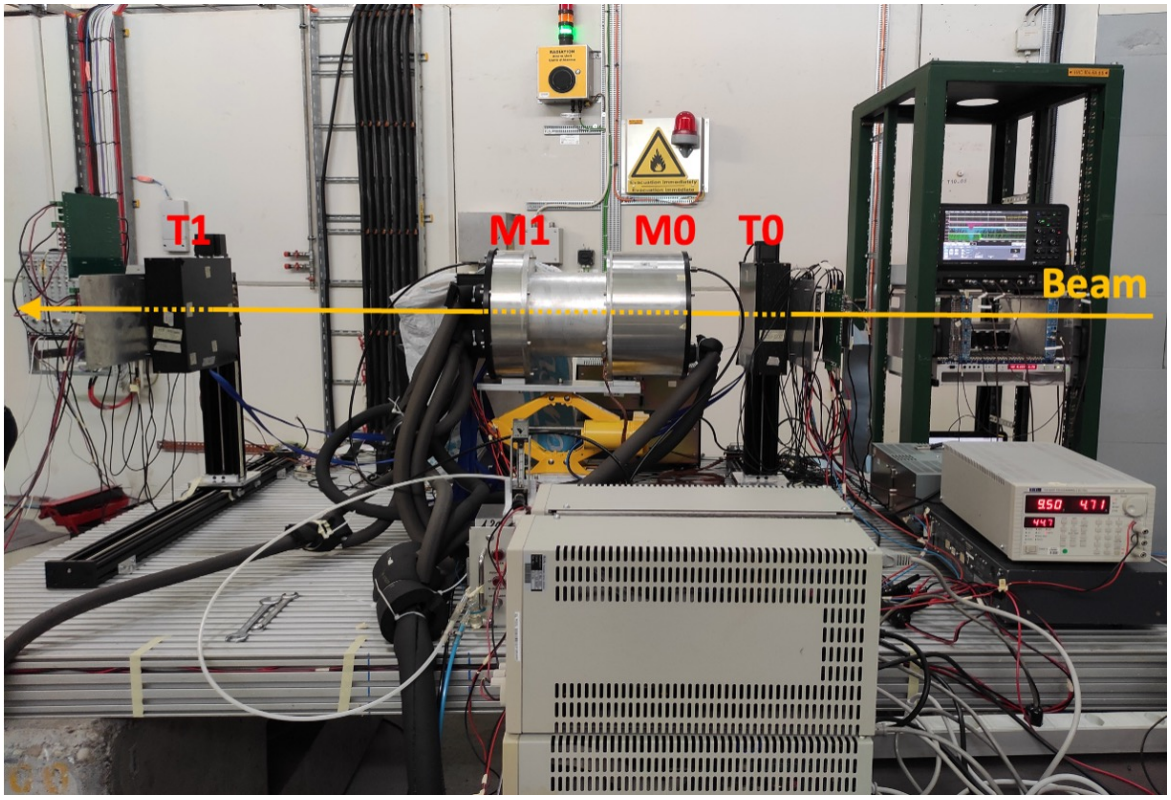


**Figure 6.11:** Photograph of the 2022-2023 beam test setup. The beam direction and the positions of the two arrays in the RICH vessel, M0 and M1, and the tracker modules, T0 and T1, are indicated.

central arrays, M0 and M1, and the tracker modules, T0 and T1, are indicated.

The left panel of Fig. 6.12 shows a photograph of the copper plate of the 2022-2023 prototype instrumented with the eight Hamamatsu S13552 linear arrays covering the aerogel ring region and the central S13361-3075AE-08 array, M1, coupled with a 1 mm thick $SiO_2$ window. The right panel of Fig. 6.12 shows a photograph of the upstream copper plate with the S13361-1350AE-08 array, M0, coupled with a 2 mm thick $SiO_2$ window.

The left panel of Fig. 6.13 shows the inside of the RICH vessel with the aerogel and the upstream copper plate mounted inside. The two corresponding Samtec HLCD-20 cables as well as the cables of the Peltier cell and the temperature sensor extend through the length of the vessel and are routed to the feed-through board mounted on the side of the main copper plate. The aerogel tile is mounted in a holder fixed by a retaining pin at a distance of 23.0 cm from the surface of the ring arrays.

The right panel of Fig. 6.13 shows the stack of the four Petiroc boards used for data acquisition: one board for the four ASICs reading the two central arrays, M0 and M1, two for the eight ASICs reading the ring arrays, and one for the four ASICs reading the S13552 arrays covering the X-Y views of the two tracker modules, T0 and T1.

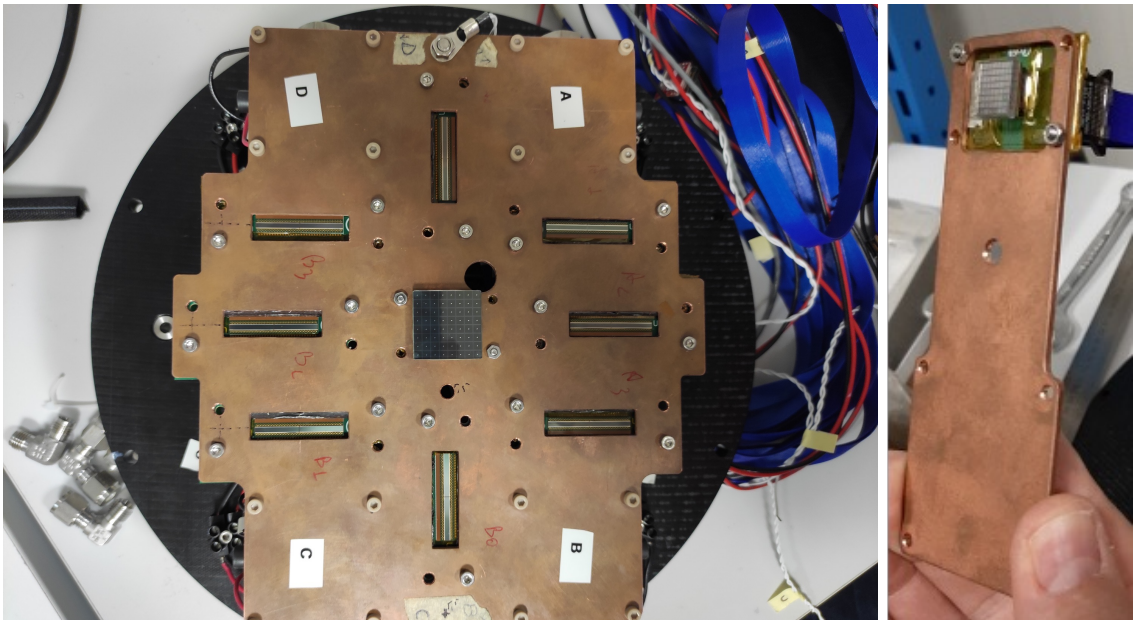


**Figure 6.12:** Photographs of copper plates in the RICH vessel of the 2022-2023 setup. Left: Main copper plate instrumented with eight Hamamatsu S13552 linear arrays covering the expected aerogel ring region, and a central S13361-3075AE-08 array coupled with a 1 mm thick fused silica window (M1). Right: Upstream copper plate instrumented with a central S13361-1350AE-08 array coupled with a 2 mm thick fused silica window.

### 6.4.1 Trigger and DAQ system

The signals from the CERN-PS T10 beam scintillator, validated in the beam spill window, were used for external triggering. The trigger was distributed to the four Petiroc boards. The full data acquisition (DAQ) chain for the 2022-2023 prototype is shown in Fig. 6.14. The Petiroc boards were operated in a master-slave configuration. In particular, the beam trigger was sent to the Petiroc board serving the two tracker modules. This master board distributed the trigger, the event tag, and a 40 MHz clock to the boards reading out the arrays within the aerogel vessel in a daisy-chain configuration. For each trigger event, a 550 ns time window for data acquisition was opened. Within this time window, the system recorded the fired channels, along with their ADC and TDC readings. Communication with the boards used the TCP/IP protocol. Data were transferred over Ethernet to the acquisition PC for offline analysis.

### 6.4.2 Collected data

Data taking with the 2022-2023 prototype was mainly carried out with the negatively charged beam at 10 GeV/$c$ momentum and the positively charged beam at 8 GeV/$c$

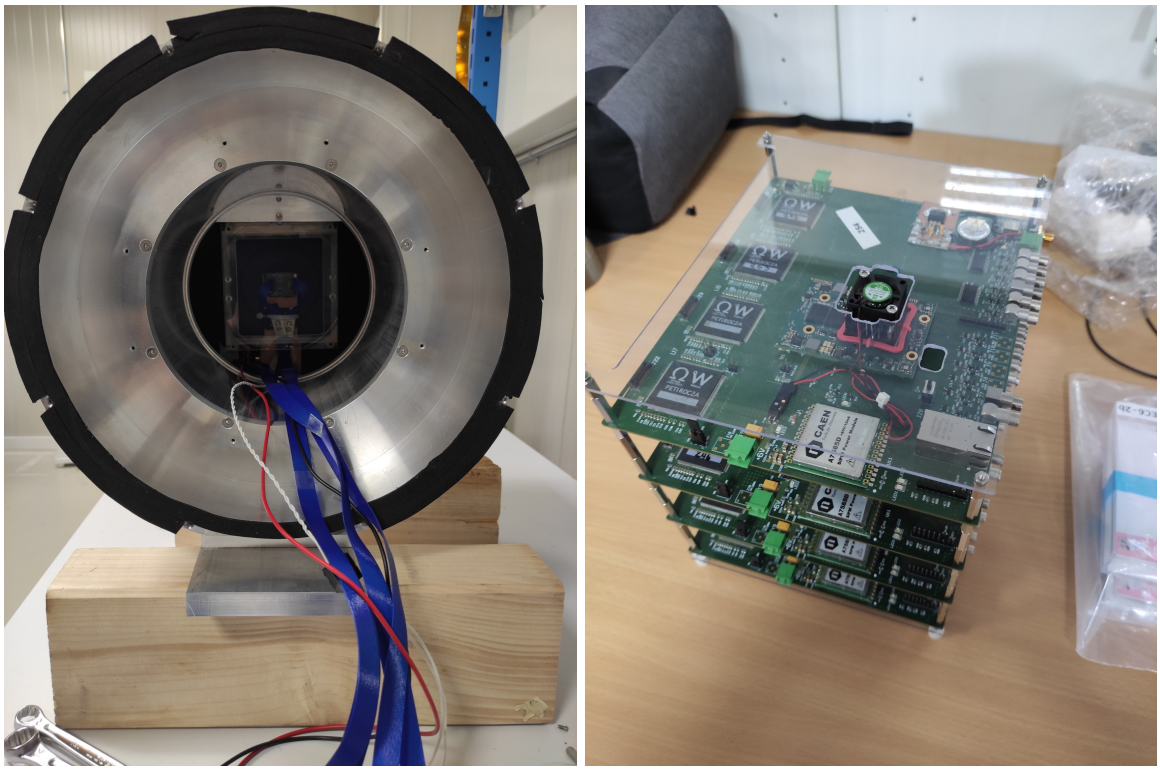

**Figure 6.13:** Left: Photograph of the open RICH vessel of the 2022-2023 setup with the aerogel and the upstream copper plate mounted inside. Right: Photograph of Petiroc boards used to read out the vessel and the tracker-module arrays.

momentum. The aerogel tiles LEC6-2b and LEC4-1a, featuring a nominal refractive index of 1.03 and a thickness of 2 cm, were tested for Cherenkov angle reconstruction studies. These studies were complemented by charged-particle timing-performance measurements, in which the relative time response of the central SiPM arrays M0 and M1 was characterized, as discussed in Section 6.2.5.

In the following, I report the main results from my analysis of 2022-2023 data, focusing on the measured Cherenkov angle reconstruction performance, the characterization of the background sources and the DCR background suppression using timing. Finally, I report the results on charged-particle timing using the central arrays, focusing on the characterization of the clusters, the efficiency and the measured time resolution.

### 6.4.3 Event selection

For the 2022-2023 beam test analysis, I selected events in which the SiPM channel with the maximum charge in M0 and in M1, and in the X and Y views of the tracker modules T0 and T1, registered at least six photoelectrons. In addition, I required that

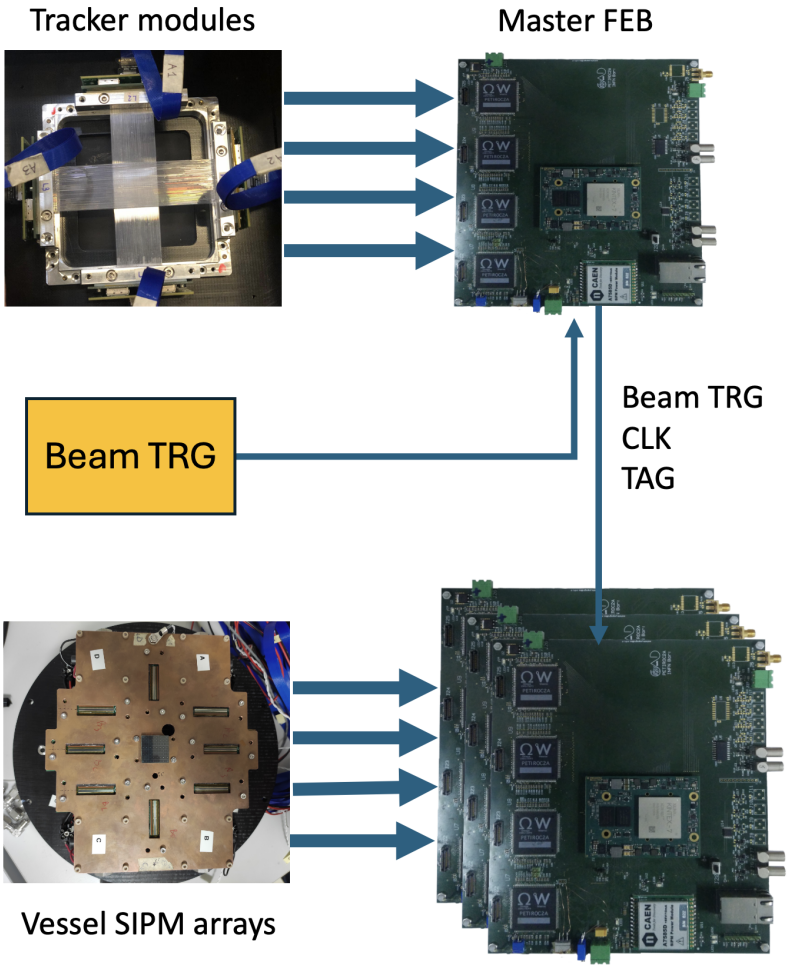


**Figure 6.14:** Data acquisition chain for the 2022-2023 prototype beam test setup.

the positions of those channels were within a central $8 \times 9$ mm$^2$ fiducial area. I also required the offset-corrected times of those channels to be within an 8 ns window to suppress the background due to wrong or ghost hits in multi-particle events.

Fig. 6.15 shows the cumulative map of the hits in the eight ring arrays in the aerogel vessel and the distribution of the extrapolated most probable X-Y photon emission points in aerogel for the negatively charged beam at 10 GeV/$c$ using tile LEC6-2b. The ring segments due to Cherenkov photons from pions are clearly visible.

### 6.4.4 Hit-track time matching and background sources

The synchrony of the four Petiroc boards enabled background studies by analysing the relative hit-track time matching. For each event, I used the SiPM cell with the largest number of detected photoelectrons in the central array M1 of the main vessel as the

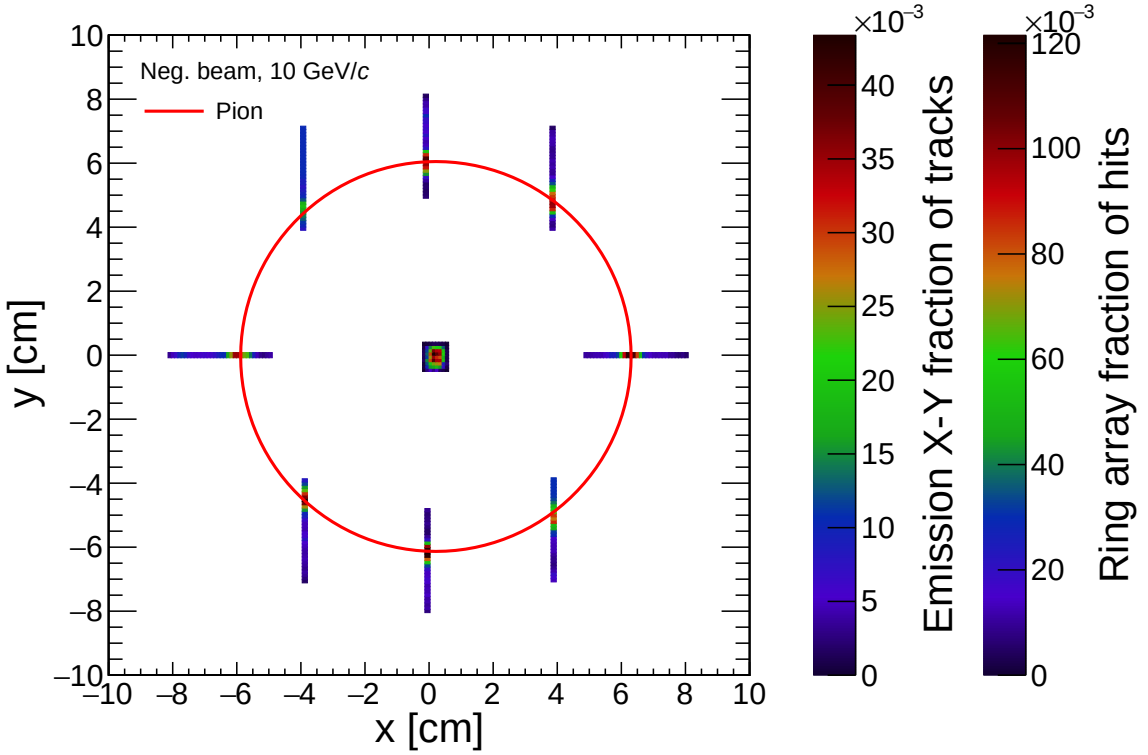


**Figure 6.15:** Spatial distribution of the extrapolated X-Y emission point at the most probable emission depth in the aerogel tile (central region) and of the hits in the eight ring arrays (ring region) for the negatively charged beam at 10 GeV/$c$ momentum using tile LEC6-2b ($n = 1.03$). The expected Cherenkov ring from pions centred in the most probable X-Y emission point is also shown.

timing reference $t_{track}$ for the considered charged track. Then I referred the times of detected hits $t_{hit}$ in the ring arrays to the reference track time.

Fig. 6.16 shows the 2D distributions of the reconstructed Cherenkov angle at the single hit level using the aerogel tile LEC6-2b ($n = 1.03$) as a function of the relative hit-track timing for the negatively charged beam at 10 GeV/$c$ and the positively charged beam at 8 GeV/$c$. The corresponding 1D projections on the relative time axis are shown in Fig. 6.17. Four different signal and background regions are clearly visible.

- The clusters at the expected Cherenkov angles for the different particle species correspond to direct Cherenkov photons. The corresponding signal hits are clustered in the Gaussian core of the distribution, having a sigma of about 450 ps.
- The horizontal bands at the nominal Cherenkov angles in Fig. 6.16 and the right tail in Fig. 6.17 originate from SiPM delayed crosstalk and afterpulsing. In channels where the single photoelectron amplitude is below threshold, delayed pulses in the same SiPM can pile-up and cross the threshold.

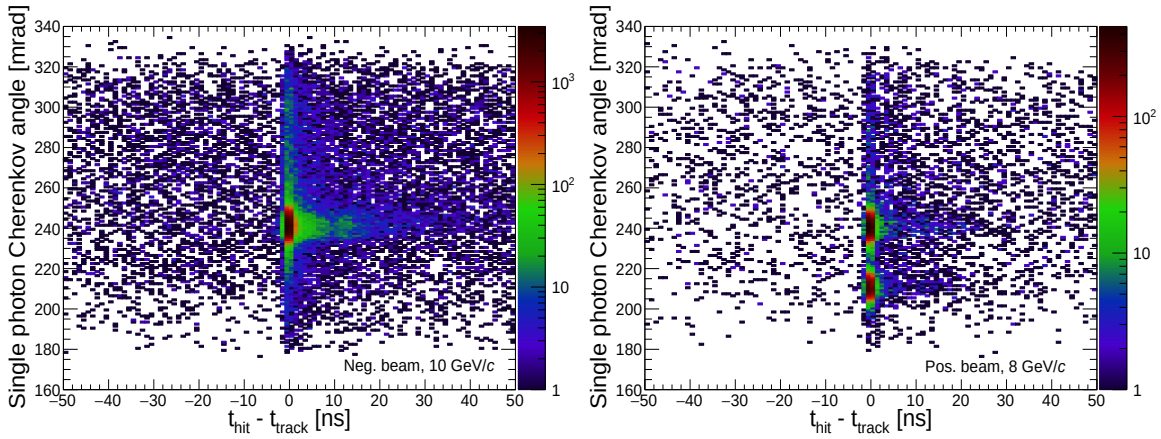


**Figure 6.16:** Distribution of the reconstructed aerogel single photon Cherenkov angle as a function of the relative time between the ring arrays $t_{hit}$ and the central array $t_{track}$ for the negatively charged beam at 10 GeV/$c$ (left) and the positively charged beam at 8 GeV/$c$ (right) using tile LEC6-2b.

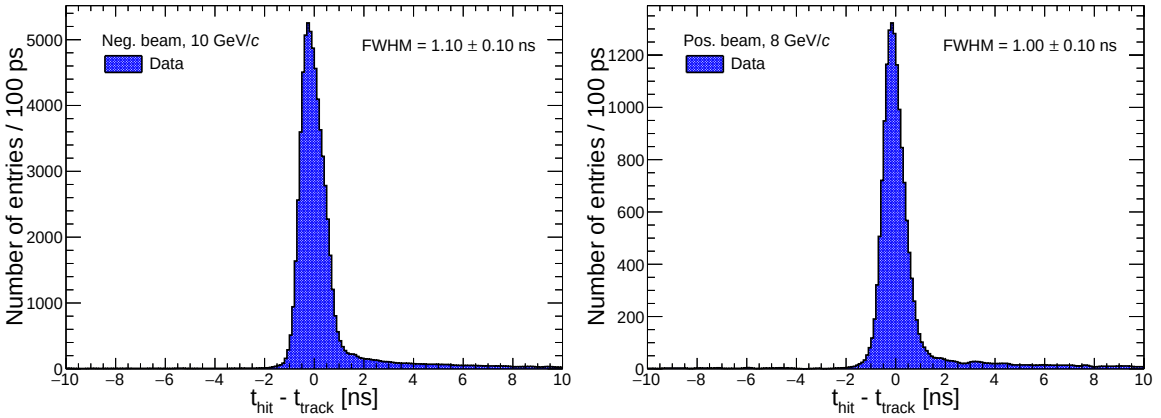


**Figure 6.17:** Distribution of the time differences between the array cell firing time $t_{hit}$ and the firing time $t_{track}$ of the central-array charged-particle cluster cell with maximum number of photoelectrons in the events with the negatively charged beam at 10 GeV/$c$ momentum (left) and with the positively charged beam at 8 GeV/$c$ momentum (right) using tile LEC6-2b.

- The vertical band superimposed to the clusters corresponds to the correlated background mainly due to Rayleigh-scattered photons in the aerogel and photons produced by secondaries, such as delta electrons. As a first approximation, this results in almost uniformly distributed background hits in each of the ring arrays.
- The sparse uniformly distributed background corresponds to uncorrelated background due to the SiPM DCR and the electronic noise.

Despite the limited time resolution of the Petiroc 2A ASIC at the single photoelectron level, Figs. 6.16 and 6.17 show that a significant suppression of uncorrelated back-

ground can be achieved by selecting hits such that $|t_{hit} - t_{track}| <$ a few ns. The impact of the considered hit-track time matching window is detailed in Section 6.4.7.

### 6.4.5 Background modelling

In order to model the uncorrelated background hits to fit the measured radial and angular distributions, I built a data-driven template background model considering the relative hit-track timing $t_{hit} - t_{track}$. I evaluated the spatial distribution of uncorrelated background hits by selecting only hits such that $|t_{hit} - t_{track}| > 50$ ns. In this region no signal hits are expected, as shown in Figs. 6.16 and 6.17 and mainly DCR hits are detected. This procedure enabled precise modelling of noisy channels and channel-by-channel fluctuations. Due to the similarities in the topology of the uncorrelated background and the expected almost uniformly distributed correlated background due to Rayleigh scattering, I assumed the same spatial distributions extrapolated for uncorrelated background to model the correlated background contribution as well, up to a multiplicative factor. The overall background model I considered for the radius and angle distributions presented in the following is then built as the relation:

$$\frac{\mathrm{d}N_{\mathrm{bkg}}}{\mathrm{dV}} = k \left( \frac{dN_{\mathrm{bkg}}}{\mathrm{dV}} \right)_{\mathrm{template}}, \tag{6.1}$$

where V is the Cherenkov radius or angle, $k$ is a free fit parameter and $(dN_{\mathrm{bkg}}/d\mathrm{V})_{\mathrm{template}}$ is the corresponding template distribution resulting from the spatial distribution of background hits evaluated from the recorded delayed hits.

### 6.4.6 Single-hit Cherenkov angle and radius

Fig. 6.18 shows the distributions of the reconstructed Cherenkov ring radius and emission angle at single hit level obtained considering all available ring array hits as candidate Cherenkov photons for the negatively charged beam at 10 GeV/$c$.

The peak due to photons from $\pi$ is clearly visible. I fitted the distributions with the sum of a Gaussian and a template background distribution, as discussed in Section 6.4.5.

It is important to note that, assuming a uniform refractive index along the tile depth, the distribution is in general not Gaussian, mainly because of the dominant nearly flat component from the geometric uncertainty on the emission depth. However, the gradient observed in Section 6.2.1 produces a natural focusing that strongly reduces this uncertainty. As a result, the distribution is well described by a simple Gaussian.

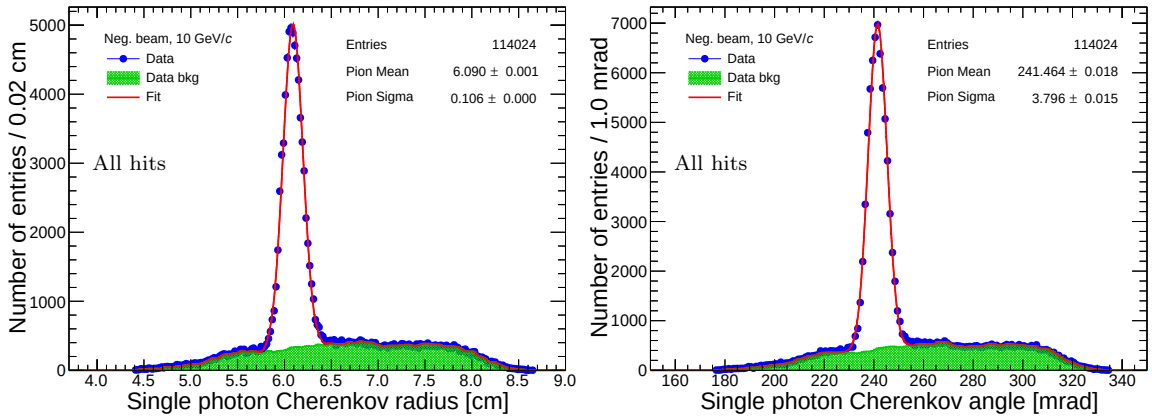


**Figure 6.18:** Distributions of the reconstructed aerogel single photon Cherenkov radius (left) and angle (right) for the negatively charged beam at 10 GeV/$c$ momentum considering all available hits using tile LEC6-2b. The vertical bars represent the statistical uncertainties. The fit with the sum of a Gaussian for the $\pi$ peak and the corresponding template background distribution is also shown.

The resulting mean ring radius and angle are about 6.1 cm and 241.5 mrad. The corresponding single hit radial and angular resolutions are about 1 mm and 3.8 mrad. They are consistent with simulations considering the measured $n$ gradient. The details on the comparisons between data and simulations are discussed in Section 6.5.12.

### 6.4.7 Uncorrelated background suppression using timing

Considering all the available hits in the ring arrays, approximately 45% of those contributing to the distributions in Fig. 6.18 comes from the cumulative uncorrelated background sampled in the full 550 ns Petiroc 2A acquisition window.

Fig. 6.19 shows the same distributions as Fig. 6.18 filtered by selecting only hits such that $|t_{hit} - t_{track}| < 5$ ns for the negatively charged beam at 10 GeV/$c$, and the positively charged beam at 8 GeV/$c$. The fit with Gaussians for the $\pi$, K and p signal peaks and the corresponding background distribution is also shown. Similar radial and angular resolutions are observed for all the observed particle species and momenta.

Excellent background suppression is achieved with timing. With the considered cut, the candidate fraction of background hits decreases from 45% down to approximately 8% at the cost of a less than 5% reduction in the overall signal photon yield, proving the effectiveness of timing to suppress the uncorrelated DCR background.

The majority of the surviving background hits is due to correlated background, such as Cherenkov photons undergoing Rayleigh scattering before leaving aerogel. Correlated

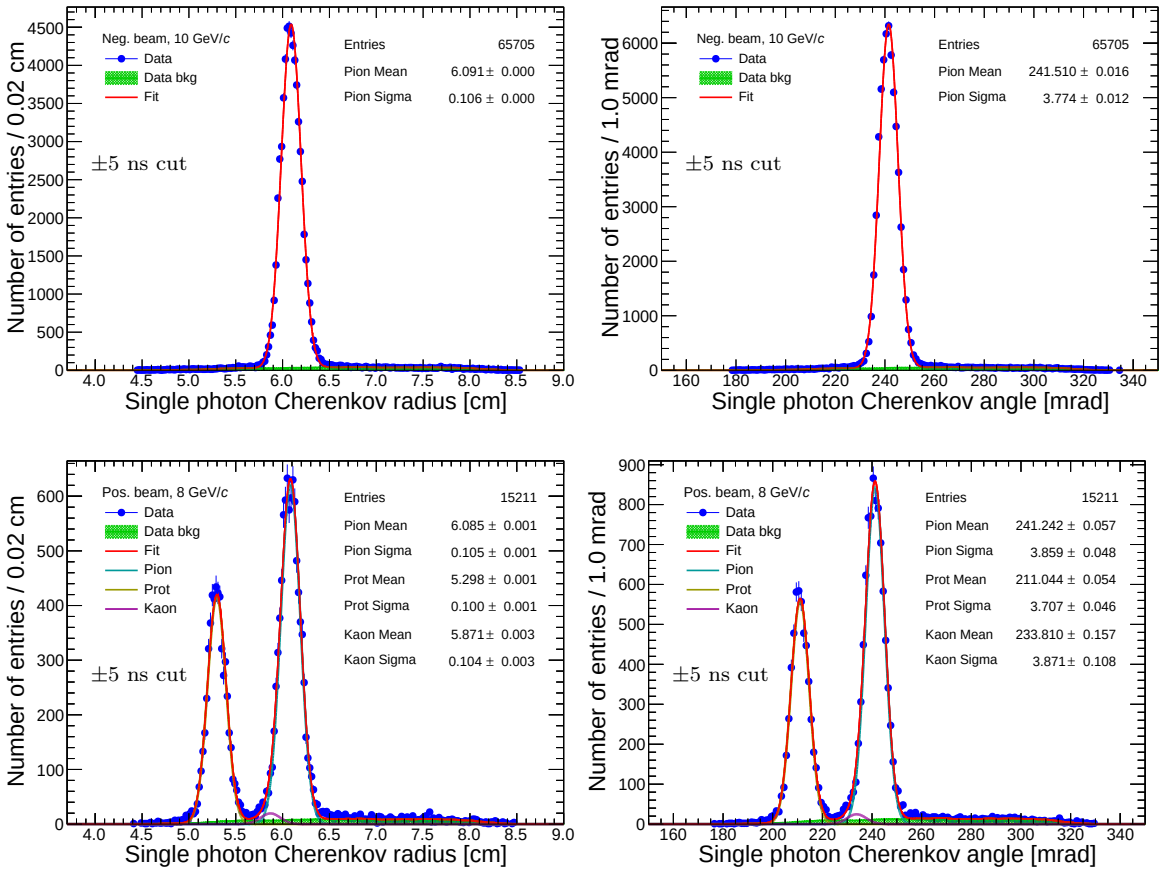


**Figure 6.19:** Distributions of the reconstructed aerogel single photon Cherenkov radius (left) and angle (right) for the negatively charged beam at 10 GeV/$c$ momentum and the positively charged beam at 8 GeV/$c$ momentum requiring hit-track matching in a ±5 ns time window using tile LEC6-2b. The vertical bars represent the statistical uncertainties. The fit with Gaussians for the signal peaks and the corresponding template background distribution is also shown.

background hits in the ring arrays are synchronous with the hits due to unscattered signal photons and cannot be discarded based on timing, as shown in Fig. 6.16.

### 6.4.8 Ring angular resolution studies

The 2023-2023 prototype allowed preliminary validation studies of the expected improvement of the angular resolution as $\propto 1/\sqrt{N_{ph}}$ with the increasing number $N_{ph}$ of detected photons. Despite the limited ring acceptance, corresponding to about 3% of the full ring, the large accumulated statistics was sufficient to extend the analysis up to $N_{ph} = 3$, 4 or 5 ring photons depending on the dataset and the considered particle species. For this study, I calculated the ring Cherenkov angle associated with a given

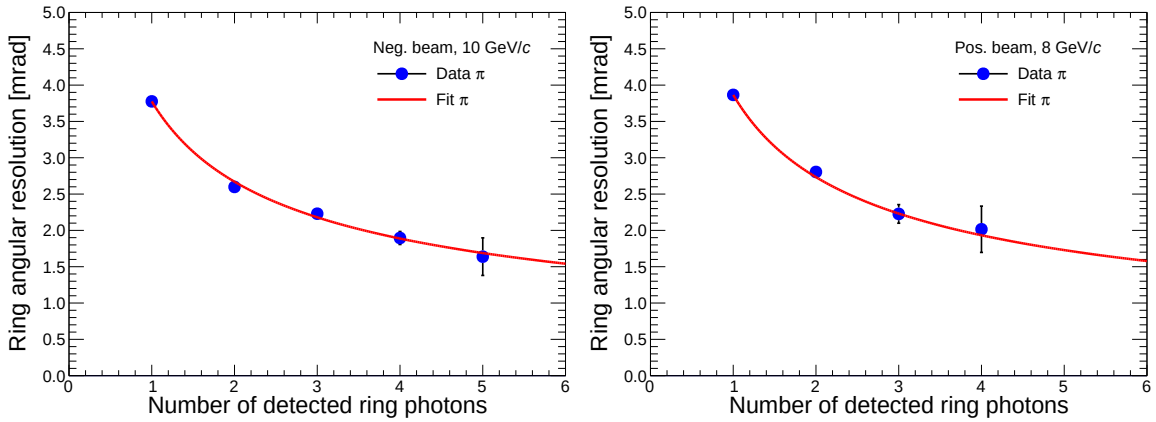


**Figure 6.20:** Cherenkov angular resolution as a function of the number $N_{\mathrm{ph}}$ of detected photons in the pion ring for the negatively charged beam at 10 GeV/$c$ momentum (top panel) and for the positively charged beam at 8 GeV/$c$ momentum (bottom panel) using tile LEC6-2b. The vertical bars represent the statistical uncertainties. The fit with the expected $1/\sqrt{N_{\mathrm{ph}}}$ scaling relative to the single photon angular resolution is also shown.

track by averaging all the reconstructed angles within the interval $[\,\theta_{\mathrm{c}} - 3\sigma_{\mathrm{c}}^{\gamma},\ \theta_{\mathrm{c}} + 3\sigma_{\mathrm{c}}^{\gamma}\,]$ such that $|\mathrm{t_{hit}} - \mathrm{t_{track}}| < 5$ ns. Here, $\theta_{\mathrm{c}}$ and $\sigma_{\mathrm{c}}^{\gamma}$ refer to the most probable Cherenkov emission angle and single photon angular resolution corresponding to the considered particle species and momentum. The resulting ring angular resolution as a function of $\mathrm{N_{ph}}$ for the negatively charged beam at 10 GeV/$c$ and the positively charged beam at 8 GeV/$c$ momentum is shown in Fig. 6.20. I extracted the value of the ring angular resolution for a given $\mathrm{N_{ph}}$ as the sigma of the Gaussian fit to the corresponding ring Cherenkov angle distributions. I fitted the available points with the expected $1/\sqrt{\mathrm{N_{ph}}}$ scaling relative to the single photon angular resolution. I extrapolated a ring angular resolution better than the target 1.5 mrad for $\mathrm{N_{ph}} > 6$ with the considered prototype.

### 6.4.9 Charged-particle timing: efficiency and time resolution

As discussed in Section 6.2.5, several combinations of arrays, window materials and window thicknesses were installed along the beam line to demonstrate the charged-particle timing performance of the SiPM-based option introduced in Section 3.6. In this section I report results for the best measured configuration, using a Hamamatsu S13361-3075AE-08 array coupled to a 1 mm $MgF_2$ window at position M0 and a Hamamatsu S13361-3075AE-08 array coupled to a 1 mm $SiO_2$ window at position M1.

Fig. 6.21 shows the distributions of the number of fired SiPMs in the track cluster for the two arrays, the total number of photoelectrons in the two arrays, the efficiency as a function of the minimum number of photoelectrons required in the cluster for

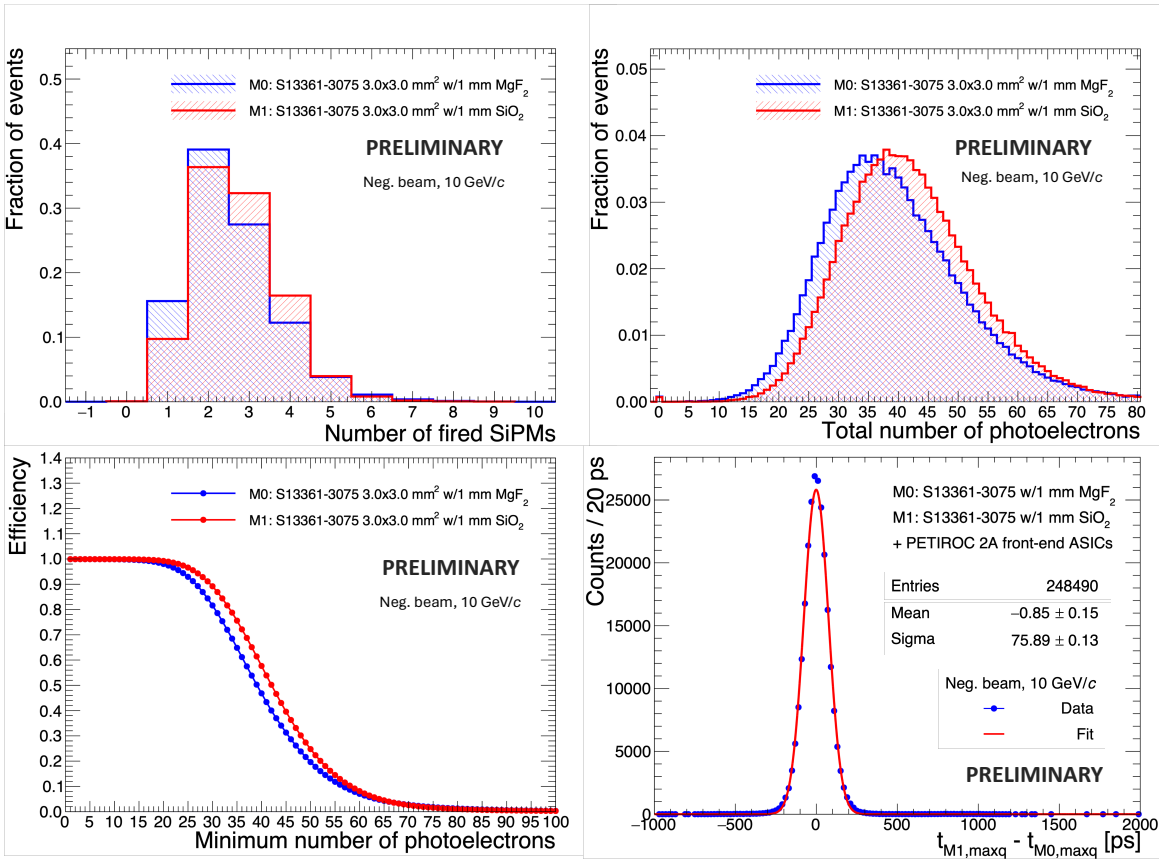


**Figure 6.21:** Distributions of the number of fired SiPMs in the track cluster (top left), the total number of photoelectrons (top right), the efficiency versus the minimum photoelectrons required in the cluster (bottom left), and the time difference between the SiPMs with maximum charge for a S13361-3075AE-08 array coupled to a 1 mm $MgF_2$ window at position M0 and a S13361-3075AE-08 array coupled to a 1 mm $SiO_2$ window at position M1 for the negatively charged beam at 10 GeV/$c$.

the two arrays, and the distribution of the time difference between the SiPMs with the maximum charge in the two arrays for the negatively charged beam at 10 GeV/$c$ momentum. With the considered $3 \times 3$ mm$^2$ SiPMs, about 2–3 SiPMs fire and share about 35–40 photoelectrons with the 1 mm window.

For each array, I evaluated the efficiency as a 4-fold/3-fold coincidence ratio, defined as the fraction of events with signals in the tracker planes T0 and T1 and in the other array, in which a cluster met or exceeded the required minimum number of photoelectrons in that array. For both arrays, efficiencies are close to 100% up to a threshold of 15 photoelectrons, proving the efficiency of the proposed timing approach.

For the timing measurements, the raw time differences were first corrected for channel-by-channel time offsets, due to the different routing of the channels, and the time-walk effect, accounting for signals with the same shape but different amplitudes crossing

the discriminator threshold at different times. A lookup-table procedure was applied. Using a subset of data, for each pair of fired SiPMs (one in each array) and for each pair of photoelectron equivalent counts in the two arrays, the distribution of the time difference was built and the resulting mean set as the reference correction of the lookup-table. The remaining data were then used for the actual analysis and corrected by subtracting the corresponding lookup-table value for the considered SiPM pair and pair of number of photoelectrons, yielding the distribution in the bottom-right panel of Fig. 6.21. The Gaussian fit to the distribution gives a time-difference resolution of about 76 ps. Assuming equal contributions from the two arrays, this corresponds to about 54 ps per array at full system level. The performance is mainly limited by the Petiroc 2A timing capabilities and by the long HLCD-20 cables between the SiPMs and the front end, which degrade signal integrity compared with an ideal direct coupling.

Nevertheless, these results constitute a proof of concept for the high efficiency and time resolution achievable with the proposed bRICH charged-particle timing option.

## 6.5 Beam test of the 2024-2025 prototype

The 2024-2025 prototype was tested on beam in a two-week period between September and October 2024 and in a one-week period in July 2025. The setup for the beam test of the 2024-2025 prototype at the PS-T10 beam line is shown in Fig. 6.22. The main vessel with the aerogel tile and the smaller upstream vessel with the arrays mounted along the beam line can be observed. The positions of the three central arrays, N0, N1 and N2, as well as the tracker modules, T0 and T1, are indicated.

The top panels of Fig. 6.23 show photographs of the copper plate of the 2024-2025 prototype instrumented with the eight Hamamatsu S13360-2050AE-08 arrays covering the expected aerogel ring region and the central S13361-3075AE-08 array, N2, directly coupled with a 1 mm thick fused silica window. The coupling of the plate to the Peltier cells at the four corners through copper cooling blocks is also shown. The bottom panels of Fig. 6.23 show the inside of the main vessel as seen from the aerogel tile, and the upstream vessel. The aerogel tile is mounted in a holder fixed by a retaining pin at a distance of 23.4 cm from the surface of the ring arrays.

Eight RadioPico boards were used for data acquisition: six boards for the central array, N2, and five ring arrays in the main vessel, and two boards for the two central arrays in the upstream, N0 and N1. In addition, two Petiroc boards were still used to read out the arrays covering the X-Y views of the two tracker modules, T0 and T1.

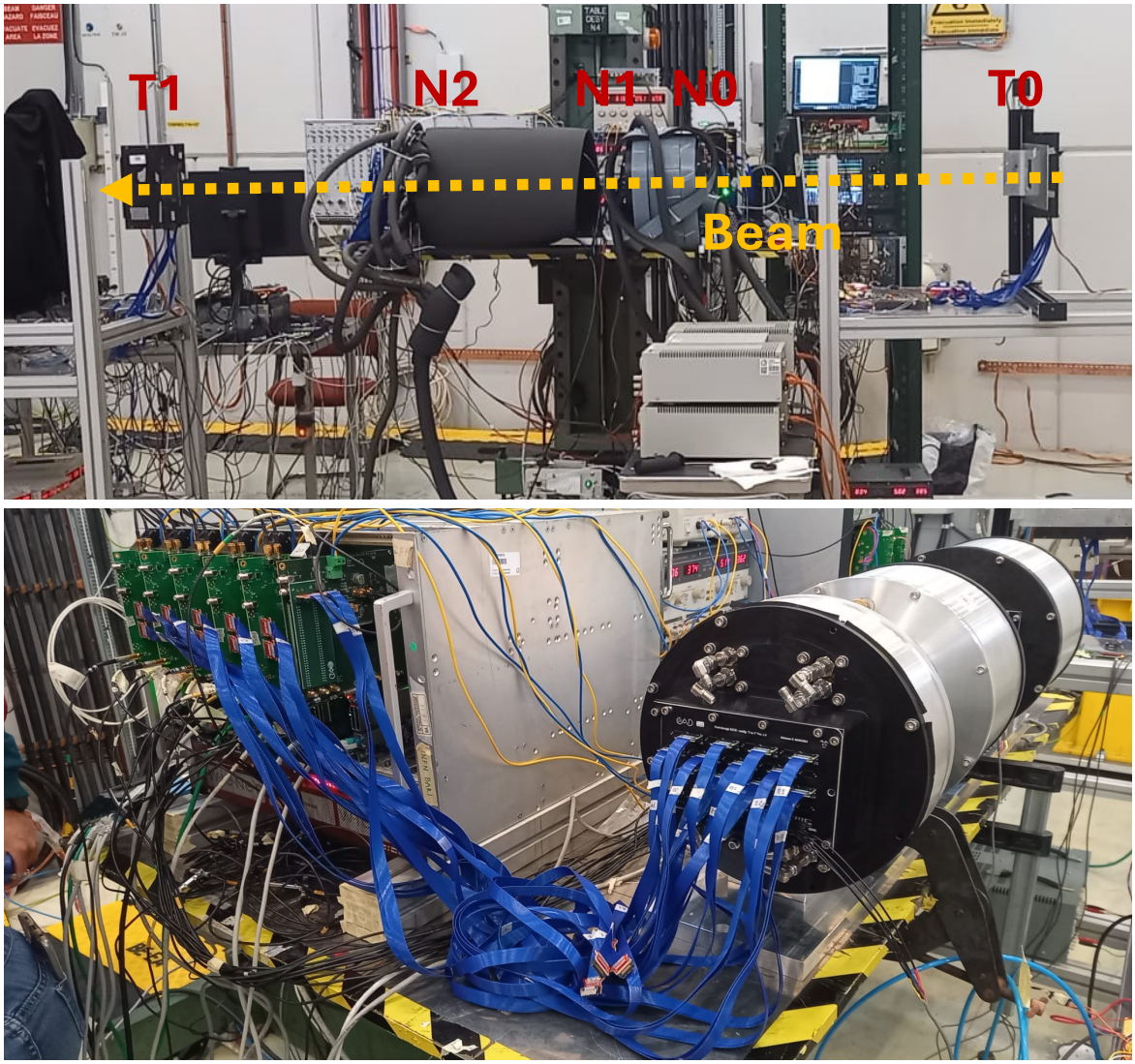


**Figure 6.22:** Photographs of the 2024-2025 beam test setup. The beam direction and the positions of the central arrays in the vessels, N0, N1 and N2, and the tracker modules, T0 and T1, are indicated.

### 6.5.1 Trigger and DAQ system

The signals from the CERN-PS T10 beam scintillator in coincidence with the signals from the Petiroc board reading the upstream tracker module T0, validated in the beam spill window, were used for triggering. The full data acquisition (DAQ) chain for the 2024-2025 prototype is shown in Fig. 6.24. The trigger signal from the Petiroc board reading the upstream tracker was sent to a CAEN DT5495 programmable logic unit (PLU) [158]. The signals from the CERN-PS T10 beam scintillator were also forwarded to the PLU, validating the coincidence in the beam spill window and producing the output trigger signal. A Skyworks SI5341-D-EVB differential clock board [159] fanned

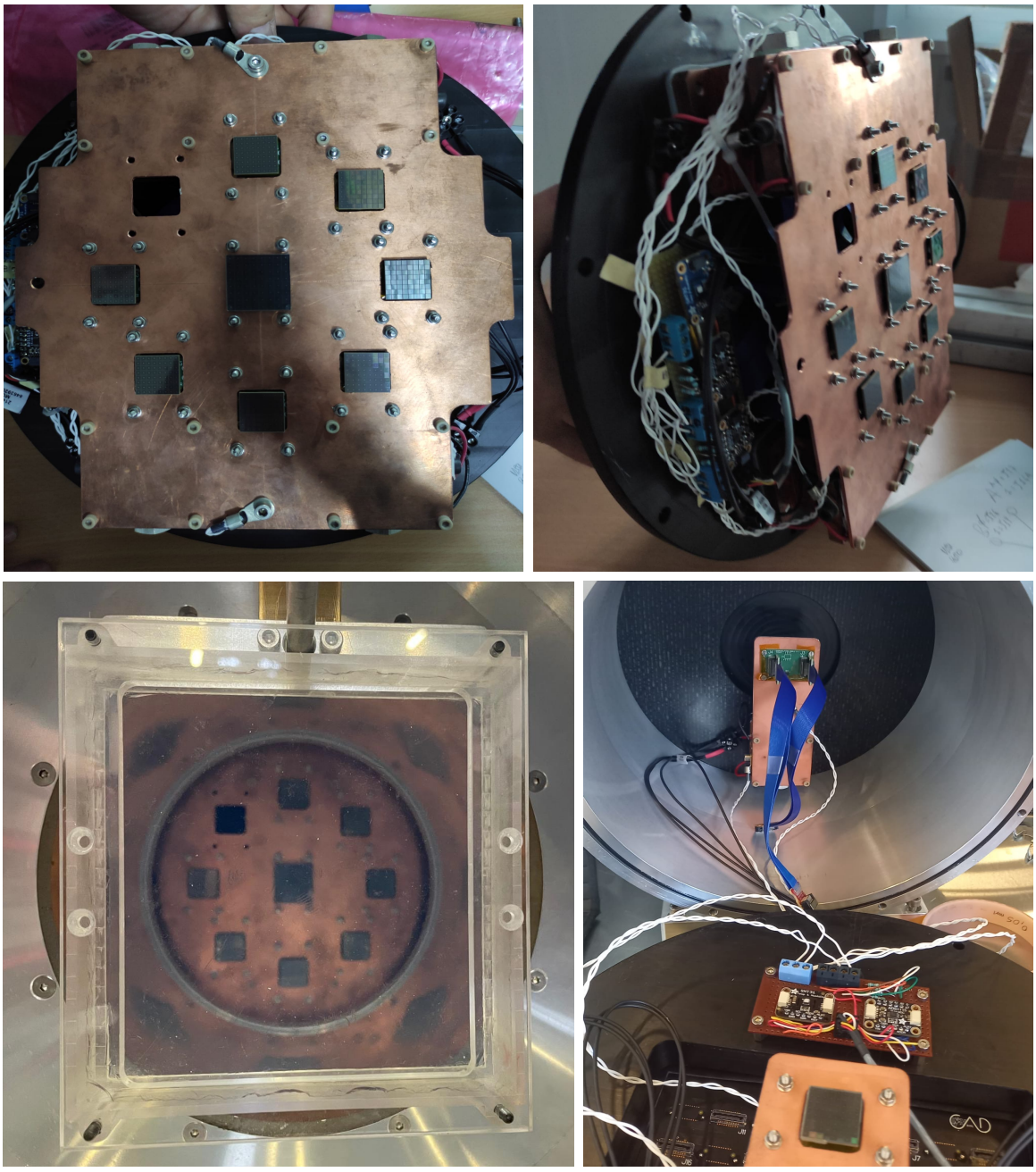

**Figure 6.23:** Photographs of the copper plates in the two vessels of the 2024-2025 setup, and of the interior of the main vessel with the aerogel tile installed. All arrays are Hamamatsu S13361-2050AE-08 ($2 \times 2$ mm$^2$ SiPMs), except the central array, which is a S13361-3075AE-08 ($3 \times 3$ mm$^2$ SiPMs).

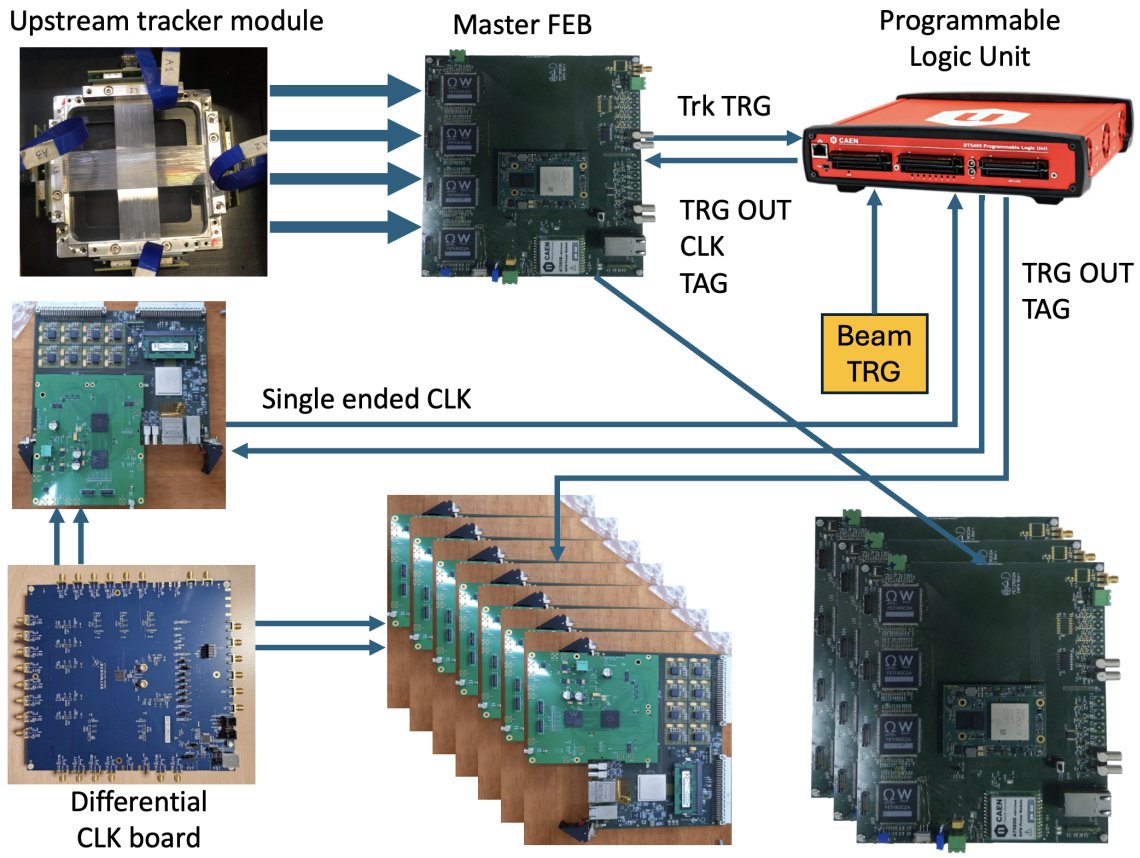


**Figure 6.24:** Data acquisition chain for the 2024-2025 prototype beam test setup.

out a 40 MHz clock to the RadioPico boards. One of the RadioPico boards forwarded a single ended copy of this clock to the PLU, which forwarded it to the master Petiroc board to have a synchronous data acquisition. The PLU distributed the output trigger and the spill signal, providing a tag for offline event matching. The master Petiroc board forwarded the trigger, spill signal, and clock to the other Petiroc boards in a daisy-chain configuration. Communication with boards was done using TCP/IP protocol. Data were transferred via Ethernet to the acquisition PC for later analysis.

### 6.5.2 Collected data

Data taking with the 2024-2025 prototype was carried out with the negatively charged beam at 10 GeV/$c$ and the positively charged beam at 8, 9 and 10 GeV/$c$ momentum. The aerogel tiles LEC6-2b and LEC4-1a, featuring a nominal refractive index of 1.03 and a thickness of 2 cm, were tested for Cherenkov angle reconstruction studies. With an acceptance of about 25% over the saturated Cherenkov rings from the aerogel and the excellent PDE of the SiPMs, this prototype proved to be ideal to validate the

pattern recognition performance in terms of photon yield and ring angular resolution and separation power, as well as its worsening with the increasing background. Ring reconstruction studies were complemented by timing studies, in which the relative time response of the central SiPM arrays at the N0, N1 and N2 positions read out by the RadioPico boards was characterized, as discussed in Section 6.2.5. Preliminary proof-of-concept studies were also performed for the gas-based e-ID option using a modified copper plate carrying four central Hamamatsu S13361-2050AE-08 SiPM arrays, with the negatively charged particle beam at momenta of 2, 3, and 4 GeV/$c$.

In the following, I report the main results from my analysis of the 2024-2025 data. First, I discuss the results on the Cherenkov angle reconstruction performance with the ALICE 3 bRICH baseline $2 \times 2$ mm$^2$ SiPMs of the S13361-2050AE-08 ring arrays and the impact of timing in suppressing the uncorrelated DCR background and the effect on the number of detected photons. Then I focus on the analysis of the pattern recognition performance and the impact of the increasing background on the Cherenkov angle reconstruction. I also show how the measured refractive index gradient allows the correct reproduction of the data with simulations. Then, I report the results on charged-particle timing using the central arrays. Finally, I show preliminary results on the validation studies for the gas-based e-ID option.

### 6.5.3 Event selection

For the 2024-2025 beam test analysis, I selected events in which the SiPM channel with the maximum charge in N0, N1 and N2, and in the X and Y views of the upstream and downstream tracker modules, T0 and T1, registered at least six photoelectrons.

Fig. 6.25 shows an example cumulative map of the hits in the five readout ring arrays in the aerogel vessel and the distribution of the extrapolated most probable X-Y photon emission points in aerogel for the negatively charged beam at 10 GeV/$c$ using tile LEC6-1a for the selected events. The expected ring centred on the most probable emission X-Y is also shown. The ring segments due to photons from pions are clearly visible. The ring arrays provide an overall acceptance for the ring photons of ≈25%.

### 6.5.4 Hit-track time matching

Following an approach similar to the one outlined for the 2022-2023 prototype analysis in Section 6.4.4, for each event, I used the SiPM cell with the largest number of detected photoelectrons in the central array N2 of the main vessel as the timing reference $t_{track}$ for the corresponding charged track. Then I referred the times of detected hits $t_{hit}$ in

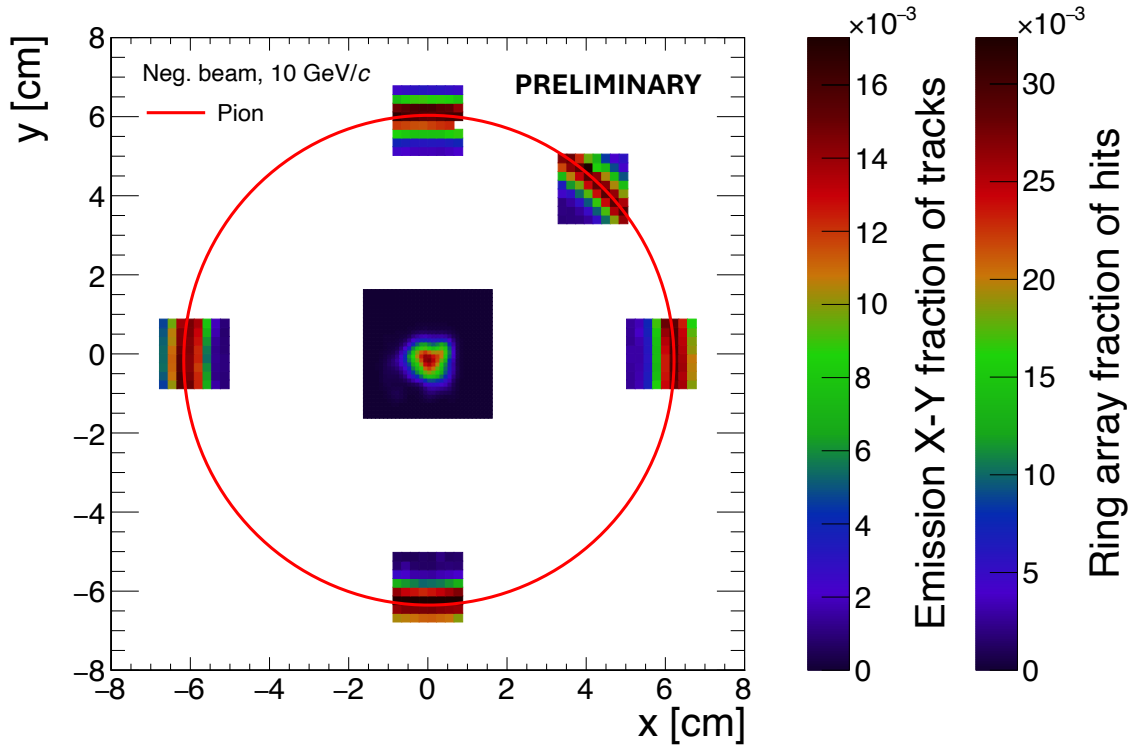


**Figure 6.25:** Spatial distribution of the extrapolated X-Y emission points at the most probable emission depth in the aerogel tile (central region) and of the hits in the five readout ring arrays (ring region) for the negatively charged beam at 10 GeV/$c$ momentum using tile LEC6-1a ($n = 1.03$). The expected Cherenkov ring from pions centred in the most probable X-Y emission point is also shown.

the ring arrays to the reference track time. Fig. 6.26 shows the 2D distributions of the reconstructed Cherenkov angle at the single hit level using the aerogel tile LEC6-2b as a function of the relative hit-track timing for the negatively charged beam at 10 GeV/$c$. The signal and background regions are highlighted.

The same considerations made for the corresponding plots obtained from beam test measurements with the 2022-2023 prototype on the signal, correlated and uncorrelated background contributions, discussed in Section 6.4.4, apply also in this case. In particular, the time distribution of the signal hits clustered at the expected pion Cherenkov angle has a Gaussian core with a sigma of approximately 340 ps. An improvement is achieved compared with the 450 ps obtained with Petiroc 2A due to the expected better single photoelectron capabilities of the Radioroc 2 coupled with the picoTDC. The main limitation of the setup, preventing the achievement of an even better resolution at single photoelectron level, mainly comes from the poor signal integrity due to the multiple connectors and cables routing the SiPM signals to the front-end ASICs.

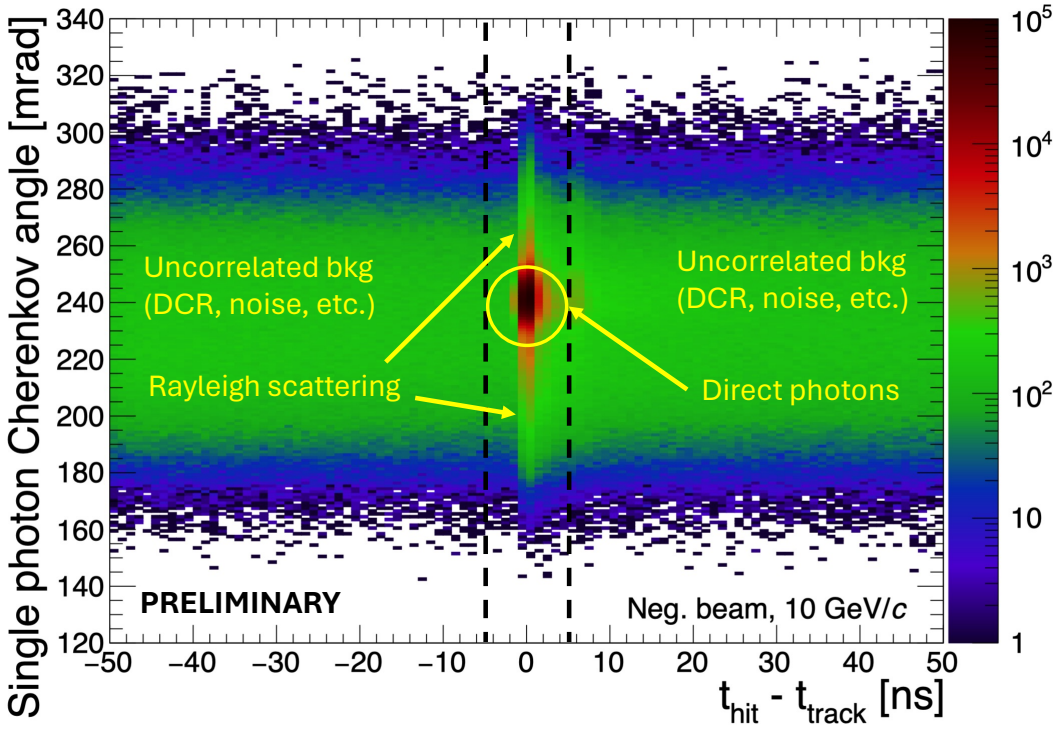


**Figure 6.26:** Distribution of the reconstructed aerogel single photon Cherenkov angle as a function of the relative time between the ring arrays $t_{hit}$ and the central array $t_{track}$ for the negatively charged beam at 10 GeV/$c$ momentum using tile LEC6-1a. The signal and background regions are highlighted.

I used the relative hit-track timing for the suppression of uncorrelated DCR hits and background modelling, following the procedures discussed in Sections 6.4.4 and 6.4.5.

### 6.5.5 Single photon angular resolution at saturation

The distribution of the reconstructed Cherenkov emission angle at single hit level obtained considering all available ring-array hits in the full 200 ns acquisition window of the picoTDC for the negatively charged beam at 10 GeV/$c$ using tile LEC6-1a is shown in Fig. 6.27. The corresponding distribution filtered by selecting only hits such that $|t_{hit} - t_{track}| < 5$ ns is also shown. I fitted the distributions with the sum of Gaussians for the signal peaks and a template background distribution, as discussed in Section 6.4.5.

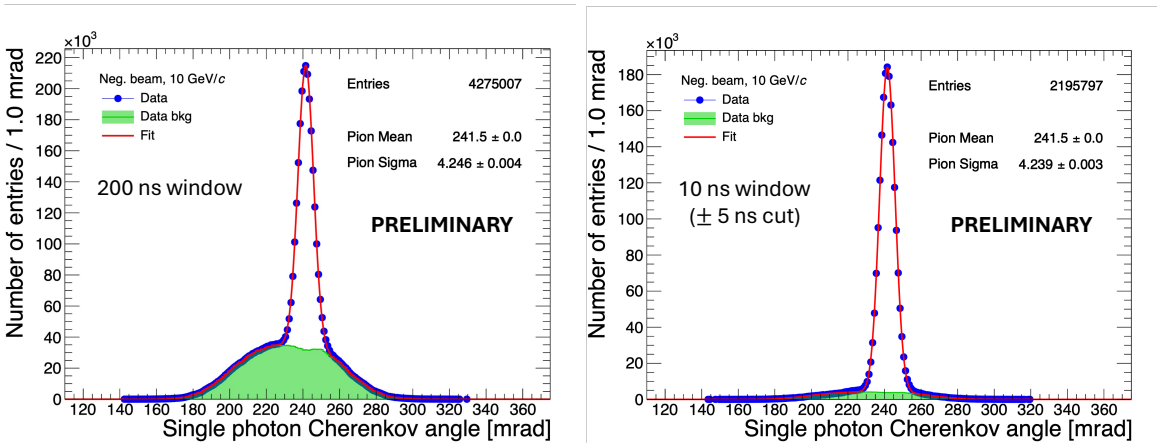


**Figure 6.27:** Single hit Cherenkov angle distribution for the negatively charged beam at 10 GeV/$c$ momentum using tile LEC6-1a considering all available ring array hits in the full 200 ns acquisition window of the picoTDC (left) and selecting only hits with relative hit-track matching in a ±5 ns time window (right). The vertical bars represent the statistical uncertainties. The fit with the sum of a Gaussian for the π peak and the corresponding template background distribution is also shown.

The Gaussian core of the distribution provides a single photon angular resolution $\sigma_c^\gamma$ of about 4.2 mrad. Despite the slightly larger expansion gap of 23.4 cm compared with the 23.0 cm of the 2022-2023 setup, a slight worsening is observed with respect to the 3.8 mrad measured with the 2022-2023 setup. This is expected due to the larger pixel size of the $2 \times 2$ mm$^2$ SiPMs of the S13361-2050-AE-08 arrays relative to the readout pitch of the $1 \times 1.625$ mm$^2$ of the S13552 arrays of the 2022-2023 setup.

Fig. 6.28 shows the corresponding angular distribution at the single hit level for runs with the positively charged beam at 9 GeV/$c$ and 8 GeV/$c$ momentum. The distributions are fitted accounting for the contribution of π, K and p. Discrepancies not larger than 0.15 mrad are observed for the single photon angular resolution of the π peak, which is always in the saturation regime, at the different momenta.

### 6.5.6 Efficiency and S/B ratio vs time matching window

Fig. 6.29 shows the signal efficiency and the signal-to-background ratio considering both all detected hits in the event and only hits in regions with measured angle $\theta_{\text{hit}}$ such that $|\theta_{\text{hit}} - \theta_\pi| < \text{N}\sigma_c^\gamma$, with N = 1, 2 and 3, as a function of the width of the hit-track timing window centred on $t_{\text{track}}$ for the negatively charged beam at 10 GeV/$c$. Here, $\theta_\pi$ and $\sigma_c^\gamma$ are the expected Cherenkov emission angle for π at 10 GeV/$c$ and the corresponding measured single photon angular resolution.

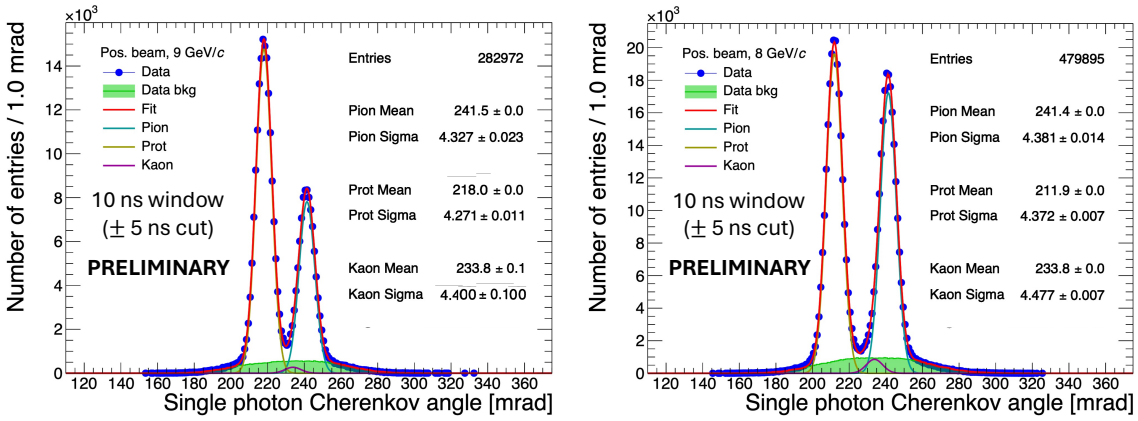


**Figure 6.28:** Single hit Cherenkov angle distribution using tile LEC6-1a selecting only hits with relative hit-track matching in a ±5 ns time window for the positively charged beam at 9 GeV/$c$ (left) and 8 GeV/$c$ (right). The vertical bars represent the statistical uncertainties. The fit with the sum of Gaussians for the π, p and K peaks and a template background distribution is also shown.

I evaluated the signal efficiency as the ratio of the area under the fit Gaussian peak for the considered time window to the area under the fit Gaussian peak considering all hits. Values above 95% were achieved considering a time window larger than 2 ns, corresponding to a $|t_{hit} - t_{track}| < 1$ ns hit-track matching cut.

I calculated the signal-to-background ratio as the ratio of the area under the fit Gaussian peak to the area under the fit background model. Values above 40, 57 and 82 were achieved at 3, 2 and 1 $\sigma_c^\gamma$, respectively, with a time window shorter than 2 ns.

### 6.5.7 Signal and background yield vs time matching window

Fig. 6.29 also shows the extrapolated mean number of detected signal hits, correlated background hits, uncorrelated background hits and total background hits per track with reconstructed angle $\theta_{hit}$ such that $|\theta_{hit} - \theta_\pi| < 3\sigma_c^\gamma$ as a function of the full width of the relative hit-track timing window for the negatively charged beam at 10 GeV/$c$.

The number of signal hits and correlated background hits increases as the time window enlarges, approaching saturation in a few ns. On the contrary, the number of uncorrelated background hits increases linearly with the time window. However, it remains lower than the amount of correlated background hits for time windows shorter than 20 ns, showing how efficiently the DCR hits are discarded using timing.

In the region covered by the five ring arrays in Fig. 6.25, corresponding to about 25% of the full ring, I found on average more than 5.5 signal hits on top of an overall background of less than 0.12 hits for a time window of 2 ns in the region $|\theta_{hit} - \theta_\pi| < 3\sigma_c^\gamma$.

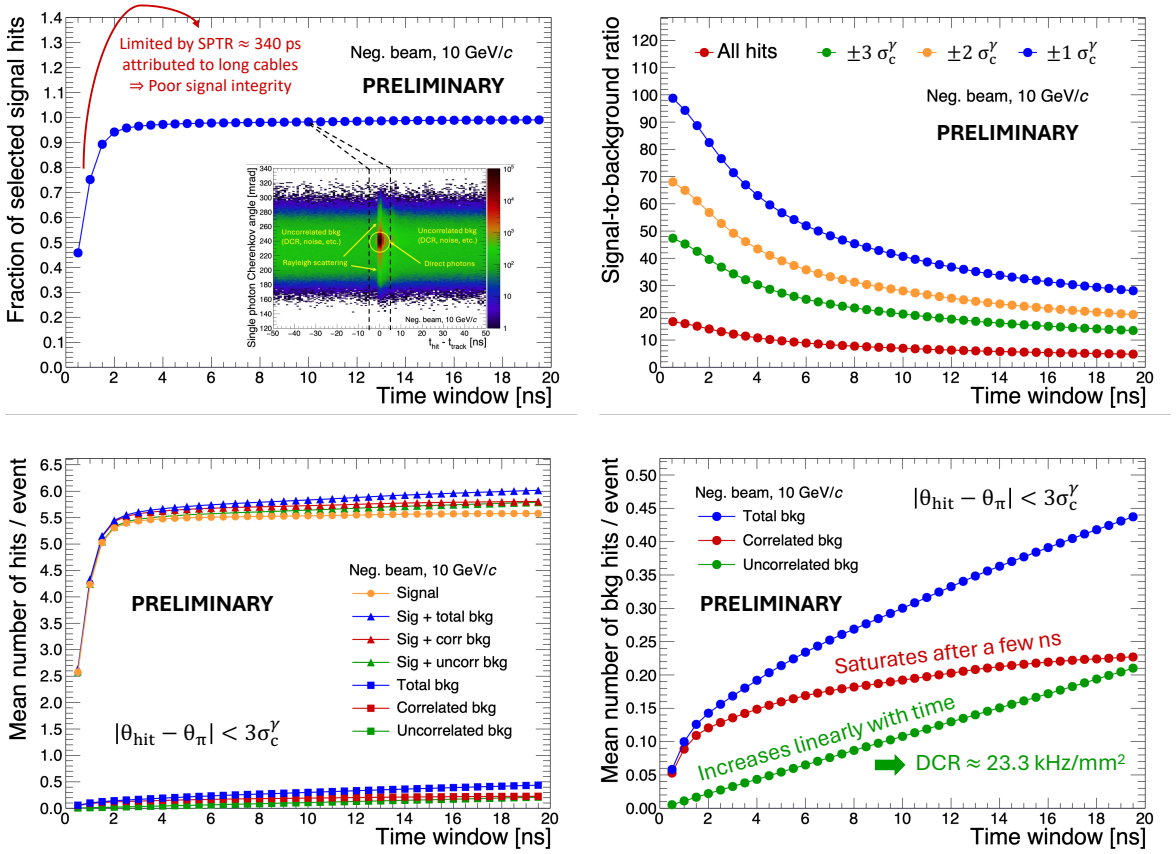


**Figure 6.29:** Signal efficiency (top left), signal-to-background ratio (top right) and extrapolated mean number of detected signal hits, correlated background hits, uncorrelated background hits and total background hits per track (bottom left and bottom right) as a function of the full width of the hit-track timing window centred on $t_{track}$ for the negatively charged beam at 10 GeV/$c$ using tile LEC6-1a. The signal-to-background ratio is evaluated considering both all detected hits in the event and only hits in regions with measured angle $\theta_{hit}$ such that $|\theta_{hit} - \theta_\pi| < N\sigma_c^\gamma$, with N = 1, 2 and 3. The mean number of signal and background hits per event is evaluated in the interval $|\theta_{hit} - \theta_\pi| < 3\sigma_c^\gamma$.

## 6.5.8 Extrapolation to the full ring acceptance

To infer the signal and background yields over the full ring acceptance within a given $\pm N\sigma_c^\gamma$ band, I constructed signal and background acceptance maps. Specifically, I scanned the XY plane at the most probable emission depth in Z and over the space of track direction cosines. At each scan point, I simulated negative–pion tracks traversing the selected position with the chosen direction.

For the signal template, for each track I generated Cherenkov photons in aerogel with the expected Cherenkov emission angle relative to track direction resulting in the measured single photon angular resolution $\sigma_c^\gamma$ on the photodetector plane and a uniform azimuth around the track. I accepted only photons satisfying $|\theta_{hit} - \theta_\pi| < N\sigma_c^\gamma$. I then

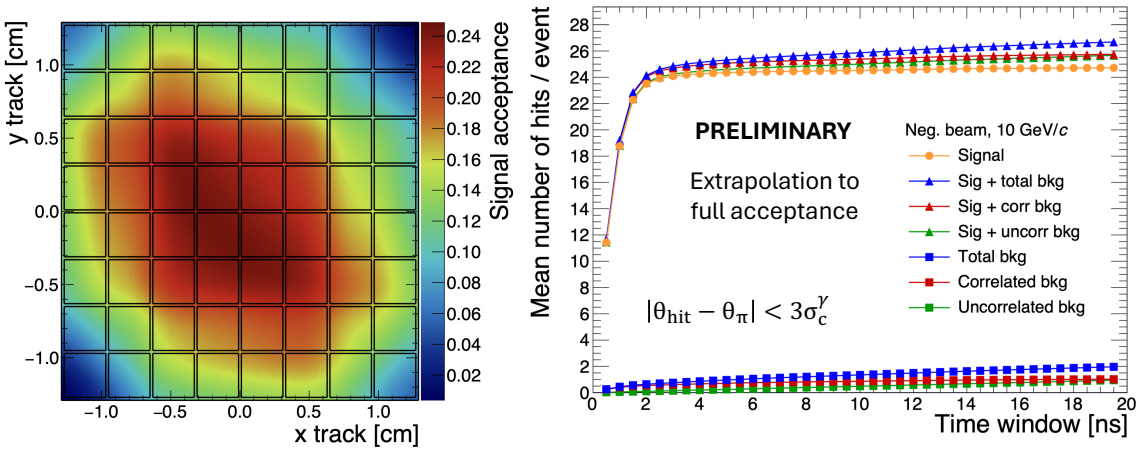


**Figure 6.30:** Simulated map of the ring acceptance of the five ring arrays as a function of the most probable X-Y photon emission point in aerogel mapped over the central array N2 (left) and extrapolation of the measured signal hits and background hits reported in the bottom-right panel of Fig. 6.29 to the full acceptance for the negatively charged beam at 10 GeV/$c$ using tile LEC6-1a.

computed, for each configuration, the fraction of accepted photons falling within the five available ring arrays, relative to all accepted photons. The left panel of Fig. 6.30 shows the resulting signal acceptance map for N = 3 at normal incidence.

For the background template, I generated uniformly distributed background hits over the full photodetector area, accepted those with $|\theta_{\rm hit} - \theta_\pi| < {\rm N}\sigma_{\rm c}^\gamma$, and evaluated their fraction in the five available ring arrays relative to all the accepted ones.

For the analysis, I assigned to each track a signal and a background acceptance weight, $w_{\rm sig}$ and $w_{\rm bkg}$, given by the corresponding maps at the most probable emission point and track direction. Finally, I rescaled the mean numbers of signal and background hits in Fig. 6.29 to full acceptance by multiplying by the number of tracks and the inverse of the sum of the weights, i.e. by $N_{\rm tracks}/\sum w_{\rm sig}$ and $N_{\rm tracks}/\sum w_{\rm bkg}$, respectively.

The right panel of Fig. 6.30 reports the extrapolated signal and background yields for N = 3 as a function of the time–matching window. The result corresponds to about 23.5 signal photon hits per event on top of fewer than 0.5 background hits per event. This is consistent with the simulation predictions, taking into account the considered operating overvoltage and the corresponding SiPM PDE profile.

Overall, these results validate the simulation in terms of the expected photon yield with the reference 2 cm thick aerogel tiles and the baseline photodetector specifications.

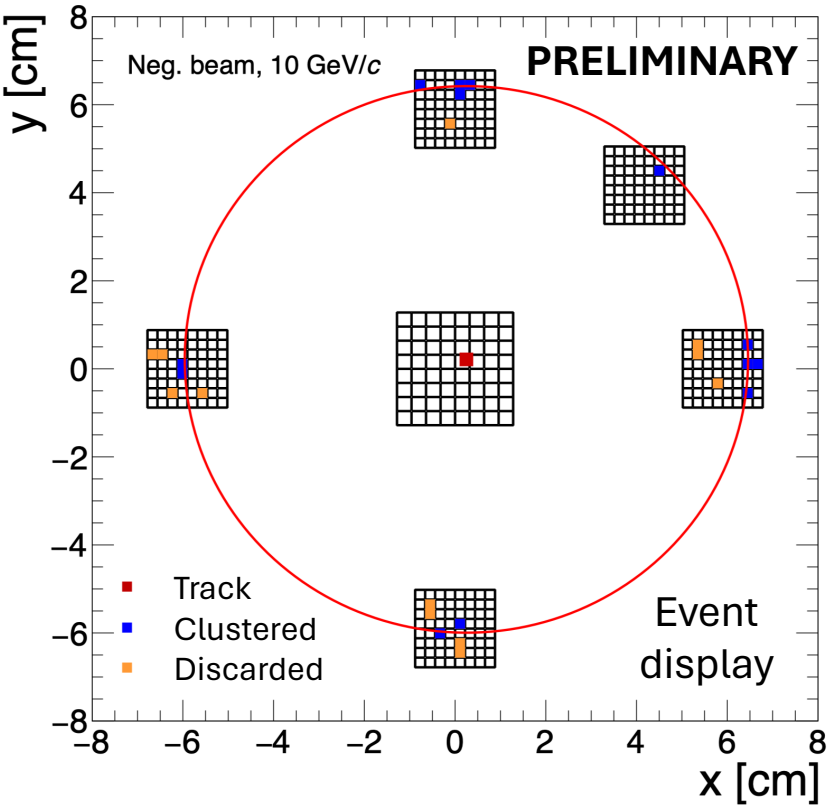


**Figure 6.31:** Event display of the most probable X-Y coordinates of the photon emission point (red) and ring array hits for the negatively charged beam at 10 GeV/$c$ using tile LEC6-1a. Pattern recognition using the Hough Transform method clusters the most probable signal hits (blue). Only hits with relative hit-track matching in a ±5 ns time window are accepted. Hits discarded due to the time matching condition or at the Hough Transform level are also shown (orange).

### 6.5.9 Pattern recognition performance

With the available ring acceptance, the 2024–2025 prototype enabled systematic studies of pattern recognition and ring reconstruction, reaching ring–angle resolutions with more than 15 detected photons per event. For all studies reported below, I used the Hough transform for pattern recognition following the procedure in Section 4.3.4.

Fig. 6.31 shows an event display for the negatively charged 10 GeV/$c$ beam using tile LEC6–1a, selecting hits within a ±5 ns hit–track time window. Hough–selected hits, with the corresponding ring fit, and rejected hits are highlighted.

To visualize the effectiveness of hit filtering with the Hough transform, Fig. 6.32 shows cumulative maps of Hough-selected hits relative to the most probable X-Y emission coordinates, selecting only hits within a ±5 ns hit–track time window, for tile LEC6–1a.

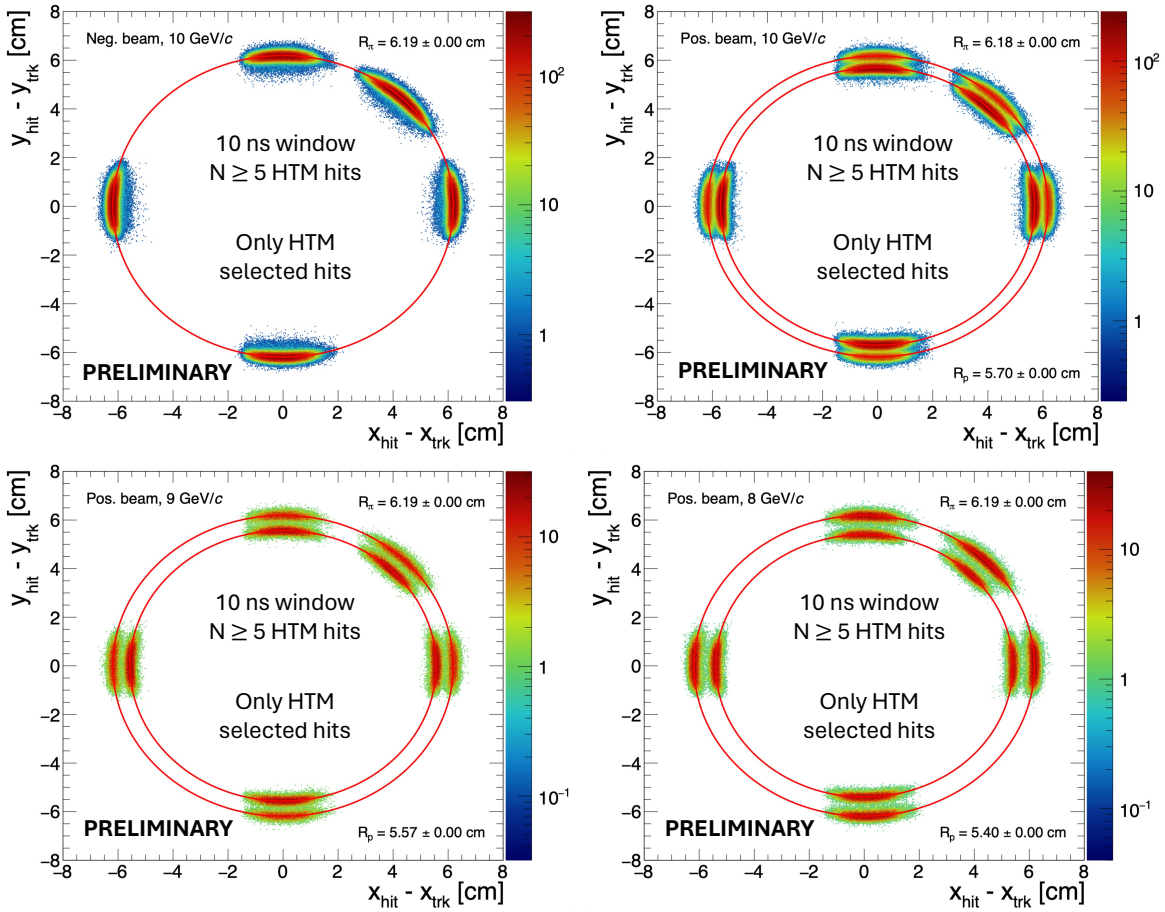


**Figure 6.32:** Cumulative hit maps of clustered hits using the Hough Transform method for pattern recognition relative to the most probable X-Y emission coordinates considering only hits with relative hit-track matching in a ±5 ns time window using the LEC6-1a aerogel tile for the negatively charged beam at 10 GeV/$c$ momentum (top left) and the positively charged beam at 10 GeV/$c$ (top right), 9 GeV/$c$ (bottom left) and 8 GeV/$c$ (bottom right) momentum. The fit rings are also shown.

The panels correspond to the negatively charged beam at 10 GeV/$c$ and the positively charged beam at 10, 9, and 8 GeV/$c$. The fitted rings are also shown. For the positive beam, the separation between the pion and proton contributions is clearly visible.

The top panels of Fig. 6.33 show, for the negatively charged beam at 10 GeV/$c$ momentum, the distribution of the mean number of Hough–selected hits and the resulting ring–angle resolution as a function of the number of Hough–selected hits. Only hits within a ±5 ns hit–track time window are considered.

With a $2 \times (2\sigma_c^{\gamma})$ Hough window, about 5.8 hits (sig+bkg) were clustered per event. Events with up to 16-17 clustered hits were recorded. With the excellent single hit angular resolution of 4.2 mrad, ring resolutions at saturation better than 1.5 mrad were measured with 10 or more clustered hits for the considered time matching window.

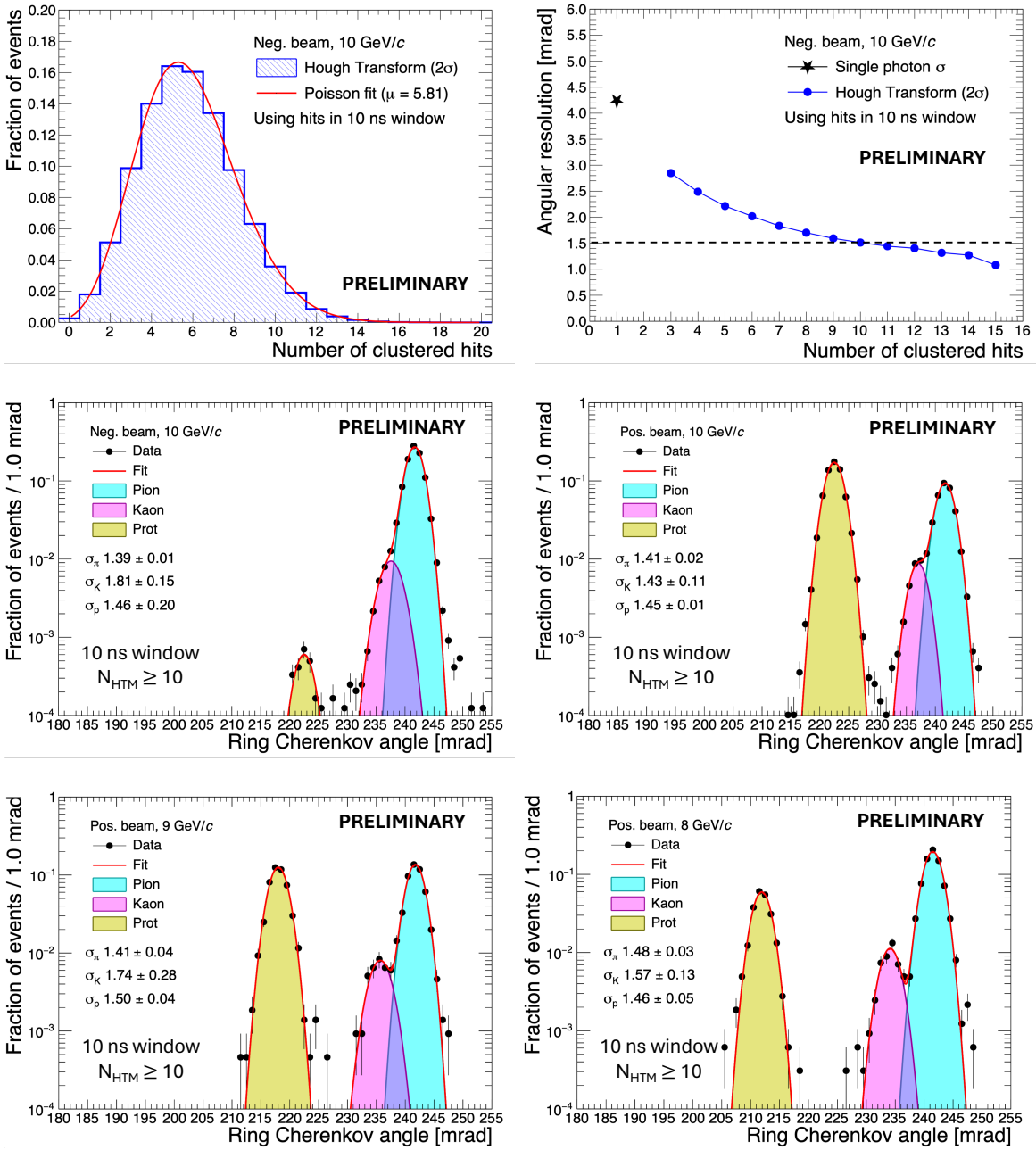


**Figure 6.33:** Distribution of the mean number of Hough-selected hits (top left), ring angular resolution as a function of the number of Hough-selected hits (top right) and distribution of the ring Cherenkov angle with at least 10 Hough-clustered hits fitted with Gaussians for π, K and p (middle left) measured selecting only hits with relative hit-track matching in a ±5 ns time window for the negatively charged beam at 10 GeV/$c$ momentum using tile LEC6-1a. The corresponding ring Cherenkov angle distributions for the positively charged beam at 10 GeV/$c$ (middle right), 9 GeV/$c$ (bottom left) and 8 GeV/$c$ (bottom right) are also shown.

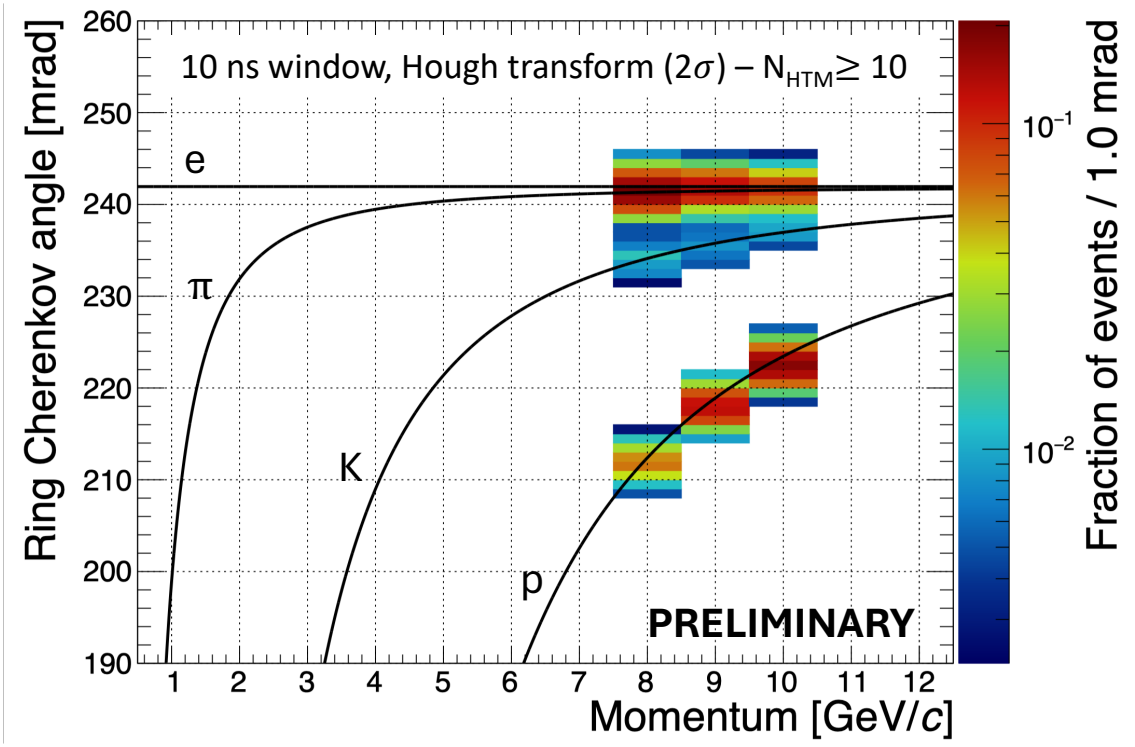


**Figure 6.34:** Reconstructed ring Cherenkov angle distribution as a function of the beam momentum considering only hits with relative hit-track matching in a ±5 ns time window and using the Hough Transform method requiring 10 or more selected hits for the runs with the positively charged beam at 8 GeV/$c$, 9 GeV/$c$ and 10 GeV/$c$ momentum. The theoretical curves for e, π, K and p are shown.

The middle and bottom panels of Fig. 6.33 show the ring Cherenkov–angle distributions obtained with at least 10 Hough–clustered hits and Gaussian fits for π, K, and p for the negatively charged 10 GeV/$c$, and the positively charged beam at 10, 9, and 8 GeV/$c$. The distributions obtained with the positively charged beam are also shown in Fig. 6.34 as a function of momentum. The theoretical curves for e, μ, π, K and p are also shown.

For all the considered datasets, momenta and particle species, the measured ring angular resolution in these conditions was always better than the target 1.5 mrad. The results indicate a separation power exceeding 3σ for all considered particle species and momenta, with the most remarkable outcome being the limiting 3σ $\pi/K$ separation at 10 GeV/$c$, one of the original bRICH design targets.

### 6.5.10 Performance stability with increasing background

The results presented in the previous section refer to the background levels achieved selecting only hits within a ±5 ns hit–track time matching window with a measured DCR of 23.3 kHz/mm$^2$ at the considered temperature and overvoltage.

To study the impact of the increasing background on the pattern recognition performance, I repeated the studies in Fig. 6.33 performing the Hough transform with various matching windows between 1 ns and 200 ns, corresponding to the full acquisition window of the picoTDC. With the increasing time window, the amount of signal and correlated background hits remains approximately the same, while the uncorrelated DCR background increases linearly with the window.

The top panels of Fig. 6.35 show, for the negatively charged 10 GeV/$c$ beam, the distribution of the mean number of Hough–selected hits and the resulting ring–angle resolution as a function of the number of Hough–selected hits for various time windows.

For a window of 1 ns, the mean number of Hough-clustered hits decreases significantly since, due to the poor SPTR of about 340 ps of the considered system, the time matching requirement is cutting the signal. For windows much larger than 10 ns the mean number of Hough-clustered hits increases since uncorrelated DCR hits are more likely to be clustered together. These background hits affect the ring resolution. For example, for 10 clustered hits the ring resolution worsens from about 1.5 mrad for a matching window of 10 ns to about 2.4 mrad for a matching window of 200 ns.

The effect can also be observed in the middle and bottom panels of Fig. 6.35, showing the ring Cherenkov–angle distributions obtained with at least 10 Hough–clustered hits and Gaussian fits for $\pi$, K, and p for the negatively charged 10 GeV/$c$, and the positively charged beam at 10, 9, and 8 GeV/$c$ considering all hits in the considered 200 ns acquisition window for pattern recognition. The larger spread of the $\pi$, K, and p peaks relative to Fig. 6.33 is clearly visible.

### 6.5.11 Extrapolation to the bRICH DCR levels

To relate these results to the expected bRICH operating conditions, accounting for DCRs at the MHz/mm$^2$ level with the reference $2 \times 2$ mm$^2$ SiPMs after irradiation, the improved SPTR anticipated from direct SiPM–front-end coupling, and a targeted acquisition window shorter than 4 ns, I performed the following study.

Considering the nominal measured DCR of 23.3 kHz/mm$^2$ in the beam test conditions, for each considered time matching window within the 200 ns picoTDC limit I evaluated the equivalent DCR under the hypothesis that all DCR hits are detected in a bRICH target acquisition window of 1 ns, 2 ns and 3 ns. As figures of merit I evaluated the mean number of Hough-selected hits as a function of the considered hit-track time matching window, i.e. the equivalent DCR, and ring angular resolution as a function of both the time window and the number of Hough-selected hits.

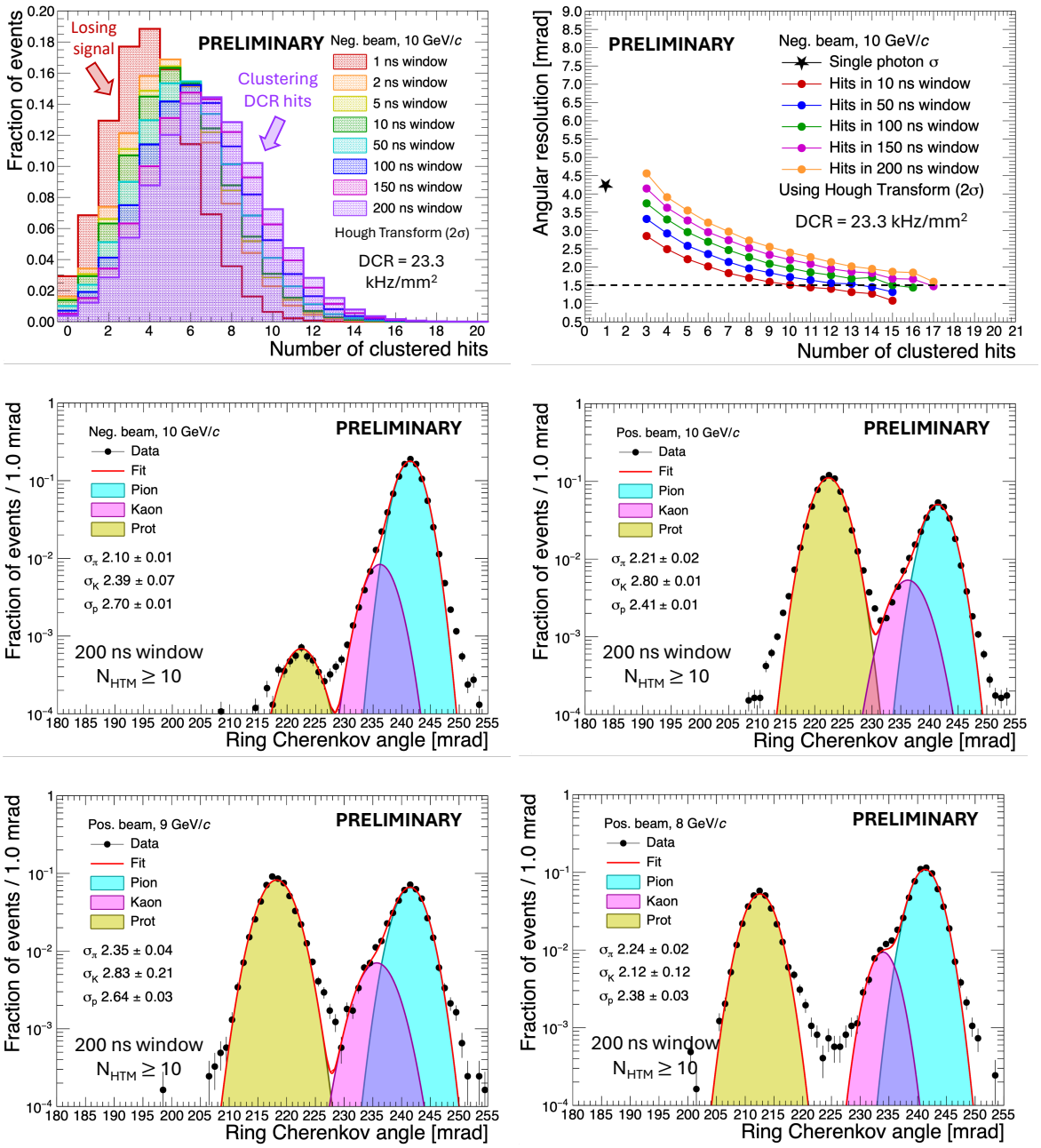


**Figure 6.35:** Distribution of the mean number of Hough-selected hits (top left) and ring angular resolution as a function of the number of Hough-selected hits (top right) measured for various hit-track time matching windows between 1 ns and 200 ns for the negatively charged beam at 10 GeV/$c$ momentum using tile LEC6-1a. The distributions of the ring Cherenkov angle with at least 10 Hough-clustered hits fitted with Gaussians for π, K and p measured considering all hits in the full 200 ns acquisition window using tile LEC6-1a with the negatively charged beam at 10 GeV/$c$ (middle left), and the positively charged beam at 10 GeV/$c$ (middle right), 9 GeV/$c$ (bottom left) and 8 GeV/$c$ (bottom right) are also shown.

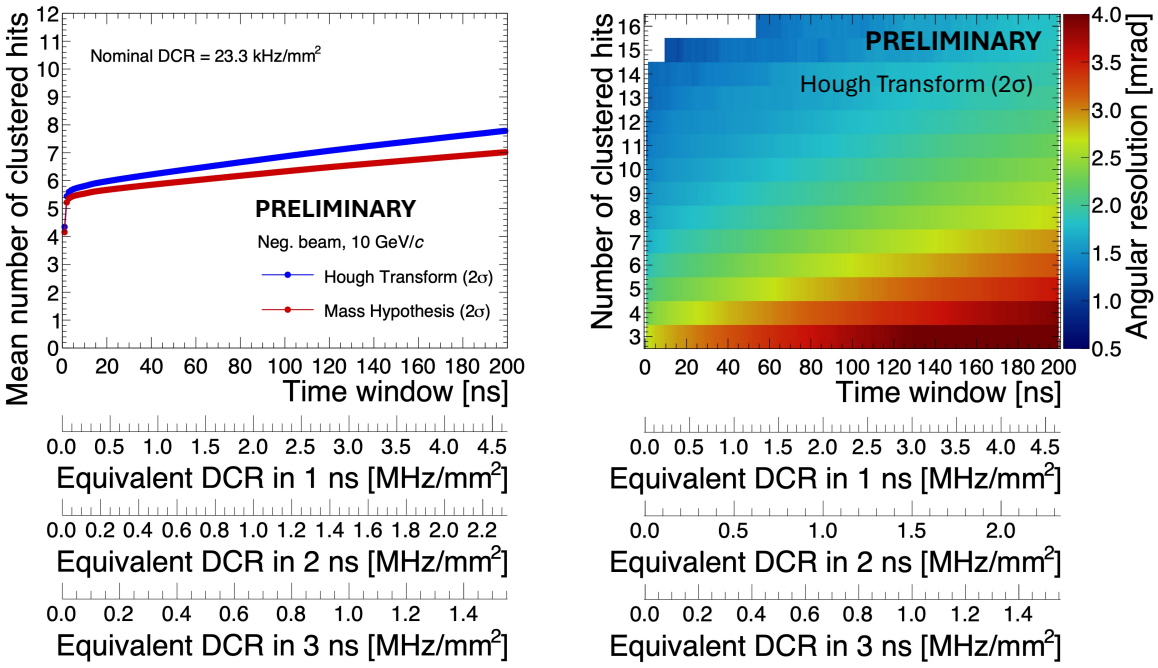


**Figure 6.36:** Mean number of Hough-selected hits as a function of the considered hit-track time matching window for the hit selection (left) and ring angular resolution as a function of both the time window and the number of Hough-selected hits (right) measured for the negatively charged beam at 10 GeV/$c$ momentum using tile LEC6-1a. The conversion of this window into an equivalent SiPM DCR if all DCR hits were detected in a 1 ns, 2 ns and 3 ns acquisition window is reported.

The results for the negatively charged beam at 10 GeV/$c$ momentum using tile LEC6-1a are shown in Fig. 6.36. For this study, the full 200 ns picoTDC acquisition window corresponds to an equivalent DCR of $\approx$ 4.6 MHz/mm$^2$ for a 1 ns bRICH window, $\approx$ 2.5 MHz/mm$^2$ for 2 ns, and $\approx$ 1.5 MHz/mm$^2$ for 3 ns.

Conversely, the reference 1 MHz/mm$^2$ level corresponds to a picoTDC window of $\approx$ 43 ns for the 1 ns bRICH window, $\approx$ 86 ns for 2 ns and $\approx$ 129 ns for the 3 ns window.

Over the full acquisition window, the mean number of selected hits in the five considered ring arrays increases from 5.8 for a picoTDC window of 10 ns to about 7.8, corresponding to about 34% extra background hits per track. The resulting ring resolution for a given number of clustered hits worsens by up to 0.9 mrad with the increasing window, since a given number of clustered hits is the result of the contribution of fewer signal hits and more background hits, as discussed in the previous section. Nevertheless, thanks to the excellent single photon angular resolution, for more than 16 hits the target 1.5 mrad ring resolution is recovered even in the worst case of a 200 ns window.

In addition, depending on the bRICH acquisition time gate, up to 4 ns, the reference 1 MHz/mm$^2$ DCR level corresponds to the hits in a time window much shorter than the maximum 200 ns picoTDC acquisition window, significantly mitigating this worsening.

Finally, with the bRICH target SPTR better than 100 ps, the time–matching procedure discussed in Section 4.3.3 further suppresses uncorrelated hits, improving the overall reconstruction performance, approaching the target performance even at high DCR.

Therefore, modulo considerations on SiPM recovery times, front-end conversion times, and the data throughput required at high DCR, which must be carefully addressed, these studies demonstrate that ring reconstruction remains stable even at these levels. The target physics performance is largely preserved, with only modest degradation, provided that the data acquisition system can sustain the corresponding rates.

### 6.5.12 Performance validation with simulations

For all the measurements presented in this chapter, I performed dedicated simulation studies for the interpretation and validation of the analysis results. One of the most striking outcomes is the observation of the expected "self–focusing" effect in the aerogel tiles, originating from the measured refractive–index gradient along the tile depth discussed in Section 6.2.1, resulting in a measured single photon angular resolution of about 4 mrad, as observed in Figs. 6.19, and 6.27. This measured resolution is notably better than the expectation for a uniform refractive index, as assumed in all the simulation studies discussed in Chapter 4, given the 2 cm aerogel thickness and the thickness of the expansion gap adopted in all beam test configurations.

As an example, Fig. 6.37 shows the simulated single-hit Cherenkov-angle distributions and the distributions of the number of Hough-clustered hits for the negatively charged 10 GeV/$c$ beam using tile LEC6-1a with the 2024-2025 setup. The results obtained assuming a uniform refractive index of $n = 1.03$ along the tile depth are compared with those including the measured quadratic $n$ gradient.

As expected, the distribution obtained with uniform $n$ is non-Gaussian. It is dominated by the nearly flat contribution from the geometric uncertainty on the emission point, modulated by Rayleigh scattering, and it yields a resolution worse than 5.8 mrad.

In contrast, including the measured refractive–index gradient in the simulation mitigates this geometric contribution and produces an almost ideal Gaussian that reproduces the measured resolution. Moreover, this modelling better reproduces the number of Hough–clustered hits under the operating conditions without any additional tuning.

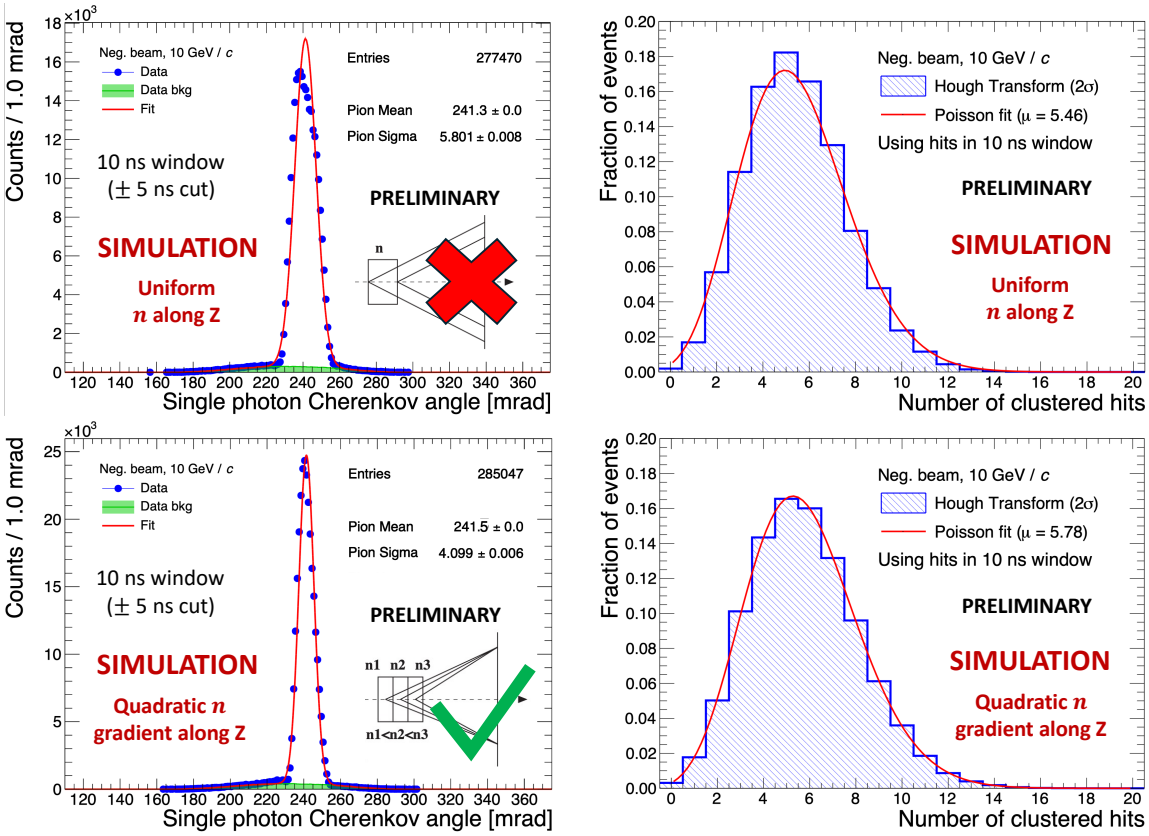


**Figure 6.37:** Simulated single hit Cherenkov angle distributions (left) and number of clustered hits using the Hough Transform for pattern recognition (right) for the negatively charged beam at 10 GeV/$c$ using tile LEC6-1a. The distributions obtained for uniform $n = 1.03$ along the tile depth (top) are compared with the ones accounting for the observed $n$ gradient along the tile depth (bottom).

All pattern-recognition results, which depend strongly on the single photon angular resolution, then follow consistently and match the data under this assumption.

This observation is crucial for the future of the bRICH project. If the same refractive-index gradient can be reliably reproduced in new tile productions, the detector would achieve substantially better pattern recognition and physics performance than those reported in Chapter 4, effectively at no extra cost.

### 6.5.13 Charged-particle timing with picoTDC

To highlight the impact of the improved front-end relative to the 2022–2023 prototype, Fig. 6.38 shows the offset- and time-walk–corrected distributions of the time difference between the SiPMs with the maximum picoTDC ToT for two pairs of arrays along the beam line (N2–N0 and N1–N2) for the negatively charged beam at 10 GeV/$c$. A S13361-3075AE-08 array with a 1 mm thick $SiO_2$ window is at position N2 and two

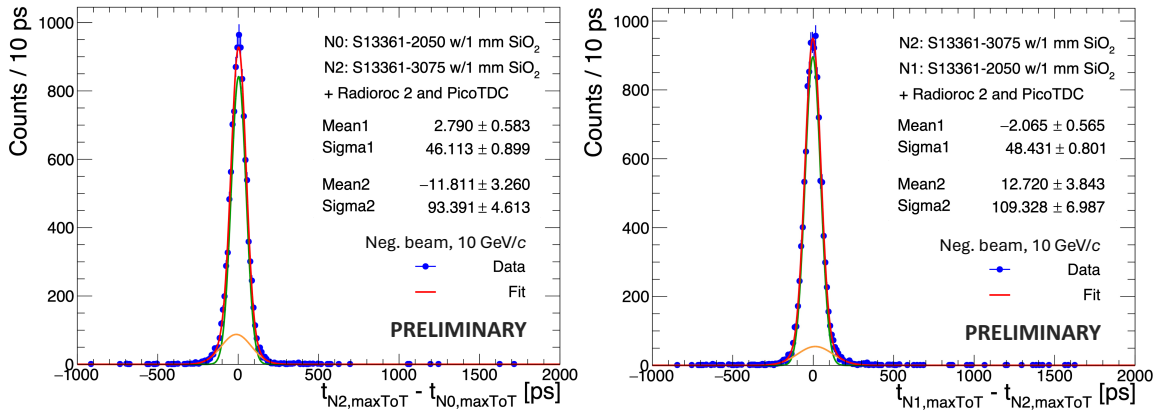


**Figure 6.38:** Distributions of the time difference between the SiPMs with the maximum picoTDC ToT for the arrays N2–N0 (left) and N1–N2 (right) for the negatively charged beam at 10 GeV/$c$.

S13361-2050AE-08 arrays with a 1 mm thick $SiO_2$ window are at positions N0 and N1.

For the channel-by-channel offset and time-walk corrections I used a lookup-table procedure similar to the one in Section 6.2.5, but based on pairs of ToT intervals rather than photoelectron equivalents. This approach is approximate, since the relation between ToT and the number of photoelectrons becomes non-linear at high signal charge, and substantially larger statistics is required to build a reliable lookup table.

The resulting distributions in Fig. 6.38 exhibit a double-Gaussian profile. The core has a sigma of about 46–48 ps, while the tail has a sigma of about 93 ps. Although the tail is still under investigation, assuming equal contributions from the two arrays, the core resolutions on the time difference between the hits in two arrays of 46–48 ps correspond to about 33–34 ps per array at the full-system level.

These results demonstrate the expected performance improvement when using Radioroc 2 and picoTDC compared with Petiroc 2A, indicating that the limiting contribution to the achievable resolution primarily arises from the front-end electronics. The performance is also constrained by the long cables between the SiPMs and the front-end. Further improvements are expected with direct coupling of the electronics to the SiPMs, potentially approaching time resolutions of order 20 ps or better.

### 6.5.14 Validation of e-ID option using high-$n$ gas

For the last measurement campaign with the 2024-2025 prototype, a modified copper plate equipped with four central Hamamatsu S13361-2050AE-08 SiPM arrays was employed to perform preliminary proof-of-concept studies of the gas-based e-ID option.

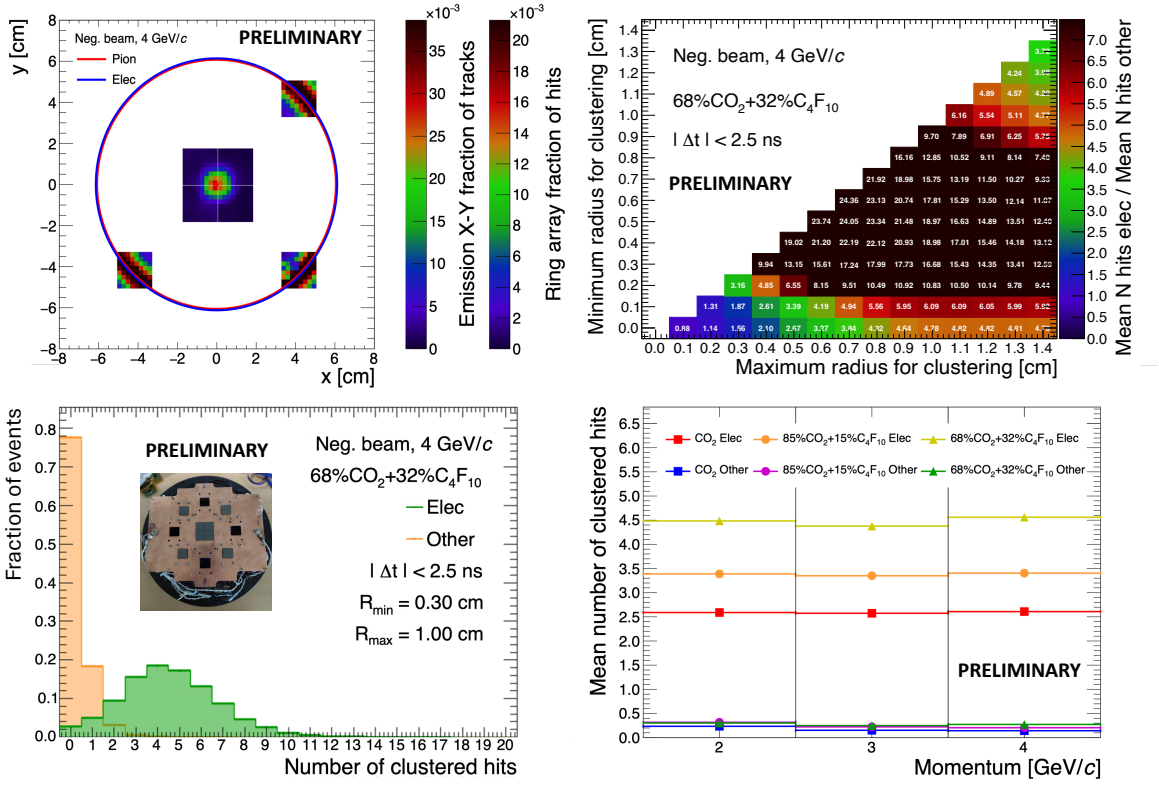


**Figure 6.39:** Very preliminary results for the gas-based e-ID study. Cumulative hit-map (top left), scan over clustering radii optimizing the e/$\pi$ separation criterion (top right), and distributions of the number of clustered hits for electron and pion samples identified with the T10 Cherenkov counters (bottom left) for the negatively charged beam at 4 GeV/$c$ with the 68% $CO_2$ + 32% $C_4F_{10}$ mixture. The bottom-right panel shows the mean number of clustered hits in narrow fiducial regions for a selection of radial and time-matching cuts for all the considered gas mixtures and momenta.

Although it was not possible to test the $C_5F_{10}O$+$CO_2$ green gas mixture discussed in Section 3.5, measurements were carried out with $CO_2$ and its mixtures with $C_4F_{10}$ to investigate performance for refractive index values around the reference 1.0006. Specifically, data were collected for refractive indices of about 1.00046 (pure $CO_2$), 1.00060 (85% $CO_2$ + 15% $C_4F_{10}$), and 1.00076 (68% $CO_2$ + 32% $C_4F_{10}$). Measurements were performed using the negatively charged particle beam at momenta of 2, 3, and 4 GeV/$c$, dominated by electrons and pions as described in Section 6.1. For each trigger, signals from the two Cherenkov counters along the T10 beam line [129] were recorded by the CAEN DT5495 logic unit to tag electron and other tracks.

I studied the clustering of hits around the track impact points for electrons and other species as a function of the gas refractive index, the beam momentum, the hit-track time matching cut, and the minimum and maximum radii used for clustering.

Fig. 6.39 shows some of the main results, including the cumulative hit-map, the scan over clustering radii to optimize the e/$\pi$ separation criterion, and the distributions of the number of clustered hits for electron and pion samples identified using the T10 Cherenkov counters for the negatively charged 4 GeV/$c$ beam. The bottom-right panel reports a summary of the results for the mean number of clustered hits for a selection of the radial and time matching cuts for the considered mixtures and momenta.

While the aerogel rings do not separate electrons from pions, the threshold-induced gas clusters do, with clear gas signal clusters for electrons and a limited amount of fake clusters for pions mainly due to DCR signals and direct charged-particle hits.

The gas-based signal exhibits the expected separation between electrons and other species up to the target 4 GeV/$c$ momentum for the considered 23.4 cm radiator gap. The best performance was obtained with the gas mixtures 85% $CO_2$ + 15% $C_4F_{10}$ and 68% $CO_2$ + 32% $C_4F_{10}$. Further optimizations based on machine-learning to maximize the electron discrimination are ongoing. Despite pending optimizations, the results validate the gas-based option for enhanced e-ID around the reference $n = 1.0006$.

# Conclusions

This thesis presented the design, optimization, and experimental validation of the barrel Ring Imaging Cherenkov detector (bRICH) proposed for the future ALICE 3 experiment planned for LHC Run 5. The work was aimed at defining an efficient and cost-effective solution for charged-particle identification (PID) to achieve the target PID requirements in the most challenging environment of central Pb–Pb collisions.

The first part of the thesis focused on the conceptual design and optimization of the detector layout. I proposed and investigated a modular projective proximity-focusing geometry, using aerogel tiles as Cherenkov radiators and SiPM-based photon detectors oriented toward the nominal interaction vertex. I optimized this configuration to enhance PID performance while minimizing the total active area and overall cost.

I also investigated the appealing option of flushing the bRICH expansion gap with an eco-friendly heavy-gas mixture to extend the electron identification reach, and assessed the feasibility of efficient charged-particle timing using the same SiPM modules coupled to a thin radiator window, achieving time resolutions of a few tens of picoseconds.

The simulation work included detailed performance studies in the high-multiplicity Pb–Pb environment, taking into account realistic worst-case SiPM dark count rate (DCR) conditions. To improve PID under these conditions, I developed fast machine-learning algorithms based on Boosted Decision Trees, trained to recognize Cherenkov-ring topologies and electron-cluster patterns. These algorithms outperformed classical approaches such as Hough-transform-based pattern recognition combined with Bayesian PID, showing that the proposed bRICH detector ensures the ALICE 3 target PID and physics requirements even in the most challenging operation conditions.

Through dedicated characterization measurements of irradiated Hamamatsu SiPM arrays, I defined a realistic operation and ageing model based on cooling down to or below -40°C and annealing cycles above 70°C to ensure operation within the reference 1 MHz/mm$^2$ DCR safety limit at the expected integrated fluences in ALICE 3 of units of $10^{11}$ MeV $n_{eq}$/cm$^2$. In addition, I explored the use of smaller SiPMs coupled with light concentrators to mitigate DCR while maintaining the same effective area.

A key result of this work came from the characterization of aerogel tiles. Measurements of hydrophobic aerogel tiles from Aerogel Factory Co., Ltd. revealed a refractive-index gradient along the tile thickness, leading to a natural focusing effect that improves the angular resolution in the proposed bRICH geometry. This effect was confirmed by beam-test data and may have potential influence on future RICH detector designs.

My design and simulation-based optimization studies were complemented by beam test activities of various prototypes at the CERN-PS T10 facility between 2022 and 2025 aimed at validating the proposed detector concept. I actively contributed to the design, preparation, and execution of these tests, as well as to the full data analysis. The results confirmed the expected photon yield, the single-photon and ring angular resolutions, and the stability of the reconstruction performance under the worst expected DCR conditions, thus validating the proposed detector layout and operation strategy.

Measurements also validated the excellent charged-particle timing performance achieved with SiPMs and the integration of the gas-based option for e-ID enhancement, proving them to be valid options to enhance the bRICH performance and physics reach.

Overall, my work demonstrated the feasibility of the proposed projective proximity-focusing bRICH design and delivered a validated, cost-effective solution that, according to simulations and beam-test measurements, met the target ALICE 3 PID goals and physics requirements with unique contributions, in particular to dielectron physics.

Thanks to the studies presented in this thesis, the proposed projective bRICH concept was accepted as the baseline detector layout in the ALICE 3 Scoping Document.

# Appendix A

# Contributions to the single photon angular resolution

In this Appendix, I discuss the main contributions to the single photon angular resolution in a proximity-focusing RICH geometry, as considered for the ALICE 3 bRICH.

The measurements necessary to define the Cherenkov angle $\theta_{\mathrm{c}}$ are the photon detection point ($x$, $y$, $z$), the particle direction ($\theta_{\mathrm{p}}$, $\phi_{\mathrm{p}}$), the depth of the photon emission point in the radiator $z_{\mathrm{e}}$ and the photon energy $E$, as illustrated in Fig. A.1. The assumption is made that these variables are uncorrelated. From the resulting functional dependence $\theta_{\mathrm{c}} = \theta_c(E, z_{\mathrm{e}}, x, y, z, \theta_{\mathrm{p}}, \phi_{\mathrm{p}})$, the uncertainty on the reconstructed Cherenkov angle at the single hit level can then be expressed according to the following equation:

$$\sigma_{\mathrm{c}}^{\gamma} = \sqrt{\sum_{\mathrm{i}} \left( \frac{\partial \theta_{\mathrm{c}}}{\partial v_{\mathrm{i}}} \sigma_{v_{\mathrm{i}}} \right)^2} \tag{A.1}$$

where the variables $v_{\mathrm{i}}$ are $E$, $z_{\mathrm{e}}$, $x$, $y$, $z$, $\theta_{\mathrm{p}}$, $\phi_{\mathrm{p}}$ and the variables $\sigma_{v_{\mathrm{i}}}$ are their respective root-mean-square (rms) uncertainties, depending on the thickness and refractive index of the radiator, the chromatic dispersion of the radiator, the refractive index of the gas in the expansion gap, and the granularity of the sensors.

## A.1 Cherenkov angle reconstruction

For the calculation of the derivatives in Eq. A.1, the Z axis is chosen normal to the RICH surfaces and the X axis such that the incident particle direction vector lies in the ZX plane, as shown in Fig. A.1. The origin of the ZXY coordinate system is taken

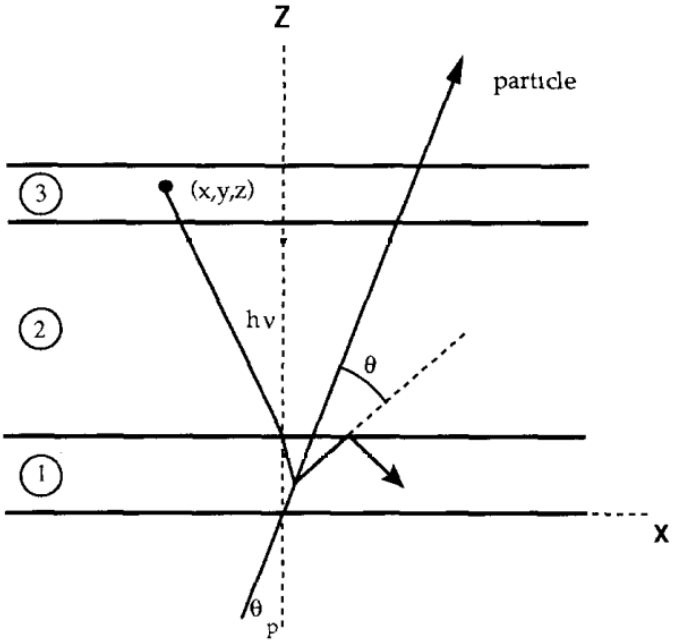


**Figure A.1:** Schematic of a proximity focusing RICH geometry. The Cherenkov radiator (1) is separated from the photodetector volume (3) by an expansion gap filled with dry gas (2).

at the point where the charged particle enters the radiator making an angle $\theta_p$ relative to the Z axis. With this choice of axes, the azimuthal angle $\phi_p$ between the X axis and the projection of the particle direction onto the XY plane is $\phi_p = 0$. The distance $z_e$ along the particle path defines the photon emission point $(z_e \cos\theta_p,\ z_e \sin\theta_p,\ 0)$.

The photon direction is defined by its polar angle $\theta_c$, relative to the particle direction, and its azimuthal angle $\phi_c$ in the plane perpendicular to the particle direction, such that $\phi_c = 0$ corresponds to a photon emitted in the plane defined by the charged track and the $X$ axis at an angle $\theta_p + \theta_c$ with respect to the $Z$ axis.

The vector direction of the emitted photons $(a_z,\ a_x,\ a_y)$ is given by

$$\begin{aligned} a_z &= \cos\theta_p \cos\theta_c - \sin\theta_p \sin\theta_c \cos\phi_c \\ a_x &= \sin\theta_p \cos\theta_c + \cos\theta_p \sin\theta_c \cos\phi_c \\ a_y &= \sin\theta_c \sin\phi_c \end{aligned} \tag{A.2}$$

where $a_x^2 + a_y^2 + a_z^2 = 1$. The photon vector ray trace including refraction at the radiator-gap surface gives the following equations for the photon coordinates

$$\begin{aligned} x &= z_e \sin\theta_p + R a_x \\ y &= R a_y \end{aligned} \tag{A.3}$$

with

$$R = \frac{T_r - z_e \cos\theta_p}{a_z} + \frac{T_g}{e_z}$$
$$e_z = \sqrt{a_z^2 + \frac{\langle n_g\rangle^2}{\langle n\rangle^2} - 1} \tag{A.4}$$

where $T_r$, $T_g$, $\langle n\rangle$ and $\langle n_g\rangle$ are the radiator thickness, the gap thickness, the radiator average refractive index and the average refractive index in the gap region. By combining Eqs. A.2 and A.3, the reconstructed angles ($\theta_c$, $\phi_c$) are obtained as a function of the measured quantities. In the approximation $T_r \ll T_g$, the following relations are obtained:

$$\cos\theta_c = \sin\theta_p \frac{\langle n_g\rangle}{\langle n\rangle} \cdot \frac{x}{r} + \cos\theta_p \sqrt{1 - \frac{\langle n_g\rangle^2}{\langle n\rangle^2} \cdot \frac{x^2+y^2}{r^2}}$$
$$\sin\theta_c \cos\phi_c = \cos\theta_p \frac{\langle n_g\rangle}{\langle n\rangle} \cdot \frac{x}{r} - \sin\theta_p \sqrt{1 - \frac{\langle n_g\rangle^2}{\langle n\rangle^2} \cdot \frac{x^2+y^2}{r^2}} \tag{A.5}$$
$$\sin\theta_c \sin\phi_c = \frac{\langle n_g\rangle}{\langle n\rangle} \cdot \frac{y}{r}$$

where $r = \sqrt{x^2+y^2+z^2}$.

## A.2 Localization and track incidence uncertainties

The uncertainties associated with the measured variables ($z$, $x$, $y$, $\theta_p$) can be directly calculated from Eq. A.5:

$$\frac{\partial\theta_c}{\partial x} = \frac{\eta}{T_g}\left(\alpha e_z \cos\phi_c - \sin\theta_p \sin\theta_c \sin^2\phi_c\right)$$
$$\frac{\partial\theta_c}{\partial y} = \frac{\eta \sin\phi_c}{T_g}\left(\cos\theta_c - \cos\theta_p \frac{1-m}{a_z}\right)$$
$$\frac{\partial\theta_c}{\partial z} = \frac{\alpha\eta}{T_g}\left(\cos\theta_p \sin\theta_c + \sin\theta_p \cos\theta_c \cos\phi_c\right) \tag{A.6}$$
$$\frac{\partial\theta_c}{\partial\theta_p} = -\cos\phi_c$$

where $\alpha = e_z/a_z$, $\eta = e_z\langle n\rangle^2/\langle n_g\rangle^2$ and $m = (\langle n_g\rangle/\langle n\rangle)^2$.

## A.3 Geometric uncertainty

The emission distance dependence $\partial\theta_c/\partial z_e$ cannot be obtained directly from Eq. A.5 since its derivation assumed $T_r \approx 0$, hence no explicit dependence is included. The dependence is obtained by considering the variation, at emission, of $x$ and $y$, i.e. $\partial x/\partial z_e = -\cos\theta_p(a_x/a_z)$ and $\partial y/\partial z_e = -\cos\theta_p(a_y/a_z)$, which leads to the result

$$\frac{\partial\theta_c}{\partial z_e} = \frac{\eta\sin\theta_c}{T_g(1+k\alpha^3\langle n\rangle^2/\langle n_g\rangle^2)}\left[\alpha^2(1-\sin^2\theta_p\sin^2\phi_c)+\lambda(\sin\theta_p\sin\phi_c)^2\right] \tag{A.7}$$

where $k = T_r/2T_g$ and $\lambda = (1+k\alpha^3)/(1+k\alpha)$.

## A.4 Chromatic uncertainty

The chromatic derivative $\partial\theta_c/\partial n$ cannot be obtained directly from Eq. A.5 since it has no explicit $n$ dependence (the $n$ in the equation is the average value). This dependence is caused by the variation, at emission, of the direction cosines $\partial a_z/\partial n = -\sin\theta_p\cos\phi_c/n\sin\theta_c$, $\partial a_x/\partial n = \cos\theta_p/n\tan\theta_c$ and $\partial a_y/\partial n = \sin\phi_c/n\sin\theta_c$ giving

$$\frac{\partial\theta_c}{\partial n} = \left(\frac{1}{\langle n\rangle\tan\theta_c}\right)\frac{\langle n\rangle^2\beta^2}{1-\tan\theta_p\tan\theta_c\cos\phi_c}. \tag{A.8}$$

## A.5 Evaluation of the rms uncertainties

The final step for the analytical treatment is the evaluation of the rms uncertainties $\sigma_{v_i}$ to be used in Eq. A.1. While the partial derivatives listed above represent a general feature of the proximity focusing configuration, the rms uncertainties are strictly related to the detector response.

The chromatic rms is calculated as $\sigma_n = (\mathrm{d}n/\mathrm{d}\lambda)\,\sigma_\lambda$. The first factor is the derivative of the radiator refractive index $n$ with respect to the photon wavelength, while the second factor is the standard deviation of the detected Cherenkov photon wavelength spectrum, resulting from the convolution of the spectrum of the emitted photons with the media transmittance and with the photodetector PDE.

The geometric rms can be estimated from the radiator thickness $T_r$ and the charged track incidence angle $\theta_p$ as $\sigma_{z_e} = T_r/(\sqrt{12}\cos\theta_p)$, where a uniform distribution is assumed for the photon emission point along the particle path in the radiator.

The localization rms includes the uncertainties of the hit coordinates $x$, $y$, and $z$ on the sensor plane. If the photodetector is segmented in pixels with size $\Delta x \times \Delta y \times \Delta z$, the corresponding rms are $\sigma_x = \Delta x/\sqrt{12}$, $\sigma_y = \Delta y/\sqrt{12}$ and $\sigma_z = \Delta z/\sqrt{12}$.

The rms on the track angles $\sigma_{\theta_p}$ and $\sigma_{\phi_p}$ depend on the precision of the tracking system.

## A.6 Magnetic field and multiple scattering errors

Multiple scattering and magnetic deflection in the radiator medium represent additional (= a) error sources $\sigma_{\rm a}$, which differ from the measurements and chromatic errors because they are momentum dependent. They have the form $\sigma_{\rm a} = p_{\rm a}/p$ with the contributions from multiple scattering (ms) or magnetic field (ma) given by:

$$\begin{aligned} p_{\rm ms} &= k_{\rm ms}\sqrt{L/X_0}, \\ p_{\rm ma} &= k_{\rm ma} BL \sin\theta_{\rm ma} \end{aligned} \tag{A.9}$$

with a resultant momentum

$$p_{\rm a} = \sqrt{p_{\rm ms^2} + p_{\rm ma}^2}. \tag{A.10}$$

The constants in Eq. A.9 are $k_{\rm ms} = (2/3)(13.6)$ MeV $= 9.1$ MeV, $k_{\rm ma} = (2/\pi)(0.3)/\sqrt{12}$ GeV/T·m $= 55.1$ GeV/T·m with $X_0$ the radiation length, $B$ the magnetic field strength and $\theta_{\rm ma}$ the particle angle relative to the magnetic field direction. The values of $k_{\rm ms}$ and $k_{\rm ma}$ are rms averages over the path length $L$ (the factor 2/3) and the image circumference (the factor $2/\pi$), respectively. This error $\sigma_{\rm a}$ must be added in quadrature to the momentum independent error $\sigma_c^\gamma$ in Eq. A.1.

# Appendix B

# Generation of the projective geometry

In this Appendix, I present the algorithm I developed to generate the projective proximity-focusing geometry of the baseline bRICH system introduced in Section 3.4.

The following assumptions are made. The system is segmented into an even number of independent sectors housed in two different symmetric cylindrical vessels, leaving a gap at $Z = 0$ for services. Each sector is further divided into modules, each including an aerogel tile and the corresponding photodetector module, aligned parallel to one another within frames shaped as isosceles trapezoidal prisms whose upstream faces subtend the same solid angle, which varies with the sector, at the nominal interaction point. Each module is then positioned such that the line connecting the intersection points of the diagonals of the upstream face of the photodetector and aerogel frames passes through the nominal interaction point and is normal to both frames. All bRICH modules within a given sector share the same expansion gap thickness and identical geometries for both the aerogel tiles and photodetector modules. The thickness of the expansion gap in each sector is maximized to optimize the single-photon angular resolution, within the constraints imposed by the radial space available to the bRICH system. The geometries of the aerogel tiles and photodetector modules are optimized to ensure maximum acceptance for the charged particles originating from the nominal interaction point. A schematic view of the proposed projective geometry concept in the $RZ$ and $XY$ planes is shown in Figs. B.1 and B.2, respectively. A 3D view of a single module in this geometry is shown in Fig. B.3. In the following sections I report the input parameters, the output geometry specifications, the implementation details of the algorithm, and the parameters used to generate the baseline geometry.

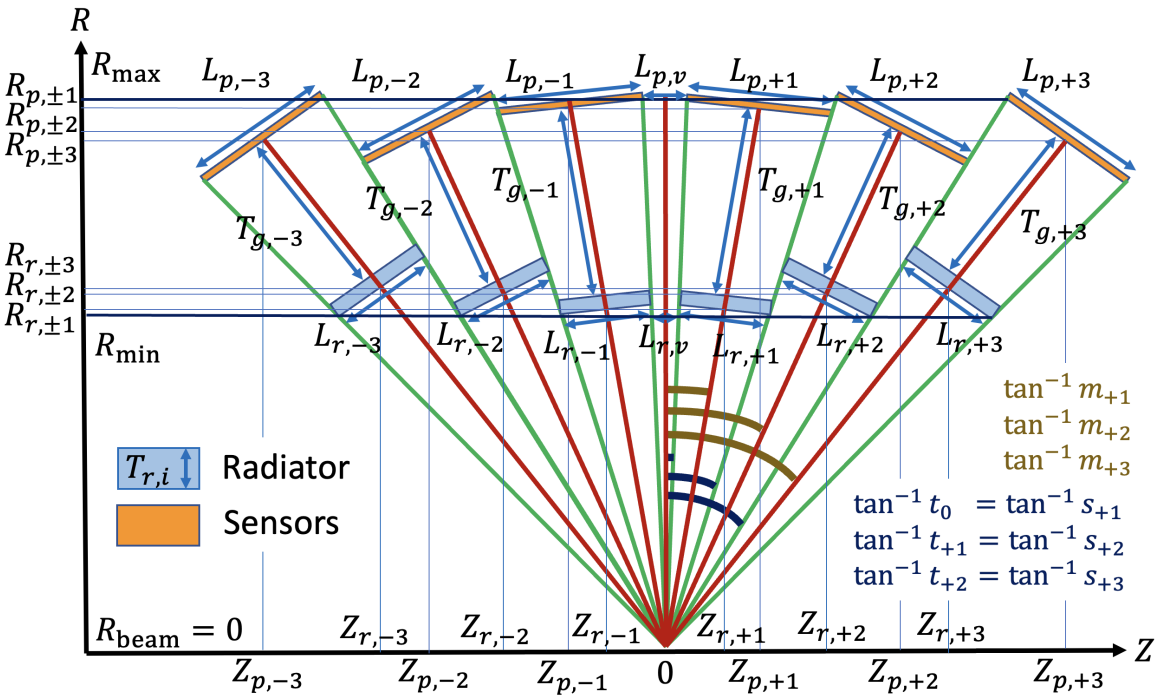


**Figure B.1:** Schematic view of projective geometry concept in the $RZ$ plane assuming $N_Z = 6$.

## B.1 Input parameters

The input parameters of the algorithm for the projective bRICH geometry are

- $N_Z$: the number of sectors. It must be an even number and each sector is labelled with an index $i = \pm 1, ..., \pm N_Z/2$, where $|i|$ increases with increasing $|Z|$. The signs + and − indicate sectors in the regions $Z > 0$ and $Z < 0$, respectively.
- $N_\phi$ is the number of modules per sector. Each module in a sector is labelled with an index $j = 1, ..., N_\phi$, with $j$ increasing in the counter-clockwise direction in the transverse $XY$ plane.
- $R^{\text{up}}_{\text{min}}$: the minimum radius of the upstream face of the frame for the aerogel tiles in the plane defined by the intersection point of the diagonals of the upstream face of the aerogel tiles and the $Z$ axis.
- $R^{\text{up}}_{\text{max}}$: the maximum radius of the upstream face of the frame for the photodetector modules in the plane defined by the intersection point of the diagonals of the upstream face of the aerogel tiles and the $Z$ axis.
- $L_{p,i}$, $i = \pm 1, ..., \pm N_Z/2$: the height of the trapezoidal section of the frames for the photodetector modules in each sector. The edges having size $L_{p,i}$ are in the

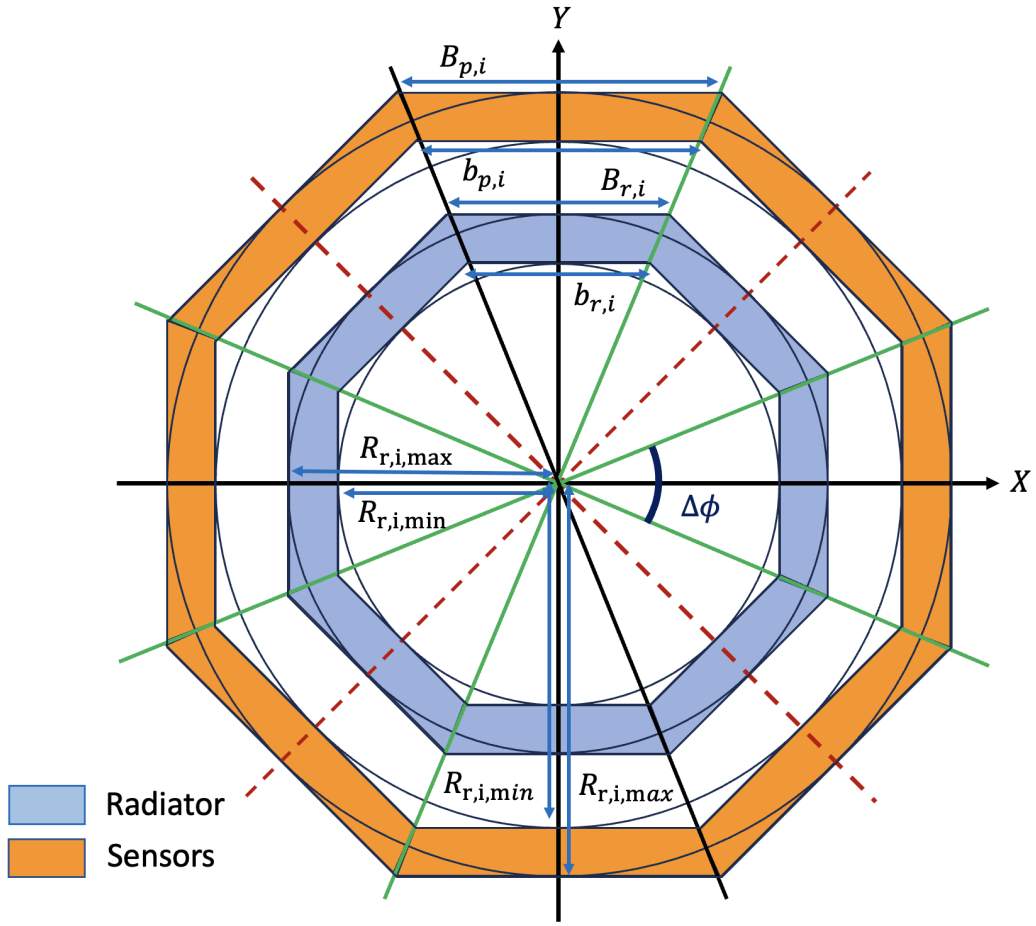


**Figure B.2:** Schematic view of projective geometry concept in the $XY$ plane assuming $N_\phi = 8$.

plane defined by the intersection point of the diagonals of the upstream face of the aerogel tiles and the $Z$ axis.

- $T_{r,i}$, $i = \pm 1, ..., \pm N_Z/2$: the thickness of the aerogel tiles in each sector.
- $L_{p,v}$: the distance along the $Z$ axis between the closest points of the upstream faces of the frames for the photodetector modules with same $j = 1, ..., N_\phi$ in the sectors $i = -1$ and $i = +1$.

## B.2 Output geometry specifications

The output specifications of the algorithm of the projective bRICH geometry are

- $L_{r,i}$, $B_{r,i}$, $b_{r,i}$ ,$i = \pm 1, ..., \pm N_Z/2$: the height, the long basis and the short basis of the trapezoidal section of frames for the aerogel tiles in each sector. The edges

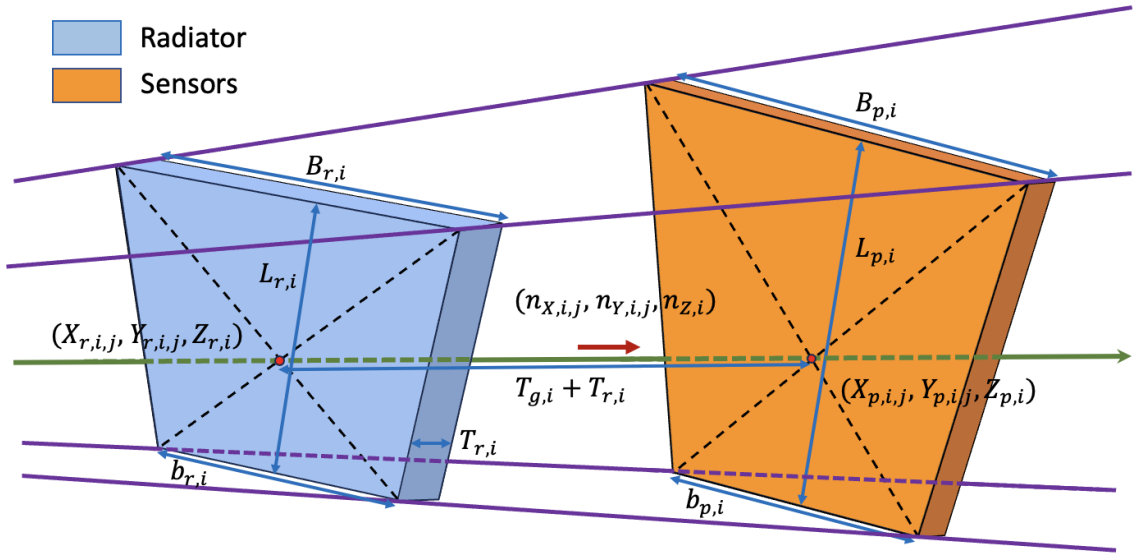


**Figure B.3:** Schematic 3D view of single module in projective geometry.

having size $L_{r,i}$ are in the plane defined by the intersection point of the diagonals of the upstream face of the aerogel tiles and the $Z$ axis, while the edges having size $B_{p,i}$ and $b_{p,i}$ are in its transverse plane passing through the $Z$ axis located at the maximum and minimum radial distance from the $Z$ axis, respectively.

- $B_{p,i}$, $b_{p,i}$ ,$i = \pm 1, ..., \pm N_Z/2$: the long basis and the short basis of the trapezoidal section of frames for the photodetector module in each sector. The edges having size $B_{p,i}$ and $b_{p,i}$ are in the plane transverse to the plane defined by the intersection point of the diagonals of the upstream face of the aerogel tiles and the $Z$ axis, passing through the $Z$ axis and are located at the maximum and minimum radial distance from the $Z$ axis, respectively.

- $X_{p,i,j}$, $Y_{p,i,j}$ and $Z_{p,i}$, $i = \pm 1, ..., \pm N_Z/2$, $j = 1, ..., N_\phi$: the $X$, $Y$ and $Z$ coordinates of the centre of the upstream face of the frame for the photodetector modules in each sector. All the modules in a given sector have the same $Z_{p,i}$.

- $X_{r,i,j}$, $Y_{r,i,j}$ and $Z_{r,i}$, $i = \pm 1, ..., \pm N_Z/2$, $j = 1, ..., N_\phi$: the $X$, $Y$ and $Z$ coordinates of the centre of the upstream face of the frame for the aerogel tiles in each sector. All the modules in a given sector have the same $Z_{r,i}$.

- $n_{X,i,j}$, $n_{Y,i,j}$, $n_{Z,i}$ , $i = \pm 1, ..., \pm N_Z/2$, $j = 1, ..., N_\phi$: the $X$, $Y$ and $Z$ direction cosines of the vector normal to the intersection points of the diagonals of the upstream face of the frames for both the aerogel tiles and the photodetector modules in each sector. All the modules in a given sector have the same $n_{Z,i}$.

- $T_{g,i}$, $i = \pm 1, ..., \pm N_Z/2$: the thickness of the expansion gap, i.e. the distance between the downstream face of the frame for the aerogel tiles and the upstream face of the frame for the corresponding photodetector modules in each sector.

## B.3 Intermediate variables

Intermediate variables are introduced to simplify the notation. They are

- $R_{r,i}$ and $R_{p,i}$, $i = \pm 1, ..., \pm N_Z/2$: the radial coordinates of the centres of the upstream face of the frame for both the aerogel tiles and the photodetector modules in each sector in the plane defined by the intersection point of the diagonals of the upstream face of the aerogel tiles and the $Z$ axis.

- $\tan^{-1}(m_i)$, $i = \pm 1, ..., \pm N_Z/2$: the angle formed by the normal to the photodetector and aerogel frames and the positive and the line $Z = 0$ in the plane defined by the intersection point of the diagonals of the upstream face of the aerogel tiles and the $Z$ axis in each sector. It takes values in $[0, \pi/2]$ for sectors in the region $Z > 0$, and in $[-\pi/2, 0]$ for those in the region $Z < 0$.

- $\tan^{-1}(t_i)$, $i = \pm 1, ..., \pm N_Z/2$: the angle formed by the line joining the points at largest Z of the photodetector and aerogel frames, also passing from the nominal interaction point as a design requirement, and the line $Z = 0$ in the plane defined by the intersection point of the diagonals of the upstream face of the aerogel tiles and the $Z$ axis in each sector. It takes values in $[0, \pi/2]$ for sectors with the points at largest $Z$ in the region $Z > 0$, and in $[-\pi/2, 0]$ for those with the points at largest $Z$ in the region $Z < 0$.

- $\tan^{-1}(s_i)$, $i = \pm 1, ..., \pm N_Z/2$: the angle formed by the line joining the points at smallest $Z$ of the photodetector and aerogel frames, also passing from the nominal interaction point as a design requirement, and the line $Z = 0$ in the plane defined by the intersection point of the diagonals of the upstream face of the aerogel tiles and the $Z$ axis in each sector. It takes values in $[0, \pi/2]$ for sectors with the points at largest $Z$ in the region $Z > 0$, and in $[-\pi/2, 0]$ for those with the points at largest $Z$ in the region $Z < 0$.

- $\Delta\phi$: the angle subtended by the edges corresponding to the long and short bases of the trapezoidal section of the photodetector and aerogel frames at the interaction point in the transverse $XY$ plane for all modules of all sectors.

- $R_{r,i,\min}$, $R_{r,i,\max}$, $i = \pm 1, ..., \pm N_Z/2$: the minimum and maximum radial coordinates of the upstream faces of the frames for the aerogel tiles in the plane defined by the intersection point of the diagonals of the upstream face of the aerogel tiles and the $Z$ axis in each sector.

- $R_{p,i,\min}$, $R_{p,i,\max}$, $i = \pm 1, ..., \pm N_Z/2$: the minimum and maximum radial coordinates of the upstream faces of the frames for the photodetector modules in the plane defined by the intersection point of the diagonals of the upstream face of the aerogel tiles and the $Z$ axis in each sector.

- $L_{r,v}$: the distance along the $Z$ axis between the closest points of the upstream faces of the frames for the aerogel tiles of the modules with same $j = 1, ..., N_\phi$ in the sectors $i = -1$ and $i = +1$. It coincides with the distance along the $Z$ axis between the inner walls of the two cylindrical vessels housing the first half ($i = -N_Z/2, ..., -1$) and the second half ($i = 1, ..., N_Z/2$) of the sectors.

## B.4 Fundamental equations

The requirement that each module is positioned such that the line connecting the intersection points of the diagonals of the upstream face of the photodetector and aerogel frames passes through the nominal interaction point and is normal to both frames can be translated, for each sector $i = \pm 1, ..., \pm N_Z/2$, into the relations:

$$Z_{p,i} = m_i R_{p,i}. \tag{B.1}$$

$$Z_{r,i} = m_i R_{r,i}, \tag{B.2}$$

The geometric constraints set by $R^{\text{up}}_{\min}$ and $R^{\text{up}}_{\max}$ with the requirement of maximizing the thickness of the expansion gap in each sector $i$ lead to the system of equations:

$$R^{\text{up}}_{\max} = R_{p,i} + \frac{L_{p,i}}{2} \sin\left(|\tan^{-1}(m_i)|\right) \tag{B.3}$$

$$R^{\text{up}}_{\min} = R_{r,i} - \frac{L_{r,i}}{2} \sin\left(|\tan^{-1}(m_i)|\right) \tag{B.4}$$

Combining B.3 and B.4, observing that, by construction,

$$\sin\left(|\tan^{-1}(m_i)|\right) = \frac{|Z_{r,i}|}{\sqrt{R^2_{r,i} + Z^2_{r,i}}} = \frac{|Z_{p,i}|}{\sqrt{R^2_{p,i} + Z^2_{p,i}}} = \frac{|m_i|}{\sqrt{1 + m_i^2}}, \tag{B.5}$$

and solving for $R_{p,i}$ and $R_{r,i}$ one obtains:

$$R_{p,i} = R^{\text{up}}_{\text{max}} - \frac{L_{p,i}}{2}\frac{|m_i|}{\sqrt{1+m_i^2}} \tag{B.6}$$

$$R_{r,i} = R^{\text{up}}_{\text{min}} + \frac{L_{r,i}}{2}\frac{|m_i|}{\sqrt{1+m_i^2}} \tag{B.7}$$

The design requirement that the upstream faces of the photodetector and aerogel frames of each module in each sector subtend the same solid angle at the nominal interaction point sets constraints on $L_{r,i}$, $B_{r,i}$, $b_{r,i}$, $B_{p,i}$ and $b_{p,i}$. The following equation is obtained in the plane defined by the intersection point of the diagonals of the upstream face of the aerogel tiles and the $Z$ axis in each sector.

$$\tan^{-1}\left(\frac{L_{p,i}}{2\sqrt{R_{p,i}^2+Z_{p,i}^2}}\right) = \tan^{-1}\left(\frac{L_{r,i}}{2\sqrt{R_{r,i}^2+Z_{r,i}^2}}\right). \tag{B.8}$$

Using Eqs. B.2 and B.1 to express $Z_{p,i}$ and $Z_{r,i}$ as a function of $R_{p,i}$ and $R_{r,i}$, and using Eqs. B.6 and B.7 for $R_{p,i}$ and $R_{r,i}$, and solving for $L_{r,i}$ one obtains:

$$L_{r,i} = \frac{\sqrt{1+m_i^2}R^{\text{up}}_{\text{min}}L_{p,i}}{\sqrt{1+m_i^2}R^{\text{up}}_{\text{max}} - |m_i|L_{p,i}} \tag{B.9}$$

In addition, the lengths of the long and the short bases of the trapezoidal section of the frames for the photodetector and the aerogel tiles of each module are constrained requiring that the corresponding edges subtend in the transverse $XY$ plane the maximum possible angle $\Delta\phi$ at the interaction point given by:

$$\Delta\phi = \frac{2\pi}{N_\phi}. \tag{B.10}$$

The values of $B_{r,i}$, $b_{r,i}$, $B_{p,i}$, $b_{p,i}$ are then obtained as the side lengths of regular polygons with $N_\phi$ sides circumscribed around circumferences with radii $R_{p,i,\text{min}}$, $R_{p,i,\text{max}}$, $R_{r,i,\text{min}}$, $R_{r,i,\text{max}}$ given by:

$$R_{r,i,\text{min}} = R^{\text{up}}_{\text{min}}, \tag{B.11}$$

$$R_{r,i,\text{max}} = R^{\text{up}}_{\text{min}} + L_{r,i}\frac{|m_i|}{\sqrt{1+m_i^2}}, \tag{B.12}$$

$$R_{p,i,\text{min}} = R^{\text{up}}_{\text{max}} - L_{p,i}\frac{|m_i|}{\sqrt{1+m_i^2}}, \tag{B.13}$$

$$R_{r,i,\max} = R^{\text{up}}_{\max}, \tag{B.14}$$

resulting in:

$$b_{r,i} = 2R_{r,i,\min} \tan\left(\frac{\Delta\phi}{2}\right) \tag{B.15}$$

$$B_{r,i} = 2R_{r,i,\max} \tan\left(\frac{\Delta\phi}{2}\right) \tag{B.16}$$

$$b_{p,i} = 2R_{p,i,\min} \tan\left(\frac{\Delta\phi}{2}\right) \tag{B.17}$$

$$B_{p,i} = 2R_{p,i,\max} \tan\left(\frac{\Delta\phi}{2}\right) \tag{B.18}$$

The values of $Z_{r,i}$ and $Z_{p,i}$ are provided by Eqs. B.2 and B.1, while the values of $X_{r,i,j}$, $Y_{r,i,j}$, $X_{p,i,j}$ and $Y_{r,i,j}$, with $j = 1, ..., N_\phi$, are determined by:

$$X_{r,i,j} = R_{r,i} \cos(j\Delta\phi) \tag{B.19}$$

$$Y_{r,i,j} = R_{r,i} \sin(j\Delta\phi) \tag{B.20}$$

$$X_{p,i,j} = R_{p,i} \cos(j\Delta\phi) \tag{B.21}$$

$$Y_{p,i,j} = R_{p,i} \sin(j\Delta\phi) \tag{B.22}$$

By construction, the vectors $(X_{r,i,j}, Y_{r,i,j}, Z_{r,i})$, or equivalently $(X_{p,i,j}, Y_{p,i,j}, Z_{p,i})$ are normal to the intersection points of the diagonals of the upstream face of the frames for the aerogel tiles and the photodetector modules. By normalizing to unity, the values of $n_{X,i,j}$, $n_{Y,i,j}$ and $n_{Z,i}$ are given by:

$$n_{X,i,j} = \frac{\cos(j\Delta\phi)}{\sqrt{1+m_i^2}}, \tag{B.23}$$

$$n_{Y,i,j} = \frac{\sin(j\Delta\phi)}{\sqrt{1+m_i^2}}, \tag{B.24}$$

$$n_{Z,i} = \frac{m_i}{\sqrt{1+m_i^2}}. \tag{B.25}$$

The value of $T_{g,i}$ in each sector is obtained by definition as:

$$T_{g,i} = \sqrt{(R_{p,i} - R_{r,i})^2 + (Z_{p,i} - Z_{r,i})^2} - T_{r,i} \tag{B.26}$$

Using Eqs. B.2 and B.1 to express $Z_{p,i}$ and $Z_{r,i}$ as a function of $R_{p,i}$ and $R_{r,i}$, and

expressing $R_{p,i}$ and $R_{r,i}$ with Eqs. B.6 and B.7, one obtains:

$$T_{g,i} = \sqrt{1+m_i^2}(R_{\max}^{\text{up}} - R_{\min}^{\text{up}}) - \frac{|m_i|}{2}(L_{p,i} + L_{r,i}) - T_{r,i} \tag{B.27}$$

The values of $\tan^{-1}(t_i)$ and $\tan^{-1}(s_i)$ in each sector $i$ are related to the corresponding value of $\tan^{-1}(m_i)$ by the relations:

$$\tan^{-1}(t_i) = \tan^{-1}(m_i) + \tan^{-1}\left(\frac{L_{p,i}/2}{\sqrt{R_{p,i}^2 + Z_{p,i}^2}}\right), \tag{B.28}$$

$$\tan^{-1}(s_i) = \tan^{-1}(m_i) - \tan^{-1}\left(\frac{L_{p,i}/2}{\sqrt{R_{p,i}^2 + Z_{p,i}^2}}\right). \tag{B.29}$$

Using Eq. B.1 to express $Z_{p,i}$ as a function of $R_{p,i}$ and using Eq. B.6 for $R_{p,i}$, Eqs. B.28 and B.29 can be written in the form:

$$\tan^{-1}(t_i) = \tan^{-1}(m_i) + \tan^{-1}\left(\frac{L_{p,i}}{2R_{\max}^{\text{up}}\sqrt{1+m_i^2} - L_{p,i}|m_i|}\right), \tag{B.30}$$

$$\tan^{-1}(s_i) = \tan^{-1}(m_i) - \tan^{-1}\left(\frac{L_{p,i}}{2R_{\max}^{\text{up}}\sqrt{1+m_i^2} - L_{p,i}|m_i|}\right). \tag{B.31}$$

All previous equations are univocally solved assuming $m_i$ to be known. An iterative procedure can be defined to iteratively constrain $m_i$ starting from the central sectors with the smallest $|Z_{p,i}|$ to the ones with the largest $|Z_{p,i}|$. A seed is required as a starting point for the positioning of all sectors. It is obtained by treating the gap between the sectors with $i = -1$ and $i = +1$ as an extra fictitious sector with $i = 0$, $L_{p,0} = L_{p,v}$, $\tan^{-1}(m_0) = 0$, and $\tan^{-1}(t_0)$ and $\tan^{-1}(s_0)$ calculated using Eqs. B.30 and B.31, respectively.

In the plane defined by the intersection point of the diagonals of the upstream face of the aerogel tiles and the $Z$ axis in each sector, the requirement that the geometries of the photodetector and aerogel frames provide maximum acceptance for the charged particles originating from the nominal interaction point is fulfilled requiring:

$$\tan^{-1}(s_i) = \tan^{-1}(t_{i-1}) \quad \text{for} \quad i = +1, ..., +N_Z/2 \tag{B.32}$$

$$\tan^{-1}(t_i) = \tan^{-1}(s_{i+1}) \quad \text{for} \quad i = -1, ..., -N_Z/2 \tag{B.33}$$

Supposing $\tan^{-1}(t_{i-1})$ and $\tan^{-1}(s_{i+1})$ to be known, expressing $\tan^{-1}(s_i)$ and $\tan^{-1}(t_i)$

using Eqs. B.31 and B.30, setting $b_i = 2R^{\text{up}}_{\text{max}}/L_{p,i}$ and solving for $m_i$ taking into account the correct development of $|m_i|$ one obtains:

$$m_i = \frac{\sqrt{b_i^2(t_{i-1}^2+1)-1} + t_{i-1}\, b_i^2}{b_i^2 - 1} \quad \text{for} \quad i = +1, ..., +N_Z/2 \tag{B.34}$$

$$m_i = \frac{s_{i+1}\, b_i^2 - \sqrt{b_i^2(s_{i+1}^2+1)-1}}{b_i^2 - 1} \quad \text{for} \quad i = -1, ..., -N_Z/2 \tag{B.35}$$

Due to the symmetry of the system, by construction, it can be noted that:

$$m_i = -m_{-i} \quad \text{for} \quad i = \pm 1, ..., \pm N_Z/2 \tag{B.36}$$

$$t_i = -s_{-i} \quad \text{for} \quad i = \pm 1, ..., \pm N_Z/2 \tag{B.37}$$

$$s_i = -t_{-i} \quad \text{for} \quad i = \pm 1, ..., \pm N_Z/2 \tag{B.38}$$

## B.5 Algorithm implementation

The specifications of the target projective geometry are obtained through an iterative procedure consisting of the following steps.

1. Treating the gap between the sectors with $i = -1$ and $i = +1$ as an extra fictitious sector with $i = 0$, $\tan^{-1}(m_0) = 0$ and $L_{p,0} = L_{p,v}$, compute the corresponding $\tan^{-1}(t_0)$ and $\tan^{-1}(s_0)$ calculated using Eqs. B.30 and B.31, respectively.

2. For each sector $i = \pm 1, ..., \pm N_Z/2$, compute the corresponding $m_i$ via Eqs. B.34 and B.35 starting from $\tan^{-1}(t_0)$ or $\tan^{-1}(s_0)$ and using the input lengths $L_{p,i}$.

3. Use the $m_i$ values to calculate the radial coordinates $R_{p,i}$ and $R_{r,i}$, as well as the radiator lengths $L_{r,i}$, via Eqs. B.6, B.7 and B.9, respectively.

4. Calculate $\Delta\Phi$ via Eq. B.10 and use the values of $L_{r,i}$ to extract the corresponding $b_{r,i}$, $B_{r,i}$, $p_{p,i}$ and $B_{p,i}$ via Eqs. B.15, B.16, B.17 and B.18, respectively.

5. Calculate the photodetector coordinates $X_{p,i,j}$, $Y_{p,i,j}$ and $Z_{p,i}$ via Eqs. B.21, B.22 and B.1, the radiator coordinates $X_{r,i,j}$, $Y_{r,i,j}$ and $Z_{r,i}$ via Eqs. B.19, B.20 and B.2, and the direction cosines of the sector normals $n_{X,i,j}$, $n_{Y,i,j}$ and $n_{Z,i}$ via Eqs. B.23, B.24 and B.25.

6. Finally, calculate the thickness of the expansion gaps $T_{g,i}$ via Eq. B.27.

**Special case: odd $N_Z$**

The algorithm illustrated here refers to the case of even $N_Z$, as planned according to the latest bRICH specifications, which include two independent vessels symmetric with respect to the plane $Z = 0$. Initial studies were performed considering the possibility of a single vessel and an odd $N_Z$, with a central sector featuring modules centered on the plane $Z = 0$ and aligned with the $Z$-axis. The proposed algorithm naturally extends to the odd $N_Z$ case by using this central sector with $i = 0$, $\tan^{-1}(m_0) = 0$, and the desired $L_{p,0}$ and $T_{r,0}$, as a seed for positioning the other sectors in step 1. The corresponding module shape and position parameters are then calculated by following steps 2–6, as for the other sectors. The sectors are then labelled with $i = 0, \pm1, ..., \pm(N_Z - 1)/2$.

## B.6 The baseline bRICH geometry

Through dedicated design optimization studies, I found the parameters in Table B.1.

| **Input** | $N_Z$ | $N_\phi$ | $R^{\text{up}}_{\text{min}}$ | $R^{\text{up}}_{\text{max}}$ | $L_{p,i}$ | $T_{r,i}$ | $L_{p,v}$ |
|---|---|---|---|---|---|---|---|
| **Value** | 24 | 36 | 90.0 cm | 117.0 cm | 18.4 cm | 2.0 cm | 1.0 cm |

**Table B.1:** Values of the input parameters defining the baseline projective bRICH geometry.

These choices are guided by physics- and integration-driven criteria. In particular, $N_Z = 24$, $N_\phi = 36$, and $L_{p,i} = 18.4$ cm result in sector and module dimensions comparable to the expected Cherenkov ring size for charged particles at saturation. The aerogel thickness, $T_{r,i} = 2.0$ cm for all sectors, is set by the required number of detected photons per ring, balancing yield against Rayleigh scattering. The values of $R^{\text{up}}_{\text{min}}$ and $R^{\text{up}}_{\text{max}}$ come from the radial constraints imposed by the space allocated to the bRICH vessel, ensuring compatibility with the other ALICE 3 subsystems. This corresponds to a minimum radius of 90 cm and a maximum radius of 120 cm, the latter also accounting for the thickness of the SiPM electronics. Furthermore, due to the segmentation of the layout, the set of points on the upstream faces of all the frames for the aerogel tiles and the photodetector modules in a given sector at fixed $Z$ can be visualized as polygons circumscribing circles with radii exceeding $R^{\text{up}}_{\text{min}}$ and $R^{\text{up}}_{\text{max}}$, respectively, by about 5 mm. Therefore, the value of $R^{\text{up}}_{\text{min}}$ is naturally set to 90 cm. Conversely, $R^{\text{up}}_{\text{max}}$ is set to 117 cm to account for the target 2 cm thickness of the photodetector module, as well as the maximum radial extension introduced by the segmentation into modules. Extra space inside $R^{\text{up}}_{\text{min}}$ and beyond $R^{\text{up}}_{\text{max}}$ must be reserved for the thermal shielding, whose design is still under development. Finally, a gap of $L_{p,v} = 1.0$ cm at $Z = 0$ is considered between the two vessels.

# Appendix C

# Alignment, tracking and angle reconstruction in beam tests

For Cherenkov angle reconstruction with beam test measurements, I implemented a Cherenkov angle reconstruction algorithm based on the one used for the simulation studies discussed in Section 4.3.1. The reconstruction requires the photon hit point on the SiPM arrays, the most probable emission point in the aerogel tile and the track direction at that point. This appendix summarizes the steps performed for the alignment, charged-particle tracking to the most probable emission point in the aerogel tile and the final single hit angle reconstruction. In the following, I assume a reference system with the positive Z-axis along the beam direction and the X and Y axes in the plane transverse to the beam.

## C.1 Track clusters in central and tracker arrays

To track the impinging charged particles, I searched for clusters in the central SiPM arrays and in the tracker modules. In the approximation of negligible mean tilt of the beam with respect to the central arrays and the tracker modules, the charged-particle Z coordinates at the central and the tracker module arrays were taken as the nominal position of the detectors along the beam line. The corresponding local X-Y coordinates were assumed according to the positions of the fired SiPM clusters.

I implemented a simple cluster finding algorithm based on the following three steps

1. **Seeding.** The cluster seed in each array was taken as the pixel with the maximum number of photoelectrons, i.e. largest ADC count and ToT for the arrays

read out with the Petiroc boards and with the RadioPico boards, respectively.

2. **Clustering.** All fired SiPM cells that were nearest neighbours to the cluster seed and to other cluster cells were iteratively associated to the cluster.

3. **Positioning.** The cluster X-Y coordinates, ($X_{\mathrm{clu}}$, $Y_{\mathrm{clu}}$), were finally calculated by averaging the nominal X-Y coordinates of the centroids of the $N_{\mathrm{clu}}$ channels in the cluster, each weighted with the number of photoelectrons $N_{\mathrm{pe}}$:

$$X_{\mathrm{clu}} = \frac{\sum_{i=1}^{N_{\mathrm{clu}}} N_{\mathrm{pe},i}\, X_i}{\sum_{i=1}^{N_{\mathrm{clu}}} N_{\mathrm{pe},i}}, \qquad Y_{\mathrm{clu}} = \frac{\sum_{i=1}^{N_{\mathrm{clu}}} N_{\mathrm{pe},i}\, Y_i}{\sum_{i=1}^{N_{\mathrm{clu}}} N_{\mathrm{pe},i}}. \tag{C.1}$$

## C.2 Alignment of arrays and tracker modules

To map the local X-Y coordinates of each array into a common global frame, I implemented a dedicated alignment procedure. Specifically, I registered the X-Y systems of all arrays mounted along the beam line, including those reading the tracker modules, to the coordinate system of the SiPM array mounted at the centre of the main vessel's copper plate. Because this reference array was rigidly coupled to the SiPM arrays used to detect Cherenkov photons from the aerogel tile, the local-to-global conversion for those arrays reduced to applying the fixed, known geometric offsets with respect to the central array. As a first approximation, I assumed a negligible average relative tilt of the beam with respect to the central arrays and the tracker modules.

My alignment procedure consisted of the following three steps:

1. **Offset initialization.** For each central array and tracker module, the relative offsets ($\Delta X, \Delta Y$) with respect to the reference array were initialized to $(0, 0)$.

2. **Coarse alignment.** For each selected event, I populated the distributions

$$\Delta X_i = X_i - X_{\mathrm{ref}} - \Delta X_{i,\mathrm{curr}} \ , \qquad \Delta Y_i = Y_i - Y_{\mathrm{ref}} - \Delta Y_{i,\mathrm{curr}} \tag{C.2}$$

where $i$ labels the considered array or tracker module, ($X_i$, $Y_i$) labels its local coordinates, and curr denotes the current offset estimate. Gaussian fits to these distributions provided means ($\mu_{X,i}$ , $\mu_{Y,i}$), which I used to update the offsets:

$$\Delta X_{i,\mathrm{new}} = \Delta X_{i,\mathrm{curr}} + \mu_{X,i} \ , \qquad \Delta Y_{i,\mathrm{new}} = \Delta Y_{i,\mathrm{curr}} + \mu_{Y,i}. \tag{C.3}$$

I iterated this step five times per array. At each new iteration, the current $\Delta X_{i,\mathrm{new}}$ and $\Delta Y_{i,\mathrm{new}}$ become the new $\Delta X_{i,\mathrm{curr}}$ and $\Delta Y_{i,\mathrm{curr}}$.

3. **Fine alignment.** Using the updated offsets, I performed straight-line fits event-by-event to $X(Z)$ and $Y(Z)$ in the X-Z and Y-Z planes, as discussed in Section C.5, using the cluster positions in the central arrays and the tracker modules. I then built the residual distributions with respect to the best-fit lines:

$$\Delta X_i = X_i - X(Z_i) - \Delta X_{i,\mathrm{curr}} \ , \qquad \Delta Y_i = Y_i - Y(Z_i) - \Delta Y_{i,\mathrm{curr}} \tag{C.4}$$

and updated the offsets of all arrays (except the reference one, which was kept fixed during this step) by adding the Gaussian–fit means ($\mu_{X,i}$ , $\mu_{Y,i}$) obtained by fitting the X and Y residual distributions to the offsets using Eq. C.3. I iterated this step five times per array. At each new iteration, the current $\Delta X_{i,\mathrm{new}}$ and $\Delta Y_{i,\mathrm{new}}$ become the new $\Delta X_{i,\mathrm{curr}}$ and $\Delta Y_{i,\mathrm{curr}}$.

The global coordinates ($X_{i,\mathrm{glob}}$ , $Y_{i,\mathrm{glob}}$) used for the final analysis were finally taken as the local cluster coordinates ($X_{i,\mathrm{loc}}$, $Y_{i,\mathrm{loc}}$ ) corrected by the final offsets ($\Delta X_i$, $\Delta Y_i$):

$$X_{i,\mathrm{glob}} = X_{i,\mathrm{loc}} - \Delta X_i \ , \qquad Y_{i,\mathrm{glob}} = Y_{i,\mathrm{loc}} - \Delta Y_i. \tag{C.5}$$

## C.3 Candidate Cherenkov photon hits

All detected hits in the arrays covering the ring were assumed as due to candidate Cherenkov photons produced by the considered charged track. The Z coordinates of the detected hits, $Z_{\mathrm{hit}}$, were assumed as the nominal Z coordinates of the surface of the arrays covering the ring region. The corresponding X-Y coordinates ($X_{\mathrm{hit}}$, $Y_{\mathrm{hit}}$) were assumed at the nominal positions of the fired channel centroids.

## C.4 Most probable emission depth in the aerogel tile

For the determination of the Cherenkov angle, the extrapolation of the most probable emission point and the track direction at that point is required. They both rely on the evaluation of the most probable emission depth in the aerogel tile.

I calculated this most probable emission depth for the tested tiles by implementing a dedicated Monte Carlo simulation accounting for the uniform emission point along the particle path length in the radiator, the wavelength dependent Cherenkov emission spectrum, given by Frank-Tamm equation (Eq. 2.7), the measured transmission length at the centre of the tested samples, and the nominal PDE curve of the SiPM arrays covering the aerogel ring. Fig. C.1 shows my simulated emission depth spectrum of

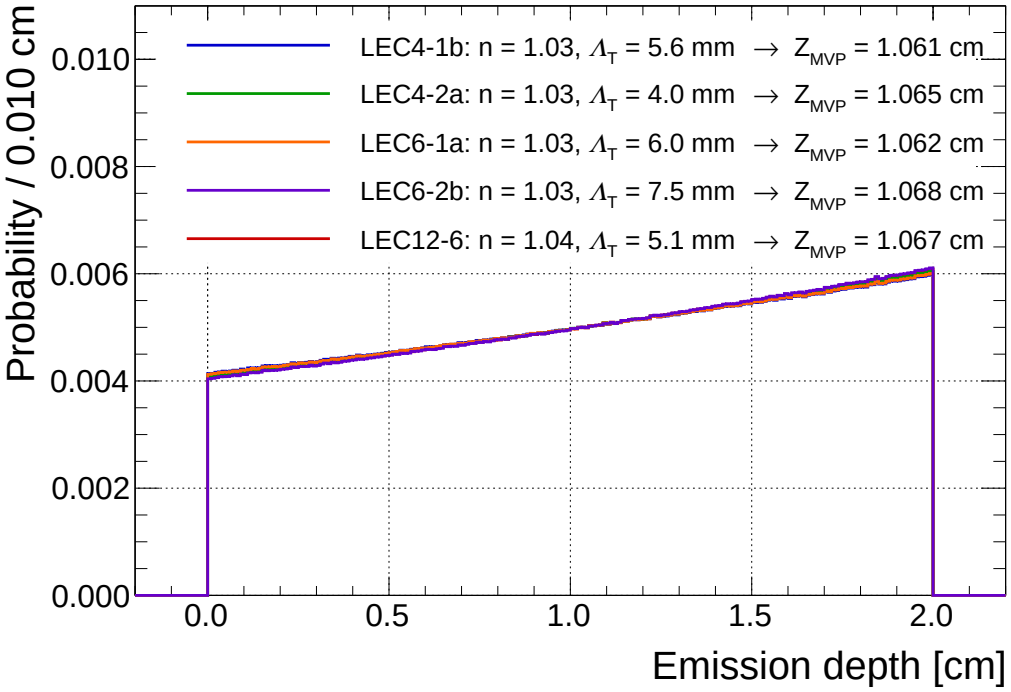


**Figure C.1:** Simulated emission depth spectrum of unscattered detected photons for various tested aerogel tiles assuming the PDE of Hamamatsu S13361-2050AE-08 SiPM arrays.

unscattered detected photons for various tested aerogel tiles assuming the PDE of S13361-2050AE-08 SiPM arrays. I extracted the most probable emission depths as the mean of the corresponding distributions. As expected, the extrapolated depths exceed the 1 cm depth of the median plane of the tile by about 600-700 µm.

## C.5 Emission point and the track direction

For Cherenkov angle reconstruction, I assumed as the Z coordinate of the photon emission point, $Z_{\mathrm{em}}$, the nominal Z coordinate of the position corresponding to the most probable emission depth of unscattered detected photons in the considered aerogel tiles. I extrapolated the corresponding X-Y coordinates ($X_{\mathrm{em}}$, $Y_{\mathrm{em}}$) and track direction cosines ($c_{\mathrm{x}}$, $c_{\mathrm{y}}$, $c_{\mathrm{z}}$) from the track cluster positions in the central arrays and the tracker modules as follows.

For each selected track, from the available points, I performed a least-squares straight line fit to extract the track parameters. In particular, I fitted the positions of the

clusters in the X-Z and Y-Z views with the following two equations:

$$\mathrm{X} = a_\mathrm{x}\mathrm{Z} + b_\mathrm{x} \qquad \mathrm{Y} = a_\mathrm{y}\mathrm{Z} + b_\mathrm{y} \tag{C.6}$$

where $a_\mathrm{x}$ and $a_\mathrm{y}$ are the slopes of the track in the X-Z and Y-Z projection planes, respectively, and $b_x$ and $b_y$ are the corresponding intercepts.

The general equation for a straight track is given by the three parametric equations:

$$\mathrm{X} = \mathrm{X}_0 + c_\mathrm{x}\, t \qquad \mathrm{Y} = \mathrm{Y}_0 + c_\mathrm{y}\, t \qquad \mathrm{Z} = \mathrm{Z}_0 + c_\mathrm{z}\, t \tag{C.7}$$

where $t$ is a parameter describing the position along the track with respect to the reference point ($\mathrm{X}_0$, $\mathrm{Y}_0$, $\mathrm{Z}_0$) and $c_\mathrm{x}$, $c_\mathrm{y}$, $c_\mathrm{z}$ are the direction cosines, satisfying:

$$c_\mathrm{x}^2 + c_\mathrm{y}^2 + c_\mathrm{z}^2 = 1\ . \tag{C.8}$$

Choosing the reference point on the plane $Z = 0$, corresponding to the copper plate with the SiPM arrays aimed at detecting Cherenkov photons from the aerogel in the vessel, it follows that:

$$Z_0 = 0, \qquad X_0 = b_x, \qquad Y_0 = b_y. \tag{C.9}$$

Assuming the beam particles to be directed along the positive z-axis in the considered reference frame, the direction cosines can then be evaluated from the slopes of the projected track in the X-Z and Y-Z planes as:

$$c_\mathrm{z} = \frac{1}{\sqrt{1 + a_\mathrm{x}^2 + a_\mathrm{y}^2}}, \qquad c_\mathrm{x} = \frac{a_\mathrm{x}}{\sqrt{1 + a_\mathrm{x}^2 + a_\mathrm{y}^2}}, \qquad c_\mathrm{y} = \frac{a_\mathrm{y}}{\sqrt{1 + a_\mathrm{x}^2 + a_\mathrm{y}^2}} \tag{C.10}$$

Then, for each track, I extrapolated the X-Y position of the photon emission point, ($X_\mathrm{em}$ and $Y_\mathrm{em}$), at the most probable emission depth in the aerogel tile $Z_\mathrm{em}$, using Eq. C.6 with the $a_\mathrm{x}$, $a_\mathrm{y}$, $b_\mathrm{x}$ and $b_\mathrm{y}$ from the fits, and assumed the track direction given by the resulting direction cosines ($c_\mathrm{x}$, $c_\mathrm{y}$, $c_\mathrm{z}$) for the Cherenkov angle reconstruction.

Constraining the track direction with two tracking modules and the SiPM arrays along the beam line, the contribution of the tracking uncertainty on the Cherenkov angle resolution was expected to be smaller than 1 mrad for all tested prototypes.

## C.6 Cherenkov angle extrapolation

For each selected track and corresponding candidate photon hit, I used the hit coordinates ($X_{\mathrm{hit}}$, $Y_{\mathrm{hit}}$, $Z_{\mathrm{hit}}$), the extrapolated most probable photon emission point ($X_{\mathrm{em}}$, $Y_{\mathrm{em}}$, $Z_{\mathrm{em}}$) and the extrapolated track direction ($c_{\mathrm{x}}$, $c_{\mathrm{y}}$, $c_{\mathrm{z}}$) through the geometric back-propagation procedure discussed in Section 6.3. In addition, I supplied as inputs to the algorithm the measured thickness $T_{\mathrm{r}}$ and refractive index $n_{\mathrm{r}}$ of the tested aerogel tile, the nominal refractive index $n_{\mathrm{g}}$ of the vessel gas, Ar [160] or the tested $CO_2$ + $C_4F_{10}$ mixtures, and the measured thickness $T_g$ of the expansion gap.

# References


[1] ALICE Collaboration. Letter of intent for ALICE 3: A next generation heavy-ion experiment at the LHC. CERN-LHCC-2022-009, 2022. https://cds.cern.ch/record/2803563.

[2] ALICE Collaboration. Scoping document for the ALICE 3 detector. CERN-LHCC-2025-002, 2025. https://cds.cern.ch/record/2925455.

[3] HotQCD Collaboration. Equation of state in $(2+1)$-flavor QCD. Phys. Rev. D, 90(9):094503, 2014. https://doi.org/10.1103/PhysRevD.90.094503.

[4] C. Gale et al. Hydrodynamic Modeling of Heavy-Ion Collisions. International Journal of Modern Physics A, 28(11):1340011, 2013. https://doi.org/10.1142/S0217751X13400113.

[5] C. A. Ogilvie. Review of nuclear reactions at the AGS. Nuclear Physics A, 698(1-4):3–12, 2002. https://doi.org/10.1016/S0375-9474(01)01343-4.

[6] U. Heinz et al. Evidence for a New State of Matter: An Assessment of the Results from the CERN Lead Beam Programme, 2000. nucl-th/0002042.

[7] M. Harrison et al. RHIC project overview. Nucl. Instrum. Meth. A, 499(2):235–244, 2003. https://doi.org/10.1016/S0168-9002(02)01937-X.

[8] ALICE Collaboration. The ALICE experiment: a journey through QCD. Eur. Phys. J. C, 84(8):813, 2024. https://doi.org/10.1140/epjc/s10052-024-12935-y.

[9] D. J. Gross. The Color Glass Condensate. Annual Review of Nuclear and Particle Science, 60:463–489, 2010. https://doi.org/10.1146/annurev.nucl.010909.083629.

[10] A. H. Mueller. Toward equilibration in the early stages after a high-energy heavy ion collision. Nucl. Phys. B, 572:227–240, 2000. https://doi.org/10.1016/S0550-3213(99)00502-7.

[11] L. McLerran et al. Computing quark and gluon distribution functions for very large nuclei. Phys. Rev. D, 49:2233–2241, 1994. https://doi.org/10.1103/PhysRevD.49.2233.

[12] C. Gale. Photon Production in Hot and Dense Strongly Interacting Matter. Landolt-Börnstein, 23, 2010. https://doi.org/10.1007/978-3-642-01539-7_15.

[13] O. S. Brüning et al. LHC Design Report. CERN Yellow Reports: Monographs. CERN, Geneva, 2004. https://doi.org/10.5170/CERN-2004-003-V-1.

[14] E. Lopienska. The CERN accelerator complex, layout in 2022. Complexe des accélérateurs du CERN en janvier 2022. 2022. General Photo.

[15] M. Vretenar et al. Linac4 design report. CERN Yellow Reports: Monographs. CERN, Geneva, 2020. https://doi.org/10.23731/CYRM-2020-006.

[16] The Proton Synchrotron Booster. 2012. https://cds.cern.ch/record/1997372.

[17] E. Regenstreif. The CERN Proton Synchrotron. CERN Yellow Reports: Monographs. CERN, Geneva, 1962. https://doi.org/10.5170/CERN-1962-003.

[18] The Super Proton Synchrotron. 2012. https://cds.cern.ch/record/1997188.

[19] Z. Q. Xie. State of the art of ECR ion sources. 1997 Particle Accelerator Conference (Cat. No.97CH36167). Vancouver, Canada, 1997. https://doi.org/10.1109/PAC.1997.752725.

[20] N. Angert et al. CERN Heavy-Ion Facility design report. CERN Yellow Reports: Monographs. CERN, Geneva, 1993. https://doi.org/10.5170/CERN-1993-001.

[21] Michel Chanel. LEIR: the low energy ion ring at CERN. Nucl. Instrum. Meth. A, 532(1):137-143, 2004. https://doi.org/10.1016/j.nima.2004.06.040.

[22] CMS Collaboration. CMS Physics: Technical Design Report Volume 1: Detector Performance and Software. Technical design report. CERN, Geneva, 2006. https://cds.cern.ch/record/922757.

[23] ATLAS Collaboration. Technical Design Report for the Phase-II Upgrade of the ATLAS TDAQ System. Technical report. CERN, Geneva, 2017. https://doi.org/10.17181/CERN.2LBB.4IAL.

[24] LHCb Collaboration. LHCb computing : Technical Design Report. Technical design report. CERN, Geneva, 2005. https://cds.cern.ch/record/835156.

[25] ALICE Collaboration. The ALICE experiment at the CERN LHC. Journal of Instrumentation, 3(08):S08002, 2008. https://doi.org/10.1088/1748-0221/3/08/S08002.

[26] ALICE Collaboration. Performance of the ALICE experiment at the CERN LHC. International Journal of Modern Physics A, 29(24):1430044, 2014. https://doi.org/10.1142/S0217751X14300440.

[27] Z. Citron et al. Future physics opportunities for high-density QCD at the LHC with heavy-ion and proton beams. CERN-LPCC-2018-07, 2018. https://cds.cern.ch/record/2650176.

[28] ALICE Collaboration. Technical Design report for the ALICE Inner Tracking System 3. Technical design report. CERN, Geneva, 2024. https://cds.cern.ch/record/2890181.

[29] ALICE Collaboration. Technical Design Report of the ALICE Forward Calorimeter (FoCal). Technical design report. CERN, Geneva, 2024. https://cds.cern.ch/record/2890281.

[30] P. M. Hohler et al. Is $\rho$-meson melting compatible with chiral restoration?. Physics Letters B, 731:103-109, 2014. https://doi.org/10.1016/j.physletb.2014.02.021.

[31] S. Ejiri et al. Hadronic fluctuations at the QCD phase transition. Phys. Lett. B, 633(2):275-282, 2006. https://doi.org/10.1016/j.physletb.2005.11.083.

[32] HotQCD Collaboration. Fluctuations and correlations of net baryon number, electric charge, and strangeness: A comparison of lattice QCD results with the hadron resonance gas model. Phys. Rev. D, 86(3):034509, 2012. https://doi.org/10.1103/PhysRevD.86.034509.

[33] LHCb Collaboration. Observation of an exotic narrow doubly charmed tetraquark. Nat. Phys., 18:751-754, 2022. https://doi.org/10.1038/s41567-022-01614-y.

[34] F. E. Low. Bremsstrahlung of Very Low-Energy Quanta in Elementary Particle Collisions. Phys. Rev., 110(4):974–977, 1958. https://doi.org/10.1103/PhysRev.110.974.

[35] CMS Collaboration. Observation of Long-Range Near-Side Angular Correlations in Proton-Proton Collisions at the LHC. JHEP, 09:091, 2010. https://doi.org/10.1007/JHEP09(2010)091.

[36] L. Yan et al. Universal Fluctuation-Driven Eccentricities in Proton-Proton, Proton-Nucleus, and Nucleus-Nucleus Collisions. Phys. Rev. Lett., 112(8):082301, 2014. https://doi.org/10.1103/PhysRevLett.112.082301.

[37] G. Aglieri Rinella et al. Characterization of analogue Monolithic Active Pixel Sensor test structures implemented in a 65 nm CMOS imaging process. Nucl. Instrum. Meth. A, 1069:169896, 2024. https://doi.org/10.1016/j.nima.2024.169896.

[38] X. Ai et al. A Common Tracking Software Project. Comput Softw Big Sci, 6(8), 2022. https://doi.org/10.1007/s41781-021-00078-8.

[39] F. Carnesecchi et al. Beam test results of 25 and 35 μm thick FBK ultra-fast silicon detectors. Eur. Phys. J. Plus, 138(99), 2023. https://doi.org/10.1140/epjp/s13360-022-03619-1.

[40] F. Carnesecchi et al. A new low gain avalanche diode concept: the double-LGAD. Eur. Phys. J. Plus, 138(990), 2023. https://doi.org/10.1140/epjp/s13360-023-04621-x.

[41] U. Follo et al. First results on monolithic CMOS detector with internal gain. 2024. https://arxiv.org/abs/2406.19906.

[42] S. Gundacker et al. The silicon-photomultiplier: fundamentals and applications of a modern solid-state photon detector. Physics in Medicine and Biology, 65(17):17TR01, 2020. https://doi.org/10.1088/1361-6560/ab7b2d.

[43] A.V. Lyashenko et al. HRPPD photosensors for RICH detectors with a high resolution timing capability. Nucl. Instrum. Meth. A, 1082:170964, 2025. https://doi.org/10.1016/j.nima.2025.170964.

[44] A. Andronic et al. The multiple-charm hierarchy in the statistical hadronization model. J. High Energ. Phys., 2021:35, 2021. https://doi.org/10.1007/JHEP07(2021)035.

[45] V. Vovchenko et al. Finite resonance widths influence the thermal-model description of hadron yields. Phys. Rev. C, 98(3):034906, 2018. https://doi.org/10.1103/PhysRevC.98.034906.

[46] Y. Kamiya et al. Femtoscopic study on $DD^*$ and $D\bar{D}^*$ interactions for $T_{cc}$ and $X(3872)$. Eur. Phys. J. A, 58:131, 2022. https://doi.org/10.1140/epja/s10050-022-00782-y.

[47] C. Lippmann. Particle identification. Nucl. Instrum. Meth. A, 666:148-172, 2012. https://doi.org/10.1016/j.nima.2011.03.009.

[48] E. Nappi et al. Ring imaging Cherenkov detectors: The state of the art and perspectives. Riv. Nuovo Cim., 28(8-9):1-130, 2005. https://doi.org/10.1393/ncr/i2006-10004-6.

[49] T. Ypsilantis et al. Theory of ring imaging Cherenkov counters. Nucl. Instrum. Meth. A, 343:30-51, 1994. https://doi.org/10.1016/0168-9002(94)90532-0.

[50] A. Di Mauro. A study of the angular resolution of the ALICE HMPID CsI-RICH detector. CERN-EP-2000-058, 2000. https://cds.cern.ch/record/436404.

[51] M. Tabata. Transparent Silica Aerogel Blocks for High-Energy Physics Research. Springer Handbook of Aerogels, 1333–1352, 2023. https://doi.org/10.1007/978-3-030-27322-4_51.

[52] A. Soleimani Dorcheh et al. Silica aerogel; synthesis, properties and characterization. Journal of Materials Processing Technology, 199(1):10-26, 2008. https://doi.org/10.1016/j.jmatprotec.2007.10.060.

[53] H.E. Jackson. The HERMES dual-radiator RICH detector. Nucl. Instrum. Meth. A, 502(1):36–40, 2003. https://doi.org/10.1016/S0168-9002(02)02154-X.

[54] The LHCb RICH Collaboration. Performance of the LHCb RICH detector at the LHC. Eur. Phys. J. C, 73(2431), 2013. https://doi.org/10.1140/epjc/s10052-013-2431-9.

[55] F. Giovacchini. Space application: The AMS RICH. Nucl. Instrum. Meth. A, 970:163657, 2020. https://doi.org/10.1016/j.nima.2020.163657.

[56] K. Uno. Operation and performance of the Belle II Aerogel RICH detector. Nucl. Instrum. Meth. A, 1056:168635, 2023. https://doi.org/10.1016/j.nima.2023.168635.

[57] M. Contalbrigo et al. The CLAS12 Ring Imaging Cherenkov detector. Nucl. Instrum. Meth. A, 964:163791, 2020. https://doi.org/10.1016/j.nima.2020.163791.

[58] D. Sharma et al. Performance of modular ring imaging Cherenkov detector for particle identification. Nucl. Instrum. Meth. A, 1061:169080, 2024. https://doi.org/10.1016/j.nima.2024.169080.

[59] S. Vallarino et al. Prototype of a dual-radiator RICH detector for the Electron–Ion Collider. Nucl. Instrum. Meth. A, 1058:168834, 2024. https://doi.org/10.1016/j.nima.2023.168834.

[60] I. Adachi et al. Study of a threshold Cherenkov counter based on silica aerogels with low refractive indices. Nucl. Instrum. Meth. A, 355:390-398, 1995. https://doi.org/10.1016/0168-9002(94)01119-2.

[61] M. Tabata et al. Hydrophobic silica aerogel production at KEK. Nucl. Instrum. Meth. A, 668:64-70, 2012. https://doi.org/10.1016/j.nima.2011.12.017.

[62] M. Tabata et al. Large-area silica aerogel for use as Cherenkov radiators with high refractive index, developed by supercritical carbon dioxide drying. The Journal of Supercritical Fluids, 110:183-192, 2016. https://doi.org/10.1016/j.supflu.2015.11.022.

[63] M. Tabata et al. Recent Progress in Silica Aerogel Cherenkov Radiator. Physics Procedia, 37:642-649, 2012. https://doi.org/10.1016/j.phpro.2012.02.410.

[64] M. Tabata et al. Development of silica aerogel with any density. IEEE Nuclear Science Symposium Conference Record, 816-818, 2005. https://doi.org/10.1109/NSSMIC.2005.1596380.

[65] A. V. Volotka et al. Rayleigh scattering of linearly polarized light: Scenario of the complete experiment. Phys. Rev. A, 102(4):042814, 2020. https://doi.org/10.1103/PhysRevA.102.042814.

[66] S. Chakraborti. Verification of the Rayleigh scattering cross section. American Journal of Physics, 75:824-826, 2007. https://doi.org/10.1119%2F1.2752825.

[67] E. Nappi. Aerogel and its applications to RICH detectors. Nuclear Physics B - Proceedings Supplements, 61(3), 1998. https://doi.org/10.1016/S0920-5632(97)00573-2.

[68] R. De Leo et al. Chromatic aberration and forward scattering of light in silica aerogel. Nucl. Instrum. Meth. A, 457:52-63, 2001. https://doi.org/10.1016/S0168-9002(00)00668-9.

[69] E. Aschenauer et al. Optical characterization of n=1.03 silica aerogel used as radiator in the RICH of HERMES. Nucl. Instrum. Meth. A, 440(2):338-347, 2000. https://doi.org/10.1016/S0168-9002(99)00923-7.

[70] L. Zhao et al. Modeling silica aerogel optical performance by determining its radiative properties. AIP Advances, 6:025123, 2016. https://doi.org/10.1063/1.4943215.

[71] I. Adachi. Status of high-quality silica aerogel radiators. Nucl. Instrum. Meth. A, 952:161919, 2020. https://doi.org/10.1016/j.nima.2019.02.046.

[72] F. Acerbi et al. Understanding and simulating SiPMs. Nucl. Instrum. Meth. A. 926:16-35, 2019. https://doi.org/10.1016/j.nima.2018.11.118.

[73] F. Acerbi et al. NUV Silicon Photomultipliers With High Detection Efficiency and Reduced Delayed Correlated-Noise. IEEE Transactions on Nuclear Science, 62(3):1318–1325, 2015. https://doi.org/10.1109/TNS.2015.2424676.

[74] P. Wang et al. Performance of NUV-HD Silicon Photomultiplier Technology. IEEE Transactions on Electron Devices. 63(3):1111–1116, 2016. https://doi.org/10.1109/TED.2016.2516641.

[75] Hamamatsu. MPPCs for precision measurements: Hamamatsu S13360 series. 2016. https://www.hamamatsu.com/content/dam/hamamatsu-photonics/sites/documents/99_SALES_LIBRARY/ssd/s13360_series_kapd1052e.pdf.

[76] A. Nepomuk Otte et al. Characterization of three high efficiency and blue sensitive silicon photomultipliers. Nucl. Instrum. Meth. A. 846:106-125, 2017. https://doi.org/10.1016/j.nima.2016.09.053.

[77] F. Acerbi et al. Cryogenic Characterization of FBK HD Near-UV Sensitive SiPMs. IEEE Transactions on Electron Devices, 64(2):521-526, 2017. https://doi.org/10.1109/TED.2016.2641586.

[78] A. L. Lacaita et al. On the bremsstrahlung origin of hot-carrier-induced photons in silicon devices. IEEE Transactions on Electron Devices, 40(3):577-582, 1993. https://doi.org/10.1109/16.199363.

[79] A. Nepomuk Otte et al. On the efficiency of photon emission during electrical breakdown in silicon. Nucl. Instrum. Meth. A, 610(1):105-109, 2009. https://doi.org/10.1016/j.nima.2009.05.085.

[80] F. Acerbi et al. Analysis of single-photon time resolution of FBK silicon photomultipliers. Nucl. Instrum. Meth. A, 787:34-37, 2015. https://doi.org/10.1016/j.nima.2014.10.057.

[81] M. Moll. Displacement Damage in Silicon Detectors for High Energy Physics. IEEE Transactions on Nuclear Science, 65(8):1561-1582, 2018. https://doi.org/10.1109/TNS.2018.2819506.

[82] G. Lindström. Radiation damage in silicon detectors. Nucl. Instrum. Meth. A, 512(1):30-43, 2003. https://doi.org/10.1016/S0168-9002(03)01874-6.

[83] L. Gonella. TID Tolerance of commercial 130nm CMOS Technologies for HEP experiments. Master's thesis, Torino, 2006. https://cds.cern.ch/record/2252791.

[84] M. Moll. Radiation damage in silicon particle detectors: Microscopic defects and macroscopic properties. PhD thesis, Hamburg, 1999. https://inspirehep.net/literature/513308.

[85] A. R. Altamura. Radiation damage of FBK Silicon Photomultipliers for HEP applications. PhD thesis, Udine, 2022. https://air.uniud.it/handle/11390/1230944.

[86] S. Krauss et al. Performance of the most recent Microchannel-Plate PMTs for the PANDA DIRC detectors at FAIR. Nucl. Instrum. Meth. A, 1057:168659, 2023. https://doi.org/10.1016/j.nima.2023.168659.

[87] A. V. Lyashenko et al. Performance of Large Area Picosecond Photo-Detectors (LAPPD$^{TM}$). Nucl. Instrum. Meth. A, 958:162834, 2020. https://doi.org/10.1016/j.nima.2019.162834.

[88] S. España et al. Performance evaluation of SiPM photodetectors for PET imaging in the presence of magnetic fields. Nucl. Instrum. Meth. A, 613(2):308-316, 2010. https://doi.org/10.1016/j.nima.2009.11.066.

[89] A. R. Altamura et al. Aerogel characterization for RICH applications. 9th International Workshop on Advances in Sensors and Interfaces, 211-216, 2023. https://doi.org/10.1109/IWASI58316.2023.10164359.

[90] Hamamatsu. MPPCs arrays in a chip size package miniaturized through the adoption of TSV structure. 2024. https://www.hamamatsu.com/content/dam/hamamatsu-photonics/sites/documents/99_SALES_LIBRARY/ssd/s13361-2050_series_kapd1055e.pdf.

[91] F. Cossio et al. ALCOR: A mixed-signal ASIC for the dRICH detector of the ePIC experiment at the EIC. Nucl. Instrum. Meth. A, 1069:169817, 2024. https://doi.org/10.1016/j.nima.2024.169817.

[92] P. Moreira et al. lpGBT: Low-Power Radiation-Hard Multipurpose High-Speed Transceiver ASIC for High-Energy Physics Experiments. IEEE Transactions on Nuclear Science, 72(1):24–37, 2025. https://doi.org/10.1109/TNS.2024.3506753.

[93] J. Troska et al. The VTRx+, an Optical Link Module for Data Transmission at HL-LHC. PoS(TWEPP-17)048, 2018. https://doi.org/10.22323/1.313.0048.

[94] O. A. de Aguiar Francisco et al. Microchannel cooling for the LHCb VELO Upgrade I. Nucl. Instrum. Meth. A, 1039:166874, 2022. https://doi.org/10.1016/j.nima.2022.166874.

[95] M. Calvi et al. Single photon detection with SiPMs irradiated up to $10^{14}$ $cm^{-2}$ 1 MeV equivalent neutron fluence. Nucl. Instrum. Meth. A, 922:243-249, 2019. https://doi.org/10.1016/j.nima.2019.01.013.

[96] G. D. Hallewell. The "green" use of fluorocarbons in Cherenkov detectors and silicon tracker cooling systems: challenges and opportunities in an unfolding era of alternatives. Eur. Phys. J. Plus, 138(1141), 2023. https://doi.org/10.1140/epjp/s13360-023-04703-w.

[97] A. Chachereau et al. Electrical insulation properties of the perfluoroketone $C_5F_{10}O$. Journal of Physics D: Applied Physics, 51(33):335204, 2018. https://doi.org/10.1088/1361-6463/aad174.

[98] G. Hallewell. A sonar-based technique for the ratiometric determination of binary gas mixtures. Nucl. Instr. Meth A, 264(2):219-234, 1988. https://doi.org/10.1016/0168-9002(88)90912-6.

[99] G. D. Hallewell. From the speed of sound to the speed of light: Ultrasonic Cherenkov refractometry. Nucl. Instr. Meth A, 876:50-53, 2017. https://doi.org/10.1016/j.nima.2017.01.014.

[100] F. Carnesecchi et al. Understanding the direct detection of charged particles with SiPMs. Eur. Phys. J. Plus, 138(337), 2023. https://doi.org/10.1140/epjp/s13360-023-03923-4.

[101] F. Carnesecchi et al. Measurements of the Cherenkov effect in direct detection of charged particles with SiPMs. Eur. Phys. J. Plus, 138(788), 2023. https://doi.org/10.1140/epjp/s13360-023-04397-0.

[102] R. Vinke et al. Optimizing the timing resolution of SiPM sensors for use in TOF-PET detectors. Nucl. Instrum. Meth. A, 610(1):188-191, 2009. https://doi.org/10.1016/j.nima.2009.05.068.

[103] F. Hénault et al. Design of light concentrators for Cherenkov telescope observatories. Nonimaging Optics: Efficient Design for Illumination and Solar Concentration X, 8834:883405, 2013. https://doi.org/10.1117/12.2024049.

[104] N. Vaidya et al. Immersion graded index optics: theory, design, and prototypes. Microsyst. Nanoeng., 8(69), 2022. https://doi.org/10.1038/s41378-022-00377-z.

[105] S. Agostinelli et al. Geant4—a simulation toolkit. Nucl. Instrum. Meth. A, 506:250-303, 2003. https://doi.org/10.1016/S0168-9002(03)01368-8.

[106] Fused silica refractive index. https://refractiveindex.info/?shelf=main&book=SiO2&page=Malitson.

[107] C. Bierlich et al. A comprehensive guide to the physics and usage of PYTHIA 8.3. SciPost Phys. Codebases, 2022. https://doi.org/10.21468/SciPostPhysCodeb.8.

[108] C. Bierlich et al. The Angantyr model for heavy-ion collisions in Pythia8. J. High Energ. Phys., 2018(134): 2018. https://doi.org/10.1007/JHEP10(2018)134.

[109] Geant4 General Particle Source. https://geant4.web.cern.ch/documentation/dev/bfad_html/ForApplicationDevelopers/GettingStarted/generalParticleSource.html.

[110] ALICE Collaboration. Centrality determination of Pb-Pb collisions at $\sqrt{s_{\mathrm{NN}}} = 2.76$ TeV with ALICE. Phys. Rev. C, 88(4):044909, 2013. https://doi.org/10.1103/PhysRevC.88.044909.

[111] E. Garutti et al. Simulation of the response of SiPMs; Part I: Without saturation effects. Nucl. Instrum. Meth. A, 1019:165853, 2021. https://doi.org/10.1016/j.nima.2021.165853.

[112] ALICE Collaboration. ALICE high-momentum particle identification: Technical Design Report. CERN, Geneva, 1998. https://cds.cern.ch/record/381431.

[113] J. Illingworth et al. A survey of the Hough transform. Computer Vision, Graphics, and Image Processing, 44(1):87-116, 1988. https://doi.org/10.1016/S0734-189X(88)80033-1.

[114] P. Mukhopadhyay et al. A survey of Hough Transform. Pattern Recognition, 48(3):993-1010, 2014. https://doi.org/10.1016/j.patcog.2014.08.027.

[115] ALICE Collaboration. Particle identification in ALICE: a Bayesian approach. Phys. J. Plus, 131(168), 2016. https://doi.org/10.1140/epjp/i2016-16168-5.

[116] J. Heaton. Applications of Deep Neural Networks with Keras. 2022. https://doi.org/10.48550/arXiv.2009.05673.

[117] G. Louppe. Understanding Random Forests: From Theory to Practice. 2015. https://doi.org/10.48550/arXiv.1407.7502.

[118] Y. Coadou. Boosted Decision Trees, Artificial Intelligence for High Energy Physics. 9-58, 2022. https://doi.org/10.1142/9789811234033_0002.

[119] T. Chen. XGBoost: A Scalable Tree Boosting System, Proceedings of the 22nd ACM SIGKDD International Conference on Knowledge Discovery and Data Mining. ACM, Aug. 2016. https://doi.org/10.1145/2939672.2939785.

[120] L. Snoj et al. A half-century of nuclear research, education and training: Story of the JSI TRIGA reactor. Annals of Nuclear Energy, 214:111122, 2025. https://doi.org/10.1016/j.anucene.2024.111122.

[121] Climats EXCAL 1423-HA climatic chamber.

[122] A. R. Altamura et al. Radiation damage on SiPMs for space applications. Nucl. Instrum. Meth. A, 1045:167488, 2023. https://doi.org/10.1016/j.nima.2022.167488.

[123] iseg SHR Series High Precision HV Source Measuring Unit. https://iseg-hv.com/en/products/detail/SHR.

[124] V. Chmill et al. Study of the breakdown voltage of SiPMs. Nucl. Instrum. Meth. A, 845:56-59, 2017. https://doi.org/10.1016/j.nima.2016.04.047.

[125] A. Bornheim et al. Integration of thermo-electric coolers into the CMS MTD SiPM arrays for operation under high neutron fluence. Journal of Instrumentation, 18(08):P08020, 2023. https://doi.org/10.1088/1748-0221/18/08/P08020.

[126] R. Preghenella et al. Study of radiation effects on SiPM for an optical readout system for the EIC dual-radiator RICH. Nucl. Instrum. Meth. A, 1056:168578, 2023. https://doi.org/10.1016/j.nima.2023.168578.

[127] J. Bernhard et al. CERN Proton Synchrotron East Area Facility: Upgrades and renovation during Long Shutdown 2. Tech. rep., CERN, Geneva, 2021. https://doi.org/10.23731/CYRM-2021-004.

[128] L. Gatignon. Design and Tuning of Secondary Beamlines in the CERN North and East Areas. CERN Document, 2020. https://doi.org/10.23731/CYRM-2021-004.

[129] M. van Dijk. Particle production and identification for the T10 secondary beamline of the CERN East Area. 2025. https://doi.org/10.48550/arXiv.2507.02567.

[130] N. Nicassio et al. A combined SiPM-based TOF+RICH detector for future high-energy physics experiments. 9th International Workshop on Advances in Sensors and Interfaces, 199-204, 2023. https://doi.org/10.1109/IWASI58316.2023.10164558.

[131] M. N. Mazziotta et al. Test beam performance of a novel RICH detector with timing capabilities for the future ALICE 3 PID system at LHC. Journal of Instrumentation, 20:C05038, 2025. https://doi.org/10.1088/1748-0221/20/05/C05038.

[132] R. Pillera et al. Beam test and performance assessment for the prototype of a novel compact RICH detector with timing capabilities for the future ALICE 3 PID system at HL-LHC. Nucl. Instrum. Meth. A, 1080:170708, 2025. https://doi.org/10.1016/j.nima.2025.170708.

[133] A. R. Altamura et al. Beam test studies for a SiPM-based RICH detector prototype for the future ALICE 3 experiment. Eur. Phys. J. C, 85(5):578, 2025. https://doi.org/10.1140/epjc/s10052-025-14287-7.

[134] PETIROC2A asic by OMEGA & weeroc. https://www.weeroc.com/read_out_chips/petiroc-2a/.

[135] T. Saleem et al. Study experimental time resolution limits of recent ASICs at Weeroc with different SiPMs and scintillators. Journal of Instrumentation, 18(10):P10005, 2023. https://doi.org/10.1088/1748-0221/18/10/P10005.

[136] S. Altruda et al. PicoTDC: a flexible 64 channel TDC with picosecond resolution. Journal of Instrumentation, 18(07):P07012, 2023. https://doi.org/10.1088/1748-0221/18/07/P07012.

[137] Agilent 900 External Diffuse Reflectance Accessory (DRA).

[138] Agilent Cary 4000 UV-Vis Spectrophotometer.

[139] A. R. Altamura et al. Silica aerogel characterization for the ePIC dRICH detector. PoS(ICHEP2024), 1116, 2025. https://doi.org/10.22323/1.476.1116.

[140] A.R. Buzykaev et al. Measurement of optical parameters of aerogel. Nucl. Instrum. Meth. A, 433(1):396-400, 1999. https://doi.org/10.1016/S0168-9002(99)00325-3.

[141] T. Bellunato et al. Refractive index dispersion law of silica aerogel. Eur. Phys. J. C, 52:759-764, 2007. https://doi.org/10.1140/epjc/s10052-007-0431-3.

[142] Thorlabs Compact Laser Modules, CPS405, CPS532, and CPS365.

[143] Hamamatsu SiPM array S13552. https://www.hamamatsu.com/eu/en/product/optical-sensors/mppc/mppc_mppc-array/S13552.html.

[144] OPTICAL CEMENT EJ-500, https://eljentechnology.com/products/accessories/ej-500.

[145] Huber Minichiller 600, https://www.huber-online.com/daisy_website_files/datenblaetter/en/3066.0024.01.PDF.

[146] TEWA TT4-10KC3-T125-M5-500. https://www.tme.eu/Document/6d2e1b5322209ea0890793c756dbc659/TT4-10KC3-T125-M5-500.pdf.

[147] ADS1115 16-Bit ADC - 4 Channel with Programmable Gain Amplifier - STEMMA QT / Qwiic. https://www.adafruit.com/product/1085.

[148] Adafruit Sensirion SHT31-D - Temperature & Humidity Sensor. https://www.adafruit.com/product/2857.

[149] M.N. Mazziotta et al. A light tracker based on scintillating fibers with SiPM readout. Nucl. Instrum. Meth. A, 1039:167040 2022. https://doi.org/10.1016/j.nima.2022.167040.

[150] R. Pillera et al. A compact, light scintillating fiber tracker with SiPM readout. Nucl. Instrum. Meth. A, 1048:167962. 2023. https://doi.org/10.1016/j.nima.2022.167962.

[151] Samtec LSHM-120-02.5-L-DV-A-N-K-TR Connector. https://www.samtec.com/products/lshm.

[152] Samtec HLCD-20-06.00-TR-TR-1. https://www.samtec.com/products/hlcd.

[153] DS18B20 1-Wire Digital Thermometer. https://www.maximintegrated.com/en/products/sensors/DS18B20.html.

[154] R. Pillera. Development of plastic scintillators with SiPM readout for satellite-borne astroparticle physics experiments. PhD thesis, Bari, 2024. https://inspirehep.net/literature/2837229.

[155] CAEN A7585D 1 Ch. 85 V/10 mA Digital Controlled SiPM Power Supply. https://www.caen.it/products/a7585/.

[156] AMD Kintex$^{TM}$ 7 FPGA Module. https://www.enclustra.com/en/products/fpga-modules/mercury-kx2.

[157] G. De Robertis et al. A MOdular System for Acquisition, Interface and Control (MOSAIC) of detectors and their related electronics for high energy physics experiment. EPJ Web Conf., 174:07002, 2018. https://doi.org/10.1051/epjconf/201817407002.

[158] CAEN DT5495 PLU, https://www.caen.it/products/dt5495.

[159] Skyworks Si5341-40 clock generator, https://www.skyworksinc.com/-/media/SkyWorks/SL/documents/public/data-sheets/si5341-40-d-datasheet.pdf.

[160] Ar $n$ vs $\lambda$. https://refractiveindex.info/?shelf=main&book=Ar&page=Larsen.

# Acknowledgements

Alla fine di questo percorso ci sono molte persone che desidero sinceramente ringraziare. Primi tra tutti i miei supervisori, tutto il gruppo ALICE 3 RICH, famiglia e amici.

Ringrazio Domenico, che mi ha fatto appassionare alla fisica fin dai tempi del liceo e che mi è stato vicino in questi tre anni, sempre pronto a mettermi alla prova e a farmi riflettere. Le sue domande, spesso spiazzanti ma sempre costruttive, mi hanno guidato verso le risposte migliori alle sfide che ho incontrato durante la mia attività di ricerca.

Un ringraziamento profondo va a Giacomo, che mi ha fatto innamorare di questo progetto, insegnato tantissime cose, seguito e guidato in ogni tappa di questo percorso non facendomi mai pesare il mio lavoro, consigliandomi e accompagnandomi in ogni scelta, e che mi ha permesso di raggiungere risultati e traguardi oltre ogni mia aspettativa.

Ringrazio Eugenio, la cui esperienza ha rappresentato un riferimento costante per lo sviluppo del mio lavoro. I suoi input e la capacità di porre sempre le domande giuste hanno affinato il mio modo di fare ricerca, dalle scelte sperimentali alla lettura critica dei dati, così come l'incoraggiamento a puntare sempre più in alto.

Un grazie sentito ad Antonello per le numerose discussioni sugli aspetti tecnici del mio progetto, che mi hanno insegnato ad avere una visione d'insieme del lavoro e ad affrontarne le sfide con maggiore consapevolezza. Grazie anche per continuare a supervisionare la mia attività durante il mio periodo come Simil Fellow al CERN.

Ringrazio Nicola per l'expertise trasmessa sull'hardware, sull'elettronica, sull'arte di condurre beam test, e per le continue discussioni che hanno arricchito la mia formazione. Insieme a lui, ringrazio il suo gruppo, Roberta, Nadia, Giuliana, Mario e Antonio, per aver reso possibile il successo delle campagne di misure fin dal 2022.

Un ringraziamento speciale va ai miei genitori e a mia sorella, che mi hanno sempre sostenuto in ogni scelta. Fin da piccolo mi hanno sempre incoraggiato a inseguire i miei sogni e le mie passioni non facendomi mai mancare nulla. La loro fiducia mi ha insegnato a credere in me stesso. Senza di loro, non sarei mai arrivato fin qui.

Ringrazio gli amici storici di Adelfia, Lorenzo, Vito, Pier, Roberto, Alessandro, Michele, Vito, Andrea, Jacopo, Daniele e tutti gli altri, per tutte le volte in cui mi avete aiutato a staccare dalla routine del lavoro, a uscire un po' e a ricaricare le energie.

Un pensiero va anche agli amici di Valenzano del liceo, Andrea, Giorgio e Iacopo, con cui, nonostante gli anni e la distanza, continuiamo a sentirci ogni tanto durante le pause dalla ricerca. È sempre un piacere ritrovarvi, anche solo per un momento.

Vorrei dedicare un ringraziamento speciale ad Alessia, una vera amica con cui ho condiviso ogni anno di università fin dal primo giorno della triennale. Sei per me un punto di riferimento. Nei momenti di difficoltà ci sei sempre stata e riesci sempre a strapparmi un sorriso. E, nonostante la distanza dopo l'inizio del dottorato, sono felice che continuiamo a sentirci quasi ogni giorno come se fossimo ancora compagni di banco. La tua amicizia è stata molto importante e mi ha dato forza in questo percorso.

Un ringraziamento davvero speciale lo dedico ad Anna Rita, la persona che più di tutte mi è stata vicina in questi tre anni. Con te ho condiviso tutto, dai periodi più intensi di lavoro a quelli più sereni. Mi hai insegnato che non esiste solo il lavoro nella vita, e che è importante fermarsi a respirare. Dispiace solo che te ne sia dovuta andare via così presto. Dovrei dedicarti un intero capitolo per dirti quanto tu sia stata importante per me, ma temo di aver finito le pagine. Mi limiterò a dirti che averti conosciuta e avuta come compagna di ufficio è stata una delle cose più belle che ricorderò di questi anni.

Ringrazio infine tutte le persone fantastiche che ho incontrato durante la mia permanenza come Simil Fellow al CERN, dai vecchi amici che ho avuto il piacere di rincontrare ai nuovi che ho avuto il piacere di conoscere. Un grazie particolare lo dedico a Noemi, Federico e Anna per la compagnia e le giornate trascorse insieme. La vostra presenza è stata preziosa, soprattutto nel periodo più delicato della stesura di questa tesi.

Grazie davvero a tutti.